Complexity

Chaos in Applied Sciences and Engineering 2021

Lead Guest Editor: Akif Akgul
Guest Editors: Jawad Ahmad, Mustafa Cagri Kutlu, Chunbiao Li, and Jesus Manuel Muñoz-Pacheco

Chaos in Applied Sciences and Engineering 2021

Complexity

Chaos in Applied Sciences and Engineering 2021

Lead Guest Editor: Akif Akgul
Guest Editors: Jawad Ahmad, Mustafa Cagri Kutlu, Chunbiao Li, and Jesus Manuel Muñoz-Pacheco

Contents

Contents

Hindawi
Complexity
Volume 2023, Article ID 9369888, 11 pages
https://doi.org/10.1155/2023/9369888

Research Article

Prediction for the Inventory Management Chaotic Complexity System Based on the Deep Neural Network Algorithm

Tengfei Lei,[1] **Rita Yi Man Li**,[2] **Nuttapong Jotikastira**,[1] **Haiyan Fu**,[3] **and Cong Wang**[3]

[1]*Rattanakosin International College of Creative Entrepreneurship, Rajamangala University of Technology Rattanakosin, Nakhon Pathom, Thailand*
[2]*Sustainable Real Estate Research Center, Department of Economics and Finance, Hong Kong Shue Yan University, North Point, Hong Kong*
[3]*Collaborative Innovation Center of Memristive Computing Application, Qilu Institute of Technology, Shandong, Jinan 250200, China*

Correspondence should be addressed to Haiyan Fu; fuhy413@126.com

Received 6 February 2022; Revised 15 July 2022; Accepted 12 September 2022; Published 12 May 2023

Academic Editor: Chun-Biao Li

Precise inventory prediction is the key to goods inventory and safety management. Accurate inventory prediction improves enterprises' production efficiency. It is also essential to control costs and optimize the supply chain's performance. Nevertheless, the complex inventory data are often chaotic and nonlinear; high data complexity raises the accuracy prediction difficulty. This study simulated inventory records by using the dynamics inventory management system. Four deep neural network models trained the data: short-term memory neural network (LSTM), convolutional neural network-long short-term memory (CNN-LSTM), bidirectional long short-term memory neural network (Bi-LSTM), and deep long-short-term memory neural network (DLSTM). Evaluating the models' performance based on RMSE, MSE, and MAE, bi-LSTM achieved the highest prediction accuracy with the least square error of 0.14%. The results concluded that the complexity of the model was not directly related to the prediction performance. By contrasting several methods of chaotic nonlinear inventory data and neural network dynamics prediction, this study contributed to the academia. The research results provided useful advice for companies' planned production and inventory officers when they plan for product inventory and minimize the risk of mishaps brought on by excess inventories in warehouses.

1. Introduction

Researchers have found chaos in physics, chemistry, ecology, geography, and economics data [1], and the discrete nonlinear management system has been widely studied by many researchers [2–8]. The concept of chaotic strategic management dates back to 1983. In 1994, Feichtinger [4] studied chaotic planning, queuing, and scheduling in management operations. Murphy [5] used chaos to study public relations' problems and crises. After reviewing the chaos management research, Joseph [6] pointed out that chaos management requires a change in rules and adaptability [1].

The main purpose of inventory is to meet the demand, so demand forecasting is the basic premise of inventory management. Boardman and others used a clustering algorithm to compare new and existing similar products and predict sales volume of new products [9]. Van der Auweraer et al. utilized auxiliary installed base data to predict the spare parts demand [10]. Yu et al. proposed a support vector machine (SVM) model to predict the newspaper demand of different stores by including 32 features in the model [11]. Shimmura and Takenaka used the SVM method to forecast the demand for convenience store inventory data by reducing the feature dimension and data quantity [12]. Tanizaki et al. used POS, Bayesian linear regression, and other methods to predict hotel passenger flow [13].

In the era of big data, the cost of acquiring, storing, and processing a large amount of data is significantly reduced. Decision makers can observe historical demand

and acquire data such as weather, prices, holidays, promotion information, and demographic information to improve demand forecasting accuracy [14, 15]. In recent years, the advantages of machine learning in processing large datasets and high-dimensional feature data have attracted the attention of scientists. The rapid increase in data changes the prediction algorithm from traditional forecasting approaches to deep learning [16–31]. For example, Kong et al. used the restricted Boltzmann machine (RBM) algorithm based on deep learning to predict traffic flow. The phase space reconstruction of the RBM algorithm constructed the polymorphic long-term model of chaotic time series [17]. Wei and Wang proposed an anomaly detection method of hierarchical spatiotemporal feature learning network based on deep learning [18]. Zhang et al. used the residual neural network framework to model time proximity, period, and trend characteristics of crowd flow [19]. Haq et al. [29] utilized the multilayer bidirectional LSTM algorithm to identify the mitochondrial protein of the Plasmodium falciparum parasite. Khan et al. [30] used deep learning algorithms to predict residential and commercial energy consumption. Azar and Vaidyanathan [1] used a new deep learning algorithm to predict and analyze renewable energy power generation. However, as a typical nonlinear system, the complex inventory management presented a chaotic and nonlinear phenomenon with high complexity and small amplitude change during the time series change. It is impossible to make accurate predictions by using traditional machine learning. Thus, finding a suitable deep learning algorithm for prediction is necessary. Having said that, however, the above mentioned deep learning algorithm can also be used in other chaotic systems [32–35].

This paper aims to:

(1) Analyze the nonlinear characteristics of inventory management using the nonlinear dynamics theory;

(2) Verify the inventory data characteristics and forecast the inventory by using LSTM, bi-LSTM, and DLSTM algorithms.

This paper predicted inventory data under complex, chaotic systems. The prediction results concluded that the bi-LSTM algorithm is better for chaotic nonlinear datasets and provided a reference for other chaotic datasets. The rest of this paper is organized as follows: in Section 2, the chaotic inventory management system, the inventory data, and the data irregularity are nonlinear y 0-1 test. Section 3 introduces prediction models: LSTM, bi-LSTM, CNN-LSTM, and DLSTM. Section 4 verifies the abovementioned algorithms by experiments, and the optimal model is obtained by comparing three indexes. Finally, the results are summarised in Section 5.

2. Inventory Management Systems and Datasets

2.1. Inventory Management Model. Many enterprises face inventory peoblems whih can be represented in form of complicated chaotic systems of equations as follows [36]:

$$\begin{cases} x_{i+1} = s + pz_{i+1}, \\ y_{i+1} = qx_{i+1} + ry_i z_i, \\ z_{i+1} = 1 - x_i - y_i + z_i, \end{cases} \tag{1}$$

where s, p, q, and r are the system parameters, s represents the initial sales base, p represents the inventory fund transfer rate, q represents the product resource rate, and r represents the inventory efficiency. x_i represents the resources for sales in period i, y_i represents the number of customers in period i, and z_i represents the inventory capital of the company in period i. Normalizing the parameters of the inventory management model [36], the results would be: $0 < x_i < 10 < y_i < 1$ and $0 < z_i < 1/r$. Where $p = 0.43$, $q = 0.38$, $s = 0.11$, and $r = 0.72$. The attractors of a system (1) are shown in Figure 1.

2.2. 0-1 Test. This study implemented the 0-1 test to investigate whether the data is chaotic. He et al. used 0-1 test algorithm to make correlation analysis on the time series of fractional order system [8]. If $\varphi(n)$ $(n = 1, 2, 3, \ldots)$ represents a one-dimensional observable iterative data, then the two real-valued functions would be [36]:

$$\begin{cases} p(n) = \sum_{i=1}^{n} \varphi(i) \cos(\theta(i)), \\ s(n) = \sum_{i=1}^{n} \varphi(i) \sin(\theta(i)), \end{cases} \tag{2}$$

where $\theta(i) = i\omega + \sum_{j=1}^{i} \varphi(j)$, the trajectories are visualised in Figure 2. If the bounded trajectory in the Figure 2 is a regular cloud shape, then the unbounded trajectory follows Brownian motion and the data is chaotic. This method was used to study the y and z sequence of the system (1). Its parameters were the same as those in Figure 2. The p-s relationship is displayed in Figure 3. The change of inventory safety threshold due to the change in stocks of goods with time is irregular, which cannot be accurately predicted by traditional algorithms [36].

3. Research Method

3.1. LSTM Model. LSTM network improves RNN. RNN neurons are shown in Figure 3. Cell memory unit structure is added to the hidden layer of RNN, which allows the model to learn the information for a long time and effectively overcome the problem of gradient disappearance or explosion [29]. LSTM introduces a memory cell structure in the hidden layer, including three gate controllers: input, forgetting, and output gates [37], allowing the network to forget historical information and update the memory state with new information. The structural diagram of LSTM neurons is shown in Figure 4.

The three gates adopt the sigmoid function, and all of them are nonlinear summation units. At the same time, the activation functions inside and outside the module are included. The multiplication operation is used to control the

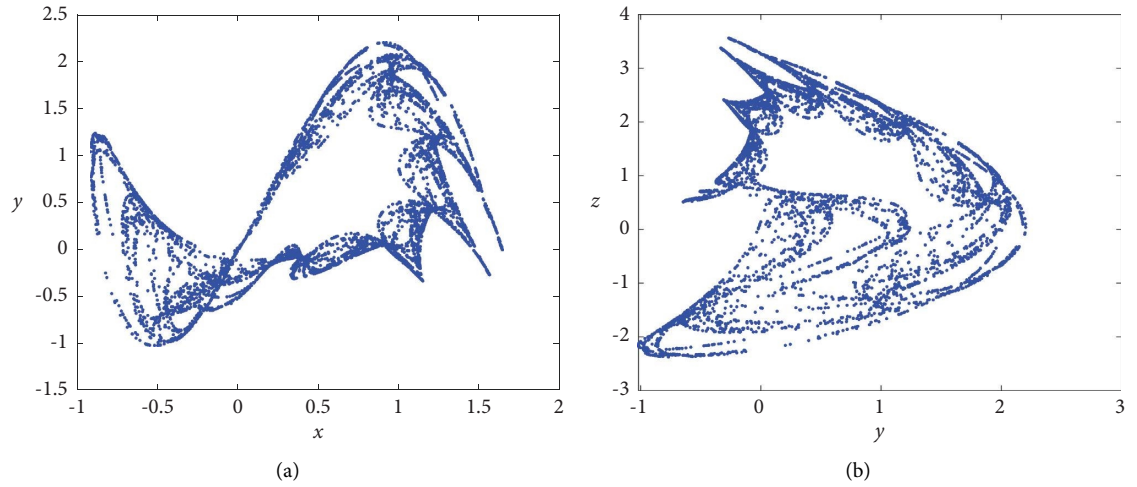

Figure 1: Attractors of system (1) with $p = 0.43$, $q = 0.38$, $s = 0.11$, and $r = 0.72$. (a) x-y phase. (b) y-z phase.

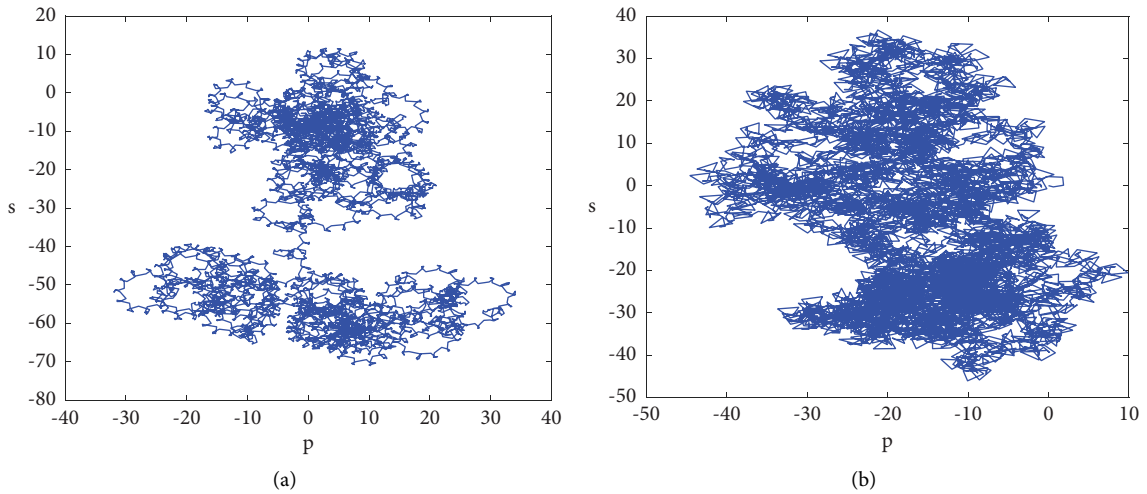

Figure 2: p-s phase diagrams of inventory system (1). (a) p-s plot of y sequence. (b) p-s plot of z sequence.

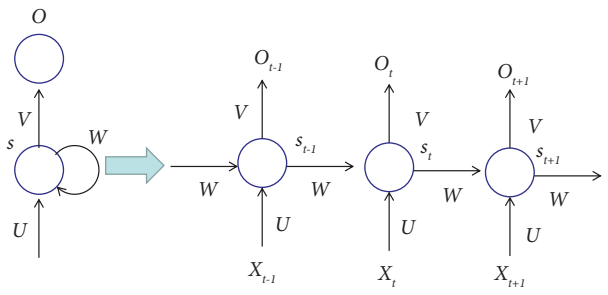

Figure 3: Framework of RNN.

activation functions of the units. The calculation consists of the following steps:

We calculate the value f_t of the forgotten gate as follows:

$$f_t = \sigma\left(W_f \cdot \left[h_{t-1}, x_t\right] + b_f\right). \tag{3}$$

We calculate the value of the input gate as follows:

$$\begin{aligned} i_t &= \sigma\left(W_i \cdot \left[h_{t-1}, x_t\right] + b_i\right), \\ \widetilde{c}_t &= \tan h\left(W_C \cdot \left[h_{t-1}, x_t\right] + b_C\right). \end{aligned} \tag{4}$$

We calculate the current time memory unit state value C_t as follows:

$$C_t = f_t * C_{t-1} + i_t * \widetilde{C}_t. \tag{5}$$

We calculate the output gate and memory output h_t of the LSTM unit as follows:

$$\begin{aligned} o_t &= \sigma\left(W_o\left[h_{t-1}, x_t\right] + b_0\right), \\ h_t &= o_t * \tan h\left(C_t\right). \end{aligned} \tag{6}$$

LSTM and RNN speculate backward data through forwarding information. Forward and backward information is used to predict the current time, strengthening the

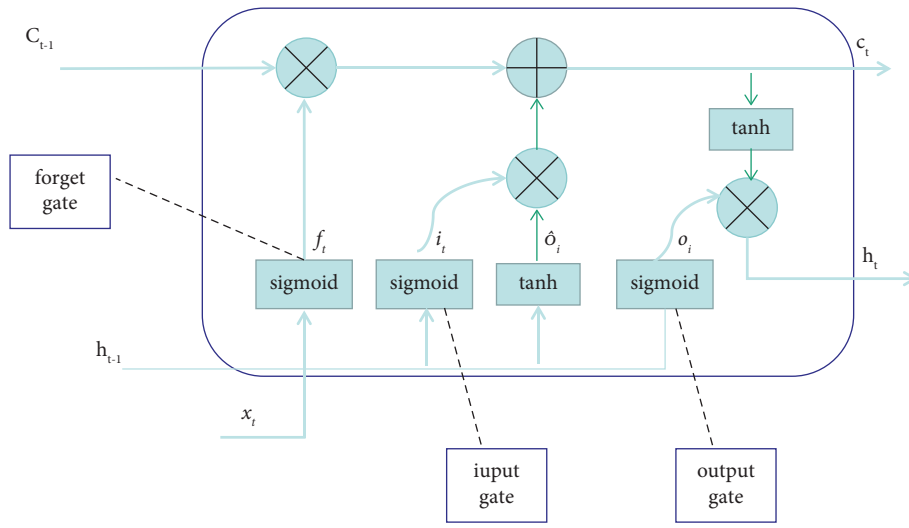

Figure 4: General framework of LSTM.

connection between feature information and predicted value and improving the model's prediction accuracy. The research shows that the LSTM network has positive results in multivariate classification and prediction.

3.2. Bi-LSTM. The LSTM prediction model only predicts through the law of unilateral data, and it cannot fully mine the time feature information, so the prediction accuracy needs further improvement. Targeting the LSTM model's deficiency, a bidirectional-LSTM (bi-LSTM) prediction model is proposed. The structural diagram of Bi-LSTM neurons is shown in Figure 5. Bi-LSTM [37] uses two unrelated LSTM models to predict data from the front and back. The output of the hidden layers of the two models is used as the input of the output layer, and finally, the built-in function of the output layer outputs the final predicted value.

$$\begin{cases} \overrightarrow{h}_t = \mathrm{LSTM}\left(x, \overrightarrow{h}_{t-1}\right), \\ \overleftarrow{h}_t = \mathrm{LSTM}\left(x, \overleftarrow{h}_{t-1}\right), \\ y_{t-1} = g\left(W_{\overrightarrow{h}y}\overrightarrow{h}_t + W_{\overleftarrow{h}y}\overleftarrow{h}_t + b_y\right). \end{cases} \tag{7}$$

Bi-LSTM, based on the time window method, refers to the prediction of the next time step by using the historical value of the time window length of data. The parameter value of the time window step represents the historical data for predicting the future value. For example, if the current value x_t and the previous values x_{t-1} and x_{t-2} are used to predict the value of the next period x_{+1}.

Regularization avoids overfitting in prediction. $L1$ and $L2$ regularization methods introduce a penalty for the problem of too large parameters in the model. The most used regularization technique for deep learning is dropout, which randomly inactivates some neurons. Each training session is equivalent to a different weak classifier, thus improving the model's generalization ability and using the dropout method to improve the model's applicability.

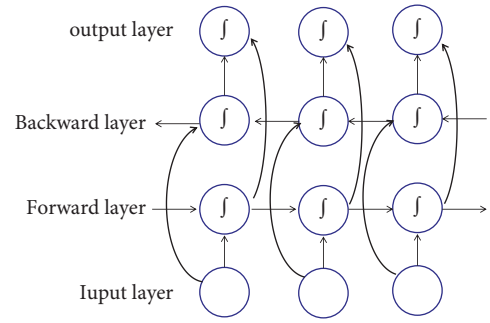

Figure 5: General framework of bi-LSTM.

According to Khan et al. [38], the hybrid network DB-Net, is proposed by combining the extended convolutional neural network (DCNN) with the bidirectional long-term and short-term memory (bi-LSTM). Sagheer and Kotb [39] put forward "CL-Net" based on a new hybrid structure T of ConvLSTM and LSTM. All the above improve LSTM and bi-LSTM deep learning models.

3.3. CNN-LSTM. A convolutional neural network (CNN) comprises five parts: input layer, convolution layer, pooling layer, full connection layer, and output layer.

$\mathbf{X} = [x_1, x_2, \ldots, x_n]$ is the input data matrix, where n represents the length of the time series and m represents the number of data features. The time-series data are convolved to obtain the following equation:

$$o_c = f_c(\mathbf{X} \otimes \mathbf{W}_c + b_c), \tag{8}$$

where $\otimes$ is the convolution operation, convolution kernel $\mathrm{WC} \in \mathbf{R}^{j*m}$ is the weight vector, j is the convolution kernel size, and b_c is the bias of this layer. $f_c(\cdot)$ represents the convolution layer activation function. o_c is the convolution kernel feature mapping result.

Pool operation selects the most critical features of the convolution layer sequence to form the pooling layer. There are two kinds of pooling operations: maximum pooling and average pooling. The commonly used pooling method is maximum pooling, and the maximum global pooling is used in the last pooling operation. The expression is:

$$\begin{cases} o_p(k) = \max\left(o_c(2k-1), o_c(2k)\right), \\ o_p = \max\left(o_c\right), \end{cases} \tag{9}$$

where $o_p(k)$ is the output result of the k^{th} pool; o_p is the output result of maximum global pooling.

A combination of timing features is realized through the full connection layer:

$$o_d = f_d\left(o_p \times \mathbf{W}_d + b_d\right). \tag{10}$$

Among them, $\mathbf{W}_d$ is the weight matrix of the full connection layer, b_d is the bias, and the activation function $f_d(\cdot)$ of the full connection layer includes ReLU, tanh, and sigmoid.

The output layer outputs the results of the full connection layer:

$$y = f_o\left(o_d \times \mathbf{W}_o + b_o\right), \tag{11}$$

$\mathbf{W}_o$ is the weight matrix of the output layer, b_o is the bias, and the activation function f_o is the softmax function.

CNN-LSTM is a combination of CNN and LSTM, which is divided into four layers:

(1) Input layer: data input after normalization.

(2) CNN layer: this layer extracts the data features through CNN, where the convolution layer and pooling layer can extract the features that more clearly reflect the inventory changes and reduce overfitting. The full connection layer can summarise and output the abovementioned features.

(3) LSTM layer: the extracted features are converted into the corresponding data format of LSTM, and time series data mining is carried out through three gate mechanisms in LSTM to obtain the internal change rule and the prediction model.

(4) Output layer: the activation function of the output layer is the Sigmoid function, and the LSTM prediction result is the output.

3.4. DLSTM. In the Deep LSTM (DLSTM) architecture, as shown in Figure 6 [40], the input at time t, x_t is introduced to the first LSTM block along with the previous hidden state $S_{t-1}{}^{(1)}$, and the superscript (1) refers to the first LSTM. The hidden state at time t, $s_t^{(1)}$ is computed and moves forward to the next step and up to the second LSTM block. The second LSTM uses the hidden state $s_t^{(1)}$ along with the previous hidden state $s_{t-1}^{(2)}$ to compute $s_t^{(2)}$, which goes forward to the next step and up to the third LSTM block and so on until the last LSTM block is compiled in the stack.

The benefit of such stacked architecture is that each layer can process some part of the desired task and subsequently pass it on to the next layer until the last accumulated layer finally provides the output. Another benefit is that such architecture allows the hidden state at each level to operate differently. The previous two benefits have a significant impact in scenarios showing the use of data with long-term dependency or in the case of handling multivariate time series datasets.

The prediction results of Bi-LSTM can be compared with LSTM. The model structure of LSTM itself is relatively complex, and training is more time-consuming than CNN. The characteristics of RNN networks determine that they cannot process data in parallel. Furthermore, although LSTM can alleviate the long-term dependence of RNN to some extent, it is difficult for longer sequence data.

4. Experimental Results

4.1. Data Sources. The experimental data in this paper come from dynamic equation (1). According to the definition of the state variable of dynamic system (1), the state variable Z is the inventory data. The first 70000 datasets were used as training datasets and the last 3000 test datasets, totalling 10000. In this paper, system (1) state Z was adopted, and 10000 samples were selected, as shown in Figure 7. The abovementioned analysis showed that the inventory data are chaotic. To fully use the time series between the data, this paper predicts and evaluates the inventory data and verifies it with the actual data.

4.2. Evaluation Index and Model Parameters. This paper used LSTM, bi-LSTM, GRU, CNN-LSTM, and other algorithmic models for prediction. To evaluate the effectiveness of these methods, mean square error (MSE), root mean square error (RMSE), and mean absolute error (MAE) were used to evaluate the model. These indicators are defined as follows [19]:

$$\begin{aligned} \text{MSE} &= \frac{1}{N}\sqrt{\sum_{i=1}^{N}\left(y_i - \widehat{y}_i\right)^2}, \\ \text{RMSE} &= \sqrt{\frac{1}{N}\sum_{i=1}^{N}\left(y_i - \widehat{y}_i\right)^2}, \\ \text{MAE} &= \frac{1}{N}\sum_{i=1}^{N}\left|y_i - \widehat{y}_i\right|, \end{aligned} \tag{12}$$

where $\widehat{y}_i$ is the observed inventory quantity, y_i is the forecast quantity of the inventory, and N is the number of test samples.

In this paper, LSTM, DLSTM, GRU, CNN-LSTM, and bi-LSTM algorithms were adopted, and the main parameter values in the algorithms are shown in Table 1.

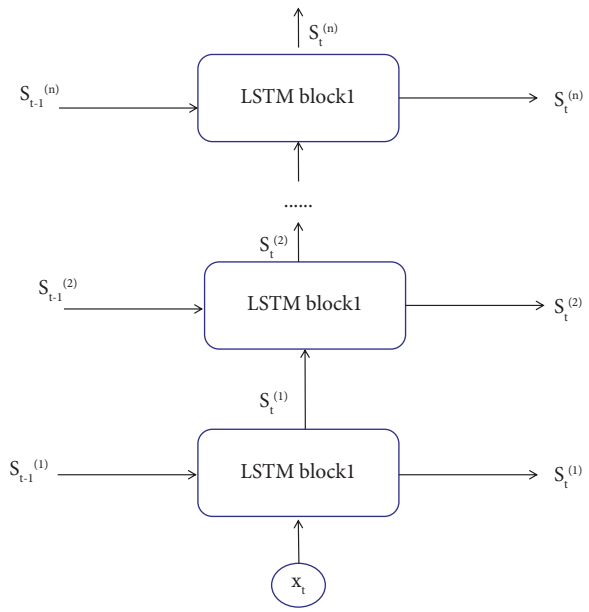

Figure 6: General framework of DLSTM.

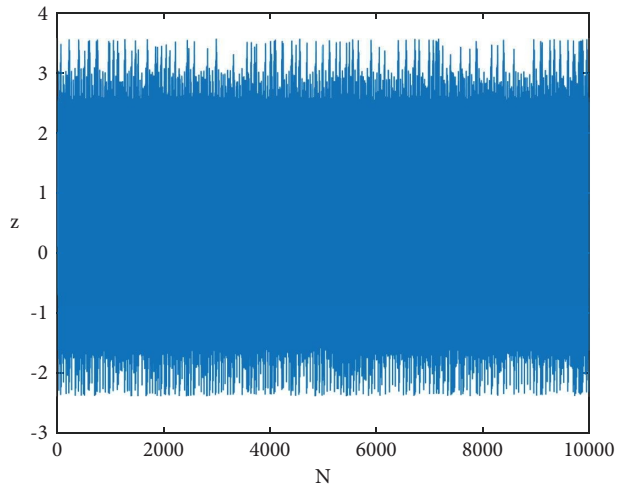

Figure 7: Inventory quantity of system (1).

4.3. Results. The inventory forecasting model adopted the LSTM algorithm, and the comparison between the predicted result and the actual value is shown in Figure 8. The change of the Loss function after 50 cycles is displayed in Figure 9. Figure 8 shows the last 150 data of the test set, allowing the readers to check the predicted and actual values. MSE was 0.005315, RMSE was 0.072905, and MAE was 0.060346. All in all, the prediction errors were quite small.

The comparison between the predicted result by using the bi-LSTM algorithm and the actual value is shown in Figure 10. The change of the Loss function after 50 cycles is shown in Figure 11. Figure 10 shows the last 150 data of the test set for the convenience of readers to check the predicted and actual values. MSE was 0.001475, RMSE was 0.038405, MAE was 0.029732, and the forecasting errors were small.

The inventory forecasting model adopted the CNN-LSTM algorithm. The comparison between the predicted result and the actual values is shown in Figure 12. The change of the Loss function after 50 cycles is shown in Figure 12. Figure 12 shows the last 150 data of the test set for the convenience of readers to check the predicted and actual values. MSE is 0.027766, RMSE is 0.166631, MAE is 0.117720, and the forecasting errors are relatively small.

The inventory forecasting model adopted Figure 13 the DLSTM algorithm. Figure 14 shows that the last 150 data of the test set were used for the convenience of readers to check

Table 1: Parameters of four models.

	LSTM	DLSTM	CNN-LSTM	Bi-LSTM
Number of neurons	80	2	80	80
Dropout	0.3	0.3	0.3	0.3
Loss function	mean_squared_error	mean_squared_error	mean_squared_error	mean_squared_error
Optimizer	Adam	Adam	Adam	Adam
Training times	50	50	50	50
Batch_size	64	1	64	64
Training set	7000	7000	7000	7000
Test set	3000	3000	3000	3000

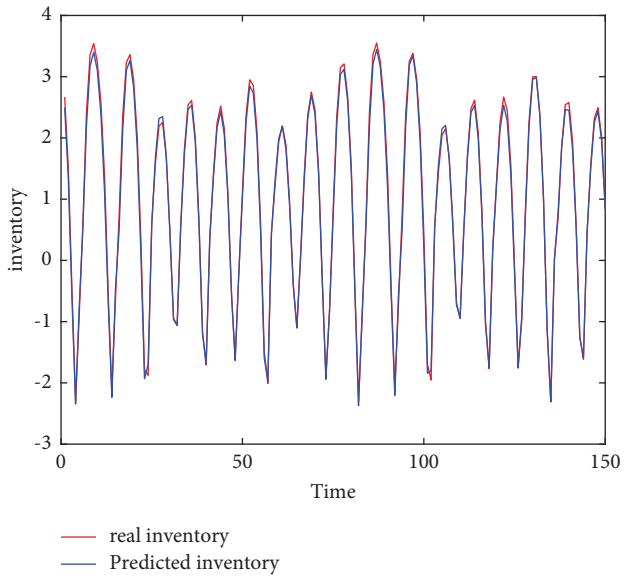

Figure 8: Timing diagram of real and predicted value (LSTM).

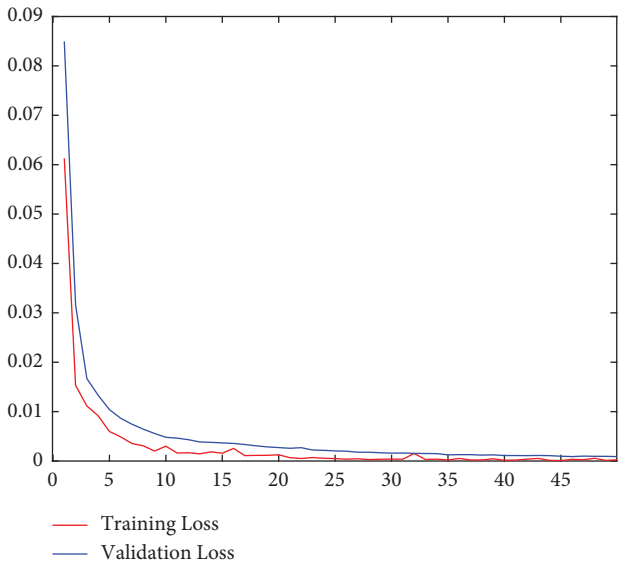

Figure 9: Training and validation loss (LSTM).

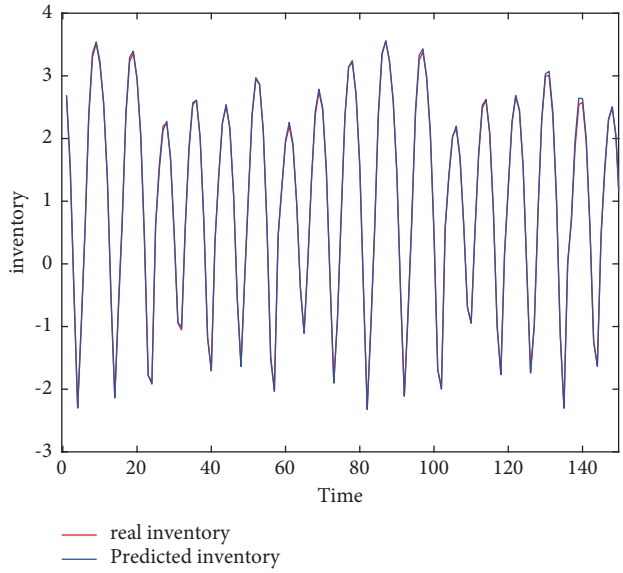

Figure 10: The timing diagram of the actual and predicted values (bi-LSTM).

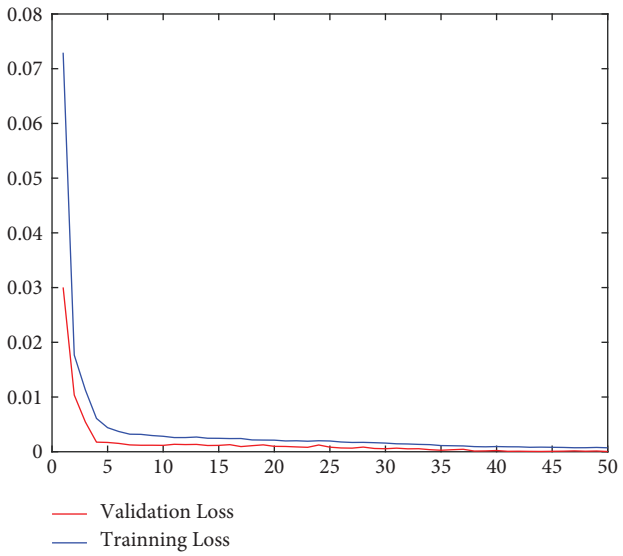

Figure 11: Training and validation loss (bi-LSTM).

the predicted and actual values. The comparison between the predicted result and the actual value is shown in Figure 14. MSE was 0.462163, RMSE was 0.6798, and MAE was 0.570947.

By comparing the abovementioned evaluating indicator, the results are shown in Table 2. The results obtained by bi-LSTM were the best with the slightest error, despite all other algorithms being used due to relatively small errors. Because the data fluctuation was not particularly large, DLSTM had no apparent advantages in this scenario. At the same time, we found no correlation between the complexity and performance of the model. For example, the DLSM algorithm is more responsible but is not the best for inventory safety prediction.

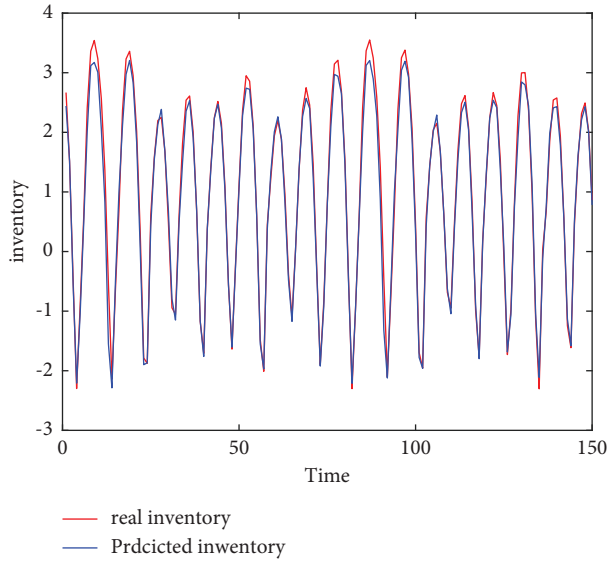

Figure 12: Timing diagram of actual and predicted value (CNN-LSTM).

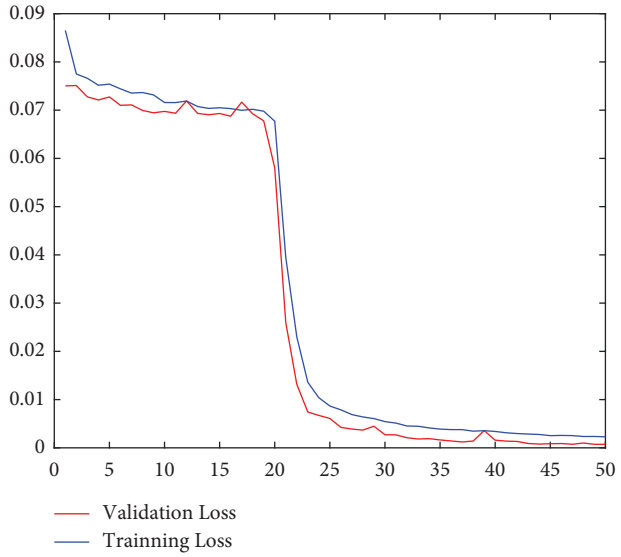

Figure 13: Training and validation loss (CNN-LSTM).

There are often uncertain factors in the production process, such as many sudden orders, temporary consumption increases, the sudden advance of delivery, late delivery, and so on. Through the abovementioned four algorithms, we can see that the bi-LSTM algorithm accurately predicted the inventory capacity, and it is of substantial value for enterprises to make purchase and demand plans.

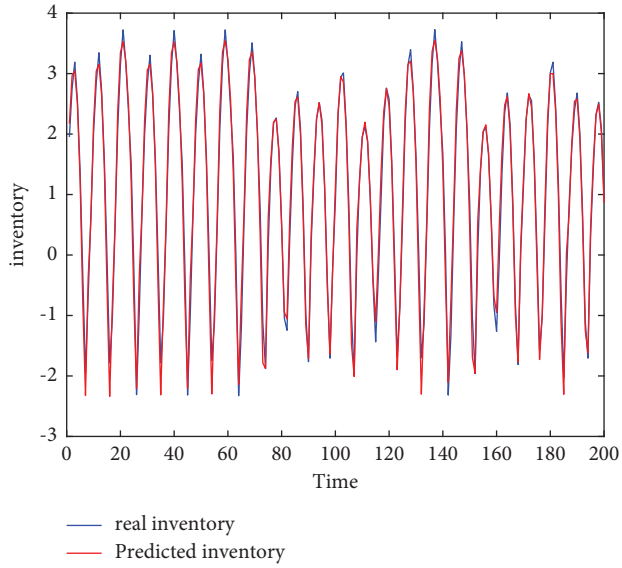

Figure 14: Timing diagram of actual and predicted value (DLSTM).

Table 2: Model results of four deep learning algorithms.

Evaluate	LSTM	Bi-LSTM	CNN-LSTM	DLSTM
MSE	0.005315	0.001475	0.027766	0.462163
RMSE	0.072905	0.038405	0.166631	0.6798
MAE	0.060346	0.029732	0.117720	0.570947

5. Conclusion

Excessive inventory capacity causes inventory backlog, directly affecting the company's production efficiency. In this paper, we focused on the prediction of inventory capacity. It used an inventory management dynamics system to obtain 10000 inventory data and used four prediction algorithms in artificial intelligence: LSTM, BI-LSTM, CNN-LSTM, and DLSTM to train and predict. The prediction results showed that bi-LSTM had the best prediction results.

This study contributed to the academic circle by comparing different forms of neural network prediction of dynamics and chaotic nonlinear inventory management data. It also provided theoretical support for other predictions. The predicted results offered practical suggestions for enterprises' planned production and inventory officers when they decide on the optimal inventory of goods and reduce the likelihood of accidents due to excessive amounts of goods in warehouses. In future work, other algorithms, such as CNN-BILSTM and CNN-DLSTM, as well as AutoML as per Li et al. [41, 42], could be used to predict inventory and compare with the four deep learning methods in this research.

Data Availability

The data used to support the findings of this study are available from the corresponding authors upon request.

Conflicts of Interest

The authors declare that they have no conflicts of interest.

Acknowledgments

This work was supported by the Major Scientific and Technological Innovation Projects of Shandong Province (Grant no. 2019JZZY010111), the Natural Science Foundation of Shandong Province (Grant no: ZR2017PA008), the Key Research and Development Plan of Shandong Province (Grant no: 2019GGX104092), and the Science and Technology Plan Projects of Universities of Shandong Province (Grant no: J18KA381).

References

[1] A. T. Azar and S. Vaidyanathan, *Chaos Modeling and Control Systems Design*, Springer, Cham, Switzerland, 2015.

[2] J. P. Pinder, "Non-linear dynamical systems and inventory management," *Managerial and Decision Economics*, vol. 17, no. 1, pp. 27–43, 1996.

[3] D. Levy, "Chaos theory and strategy: theory, application, and managerial implications," *Strategic Management Journal*, vol. 15, no. 2, pp. 167–178, 2007.

[4] G. Feichtinger, C. H. Hommes, and W. Herold, "Chaos in a simple deterministic queueing system," *ZOR - Methods and Models of Operations Research*, vol. 40, no. 1, pp. 109–119, 1994.

[5] P. Murphy, "Chaos theory as a model for managing issues and crises," *Public Relations Review*, vol. 22, no. 2, pp. 95–113, 1996.

[6] E. C. Joseph, "Chaos & postmodernism forecasting & futuring insights," *Futurics,Summer-Fall*, pp. 1–12, 1994.

[7] Y. Ding and J. Cao, "Bifurcation analysis and chaos switchover phenomenon in a nonlinear financial system with delay feedback," *International Journal of Bifurcation and Chaos*, vol. 25, no. 12, Article ID 1550165, 2015.

[8] S. Wang, S. He, A. Yousefpour, H. Jahanshahi, R. Repnik, and M. Perc, "Chaos and complexity in a fractional-order financial system with time delays," *Chaos, Solitons & Fractals*, vol. 131, Article ID 109521, 2020.

[9] L. Baardman, I. Levin, G. Perakis, and D. Singhvi, "Leveraging comparables for new product sales forecasting," *Production*

and Operations Management, vol. 27, no. 12, pp. 2340–2343, 2018.

[10] S. Van der Auweraer, R. N. Boute, and A. A. Syntetos, "Forecasting spare part demand with installed base information: a review," *International Journal of Forecasting*, vol. 35, no. 1, pp. 181–196, 2019.

[11] X. Yu, Z. Qi, and Y. Zhao, "Support vector regression for newspaper/magazine sales forecasting," *Procedia Computer Science*, vol. 17, pp. 1055–1062, 2013.

[12] T. Shimmura and T. Takenaka, "Selecting rows and columns for training support vector regression models with large retail datasets," *European Journal of Operational Research*, vol. 226, no. 3, pp. 679–683, 2013.

[13] T. Tanizaki, T. Hoshino, T. Shimmura, and T. Takenaka, "Demand forecasting in restaurants using machine learning and statistical analysis," *Procedia CIRP*, vol. 79, pp. 679–683, 2019.

[14] J. Meller, F. Taigel, and R. Pibernik, "Prescriptive analytics for inventory management: a comparison of new approaches," *SSRN Electronic Journal*, 2018.

[15] A. L. Beutel and S. Minner, "Safety stock planning under causal demand forecasting," *International Journal of Production Economics*, vol. 140, no. 2, pp. 637–645, 2012.

[16] A. Koesdwiady, R. Soua, and F. Karray, "Improving traffic flow prediction with weather information in connected cars: a deep learning approach," *IEEE Transactions on Vehicular Technology*, vol. 65, no. 12, pp. 9508–9517, 2016.

[17] F. Kong, J. Li, B. Jiang, and H. Song, "Short-term traffic flow prediction in smart multimedia system for Internet of Vehicles based on deep belief network," *Future Generation Computer Systems*, vol. 93, no. 4, pp. 460–472, 2019.

[18] G. Wei and Z. Wang, "Adoption and realization of deep learning in network traffic anomaly detection device design," *Soft Computing*, vol. 25, no. 2, pp. 1147–1158, 2021.

[19] J. Zhang, Y. Zheng, and D. Qi, "Deep spatio-temporal residual networks for citywide crowd flows prediction," *Proceedings of the AAAI Conference on Artificial Intelligence*, vol. 31, no. 1, pp. 1655–1661, 2017.

[20] Y. Lv, Y. Duan, W. Kang, Z. Li, and F. Y. Wang, "Traffic flow prediction with big data: a deep learning approach," *IEEE Transactions on Intelligent Transportation Systems*, vol. 16, no. 2, pp. 865–873, 2015.

[21] D. Zhang and M. R. Kabuka, "Combining weather condition data to predict traffic flow: a GRU-based deep learning approach," *IET Intelligent Transport Systems*, vol. 12, no. 7, pp. 578–585, 2018.

[22] S. Du, T. Li, X. Gong, Y. Yang, and S. J. Horng, "Traffic flow forecasting based on hybrid deep learning framework," in *Proceedings of the 12th International Conference on Intelligent Systems and Knowledge Engineering*, pp. 1–6, Nanjing, China, November 2017.

[23] A. S. Mihaita, H. Li, Z. He, and M. A. Rizoiu, "Motorway traffic flow prediction using advanced deep learning," in *Proceedings of the 2019 IEEE Intelligent Transportation Systems Conference (ITSC)*, pp. 1683–1690, Auckland, New Zealand, October 2019.

[24] L. Qu, W. Li, W. Li, D. Ma, and Y. Wang, "Daily long-term traffic flow forecasting based on a deep neural network," *Expert Systems with Applications*, vol. 121, no. 5, pp. 304–312, 2019.

[25] Y. Kim, P. Wang, and L. Mihaylova, "Scalable learning with a structural recurrent neural network for short-term traffic prediction," *IEEE Sensors Journal*, vol. 19, no. 23, pp. 11359–11366, 2019.

[26] Y. Chen, L. Shu, and L. Wang, "Traffic flow prediction with big data: a deep learning based time series model," in *Proceedings of the 2017 IEEE Conference on Computer Communications Workshops (INFOCOM WKSHPS)*, pp. 1010-1011, Atlanta, GA, USA, May 2017.

[27] H. F. Yang, T. S. Dillon, and Y. P. P. Chen, "Optimized structure of the traffic flow forecasting model with a deep learning approach," *IEEE Transactions on Neural Networks and Learning Systems*, vol. 28, no. 10, pp. 2371–2381, 2017.

[28] S. U. Khan and R. Baik, "MPPIF-net: identification of Plasmodium falciparum parasite mitochondrial proteins using deep features with multilayer Bi-directional LSTM," *Processes*, vol. 8, no. 6, p. 725, 2020.

[29] I. U. Haq, A. Ullah, S. U. Khan et al., "Sequential learning-based energy consumption prediction model for residential and commercial sectors," *Mathematics*, vol. 9, 2021.

[30] N. Khan, F. Ullah, I. U. Haq, S. U. Khan, M. Y. Lee, and S. W. Baik, "AB-net: a novel deep learning assisted framework for renewable energy generation forecasting," *Mathematics*, vol. 9, no. 19, p. 2456, 2021.

[31] X.. Gao, J. Mou, L. Xiong, Y. Sha, H. Yan, and Y. Cao, "A fast and efficient multiple images encryption based on single-channel encryption and chaotic system," *Nonlinear Dynamics*, vol. 108, no. 1, pp. 613–636, 2022.

[32] X. Ma, J. Mou, J. Liu, C. Ma, F. Yang, and X. Zhao, "A novel simple chaotic circuit based on memristor-memcapacitor," *Nonlinear Dynamics*, vol. 100, no. 3, pp. 2859–2876, 2020.

[33] X. Li, J. Mou, Y. Cao, and S. Banerjee, "An optical image encryption algorithm based on a fractional-order laser hyperchaotic system," *International Journal of Bifurcation and Chaos*, vol. 32, no. 03, 2022.

[34] X. Gao, J. Mou, S. Banerjee, Y. Cao, L. Xiong, and X. Chen, "An effective multiple-image encryption algorithm based on 3D cube and hyperchaotic map," *Journal of King Saud University-Computer and Information Sciences*, vol. 34, no. 4, pp. 1535–1551, 2022.

[35] S. Hochreiter and J. Schmidhuber, "Long short-term memory," *Neural Computation*, vol. 9, no. 8, pp. 1735–1780, 1997.

[36] T. Lei, R. Y. M. Li, and H. Fu, "Dynamics analysis and fractional-order approximate entropy of nonlinear inventory management systems," *Mathematical Problems in Engineering*, vol. 2021, Article ID 5516703, 8 pages, 2021.

[37] Z. Li, J. P. Zhu, X. J. Xu, and Y. Yao, "RDense: a protein-RNA binding prediction model based on bidirectional recurrent neural network and densely connected convolutional networks," *IEEE Access*, vol. 8, pp. 14588–14605, 2020.

[38] N. Khan, I. U. Haq, S. U. Khan, S. Rho, M. Y. Lee, and S. W. Baik, "DB-Net: a novel dilated CNN based multi-step forecasting model for power consumption in integrated local energy systems," *International Journal of Electrical Power & Energy Systems*, vol. 133, Article ID 107023, 2021.

[39] N. Khan, I. U. Haq, F. U. M. Ullah, S. U. Khan, and M. Y. Lee, "CL-net: ConvLSTM-based hybrid architecture for batteries' state of health and power consumption forecasting," *Mathematics*, vol. 9, no. 24, p. 3326, 2021.

[40] A. Sagheer and M. Kotb, "Time series forecasting of petroleum production using deep LSTM recurrent networks," *Neurocomputing*, vol. 323, pp. 203–213, 2019.

[41] R. Y. M. Li, L. Song, B. Li, M. J. C. Crabbe, and X. G. Yue, "Predicting carpark prices using real estate indices and AutoML," *CMES-Computer Modeling in Engineering & Science*, vol. 134, no. 3, pp. 2247–2282, 2022.

[42] R. Y. M. Li, K. W. Chau, and D. C. W. Ho, *Current State of Art in Artificial Intelligence and Ubiquitous Cities*, Springer, Berlin, Germany, 2022.

Hindawi
Complexity
Volume 2022, Article ID 3154650, 21 pages
https://doi.org/10.1155/2022/3154650

Research Article

DWT-SVD Based Watermarking for High-Resolution Medical Holographic Images

Fahrettin Horasan,[1] **Muhammed Ali Pala**,[2,3] **Ali Durdu**,[4] **Akif Akgül**,[5] **Ömer Faruk Akmeşe**,[5] **and Mustafa Zahid Yıldız**[2,3]

[1]*Department of Computer Engineering, Faculty of Engineering and Architecture, Kırıkkale Universityz, Yahşihan 71450, Kırıkkale, Turkey*
[2]*Department of Electrical and Electronics Engineering, Faculty of Technology, Sakarya University of Applied Sciences, Sakarya 54050, Turkey*
[3]*Biomedical Technologies Application and Research Center (BIYOTAM), Sakarya University of Applied Sciences, Sakarya, Turkey*
[4]*Department of Management Information Systems, Faculty of Political Sciences, Social Sciences University of Ankara, Altındag 06050, Ankara, Turkey*
[5]*Department of Computer Engineering, Faculty of Engineering, Hitit University, Corum 19030, Turkey*

Correspondence should be addressed to Muhammed Ali Pala; pala@subu.edu.tr

Received 19 February 2022; Revised 23 June 2022; Accepted 11 July 2022; Published 29 August 2022

Academic Editor: Ning Cai

Watermarking is one of the most common techniques used to protect data's authenticity, integrity, and security. The obfuscation in the frequency domain used in the watermarking method makes the watermarking stronger than the obfuscation in the spatial domain. It occupies an important place in watermarking works in imperceptibility, capacity, and robustness. Finding the optimal location to hide the watermarking is one of the most challenging tasks in these methods and affects the method's performance. In this article, sample identification information is processed with the method of watermaking on the hiding environment created by using a chaos-based random number generator on biomedical data to provide solutions to problems such as visual attack, identity theft, and information confusion. In order to obtain biomedical data, a lensless digital in-line holographic microscopy (DIHM) setup was designed, and holographic data of human blood and cancer cell lines, which are widely used in the laboratory environment, were obtained. The standard USAF 1951 target was used to evaluate the resolution of our imaging setup. Various QR codes were generated for medical sample identification, and the captured medical data were processed by watermarking it with chaos-based random number generators. A new method using chaos-based discrete wavelet transform (DWT) and singular value decomposition (SVD) has been developed and applied to high-resolution data to eliminate the problem of encrypted data being directly targeted by third-party attacks. The performance of the proposed new watermarking method has been demonstrated by various robustness and invisibility tests. Experimental results showed that the proposed scheme reached an average PSNR value of 564588 dB and SSIM value of 0.9972 against several geometric and destructive attacks, which means that the proposed method does not affect the image quality and also ensures the security of the watermarking information. The results of the proposed method have shown that it can be used efficiently in various fields.

1. Introduction

In recent years, significant developments in medical imaging technologies have brought many new perspectives to hospital and laboratory environments. These developments have resulted in large databases of information such as medical images, experimental procedure records, diagnostic and treatment reports, and patient records. The secure management, indexing, and archiving of these digitized data that emerged with these technologies become a significant issue. Illegal access, copying, and unlawful data modification cause serious security problems [1, 2]. A high degree of

security procedures is required to store, record, and transmit these data securely. In addition, other identifying data attached to images may be lost, hacked, or archived incorrectly. Although various methods have been proposed in the literature to solve these problems, the watermarking technique is one of the most popular methods [3–5].

Watermarking is defined as embedding the data in another signal; it is embedding additional information directly into the data by gradually altering the original data or some transformed version of these data. The characteristics of a watermarking algorithm vary depending on the application for which it is designed. Undetectability, robustness, and security are essential criteria for a successful watermarking operation [6]. Undetectability defines the confidentiality of the presence of the watermark in the data, and the signal embedded in the data should not be noticed. The watermark embedded in the data must survive any reasonable action applied to the carrier. Otherwise, it is called fragile if it is not detected after the slightest change. In addition, embedded data should be resistant to unauthorized access and should not show any hint of the presence of the watermark. With the digital watermarking process, data corruption and access by unauthorized persons are highly restricted, producing results that are highly resistant to attacks [6–10]. In addition, a digital watermark is used to check for privacy, integrity, and malpractice obligations and tackle ethical and legal issues [11–13]. The watermarking of medical data brings with it various advantages. Thanks to the embedded data that contribute to savings in archiving large-scale digitized data. Embedded data reduce the need for additional bandwidth in transmission processes and increases the transfer rate. Thanks to the metadata hidden in the image data; it increases the safety of patients' records in the hospital and the safety of experiments in laboratory environments. This situation primarily provides advantages in archiving and proper classification and prevents unauthorized access to these data from outside [14, 15].

In recent years, many studies have been conducted on watermarking medical data. Alshaikn et al. [16] tried to determine the most suitable region to embed the watermark in the discrete cosine transform (DCT) based watermarking approach. They use a modified pigeon algorithm to determine the optimal burial path. Hsu et al. [17] proposed a high-capacity QR decomposition (QRD) based blind watermarking algorithm with artificial intelligence technologies for color images. Applying the watermark involves dividing the main image into nonoverlapping blocks of 4×4 pixels and then applying the QRD to each block. Ernawan et al. [18] proposed a self-embedded watermark using a spiral block mapping for tamper detection and restoration. They implemented a 3×3 block-based encoding, self-embedding watermark with two authentication bits and seven recovery bits. Muigai et al. [19] proposed an imperceptible and reversible medical image watermarking (MIW) scheme based on image segmentation, image estimation, and nonlinear difference broadening for the integrity and authenticity of medical images and detection of both intentional and unintentional manipulations.

Huang and Wu [20] proposed a new visual information hiding technique called optical watermarking for authenticating original printed documents. An optical watermark is a two-dimensional binary image. It can be of any shape and can be printed anywhere in a document. An optical watermark is created by overlaying many two-dimensional binary images, each of which has different carrier structural patterns that embed confidential information. The hidden information is embedded in each layer using phase modulation. Xie and Arce [21] developed a blind watermarking technique with a digital image signature for authentication. The signature algorithm is first implemented in the discrete wavelet transform (DWT) domain and then combined into the SPIHT compression algorithm. The capacity of the watermarking method is determined by the upper limit of the bit rate of information that can be hidden in the image using the binary engraving and multibit engraving methods. Arena et al. [22] proposed digital watermarks to validate both video and images. In such embodiments, the watermark is embedded in a master image, so that subsequent changes in the watermarked image can be detected with a high probability. The study presents the possibility of applying a real-time watermark on a video stream. Sidiropoulas et al. [23] proposed a new technique combining localization and reversibility. Moreover, the watermark dependency on the original image and the nonlinear watermark placement procedure ensured that no malicious attack would generate information leakage.

Thakkar et al. proposed a blind image watermarking scheme based on discrete wavelet transform (DWT) and singular value decomposition (SVD). This study applied DWT to the medical image's ROI (region of interest) to obtain different frequency subbands of wavelet decomposition [13]. Dhanalakshmi and Thaiyalnayaki proposed a binary watermarking method based on DWT-SVD and chaos cryptography [6]. A different spatial domain-based digital image watermarking method has been proposed by Lin et al. [24]. Today, encryption and watermarking methods have begun to work together to extend security to the electronic patient report (EPR) medical data [4]. An excellent watermarking algorithm must be robust and reliable against attacks [8]. Also, some studies have proposed the wavelet-based watermarking method for medical images [25–30].

In the SVD method, the diagonal elements of the singular value matrices are less subject to change against possible attacks after watermarking [31]. In more detail, the large-valued ones of the singular value matrix do not undergo significant change. In addition, the imperceptibility of the cover image is better as it allows for hiding less data belonging to the watermark. The most important advantage of using the DWT-SVD method is reducing the SVD process cost [32]. For this, the scaling feature of the DWT technique was used. R-DWT is applied to realize the most appropriate scaling. Thus, a robust, transparent, and less costly scheme is obtained [33]. The disadvantage of the SVD method is the false positive problem. This is the case when another watermark (actually another logo or image that is not watermarked) could be extracted from the watermarked image.

This study used chaos-based random number generators to counter the false positive problem. Watermarking is performed on randomly selected pixels. Thus, it is possible to remove the watermark only by those who know these chaotic keys.

This study developed a new method using chaos-based discrete wavelet transform (DWT) and singular value decomposition (SVD) for watermarking with high imperceptibility and robustness. In addition, a new application area has been gained by applying the proposed method to the data obtained from the DIHM system. In the following sections of this article, the theoretical details of holography and the design parameters of our microscopy setup are explained in detail. The standard USAF 1951 target was used to evaluate the resolution of the imaging setup. Human blood and cancer cell culture cells, which are widely investigated in clinical and laboratory applications, were used as medical samples. A QR code was created for information such as medical sample preparation procedures and patient information. The chaotic system is used for random number generators. The dynamic analysis results of the chaotic system determined as suitable for the watermarking process are shown. The randomness performance of random number generators has been demonstrated by NIST and ENT statistical tests. The new method using discrete wavelet transform (DWT) and singular value decomposition (SVD) intended for watermarking is explained in detail. The performance of the proposed new watermarking method has been demonstrated by various robustness and invisibility tests.

2. Lensless Digital In-Line Holographic Microscopy

Microscopy systems that allow imaging at the micro-nano level have an undeniable effect on the development of today's scientific world. Micro-nano level sensors developed based on semiconductor technology have expanded the usage area of microscopy systems and caused this development to progress. With these developments, DIHM has begun to be used in many application areas, from physics to medical imaging [34–37]. With its advantages such as wide field of view, high spatial resolution, easy integration, and low cost, DIHM has become a tool that performs essential functions, especially in the laboratory and clinical stages of medical imaging. DIHM is used in laboratory conditions to imaging microorganisms such as cancer cells, bacteria, yeast cells, or sperm cells, perform viability analyses, track the cells in 2D, and determine sample 3D localizations [38–42]. It is used in the clinic for human-level counting and classifying blood cells, morphological examination of medical samples, and disease diagnosis [43–45]. Considering all these areas of use, the commercial studies of DIHM systems are currently used for clinical and laboratory experiments. With DIHM, where algorithm integration is easy, various analyses can be obtained with high accuracy rates with traditional image processing methods, segmentation methods, or deep neural network methods [46, 47]. This situation constitutes an excellent alternative to the methods accepted as a gold standard, and it seems likely to reach more areas of use in the future. In this section, the basic principles of holography are mentioned, and the design parameters of our imaging system are detailed.

2.1. Hologram Theory. DIHM is based on Gabor's holographic principle [48]. The interaction of the light source and the rays emanating from this light source with the sample and the diffraction patterns resulting from this interaction are recorded by charge-matched semiconductors (CCD) or complementary metal oxide semiconductors (CMOS). The interaction of the beams emitted from the light source with the sample and the diffraction patterns resulting from this interaction are recorded via charge-coupled devices (CCD) or complementary metal oxide semiconductors (CMOS) [49]. Coherent sources are used as light sources, and spatially filtered light-emitting diodes (LED) are used in many applications in the literature [38, 50]. DIHM, in which no optical lens is used, uses Fourier optics' principles numerically in its image creation processes. According to the in-line principle, the hologram ($H(x, y)$) can be expressed as

$$H(x, y) = |I(x, y)|^2 = |R(x, y)|^2 + |O(x, y)|^2 + R^*(x, y)O(x, y) + O^*(x, y)R(x, y), \tag{1}$$

where $|I(x, y)|^2$ is the diffraction image, $R(x, y)$ is the reference wave, $O(x, y)$ is the diffraction of the object, $R(x, y)^2$ the intensity of the reference wave (constant term), and $O(x, y)^2$ is the zero-order diffraction of the object and is very small compared to other terms, so that it can be neglected. $R^*(x, y)O(x, y)$ is the real image and $O^*(x, y)R(x, y)$ is the twin image. The hologram needs to be normalized [51]. For this, the constant DC ($|R(x, y)|^2 \cong |R(x, y)|^2 + |O(x, y)|^2$) term in (1) can be extracted from the hologram intensity data by recording between the sensor and the object plane without an object. It can be normalized with the average intensity value of the background of the hologram data. Normalization or background removal eliminates the inhomogeneous light distribution or unwanted noise in the hologram. In addition, the obtained hologram data can be obtained regardless of the reference wave or the imaging sensor's sensitivity [52]. Therefore, the hologram's real image and twin image terms must remain in the equation to obtain the object information. Thus, the result of background normalization is

$$\widetilde{H}(x, y) = \frac{|I(x, y)|^2}{|R(x, y)|^2} \cong 1 + \frac{R^*(x, y)O(x, y) + O^*(x, y)R(x, y)}{|R(x, y)|^2}. \tag{2}$$

2.2. Microscopy Setup and Imaging Evaluation. Our DIHM setup consists of a light source, pinhole, imaging sensor, and electronic components. All mechanical parts were 3D printed, and electronic components were controlled with a microcomputer. Due to the diffraction phenomenon, short-wavelength illumination sources can achieve higher spatial

resolution [53]. For this reason, a Power LED source of 430 nm wavelength has been used as the light source. The power LED source was driven with a 250 mA constant current source. The microcomputer provides the PWM signal to coordinate the light source with the imaging sensor during hologram acquisition. With the PWM control, the heating of the light source is prevented, and therefore the temperature-dependent change of the wavelength is prevented. A 150 μm diameter laser cut pinhole was placed in front of the LED source to provide spatial filtering and make the light source partially coherent. Sony IMX 219PQ was used as the imaging sensor. The CMOS sensor has a maximum resolution of 3280 × 2464 and a pixel pitch is 1.12 μm. The imaging sensor has an approximately 10mm^2 active sensor area, which is equal to the field of view of the DIHM. All data obtained during the study were collected and processed at this resolution. The medical samples and the calibration slide were placed directly on the imaging sensor. The imaging sensor was connected to the microcomputer with the help of a flex cable, and parameters such as exposure time, gain, and white balance were adjusted. Considering the magnification factor in the produced imaging system, the distance between the sensor and the object (z_2) was chosen as less than 1 cm, and the distance between the imaging sensor and the light source (z_1) was chosen as 6 cm. Figure 1 shows a schematic representation of the DIHM system.

After the light source interacts with the object plane, the interference of the object's diffraction waves and reference waves on the imaging sensor generate the hologram. The hologram and background images collected with the help of the microcomputer were recorded as color images and then transferred to the PC to perform the image processing steps. Since the imaging sensor has a Bayer filter, only the green channel is used to obtain maximum light information. Background data were extracted from the hologram, and images were converted to [0, 255] scale. The normalized hologram data is backpropagated in the z optical axis between the sensor and object planes via the angular spectrum method [47, 54]. The angular spectrum method uses no approximations and is appropriate for small z_2 distances [55]. Fast Fourier transform (FFT) first transferred the hologram to the spatial frequency domain. Then, the hologram in the frequency domain is multiplied by the created transfer function. Finally, the images that have been multiplied in the frequency domain are converted to the spatial domain by inverse fast Fourier transform (IFFT). The angular spectrum method used in creating the transfer function can be mathematically expressed as follows:

$$I(x,y;z) = \mathfrak{F}^{-1}\left\{\mathfrak{F}\{I(x,y;0)\}\exp\left\{i\frac{2\pi z}{\lambda}\sqrt{1-(\lambda f_x)^2-(\lambda f_y)^2}\right\}\right\}, \tag{3}$$

where $\mathfrak{F}$ represents the FFT and $\mathfrak{F}^{-1}$ represents the IFFT. x and y are the spatial coordinates in the image plane, z is the propagation distance, f_x and f_y represent th spectral coordinates in the Fourier space, and λ is the wavelength. $I(x, y; 0)$ is the expression of the hologram's light-intensity field on the imaging sensor and $I(x, y; z)$ the reconstructed image in the optic axis direction.

When creating the transfer function, the distance between the required image sensor and the sample may not be known in some cases. In order to solve this problem, it must be solved numerically by multiplying the transfer function formed from a small reconstruction distance with the hologram. In the study, 50 transfer functions were created with a 10 μm step size, multiplied with a hologram, and the sample images were obtained. Tenenbaum gradient, Brenner gradient, and Tamura gradient of all images were calculated to find the optimum distance through the images [56, 57]. The local maximum values of the calculated functions are taken as the best image. In order to improve the hologram images, methods such as phase retrieval and twin image elimination can be applied to images [58, 59]. However, in this study, these routines were not applied within the scope of the study, and the basic system microscopy scheme was considered.

The standard USAF 1951 resolution target was used to evaluate the resolution capability of our microscopy setup. USAF 1951 target has a maximum of seven groups and six elements. The raw hologram obtained by USAF 1951 is shown in Figure 2(a), the region of interest (ROI) is shown in Figure 2(a), the image resulting from the reconstruction of the ROI is shown in Figure 2(c), and the group is shown in Figure 2(d), the normalized pixel intensity value of group 7 and elements 6 is given. The figures show that the microscope designed for imaging resolves 228.1 (lp/mm).

2.3. Sample Preparation and Data Collection. As for medical data, the most analyzed medical samples in clinics and laboratories were preferred. Human blood cells were imaged as the first medical sample. The sample blood samples used in this study were approved by the Sakarya University Ethics Committee's decision number 050.01.04/291. The participant was healthy laboratory personnel, verbal and written information was given about the study, and the samples were used with permission. Blood samples were prepared in 5 μL, and the samples were placed on a glass slide. MCF-7 breast cancer cell culture was used as a secondary medical sample, and MCF-7 cell culture is one of the most frequently used cell cultures in laboratory research. The MCF-7 cell line was supported and grew with 10% fetal bovine serum and 1% penicillin and incubated at 37°C with 5% CO_2. Trypan blue was added to the cells in a ratio of 1 : 1. It was taken in the same volume as the blood sample and imaged in DIHM. In Figure 3, images of the obtained medical samples and regions of interest are given.

3. The Used Chaotic System, Its Dynamic Analysis, and RNG Design

Edward Lorenz introduced the concept of chaos and the attractor, which is very sensitive to initial conditions, in 1963 [60]. In recent years, developments related to chaotic systems have attracted the attention of researchers [61, 62]. The science of chaos, briefly defined as the order in disorder, is encountered in many applications such as electronics,

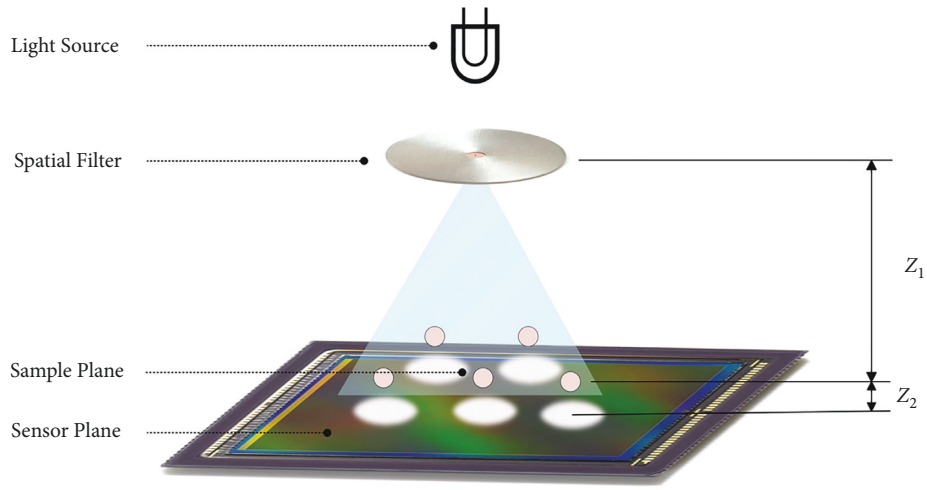

FIGURE 1: Schematic representation of the DIHM system, z_2 distance less than 1 cm and z_1 distance 6 cm.

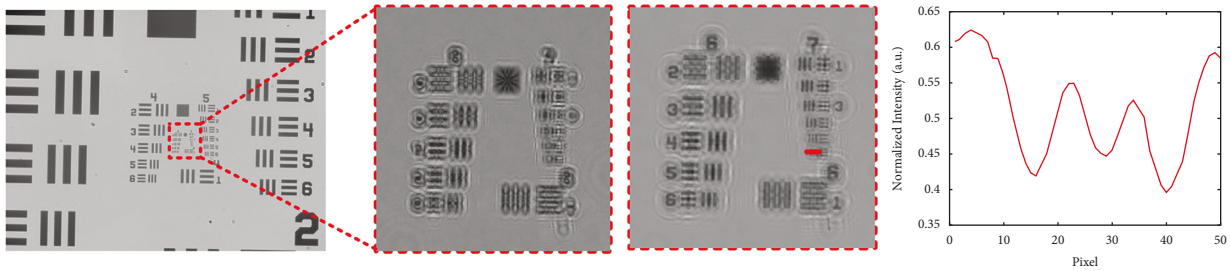

(a) (b) (c) (d)

FIGURE 2: Resolution evaluation of the imaging system: (a) raw hologram data obtained in size 3280 × 2464; (b) the raw hologram of the target region of interest; (c) reconstructed hologram; (d) normalized intensity profile of group 7 element 6.

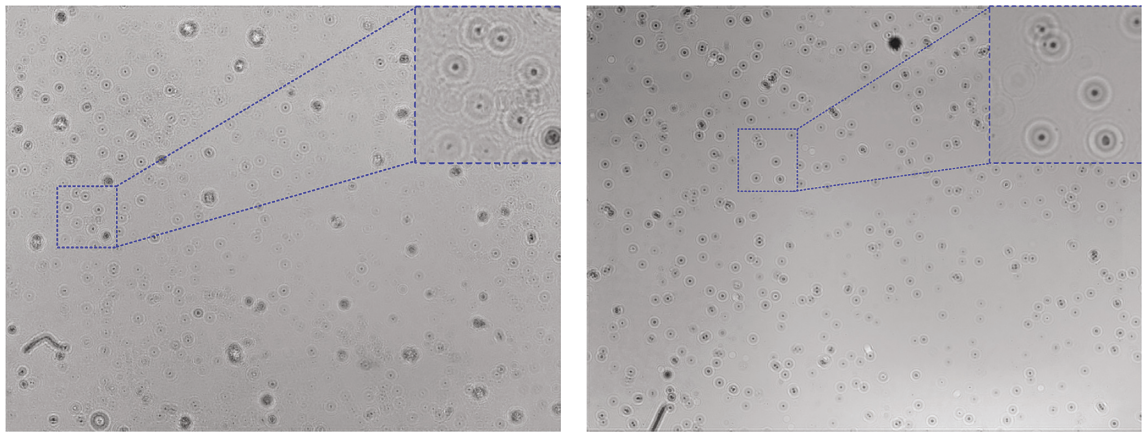

(a) (b)

FIGURE 3: Medical samples were obtained with DIHM. (a) Image of human blood cells and selected ROI. (b) MCF-7 cell line and selected ROI.

computers, control, finance, and health because it is mathematically simple and can be used in practice [63–67].

This section discusses the fundamental dynamic analysis of the chaotic system without equilibrium points used for watermarking. The chaos-based random generator will form the basis of watermarking work and its statistical tests. The equations for the chaotic system without equilibrium points used for the chaos-based random number generator are

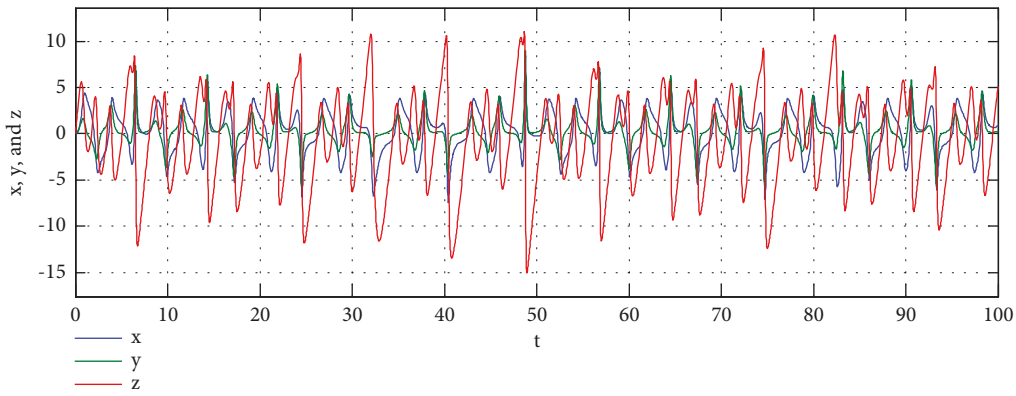

Figure 4: Time series for x, y, and z outputs.

$$\begin{aligned}\dot{x} &= ay - x + zy,\\ \dot{y} &= -bxz - cx + yz + d,\\ \dot{z} &= e - fxy - x^2.\end{aligned} \tag{4}$$

The random numbers required for the watermarking application are generated from chaotic systems. 3D continuous-time chaotic system has six parameters. The values of these parameters are $a = 2.8, b = 0.2, c = 1.4, d = 1, e = 10$, and $f = 2$. In addition, the initial conditions of the chaotic system are $x(0) = 0, y(0) = 0, z(0) = 0$. In other cases, the system may emerge from chaos. In (5), the set of equations can be seen with parameter values entered. The watermarking application generated random numbers according to the parameter values and initial conditions selected in the article study. In order to show that the system is chaotic, some analyzes are given in the article and it is shown that the system is chaotic. With the system that proved to be chaotic, random number generation was made as given in algorithm 1, and the watermarking application was carried out as a result of successful test processes.

$$\begin{aligned}\dot{x} &= 2.8y - x + zy,\\ \dot{y} &= -0.2xz - 1.4x + yz + 1,\\ \dot{z} &= 10 - 2xy - x^2.\end{aligned} \tag{5}$$

3.1. Dynamic Analysis. The time series analysis, sensitivity to initial conditions, and phase portraits of the chaotic system used in the article are shown in Figures 4–6. The sensitivity analysis of the initial conditions shows that the system exhibits different behavior with a minimal change. For this reason, the chosen chaotic system is suitable for essential studies such as encryption, data hiding, and watermarking.

3.2. Random Number Generation. Random numbers are generally divided into pseudo (PRNG) and true (TRNG). If we obtain different random numbers every time we start a system, this system is called TRNG. Because of the production of different random numbers each time, the use of TRNG is, in some cases, not suitable for studies such as encryption. For this reason, PRNG *s* can be preferred to get the same numbers when the system is started from the beginning. In this article, pseudorandom numbers were preferred because the same random numbers were needed when the system was rerun for the watermarking application. The pseudocode for how random numbers are generated is given in Algorithm 1.

If Algorithm 1 is explained, a chaotic system without an equilibrium point selected for the PRNG design is discretized by the RK4 numerical analysis algorithm since it is a continuous-time system. After the discretization process, the obtained point-based numbers were converted to a binary number system. After the conversion process, a 32 bit binary number system is produced for each point-based number. This study created random number sequences by selecting low-significant 16 bit number series from the 32nd bit to the 17th bit of each generated number.

3.3. Statistical Tests. NIST-800-22 statistical tests with the highest standards at the international level were used to measure the randomness performance of the numbers produced. Although the NIST-800-22 tests consist of 16 different tests, a series of numbers consisting of a minimum of 1 Mbit "0" and "1" is required. If one or more NIST-800-22 tests fail, the bit series must be rebuilt and the test repeated. All tests must be successful for the produced series of bits to be successful. The NIST-800-22 Test results are interpreted according to *P* values. The result must be greater than the defined *P*-value for the test to be considered successful. The random bit series created successfully passed this study's NIST-800-22 statistical tests. The chosen chaotic system is three-dimensional. Therefore, three different outputs can be obtained: *x*, *y*, and *z*. However, in this study, the tests were performed only with random numbers obtained from the output "*x*" and the results are given in Table 1.

According to Table 1, all *P* values are greater than 0.001. Therefore, the generated random bit series has successfully passed all NIST-800-22 statistical tests. Generated random numbers can be safely used in encryption, data hiding, and watermarking applications due to the test's success.

Another reliable statistical test, the ENT test, is a test application developed by John Walker that applies various

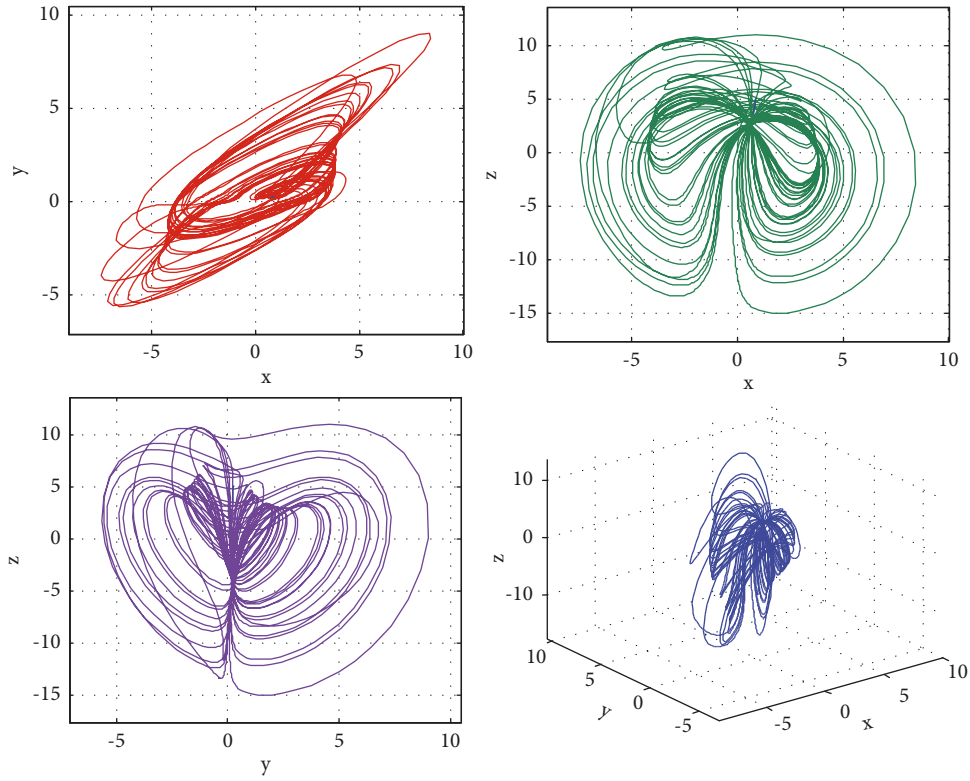

Figure 5: Phase portraits for x-y, x-z, y-z, and x-y-z.

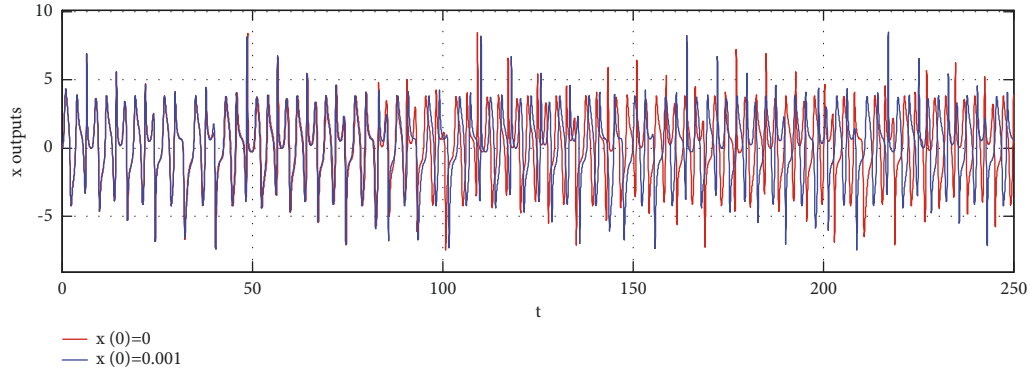

Figure 6: Sensitivity to initial conditions for x output.

tests to byte sequences produced by pseudorandom number generator applications [25]. There are five different statistical tests found in the ENT test that define the randomness of bit sequences. ENT test results mean values of random numbers obtained from output x are given in Table 2. According to Table 2, it was concluded that the random numbers generated from the last 16 bit values of the x output, which passed all tests, provided randomness.

4. DWT-SVD Based Watermarking Application

This section describes watermarking the cover image and removing the watermark from the watermarked image. First, a 256×256 dimensional matrix (selected blocks) is obtained from the high-resolution medical images of blood and cancer cells through chaos-based random numbers. In other words, it forms the $B \in R^{M \times M}$ matrix, we call selected blocks, which consists of randomly selected pixels that we obtained from the large-size image we call cover image (C). R-level wavelet transform algorithm is applied to this obtained image. The watermarking process uses singular value decomposition (SVD) for the $M \times M$ size image to be watermarked and the $N \times N$ size watermark. In the continuation of this section, details of the discrete wavelet transform, singular value decomposition, and watermarking algorithm are given.

4.1. Generating Selected Blocks Matrix from Cover/Watermarked Cover Image. This study hides the watermark in the B matrix created from the pixels selected with CBRNG from the original image. Then, this matrix with a watermark is

Input: System Parameters ($a = 2.8$, $b = 0.2$, $c = 1.4$, $d = 1$, $e = 10$, $f = 2$), Initial condition (x(0) = 0, y(0) = 0, z(0) = 0)
Output: Chaos-Based Random Numbers (CBRNG)
(1) Start
(2) Determination of the appropriate value of Δh (0.05)
(3) while minimum 1Mbit data do
    Solving the chaotic system using the RK-4 algorithm
    Obtaining time series
    Convert float to binary
    Select "$s = 16$" bit LSB
  end while
(4) Apply randomness tests
(5) if test results = = pass then
    Ready-tested random numbers for engineering application
  else
    Test results = = false
    return Start
  end if
(6) Exit.

Algorithm 1: Chaos-Based Random Number Generator (CBRNG).

Table 1: RNG NIST-800-22 tests with a 3D chaotic system without equilibrium points.

Statistical tests	P value (x)	Result
Frequency (monobit) test	0.6326	Successful
Block-frequency test	0.4965	Successful
Cumulative-sums test	0.6356	Successful
Runs test	0.0684	Successful
Longest-run test	0.8196	Successful
Binary matrix rank test	0.1178	Successful
Discrete Fourier transform test	0.7342	Successful
Nonoverlapping templates test	0.0053	Successful
Overlapping templates test	0.2708	Successful
Maurer's universal statistical test	0.2039	Successful
Approximate entropy test	0.6650	Successful
Random excursions test	0.4787	Successful
Random excursions variant test	0.6745	Successful
Serial test 1	0.5894	Successful
Serial test 2	0.6463	Successful
Linear complexity test	0.3089	Successful

placed on the cover image, pixel by pixel, to its previous positions with CBRNG. In this way, it is aimed to discover watermarking difficult.

According to Figure 7, random numbers were generated (CBRNG) with the proposed chaotic system according to the size (256×256) of the B matrix to be obtained. Then, the N-dimensional RNG array was obtained. In Figure 7, the B matrix is created by selecting the green pixel values of the CBRNG array of the cover image. With the watermark hidden in the B matrix with the proposed method, the 256×256 matrix B with the watermark shown in red in Figure 7 is obtained. As a result of the watermarking, the watermarked matrix is repositioned to the CBRNG array pixels marked in red. Since the watermarking process is performed on random numbers indicated by the CBRNG series, the chaotic system that makes up the CBRNG number system must be known to obtain the secret watermark.

The algorithm's pseudocode for generating the B matrix in the proposed chaos-based RNG watermarking method is given in Algorithm 2.

According to Algorithm 2, the width (Width1) and height (Height1) values of matrix B are taken as input. Then, the cover image (img1) to be processed is selected, and the width (Width) and height (Height) values are read. By selecting the RNG file, the CBRNG sequence is divided into two: CBRNG X and Y. The values in the CBRNG array are checked and parsed as repetitive values. This is to avoid using the same location twice, thanks to unique values. The elements of the CBRNG X array are normalized with the width value and the elements of the CBRNG Y array with the height value, so the array number values are adjusted according to the width and height limit of the original image. An empty array is created according to the desired Width1 and Height1 values for the B matrix to be obtained. Two nested loops are created. It starts from the first row and first column of matrix B. All the image pixels are processed until the outer loop to the value of Height1 in the first iteration and the value of Width1 in the first iteration of the inner loop. In Algorithm 2, the outer loop variable i shows the rows in the cover image; if the inner loop variable j shows the column row, CBRNG Y shows the rows, and CBRNG X shows the random number generator values for the columns. In each step of the loop, the pixel of the cover image is taken at the position determined by the CBRNG sequence and placed in the next pixel of the B matrix. This process continues until all pixels of matrix B have been generated.

4.2. Obtaining Cover/Watermarked Cover Image from Selected Blocks Matrix. In the proposed chaos-based CBRNG watermarking method, the flow diagram of the algorithm for placing the watermarked matrix B back to its previous positions in the cover image is given in Algorithm 3. By selecting the watermarked matrix B to be obtained according to Algorithm 3, the width (Width1) and height (Height1)

Table 2: ENT test results of random numbers obtained from x output.

Test name	Average	Ideal results	Result
Arithmetic mean	127.4068	127,5	Successful
Entropy	7.9985	8	Successful
Correlation	0.0012006	0	Successful
Chi-square	252.137	Between 10% and 90%	Successful
Monte Carlo	3.1331 (error = 0.0027013)	Pi number	Successful

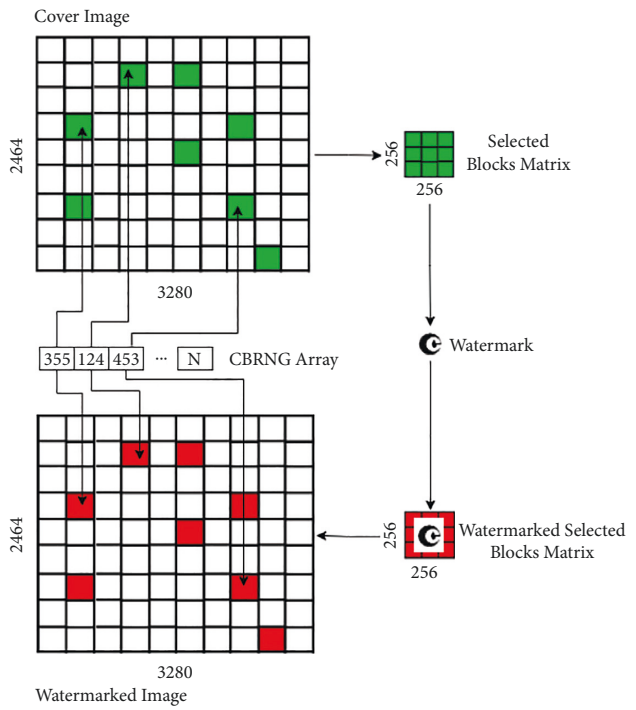

Figure 7: Working principle of the proposed chaos-based RNG watermarking method.

values are read. Then, by selecting the cover image (img1) to be processed, the width (Width) and height (Height) values are obtained. By selecting the CBRNG file, the CBRNG sequence is divided into two CBRNG X, and Y. Duplicate values are parsed by checking the values in the CBRNG array. This avoids using the same location twice, thanks to unique values. The elements of the CBRNG X array are normalized with the width value, and the elements of the CBRNG Y array with the height value so that the array number values are set according to the width and height limit of the original image. Two nested loops are created. It starts from the first row and first column of matrix B. All the image pixels are processed until the outer loop to the value of Height1 in the 1st iteration and the value of Width1 in the 1st iteration of the inner loop. In Algorithm 3, the outer loop variable i represents the rows in the original image; if the inner loop variable j is the column row, CBRNG Y represents the rows, and CBRNG X represents the random number generator values for the columns. At each step of the loop, the pixel of matrix B in the j column position of the i row is taken and placed in the cover image pixel at the position determined by the CBRNG array. This process continues until all the indices of the watermarked matrix B have been placed back. Thus, a watermarked image is obtained by using CBRNG from matrix B. This process is also used in the watermarking and watermark removal algorithm.

4.3. DWT and SVD Methods. Discrete wavelet transform is one of the most basic methods that transform digital images from the spatial domain to the frequency domain. DWT is a feature extraction technique that allows the processing of images at different resolutions. It is especially preferred in watermarking research because it is resistant to attacks applied to the image [68]. In this study, R-level DWT, which considers the size of the selected blocks matrix and the watermark size, is used. Here, R is determined according to the result of the expression $\log_2(M/N)$. For example, if $M = 512$ and $N = 128$, $R = 2$. Therefore, 2-level DWT is applied. After the DWT process, LL for low frequency, HL for horizontal mid-frequency, LH for vertical mid-frequency, and HH for high frequency are obtained. Performing the DWT process R times on these subbands obtained from the previous DWT operation is called R-LEVEL DWT. For example, Figure 8 shows the subbands obtained due to 1-level DWT and 2-level DWT.

Singular value decomposition (SVD), mainly used for dimension reduction in signal processing studies, is preferred in watermarking because it is more resistant to attacks. Assuming $A \in \mathbb{R}^{m \times n}$ and $m > n$, A is factored by the SVD operation as shown in the following equation:

$$A = U\Sigma V^T. \tag{6}$$

The matrices U and V here are orthogonal and satisfy the conditions $UU^T = U^TU = I$ and $VV^T = V^TV = I$, respectively. The Σ is a diagonal matrix, and it satisfies the condition $\sigma_1 > \sigma_2 > , \ldots , > \sigma_m$, the diagonal elements being $\sigma_1, \sigma_2, \ldots, \sigma_m$, respectively.

4.4. Proposed Watermarking Scheme. In this article, numbers produced by a chaos-based number generator and watermarking techniques were combined to protect medical confidentiality, and digital watermarking was made on medical images. The study considers a new binary watermarking scheme that includes encryption to improve medical images' tenure, protection, and robustness. The security feature of the proposed watermarking technique is enhanced by chaos-based and uniquely number generation. The watermarked primary image is encrypted using the chaos-based encryption technique. It is then placed in the image and transmitted. The chaotic encryption scheme

```
    Input: Cover/Watermarked Image
    Output: Selected Block Matrix (B)
(1) Start
(2) Read Cover Image (img1)
(3) Get Width and Height from img1
(4) Select CBRNG file
(5) Divide CBRNG numbers by CBRNG X and CBRNG Y
(6) Normalize the values in the CBRNG X array by modulo with Width
(7) Normalize the values in the CBRNG Y array by modulo with Height
(8) Discard repetitive values in CBRNG X and Y
(9) Get Width1 and Height1 from B
(10) Create an array of size B
(11) for i = 1: Height1: 1
        for j = 1: Width1: 1
        B(i, j) = img1(CBRNG Y(i), CBRNG X(j))
     end for
(12) Return B
(13) End
```

Algorithm 2: Generating the Selected Blocks Matrix.

```
    Input: Cover Image, B*
    Output: Watermarked Image (C*)
(1) Start
(2) Read Cover Image (img1)
(3) Get Width and Height from img1
(4) Select CBRNG file
(5) Divide CBRNG numbers by CBRNG X and CBRNG Y
(6) Normalize the values in the CBRNG X array by modulo with Width
(7) Normalize the values in the CBRNG Y array by modulo with Height
(8) Discard repetitive values in CBRNG X and Y
(9) Get array B*
(10) Get Width1 and Height1 from B*
(11) for i = 1: Height1: 1
        for j = 1: Width1: 1
        img1(CBRNG Y(i), CBRNG X(j)) = B* (i,j)
     end for
(12) Create C* from img1 array
(13) Return C*
(14) End
```

Algorithm 3: Generating the Watermarked Image.

provides a large key space and high key precision, and the password can resist brute force attacks and statistical analyses. The proposed method is secure against third-party attacks and can meet the need for image encryption. A reliable watermark decryption scheme and an extraction scheme for both the primary and secondary watermark are established to remove the watermark. In the proposed method, the watermark is hidden in the image created by selecting random pixels with the numbers produced by RNG from the original image with medical content. The 8 bit images containing human blood and cancer cell samples were used. In the method, first, the watermark is hidden in the image created from the pixels selected with RNG from the original image. Then, the watermarked image is placed on the original image with RNG, pixel by pixel, to its previous positions. In this way, the method makes watermark detection difficult and makes it difficult to discover the watermark. The watermarked image recreated at the end of the method is not distinguishable from the original image. The watermark can be removed lossless from the watermarked image. The RNG sequence created through the chaotic system is needed for the watermark extraction process. By operating the chaotic system with the same initial conditions at the receiving end, the same RNG sequence can be produced, or a standard RNG sequence can be used. RNG sequence can be considered the proposed method's chaotic encryption algorithm. Different encryptions can be made by changing the RNG sequence. This

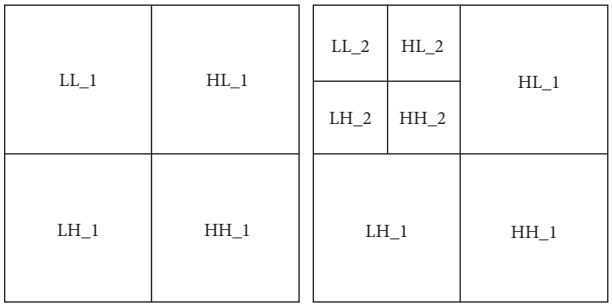

Figure 8: 1-level DWT and 2-level DWT.

increases the system's security and prevents malicious people from destroying the watermark.

In the next section, watermarking embedding and watermarking extraction algorithms are explained. In this algorithm, the cover image, selected block obtained with chaos-based random numbers, and the watermark are represented by $C \in \mathbb{R}^{x\times y}$, $B \in \mathbb{R}^{m\times m}$, and $W \in \mathbb{R}^{n\times n}$, respectively. After the watermarking embedding, $C^* \in \mathbb{R}^{x\times y}$ and $B^* \in \mathbb{R}^{m\times m}$ are obtained. After the watermarking extraction, $W^* \in \mathbb{R}^{n\times n}$ is obtained. Here, the condition $\forall x \forall y\,(x \geq m \geq n \wedge y \geq m \geq n)$ is met.

4.4.1. Watermarking Embedding Algorithm. First, B is obtained from the cover image (C) using CBRNG. In the second step, R-level DWT is applied to matrix B. The SVD is applied to the R^{th} LL (LL_R) obtained with the R-level DWT. U_B, Σ_B and V_B^T are obtained from this process. Also, singular value decomposition is applied to the W matrix and U_W, Σ_W and V_W^T matrices are obtained. Σ_B^* is obtained by taking into account the singular values (Σ_B and Σ_W) and the scaling factor (α) in

$$\Sigma_B^* = \Sigma_B + \alpha\Sigma_W. \tag{7}$$

In (8), using Σ_B^*, U_B, and V_B^T, LL_R^* is obtained.

$$LL_R^* = U_B\Sigma_B^*V_B^T. \tag{8}$$

With LL_R^*, the reverse of the R-level DWT process is applied and B^* is obtained. Then, using B^* and CBRNG, the pixels in C are updated and C^* is obtained. The watermarking embedding process is explained step by step in Algorithm 4. Figure 9 shows the proposed watermarking embedding scheme.

4.4.2. Watermarking Extraction Algorithm. In this algorithm, Watermarked hologram Image (C^*) and the CBRNG used in the watermarking embedding algorithm are taken as inputs. As the output, the extracted watermark W^* is obtained. As in the watermarking embedding algorithm, the watermarked selected block (B^*) is obtained from the C^* image using the same CBRNG.

Then, R-level DWT is applied to the B^* matrix and LL_W^*, HL_W^*, LH_W^* is obtained. SVD is applied to the LL_W^* and U_E, Σ_E and V_E^T matrices are obtained. Then, the singular

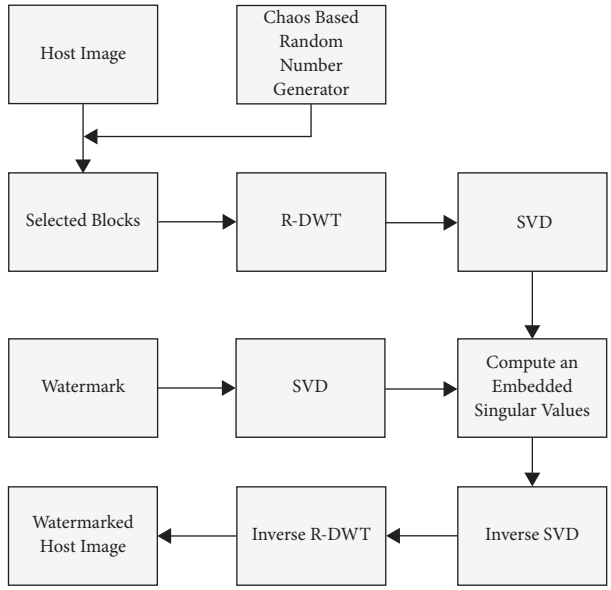

Figure 9: Proposed watermarking embedding scheme.

values of the watermark are extracted using the Σ_B obtained during watermarking embedding process with

$$\Sigma_W^* = \frac{(\Sigma_E - \Sigma_B)}{\alpha}. \tag{9}$$

Using the Σ_W^* and U_W, and V_W^T, the extracted watermark W^* is obtained by equation (10). The watermarking extraction process is explained step by step in Algorithm 5. Figure 10 shows the proposed watermarking extraction scheme.

$$W^* = U_W\Sigma_W^*V_W^T. \tag{10}$$

5. Experimental Results and Safety Analysis

In this section, performance tests were conducted to analyze the invisibility and the robustness of the proposed technique in this study. The human blood and cancer cell line images shown in Figure 11 are used as the cover image. The textual data in Figure 12(a) for blood images and Figure 12(b) for cancer images were used as watermarks. The QR codes as the visual representation of the texts given in Figures 12(a) and 12(b) are shown in Figure 13, respectively. All of the experiments were carried out on a Workstation with an Intel dual-core 2.7 GHz CPU with 32 GB of RAM, using the MATLAB R2018b version.

The proposed model's time complexity is relatively low, considering that the watermark size is much smaller than the cover image size. The size of the watermark image is $a \times b$. Here the condition $a > b$ and $a < \min(m, n)$ is satisfied. Accordingly, the time complexity of the proposed method is ab^2. Here, a and b values are smaller than the dimensions of the cover image (m and n). The a and b values are very small relative to the dimensions of the cover image (m and n). Therefore, the time complexity of the proposed algorithm is not dependent on the size of the cover image.

Input: Cover Image (C), Watermark Image (W), scaling factor (α)
Output: Watermarked Hologram Image (H^*)
(1) Start
(2) B = Generating the Selected Blocks Matrix (C)
(3) $[LL_R, HL_R, LH_R$ ve $HH_R] = R\_\text{Level\_DWT(B)}$
(4) SVD is applied to the LL_R and U_B, Σ_B and V_B^T are obtained.
(5) SVD is applied to the W and U_W, Σ_W and V_W^T are obtained.
(6) $\Sigma_B^* = \Sigma_B + \alpha\Sigma_W$
(7) $LL_R^* = U_B\Sigma_B^* V_B^T$
(8) B^* = InverseRlevelDWT$(LL_R^*, HL_R, LH_R HH_R)$
(9) C^* = Generating the Watermarked Image (C, B^*)
(10) return C^*.
(11) End.

Algorithm 4: Watermarking Embedding Algorithm.

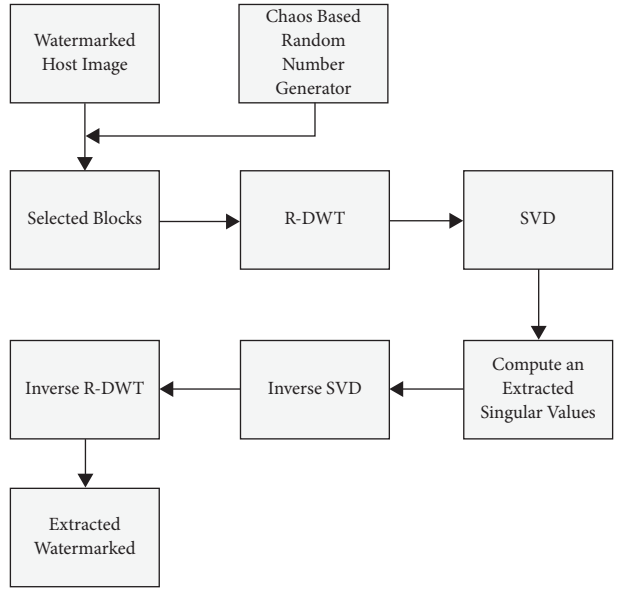

Figure 10: Proposed watermarking extraction scheme.

Input: Watermarked Cover Image (C^*)
Output: Extracted watermark (W^*)
(1) Start
(2) B^* = Generating the Selected Blocks Matrix (C^*)
(3) $[LL_W^*, HL_W^*, LH_W^*, HH_W^*] = R\_\text{Level\_DWT}\ (B^*)$
(5) SVD is applied to the LL_W^* and U_E, Σ_E ve V_E^T are obtained.
(6) $\Sigma_W^* = (\Sigma_E - \Sigma_B)/\alpha$
(7) $W^* = U_W\Sigma_W^* V_W^T$
(8) return W^*.
(9) End.

Algorithm 5: Watermarking Extraction Algorithm.

The chaos-based random numbers were used to cope with the false positive problem encountered in the SVD technique used in the study. Tests were carried out to see if the proposed model was resistant to false positive problems. Table 3 provides the images and robustness results of the extracted watermark in cases where the chaotic keys are entered correctly or incorrectly. The results were obtained using the blood cell cover image and a 256×256 watermark. It is understood from the table that the watermark was not extracted correctly in all rows except the first row, where the

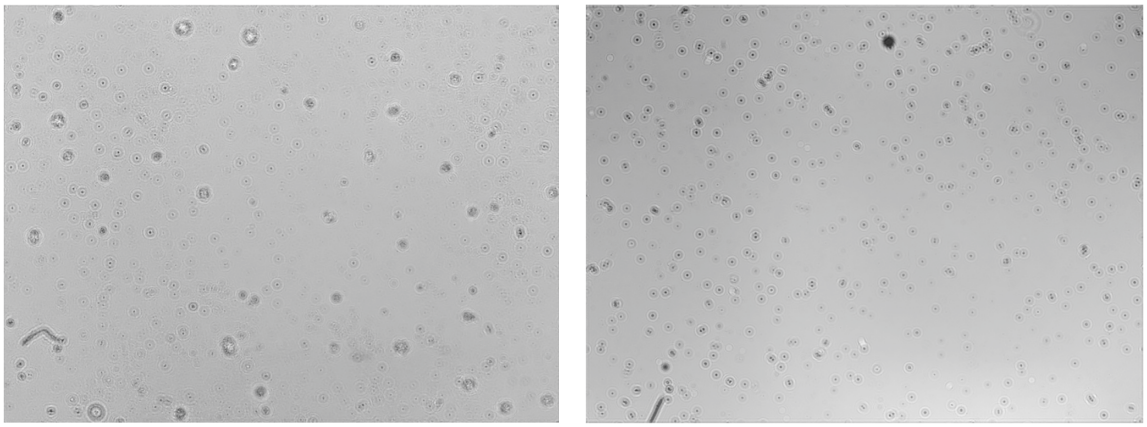

(a) (b)

Figure 11: Sample blood and cancer cell images (256 × 256).

TESTDATE:30.04.2021
ID:12345
PATIENTNUMBER:182654
NAME: MUHAMMED ALI
SURMANE:PALA
SEX:M
DATE OF BIRTH:01.01.1994
PHONE NUMBER:+90264295
ALLERGIES:NONE
ADRESS:NONE

(a)

CELL LINE NAME: MCF7
SPECIES: HUMAN
DOUBLING TIME: 25.4
DISEASE: ADENOCARCINOMA
CULTURE: ADHERENT
VIABILITY PROTOCOL: WST-1
OTHER INFORMATON: NONE

(b)

Figure 12: Watermark texts (a) for cancer cell image and (b) blood image.

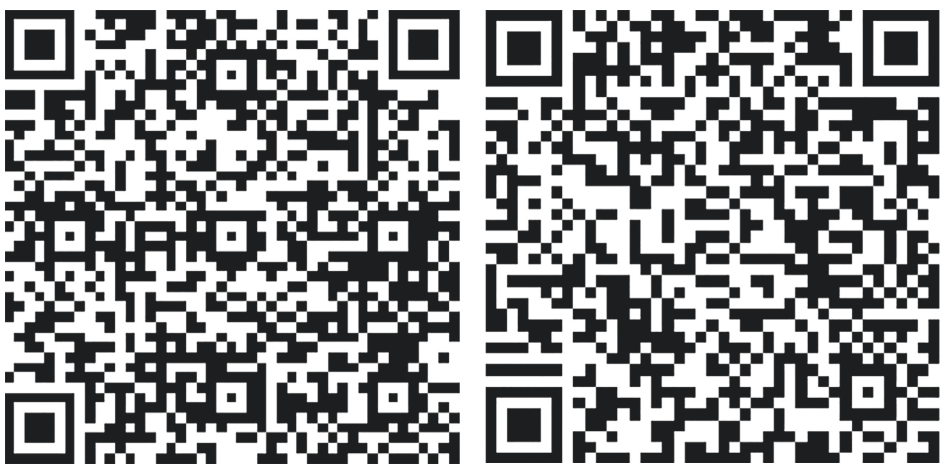

(a) (b)

Figure 13: Watermark QR codes (256 × 256). (a) Watermark QR code for blood images and (b) cancer cell line images.

Table 3: FPP analysis result.

System parameters	Initial condition	NC
$a = 2.8,\ b = 0.2,\ c = 1.4,\ d = 1,\ e = 10,\ f = 2$	$x0 = 0,\ y0 = 0,\ z0 = 0$	1
$a = 1.8,\ b = 0.2,\ c = 1.4,\ d = 1,\ e = 10,\ f = 2$	$x1 = 1,\ y0 = 0,\ z0 = 0$	0.5912
$a = 1.8,\ b = 0.4,\ c = 1.4,\ d = 1,\ e = 10,\ f = 2$	$x1 = 1,\ y0 = 1,\ z0 = 0$	0.5221
$a = 1.8,\ b = 0.4,\ c = 1.0,\ d = 1,\ e = 10,\ f = 2$	$x1 = 1,\ y0 = 1,\ z0 = 1$	0.4766
$a = 1.8,\ b = 0.4,\ c = 1.0,\ d = 2,\ e = 10,\ f = 2$	$x1 = 1,\ y0 = 1,\ z0 = 1$	0.4643
$a = 1.8,\ b = 0.4,\ c = 1.0,\ d = 2,\ e = 5,\ f = 2$	$x1 = 1,\ y0 = 1,\ z0 = 1$	0.4539
$a = 1.8,\ b = 0.4,\ c = 1.0,\ d = 2,\ e = 5,\ f = 1$	$x1 = 1,\ y0 = 1,\ z0 = 1$	0.4304

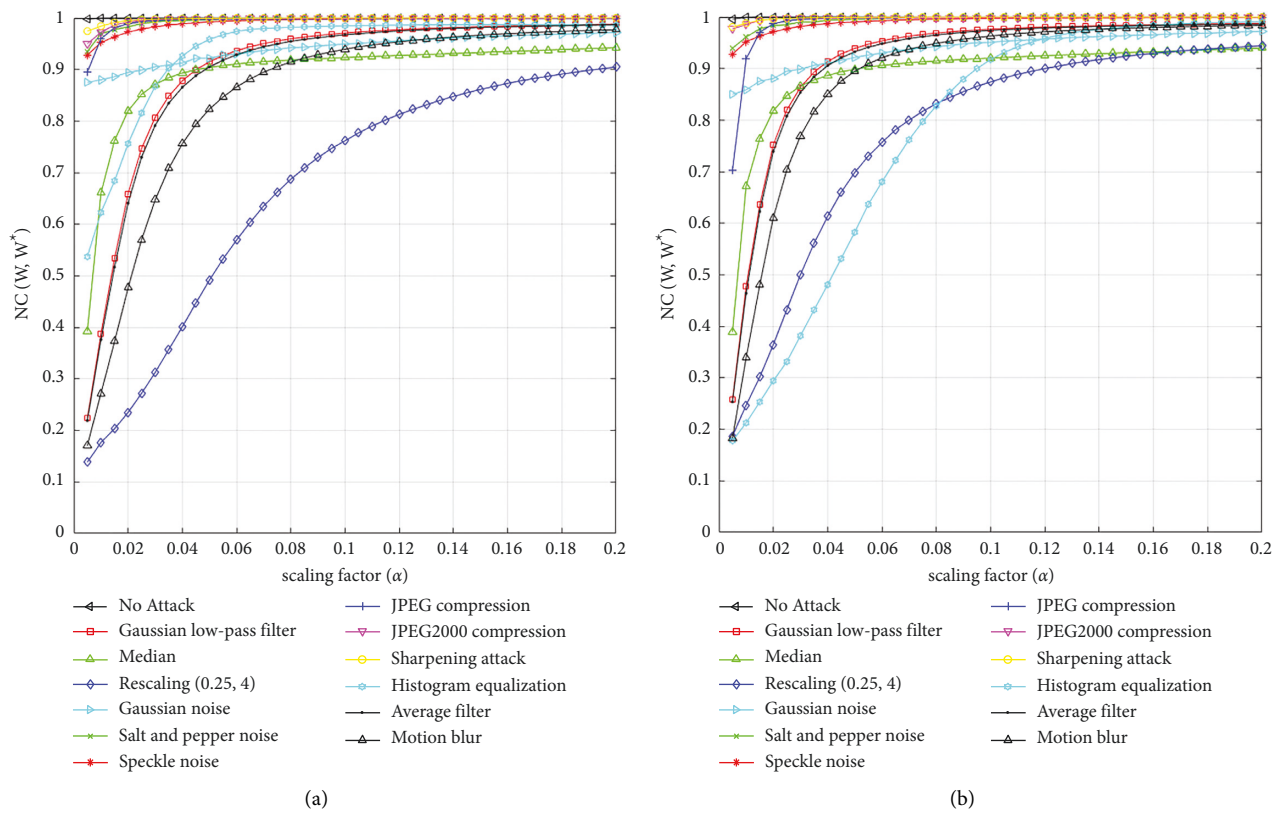

Figure 14: NC results of tests under different attacks according to scaling factor change. (a) Human blood. (b) Cancer cell line.

correct keys were entered. Accordingly, it is impossible to extract the watermark for someone who does not know the keys of the random number generator and the chaos function used in the proposed model.

In order to obtain the best performance in the watermarking algorithm, the optimal scaling factor must be found. Normalized correlation (NC) is used for watermark robustness for performance analysis. In contrast, peak signal-to-noise ratio (PSNR) and structural similarity index measure (SSIM) metrics measure watermark imperceptibility. The calculation of the NC is shown in the following equation.

$$\mathrm{NC}(W, W^*) = \frac{\sum_{i=1}^{N}\sum_{j=1}^{N} W_{i,j} W^*_{i,j}}{\sqrt{\sum_{i=1}^{N}\sum_{j=1}^{N} W^2_{i,j}}\sqrt{\sum_{i=1}^{N}\sum_{j=1}^{N} W^{*2}_{i,j}}}. \tag{11}$$

Equations for calculating MSR, PSNR, and SSIM metrics are

$$\mathrm{MSE}(C, C^*) = \frac{\sum_{i=1}^{N}\sum_{j=1}^{N}\left(C_{i,j} - C^*_{i,j}\right)}{M^2}, \tag{12}$$

$$\mathrm{PSNR}(C, C^*) = 10\log_{10}\frac{C^2_{\max}}{MSE(C, C^*)}, \tag{13}$$

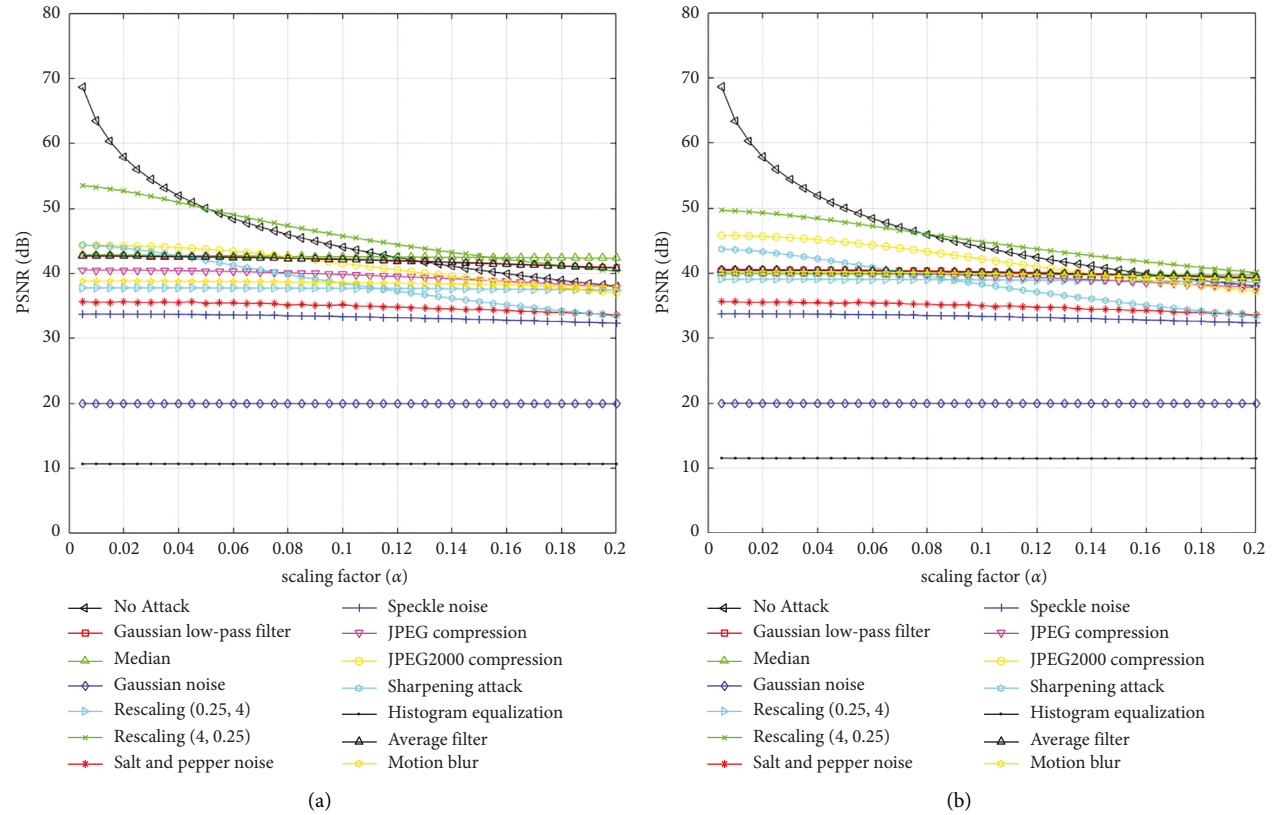

Figure 15: PSNR results of tests under different attacks according to scaling factor change. (a) Human blood. (b) Cancer cell line.

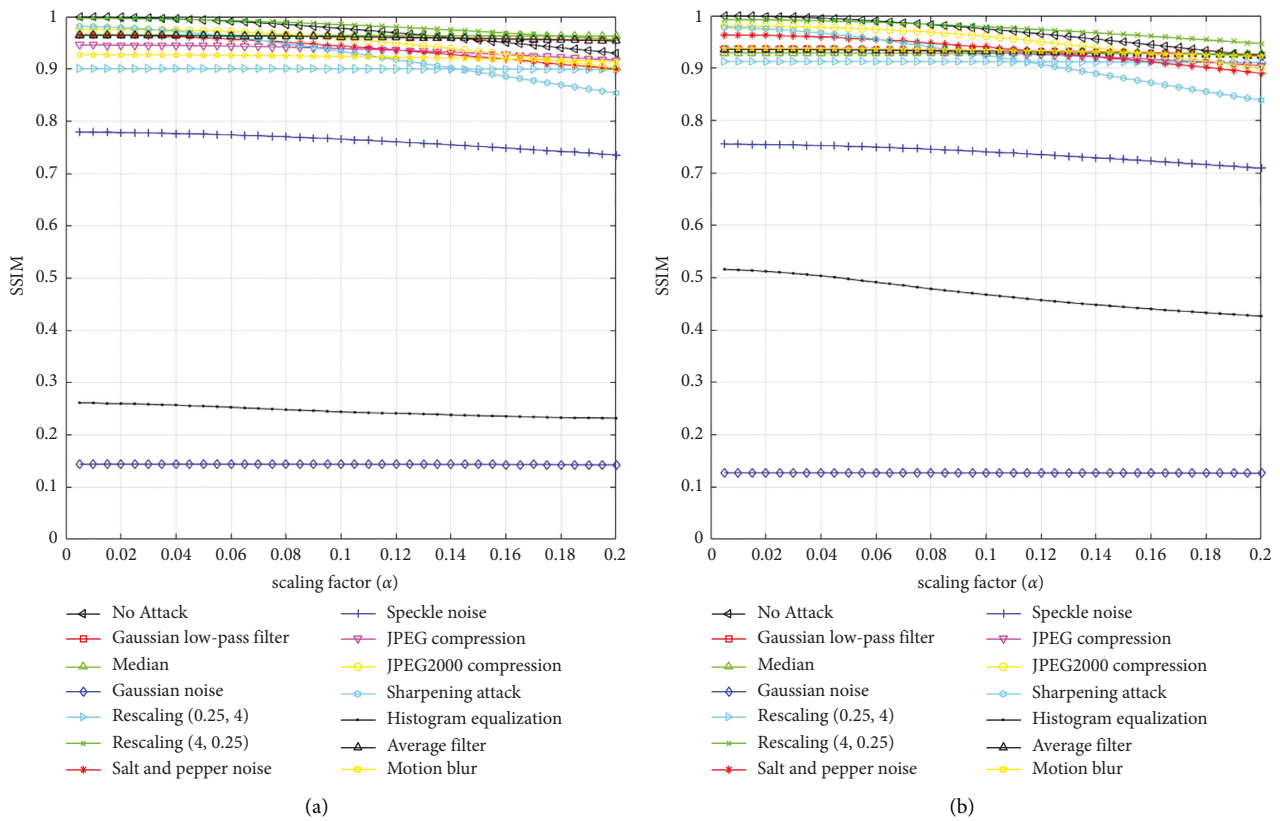

Figure 16: SSIM results of tests under different attacks according to scaling factor change. (a) Human blood. (b) Cancer cell line.

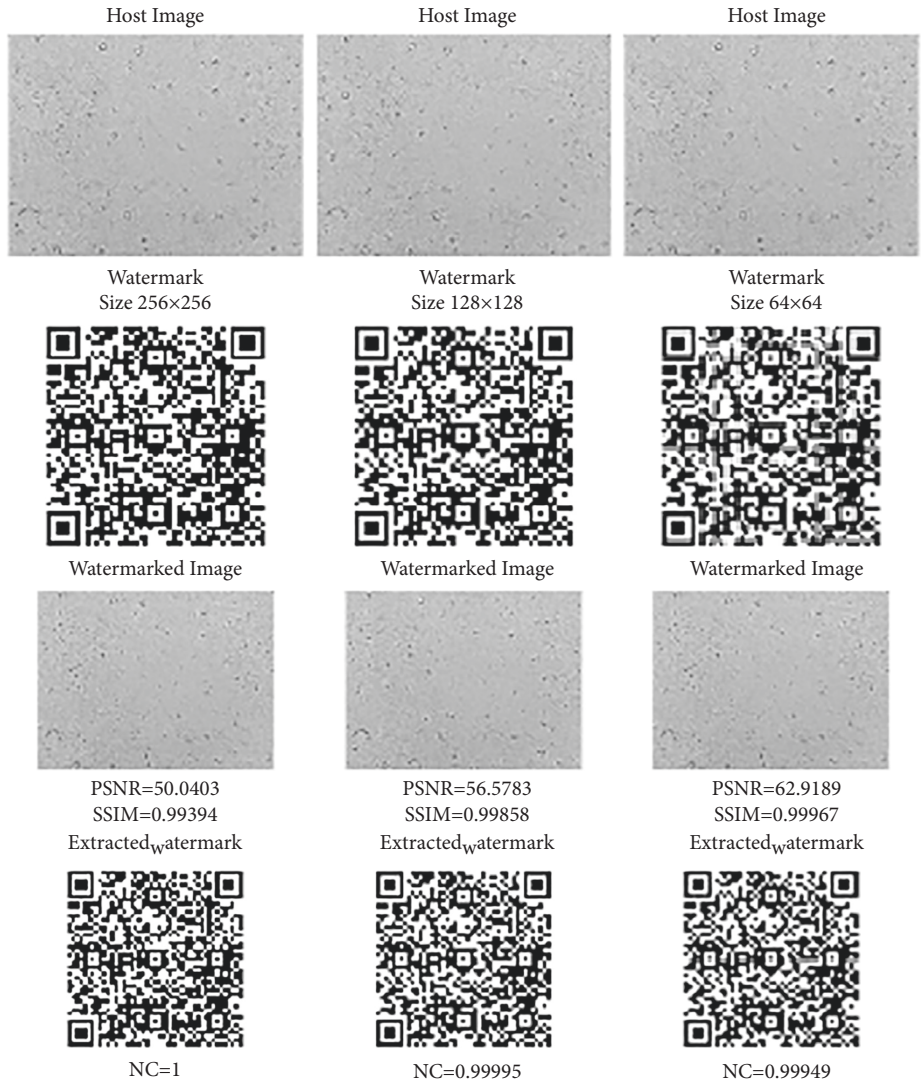

Figure 17: Invisibility performance of blood image.

$$\mathrm{SSIM}\left(C, C^*\right) = \frac{2\mu_c\mu_{c^*} + v_1}{\mu_C^2 + \mu_{C^*}^2 + v_1} \cdot \frac{\alpha_{CC^*} + v_2}{\alpha_C^2 + \alpha_{C^*}^2 + v_2}. \tag{14}$$

The μ_c and μ_{c^*} in the equations are the mean of C and C^*, respectively. α_C^2 and $\alpha_{C^*}^2$ are the variances of C and C^*. v_1 and v_2 are two variables used to balance the partition with a weak denominator. Finally, α_{CC^*} is the covariance of C and C^*.

For the robustness and invisibility analysis of the watermark, three forms of watermarks (64×64, 128×128, and 256×256) were used. The best scaling factors for all three forms and each cover image were determined by considering the changes in NC, PSNR, and SSIM metrics. For the robustness analysis, various attacks were applied to the watermarked image, and the watermark's invisibility was examined. In addition, robustness analyses were performed on the watermark extracted from the watermarked image. The applied attacks are basically noise (Gaussian, salt and peppers, and speckle noises), filter (median, Gaussian low-pass, and average), compression (JPEG with quality factor (QF) 50 and JPEG2000 with compression ratio (CR) 12), rescaling (0.25, 4), histogram equalization (HE), sharpening (threshold = 0.8), and motion blur (with Theta = 4, Len = 7) attacks.

It is necessary to analyze the durability of watermark and the cover image's imperceptibility to determine the optimum scaling factor. For this, both NC values, as well as PSNR and SSIM metrics, were examined. Accordingly, cases where all three metrics are good can be selected as the scaling factor. In order to determine the optimum scaling factor, NC change under various attacks is shown in Figure 14 for blood and cancer cell line images, respectively. PSNR and SSIM results are also shown in Figures 15 and 16, respectively. When the changes are examined, the NC value increases as the alpha increases, while the PSNR and SSIM results decrease. In cases where noisy attacks such as Gaussian noise, speckle noise, salt and pepper noise, compression, and sharpening attacks are applied, the results give good results even at smaller alpha values. For example, relevant results

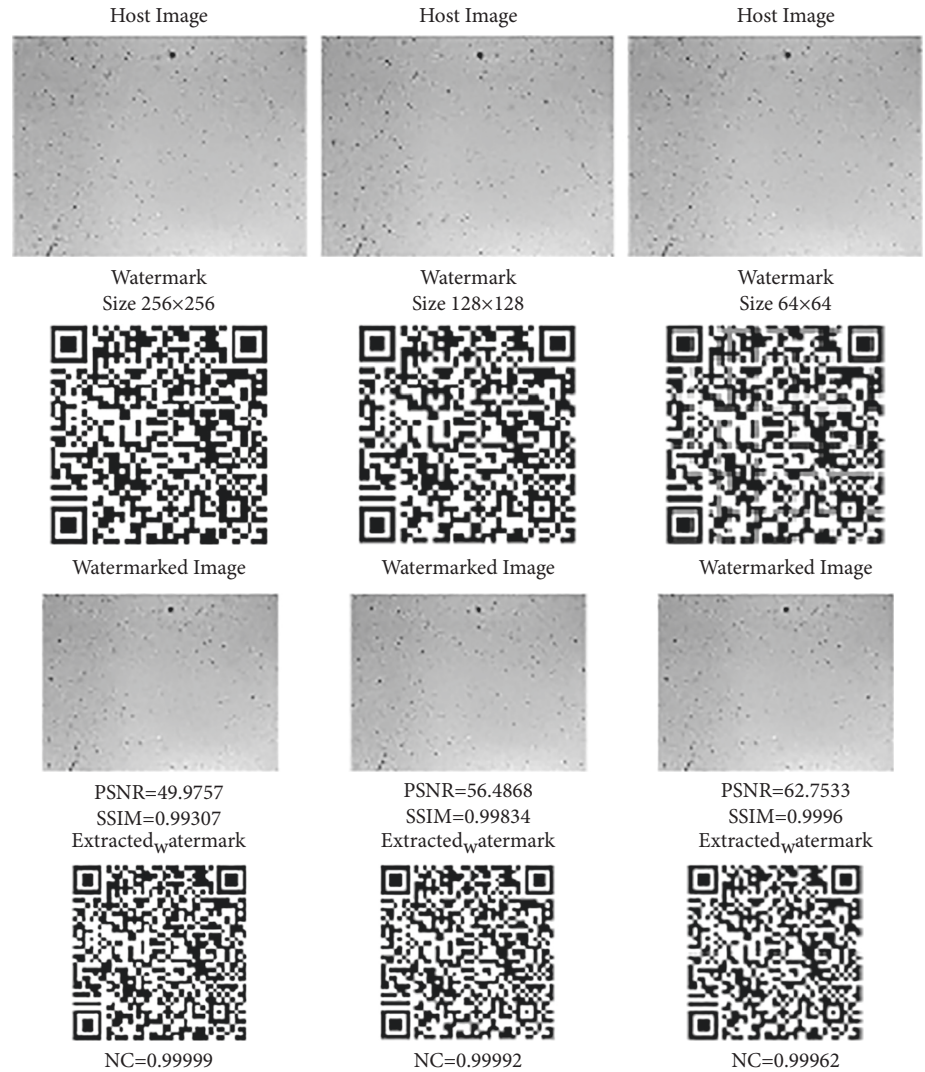

Figure 18: Invisibility performance of cancer cell line image.

were obtained when these attacks were applied even when $\alpha = 0.01$.

Another issue to be measured in watermarking studies is invisibility. The fact that people cannot notice the watermarked information is essential for the security of the data. In this case, it is aimed that the watermarked image obtained after watermarking does not look much different from the original. For this reason, invisibility measurement is essential in order not to understand the watermark in the watermarked image. Figures 17 and 18 show the invisibility and robustness results obtained for exemplary blood and cancer cell line images, respectively. The watermark texts were transformed into QR codes in 256×256, 128×128, and 64×64 sizes. Here, the performance results after these three different watermarking are listed.

When Figures 17 and18 are examined, 100% successful access to the texts is achieved from the QR codes obtained. The literature states that acceptable invisibility is when the measured values for invisibility are PSNR>0.37 dB and

Table 4: The robustness performance of the watermarked blood image obtained using different-sized watermarks.

Attack	Watermark size		
	256×256	128×128	64×64
No attack	1	0.99999	0.99994
Gaussian low-pass filter	0.98809	0.96782	0.95473
Median	0.94269	0.92397	0.94444
Gaussian noise	0.97201	0.97087	0.98694
Rescaling (0.25, 4)	0.90461	0.88459	0.86823
Rescaling (4, 0.25)	0.99985	0.99956	0.99923
Salt and pepper noise	0.99971	0.99973	0.99961
Speckle noise	0.9994	0.99933	0.99948
JPEG compression	0.99875	0.99353	0.97793
JPEG2000 compression	0.99959	0.99915	0.99391
Sharpening attack	0.99995	0.98755	0.98443
Histogram equalization	0.98631	0.97033	0.96303
Average filter	0.98684	0.96459	0.94941
Motion blur	0.9775	0.95125	0.93015

Table 5: The robustness performance of the watermarked cancer cell line image obtained using different-sized watermarks.

Attack	Watermark size		
	256 × 256	128 × 128	64 × 64
No attack	0.99988	0.99999	0.99996
Gaussian low-pass filter	0.98733	0.97427	0.96717
Median	0.93992	0.93212	0.94764
Gaussian noise	0.97206	0.96799	0.98251
Rescaling (0.25.4)	0.94459	0.89711	0.87132
Rescaling (4.0.25)	0.99944	0.99947	0.99914
Salt and pepper noise	0.99953	0.99954	0.99955
Speckle noise	0.99899	0.99925	0.99944
JPEG compression	0.99919	0.99268	0.97928
JPEG2000 compression	0.99943	0.99915	0.99740
Sharpening attack	0.9997	0.98721	0.98400
Histogram equalization	0.9911	0.84563	0.83418
Average filter	0.98625	0.97174	0.96350
Motion blur	0.98371	0.9686	0.95394

SSIM>0.93. When all the images here are examined, it is observed that a value far above these limits is obtained. In addition, if the QR code images are taken into account, it has been observed that the NC results of the recalled watermarks are very close to 1.

Tables 4 and 5 provide the normalized correlation (robustness) of images against various attacks. Here, 256 × 256, 128 × 128, and 64 × 64 sized QR codes were watermarked separately, and the results were listed after these three different watermarks.

When Tables 4 and 5 are examined, it is seen that a robust watermarking process is performed for the sample blood and the sample cancer cells in the no attack condition. As the watermark size decreased, the performance decreased slightly, but outstanding results were still obtained.

There is almost no loss in the watermark after the applied noise (Gaussian, salt and peppers, and speckle noises) attacks. Similarly, outstanding performances were obtained in each Gaussian low-pass filter, rescaling (4, 0.25), JPEG compression, JPEG2000 compression, and sharpening attacks. It has been observed that the median and average filter attacks, rescaling (0.25.4), histogram equalization, and motion blur attacks are good enough but not as good as the above attacks. Outstanding results were obtained in all attacks, mainly when a 256 × 256 watermark was applied. Although the results obtained for Histogram equalization and Rescaling (0.25.4) attacks were sufficient when 128 × 128 and 64 × 64 size watermarks were applied, the robustness decreased more than the others. Lossless results were obtained in almost all of the proposed watermark methods against all attacks except these attacks. After the QR code of all watermarks is converted back to the text, completely lossless watermark texts are obtained.

6. Conclusion

Watermarking has excellent potential to provide valuable solutions for medical applications such as identity theft, data security, health data management, and storage. This study developed a new method using chaos-based discrete wavelet transform (DWT) and singular value decomposition (SVD) for watermarking with high imperceptibility and robustness. In order to obtain a high-resolution biomedical image, a low-cost, large field of view and easy-to-integrate LED-based DIHM setup was designed. The resolution capability of the imaging system is demonstrated with the standard USAF 1951 resolution target. The captured diffraction patterns of medical samples were reconstructed using the angular spectrum method. Images of human blood and cancer cell lines, which are widely used in the laboratory environment, were obtained. For the security feature of the proposed watermarking technique, chaos-based random number generators are used. Specifically, chaos-based random number generators were used to eliminate the false positive problem, which is the disadvantage of the SVD method. The chaotic system without equilibrium points is preferred for the chaos-based random number generator. The suitability of the selected chaotic system for use in studies such as encryption, data hiding, and watermarking has been proven by dynamic analysis. Random numbers are generated with CBRNG as the same random numbers are needed when the system is rerun for the watermarking application. NIST-800-22 and ENT statistical tests with the highest standards at the international level were used to measure the randomness performance of the numbers produced. For the watermarking process, a new method using chaos-based discrete wavelet transform (DWT) and singular value decomposition (SVD) has been developed and applied to high-resolution data in order to eliminate the problem of encrypted data being directly targeted by third-party attacks. The performance of the proposed new watermarking method has been demonstrated by various robustness and invisibility tests. Robustness and invisibility results show the watermarked host images have good visual quality, PSNRs, and SSIMs. Experimental results showed that the proposed scheme reached an average PSNR value of 564588 dB and an SSIM value of 0.9972 against several geometric and destructive attacks. Furthermore, the watermarks can be clearly extracted from the watermarked host image, and even for the watermarks with different sizes, the proposed image watermarking method achieved good invisibility and robustness. To the best of our knowledge, the proposed method has been applied for the first time in DIHM systems, along with producing solutions to the problems in the watermarking process. The proposed method can be applied to medical images obtained in both clinical and laboratory conditions and has the potential to be applied to many different high-resolution data. We can apply our proposed method to color images and many other areas in our future work. It is also possible to construct a blind and more secure watermarking system using some cutting-edge techniques like blockchain, deep learning, or machine learning, and better error-correcting code.

Data Availability

The datasets generated during and/or analyzed during the current study are available from the corresponding author upon request.

Conflicts of Interest

The authors declare that they have no conflicts of interest.

Acknowledgments

This work was supported by the Sakarya University of Applied Science Scientific Research Projects Coordination Unit (SUBU BAPK, Project Number: 2020-01-01-011). The author, Muhammed Ali PALA, is grateful to The Scientific and Technological Research Council of Turkey for granting a scholarship (TUBITAK, 2211-C) for his Ph.D. studies.

References

[1] K. Y. Ngiam and I. W. Khor, "Big data and machine learning algorithms for health-care delivery," *The Lancet Oncology*, vol. 20, no. 5, pp. 262–273, 2019.

[2] G. Manogaran, C. Thota, D. Lopez, V. Vijayakumar, K. M. Abbas, and R. Sundarsekar, *Big Data Knowledge System in Healthcare*, pp. 133–157, Springer, Cham, Switzerland, 2017.

[3] R. Thanki, S. Borra, V. Dwivedi, and K. Borisagar, "An efficient medical image watermarking scheme based on FDCuT–DCT," *Engineering Science and Technology, an International Journal*, vol. 20, no. 4, pp. 1366–1379, 2017.

[4] S. M. Mousavi, A. Naghsh, and S. A. R. Abu-Bakar, "Watermarking techniques used in medical images: a survey," *Journal of Digital Imaging*, vol. 27, no. 6, pp. 714–729, 2014.

[5] S. Sharma, H. Sharma, J. B. Sharma, and R. C. Poonia, "A secure and robust color image watermarking using nature-inspired intelligence," *Neural Computing & Applications*, pp. 1–19, Jan. 2021.

[6] R. Dhanalakshmi and K. Thaiyalnayaki, "Dual watermarking scheme with encryption," *International Journal of Computer Science and Information Security*, vol. 7, no. 1, pp. 248–253, 2010.

[7] S. Sharma, H. Sharma, and J. B. Sharma, "Artificial intelligence based watermarking in hybrid DDS domain for security of colour images," *International Journal of Intelligent Engineering Informatics*, vol. 8, no. 4, p. 331, 2020.

[8] A. K. Singh, B. Kumar, M. Dave, and A. Mohan, "Robust and imperceptible dual watermarking for telemedicine applications," *Wireless Personal Communications*, vol. 80, no. 4, pp. 1415–1433, 2015.

[9] S. A. K. Mostafa, N. El-sheimy, A. S. Tolba, F. M. Abdelkader, and H. M. Elhindy, "Wavelet packets-based blind watermarking for medical image management," *The Open Biomedical Engineering Journal*, vol. 4, no. 1, pp. 93–98, 2010.

[10] S. Sharma, H. Sharma, and J. B. Sharma, "An adaptive color image watermarking using RDWT-SVD and artificial bee colony based quality metric strength factor optimization," *Applied Soft Computing*, vol. 84, Article ID 105696, 2019.

[11] R. Pandey, A. K. Singh, B. Kumar, and A. Mohan, "Iris based secure NROI multiple eye image watermarking for teleophthalmology," *Multimedia Tools and Applications*, vol. 75, no. 22, Article ID 14381, 2016.

[12] H. Nyeem, W. Boles, and C. Boyd, "A review of medical image watermarking requirements for teleradiology," *Journal of Digital Imaging*, vol. 26, no. 2, pp. 326–343, 2013.

[13] F. N. Thakkar and V. K. Srivastava, "A blind medical image watermarking: DWT-SVD based robust and secure approach for telemedicine applications," *Multimedia Tools and Applications*, vol. 76, no. 3, pp. 3669–3697, 2017.

[14] A. K. Singh, M. Dave, and A. Mohan, "Hybrid technique for robust and imperceptible multiple watermarking using medical images," *Multimedia Tools and Applications*, vol. 75, no. 14, pp. 8381–8401, 2016.

[15] K. A. Navas and M. Sasikumar, "Survey of medical image watermarking algorithms," in *Proceedings of the 4 th International conference: Sciences of Electronic, Technologies of Information and Telecommunications*, pp. 25–29, Tunisia, July 2007.

[16] M. AlShaikh, M. Alzaqebah, and S. Jawarneh, "Robust watermarking based on modified Pigeon algorithm in DCT domain," *Multimedia Tools and Applications*, pp. 1–21, 2022.

[17] L. Y. Hsu, H. T. Hu, and H. H. Chou, "A high-capacity QRD-based blind color image watermarking algorithm incorporated with AI technologies," *Expert Systems with Applications*, vol. 199, Article ID 117134, 2022.

[18] F. Ernawan, A. Aminuddin, D. Nincarean, M. F. A. Razak, and A. Firdaus, "Three layer authentications with a spiral block mapping to prove authenticity in medical images," *International Journal of Advanced Computer Science and Applications*, vol. 13, no. 4, pp. 211–223, 2022.

[19] D. Muigai, E. Mwangi, and E. T. Mharakurwa, "A prediction error nonlinear difference expansion reversible watermarking for integrity and authenticity of DICOM medical images," *International Journal of Advanced Computer Science and Applications*, vol. 13, no. 3, pp. 201–210, 2022.

[20] S. Huang and J. K. Wu, "Optical watermarking for printed document authentication," *IEEE Transactions on Information Forensics and Security*, vol. 2, no. 2, pp. 164–173, Jun. 2007.

[21] L. Xie and G. R. Arce, "Joint wavelet compression and authentication watermarking," *IEEE Int. Conf. Image Process.*vol. 2, pp. 427–431, 1998.

[22] P. Arena, A. Basile, L. Fortuna, M. E. Yalçin, and J. Vandewalle, "Watermarking for the authentication of video on CNN-UM," *Proceedings of the 2002 7th IEEE International Workshop on Cellular Neural Networks and Their Applications*, vol. 2002, Article ID 1035038, 83 pages, 2002.

[23] P. Sidiropoulos, N. Nikolaidis, and I. Pitas, "Invertible chaotic fragile watermarking for robust image authentication," *Chaos, Solitons & Fractals*, vol. 42, no. 5, pp. 2667–2674, 2009.

[24] W. H. Lin, S. J. Horng, T. W. Kao et al., "Image copyright protection with forward error correction," *Expert Systems with Applications*, vol. 36, no. 9, Article ID 11888, 2009.

[25] J. Zain and M. Clarke, *Security in Telemedicine: Issues in Watermarking Medical Images*, Brunel University, London, UK, 2005.

[26] M. M. Soliman, A. E. Hassanien, N. I. Ghali, and H. M. Onsi, "An adaptive watermarking approach for medical imaging using swarm intelligent," *Int. J. Smart Home*, vol. 6, no. 1, pp. 37–50, 2012.

[27] K. Pal, G. Ghosh, and M. Bhattacharya, "Biomedical image watermarking in wavelet domain for data integrity using bit majority algorithm and multiple copies of hidden information," *American Journal of Biomedical Engineering*, vol. 2, no. 2, pp. 29–37, 2012.

[28] N. A. Memon and S. A. M. Gilani, "NROI watermarking of medical images for content authentication," in *Proceedings of the 2008 IEEE International Multitopic Conference 2008 12th IEEE Int. Multitopic Conf. - Conf. Proc*, pp. 106–110, IEEE, Karachi, Pakistan, December 2008.

[29] C. C. Lai and C. C. Tsai, "Digital image watermarking using discrete wavelet transform and singular value

decomposition," *IEEE Transactions on Instrumentation and Measurement*, vol. 59, no. 11, pp. 3060–3063, 2010.

[30] A. Kannammal, K. Pavithra, and S. SubhaRani, "Double watermarking of dicom medical images using wavelet decomposition technique," *European Journal of Scientific Research*, vol. 70, no. 1, pp. 46–55, 2012.

[31] A. Anand and A. K. Singh, "An improved DWT-SVD domain watermarking for medical information security," *Computer Communications*, vol. 152, pp. 72–80, Feb. 2020.

[32] P. Kadian, N. Arora, and S. M. Arora, "Performance evaluation of robust watermarking using DWT-SVD and RDWT-SVD," in *Proceedings of the 2019 6th International Conference on Signal Processing and Integrated Networks (SPIN)*, pp. 987–991, IEEE, Noida, India, May 2019.

[33] N. Zermi, A. Khaldi, M. R. Kafi, F. Kahlessenane, and S. Euschi, "A lossless DWT-SVD domain watermarking for medical information security," *Multimedia Tools and Applications*, vol. 80, no. 16, Article ID 24823, 2021.

[34] E. McLeod and A. Ozcan, "Unconventional methods of imaging: computational microscopy and compact implementations," *Reports on Progress in Physics*, vol. 79, no. 7, Article ID 076001, 2016.

[35] W. Zhang, L. Cao, D. J. Brady et al., "Twin-image-Free holography: a compressive sensing approach," *Physical Review Letters*, vol. 121, no. 9, Article ID 093902, 2018.

[36] G. DIng, J. Wang, J. Zou et al., "A novel method based on optofluidic lensless-holography for detecting the composition of oil droplets," *IEEE Sensors Journal*, vol. 20, no. 13, pp. 6928–6936, 2020.

[37] M. A. Pala and M. Z. Yıldız, "Development of embedded system-based lens-less microscopy system and testing on tissue samples," *European Journal of Science and Technology*, vol. 28, no. 28, pp. 357–361, Nov. 2021.

[38] A. B. Dharmawan, S. Mariana, G. Scholz et al., "Nonmechanical parfocal and autofocus features based on wave propagation distribution in lensfree holographic microscopy," *Scientific Reports*, vol. 11, no. 1, p. 3213, 2021.

[39] G. Scholz, S. Mariana, I. Syamsu et al., "Continuous live-cell culture monitoring by compact lensless LED microscopes," *Proceedings*, vol. 2, no. 13, p. 877, 2018.

[40] Y. Wang, P. Ju, S. Wang, J. Su, W. Zhai, and C. Wu, "Identification of living and dead microalgae cells with digital holography and verified in the East China Sea," *Marine Pollution Bulletin*, vol. 163, Article ID 111927, 2021.

[41] G. Li, M. Wei, J. Sun, Y. Zhang, and R. Zhang, "Low false positive and accurate detection of yeast cell viability and concentration using an automatic staining and lensfree imaging platform," *Biochemical and Biophysical Research Communications*, vol. 525, no. 3, pp. 793–799, 2020.

[42] M. A. Pala, M. E. Çimen, A. Akgül, M. Z. Yıldız, and A. F. Boz, "Fractal dimension-based viability analysis of cancer cell lines in lens-free holographic microscopy via machine learning," *The European Physical Journal - Special Topics*, vol. 231, no. 5, pp. 1023–1034, 2021.

[43] D. Ahn, J. Lee, S. Moon, and T. Park, "Human-level blood cell counting on lens-free shadow images exploiting deep neural networks," *Analyst*, vol. 143, no. 22, pp. 5380–5387, 2018.

[44] T. O'Connor, C. Hawxhurst, L. M. Shor, and B. Javidi, "Red blood cell classification in lensless single random phase encoding using convolutional neural networks," *Optics Express*, vol. 28, no. 22, Article ID 33504, 2020.

[45] M. A. Pala, M. E. Çimen, M. Z. Yıldız, G. Güney Eskiler, and A. Deveci Özkan, "Holografik görüntülerde kenar tabanlı fraktal özniteliklerin hücre canlılık analizlerinde başarısı," *Journal of Smart Systems Research*, vol. 2, no. 2, pp. 86–94, Dec. 2021.

[46] Y. Rivenson, Y. Wu, and A. Ozcan, "Deep learning in holography and coherent imaging," *Light: Science & Applications*, vol. 8, no. 1, p. 85, 2019.

[47] Z. Ren, Z. Xu, and E. Y. Lam, "End-to-end deep learning framework for digital holographic reconstruction," *Advanced Photonics*, vol. 1, no. 01, p. 1, 2019.

[48] D. Gabor, "A new microscopic principle," *Nature*, vol. 161, pp. 777-778, 1948.

[49] W. Luo, Y. Zhang, A. Feizi, Z. Göröcs, and A. Ozcan, "Pixel super-resolution using wavelength scanning," *Light: Science & Applications*, vol. 5, no. 4, Article ID 16060, 2015.

[50] Y. Bian, W. Wang, A. Hussian, C. Kuang, H. Li, and X. Liu, "Experimental analysis and designing strategies of lens-less microscopy with partially coherent illumination," *Optics Communications*, vol. 434, pp. 136–144, 2019.

[51] T. Latychevskaia and H.-W. Fink, "Practical algorithms for simulation and reconstruction of digital in-line holograms," *Optica*, vol. 54, 2015.

[52] N. C. Lindquist, "An Introduction to Lensless Digital Holographic Microscopy," *Miniature Fluidic Devices for Rapid Biological Detection*, Springer, Cham, Switzerland, pp. 147–170, 2018.

[53] J. Zhang, J. Sun, Q. Chen, and C. Zuo, "Resolution Analysis in a Lens-free On-Chip Digital Holographic Microscope," 2019, http://arxiv.org/abs/1906.06231.

[54] G. Li, R. Zhang, M. Wei, C. Yin, J. Sun, and Y. Zhang, "Lensfree diffraction reconstruction approach enables early detection of cancer in vitro based on molecular diagnosis," *ACS Sensors*, vol. 5, no. 10, pp. 3091–3098, 2020.

[55] D. G. Voelz, *Computational Fourier Optics: A MATLAB Tutorial*, New Mexico State University, New Mexico, NM, USA, 2011.

[56] H. A. İlhan, M. Doğar, and M. Özcan, "Autofocusing in digital holography," *SPIE Proceedings*, vol. 8644, Article ID 86440C, 2013.

[57] M. Trusiak, J. A. Picazo-Bueno, P. Zdankowski, and V. Micó, "DarkFocus: numerical autofocusing in digital in-line holographic microscopy using variance of computational dark-field gradient," *Optics and Lasers in Engineering*, vol. 134, no. April, Article ID 106195, 2020.

[58] J. Mariën, R. Stahl, A. Lambrechts, C. van Hoof, and A. Yurt, "Color lens-free imaging using multi-wavelength illumination based phase retrieval," *Optics Express*, vol. 28, no. 22, Article ID 33002, 2020.

[59] H. Li, X. Chen, Z. Chi, C. Mann, and A. Razi, "Deep DIH: single-shot digital in-line holography reconstruction by deep learning," *IEEE Access*, vol. 8, Article ID 202648, 2020.

[60] E. N. Lorenz, "Deterministic nonperiodic flow," pp. 367–378, Universality in Chaos, Tyrol, Austria, 1963.

[61] Y. Tang, J. Kurths, W. Lin, E. Ott, and L. Kocarev, "Introduction to Focus Issue: when machine learning meets complex systems: networks, chaos, and nonlinear dynamics," *Chaos*, vol. 30, Article ID 063151, 6 pages, 2020.

[62] G. Quaranta, W. Lacarbonara, and S. F. Masri, "A review on computational intelligence for identification of nonlinear dynamical systems," *Nonlinear Dynamics*, vol. 99, no. 2, pp. 1709–1761, 2020.

[63] N. Tsafack, A. M. Iliyasu, N. J. De Dieu et al., "A memristive RLC oscillator dynamics applied to image encryption," *Journal of Information Security and Applications*, vol. 61, Article ID 102944, 2021.

[64] A. Sambas, S. Vaidyanathan, E. Tlelo-Cuautle et al., "A 3-D multi-stable system with a peanut-shaped equilibrium curve: circuit design, FPGA realization, and an application to image encryption," *IEEE Access*, vol. 8, Article ID 137116, 2020.

[65] A. Akgül, S. Kaçar, B. Aricioglu, and I. Pehlivan, "Text encryption by using one-dimensional chaos generators and nonlinear equations," in *Proceedings of the 2013 8th International Conference on Electrical and Electronics Engineering (ELECO)*, pp. 320–323, IEEE, Bursa, Turkey, November 2013, Article ID 6713853.

[66] Q. Lai, X. W. Zhao, K. Rajagopal, G. Xu, A. Akgul, and E. Guleryuz, "Dynamic analyses, FPGA implementation and engineering applications of multi-butterfly chaotic attractors generated from generalised Sprott C system," *Pramana - Journal of Physics*, vol. 90, no. 1, pp. 6–12, 2018.

[67] K. Rajagopal, V. T. Pham, F. R. Tahir, A. Akgul, H. R. Abdolmohammadi, and S. Jafari, "A chaotic jerk system with non-hyperbolic equilibrium: dynamics, effect of time delay and circuit realisation," *Pramana - Journal of Physics*, vol. 90, no. 4, pp. 52–58, 2018.

[68] J. Liu, J. Huang, Y. Luo et al., "An optimized image watermarking method based on HD and SVD in DWT domain," *IEEE Access*, vol. 7, Article ID 80849, 2019.

Hindawi
Complexity
Volume 2022, Article ID 9084394, 21 pages
https://doi.org/10.1155/2022/9084394

Research Article

Thermal Convective Instabilities and Chaos in a Rotating Hybrid Nanofluid Layer with Cattaneo–Christov Heat Flux Model

Sèmako Justin Dèdèwanou,[1] **Adjimon Vincent Monwanou**,[1] **Aimé Audran Koukpémèdji**,[1,2,3] **Amoussou Laurent Hinvi**,[1,4] **Clément Hodévèwan Miwadinou**,[1,3,5] **and Jean Bio Chabi Orou**[1]

[1]*Laboratoire de la Mécanique des Fluides, de la Dynamique Non-Linéaire et de la Modélisation des Systèmes Biologiques (LMFDNMSB), Institut de Mathématiques et de Sciences Physiques (IMSP), Université d'Abomey-Calavi (UAC), Godomey, Benin*
[2]*Département de Physique, FAST-Natitingou, Université Nationale des Sciences, Technologies, Ingénierie et Mathématiques (UNSTIM) d'Abomey, Abomey, Benin*
[3]*Laboratoire de Physique et Applications du Centre Universitaire de Natitingou, Université Nationale des Sciences, Technologiques, Ingénierie et Mathématiques (UNSTIM) d'Abomey, Abomey, Benin*
[4]*Department of Industrial Computer and Electrical Engineering, Université Nationale des Sciences, Technologiques, Ingénierie et Mathématiques (UNSTIM) d'Abomey, Abomey, Benin*
[5]*Département de Physique, ENS-Natitingou, Université Nationale des Sciences, Technologies, Ingénierie et Mathématiques (UNSTIM) d'Abomey, Abomey, Benin*

Correspondence should be addressed to Aimé Audran Koukpémèdji; kaudranus2000@gmail.com

Received 23 February 2022; Accepted 27 June 2022; Published 22 August 2022

Academic Editor: Akif Akgul

The linear and nonlinear dynamics of thermal convection of a rotating hybrid nanofluid layer heated from below with the Cattaneo–Christov heat flux model are studied in this paper. Starting from the flow equations of a hybrid nanofluid and exploiting the free boundary conditions, the analytical expressions of the stationary and oscillatory Rayleigh numbers of the base fluid are determined as a function of the dimensionless parameters of the heat transfer fluid and the thermophysical properties of the hybrid nanofluid. The effects of hybrid nanoparticles and Taylor number on the onset of stationary convection in the base fluid are investigated graphically. Then, a numerical study of the transition from natural convection to chaotic behaviour of the hybrid nanofluid is made using the truncated Galerkin approximation. This approximation allowed us to find a novel six-dimensional nonlinear system depending on the parameters of the base fluid and the thermophysical properties of the hybrid nanofluid that can be reduced to five, four, or three dimensions when we tend some parameters to zero. The different results showed that the addition of hybrid nanoparticles (alumina-copper) to a thermal fluid (water) subjected to the rotation force in the presence or absence of the thermal relaxation time allows control of the chaotic convection in the base fluid. On the other hand, the increase of the rescaled Taylor number and the Cattaneo number widens the domain of chaos in the hybrid nanofluid with the increase of the rescaled Rayleigh number of the base fluid.

1. Introduction

In 1995, Choi introduced, at the Argonne National Laboratory of the University of Chicago in the U.S., the concept of nanofluid [1]. This new generation of fluids consists of dispersing nanoparticles (assemblies of a few hundred to a few thousand atoms, leading to an object with at least one dimension of thousands of atoms, leading to an object of which at least one of the dimensions is of nanometric size) in a base liquid (water, oil, ethylene glycol, toluene). The use of

these nanofluids in some industrial operations that involve heat transfer by convection is a promising alternative solution to improve thermal performance. Thus, the problem of natural convection in a nanofluid layer heated from below has been studied by several researchers [2–6] with the Fourier law. The flow and heat transport of nanomaterial with quadratic radiative heat flux and aggregation kinematics of nanoparticles reported by Mahanthesh [7] revealed that the suspension of the nanoparticles increases the thermal conductivity and, thus, improves the temperature and reduces the heat flux at the plate. The Rayleigh-Bénard convection in nanofluid submerged with dust particles was investigated by Shalini and Mahanthesh [8]. They pointed out that the inclusion of nano and dust particles reduces the Rayleigh number while the rotation postpones the onset of convection and stabilizes the system.

Ahuja and Sharma [9] conducted a comprehensive review of the instability of Rayleigh-Bénard convection in nanofluids by summarizing in their work the studies related to the instability of a horizontal nanofluid layer under the impact of various parameters such as rotation magnetic field, Hall currents, and LTNE (local thermal nonequilibrium) effects in porous and nonporous media. The thermal convection in a rotating fluid layer provides a system to study hydrodynamic instabilities, pattern formation, and spatiotemporal chaos in nonlinear dynamical systems with many practical applications in engineering, such as food processing, chemical processes, solidification, centrifugal casting of metals, and rotating machines [10].

To compensate for the defect and all the disadvantages of mono nanofluids, it is essential to combine several nanoparticles to prepare a hybrid nanofluid [11]. Natural magnetohydrodynamic convection in a triangular cavity filled with a hybrid (copper-alumina)/water nanofluid with localized heating from below and internal heat has been investigated by Rashad et al. [12]. They concluded that a hybrid nanofluid composed of equal amounts of copper and alumina nanoparticles dispersed in water has no significant improvement on the average Nusselt number compared to the mono nanofluid and that the effect of increasing the hybrid nanoparticles becomes significant in the case where natural convection is very low. Aladin et al. [13] also studied the significant effects of suction and magnetic field on a moving plate containing a hybrid (copper-alumina)/water nanofluid. They have proved that the hybrid nanofluid gives better results than the mono nanofluid.

According to Myson and Mahanthesh [14], the hybrid nanofluid delays the convection and will further enhance the heat transfer rate, but the Casson parameter advances the convection while reducing the heat transfer rate. Mackolil and Mahanthesh [15] illustrated the optimization of heat transfer in the thermal Marangoni and nonlinear convective flow of a hybrid nanomaterial with sensitivity analysis. It is shown that the hybrid nanomaterial possesses enhanced thermal fields for nanoparticle volume fractions less than 0.02. The sensitivity computation of nonlinear convective heat transfer in hybrid nanomaterial between two concentric cylinders with irregular heat sources was also made by Thriveni and Mahanthesh [16].

Given its advantages and industrial applications, especially in chemical reactions, biological systems, crystal production, petroleum reservoir modeling, and packed-bed catalytic filtration, chaotic convection in a hybrid nanofluid layer should receive considerable attention due to the performance of nanofluids. Jawdat et al. [17], Moaddy et al. [18, 19], and Bhardwaj and Chawla [20] all contributed well to nonlinear dynamical analysis of the thermal convection in a horizontal nanofluid layer heated from below in the presence or absence of a magnetic field. They studied the effect of nanoparticles on chaotic convection in a layer of fluid (water) heated from below and noticed that the stability region can be increased by using nanofluids and that the onset of chaotic convection can be delayed under the influence of nanoparticles. Also, variations in temperature and magnetic field strength cause the system to transition from a steady state to chaos and back to a steady state. The case of hybrid nanofluid was first presented by Dèdèwanou et al. [21] with the Fourier law. They found that the copper nanofluid makes it possible to quickly switch from chaotic to periodic regimes compared to the alumina nanofluid, and the use of hybrid nanoparticles allows further control of the chaos in the base fluid by expanding the convective flow and reducing the chaotic flow.

Furthermore, Maxwell and Cattaneo modified Fourier's law by taking into account the aspect of thermal relaxation time in the propagation of heat [22]. In order to eliminate the heat flow and thus obtain a single equation for the temperature field, Christov [23] proposed a generalization of the material-invariant Maxwell–Cattaneo law, in which the relaxation time of the heat flow is given by the convex Oldroyd upper derivative. This new law was used by Straughan [24] to study thermal convection in an ordinary fluid. He concluded that the thermal relaxation time is significant if the Cattaneo number is large enough, and the convection mechanism changes from stationary to oscillatory convection with narrower cells. Indeed, some researchers used the Cattaneo–Christov model to appreciate the effects of temporal relaxation on the thermal behavior of a nanofluid [25–31]. Alebraheem and Ramzan [26] have studied the heat and mass transfer of Casson nanofluid flow containing gyrotactic microorganisms past a swirling cylinder by considering the Cattaneo-Christov heat flux model. According to their numerical solution of the subject system, which is framed via the bvp4c technique of MATLAB software, the concentration of the fluid is reduced owing to the increase in values of the brownian motion parameter and local Reynolds number, but the diminishing density of microorganisms is perceived for mounting estimates of the bioconvection Péclet number. Multiple slip impacts in the MHD hybrid nanofluid flow with Cattaneo–Christov heat flux and autocatalytic chemical reaction were investigated by Gul et al. [32]. They found that the fluid temperature is diminishing function of the thermal slips parameters but increased for high estimates of the heat source-sink and nanoparticle volume concentration parameters while entropy number augmented for higher thermal relaxation parameter and Reynolds number. Lu et al. [33] have also studied a thin film flow of nanofluid comprising carbon

nanotubes influenced by Cattaneo–Christov heat flux and entropy generation. They showed that the velocity and temperature distributions increase as the solid volume fraction escalates. Recently, a three-dimensional flow of gold-silver/engine oil hybrid nanofluid owing to a rotating disk of variable thickness with Cattaneo–Christov heat flux has been addressed by Zhang et al. [34]. They proved that the performance of the hybrid nanofluid is far better than the common nanofluid according to the surface temperature and heat transfer rate. This same remark is made from the results obtained for the model-based comparative study of magnetohydrodynamics unsteady hybrid nanofluid flow between two infinite parallel plates with particle shape effects [35]. Considering hybrid nanofluid Yamada-Ota and Xue flow models in a rotating channel with the modified Fourier law, it is observed that the velocity profile decreases for the higher rotation parameter while it increases for the escalated slip parameter, but the fluid concentration and temperature are on the decline for higher surface catalyzed reaction and thermal relaxation parameters respectively [36]. Ramdan et al. [37] have analyzed the hydrodynamic and heat characteristics of the three-dimensional flow of a steady, laminar, and incompressible convective graphene-copper oxide/water and graphene-silver/water hybrid nanofluids (used as a solar energy absorber) with varied particle shapes in a porous medium. Their study revealed that the rotational parameter has declined the velocity profiles but enhanced the temperature profiles, and the decline effect is significant in the case of graphene-copper oxide/water whereas the enhancement effect of temperature is significant for graphene-silver/water. A comparative analysis of magnetized partially ionized copper, copper oxide-water, and kerosene oil nanofluid flow with Cattaneo–Christov heat flux was made by Abid et al. [38]. They noted the greater effective thermal conductivity for copper-water partially ionized nanofluid as compared to other given partially ionized nanofluids (copper-kerosene oil, copper oxide-water/kerosene oil partially ionized nanofluids). Ramzan et al. [39] developed a mathematical model for the nanofluid flow containing carbon nanotubes with ethylene glycol as a base fluid in a rotating channel with an upper permeable wall by adding the Cattaneo–Christov heat flux's impact with thermal stratification. The displacement of the lower plate at variable velocity, caused by the rotation of the fluid, produces forced convection with rotation and centripetal impact. Nevertheless, the upper plate is porous. Chu et al. [40] investigated a numerical solution for MHD Maxwell nanofluid with gyrotactic microorganisms, a higher-order chemical reaction in the presence of variable source/sink, and Newtonian heating in a rotating flow on a deformable surface and noted that on incrementing the conjugate heat parameter and thermal relaxation time, the rate of heat transfer augments, but the rate of heat transfer decreases on varying the fluid relaxation time.

Despite all the above, the study of nanoparticles requires more attention due to their industrial uses. After inspecting the scientific literature, we noted that no work has yet addressed the chaotic aspect of thermal convection in hybrid nanofluids, taking into account the thermal relaxation time, although this would be very useful in some applications like petroleum reservoir modeling, chemical reactions, thermal transport in biological tissue, and surgical operations. Nevertheless, Layek and Pati [41] studied the effects of thermal lag on the onset of convection, its bifurcations, and the chaos of a horizontal layer of the heated Boussinesq fluid underneath via a five-dimensional nonlinear system. A comparative study of the five-dimensional system obtained for the case of a hybrid nanofluid was made by Dèdèwanou et al. [42]. Therefore, the objective of the present paper is to investigate the effects of hybrid nanoparticles on the occurrence of thermal convection instability and chaos in a rotating fluid layer heated from below with the Cattaneo–Christov heat flux model. A specific objective is to determine the analytical expression for the stationary Rayleigh number that can be used to study the nonlinear dynamics of thermal convection in rotating hybrid nanofluid flow in the presence of thermal relaxation time. This work aims to study the different transition regimes as a function of the thermophysical properties of nanofluids and then to show the effects of hybrid nanoparticles, Taylor number, and Cattaneo number on the chaotic behavior of natural convection in a basic fluid such as water via dynamical systems.

In the next section, the thermal convection in an infinite horizontal rotating hybrid nanofluid layer with the hyperbolic Cattaneo–Christov heat flux is outlined. Section 3 discusses the theory of conduction, stationary convection, and oscillatory convection, where we generalize and simplify the expression for the Rayleigh number by deriving a number of new analytical results. In order to reduce the set of equations governing the dynamic behavior of thermal convection in the hybrid (alumina-copper)/water nanofluid, discretized models in four and six dimensions are developed in Section 4 using the Galerkin expansion. We have studied the nature of the nonlinear dynamics of the obtained dynamical systems and determined the fixed points by analyzing the stability of the stationary solutions. These analyses have allowed us to justify the influence of the hybrid alumina-copper nanoparticle, the Cattaneo number, and the Taylor number on number on the transition from chaos to periodicity and vice versa in the fluid. In Section 5, we present the different simulations performed, and the results obtained are discussed. The conclusions are drawn in Section 6.

2. Mathematical Modeling

2.1. Problem Formulation. We consider an infinite rectangular cavity with two horizontal walls maintained at different temperatures. This cavity, heated from below with a thermal relaxation time, is filled with a hybrid nanofluid (water and nanoparticles), subject to gravity acting downwards and to rotation. In order to develop our numerical model, it is necessary to adopt certain assumptions, namely, the flow is assumed to be permanent and incompressible, the mixture is assumed to be homogeneous, single-phase, Newtonian, the nanoparticles are spherical, and the mass transfer between the particles and the fluid is negligible. The Cartesian coordinate system used is such that the y-axis follows the

horizontal and the vertical z-axis is collinear with gravity. The geometry of our problem is presented in Figure 1.

2.2. Governing Equations. In this section, we have studied the equations governing the dynamic and thermal fluxes with boundary conditions and nondimensional parameters characterizing the thermal convection in a rotating hybrid nanofluid layer in the presence of thermal relaxation time. Taking into account the listed assumptions and using the hybrid nanofluid model proposed in Section 3, the equations governing the conservation of mass, momentum, energy, and heat flux for a laminar flow of the hybrid nanofluid are written in their dimensional form respectively as follows [10, 42]:

$$\frac{\partial v_i}{\partial x_i} = 0, \tag{1}$$

$$\rho_{hf}\left[\frac{\partial v_i}{\partial t} + \left(v_j \frac{\partial v_i}{\partial x_j}\right)\right] = -\frac{\partial p}{\partial x_i} - \rho g e_i + \mu_{hf}\nabla^2 v_i + 2\rho_{hf}\Omega_j \frac{\partial v_i}{\partial x_j} e_i, \tag{2}$$

$$(\rho Cp)_{hf}\left[\frac{\partial T}{\partial t} + \left(v_j \frac{\partial T}{\partial x_j}\right)\right] = -\frac{\partial Q_j}{\partial x_j}, \tag{3}$$

$$\left[\frac{\partial Q_i}{\partial t} + \left(v_j \frac{\partial Q_i}{\partial x_j}\right)\right] + Q_i = -k_{hf}\frac{\partial T}{\partial x_i}. \tag{4}$$

In equation (2), $e_i = (0, 0, 1)$ is the unit vector and $\nabla^2 = (\partial^2/\partial x^2) + (\partial^2/\partial y^2) + (\partial^2/\partial z^2)$ is the Laplacian operator. The use of the Boussinesq approximation allows us to define the density as a function of temperature as

$$\rho = \rho_{hnf}\left[1 - \beta_{hf}(T - T_0)\right]. \tag{5}$$

The density, thermal expansion coefficient, heat capacity, dynamic viscosity, thermal conductivity of the dynamic viscosity, and thermal conductivity of the hybrid nanofluid, respectively, are defined as follows:

$$\begin{aligned}
\rho_{hf} &= (1-\varphi_2)\left[(1-\varphi_1)\rho_f + \varphi_1\rho_{s1}\right] + \varphi_2\rho_{s2},\\
(\rho\beta)_{hf} &= (1-\varphi_2)\left[(1-\varphi_1)(\rho\beta)_f + \varphi_1(\rho\beta)_{s1}\right] + \varphi_2(\rho\beta)_{s2},\\
(\rho Cp)_{hf} &= (1-\varphi_2)\left[(1-\varphi_1)(\rho Cp)_f + \varphi_1(\rho Cp)_{s1}\right] + \varphi_2(\rho Cp)_{s2},\\
(\rho Cp)_{hf} &= (1-\varphi_2)\left[(1-\varphi_1)(\rho Cp)_f + \varphi_1(\rho Cp)_{s1}\right] + \varphi_2(\rho Cp)_{s2},\\
\mu_f &= \mu_{hf}(1-\varphi_1)^{-2.5}(1-\varphi_2)^{-2.5},\\
k_{hf} &= k_{gf}\left[\frac{\left(k_{s2} + \eta k_{gf}\right) - \eta\varphi_2\left(k_{gf} - k_{s2}\right)}{\left(k_{s2} + \eta k_{gf}\right) + \varphi_2\left(k_{gf} - k_{s2}\right)}\right],
\end{aligned} \tag{6}$$

to

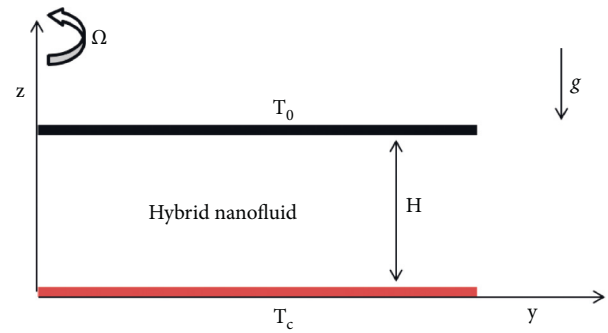

Figure 1: Configuration of the problem.

$$k_{hnf} = k_{hf}\left[\frac{\left(k_{s1} + \eta k_{hf}\right) - \eta\varphi_1\left(k_{hf} - k_{s1}\right)}{\left(k_{s1} + \eta k_{hf}\right) + \varphi_1\left(k_{hf} - k_{s1}\right)}\right], \tag{7}$$

where

$$\eta = m - 1. \tag{8}$$

The thermophysical properties of nanoparticles and water used in this work are summarized in Table 1 (see [13]).

3. Linear Stability Analysis

We consider a classical Rayleigh-Bénard problem of linear stability of convective rolls in a horizontal fluid layer with unconstrained boundary conditions. Thus, the temperature boundary conditions are $T = T_c$ at $z = 0$ and $T = T_0$ at $z = 1$ with $T_c > T_0$. As for the velocity, its component along the z axis is zero at the boundaries.

3.1. Steady-State Solutions. A time-independent quiescent solution of equations (1)–(4) with temperature and heat flux varying in the z direction only, is obtained by reducing equations (2)–(4) to

$$\begin{aligned}
\rho_{hf}\left(v_j \frac{\partial v_i}{\partial x_j}\right) + \frac{\partial p}{\partial x_i} + \rho g e_i - \mu_{hf}\nabla^2 v_i - 2\rho_{hf}\Omega_j \frac{\partial v_i}{\partial x_j} e_i = 0,\\
(\rho Cp)_{hf}\left(v_j \frac{\partial T}{\partial x_j}\right) + \frac{\partial Q_j}{\partial x_j} = 0,\\
\left(v_j \frac{\partial Q_i}{\partial x_j}\right) + Q_i + k_{hf}\frac{\partial T}{\partial x_i} = 0.
\end{aligned} \tag{9}$$

Then, the steady state solutions are given

$$\begin{aligned}
v_b(z) &= 0,\\
T_b &= T_c - \chi x_j e_j,\\
Q_b(z) &= \chi k_{hf} \text{ and } P_b(z) = P_0,
\end{aligned} \tag{10}$$

with the temperature gradient χ and the profile of P_0 defined by

Table 1: The thermophysical properties of the water and nanoparticles at 293 K.

	ρ	Cp	k	$\beta \times 10^{-5}$
Water	997.1	4179	0.613	21
Alumina	3970	765	40	0.85
Copper	8933	385	401	1.67

$$\chi = \left|\frac{\partial T}{\partial x_i}\right| \text{ and}$$
$$\frac{\partial p_0}{\partial x_i} = \rho(T_b) g e_i. \tag{11}$$

3.2. Simplified Set of Equations. In order to simplify the parametric representation of this physical problem and to find the characteristic properties of the system, it is necessary to recast the flow equations. Thus, the following normalized quantities are introduced:

$$\widetilde{x}_i = \frac{x_i}{H},$$
$$\widetilde{v}_i = \frac{\rho_f H.v_i}{\mu_f},$$
$$\widetilde{P} = \frac{H^2.P}{\rho_{f.}\nu_f},$$
$$t_* = \frac{\mu_f t}{\rho_{f.} H^2}, \tag{12}$$
$$\widetilde{T} = \sqrt{\frac{\beta_f g k_f H^2}{\chi \nu_f (\rho C p)_f}}\, T,$$
$$\widetilde{Q}_i = \frac{H}{k_f}\left(\frac{\widetilde{T}}{T}\right) Q_i.$$

Considering small perturbations on the basic solutions as follows:

$$\begin{aligned} \widetilde{v}_i &= \widetilde{v}_b + \widetilde{v}_i', \\ \widetilde{T} &= \widetilde{T}_b + T', \\ \widetilde{Q}_i &= \widetilde{Q}_b + Q_i', \\ \widetilde{P} &= \widetilde{P}_b + \widetilde{P}', \end{aligned} \tag{13}$$

and neglecting the products of the primed quantities, we obtain the following dimensional equations:

$$\frac{\partial \widetilde{v}_i'}{\partial \widetilde{x}_i'} = 0, \tag{14}$$

$$\frac{\partial \widetilde{v}_i'}{\partial \widetilde{t}'} = -\frac{\partial \widetilde{P}'}{\partial \widetilde{x}_i'} + \left(\frac{\mu_{hf}}{\mu_f}\frac{\rho_f}{\rho_{hf}}\right)\nabla^2 \widetilde{v}_i' + \frac{(\rho\beta)_{hf}}{(\rho\beta)_f}\sqrt{Ra_f}\,\widetilde{T} e_i + \sqrt{Ta}\,\frac{\partial \widetilde{v}_i'}{\partial \widetilde{x}_j} e_i, \tag{15}$$

$$\left(\frac{(\rho C p)_{hf}}{(\rho C p)_f}\right)\left(Pr_f \frac{\partial \widetilde{T}'}{\partial \widetilde{t}'} - \sqrt{Ra_f}\,\widetilde{w}'\right) = -\frac{\partial \widetilde{Q}_i'}{\partial \widetilde{x}_j'}, \tag{16}$$

$$2Pr_f C_f \frac{\partial \widetilde{Q}_i'}{\partial \widetilde{t}'} + \widetilde{Q}_i' = -\left(\frac{k_{hf}}{k_{hf}}\right)\frac{\partial \widetilde{T}'}{\partial \widetilde{x}_i'}, \tag{17}$$

where the dimensionless parameters are defined by

$$\begin{aligned} Pr_f &= \frac{\mu_f}{\rho_f \alpha_f}, \\ C_f &= \frac{\alpha_f \tau}{2H^2}, \\ Ra_f &= \frac{g.H^4 \beta_f \chi}{\alpha_f \nu_f}. \end{aligned} \tag{18}$$

Now we eliminate the pressure from the nondimensional equations (14)–(17) by taking the curl-curl of equation (15), the divergence of equation (15), the inner product of any vector equation with e_i;, and denoting the divergence of the heat flux $Q = (\partial \widetilde{Q}_i / \partial \widetilde{x}_i)$, to obtain, after dropping the tilde notation for brevity, the equations

$$\frac{\partial}{\partial t}\left(\nabla^2 w\right) = \sqrt{Ra_f}\,\frac{(\rho\beta)_{hf}}{(\rho\beta)_f}\left(\frac{\partial^2 T}{\partial x^2} + \frac{\partial^2 T}{\partial y^2}\right) + \left(\frac{\mu_{hf}}{\mu_f}\frac{\rho_f}{\rho_{hf}}\right)\nabla^4 w + \sqrt{Ta}\,\frac{\partial \zeta}{\partial z}, \tag{19}$$

$$\left(\frac{(\rho C p)_{hf}}{(\rho C p)_f}\right)\left(Pr_f \frac{\partial T}{\partial t} - \sqrt{Ra_f}\, w\right) = -Q, \tag{20}$$

$$2Pr_f C_f \frac{\partial Q}{\partial \widetilde{t}'} + Q = -\left(\frac{k_{hf}}{k_{hf}}\right)\nabla^2 T. \tag{21}$$

which describe the evolution of the conduction steady state perturbations in a conveniently simplified form with four variables such as the z-component of the velocity field, the vorticity $\zeta = \partial v/\partial x - \partial u/\partial y$, the heat flux Q, and the temperature T.

An evolutionary equation for the vorticity can be obtained from the equation of motion by taking curl, then the dot product with e_3 for the vertical component. Thus, eliminating the pressure and introducing the vorticity in equation (2) allows us to obtain the following:

$$\left[\left(\frac{\mu_{hf}}{\mu_f}\frac{\rho_f}{\rho_{hf}}\right)\nabla^2 - \frac{\partial}{\partial t}\right]\zeta = -\sqrt{Ta}\,\frac{\partial w}{\partial z}. \tag{22}$$

From equations (19) and (22), we obtain the following:

$$\left[\left(\left(\frac{\mu_{hf}}{\mu_f}\frac{\rho_f}{\rho_{hf}}\right)\nabla^2-\frac{\partial}{\partial t}\right)\left(\frac{\partial}{\partial t}\nabla^2-\left(\frac{\mu_{hf}}{\mu_f}\frac{\rho_f}{\rho_{hf}}\right)\nabla^4+Ta\frac{\partial^2}{\partial z^2}\right)\right]w$$
$$-\sqrt{Ra_f}\,\frac{(\rho\beta)_{hf}}{(\rho\beta)_f}\left[\left(\frac{\mu_{hf}}{\mu_f}\frac{\rho_f}{\rho_{hf}}\right)\nabla^2-\frac{\partial}{\partial t}\right]\left(\frac{\partial^2 T}{\partial x^2}+\frac{\partial^2 T}{\partial y^2}\right)=0. \tag{23}$$

3.3. Normal Modes and Analytical Solution. The linear stability of the conduction solutions is studied by writing the perturbations in separable form and assuming an exponential time dependence

$$\begin{aligned} w &= W(z)h(x,y)e^{\sigma t},\\ T &= \Theta(z)h(x,y)e^{\sigma t},\\ Q &= \Phi(z)h(x,y)e^{\sigma t}, \end{aligned} \tag{24}$$

with the plane tiling function satisfying

$$\nabla^2 h(x,y) = -\kappa^2 h(x,y), \tag{25}$$

where W, Θ, Φ are eigenfunctions. The substitution of equation (24) into the differential equations (20), (21), and (23) leads to

$$\begin{aligned} \left[\left(D^2-\kappa^2\right)\left(\gamma_1\left(D^2-\kappa^2\right)-\sigma\right)^2+TaD^2\right]&\\ W=\kappa^2\gamma_2\sqrt{Ra_f}\left[\gamma_1\left(D^2-\kappa^2\right)-\sigma\right]\Theta,& \end{aligned} \tag{26}$$

$$\sigma Pr_f\Theta = \sqrt{Ra_f}W-\gamma_3\Phi, \tag{27}$$

$$2\sigma Pr_f C_f\Phi+\Phi=-\gamma_4\left(D^2-\kappa^2\right)\Theta, \tag{28}$$

where $D = d/dt, D^2 = d^2/dt^2$ and

$$\begin{aligned} \gamma_1 &= \frac{\mu_{hf}}{\mu_f}\frac{\rho_f}{\rho_{hf}},\\ \gamma_2 &= \frac{(\rho\beta)_{hf}}{(\rho\beta)_f},\\ \gamma_3 &= \frac{(\rho Cp)_f}{(\rho Cp)_{hf}},\\ \gamma_4 &= \frac{k_{hf}}{k_{hf}}. \end{aligned} \tag{29}$$

Equations (26)–(28), which represent the starting point for analytical and numerical calculations on thermal convective instability are used to study the occurrence of stationary and oscillatory convection in nanofluids. They are equivalent to those obtained by Straughan [24] and Bissell [43, 44] in the case of an ordinary fluid not subjected to a Coriolis force, i.e. when $\varphi_1 = \varphi_2 = 0$ and $Ta = 0$. The disappearance of tangent shear stresses at the free surface and the conservation of the mass equation allow us to obtain the boundary conditions of the free surface defined by

$$\begin{aligned} W &= 0,\\ D^2W &= 0 \text{ and}\\ \Theta &= 0 \text{ at } z = 0, 1. \end{aligned} \tag{30}$$

In order to obtain an approximate solution of equations (26)–(28), we used the Galerkin weighted residual method by choosing the test function written as

$$\begin{aligned} W &= W_0\sin(\pi z),\\ \Theta &= \Theta_0\sin(\pi z),\\ \Phi &= \Phi_0\sin(\pi z), \end{aligned} \tag{31}$$

which fulfill the conditions at the borders mentioned in equation (30).

By substituting the test functions defined in equation (31) into equations (26)–(28) and performing some integrations, we obtain the following matrix equation:

$$\begin{pmatrix} \left[J\left(\gamma_1 J+\sigma\right)+\dfrac{\pi^2 Ta}{\left(\gamma_1 J+\sigma\right)}\right] & -\kappa^2\gamma_2\sqrt{Ra_f} & 0\\ -\sqrt{Ra_f} & \sigma Pr_f & \gamma_3\\ 0 & -\gamma_4 J & \left(2\sigma Pr_f C_f+1\right) \end{pmatrix} \times \begin{pmatrix} W_0\\ \Theta_0\\ \Phi_0 \end{pmatrix} = \begin{pmatrix} 0\\ 0\\ 0 \end{pmatrix}, \tag{32}$$

where $J = D^2 - \kappa^2$. For this matrix equation (32) to admit a nontrivial solution, the Rayleigh number of the base fluid must be in the following form:

$$Ra_f = \frac{\left[\gamma_3\gamma_4 J+\sigma Pr_f\left(2\sigma Pr_f C_f+1\right)\right]\left[J\left(\gamma_1 J+\sigma\right)+\left(\pi^2 Ta/\left(\gamma_1 J+\sigma\right)\right)\right]}{\kappa^2\gamma_2\left(2\sigma Pr_f C_f+1\right)}. \tag{33}$$

For the following, let $\sigma = j\omega$ with $j^2 = -1$ and ω the real frequency. Thus, the expression for the Rayleigh number defined in equation (33) becomes

$$Ra_f = \Delta_1 + j\omega\Delta_2, \tag{34}$$

with

$$\begin{aligned}\Delta_1 = &\left[\kappa^2\gamma_2\left(1 + 4\omega^2 Pr_f^2 C_f^2\right)\right]^{-1} \\ &\cdot \left[J\left(\gamma_1\gamma_3\gamma_4 J^2 - \omega^2 Pr_f\right) + \frac{\pi^2 Ta\left(\gamma_1\gamma_3\gamma_4 J^2 + \omega^2 Pr_f\right)}{\left(\gamma_1 J\right)^2 + (\omega)^2}\right. \\ &\left. + 2J\omega^2 Pr_f C_f\left(\gamma_3\gamma_4 J - 2\omega^2 Pr_f^2 C_f\right) + \frac{2\pi^2\omega^2 Pr_f C_f Ta\left(2\omega^2 Pr_f^2 C_f - \gamma_3\gamma_4 J\right)}{\left(\gamma_1 J\right)^2 + (\omega)^2}\right],\end{aligned} \tag{35}$$

$$\begin{aligned}\Delta_2 = &\left[\kappa^2\gamma_2\left(1 + 4\omega^2 Pr_f^2 C_f^2\right)\right]^{-1} \\ &\cdot \left[J^2\left(\gamma_3\gamma_4 + \gamma_1 J\right) + \frac{\pi^2 JTa\left(\gamma_1 - \gamma_3\gamma_4\right)}{\left(\gamma_1 J\right)^2 + (\omega)^2} + 2JPr_f C_f\left(2\gamma_1 J\omega^2 Pr_f^2 C_f - \gamma_1\gamma_3\gamma_4 J^2\right) + \frac{2\pi^2\gamma_1 JPr_f C_f Ta\left(2\omega^2 Pr_f^2 C_f - \gamma_3\gamma_4 J\right)}{\left(\gamma_1 J\right)^2 + (\omega)^2}\right].\end{aligned} \tag{36}$$

Since the Rayleigh number is a real and positive physical quantity, then for the expression equation (33) to exist, ω must be zero or $\Delta_2 = 0$.

3.4. Stationary Convection. According to the stability exchange principle for the stationary case, the stability margin is characterized by the frequency equal to zero. This condition allows to obtain from the expression equation (33), the Rayleigh number of the base fluid of the stationary convection expressed as follows:

$$Ra_f^{st} = \frac{\gamma_3\gamma_4}{\kappa^2\gamma_2}\left[\gamma_1\left(\kappa^2 + \pi^2\right)^3 + \frac{\pi^2 Ta}{\gamma_1}\right]. \tag{37}$$

If $\gamma_1 = \gamma_2 = \gamma_3 = \gamma_4 = 1$ and the cavity is not rotating, i.e. $\varphi_1 = \varphi_2 = 0$ and $Ta = 0$, equation (37) is equivalent to the classical Rayleigh number of stationary convection in ordinary fluids [42].

In the absence of the rotation force, we have

$$Ra_f^{st} = \frac{\gamma_1\gamma_3\gamma_4}{\gamma_2}\frac{\left(\kappa^2 + \pi^2\right)^3}{\kappa^2}. \tag{38}$$

The absolute critical Rayleigh number of the hybrid nanofluid in this case is defined as

$$Ra_f^{st} = \frac{27\pi^4}{4}\frac{\gamma_1\gamma_3\gamma_4}{\gamma_2}, \tag{39}$$

with the corresponding wavenumber

$$\kappa_c^{st} = \frac{\pi}{\sqrt{2}}. \tag{40}$$

We note that the Rayleigh number obtained for stationary convection in nanofluids is not a function of the Prandtl number or the Cattaneo number of the base fluid. Thus, the same results can be associated with the more usual Fourier law for mono nanofluids or hybrid nanofluids.

3.5. Oscillatory Convection. Now, we study the effects of the Cattaneo number, the nanoparticles, and the rotation on the oscillating convection. In this case, we must have $\omega \neq 0$ and $\Delta_2 = 0$. Therefore, the Rayleigh number of the base fluid for oscillatory convection is given by

$$\begin{aligned}Ra_f^{os} = &\left[\kappa^2\gamma_2\left(1 + 4\omega^2 Pr_f^2 C_f^2\right)\right]^{-1} \\ &\cdot \left[J\left(\gamma_1\gamma_3\gamma_4 J^2 - \omega^2 Pr_f\right) + \frac{\pi^2 Ta\left(\gamma_1\gamma_3\gamma_4 J^2 + \omega^2 Pr_f\right)}{\left(\gamma_1 J\right)^2 + (\omega)^2}\right. \\ &+ 2J\omega^2 Pr_f C_f\left(\gamma_3\gamma_4 J - 2\omega^2 Pr_f^2 C_f\right) \\ &\left. + \frac{2\pi^2\omega^2 Pr_f C_f Ta\left(2\omega^2 Pr_f^2 C_f - \gamma_3\gamma_4 J\right)}{\left(\gamma_1 J\right)^2 + (\omega)^2}\right].\end{aligned} \tag{41}$$

The corresponding oscillatory frequency ω must verify the following equations:

$$\begin{aligned}&\left(4\gamma_1 J^2 Pr_f^3 C_f^2\right)\omega^4 + \left[J^2\left(\gamma_3\gamma_4 + \gamma_1 Pr_f\right)\right.\\&+ 4\gamma_1 JPr_f^3 C_f^2\left(\gamma_1 J^3 + \pi^2 Ta\right) - 2\gamma_1\gamma_3\gamma_4 Pr_f C_f J^3\left.\right]\omega^2\\&+ \left[\gamma_1^2 J\left(\gamma_3\gamma_4 + \gamma_1 Pr_f\right) + \pi^2 JTa\left(\gamma_1 - \gamma_3\gamma_4\right)\right.\\&\left.- 2\gamma_1\gamma_3\gamma_4 Pr_f C_f J^2\left(\gamma_3\gamma_4 + \gamma_1 Pr_f\right)\right] = 0.\end{aligned} \tag{42}$$

For oscillatory instability to be possible, the value of ω^2 generated by equation (42) must be positive.

4. Dynamical System Analysis

In order to explore how thermal relaxation time, hybrid nanoparticles, and rotation affect the nonlinear stability of the onset of thermal convection in a horizontal layer of ordinary fluid such as water, we reduce the problem to the classical case of two-dimensional convective rolls in a fluid layer with unconstrained horizontal boundaries. Thus, we assume that all physical quantities are independent of x. We consider the early stages of nonlinear convection when the basic structure of the convective rolls is still determined by the dynamic behavior of the linearized solution. The real components of the fluid velocity are expressed in terms of partial derivatives of the stream function as follows:

$$\begin{aligned}u &= -\frac{\partial\psi(y,z,t)}{\partial z},\\ w &= \frac{\partial\psi(y,z,t)}{\partial y}.\end{aligned} \tag{43}$$

Eliminating the pressure from equation (2) and introducing the expressions of the stream function defined in equations (43) into the resulting equation and equations (3) and (4), we obtain with the appropriate dimensionless variables [10, 42], the following new equations:

$$\left[\left(\frac{1}{Pr_f}\frac{\partial}{\partial t_*} - \gamma_5\nabla^2\right)^2 - Ta\frac{\partial^2}{\partial z_*^2}\right]\frac{\partial^2\psi_*}{\partial y_*^2} = \gamma_6 Ra_f\left(\frac{1}{Pr_f}\frac{\partial}{\partial t_*} - \gamma_5\nabla^2\right)\frac{\partial^2 T_*}{\partial y_*^2}, \tag{44}$$

$$\left(1 + 2C_f\frac{d}{dt_*}\right)\left(\frac{dT_*}{dt_*} - \frac{\partial\psi_*}{\partial y_*}\right) = \gamma_7\left(\frac{\partial^2 T_*}{\partial y_*^2} + \frac{\partial^2 T_*}{\partial z_*^2}\right), \tag{45}$$

with

$$\begin{aligned}\frac{d}{dt_*} &= \frac{\partial}{\partial t_*} - \frac{\partial\psi_*}{\partial z_*}\frac{\partial}{\partial y_*} + \frac{\partial\psi_*}{\partial y_*}\frac{\partial}{\partial z_*},\\ Ra_f &= \frac{g.H^3\beta_f\left(T_c - T_0\right)}{\alpha_f\nu_f},\\ Pr_f &= \frac{\nu_f}{\alpha_f},\\ C_f &= \frac{\tau\alpha_f}{2H^2},\\ \gamma_5 &= \frac{\mu_{hf}}{\mu_f}\frac{\rho_f}{\rho_{hf}}\frac{k_f}{k_{hf}}\frac{(\rho Cp)_{hf}}{(\rho Cp)_f},\\ \gamma_6 &= \frac{(\rho\beta)_{hf}}{(\rho\beta)_f}\frac{\rho_{hf}}{\rho_{hf}},\\ \gamma_7 &= \frac{k_{hf}}{k_f}\frac{(\rho Cp)_f}{(\rho Cp)_{hf}}.\end{aligned} \tag{46}$$

The ratio of the Rayleigh number of the hybrid nanofluid to that of the base fluid gives the effective Rayleigh number of the hybrid nanofluid as a function of the thermophysical properties and Rayleigh number of the heat transfer fluid defined as

$$Ra_f = \left(\frac{(\rho\beta)_{hf}}{(\rho\beta)_f}\right)\left(\frac{k_f}{k_{hf}}\right)\left(\frac{(\rho Cp)_{hf}}{(\rho Cp)_f}\right)\left(\frac{\mu_f}{\mu_{hf}}\right)Ra_f. \tag{47}$$

Similarly, the Cattaneo number of the hybrid nanofluid is defined as follows:

$$C_{hf} = \gamma_7 C_f. \tag{48}$$

4.1. Reduced Set of Equations. The solution of the coupled nonlinear system of partial differential equations (44) and (45) will be obtained by representing the current function and the temperature using the Galerkin expansion in the following form [42]:

$$\begin{aligned}\psi_*\left(y_* z_* t_*\right) &= A_{11}\left(t_*\right)\sin\left(\kappa y_*\right)\sin\left(\pi z_*\right),\\ T_*\left(y_* z_* t_*\right) &= B_{11}\left(t_*\right)\cos\left(\kappa y_*\right)\sin\left(\pi z_*\right)\\ &\quad + B_{02}\left(t_*\right)\sin\left(\pi z_*\right).\end{aligned} \tag{49}$$

This representation is equivalent to a Galerkin expansion of the solution in the y and z directions, truncated when $i + j = 2$, where i is the Galerkin summation index in the y direction and j is the Galerkin summation index in the z direction. Substituting equations (49) into equations (44) and (45), multiplying the equations by the orthogonal eigenfunctions corresponding to equations (44), and integrating over the domain and wavelength of the convection cell in the vertical and horizontal directions respectively, i.e., $\int_0^{\pi/\kappa} dy \int_0^1 dz\,(.)$, we obtain a set of three ordinary differential

equations for the time evolution of the second-order amplitudes expressed by

$$\frac{d^2A_{11}}{dt_*^2} = -2\gamma_5 Pr_f\left(\kappa^2+\pi^2\right)\frac{dA_{11}}{dt_*} - \gamma_5^2 Pr_f^2\left(\kappa^2+\pi^2\right)^2 A_{11} - \pi^2 Pr_f^2 Ta A_{11} + \frac{\gamma_6\kappa^2 Pr_f Ra_f}{\left(\kappa^2+\pi^2\right)}A_{11} + \gamma_6\kappa^2 Pr_f Ra_f\left(\gamma_5 Pr_f - \gamma_7\right),$$

$$\frac{d^2B_{02}}{dt_*^2} = \frac{1}{2C_f}\left[\frac{dB_{02}}{dt_*} + \frac{\pi\kappa}{2}A_{11}B_{11} - 4\pi^2\gamma_7 B_{02}\right] - \frac{\pi\kappa^2}{2}A_{11}^2 + \frac{\pi\kappa}{2}\left(A_{11}\frac{dB_{11}}{dt_*} + B_{11}\frac{dA_{11}}{dt_*}\right) + \pi^2\kappa^2 A_{11}^2 B_{11} + \pi\kappa A_{11}\frac{dB_{11}}{dt_*}, \tag{50}$$

$$\frac{d^2B_{02}}{dt_*^2} = \frac{1}{2C_f}\left[\frac{dB_{02}}{dt_*} + \frac{\pi\kappa}{2}A_{11}B_{11} - 4\pi^2\gamma_7 B_{02}\right] - \frac{\pi\kappa^2}{2}A_{11}^2 + \frac{\pi\kappa}{2}\left(A_{11}\frac{dB_{11}}{dt_*} + B_{11}\frac{dA_{11}}{dt_*}\right) + \pi^2\kappa^2 A_{11}^2 B_{11} + \pi\kappa A_{11}\frac{dB_{11}}{dt_*}.$$

After introducing new variables of amplitudes defined as

$$\begin{aligned} U &= \frac{(\kappa/\kappa_c)A_{11}}{(\kappa/\kappa_c)^2+2}, \\ Y &= \kappa R_f B_{11}, \\ Z &= \pi R_f B_{02}, \end{aligned} \tag{51}$$

and the expressions

$$\begin{aligned} R_f &= \frac{Ra_f}{Ra_{fc}}, \\ t_* &= \left(\kappa^2+\pi^2\right)t, \\ \lambda &= \frac{8}{\left[(\kappa/\kappa_c)^2+2\right]}, \\ Ra_{fc} &= \frac{\epsilon\left(\kappa^2+\pi^2\right)^3}{\kappa^2}, \\ \delta &= \frac{1}{2C_f\left(\kappa^2+\pi^2\right)}, \\ T_f &= \frac{\pi^2 Ta}{\left(\kappa^2+\pi^2\right)^3}, \\ \epsilon &= \frac{(\rho\beta)_f}{(\rho\beta)_{hf}}\frac{\alpha_{hf}}{\alpha_f}\frac{\mu_{hf}}{\mu_f}, \\ \kappa_c &= \frac{\pi}{\sqrt{2}}, \end{aligned} \tag{52}$$

in equations 50, we obtain the following system:

$$\begin{cases} \ddot{U} = -2\gamma_5 Pr_f\dot{U} + Pr_f\left[\gamma_6\epsilon R_f - Pr_f\left(T_f+\gamma_5^2\right)\right]U - \gamma_6 Pr_f\left[UZ - \left(\gamma_5 Pr_f - \gamma_7\right)\right]Y, \\ \ddot{Y} = \epsilon R_f\dot{U} + U^2 Y - 2U\dot{Z} - \dot{U}Z + \delta\left(\epsilon R_f U - \dot{Y} - UZ - \gamma_7 Y\right), \\ \ddot{Z} = \dot{U}Y + 2U\dot{Y} - \epsilon R_f U^2 + U^2 Z + \delta\left(UY - \dot{Y} - \lambda\gamma_7 Z\right). \end{cases} \tag{53}$$

Therefore, we can reduce the amplitude equations of system (53) to a system of first-order nonlinear equations by introducing the amplitudes $V = \dot{U}$, $P = \epsilon R_f U - \dot{Y} - UZ$, and $S = UY - \dot{Z}$. Thus, we obtain the six-dimensional system by describing the nonlinear dynamic behavior of thermal convection in mono or hybrid nanofluids, presented as follows:

$$\begin{cases} \dot{U} = V, \\ \dot{Y} = \epsilon R_f U - P - UZ, \\ \dot{Z} = UY - S, \\ \dot{P} = US - \delta\left(P - \gamma_7 Y\right), \\ \dot{S} = UP - \delta\left(S - \lambda\gamma_7 Z\right), \\ \dot{V} = -2\gamma_5 Pr_f V + Pr_f\left[\gamma_6\epsilon R_f - Pr_f\left(T_f+\gamma_5^2\right)\right]U - \gamma_6 Pr_f\left[UZ - \left(\gamma_5 Pr_f - \gamma_7\right)\right]Y, \end{cases} \tag{54}$$

where the dot (.) denote the time derivative d/dt.

When $\varphi_1 = \varphi_2 = 0$, $\varphi_1 \neq 0$ and $\varphi_2 = 0$, $\varphi_1 = 0$ and $\varphi_2 = 0$, system equation (63) corresponds to the base fluid, alumina-water nanofluid, copper-water nanofluid, respectively.

When $T_f = 0$, system (63) is equivalent to the system obtained by Dèdèwanou et al. [42]. When $\varphi_1 = \varphi_2 = 0$, $C_f = 0$, system (54) is equivalent to the system obtained by Gupta et al. [10].

When $\varphi_1 = \varphi_2 = 0$, $T_f = 0$, system (54) is equivalent to the system obtained by Layek and Pati [41].

In the absence of the thermal relaxation time, (54) and (46) are reduced to the following system:

$$\begin{cases} \dot{U} = V, \\ \dot{Y} = \epsilon R_f U - \gamma_7 Y - UZ, \\ \dot{Z} = UY - \lambda\gamma_7 Z, \\ \dot{V} = -2\gamma_5 Pr_f V + Pr_f\left[\gamma_6 \epsilon R_f - Pr_f\left(T_f + \gamma_5^2\right)\right]U - \gamma_6 Pr_f\left[UZ - \left(\gamma_5 Pr_f - \gamma_7\right)\right]Y. \end{cases} \tag{55}$$

Lorenz [45] has investigated the nonlinear analysis of convection in pure fluid confined in a nonporous cavity by using the Fourier law. His nonlinear dynamic system has been analyzed and solved for $Pr_f = 10$, so that there are convection cells in the domain and that the boundary conditions are satisfied [45, 46]. Bissell [43] analyzed the oscillatory convection with the Cattaneo–Christov hyperbolic heat-flow model and included the effects owing to Prandtl number, which in some circumstances can be used as a control parameter. He showed that the Cattaneo threshold can be conceived equivalently as a Prandtl threshold, so that system bifurcations could potentially be triggered by varying the Prandtl number. For small values of Cattaneo number, a five-dimensional nonlinear system obtained by Layek and Pati [41] undergoes a subcritical transition to chaos similar to the Lorenz system but undergoes a period-doubling transition to chaos when $Pr_f = 5$ and $C_f = 0.001$. For increasing values of Prandtl number, he found that the fine-structure of the period-doubling cascade is interrupted and that this is due to the generation of internal noise that fastens the transitional process. With the critical value of the wavenumber corresponding to the convection threshold, the expression of the Rayleigh number of the base fluid defined in equation (53) gives: $Ra_{fc} = 27\pi^4\epsilon/4$.

4.2. Dissipation Effect. The nonlinear dynamical system (54) has the reflection symmetry $(U, Y, P) \longrightarrow -(U, Y, P)$ and

$$\begin{aligned} \vec{\nabla}.\vec{\vartheta} &= \frac{\partial \dot{U}}{\partial U} + \frac{\partial \dot{Y}}{\partial Y} + \frac{\partial \dot{Z}}{\partial Z} + \frac{\partial \dot{P}}{\partial P} + \frac{\partial \dot{S}}{\partial S} + \frac{\partial \dot{V}}{\partial V}, \\ \vec{\nabla}.\vec{\vartheta} &= -\left[Pr_f\left(2\gamma_5 + \gamma_6\right) + 2\delta\right]. \end{aligned} \tag{56}$$

We note that $\vec{\nabla}.\vec{\vartheta} < 0$ whatever the values of Pr_f, γ_5, γ_6 and δ. Then system (54) is dissipative and its solutions are bounded in phase space. Therefore, if a set of initial points in phase space occupies the region $\vartheta(0)$ at $t = 0$, then after some time, t, the end points of the corresponding trajectories will fill a volume

$$\vartheta(t) = \exp\left\{-\left[Pr_f\left(2\gamma_5 + \gamma_6\right) + 2\delta\right]t\right\}. \tag{57}$$

4.3. Equilibrium Points and Their Stability. In this section, the nature of the nonlinear dynamics of systems (54) and (55) is determined around the fixed points by analyzing the stability of stationary solutions. The hybrid nanofluid is confined in a nonporous cavity so that there are convection cells in the domain and the boundary conditions are satisfied.

4.3.1. The Case of $C_f = 0$. Considering the general form of system (54) defined by $\dot{X} = F(X_s)$ and the equilibrium (stationary or fixed) points X_s defined by $F(X_s) = 0$, we obtained three fixed equilibrium points of the system, including the first one

$$U_1 = Y_1 = Z_1 = P_1 = S_1 = V_1 = 0, \tag{58}$$

is the stationary solution and the other two

$$\begin{aligned} U_{2,3} &= \pm\sqrt{\frac{-\lambda\gamma_5\gamma_6\gamma_7}{\left(T_f + \gamma_5^2\right)}\left[\frac{\gamma_7}{\gamma_5\gamma_6}\left(T_f + \gamma_5^2\right) - \epsilon R_f\right]}, \\ Y_{2,3} &= \pm\sqrt{\frac{-\lambda\gamma_7}{\gamma_5\gamma_6}\left(T_f + \gamma_5^2\right)\left[\frac{\gamma_7}{\gamma_5\gamma_6}\left(T_f + \gamma_5^2\right) - \epsilon R_f\right]}, \\ Z_{2,3} &= \epsilon R_f - \frac{\gamma_7}{\gamma_5\gamma_6}\left(T_f + \gamma_5^2\right), \\ V_{2,3} &= 0, \end{aligned} \tag{59}$$

are the convection solutions. The linear stability of the points can be obtained by linearizing the nonlinear dynamical system equation (55). Thus, the resulting Jacobian matrix is as follows:

$$M = \begin{pmatrix} 0 & 0 & 0 & 1 \\ \varepsilon r_f - Z & -\gamma_7 & -U & 0 \\ Y & U & -\lambda Pr_f & 0 \\ Pr_f\left[\gamma_6 \varepsilon r_f - Pr_f\left(T_f + \gamma_5^2\right)\right] & \gamma_6 Pr_f\left(\gamma_5 Pr_f - \gamma_7\right) & -\gamma_6 Pr_f U & 2\gamma_5 Pr_f \end{pmatrix}. \tag{60}$$

Using test solutions of the form $\exp(\xi t)$, $\xi \in \mathbb{C}$, the stability of the fixed point corresponding to the conduction solution is controlled by the roots of the following characteristic polynomial equation:

$$(\lambda\gamma_7 + \xi)\left\{\xi^3 + \left(2\gamma_5 Pr_f + \gamma_7\right)\xi^2 + \left[Pr_f^2\left(T_f + \gamma_5^2\right) + Pr_f\left(2\gamma_5\gamma_7 - \gamma_6 \epsilon R_f\right)\right]\xi^2 + Pr_f^2\left[\left(T_f + \gamma_5^2\right) - \gamma_5\gamma_6\,\epsilon\, R_f\right]\right\} = 0. \tag{61}$$

This equation (61) generates four eigenvalues. The first one given by $\xi = -\lambda\gamma_7$ is always negative, and the other three are the solutions of the following equation:

$$\xi^3 + \left(2\gamma_5 Pr_f + \gamma_7\right)\xi^2 + \left[Pr_f^2\left(T_f + \gamma_5^2\right) + Pr_f\left(2\gamma_5\gamma_7 - \gamma_6\,\epsilon\, R_f\right)\right]\xi + Pr_f^2\left[\gamma_7\left(T_f + \gamma_5^2\right) - \gamma_5\gamma_6\,\epsilon\, R_f\right] = 0. \tag{62}$$

From this equation, the fixed point of the stationary solution is stable if and only if $\gamma_5\gamma_6\,\epsilon\, R_f < \gamma_7\left(T_f + \gamma_5^2\right)$. Thus, the critical value of the rescaled Rayleigh number of the base fluid at which the fixed point of the stationary solution loses its stability and that of the convection solution takes over is expressed by

$$R_{fc1} = \frac{\gamma_7}{\epsilon\gamma_5\gamma_6}\left(T_f + \gamma_5^2\right). \tag{63}$$

This expression is a function of the thermophysical properties of the hybrid nanofluid and the rescaled Taylor number, so the transition from conduction to stationary convection depends on the volume fraction of the nanoparticles and the effect of rotation as shown in Figure 2.

Data analysis of the curves constructed in Figure 2 shows that when the value of Taylor number is less than about 0.33, 0.315, 0.30, and 0.293 for $\varphi_1 = \varphi_2 = 0.01, 0.02, 0.03$, and 0.04, respectively, R_{fc1} decreases but increases for higher values of T_f. Taking $T_f = 0$ for example, we found $R_{fc1} = 1.2$ like Gupta [10] for the ordinary fluids ($\varphi = 0$). But when $\varphi_1 = \varphi_2 = 0.01, 0.02, 0.03, 0.04$; we have $R_{fc1} \approx 1.176$, 1.157, 1.142, 1.13. Thus, it is then possible to reduce or increase conduction in a heat transfer fluid using hybrid nanoparticles under the effect of rotation. Using the same test solutions of the form $\exp(\xi t)$, $\xi \in \mathbb{C}$, the stability of the fixed points corresponding to the convection solution is controlled by the roots of the following characteristic polynomial equation:

$$\begin{aligned} &\xi^4 + \left[\gamma_7(1+\lambda) + 2\gamma_5 Pr_f\right]\xi^3 + \left[\frac{\lambda\gamma_5\gamma_6\gamma_7\varepsilon R_f}{\left(T_f + \gamma_5^2\right)} + 2\gamma_5\gamma_7 Pr_f(1+\lambda) + Pr_f\left(Pr_f - \frac{\gamma_7}{\gamma_5}\right)\left(T_f + \gamma_5^2\right)\right]\xi^2 \\ &+ \left\{\frac{2\lambda\gamma_5^2\gamma_6\gamma_7\varepsilon R_f}{\left(T_f + \gamma_5^2\right)} + \lambda\gamma_7 Pr_f\left[\left(Pr_f - \frac{2\gamma_7}{\gamma_5}\right)\left(T_f + \gamma_5^2\right) + \gamma_6\varepsilon R_f\right]\right\}\xi = 0. \end{aligned} \tag{64}$$

This equation is solved numerically for different values of the parameters to study the stability of the fixed points of the convection solutions.

4.3.2. The Case of $\mathbf{C_f} \neq 0$. In the presence of the thermal relaxation time, the elimination of a quadratic factor, which is not associated with the beginning of the instability,

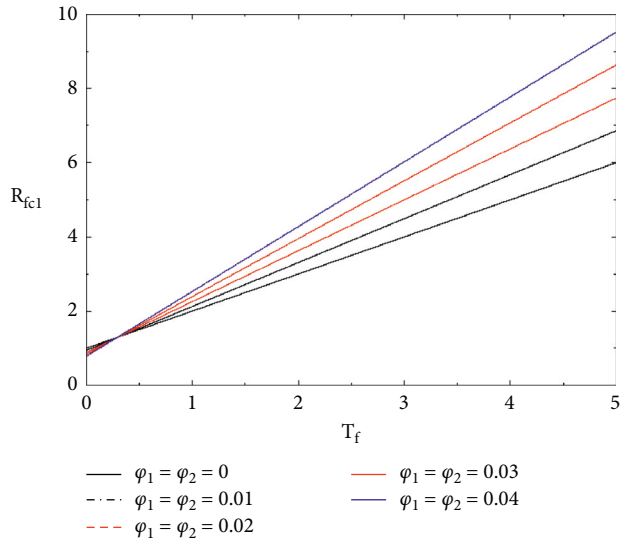

Figure 2: Variation of the critical Rayleigh number of the stationary solution as a function of the Taylor number with increasing nanoparticle volume fraction.

allowed us to find the characteristic polynomial equation of the fixed point corresponding to the immobile support at the origin whose roots control its stability, which is presented as follows:

$$\begin{aligned}&\xi^4 + \left(2\gamma_5 Pr_f + \delta\right)\xi^3 + \left\{\delta\left(2\gamma_5 Pr_f + \delta\right) - Pr_f\left[\gamma_6 \epsilon R_f - Pr_f\left(T_f + \gamma_5^2\right)\right]\right\}\\ &\xi^2 + \left\{2\gamma_5\gamma_7\delta Pr_f - \gamma_6 Pr_f\left(2\gamma_5 Pr_f - \gamma_7\right)\epsilon R_f - \delta Pr_f\left[\gamma_6\epsilon R_f - Pr_f\left(T_f + \gamma_5^2\right)\right]\right\}\\ &\quad + \delta Pr_f^2\left[\gamma_7\left(T_f + \gamma_5^2\right) - \gamma_5\gamma_6\,\epsilon R_f\right] = 0.\end{aligned} \tag{65}$$

When $\xi = 0$, a stability exchange occurs and stationary convection takes over. The corresponding critical rescaled Rayleigh number of the base fluid from which this phenomenon is observed is equivalent to equation (63).

5. Results and Discussion

We performed numerical simulations to investigate the influence of hybrid nanoparticles and rotation on the dynamic behavior of thermal convection in a base fluid (water) in the presence of thermal relaxation time. Using free boundary conditions, we determined the analytical expressions of Rayleigh numbers of the base fluid for stationary and oscillatory convection as a function of the thermophysical properties of the hybrid nanofluid. We observe that the stationary Rayleigh number of the base fluid does not depend on the Prandtl number and the Cattaneo number. Figure 3 shows the variation of the stationary Rayleigh number of the base fluid as a function of wavelength for different values of the volume fraction of the hybrid nanoparticles (alumina-copper) with a fixed value of Taylor number. From these plotted curves, we find that the stationary Rayleigh number increases with the value of the volume fraction of hybrid nanoparticles. Thus, the addition of the hybrid nanoparticles (alumina-copper) to the base fluid (water) subjected to the rotation stabilizes the stationary convection. Figure 4 shows the variation of the stationary Rayleigh number of the base fluid as a function of the wavelength for different values of the Taylor number with a fixed value of the volume fraction of the hybrid nanoparticles (alumina-copper).

From these plotted curves, it can be seen that the stationary Rayleigh number increases with an increasing Taylor number. Thus, the rotation stabilizes the stationary convection in the hybrid nanofluid.

The fourth-order Runge–Kutta method, the polynomial companion matrix, and the standard eigenvalue solver of the Lapack method are used to numerically solve systems equations (54) and (55). We took the initial conditions $U(0) = Y(0) = 0.8, Z(0) = 0.92195, P(0) = 0.8, S(0) = 0.92195$ and $V(0) = 0.8$. In order to guarantee the results, our different numerical simulations are compared with the results obtained by Dèdèwanou et al. [42] and Gupta [10]. We present in Figures 5–8, the bifurcation diagrams representing the minima and maxima of the posttransient regimes of the solutions of the amplitude $Z(t)$ as a function of function of R_f when the thermal relaxation time is zero using $Pr_f = 10$ and $\lambda = 8/3$. These diagrams show that system equation (55) can have chaotic, periodic, or multiperiodic behavior depending on the parameter values chosen. By comparing the diagrams in Figures 5–7, we notice that, for $T_f = 0.2$, when the volume fraction of the hybrid nanoparticles increases, the

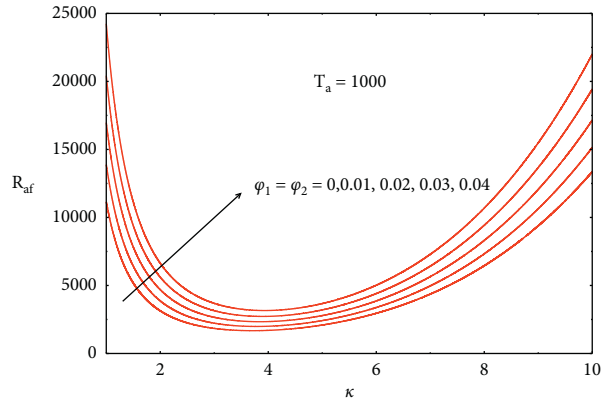

Figure 3: Variation of the stationary Rayleigh number of the base fluid as a function of the volume fraction of hybrid (aluminum-copper) nanoparticles.

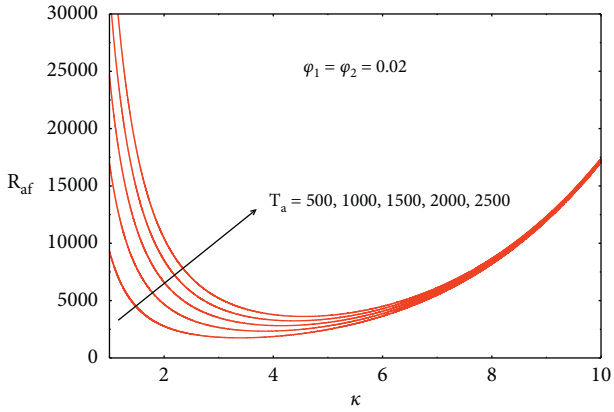

Figure 4: Variation of the stationary Rayleigh number of the base fluid as a function of the Taylor number.

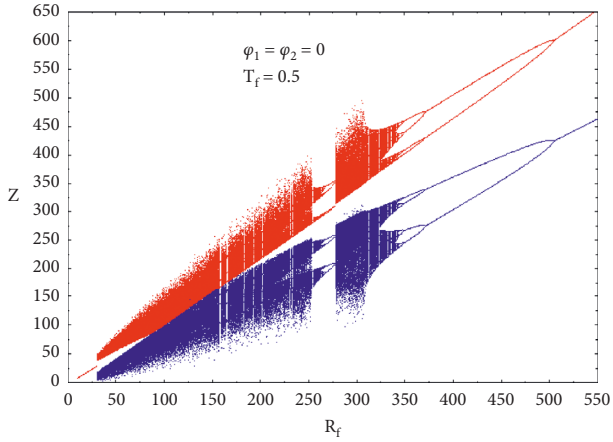

Figure 5: Bifurcation diagram of Z versus R_f representing maxima and minima of the posttransient solution of $Z(t)$ for hybrid nanofluid $\varphi_1 = \varphi_2 = 0$) with $T_f = 0.2$.

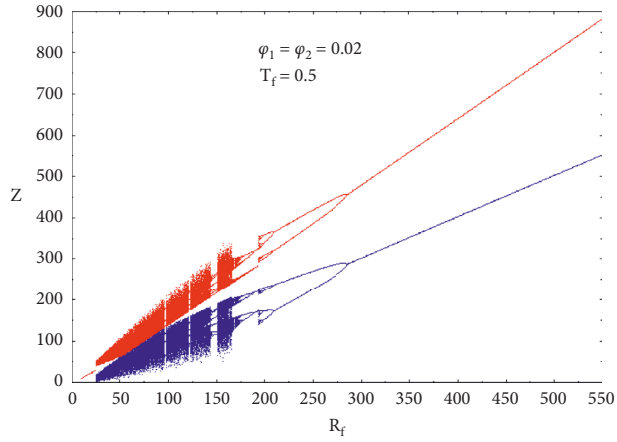

Figure 6: Bifurcation diagram of Z versus R_f representing maxima and minima of the posttransient solution of $Z(t)$ for hybrid nanofluid $\varphi_1 = \varphi_2 = 0.02$) with $T_f = 0.5$.

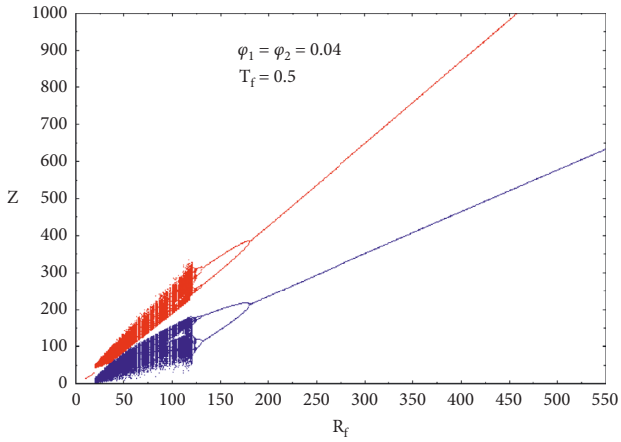

Figure 7: Bifurcation diagram of Z versus R_f representing maxima and minima of the posttransient solution of $Z(t)$ for hybrid nanofluid $\varphi_1 = \varphi_2 = 0.04$) with $T_f = 0.5$.

domain of the chaotic behavior chaotic behavior decreases with the increase of the values of the rescaled Rayleigh number of the number of the base fluid. On the other hand, comparison of the plots in Figures 6 and 8 shows that, for $\varphi_1 = \varphi_2 = 0.02$, increasing the values of the Taylor number increases the domain of chaotic behavior with increasing values of the rescaled Rayleigh number of the base fluid.

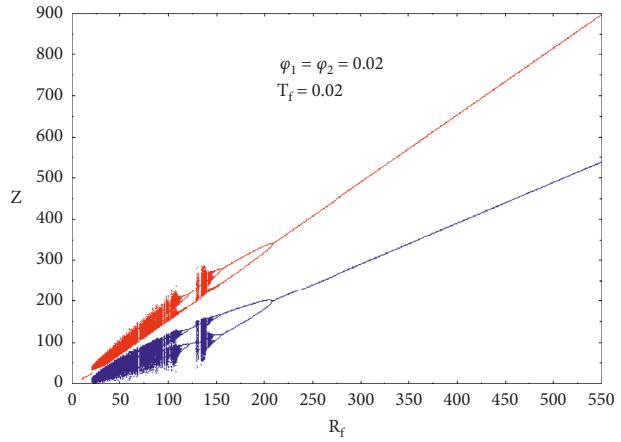

FIGURE 8: Bifurcation diagram of Z versus R_f representing maxima and minima of the posttransient solution of $Z(t)$ for hybrid nanofluid $\varphi_1 = \varphi_2 = 0.02$) with $T_f = 0.2$.

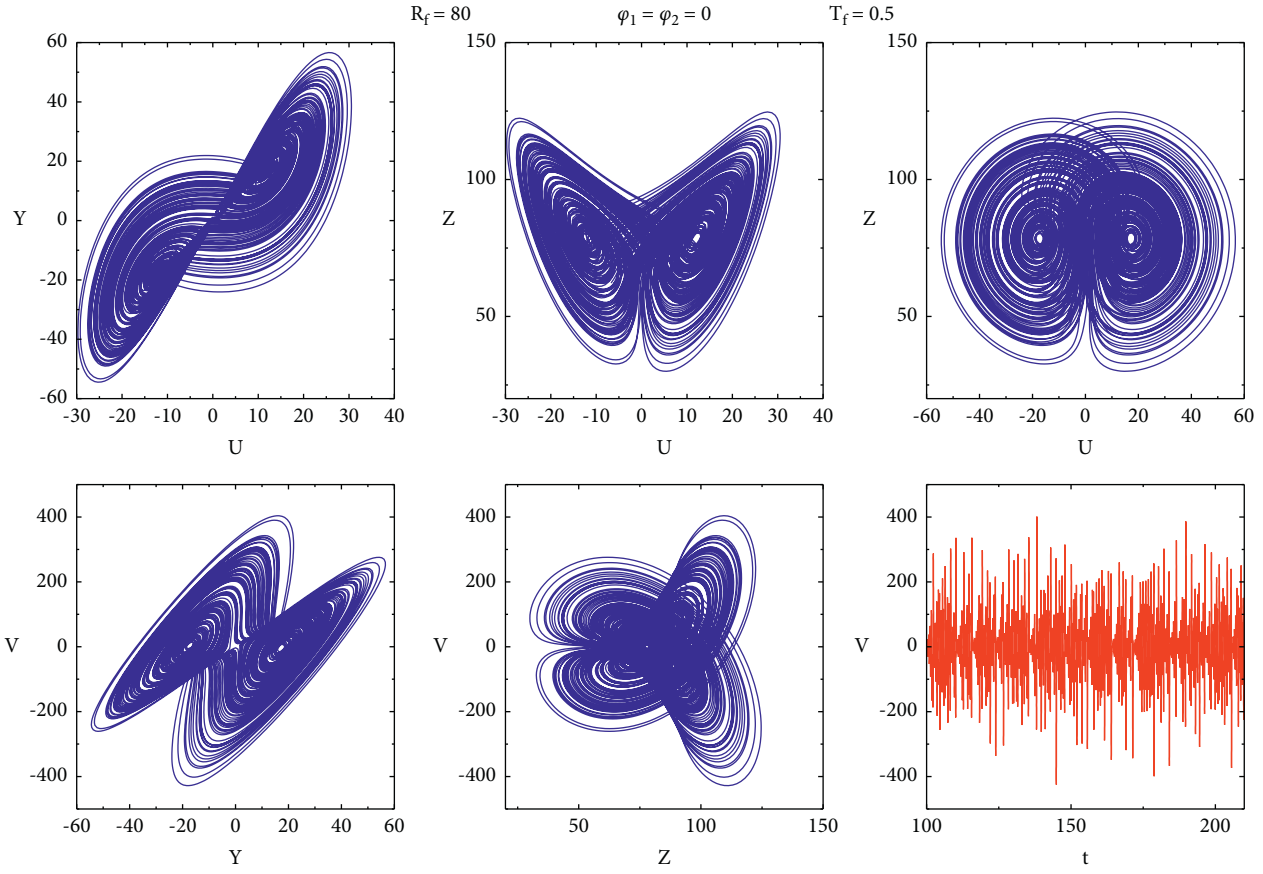

FIGURE 9: Phase portrait and its corresponding time story for $\varphi_1 = \varphi_2 = 0$), $R_f = 80$ and $T_f = 0.5$.

To confirm this prediction of the bifurcation diagrams, we constructed in Figure 9, the chaotic behavior of the system in the base fluid case by choosing $R_f = 80$ and $T_f = 0.5$. As shown in Figure 10, we set the values of the rescaled Taylor and Rayleigh numbers by varying the volume fraction of the hybrid nanoparticles to construct the in-plane

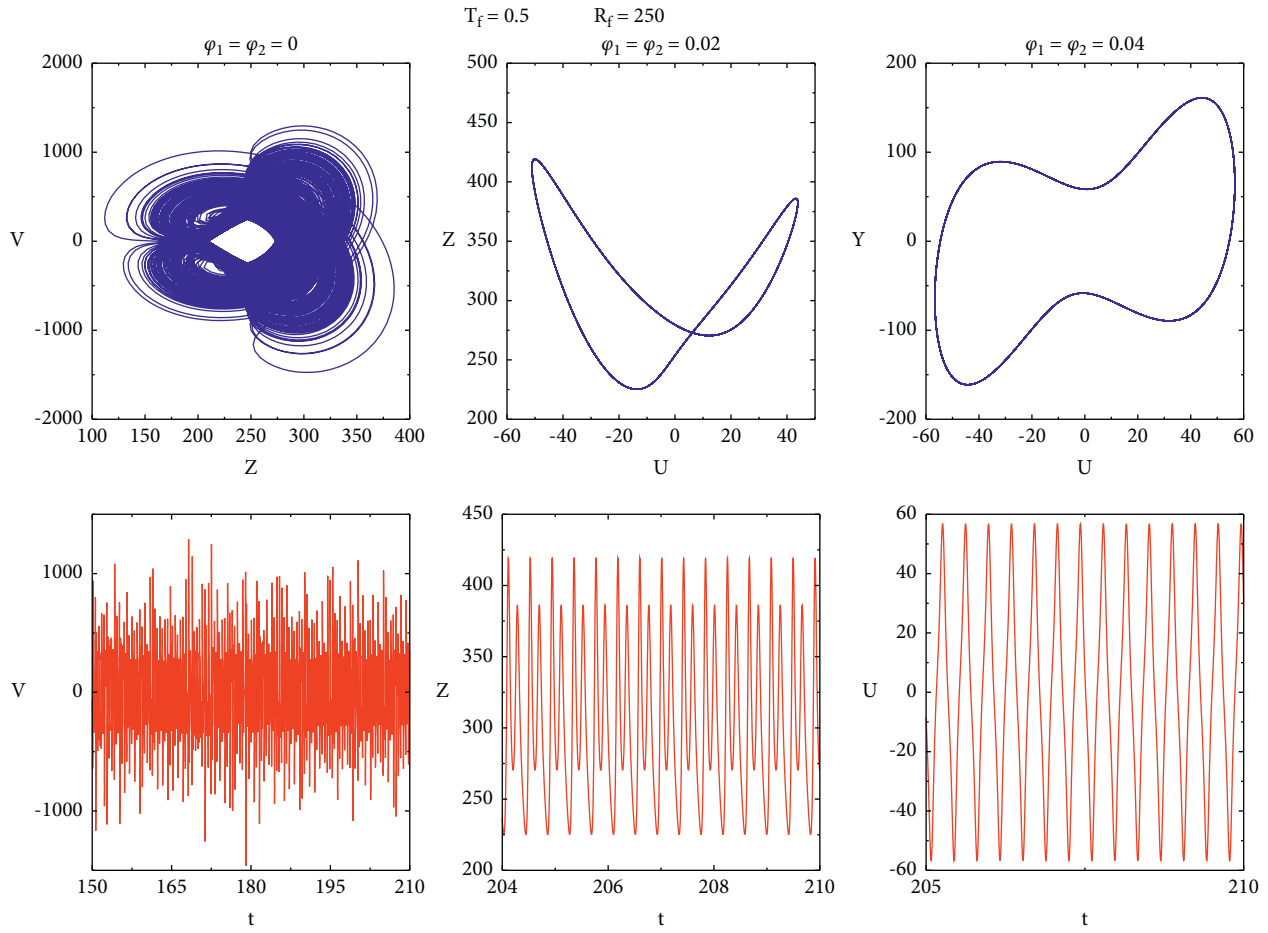

Figure 10: Phase portrait and its corresponding time story for $R_f = 250$, $T_f = 0.5$ and $\varphi_1 = \varphi_2 = 0$, 0.02, 0.04.

phase spaces with their corresponding time evolutions. For $\varphi_1 = \varphi_2 = 0, 0.02$ and 0.04, the system is chaotic in period 2 and period 1, respectively. Therefore, by analyzing these curves shown in Figure 10, it can be deduced that the addition of the hybrid nanoparticles in a heat transfer fluid makes the convection periodic. On the other hand, in the case of Figure 11, we have fixed the values of the volume fraction of hybrid nanoparticles and the rescaled Rayleigh number of the base fluid by varying the value of the rescaled Taylor number. The analysis of these curves shows that the system leaves the chaotic regime to the periodic regime when the value of the rescaled Taylor number decreases. Therefore, increasing the rescaled Taylor number increases the periodicity of the system.

Furthermore , we present in Figures 12–15, the bifurcation diagrams representing the minima and maxima of the post-transient regimes of the solutions of the amplitude $Z(t)$ as a function of R_f when the thermal relaxation time exists using $Pr_f = 5$ like Layek and Pati [41]. These diagrams show that system 63 can also have chaotic, periodic, or multiperiodic behavior depending on the parameter values chosen. Comparing the diagrams in Figures 12–14, it can be seen that, for $T_f = 0.2$ and $C_f = 0.001$, increasing the volume fraction of the nanoparticles hybrid nanoparticles decreases the domain of chaotic behavior with the increase of the Rayleigh number values of the base fluid. On the other hand, the comparison of the diagrams in Figures 13 and 15 show that, for $\varphi_1 = \varphi_2 = 0.02$ and $T_f = 0.2$, increasing the values of the Cattaneo number largely increases the range of chaotic behavior with increasing values of the Rayleigh number of the base fluid. Referring to Figure 14, for $\varphi_1 = \varphi_2 = 0.04$, $T_f = 0.2$ and $C_f = 0.001$, the system is chaotic for $14 < R_f < 16$.

In Figures 16 and 17, we have constructed the phase spaces in the $X - Z$ plane for different values of the control parameters of system equation (54). When we set $T_f = 0.2$ and $C_f = 0.001$ (see Figure 16), we notice in the base fluid case $(\varphi_1 = \varphi_2 = 0)$ that the system is in period 4 for $R_f = 166$. For $\varphi_1 = \varphi_2 = 0.02$, the system is in period 2 and for $\varphi_1 = \varphi_2 = 0.04$, the system has quasi-chaotic behavior. For $\varphi_1 = \varphi_2 = 0.02$ and $R_f = 100$ fixed, the system is in period 1 for $T_f = 0.2$ and $C_f = 0.001$. On the other hand, for $T_f = 0.2$ and $C_f = 0.003$, $T_f = 0.2$ and $C_f = 0.005$, $T_f = 0.3$ and $C_f = 0.005$, $T_f = 0.5$ and $C_f = 0.001$, and $T_f = 1.7$ and $C_f = 0.005$, the system is chaotic.

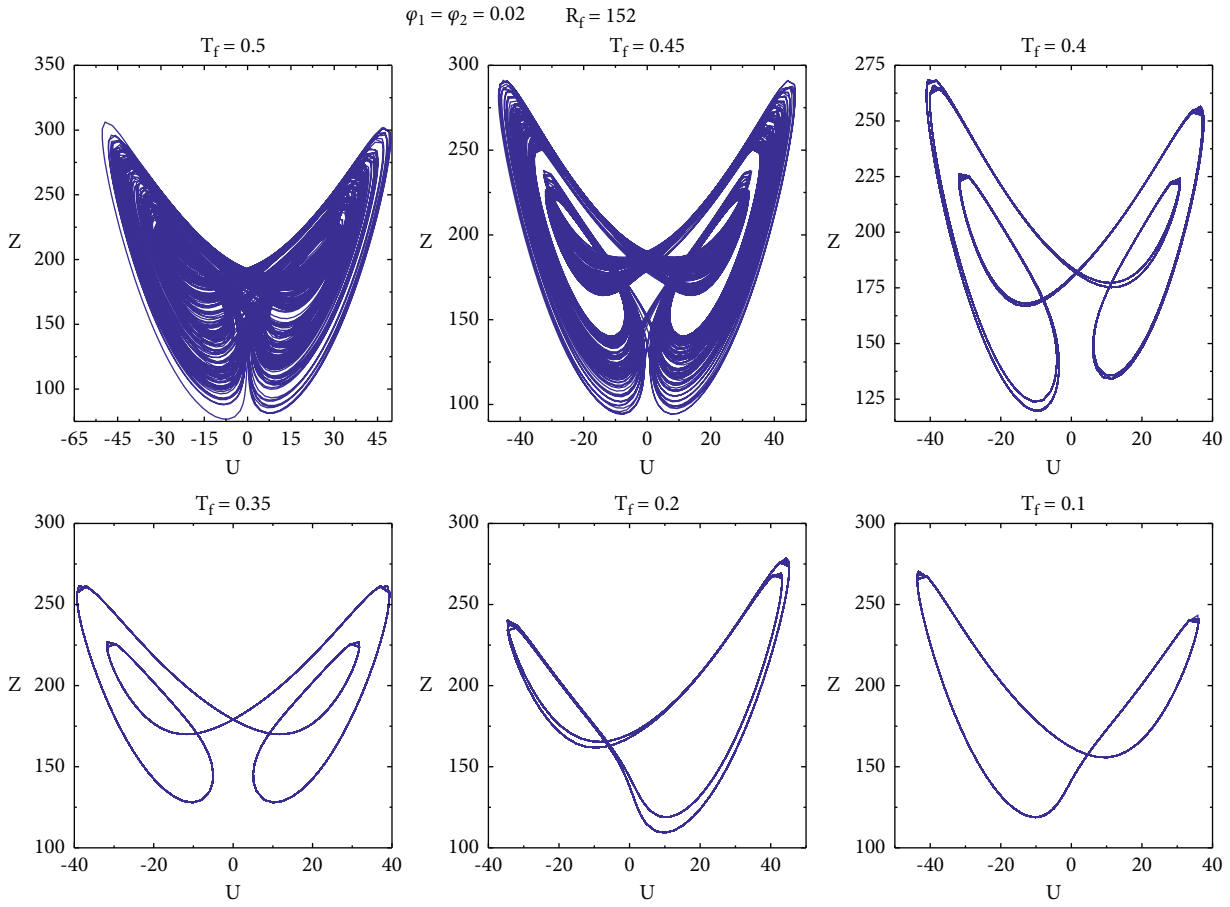

Figure 11: Phase portrait for $R_f = 152$ and $\varphi_1 = \varphi_2 = 0.02$ with different values of T_f.

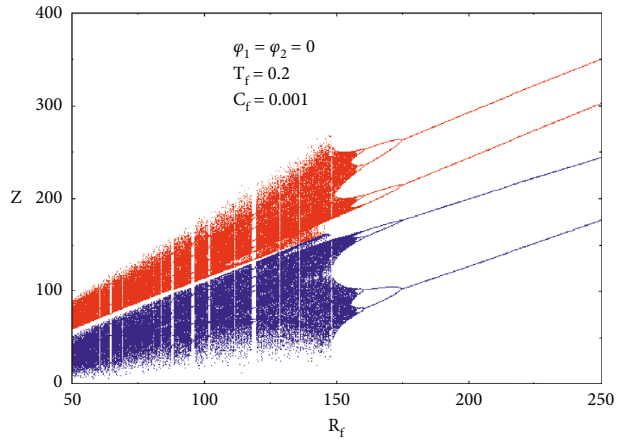

Figure 12: Bifurcation diagram of Z versus R_f representing maxima and minima of the posttransient solution of $Z(t)$ for base fluid ($\varphi_1 = \varphi_2 = 0$) with $T_f = 0.2$ and $C_f = 0.001$.

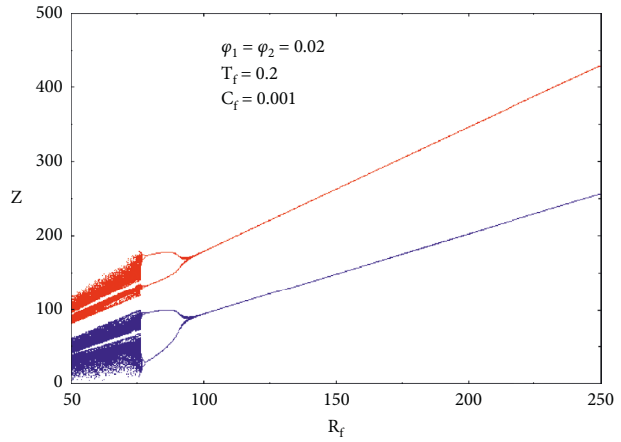

Figure 13: Bifurcation diagram of Z versus R_f representing maxima and minima of the posttransient solution of $Z(t)$ for hybrid nanofluid ($\varphi_1 = \varphi_2 = 0.02$) with $T_f = 0.2$ and $C_f = 0.001$.

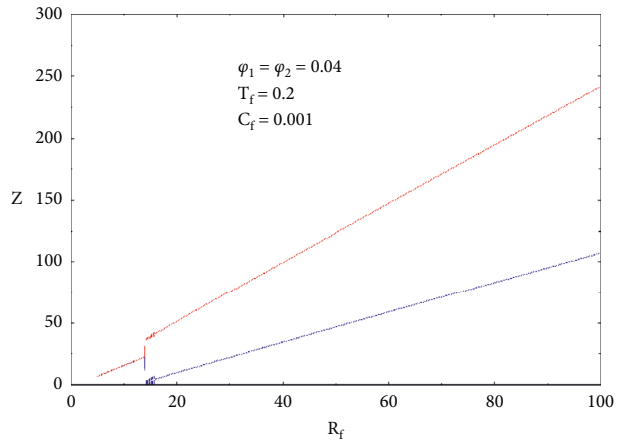

Figure 14: Bifurcation diagram of Z versus R_f representing maxima and minima of the posttransient solution of $Z(t)$ for hybrid nanofluid ($\varphi_1 = \varphi_2 = 0.04$) with $T_f = 0.2$ and $C_f = 0.001$.

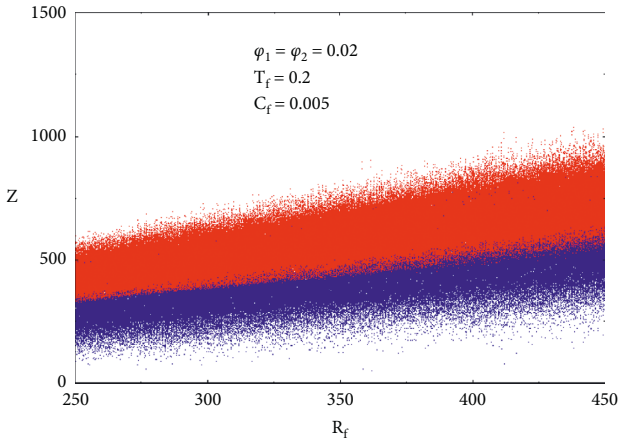

Figure 15: Bifurcation diagram of Z versus R_f representing maxima and minima of the posttransient solution of $Z(t)$ for hybrid nanofluid ($\varphi_1 = \varphi_2 = 0.02$) with $T_f = 0.2$ and $C_f = 0.005$.

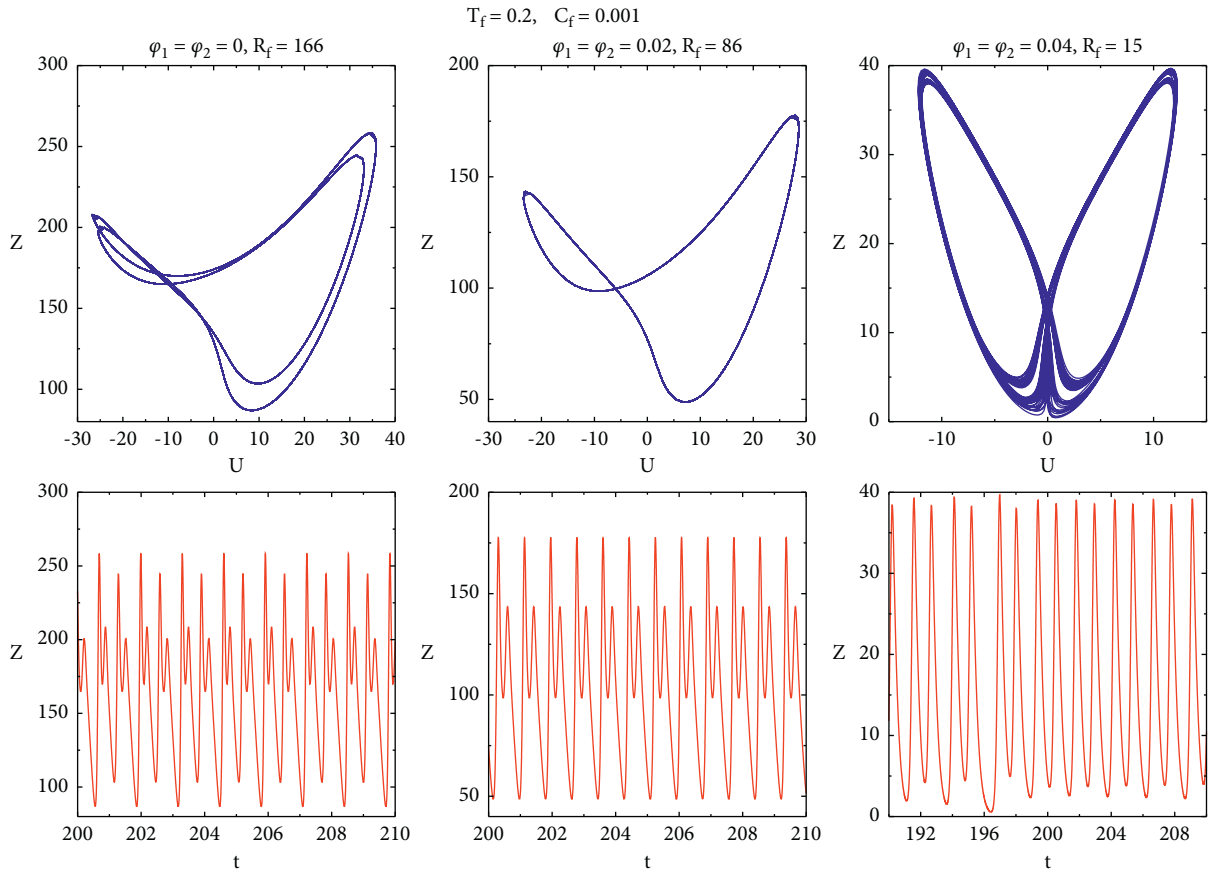

Figure 16: Phase portrait and its corresponding time story for $T_f = 0.2$ and $C_f = 0.001$.

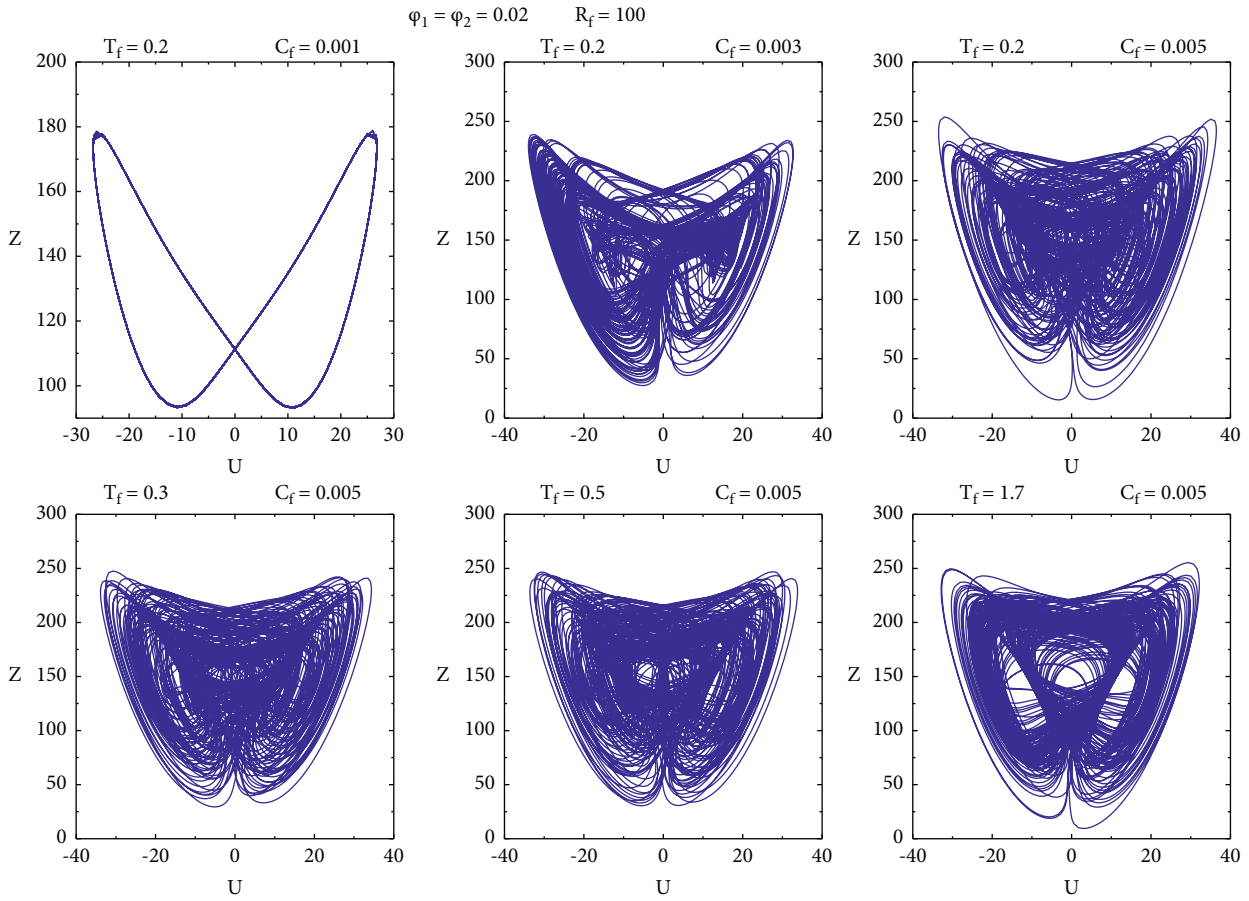

Figure 17: Phase portrait and its corresponding time story for $\varphi_1 = \varphi_2 = 0.02$ and $R_f = 100$.

6. Conclusions

We have studied the occurrence of thermal convective instabilities and chaos in a rotating infinite horizontal hybrid nanofluid layer heated from below with the Cattaneo–Christov heat flux model and subjected to unconstrained boundary conditions. The linear study of the mass, momentum, energy, and heat flow equations governing natural convection allowed us to find the general expression for the stationary Rayleigh number of the base fluid that can be used for the nonlinear dynamic analysis of thermal convection in nanofluids. We noticed that the rotation and the addition of nanoparticles in the base fluid have stabilizing effects on the stationary convection. With the obtained low-dimensional dynamical systems, we notice that the addition of hybrid nanoparticles in the heat transfer fluid subjected to rotation and/or in the presence of the thermal relaxation time reduces the domain of chaos and enlarges the domain of periodicity with the increase of the Rayleigh number of the base fluid. On the other hand, the increase of the Taylor number and Cattaneo number increases the chaotic domain with the increase of the Rayleigh number of the base fluid. The obtained nonlinear system depends on the parameters of the base fluid and the thermophysical properties of the hybrid nanofluid; it will be very useful to predict or control the chaotic behaviour of thermal convection in dynamic and biological systems. Thus, the hybrid nanofluid confers a great advantage for chaos control in many industrial applications like food processing, chemical processes, solidification and centrifugal casting of metals, and rotating machines to achieve the desired results. Obtained results and comparative studies show that the use of hybrid nanoparticles can be useful to control the small thermal relaxation time due to thermal inertia for thermal transport in biological tissues and surgical operations.

Latin symbols

A_{11}: Stream function amplitude
B_{11}, B_{02}: Temperature amplitude
C: Cattaneo number
Cp: Specific heat at constant pressure ($J.kg^{-1}: K^{-1}$)
d/dt: Material derivative
$\vec{e}_n$: Unit vector normal to the boundary
$h(x; y)$: Plane tiling function
$\vec{g}$, g: Acceleration vector of gravity, gravity intensity ($m.s^{-2}$)
k: Thermal conductivity ($W.m^{-1}.K^{-1}$)
m: Particle shape factor
M: Matrix associated to the origin fixed point
P: Pressure (Pa)
Pr: Prandtl number
Q: Heat flux
Ra: Thermal Rayleigh number
R_f: Rescaled Rayleigh number of the base fluid
t: Time (s)
Ta: Taylor number
T_f: Rescaled Taylor number
T_c: Hot temperature (K)
T_0: Cold temperature (K)
T: Temperature at time t (K)
$U; Y; Z; P; S; V$: Rescaled amplitudes
$\vec{v}$: velocity vector
W: Velocity eigenfunction
(x, y, z): Cartesian coordinates

Greek symbols

α: Thermal diffusivity of the fluid ($m^{-2}.s^{-1}$)
β: Coefficient of thermal expansion (K^{-1})
γ_i: Nanofluid parameters
δ: Rescaled Cattaneo number
ϵ: Parameter related to nanofluid properties
ζ: Vorticity
ϑ: Volume
κ: Wavenumber
μ: Dynamic viscosity ($kg.m^{-1}.s^{-1}$)
ξ: Eigenvalues
ρ: Density ($kg.m^{-3}$)
τ: Thermal relaxation time
φ_1: Alumina volume fraction
φ_2: Copper volume fraction
χ: Temperature gradian
ω: Oscillatory frequency
Θ: Temperature eigenfunction
Φ: Heat-flux eigenfunction
ψ: Stream function
Ω: Angular velocity

Subscripts

$*$: Dimensionless
$\sim$: Small quantity
b: Basic solution
c: Critical
f: Base fluid
hf: Hybrid nanofluid
s: Nanoparticle
0: Reference.

Data Availability

No data were used to support this study.

Conflicts of Interest

The authors declare that they have no conflicts of interest.

Acknowledgments

The authors thank the IMSP-UAC for its support. The authors also thank Dr. P. Hounsou for his collaboration.

References

[1] S. U. S. Choi and J. A. Eastman, "Enhancing thermal conductivity of fluids with nanoparticles," in *Proceedings of the 1995 International Machanical Engineering Congress and*

Exposition, vol. 66, no. 4356, pp. 99–105, ASME, San Francisco, NY, USA, November 1995.

[2] H. F. Oztop and E. Abu-Nada, "Numerical study of natural convection in partially heated rectangular enclosures filled with nanofluids," *International Journal of Heat and Fluid Flow*, vol. 29, no. 5, pp. 1326–1336, 2008.

[3] E. Abu-Nada, Z. Masoud, and A. Hijazi, "Natural convection heat transfer enhancement in horizontal concentric annuli using nanofluids," *International Communications in Heat and Mass Transfer*, vol. 35, no. 5, pp. 657–665, 2008.

[4] M. K. Das and P. Shridhar Ohal, "Natural convection heat transfer augmentation in a partially heated and partially cooled square cavity utilizing nanofluids," *International Journal of Numerical Methods for Heat and Fluid Flow*, vol. 19, no. 3/4, pp. 411–431, 2009.

[5] K. C. Lin and A. Violi, "Natural convection heat transfer of nanofluids in a vertical cavity: effects of non-uniform particle diameter and temperature on thermal conductivity," *International Journal of Heat and Fluid Flow*, vol. 31, no. 2, pp. 236–245, 2010.

[6] B. Elhajjar, G. Bachir, A. Fakih, and C. Charrier-Mojtabi, "Modeling of Rayleigh-Bénard natural convection heat transfer in nanofluids," *Comptes Rendus Mecanique*, vol. 338, no. 6, pp. 350–354, 2010.

[7] B. Mahanthesh, "Flow and heat transport of nanomaterial with quadratic radiative heat flux and aggregation kinematics of nanoparticles," *International Communications in Heat and Mass Transfer*, vol. 127, Article ID 105521, 2021.

[8] G. Shalini and B. Mahanthesh, "Rayleigh-benard convection in a dusty Newtonian nanofluid with and without Coriolis force," *Journal of Nanofluids*, vol. 7, no. 6, pp. 1240–1246, 2018.

[9] J. Ahuja and J. Sharma, "Rayleigh-Bénard instability in nanofluids: a comprehensive review," *Micro and Nano Systems Letters*, vol. 8, no. 1, p. 15, 2020.

[10] V. K. Gupta, B. S. Bhadauria, I. Jawdat, J. Singh, and A. Singh, "Chaotic convection in a rotating fluid layer," *Alexandria Engineering Journal*, vol. 54, no. 4, pp. 981–992, 2015.

[11] A. Jan, B. Mir, and A. A. Mir, "Hybrid nanofluids: an overview of their synthesis and thermophysical properties," in *Proceedings of the Tech. Conf. And Exhibition on Integration and Packaging of MEMS, NEMS, and Electronic System*, pp. 343–353, 2019.

[12] A. M. Rashad, A. J. Chamkha, and M. A. Ismael, "MHD natural convection in a triangular cavity filled with a Cu-Al_2O_3/water hybrid nanofluid with localized heating from below and internal heat generation," *Journal of Heat Transfer*, vol. 140, no. 7, Article ID 072502, 13 pages, 2018.

[13] N. A. L. Aladin, N. Bachok, and I. Pop, "Water hybrid nanofluid flow over a permeable moving surface in presence of hydromagnetic and suction effects," *Alexandria Engineering Journal*, vol. 59, no. 2, pp. 657–666, 2020.

[14] S. Myson and B. Mahanthesh, "Rayleigh-bénard convection in Casson and hybrid nanofluids: an analytical investigation," *Journal of Nanofluids*, vol. 8, no. 1, pp. 222–229, 2019.

[15] J. Mackolil and B. Mahanthesh, "Optimization of heat transfer in the thermal Marangoni convective flow of a hybrid nanomaterial with sensitivity analysis," *Applied Mathematics and Mechanics*, vol. 42, no. 11, pp. 1663–1674, 2021.

[16] K. Thriveni, B. Mahanthesh, Sensitivity computation of nonlinear convective heat transfer in hybrid nanomaterial between two concentric cylinders with irregular heat sources," *International Communications in Heat and Mass Transfer*, vol. 129, Article ID 105677, 2021.

[17] J. M. Jawdat, I. Hashim, and S. Momani, "Dynamical system Analysis of thermal convection in a horizontal layer of nanofluids heated from below," *Mathematical Problems in Engineering*, vol. 2012, Article ID 128943, 13 pages, 2012.

[18] K. Moaddy, "Control and stability on chaotic convection in porous media with time delayed fractional orders," *Advances in Difference Equations*, vol. 2017, no. 1, 2017.

[19] K. Moaddy, A. Radwan, and J. Jawdat, "Bifurcation behaviour and control on chaotic convection of nanofluids with fractional-orders," *Recent Advances in Mathematical Methods and Computational Techniques in Modern Science*, pp. 63–72, 2013.

[20] R. Bhardwaj and M. Chawla, "Convection dynamics of nanofluids for temperature and magnetic field variations," *Advances in Intelligent Systems and Computing*, vol. 1165, pp. 271–289, 2020.

[21] S. J. Dèdèwanou, A. L. Hinvi, and H. C. Miwadinou, "Chaotic convection in a hyorizontal cavity filled with (alumina–copper)/water hybrid nanofluid Heated from below in Presence of Magnetic Field," *Brazilian Journal of Physics*, vol. 51, no. 4, pp. 1079–1095, 2021.

[22] C. I. Christov and P. M. Jordan, "Heat conduction paradox involving second-sound propagation in moving media," *Physical Review Letters*, vol. 94, no. 15, Article ID 154301, 2005.

[23] C. I. Christov, "On frame indifferent formulation of the Maxwell-Cattaneo model of finite-speed heat conduction," *Mechanics Research Communications*, vol. 36, no. 4, pp. 481–486, 2009.

[24] B. Straughan, "Thermal convection with the Cattaneo-Christov model," *International Journal of Heat and Mass Transfer*, vol. 53, no. 1-3, pp. 95–98, 2010.

[25] B. Mahanthesh, B. J. Gireesha, and C. S. K. Raju, "Cattaneo-Christov heat flux on UCM nanofluid flow across a melting surface with double stratification and exponential space dependent internal heat source," *Informatics in Medicine Unlocked*, vol. 9, pp. 26–34, 2017.

[26] J. Alebraheem and M. Ramzan, "Flow of nanofluid with Cattaneo-Christov heat flux model," *Applied Nanoscience*, vol. 10, no. 8, pp. 2989–2999, 2020.

[27] A. S. Dogonchi and D. D. Ganji, "Impact of Cattaneo-Christov heat flux on MHD nanofluid flow and heat transfer between parallel plates considering thermal radiation effect," *Journal of the Taiwan Institute of Chemical Engineers*, vol. 80, pp. 52–63, 2017.

[28] S. Jakeer, P. BalaAnki Reddy, A. M. Nabwey, and H. A. Nabwey, "Impact of heated obstacle position on magneto-hybrid nanofluid flow in a lid-driven porous cavity with Cattaneo-Christov heat flux pattern," *Alexandria Engineering Journal*, vol. 60, no. 1, pp. 821–835, 2021.

[29] A. Hafeez, M. Khan, A. Ahmed, and J. Ahmed, "Rotational flow of Oldroyd-B nanofluid subject to Cattaneo-Christov double diffusion theory," *Applied Mathematics and Mechanics*, vol. 41, no. 7, pp. 1083–1094, 2020.

[30] A. Ahmed, M. Khan, M. Ahmed, J. Iqbal, and Z. Iqbal, "Forced convection in 3D Maxwell nanofluid flow via Cattaneo-Christov theory with Joule heating," *Proceedings of the Institution of Mechanical Engineers - Part E: Journal of Process Mechanical Engineering*, vol. 235, no. 4, pp. 747–757, 2021.

[31] A. Saeed, S. Islam, A. Shah, Z. Kumam, P. Khan, and W. Khan, "Influence of cattaneo-christov heat flux on MHD jeffrey, Maxwell, and Oldroyd-B nanofluids with homogeneous-heterogeneous reaction," *Symmetry*, vol. 11, no. 3, p. 439, 2019.

[32] H. Gul, M. Ramzan, J. D. Chu, Y. M. Kadry, and S. Kadry, "Multiple slips impact in the MHD hybrid nanofluid flow with Cattaneo-Christov heat flux and autocatalytic chemical reaction," *Scientific Reports*, vol. 11, no. 1, Article ID 14625, 2021.

[33] D. Lu, M. Ramzan, M. Howari, F. Chung, and J. D. Chung, "A thin film flow of nanofluid comprising carbon nanotubes influenced by Cattaneo-Christov heat flux and entropy generation," *Coatings*, vol. 9, no. 5, p. 296, 2019.

[34] Y. Zhang, N. Shahmir, M. Alotaibi, H. Aljohani, and H. M. Aljohani, "Upshot of melting heat transfer in a Von Karman rotating flow of gold-silver/engine oil hybrid nanofluid with Cattaneo-Christov heat flux," *Case Studies in Thermal Engineering*, vol. 26, Article ID 101149, 2021.

[35] S. B. Yu-Ming Chu and M. Ramzan, "Model-based Comparative Study of Magnetohydrodynamics Unsteady Hybrid Nanofluid Flow between Two Infinite Parallel Plates with Particle Shape Effects," *Mathmatical Methods in applied Sciences*, Wiley Online Library, NJ, USA, 2022.

[36] M. Ramzan, H. Gul, M. Y. Baleanu, D. Nisar, and K. S. Nisar, "On hybrid nanofluid Yamada-Ota and Xue flow models in a rotating channel with modified Fourier law," *Scientific Reports*, vol. 11, no. 1, Article ID 19590, 2021.

[37] M. Ramdan, N. Shahmir, H. A. S. Nisar, K. S. Alharbi, F. M. Yahia, and I. S. Yahia, "Hydrodynamic and heat transfer analysis of dissimilar shaped nanoparticles-based hybrid nanofluids in a rotating frame with convective boundary condition," *Scientific Reports*, vol. 12, no. 1, 2022.

[38] N. Abid, M. Ramzan, J. D. Kadry, S. Chu, and Y. M. Chu, "Comparative analysis of magnetized partially ionized copper, copper oxide-water and kerosene oil nanofluid flow with Cattaneo-Christov heat flux," *Scientific Reports*, vol. 10, no. 1, p. 436, 2020.

[39] M. Ramzan, H. Gul, and S. Kadry, "Onset of Cattaneo-Christov heat flux and thermal stratification in ethylene-glycol based nanofluid flow containing carbon nanotubes in a rotating frame," *IEEE Access*, vol. 7, pp. 146190–146197, 2019.

[40] Y. M. Chu, M. Ramzan, N. Shaheen et al., "Analysis of Newtonian heating and higher-order chemical reaction on a Maxwell nanofluid in a rotating frame with gyrotactic microorganisms and variable heat source/sink," *Journal of King Saud University Science*, vol. 33, no. 8, Article ID 101645, 2021.

[41] G. C. Layek and N. C. Pati, "Bifurcations and chaos in convection taking non-Fourier heat-flux," *Physics Letters A*, vol. 381, no. 41, pp. 3568–3575, 2017.

[42] S. J. Dèdèwanou, A. V. Monwanou, A. A. Koukpémèdji, L. A. Hinvi, C. H. Miwadinou, and J. B Chabi Orou, "Thermal instability and chaos in a hybrid nanofluid flow," *International Journal of Bifurcation and Chaos*, vol. 32, no. 07, Article ID 2250102, 21 pages, 2022.

[43] J. J. Bissell, "On oscillatory convection with the Cattaneo-Christov hyperbolic heat-flow model," *Proceedings of the Royal Society A: Mathematical, Physical & Engineering Sciences*, vol. 471, no. 2175, Article ID 38527619, 2015.

[44] S. Chandrasekhar, *Hydrodynamic and Hydromagnetic Stability*, Dover, NY, USA, 1981.

[45] E. N. Lorenz, "Deterministic nonperiodic flow," *Journal of the Atmospheric Sciences*, vol. 20, no. 2, pp. 130–141, 1963.

[46] C. Sparrow, "The Lorenz Equations: Bifurcations, Chaos and Strange Attractors," *Applied Mathematical Sciences I*, vol. 41, 1982.

Hindawi
Complexity
Volume 2022, Article ID 3505634, 14 pages
https://doi.org/10.1155/2022/3505634

WILEY | Hindawi

Research Article

Existence of Solution and Self-Exciting Attractor in the Fractional-Order Gyrostat Dynamical System

Muhammad Marwan,[1] **Gauhar Ali**,[2] **and Ramla Khan**[3]

[1]*College of Mathematics and Computer Science, Zhejiang Normal University, Jinhua, Zhejiang 321004, China*
[2]*Department of Mathematics, University of Malakand, Malakand, Pakistan*
[3]*School of Environment Earth and Ecosystem Sciences (EEES) School, The Open University, Milton Keynes MK76AA, UK*

Correspondence should be addressed to Gauhar Ali; gauharali4@gmail.com

Received 25 March 2022; Revised 5 May 2022; Accepted 9 May 2022; Published 18 July 2022

Academic Editor: Chun-Biao Li

This work identifies the influence of chaos theory on fractional calculus by providing a theorem for the existence and stability of solution in fractional-order gyrostat model with the help of a fixed-point theorem. We modified an integer order gyrostat model consisting of three rotors into fractional order by attaching rotatory fuel-filled tank and provided an iterative scheme for our proposed model as a working rule of obtained analytical results. Moreover, this iterative scheme is injected into algorithms for a system of integer order dynamical systems to observe Lyapunov exponents and a bifurcation diagram for our proposed fractional-order dynamical model. Furthermore, we obtained five equilibrium points, including four unstable spirals and one saddle node, using local dynamical analysis which acted as self-exciting attractors and a separatrix in a global domain.

1. Introduction

System of ordinary differential equations [1]

$$\dot{x} = f(x, \beta). \tag{1}$$

Is called the dynamical system, and a parameter $\beta \in \mathbb{R}$ in the velocity vector field is termed as bifurcation parameter if system (1) changes its topological structure with the variation in parameter values, whereas the process of changing in qualitative structures is known as bifurcation. There are several types of bifurcation including saddle node [2], Hopf [3–7], and zero-Hopf [8–11]. The bifurcation diagram [12] for the parameter makes it easy for predicting the type of bifurcation and existence of chaos in system (1). Chaos has a vital role in engineering [13–17], medical [18–20], aeronautics [14, 21] and fluid dynamics [22–24]. Apart from the above cited applications, its great influence can also be found in fractional calculus [25–27] and reference therein. Dynamical systems based on ordinary differential equations with an integer order, $\gamma = 1$, describe velocity vectors, but for fractional order, $\gamma \in (0, 1)$, researchers aim to target velocity vectors and replace it by differential equation with order between 0 and 1. Several discretization techniques such as fractional linear multistep [28], Adam [29], predictor-corrector [30], and Adam–Bashforth/Moulton [31] are used to solve fractional-order dynamical systems since decade, but the most flexible scheme with fast convergence in solving nonlinear problems is the variation iteration method (VIM). This technique was used for integer order dynamical systems, but later on modified for fractional-order systems by introducing Lagrangian multiplier [32] into it. Many researchers have enhanced its importance by using it in several engineering-based complex problems, such as in 2006, the variation iteration scheme was utilized for fractional-order systems by Odibat and Momani [33], whereas new development in the VIM was carried by Wu and Baleanu [32] in 2013 to overcome its limitation. Recently in 2021, Kumar and Gupta [34] worked on application of the VIM in a fuzzy-based system.

It has been observed from the above-cited work and our knowledge from the literature that dynamical systems related to spacecrafts or its attached devices such as beam and gyrostat have never been considered for the existence of

solution and self-exciting attractors in a fractional-order form. Therefore, we have restructured the gyrostat chaotic system [35] into a fractional order along with the addition of a rotatory liquid-filled tank to discuss its unique solution, bounds, and stability using the fixed point theory. Moreover, for bringing novelty into our work, a variation iteration scheme has been used in our proposed fractional-order system to observe chaos into it. For this purpose, several algorithms such as by Wolf et al. [36] and the bifurcation diagram [37] were modified by injecting the VIM iteration scheme into these algorithms. Finally, analyzing local dynamics of our proposed model, trajectories around five equilibrium points with four unstable spirals and a single saddle node motivated us to search for self-exciting attractors with a separatrix in a global domain.

The following pattern can be followed for understanding the rest of the paper. In Section 2, the gyrostat chaotic system is remodeled by adding rotatory liquid-filled tank and modified into fractional order. Several theorems have been proved in Section 3 for the existence of solution and stability. An iteration scheme for our proposed model has been introduced in Section 4, while several applications of this scheme related to dynamical analysis are discussed in Section 5. Finally, Section 6 comprises concluding remarks and future target.

2. Modeling of Gyro Chaotic System Attached with Fuel-Filled Tank

Gyrostat is a device consisting of rotors, used as an attachment in larger objects for bringing stability in their dynamics with the passage of time. The system of three-dimensional ordinary differential equations for the gyrostat model is designed by Qi et al. [35]:

$$\begin{cases} I_x\dot{x} = \left(I_y - I_z\right)yz - yh_z + zh_y - T_x + L_x, \\ I_y\dot{y} = \left(I_z - I_x\right)zx - zh_x + xh_z - T_y + L_y, \\ I_z\dot{z} = \left(I_x - I_y\right)xy - xh_y + yh_x - T_z + L_z, \end{cases} \tag{2}$$

where $X = [xyz]^T$ is the angular velocity vector, $I = [I_x, I_y, I_z]$ are the principal moments of inertia of the gyrostat in the body axis frame, $H = [h_x, h_y, h_z]$ are constants of total angular momentum, whereas $L = [L_x, L_y, L_z]$ and $T = [T_x, T_y, T_z]$ are external and disturbed torques applied on the gyrostat, respectively.

A tank, rotating about an angle θ at desired point $(\overline{x}, \overline{y}, \overline{z})$ (shown in Figure 1), is attached with an originally disturbed gyrostat system given in (2). It is observed that $L = (L_x, L_y, L_z)$ is a vector of external forces applied on the gyrostat. Therefore, we have attached a tank containing fuel which exert external forces on the gyrostat due to rotation of the attached tank with respect to $z-$ axis about angle θ at desired point $(\overline{x}, \overline{y}, \overline{z})$. Hence, we replaced L with

$$R = R_z(\theta)\overline{d}(x), \tag{3}$$

where $R = (R_x, R_y, R_z)$, $R_z(\theta)$ is the rotation matrix for $z-$ axis and $\overline{d}(x)$ is a desired point about which one can rotate the attached tank. Therefore, using vector T in ((2) [38]) and R given in (3) into (2), we obtain the following equation:

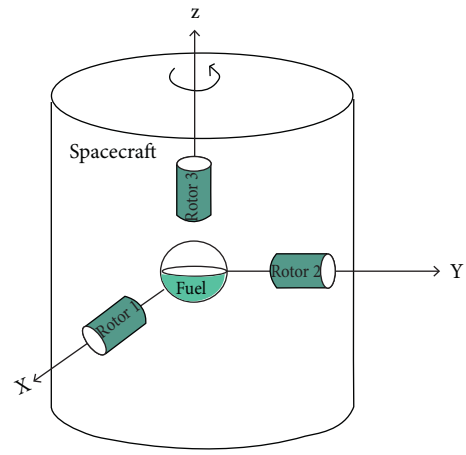

Figure 1: Spacecraft attached with partially filled fuel tank and three rotors. This figure is reproduced from the work of Sabir et al. [7] with the assumption that the third rotor is rotating about z-axis.

$$\begin{cases} I_x^C\mathscr{D}^\gamma x = \left(I_y - I_z\right)yz - yh_z + zh_y - \mu_x x + \overline{x}\cos(\theta) - \overline{y}\sin(\theta), \\ I_y^C\mathscr{D}^\gamma y = \left(I_z - I_x\right)zx + xh_z + \mu_y y + \overline{x}\sin(\theta) + \overline{y}\cos(\theta), \\ I_z^C\mathscr{D}^\gamma z = \left(I_x - I_y\right)xy - xh_y - \mu_z z + \overline{z}, \end{cases} \tag{4}$$

System (4) is a fractional-order mathematical representation of the model given in Figure 1 in which γ is the fractional number between 0 and 1 exclusive, $u = (u_x, u_y, u_z)$ is a damping constant vector, while X, I, and H are defined in equation (2). Moreover, system (4) shows chaotic behavior for $X = [0.1, 0.1, 0.1]$, $I = [0.85, 0.45, 0.2]$, $u = [6, 6.42, 5.8]$, $H = [0, 0.57416, 2, 38]$, and $R = [-20, 2, 20]$. The phase portrait of system (4) with given initial and parameter values can be seen in region 10 of Figure 2.

3. Existence and Stability of Solution

In this part of our paper, we determined results based on the existence theory for system (4) using the fixed point theorem with Banach space. Therefore, basic definitions and important lemmas are considered for the understanding of this work.

Definition 1 (see [39]). The integral of fractional order $\gamma 0$ for a function ϖ is given by

$$\mathscr{I}^\gamma\varpi(t) = \frac{1}{\Gamma(\gamma)}\int_0^t (t-\eta)^{\gamma-1}\varpi(\eta)d\eta\ . \tag{5}$$

Definition 2 (see [39]). The Caputo fractional derivative of order $\gamma 0$ of a continuous function ϖ is given by

$${}^C\mathscr{D}^\gamma\varpi(t) = \frac{1}{\Gamma(n-\gamma)}\int_0^t (t-\eta)^{n-\gamma-1}\varpi^{(n)}(\eta)d\eta\ , \tag{6}$$

where $n = [\gamma] + 1$.

Following two lemmas have importance in achieving the solutions of the systems consisting of fractional differential equations.

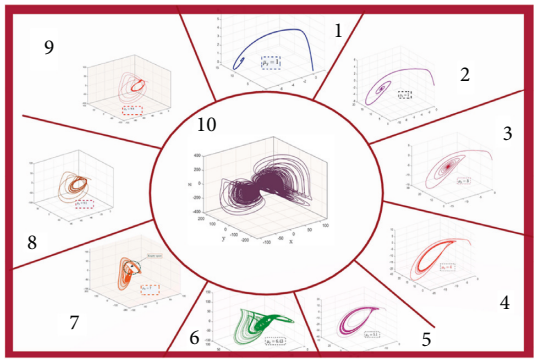

FIGURE 2: Existence of chaos in clockwise and anticlockwise directions.

Lemma 1 (see [39]). *Assume $\varpi \in C(0,1)$, then the solution of fractional differential equation*

$$^{C}\mathscr{D}^{\gamma}\varpi(t) = 0, \tag{7}$$

Of order $\gamma 0$ is

$$\varpi(t) = c_0 + c_1 t + \cdots + c_{n-1}t^{n-1}, \quad c_i \in \mathscr{R},\ i = 0, 2, \ldots, n-1. \tag{8}$$

Lemma 2 (see [39]). *Let us consider $\varpi \in C(0,1)$, with a derivative of fractional order γ, then*

$$\mathscr{I}^{\gamma\,C}\mathscr{D}^{\gamma}\varpi(t) = \varpi(t) + c_0 + c_1 t + \cdots + c_{n-1}t^{n-1}, \quad c_i \in \mathscr{R},\ i = 0, 2, \ldots, n-1. \tag{9}$$

We begin our work by introducing ϖ_1, ϖ_2, and ϖ_3 on the right side of equation (4) and for convenience, we use the following notions:

$$\chi(t) = \begin{cases} x(t), \\ y(t), \chi_0 = \\ z(t), \end{cases} \begin{cases} x(0), \\ y(0), \Psi(t, \chi(t)) = \\ z(0), \end{cases} \begin{cases} \varpi_1(t,x,y,z), \\ \varpi_2(t,x,y,z), \\ \varpi_3(t,x,y,z), \end{cases} \tag{10}$$

and

$$\Psi_0 = \begin{cases} \varpi_1(0, x(0), y(0), z(0)), \\ \varpi_2(0, x(0), y(0), z(0)), \\ \varpi_3(0, x(0), y(0), z(0)), \end{cases} \tag{11}$$

System (4) can be rewritten, using (5) as

$$\begin{aligned} {}^{C}D_t^{\gamma}[\chi(t)] &= \Psi(t, \chi(t)), t \in [0, \tau], \\ \chi(0) &= \chi_0. \end{aligned} \tag{12}$$

According to Lemma 2, problem (12) can be converted into an integral equation

$$\chi(t) = \chi_0 + \frac{1}{\Gamma(\gamma)}\int_0^t (t-\eta)^{\gamma-1}\Psi(\eta, \chi(\eta))d\eta\ . \tag{13}$$

Definition 3. Let us consider $X = C([0,\tau]$ a Banach space under the suitable norm

$$\|\chi\| = \sup_{t\in J}\{|\chi|: \chi \in X\}, \tag{14}$$

and the operator is defined as

$$\tau\chi(t) = \chi_0 + \frac{1}{\Gamma(\gamma)}\int_0^t (t-\eta)^{\gamma-1}\Psi(\eta, \chi(\eta))d\eta\ , \tag{15}$$

where $0 \le t \le \tau < \infty$ and $J = [0, \tau]$. Then, the following assumptions are true:

$[(A_1)]$ There exists a positive constant $_{\Psi} > 0$ such that

$$\left|\Psi(t, \chi(t)) - \Psi(t, \overline{\chi}(t))\right| \le {}_{\Psi}\left|\chi(t) - \overline{\chi}(t)\right|. \tag{16}$$

$[(A_2)]$ The following inequality holds for positive constants $M_{\Psi}, G_{\Psi} > 0$:

$$|\Psi(t, \chi(t))| \le M_{\Psi}|\chi| + G_{\Psi}. \tag{17}$$

Theorem 1. *Let us consider that $_{\Psi}\tau^{\gamma} < \Gamma(\gamma+1)$ and assumption (A_2) is satisfied. Then, there exists a unique solution of system (4) with the contraction of operator τ.*

Proof. Let $\chi, \overline{\chi} \in X$, then one has

$$\begin{aligned} \|\tau\chi - \tau\overline{\chi}\| &= \sup_{t\in J}\left|\chi_0 + \frac{1}{\Gamma(\gamma)}\int_0^t (t-\eta)^{\gamma-1}\Psi(\eta, \chi(\eta))d\eta\right. \\ &\quad \left. -\left(\chi_0 + \frac{1}{\Gamma(\gamma)}\int_0^t (t-\eta)^{\gamma-1}\Psi(\eta, \overline{\chi}(\eta))d\eta\right)\right| \\ &\le \frac{1}{\Gamma(\gamma)}\int_0^{\tau} (t-\eta)^{\gamma-1}|\Psi(\eta, \chi(\eta)) - \Psi(\eta, \overline{\chi}(\eta))|d\eta \\ &\le \frac{1}{\Gamma(\gamma)}\int_0^{\tau} (t-\eta)^{\gamma-1}d\eta\ {}_{\Psi}|\chi(\eta)) - \overline{\chi}(\eta)| \\ &\le \frac{{}_{\Psi}\tau^{\gamma}}{\Gamma(\gamma+1)}\|\chi - \overline{\chi}\|. \end{aligned} \tag{18}$$

This shows that τ is a contraction. Hence, our desired result is obtained, that system (4) has a unique solution. □

Theorem 2. *The integral equation (8) has at least one solution if $_{\Psi} < \mathbb{G}(\gamma)$ under the assumptions of A_1 and A_2.*

Proof. For existence of a solution for operator τ, it is enough to show that τ is completely continuous, and there exists an

element $\chi \in X$ such that $\chi = \delta\tau(\chi)$ for $\delta \in (0,1)$. Therefore, our proof will pass through three steps for achieving our desired results. □

Step 1. Let us consider a sequence $\chi_n \longrightarrow \chi$ in X and for each $t \in J$, we have

$$\begin{aligned}\|\tau\chi_n - \tau\chi\| &= \sup_{t\in J} |\chi_0 + \frac{1}{\Gamma(\gamma)}\int_0^t (t-\eta)^{\gamma-1}\Psi(\eta,\chi_n(\eta))d\eta \\ &\quad -\left(\chi_0 + \frac{1}{\Gamma(\gamma)}\int_0^t (t-\eta)^{\gamma-1}\Psi(\eta,\chi(\eta))d\eta\right)| \\ &\leq \frac{1}{\Gamma(\gamma)}\int_0^\tau (t-\eta)^{\gamma-1}|\Psi(\eta,\chi_n(\eta)) - \Psi(\eta,\chi(\eta))|d\eta\,.\end{aligned} \tag{19}$$

Hence, $\tau\chi_n$ approaches $\tau\chi$ as time t tends to infinity

$$\|\tau\chi_n - \tau\chi\| \longrightarrow 0 as n \longrightarrow \infty. \tag{20}$$

Equation (20) identifies continuity of an operator τ.

Step 2. Let us consider a bounded set $B_r = \{\chi \in X: \|\chi\| \leq r\}$, where r is a positive real number. Then, for any $\chi \in B_r$, we have

$$\begin{aligned}\|\tau\chi\| &= \sup_{t\in J}\left|\chi_0 + \frac{1}{\Gamma(\gamma)}\int_0^t (t-\eta)^{\gamma-1}\Psi(\eta,\chi(\eta))d\eta\right| \\ &\leq \chi_0 + \frac{1}{\Gamma(\gamma)}\int_0^\tau (\tau-\eta)^{\gamma-1}|\Psi(\eta,\chi(\eta))|d\eta \\ &\leq \chi_0 + \frac{M_\Psi|\chi| + G_\Psi}{\Gamma(\gamma)}\int_0^\tau (\tau-\eta)^{\gamma-1}d\eta \\ &\leq \chi_0 + \frac{(M_\Psi r + G_\Psi)\tau^\gamma}{\Gamma(\gamma+1)} = l.\end{aligned} \tag{21}$$

Hence, τ maps a bounded set into a bounded set.

Step 3. The image of a bounded set under τ is equicontinuous in X.

Let $t_1 \langle t_2$ in J and $\chi \in B_r$, we have

$$\begin{aligned}|\tau\chi(t_2) - \tau\chi(t_1)| &= |\chi_0 + \frac{1}{\Gamma(\gamma)}\int_0^{t_2} (t_2-\eta)^{\gamma-1}\Psi(\eta,\chi(\eta))d\eta \\ &\quad -\left(\chi_0 + \frac{1}{\Gamma(\gamma)}\int_0^{t_1} (t_1-\eta)^{\gamma-1}\Psi(\eta,\chi(\eta))d\eta\right)| \\ &= |\frac{1}{\Gamma(\gamma)}\left(\int_0^{t_1} (t_2-\eta)^{\gamma-1}\Psi(\eta,\chi(\eta))d\eta\right. \\ &\quad \left. + \int_{t_1}^{t_2} (t_2-\eta)^{\gamma-1}\Psi(\eta,\chi(\eta))d\eta - \int_0^{t_1} (t_1-\eta)^{\gamma-1}\Psi(\eta,\chi(\eta))d\eta\right)| \\ &\leq \frac{1}{\Gamma(\gamma)}\left(\int_0^{t_1} (t_2-\eta)^{\gamma-1} + (t_1-\eta)^{\gamma-1}\Psi(\eta,\chi(\eta))d\eta + \int_{t_1}^{t_2} (t_2-\eta)^{\gamma-1}\Psi(\eta,\chi(\eta))d\eta\right. \\ &\leq \frac{M_\Psi r + G_\Psi}{\Gamma(\gamma+1)}\left\{\int_0^{t_2} (t_2-\eta)^{\gamma-1}d\eta - \int_0^{t_1} (t_1-\eta)^{\gamma-1}d\eta\right\} \leq \frac{M_\Psi r + G_\Psi}{\Gamma(\gamma+1)}\{t_2^\gamma - t_1^\gamma\}.\end{aligned} \tag{22}$$

As $t_2 \longrightarrow t_1$, then $|\tau\chi(t_2) - \tau\chi(t_1)| \longrightarrow 0$, and thus, τ is continuous and bounded. Hence, $\|\tau\chi(t_2) - \tau\chi(t_1)\| \longrightarrow 0$ shows uniform continuity of τ. Therefore, steps 1 – 3 show that τ is completely continuous.

Step 4. Finally, we have to show that $\mathscr{B} = \{\chi \in X: \chi = \delta\tau(\chi)\}$ for some $\delta \in [0,1]$, is bounded. Let $\chi \in \mathscr{B}$ and for any t, we have

$$\begin{aligned}\|\chi\| &= \sup_{t\in J} |\delta T(\chi)| \\ &= \sup_{t\in J} |\delta\chi_0 + \frac{\delta}{\Gamma(\gamma)}\int_0^t (t-\eta)^{\gamma-1}\Psi(\eta,\chi(\eta))d\eta| \\ &\leq \chi_0 + \frac{1}{\Gamma(\gamma)}\int_0^\tau (\tau-\eta)^{\gamma-1}|\Psi(\eta,\chi(\eta))|d\eta\ , as \delta \leq 1, \\ &\leq \chi_0 + \frac{M_\Psi|\chi| + G_\Psi}{\Gamma(\gamma)}\int_0^\tau (\tau-\eta)^{\gamma-1}d\eta\ , \\ \|\chi\| &\leq \chi_0 + \frac{(M_\Psi\|\chi\| + G_\Psi)\tau^\gamma}{\Gamma(\gamma+1)}.\end{aligned} \tag{23}$$

Simplifying inequality (19) yields

$$\|\chi\| \leq \frac{\chi_0 \Gamma(\gamma+1) + G_\Psi \tau^\gamma}{\Gamma(\gamma+1) - M_\Psi \tau^\gamma}. \tag{24}$$

This shows that the defined set $\mathscr{B}$ is bounded. Hence using Schaefer's theorem [40], system (4) has at least one solution.

For achieving stability, a negligible perturbation parameter $\theta(t)$ can be included in ${}_0^{CF}D_t^\gamma \chi(t)$ such that

(i) ${}_0^{CF}D_t^\gamma \chi(t) = \Psi(t, \chi(t)) + \theta(t)$
(ii) $|\theta(t)| < \varepsilon$ for $\varepsilon 0$

Lemma 3. *Solution of the perturbed problem*

$${}_0^{CF}D_t^\gamma \chi(t) = \Psi(t, \chi(t)) + \theta(t) \chi(0) = \chi_0, \tag{25}$$

Satisfies the following relation:

$$\left| \chi(t) - \left(\chi_0 + [\Psi(t, \chi(t)) - \Psi_0] \frac{(1-\gamma)}{\mathbb{G}(\gamma)} + \frac{\gamma}{\mathbb{G}(\gamma)} \int_0^t \Psi(\eta, \chi(\eta)) d\eta \right) \right| \leq L_\Psi \varepsilon. \tag{26}$$

Theorem 3. *Gyrostat system (4) achieves Ullam–Hyers stability if* $L_\Psi < 1$ *and assumption* A_2*, together with Lemma 3 is satisfied.*

Proof. Let $\chi \in X$ be any solution and $\overline{\chi} \in X$ is a unique solution, then

$$\begin{aligned} |\chi(t) - \overline{(Y)}(t)| &= \left| \chi(t) - \left(\chi_0 + [\Psi(t, \overline{\chi}(t)) - \Psi_0] \frac{(1-\gamma)}{\mathbb{G}(\gamma)} + \frac{\gamma}{\mathbb{G}(\gamma)} \int_0^t \Psi(\eta, \overline{\chi}(\eta)) d\eta \right) \right| \\ &\leq \left| \chi(t) - \left(\chi_0 + [\Psi(t, \chi(t)) - \Psi_0] \frac{(1-\gamma)}{\mathbb{G}(\gamma)} + \frac{\gamma}{\mathbb{G}(\gamma)} \int_0^t \Psi(\eta, \chi(\eta)) d\eta \right) \right| \\ &\quad + \left| \left(\chi_0 + [\Psi(t, \chi(t)) - \Psi_0] \frac{(1-\gamma)}{\mathbb{G}(\gamma)} + \frac{\gamma}{\mathbb{G}(\gamma)} \int_0^t \Psi(\eta, \chi(\eta)) d\eta \right) \right. \\ &\quad \left. - \left(\chi_0 + [\Psi(t, \overline{\chi}(t)) - \Psi_0] \frac{(1-\gamma)}{\mathbb{G}(\gamma)} + \frac{\gamma}{\mathbb{G}(\gamma)} \int_0^t \Psi(\eta, \overline{\chi}(\eta)) d\eta \right) \right| \\ &\leq L_\Psi \varepsilon + L_\Psi \|\chi - \overline{\chi}\|. \end{aligned} \tag{27}$$

This implies that

$$\|\chi - \overline{\chi}\| \leq \frac{L_\Psi}{1 - L_\Psi} \varepsilon. \tag{28}$$

Hence, solution of the proposed system (4) is Ullam–Hyers stable. □

4. Variational Iterative Scheme for System (4)

An iterative scheme, variational iterative method (VIM), is introduced in this section using successive approximations of the solution for rapid convergence and analytical results discussed in Section 2.

4.1. Working Rule. To express the VIM, we consider general nonlinear differential equation as

$$\mathscr{L}\chi(t) + \mathscr{N}\chi(t) = h(t), \tag{29}$$

where $\mathscr{L}$, $\mathscr{N}$, and h are linear, nonlinear, and source functions, while the corrector function for (29) is considered as

$$\chi_{n+1}(t) = \chi_n(t) + \int_0^t \Lambda(\eta) (\mathscr{L}\chi(\eta) + \widetilde{\mathscr{N}}\chi(\eta) - h(\eta)) d\eta \,. \tag{30}$$

Λ in (30) is defined as $(-1)^n (t-\eta)^{n-1} / \Gamma(n)$, whereas $\widetilde{\mathscr{N}}$ is used as a restricted value with $\sigma\mathscr{N} = 0$. Then, the exact solution can be obtained as

$$\chi(t) = \lim_{n \longrightarrow \infty} \chi_n(t). \tag{31}$$

System (4) can be discretized using VIM as

$$\begin{aligned} x_{n+1} &= x_n - \mathcal{F}^{\gamma}\left(I_x^C\mathcal{D}^{\gamma}x_n - \left(I_y - I_z\right)y_n z_n + y_n h_z - z_n h_y + \mu_x x_n - \overline{x}\cos(\theta) + \overline{y}\sin(\theta)\right),\\ y_{n+1} &= y_n - \mathcal{F}^{\gamma}\left(I_y^C\mathcal{D}^{\gamma}y_n - (I_z - I_x)z_n x_n - x_n h_z - \mu_y y_n - \overline{x}\sin(\theta) - \overline{y}\cos(\theta)\right),\\ z_{n+1} &= z_n - \mathcal{F}^{\gamma}\left(I_z^C\mathcal{D}^{\gamma}z - \left(I_x - I_y\right)x_n y_n + x_n h_y + \mu_z z_n + \overline{z}\right), \end{aligned} \tag{32}$$

where $x(0) = x_0$, $y(0) = y_0$, and $z(0) = z_0$.

For $n = 0, 1$

$$\begin{cases} x_1 = x_0 + \dfrac{x^{\gamma}\kappa_{x1}}{\Gamma(\gamma+1)}, \\ y_1 = y_0 + \dfrac{y^{\gamma}\kappa_{y1}}{\Gamma(\gamma+1)}, \\ z_1 = z_0 + \dfrac{z^{\gamma}\kappa_{z1}}{\Gamma(\gamma+1)}, \end{cases} \begin{cases} x_2 = x_0 + \dfrac{\kappa_{x2}}{\Gamma(\gamma+1)}x^{\gamma} - \dfrac{\mu_x\kappa_{x1}}{\Gamma(2\gamma+1)}x^{2\gamma}, \\ y_2 = y_0 + \dfrac{\kappa_{y2}}{\Gamma(\gamma+1)}y^{\gamma} + \dfrac{\kappa_{y1}}{\Gamma(2\gamma+1)}y^{2\gamma}, \\ z_2 = z_0 + \dfrac{\kappa_{z2}}{\Gamma(\gamma+1)}z^{\gamma} - \dfrac{\left(\mu_z - h_y\right)\kappa_{z1}}{\Gamma(2\gamma+1)}z^{2\gamma}, \end{cases} \tag{33}$$

where

$$\begin{cases} \kappa_{x1} = -\left(I_y - I_z\right)y_0 z_0 + y_0 h_z - z_0 h_y + \mu_x x_0 - \overline{x}\cos(\theta) + \overline{y}\sin(\theta), \\ \kappa_{x2} = \kappa_{x1}(1 + I_x) - \left(I_y - I_z\right)y_1 z_1 + y_1 h_z - z_1 h_y + \mu_x x_0 - \overline{x}\cos(\theta) + \overline{y}\sin(\theta), \\ \kappa_{y1} = -(I_z - I_x)z_0 x_0 - x_0 h_z - \mu_y y_0 - \overline{x}\sin(\theta) - \overline{y}\cos(\theta), \\ \kappa_{y2} = L_y\left(1 + I_y\right) - (I_z - I_x)z_1 x_1 - x_1 h_z - \mu_y y_0 - \overline{x}\sin(\theta) - \overline{y}\cos(\theta), \\ \kappa_{z1} = -\left(I_x - I_y\right)x_0 y_0 + x_0 h_y + \mu_z z_0 - \overline{z}, \\ \kappa_{z2} = L_z(1 + I_z) - \left(I_x - I_y\right)x_1 y_1 + x_1 h_y + \mu_z z_1 - \overline{z}. \end{cases} \tag{34}$$

For $n = 2$, we have

$$\begin{cases} x_3 = x_0 + \dfrac{\rho 1/x}{\Gamma(\gamma+1)}x^{\gamma} - \dfrac{\rho 2/x}{\Gamma(2\gamma+1)}x^{2\gamma} + \dfrac{\rho 3/x}{\Gamma(3\gamma+1)}x^{3\gamma}, \\ y_3 = y_0 + \dfrac{1/y}{\Gamma(\gamma+1)}y^{\gamma} + \dfrac{2/y}{\Gamma(2\gamma+1)}y^{2\gamma} + \dfrac{3/y}{\Gamma(3\gamma+1)}y^{3\gamma}, \\ z_3 = z_0 + \dfrac{\varsigma 1/z}{\Gamma(\gamma+1)}z^{\gamma} - \dfrac{\varsigma 2/z}{\Gamma(2\gamma+1)}z^{2\gamma} + \dfrac{\varsigma 3/z}{\Gamma(3\gamma+1)}z^{3\gamma}. \end{cases} \tag{35}$$

The values of ρ_x^i, ϱ_y^i and ς_z^i, $i = 1, 2, 3$ in (35) are given in Appendix *A*. In the next section, we have discussed system (4) analytically and qualitatively. For numerical simulations, our designed algorithm is used to plot Lyapunov exponents and bifurcation diagram in integer order as well as fractional-order chaotic systems.

5. Dynamical Analysis

The fractional-order dynamical system exhibits chaos for some values of fractional term, γ, but using a hit and trial method for such purpose is difficult to investigate chaos in dynamical systems. Therefore, we plotted the bifurcation diagram for

system (4) with respect to fractional term, γ. A noisy dense area is observed in Figure 3 that illustrates occurrence of chaos in the fractional-order gyrostat system beginning with $\gamma = 0.86$.

In section 2, we used the concept of the fixed point theory to obtain at least one solution of system (4). Hence, for fixed points, we consider the following function ϖ_i, $i = 1, 2, 3$ equals to zero:

$$\begin{cases} \varpi_1 = \left(I_y - I_z\right)yz - yh_z + zh_y - \mu_x x + \overline{x}\cos(\theta) - \overline{y}\sin(\theta) = 0, \\ \varpi_2 = \left(I_z - I_x\right)zx + xh_z + \mu_y y + \overline{x}\sin(\theta) + \overline{y}\cos(\theta) = 0, \\ \varpi_3 = \left(I_x - I_y\right)xy - xh_y - \mu_z z + \overline{z} = 0. \end{cases} \tag{36}$$

After fixing all parameters given in section (1), then we solve equation (36) to get the following five equilibrium points:

$$\begin{cases} E_1 = [-0.819, 3.141, 3.352]^T, \\ E_2 = [-11.078, 14.8464, -6.79773]^T, \\ E_3 = [12.445, -15.8945, -11.4255]^T, \\ E_4 = [11.5523, 22.4277, 20.1731]^T, \\ E_5 = [-12.4328, -23.1278, 24.5096]^T. \end{cases} \tag{37}$$

In Theorem 4 local dynamical analysis of system (4) is used for observing trajectories around equilibrium points (27).

Theorem 4. *A gyrostat chaotic system (4) is composed of five equilibrium points, in which E_1 is the saddle node and $E_{2,3,4,5}$ are all unstable saddle spirals. Moreover, these spirals lead to four attractors and one saddle node E_1 that act as a separatrix as t extends.*

Proof. Five equilibrium points are calculated in equation (27). The Jacobian matrix plays a vital role in the system of differential equations for local dynamical analysis. Therefore, the Jacobian matrix of system (4) is

$$J = \begin{pmatrix} \frac{-120}{17} & \frac{5z}{17} - \frac{14}{5} & \frac{5y}{17} + \frac{7177}{10625} \\ \frac{238}{45} - \frac{(13z)}{9} & \frac{214}{15} & -\frac{(13x)}{9} \\ 2y - \frac{7177}{2500} & 2x & -29 \end{pmatrix}. \tag{38}$$

And the Jacobian matrix for fixed parameter values at E_1 is

$$J|_{E_1} = \begin{pmatrix} -7.0588 & -1.8142 & 1.5993 \\ 0.4473 & 14.2667 & 1.1842 \\ 3.4111 & -1.6397 & -29.0000 \end{pmatrix}. \tag{39}$$

The characteristic equations of the Jacobian matrix (29) is

$$\lambda_1^3 + 21.79\lambda_1^2 - 312.44\lambda_1 - 2796.9. \tag{40}$$

Solution of (40) results into single positive and two negative eigenvalues:

$$\lambda_{11} = -29.21, \lambda_{12} = -6.75, \lambda_{13} = 14.17. \tag{41}$$

Equation (41) illustrates that two states will move away from E_1, while a single state will move inward towards equilibria: E_1, and such information shows occurrence of the saddle. The Jacobian matrix at E_2 is

$$J|_{E_2} = \begin{pmatrix} -7.0588 & -4.7993 & 5.0421 \\ 15.1078 & 14.2667 & 16.0016 \\ 26.8220 & -22.1560 & -29.0000 \end{pmatrix}. \tag{42}$$

And the corresponding characteristic equation is

$$\lambda_2^3 + 21.79\lambda_2^2 - 17.93\lambda_2 + 7361.79. \tag{43}$$

Solution of (43) gives three eigenvalues with one negative real and two complex numbers with positive real part:

$$\begin{aligned} \lambda_{21} &= -30.37, \\ \lambda_{223} &= 4.2871 \pm 14.9684\iota. \end{aligned} \tag{44}$$

Equation (44) describes occurrence of the unstable spiral. In a similar fashion, one can achieve

$$\begin{aligned} \lambda_{31} &= -30.4682, \\ \lambda_{323} &= 4.3380 \pm 19.4641\iota, \\ \lambda_{41} &= -35.8534, \\ \lambda_{423} &= 7.0306 \pm 17.3188\iota, \\ \lambda_{51} &= -35.8109, \\ \lambda_{523} &= 7.0094 \pm 20.5301\iota. \end{aligned} \tag{45}$$

Eigenvalues of E_3, E_4, and E_5. In view of (45), equilibrium points, $E_{3,4,5}$ are also unstable spirals.

Analytical results (29–35) are explained in Figure 4, which illustrate trajectories of system (4) around their equilibrium points. Five different colors are used for each equilibrium point, which are also highlighted as a legend in Figure 4. It is observed that $E_{2,3,4,5}$ are unstable spirals plotted in green, brown, blue, and black colors, while red color shows the saddle node. In detail, we can see that the red trajectory starts from E_1 and passes through the regions of E_2, E_3, E_4, and E_5 with the passage of time. The trajectory for E_2 shows a spiral emerging from its equilibrium point and is

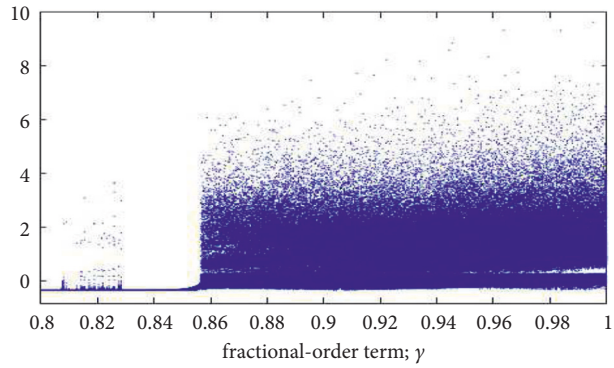

Figure 3: Bifurcation diagram of system (4) with respect to γ.

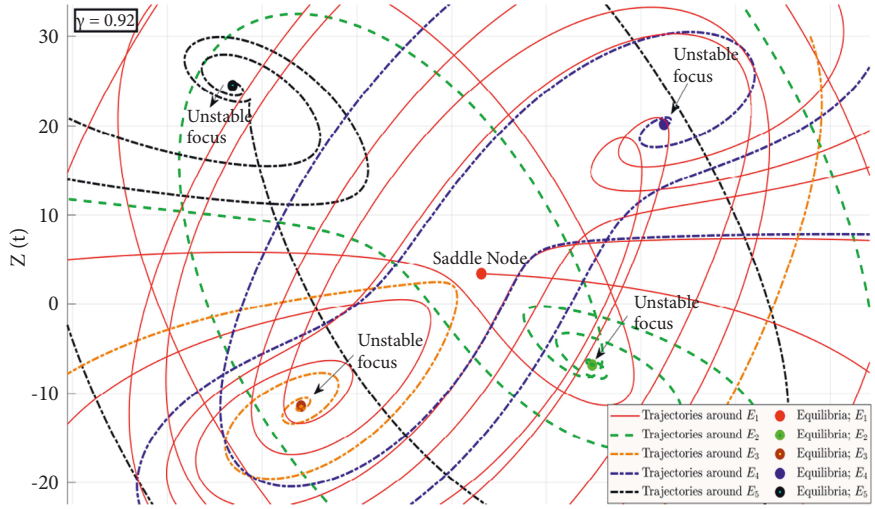

Figure 4: Trajectories of system (4) around equilibrium points.

moving away from it. After some time it has been observed that the green trajectory is acting as a heteroclinic orbit: E_5. The same theory can be observed between E_2 and E_3, when a brown colored orbit starts with high unstable oscillations and approaches to a region occupied by E_2. Apart from these four unstable spirals, one can also locate saddle node equilibria E_1 in the red color, in which its trajectory passes through regions acquired by unstable spirals and act as a separatrix between them. For further analysis, we have extended time for observing the trajectories around five equilibrium points in the greater domain. It has been analyzed that four unstable equilibrium points are self-exciting attractors and occupy four basins. Moreover, the combination of all these four regions leads to the concept of a strange attractor in system (4). Studying in more depth, it has been also observed that the saddle node in the global domain is busy in separating regions of self-exciting attractors. For getting more knowledge about chaoticity in the fractional-order gyrostat system (4), some basic results are used for the possibility and detection of chaos. □

5.1. Lyapunov Exponents. The Lyapunov exponent is one of the fundamental results, which help researchers in pointing out existence of unpredictability in trajectories of their corresponding systems. Moreover, in a three-dimensional autonomous system of ordinary differential equations, there exist three Lyapunov exponents λ_i, $i = 1, 2, 3$. Now, if $(\lambda_1, \lambda_2, \lambda_3) = (+ive, 0, -ive)$, then it shows existence of chaos, whereas $(-ive, -ive, +ive)$ illustrates the existence of periodic solutions. In Figure 5, three Lyapunov exponents can be observed, emerging from $(-9, 11, -30)$ and leading to $(-26.51, 0, 4.87)$, which motivated us to work further on it and find out chaotic trajectories in it. For further investigation, we have used the concept of the bifurcation diagram [12].

5.2. Bifurcation Leading to Chaos. For confirmation of existence of chaos in our proposed model (4), we fixed all other parameter values except for μ_y. For damping coefficient, μ_y, it is observed in Figure 6 that there seems no bifurcation in system (4) for $\mu_y \in (1, 3.6)$. The single bifurcation emerges at $\mu_y = 3.6$ and continues till $\mu_y = 5$, which changes into period doubling bifurcation (**PDB**) for $5 \leq \mu_y \leq 5.2$. Trajectories of our proposed system jump into the chaotic region for μ_y lying in interval $(5.2, 6.5)$. One can observe symmetric behavior in sense of bifurcation leading to chaos in Figure 6. If we start from $\mu_y = 11$, two lines can be observed that are

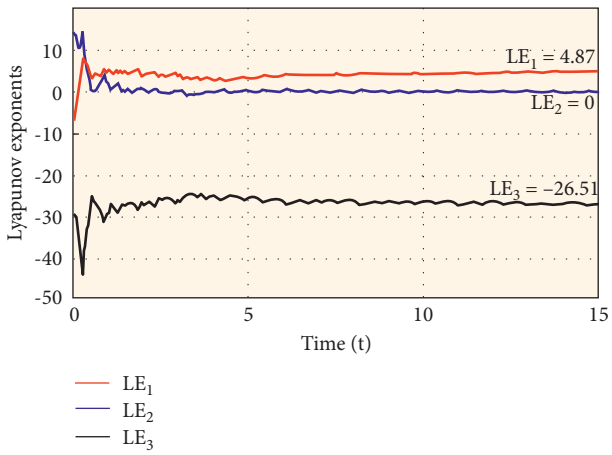

Figure 5: Lyapunov exponents of system (4).

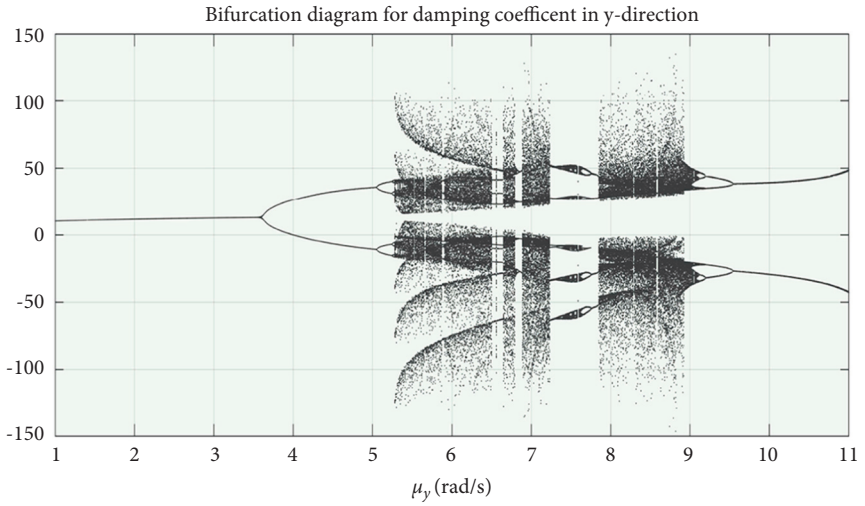

Figure 6: Bifurcation diagram for damping coefficient, μ_y in system (4).

converted into period doubling bifurcations, then period 2 ⟶ period 4 ⟶ 8 ⟶ chaotic region. This concept is also explained with the aid of a series of phase portraits, which confirms chaotic behavior in our proposed system. Therefore, we have divided bifurcation diagram 5 in nine regions and plotted phase portraits to their corresponding values.

Figure 2 is validation of Figure 6, which explains existence of chaos in detail by moving clockwise or anticlockwise. Therefore, we have an indexed sequence of phase portraits for μ_y. If we start from region 1, a spiral trajectory can be observed and is expanding in regions 2 and 3. This trajectory is converted into period doubling and period 4 bifurcations in region 4 and 5 for $\mu_y = 4$ to 5.1, respectively. In region 6, chaotic movement of trajectories can be observed, which gradually declines to period 8 ⟶ period 4 ⟶ period 2 bifurcations by moving in the anticlockwise direction from region 6 to 9. Similarly, if we begin in the clockwise direction, region 9 to 1, one can see trajectory starts with period doubling bifurcation for $\mu_y = 9.6$ is gradually increasing to period 4 ⟶ period 8 ⟶ chaos from region 9 to 6, then decline in a symmetric way is observed from chaos to the period doubling bifurcation till region 4 which finally shrinks into spiral and bifurcation disappearing in region 3 to 1.

Figure 7 is the series of Lyapunov exponents corresponding to each subregion of the bifurcation diagram (plotted in Figure 6). In Figure 2, the existence of chaos in a symmetrical way is thoroughly discussed, but in Figures 7(a)–7(h) the same concept is explained in more detail where for each value of the damping coefficient μ_y; there exist different values of Lyapunov exponents. Moreover, it is also observed that the Lyapunov exponent of system (4) tends to $(-ive, 0, +ive)$ as the damping coefficient μ_y approaches to 6.43.

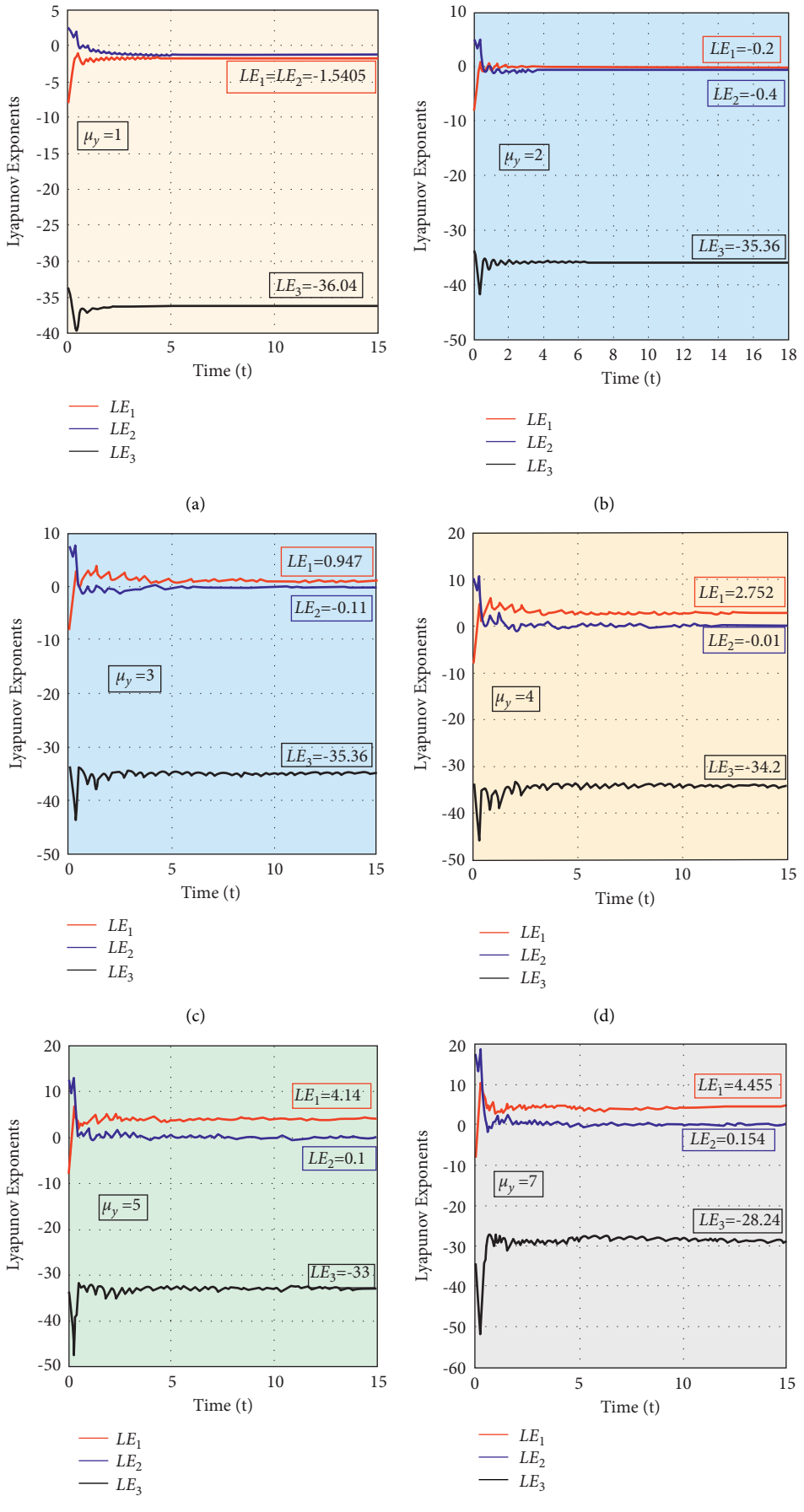

Figure 7: Continued.

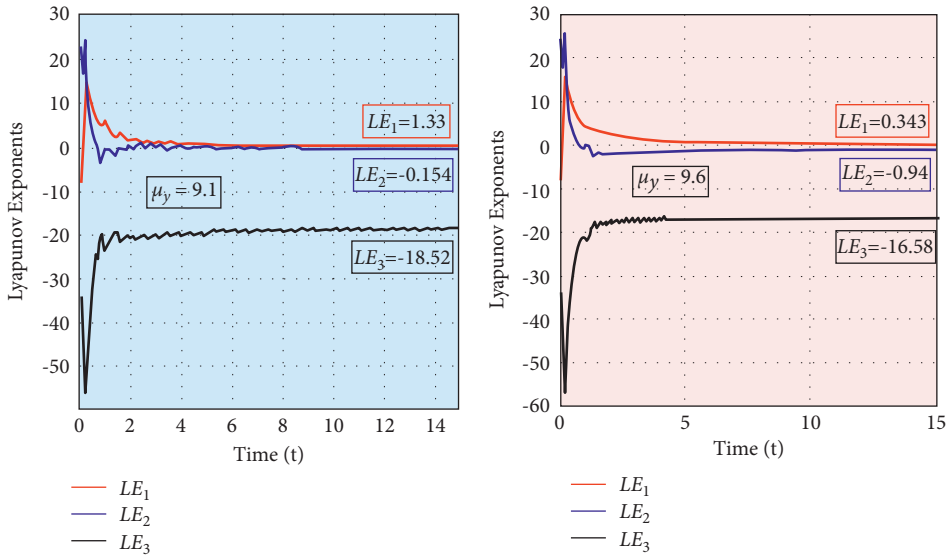

Figure 7: Lyapunov exponents corresponding to each subregion in Figure 6.

6. Conclusion and Future Work

An integer ordered dynamical system of the gyrostat was considered by researchers since decade, and a variety of work related to chaos was achieved with the help of sensitivity in its initial conditions. But we have analyzed the gyrostat model with modification by attaching a rotatory cylinder and conversion into fractional order for the first time. Several theorems were proved in this work for the existence of solution and Ullam–Hyers stability. Moreover, dealing with the fractional-order system does not work on *ODE*45; therefore, an iterative scheme was designed for system (4) to attain chaos in the fractional order. Studying local dynamics of system (4) leads to five solutions with four unstable spirals and one saddle node, but observing trajectories around these equilibrium points in global domain acted as a self-exciting attractor and separatrix. In future, we aim to target fractional-order dynamical systems for codimension 2 bifurcations, which itself is a tedious task due to a large number of involved parameters. Apart from bifurcation, our future aim also involves application of (integer and fractional) ordered chaotic systems in strategy-based mobile gaming.

Appendix

Our discretization scheme is based on an iterative technique; therefore, for $n = 0$ and 1, analytical work is presented in Section 3. But increasing the number of n leads to tedious analytic. Hence, for $n = 2$, the leftover calculation in equation (25) is done here:

$$\begin{cases} \rho_x^1 = \kappa_{x2}(1 - I_x) + (I_y - I_z)\rho_x\rho_{x1} - \rho_x(h_z - h_y) - \mu_x x_0 + \overline{x}\cos(\theta) - \overline{y}\sin(\theta), \\ \rho_x^2 = \mu_x\kappa_{x1} - \dfrac{I_x\mu_x\kappa_{x1}}{\Gamma(\gamma+1)} + \dfrac{\rho_x\kappa_{x1}(I_y - I_z)[(I_x - I_y)y_1 - h_y](h_z + 1)}{(\Gamma(\gamma+1))^2}z^\gamma \\ + \dfrac{\rho_x\kappa_{x1}(I_y - I_z)[(I_z - I_x)z_1 - h_y](h_y + 1)}{(\Gamma(\gamma+1))^2}y^\gamma - \dfrac{\mu_x\kappa_{x2}}{\Gamma(\gamma+1)}, \\ \rho_x^3 = \dfrac{[(I_z - I_x)z_1 - h_y][(I_x - I_y)y_1 - h_y]\kappa_{x1}^2}{(\Gamma(\gamma+1))^4}y^\gamma z^\gamma + \dfrac{\mu_x\kappa_{x1}}{\Gamma(2\gamma+1)}, \end{cases} \tag{A.1}$$

where

$$\begin{aligned}\rho_x &= \frac{\kappa_{y1}\left(1+I_y\right)-\left(I_z-I_x\right)z_1x_0+x_0h_y-\mu_y y_0-\overline{x}\sin\left(\theta\right)-\overline{y}\cos\left(\theta\right)}{\Gamma\left(\gamma+1\right)}y^{\gamma}+y_0+\frac{\kappa_{y1}}{\Gamma\left(2\gamma+1\right)}y^{2\gamma},\\ \rho_{x1} &= \frac{\kappa_{z1}\left(1+I_z\right)-\left(I_x-I_y\right)y_1x_0+x_0h_y-\left(\mu_z-h_y\right)z_0-\overline{z}}{\Gamma\left(\gamma+1\right)}z^{\gamma}+z_0+\frac{\left(\mu_z-h_y\right)\kappa_{z1}}{\Gamma\left(2\gamma+1\right)}z^{2\gamma}.\end{aligned} \tag{A.2}$$

In a similar way, the values of ϱ_y^i are calculated as

$$\begin{cases}\varrho_y^1=\kappa_{y2}\left(1-I_y\right)+\left(I_z-I_x\right)\tilde{\mathrm{n}}_y\tilde{\mathrm{n}}_{y1}-\tilde{\mathrm{n}}_{y1}h_z+\mu_y y_0+\overline{x}\sin\left(\theta\right)+\overline{y}\cos\left(\theta\right),\\ \varrho_y^2=\kappa_{y1}-\frac{\kappa_{y1}}{\Gamma\left(\gamma+1\right)}-\frac{\varrho_y\left[\left(I_y-I_z\right)z_1-h_z\right]\kappa_{y1}}{\left(\Gamma\left(\gamma+1\right)\right)^2}x^{\gamma}-\frac{\mu_y\kappa_{y2}}{\Gamma\left(\gamma+1\right)}-\frac{\varrho_{y1}\left(I_z-I_x\right)\left(I_x-I_y\right)x_1\kappa_{y1}}{\left(\Gamma\left(\gamma+1\right)\right)^2}z^{\gamma},\\ \varrho_y^3=\frac{\left(I_x-I_y\right)\left(I_z-I_y\right)\left[\left(I_y-I_z\right)z_1-h_z\right]\kappa_{y1}}{\left(\Gamma\left(\gamma+1\right)\right)^4}x^{\gamma}y^{\gamma}+\frac{\mu_y\kappa_{y1}}{\Gamma\left(2\gamma+1\right)},\end{cases} \tag{A.3}$$

With

$$\begin{aligned}\varrho_y &= \frac{\kappa_{z1}\left(1+I_z\right)-\left(I_x-I_y\right)x_1y_0+x_1h_y+\left(\mu_z-h_y\right)z_0+\overline{z}}{\Gamma\left(\gamma+1\right)}z^{\gamma}+z_0-\frac{\left(\mu_z-h_y\right)\kappa_{z1}}{\Gamma\left(2\gamma+1\right)}z^{2\gamma},\\ \varrho_{y1} &= \frac{\kappa_{x1}\left(1+I_x\right)-\left(I_y-I_z\right)z_1y_0+y_0h_z-z_1h_y-\mu_x x_0-\overline{x}\cos\left(\theta\right)+\overline{y}\sin\left(\theta\right)}{\Gamma\left(\gamma+1\right)}y^{\gamma}+x_0-\frac{\mu_x\kappa_{x1}}{\Gamma\left(2\gamma+1\right)}x^{2\gamma}.\end{aligned} \tag{A.4}$$

Finally, the values of ς_z^i are

$$\begin{cases}\varsigma_z^1=\kappa_{z2}\left(1-I_z\right)+\left(I_x-I_y\right)C_z\varsigma_{z1}-\varsigma_z-\varsigma_{z1}\left(\mu_z-h_y\right)-\overline{z},\\ \varsigma_z^2=\left(\mu_z-h_y\right)L_z+\frac{\left(\mu_z-h_y\right)I_zL_z}{\Gamma\left(\gamma+1\right)}-\frac{x_1\kappa_{z1}\left(I_z-I_x\right)\left[\varsigma_z\left(I_x-I_y\right)+\left(\mu_z-h_y\right)\right]}{\left(\Gamma\left(\gamma+1\right)\right)^2}y^{\gamma}-\frac{\kappa_{z1}\left(\left(I_y-I_z\right)y_1+h_y\right)\left[\varsigma_{z1}\left(I_x-I_y\right)+h_y\right]}{\left(\Gamma\left(\gamma+1\right)\right)^2}x^{\gamma},\\ \varsigma_z^3=\frac{x_1\kappa_{z1}^2\left(I_x-I_y\right)\left(I_z-I_x\right)\left[\left(I_y-I_z\right)+h_y\right]}{\left(\Gamma\left(\gamma+1\right)\right)^4}x^{\gamma}y^{\gamma},\end{cases} \tag{A.5}$$

where

$$\begin{aligned}\varsigma_z &= \frac{I_x\kappa_{x1}+\mu_x x_0+y_2h_z-\left(\left(I_y-I_z\right)y_1+h_y\right)z_0-\overline{x}\cos\left(\theta\right)+\overline{y}\sin\left(\theta\right)}{\Gamma\left(\gamma+1\right)}x^{\gamma}+x_0-\frac{\mu_x}{\kappa_{x1}}\Gamma\left(2\gamma+1\right)x^{2\gamma},\\ \varsigma_{z1} &= \frac{L_y\left(1+I_y+x_1h_y-\mu_y y_0-\left(I_z-I_x\right)x_1z_0-\overline{x}\sin\left(\theta\right)-\overline{y}\cos\left(\theta\right)\right)}{\Gamma\left(\gamma+1\right)}y^{\gamma}+y_0+\frac{\kappa_{y1}}{\Gamma\left(2\gamma+1\right)}y^{2\gamma}.\end{aligned} \tag{A.6}$$

For further iterations, things were very tedious; therefore, we used MATLAB for further numerical calculations.

Data Availability

MATLAB is used for graphs and tedious calculations in this work, and codes are available upon reasonable request from the corresponding author.

Ethical Approval

This paper does not contain any studies with human participants or animals performed by any of the author.

Conflicts of Interest

All authors declare that they have no conflicts of interest.

Authors' Contributions

All authors contributed equally to the writing of this paper. All authors read and approved the final manuscript. Muhammad Marwan conducted formal analysis, methodology, investigation, and writing of the original draft. Gauhar Ali conducted formal analysis, methodology, and conceptualization. Ramla Khan conducted methodology, software, conceptualization, and writing.

References

[1] J. Guckenheimer and P. Holmes, "Nonlinear oscillations, dynamical systems, and bifurcations of vector fields," *Springer Science & Business Media*, vol. 42, 2013.

[2] Q. Yang and G. Chen, "A chaotic system with one saddle and two stable node-foci," *International Journal of Bifurcation and Chaos*, vol. 18, no. 05, pp. 1393–1414, 2008.

[3] M. Marwan, M. Mehboob, S. Ahmad, and M. Aqeel, "Hopf bifurcation of forced chen system and its stability via adaptive control with arbitrary parameters," *Soft Computing*, vol. 24, no. 6, pp. 4333–4341, 2020.

[4] M. Fiaz, M. Aqeel, M. Marwan, and M. Sabir, "Retardational effect and hopf bifurcations in a new attitude system of quadrotor unmanned aerial vehicle," *International Journal of Bifurcation and Chaos*, vol. 31, no. 09, Article ID 2150127, 2021.

[5] X. Zhang and H. Zhu, "Hopf bifurcation and chaos of a delayed finance system," *Complexity*, vol. 2019, Article ID 6715036, 2019.

[6] K. Zhuang, J. Gao, and D. Liu, "Stability and hopf bifurcation in a three-component planktonic model with spatial diffusion and time delay," *Complexity*, vol. 2019, Article ID 4590915, , 2019.

[7] M. Sabir, S. Ahmad, and M. Marwan, "Hopf bifurcation analysis for liquid-filled gyrostat chaotic system and design of a novel technique to control slosh in spacecrafts," *Open Physics*, vol. 19, no. 1, pp. 539–550, 2021.

[8] M. Fiaz, M. Aqeel, M. Marwan, and M. Sabir, "Integer and fractional order analysis of a 3d system and generalization of synchronization for a class of chaotic systems," *Chaos, Solitons & Fractals*, vol. 155, Article ID 111743, 2022.

[9] Diz-Pita Erika, L. Jaume, M. Otero-Espinar Victoria, and V. Claudia, "The zero-hopf bifurcations in the Kolmogorov systems of degree 3 in r3," *Communications in Nonlinear Science and Numerical Simulation*, vol. 95, Article ID 105621, 2021.

[10] B. Francisco and C. Mereu Ana, "Zero – hopf bifurcation in a 3d jerk system," *Nonlinear Analysis: Real World Applications*, vol. 59, Article ID 103245, 2021.

[11] M. R. Cândido and J. Llibre, "Zero-Hopf bifurcations in 3-dimensional differential systems with no equilibria – hopf bifurcations in 3 – dimensional differential systems with no equilibria," *Mathematics and Computers in Simulation*, vol. 151, pp. 54–76, 2018.

[12] M. Marwan and S. Ahmad, "Bifurcation analysis for energy transport system and its optimal control using parameter self-tuning law," *Soft Computing*, vol. 24, no. 22, Article ID 17221, 2020.

[13] G. Qi, "Energy cycle of brushless dc motor chaotic system," *Applied Mathematical Modelling*, vol. 51, pp. 686–697, 2017.

[14] Y. F. Zhang, M. H. Yao, W. Zhang, and B. C. Wen, "Dynamical modeling and multi-pulse chaotic dynamics of cantilevered pipe conveying pulsating fluid in parametric resonance," *Aerospace Science and Technology*, vol. 68, pp. 441–453, 2017.

[15] Y. Yang and G. Qi, "Comparing mechanical analysis with generalized-competitive-mode analysis for the plasma chaotic system," *Physics Letters A*, vol. 383, no. 4, pp. 318–327, 2019.

[16] M. Sabir, M. Marwan, S. Ahmad, M. Fiaz, and F. Khan, "Observer and descriptor satisfying incremental quadratic constraint for class of chaotic systems and its applications in a quadrotor chaotic system," *Chaos, Solitons & Fractals &*, vol. 137, Article ID 109874, 2020.

[17] M. Marwan, M. Z. Abidin, H. Kalsoom, and M. Han, "Generalized full order observer subject to incremental quadratic constraint (IQC) for a class of fractional order chaotic systems," *Fractal and Fractional*, vol. 6, no. 4, 2022.

[18] J. Iqbal, S. Ahmad, M. Marwan, and M. Shaukat, "Control and numerical analysis for cancer chaotic system," *Archive of Applied Mechanics*, vol. 90, no. 12, pp. 2597–2608, 2020.

[19] A. E. Matouk, "Complex dynamics in susceptible-infected models for covid-19 with multi-drug resistance," *Chaos, Solitons & Fractals*, vol. 140, Article ID 110257, 2020.

[20] D. Nadjette, O. Adel, M. B. Iqbal, and G. Giuseppe, "Chaotic dynamics in a novel covid-19 pandemic model described by commensurate and incommensurate fractional-order derivatives," *Nonlinear Dynamics*, vol. 2021, pp. 1–13, 2021.

[21] L. F. Santos and M. Rui, "Bifurcation of equilibria for general case of gyrostat satellite on a circular orbit," *Aerospace Science and Technology*, vol. 105, Article ID 106058, 2020.

[22] M. Z. Abidin and J. Chen, "Global well-posedness of the generalized rotating magnetohydrodynamics equations in variable exponent Fourier – Besov spaces," *Journal of Applied Analysis & Computation*, vol. 11, no. 3, pp. 1177–1190, 2021.

[23] M. Marwan, S. Ahmad, M. Aqeel, and M. Sabir, "Control analysis of rucklidge chaotic system," *Journal of Dynamic Systems, Measurement, and Control*, vol. 141, no. 4, 2018.

[24] M. Z. Abidin, N. Ullah, and Omer Abdalrhman Omer, "Global well-posedness and analyticity of the primitive equations of geophysics in variable exponent Fourier – Besov spaces," *Symmetry*, vol. 14, no. 1, 2022.

[25] A. M. AbdelAty, M. E. Fouda, and A. M. Eltawil, "On numerical approximations of fractional-order spiking neuron models," *Communications in Nonlinear Science and Numerical Simulation*, vol. 105, Article ID 106078, 2022.

[26] Q. Li, S. Liu, and Y. Chen, "Combination event-triggered adaptive networked synchronization communication for nonlinear uncertain fractional-order chaotic systems,"

Applied Mathematics and Computation, vol. 333, pp. 521–535, 2018.

[27] J. Hadi, Y. Amin, M. Munoz-Pacheco Jesus, K. Sezgin, P. Viet-Thanh, and A. Fawaz, "A new fractional-order hyperchaotic memristor oscillator: dynamic analysis, robust adaptive synchronization, and its application to voice encryption," *Applied Mathematics and Computation*, vol. 383, Article ID 125310, 2020.

[28] R. Garrappa, "Trapezoidal methods for fractional differential equations: theoretical and computational aspects," *Mathematics and Computers in Simulation*, vol. 110, pp. 96–112, 2015.

[29] D. Kai, N. Ford, and D. Freed Alan, "Detailed error analysis for a fractional adams method," *Numerical Algorithms*, vol. 36, pp. 31–52, 2004.

[30] R. Garrappa, "On linear stability of predictor-corrector algorithms for fractional differential equations," *International Journal of Computer Mathematics*, vol. 87, no. 10, pp. 2281–2290, 2010.

[31] M. Zayernouri and A. Matzavinos, "Fractional adams–bashforth/moulton methods: an application to the fractional keller –– segel chemotaxis system," *Journal of Computational Physics*, vol. 317, no. 1–14, 2016.

[32] G. C. Wu and D. Baleanu, "Variational iteration method for fractional calculus – a universal approach by laplace transform," *Advances in Difference Equations*, vol. 18, 2013.

[33] Z. M. Odibat and S. Momani, "Application of variational iteration method to nonlinear differential equations of fractional order," *International Journal of Nonlinear Sciences and Numerical Stimulation*, vol. 7, no. 1, pp. 27–34, 2006.

[34] S. Kumar and V. Gupta, "An application of variational iteration method for solving fuzzy time-fractional diffusion equations," *Neural Computing & Applications*, vol. 33, no. 24, Article ID 17659, 2021.

[35] G. Qi and X. Yang, "Modeling of a chaotic gyrostat system and mechanism analysis of dynamics using force and energy," *Complexity*, vol. 1, no. 13, 2019.

[36] A. Wolf, J. B. Swift, H. L. Swinney, and J. A. Vastano, "Determining lyapunov exponents from a time series," *Physica D: Nonlinear Phenomena*, vol. 16, no. 3, pp. 285–317, 1985.

[37] M. Schmutz and M. Rueff, "Bifurcation schemes of the lorenz model," *Physica D: Nonlinear Phenomena*, vol. 11, no. 1, pp. 167–178, 1984.

[38] H. Bi, G. Qi, and J. Hu, "Modeling and analysis of chaos and bifurcations for the attitude system of a quadrotor unmanned aerial vehicle," *Complexity*, vol. 2019, Article ID 6313925, , 2019.

[39] Anatoliui Aleksandrovich Kilbas, H. M. Srivastava, and J. J. Trujillo, *Theory and applications of fractional differential equations*, Vol. 204, Elsevier, , Amsterdam, 2006.

[40] T. Burton and C. Kirk, "A fixed point theorem of krasnoselskii—schaefer type," *Mathematische Nachrichten*, vol. 189, no. 1, pp. 23–31, 1998.

Hindawi
Complexity
Volume 2022, Article ID 2596924, 15 pages
https://doi.org/10.1155/2022/2596924

Research Article

Development of a New Multi-step Iteration Scheme for Solving Non-Linear Models with Complex Polynomiography

Amanullah Soomro,[1] **Amir Naseem**,[2] **Sania Qureshi**,[1,3] **and Nasr Al Din Ide**[4]

[1]*Department of Basic Sciences and Related Studies, Mehran University of Engineering and Technology, Jamshoro 76062, Pakistan*
[2]*Department of Mathematics, University of Management and Technology, Lahore 54770, Pakistan*
[3]*Department of Mathematics, Near East University TRNC, Mersin 10, Turkey*
[4]*Department of Mathematics, Faculty of Science, Aleppo University, Syria*

Correspondence should be addressed to Amir Naseem; amir.kasuri89@gmail.com and Nasr Al Din Ide; ide1112002@yahoo.ca

Received 28 March 2022; Revised 11 May 2022; Accepted 12 May 2022; Published 27 June 2022

Academic Editor: Jesus M. Munoz-Pacheco

The appearance of nonlinear equations in science, engineering, economics, and medicine cannot be denied. Solving such equations requires numerical methods having higher-order convergence with cost-effectiveness, for the equations do not have exact solutions. In the pursuit of efficient numerical methods, an attempt is made to devise a modified strategy for approximating the solution of nonlinear models in either scalar or vector versions. Two numerical methods of second-and sixth-order convergence are carefully merged to obtain a hybrid multi-step numerical method with twelfth-order convergence while using seven function evaluations per iteration, resulting in the efficiency index of about 1.4262. The convergence is also ascertained theoretically, and the asymptotic error constant is computed. Furthermore, various numerical methods of varying orders are used to compare the numerical results obtained with the proposed hybrid method in approximate solution, number of iterations, absolute error, absolute functional value, and the machine time measured in seconds. The obtained results outperformed the chosen methods when applied models arising from physical and natural fields were solved. Finally, to observe the convergence graphically, some complex polynomials are plotted as polynomiographs, wherein the rapid convergence of the proposed method is guaranteed.

1. Introduction

Computing the approximate zeros of the nonlinear scalar and vector functions is one of the most important and interesting research areas in the modern age. There are many applications of the root-finding methods in different disciplines of science as well as in arts and economics. With the help of several mathematical techniques, a variety of complex problems in different applied sciences can be modulated in the form of nonlinear equations and then can be readily solved via different root-finding techniques. A root-finding method in mathematics and computer technology is a method for finding zeros, commonly known as "roots" of continuous functions. A zero of a real-valued or a complex-valued function f, is a value r such that $f(r) = 0$. Mostly, the root-finding techniques give approximations to zeros, expressed either as floating-point integers or as tiny isolating intervals, or discs for real or complex roots, because the zeros of a function cannot be calculated accurately with available analytical techniques.

Most numerical approaches for root-finding rely on the iteration process, which generates a series of discrete points that should converge towards the root as a limit. These iteration schemes start with one or more estimations of the root as initial inputs, and every iteration of the process generates a more accurate estimation of the exact root [1–4].

Since iterations must be ended at some point, these approaches yield estimation to the root rather than a precise solution. Many approaches compute successive

approximations by considering an auxiliary function on the values that came before them. Therefore, the limit is a fixed point of the function f, which is selected to have the solution of the original equation as fixed points and to converge to these fixed points quickly. In pursuing accurate and efficient roof-finding techniques, several techniques have been proposed in the past and current literature from the Newton method through the techniques proposed in the ongoing year.

Perhaps, the most commonly used root-finding method is the Newton Rahpson method $N2$ [5] with quadratic convergence. Its computational step is shown below that uses two function evaluations: 1 for the function $f(x)$ itself and 1 for the first-order derivative $f'(x)$:

$$x_{i+1} = x_i - \left(\frac{f(x_i)}{f'(x_i)}\right), \quad i = 0, 1, 2, \tag{1}$$

where $f'(x_i) \neq 0$.

The researchers in [6] devised a modified version of an existing algorithm aiming at the removal of first-order derivatives. They came up with a two-step method with fourth-order convergence abbreviated by $N4$. One of the advantages of the algorithm was the use of only four function evaluations per iteration, as depicted in the following computational scheme:

$$\begin{aligned} y_i &= x_i - \frac{f(x_i)}{\kappa(x_i)}, \\ x_{i+1} &= y_i - \frac{f(y_i)}{\kappa(y_i)} - \frac{f^2(y_i) f(x_i.y_i)}{2f^3(y_i)}, \quad i = 0, 1, \ldots, \end{aligned} \tag{2}$$

where

$$\begin{aligned} \kappa(x_i) &= \frac{f(x_i + f(x_i)) - f(x_i)}{f(x_i)}, \\ \kappa(y_i) &= \frac{f(y_i + f(y_i)) - f(y_i)}{f(y_i)}, \\ f(x_i, y_i) &= \frac{\kappa(y_i) - \kappa(x_i)}{f(y_i) - f(x_i)}. \end{aligned} \tag{3}$$

The researchers in [7] devised a three-step method having eighth-order convergence as denoted by W_8. Despite being eighth-order convergent, one of the advantages of the algorithm was the use of only four function evaluations per iteration, as depicted in the following computational scheme:

$$\begin{aligned} y_i &= x_i - \frac{f(x)_i}{f'(x_i)}, \\ z_i &= x_i - \frac{f(x_i)}{f'(x_i)} \frac{4f(x_i)^2 - 5f(x_i)f(y_i) - f(y_i)^2}{4f(x_i)^2 - 9f(x_i)f(y_i)}, \quad i = 0, 1, 2, \ldots, \\ x_{i+1} &= z_i - \frac{f(z_i)}{f'(x_i)} \left[1 + 4\frac{f(z_i)}{f(x_i)}\right] \left[\frac{8f(y_i)}{4f(x_i) - 11f(y_i)} + 1 + \frac{f(z_i)}{f(y_i)}\right]. \end{aligned} \tag{4}$$

A ninth-order convergence for a method as denoted by $N9$ was proved in [8]. The algorithm merely needs 5 function evaluations per iteration, as depicted in the following computational scheme:

$$\begin{aligned} y_i &= x_i - \frac{f(x_i)}{f'(x_i)}, \\ z_i &= y_i - \left(1 + \left(\frac{f(y_i)}{f(x_i)}\right)^2\right) \frac{f(y_i)}{f'(y_i)}, \quad i = 0, 1, 2, \ldots, \\ x_{i+1} &= z_i - \left(1 + 2\left(\frac{f(y_i)}{f(x_i)}\right)^2 + 2\frac{f(z_i)}{f(y_i)}\right) \frac{f(z_i)}{f'(y_i)}. \end{aligned} \tag{5}$$

Another higher-order three-step iterative method as denoted by $P10$ is in [9]. The method is shown to be three-step that requires only 6 function evaluations per iteration, as depicted in the following computational scheme:

$$\begin{aligned} y_i &= x_i - \frac{f(x_i)}{f'(x_i)}, \\ z_i &= y_i - \frac{f(y_i)}{f'(y_i)}, \\ x_{x+1} &= z_i - \left(\frac{f(z_i)f'(z_i) + 3f(z_i)f'(y_i)}{5f'(y_i)f'(z_i) - f'^2(y_i)}\right). \end{aligned} \tag{6}$$

for

We have also chosen an iterative process with eleventh-order convergence as denoted by $N11$ in [10]. The process consists of four steps and requires 7 function evaluations per iteration, as depicted in the following computational scheme:

$$
\begin{aligned}
y_i &= x_i - \frac{f(x_i)}{f'(x_i)},\\
z_i &= y_i - \left(1 + \left(\frac{f(y_i)}{f(x_i)}\right)^2\right)\frac{f(y_i)}{f'(y_i)},\\
w_i &= z_i - \left(1 + 2\left(\frac{f(y_i)}{f(x_i)}\right)^2 + 2\frac{f(z_i)}{f(y)_i}\right)\frac{f(z_i)}{f'(y_i)}, \quad i = 0, 1, 2, \ldots,\\
x_{i+1} &= w_i - \frac{f(w_i)}{f'(w_i)}.
\end{aligned}
\tag{7}
$$

Finally, a three-step iterative method with twelfth-order convergence as denoted by $N12$ is in [11, 12]. The method consists of 5 function evaluations per iteration, as depicted in the following computational scheme:

$$
\begin{aligned}
y_i &= x_i - \frac{f(x_i)}{f'(x_i)},\\
z_i &= y_i - \frac{(x_i - y_i)f(y_i)}{f(x_i) - 2f(y_i)}, \quad i = 0, 1, 2, \ldots,\\
x_{i+1} &= z_i - \frac{f(z_i)f'(z_i)}{(1 - 0.5f(z_i))(f'(z_i))^2}.
\end{aligned}
\tag{8}
$$

2. Formulation of the Proposed Method

It has been observed in the current literature that new modified root-finding techniques are being proposed because of increasing the efficiency of the existing ones. In search of such algorithms, some researchers have merged two existing iterative methods of convergence order m and n to obtain a hybrid method with convergence order mn. In this respect, the convergence order is improved. Nonetheless, the computational aspect was ignored, resulting in an increased number of function evaluations in most newly modified hybrid approaches. For example, authors in [13] proposed an iterative third-order method with five function evaluations required per iteration, including another algorithm presented in the same research work with a fourth-order three-step method that requires eight function evaluations. Likewise, authors in [14,15] have employed an excessive number of first-order derivatives, leading to high computational effort and machine time. The primary concern of the present work is to propose a hybrid method with possible higher-order convergence with the minimum number of function evaluations so that the computational cost in terms of arithmetic operations and CPU time be reduced. The proposed method comes from Newton's method ($m = 2$) and a three-step method ($n = 6$) in [16,17], leading to produce the proposed approach with convergence order mn = 12 while using just seven function evaluations per iteration. The four-step proposed method results in the following computational steps, whose flowchart is depicted in Figure 1:

$$
\begin{aligned}
w_i &= x_i - \frac{f(x_i)}{f'(x_i)},\\
y_i &= w_i - \frac{f(w_i)}{f'(w_i)},\\
z_i &= y_i - \frac{f(y_i)}{f'(y_i)},\\
x_{i+1} &= y_i - \left[\frac{f(y_i) + f(z_i)}{f'(y_i)}\right].
\end{aligned}
\tag{9}
$$

for $i = 0, 1, 2, \ldots$.

The methods as mentioned earlier, including the one proposed as the four-step hybrid method in the present article, are compared in Figure 2 with each other based on efficiency index ($p^{1/n}$), order of convergence (p), and the number of function evaluations (n) used by each method per iteration.

3. Convergence Analysis of the Proposed Method

This section has been divided into two sections wherein the convergence of the proposed four-step hybrid method in both scalar and vector form has been discussed in detail. It is noted that the twelfth-order convergence is theoretically verified in each case with the aid of Taylor's expansion.

3.1. Convergence Theory with Scalar Form. In this subsection, we theoretically prove the local order of convergence for the proposed method given in (9).

Theorem 1. *Suppose that $\alpha \in Q$ be the required simple root for a sufficiently differentiable function $f: Q \subseteq \mathbb{R} \longrightarrow \mathbb{R}$ within an open real interval Q. Then, the proposed four-step numerical method (9) possesses twelfth-order convergence with the error equation given by:*

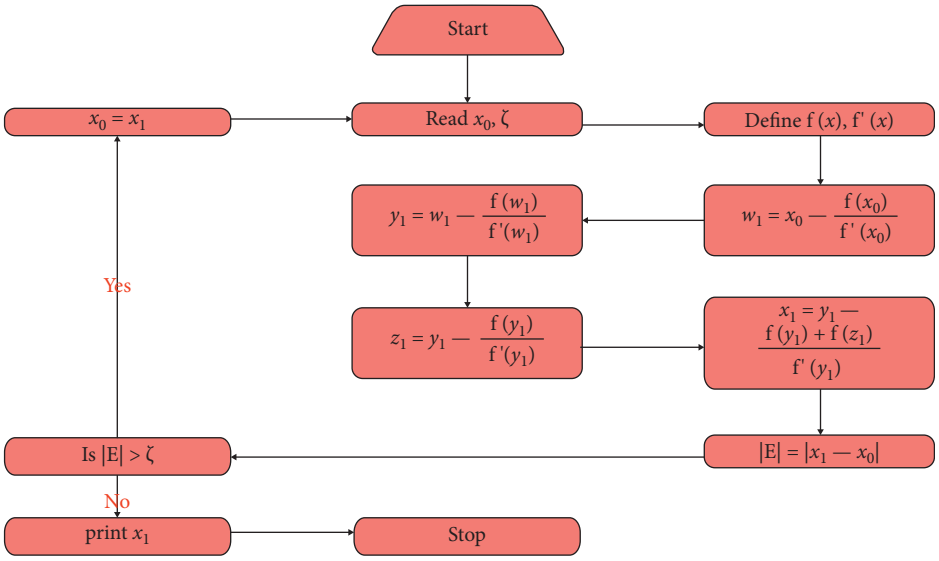

Figure 1: Flow chart for the proposed four-step hybrid method given in (9).

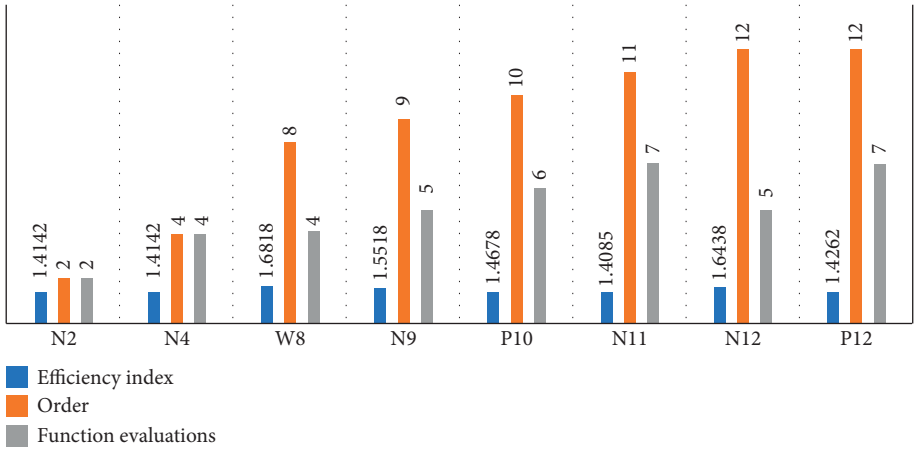

Figure 2: Comparison of the methods under consideration on the basis of efficiency index, order of convergence, and number of function evaluations.

$$\zeta_{i+1} = 2\left(\frac{f_2}{2f_1}\right)^{11}\zeta_i^{12} + \mathcal{O}\left(\zeta_i^{13}\right), \tag{10}$$

where $f_i = f^{(i)}(\alpha)$ *and* $\zeta_i = x_i - \alpha, \quad i = 1, 2, \ldots$

Proof. Suppose α be a simple root of $f(x)_i = 0$, where x_i be the i th approximation for the root by the proposed method (9), and $\zeta_i = x_i - \alpha$ be the error term in variable x at the i th iteration step. Employing the single real variable Taylor's series in [9] for $f(x_i)$ around α, we obtain

$$f(x_i) = f_1\zeta_i + \frac{f_2}{2!}\zeta_i^2 + \frac{f_3}{3!}\zeta_i^3 + \frac{f_4}{4!}\zeta_i^4 + \mathcal{O}\left(\zeta_i^5\right). \tag{11}$$

Similarly, using the Taylor's series for $1/f'(x_i)$ around α, we obtain

$$\frac{1}{f'(x_i)} = f_1^{-1} - \frac{f_2\zeta_i}{f_1^2} + \frac{\zeta_i^2}{f_1}\left(-\frac{f_3}{2f_1} + \frac{f_2^2}{f_1^2}\right) + \frac{\zeta_i^3}{f_1}\left(-\frac{f_4}{6f_1} + \frac{f_2f_3}{2f_1^2} + \frac{\left(f_3f_1 - 2f_2^2\right)f_2}{2f_1^3}\right) + \mathcal{O}\left(\zeta_i^4\right). \tag{12}$$

Multiplying (11) and (12), we obtain

$$\frac{f(x_i)}{f'(x_i)} = -\frac{\left(2f_4f_1^2 - 7f_3f_2f_1 + 6f_2^3\right)\zeta_i^4}{12f_1^3} - \frac{\left(2f_3f_1 - 3f_2^2\right)\zeta_i^3}{6f_1^2} - \frac{\zeta_i^2 f_2}{2f_1} + \zeta_i. \tag{13}$$

Substituting (13) in the first step of (9), we obtain

$$\eta_i = \frac{\left(2f_4f_1^2 - 7f_3f_2f_1 + 6f_2^3\right)\zeta_i^4}{12f_1^3} + \frac{\left(2f_3f_1 - 3f_2^2\right)\zeta_i^3}{6f_1^2} + \frac{\zeta_i^2 f_2}{2f_1}, \tag{14}$$

where $\eta_i = w_i - \alpha$. Using the Taylor's series for $f(w_i)$ around α, we obtain

$$f(w_i) = f_1\eta_i + \frac{f_2}{2!}\eta_i^2 + \frac{f_3}{3!}\eta_i^3 + \frac{f_4}{4!}\eta_i^4 + \mathcal{O}\left(\eta_i^5\right). \tag{15}$$

Similarly, using the Taylor's series for $1/f'(w_i)$ around α, we obtain

$$\frac{1}{f'(w_i)} = f_1^{-1} - \frac{f_2\eta_i}{f_1^2} + \frac{\eta_i^2}{f_1}\left(-\frac{f_3}{2f_1} + \frac{f_2^2}{f_1^2}\right) + \frac{\eta_i^3}{f_1}\left(-\frac{f_4}{6f_1} + \frac{f_2f_3}{2f_1^2} + \frac{\left(f_3f_1 - 2f_2^2\right)f_2}{2f_1^3}\right) + \mathcal{O}\left(\eta_i^4\right). \tag{16}$$

Multiplying (15) and (16), we obtain

$$\frac{f(w_i)}{f'(w_i)} = -\frac{\left(2f_4f_1^2 - 7f_3f_2f_1 + 6f_2^3\right)\eta_i^4}{12f_1^3} - \frac{\left(2f_3f_1 - 3f_2^2\right)\eta_i^3}{6f_1^2} - \frac{\eta_i^2 f_2}{2f_1} + \eta_i. \tag{17}$$

Substituting (17) in the second step of (9), we obtain

$$\nu_i = \frac{\left(2f_4f_1^2 - 7f_3f_2f_1 + 6f_2^3\right)\eta_i^4}{12f_1^3} + \frac{\left(2f_3f_1 - 3f_2^2\right)\eta_i^3}{6f_1^2} + \frac{\eta_i^2 f_2}{2f_1}. \tag{18}$$

where $\nu_i = y_i - \alpha$. Using the Taylor's series for $f(y_i)$ around α, we obtain

$$f(y_i) = f_1\nu_i + \frac{f_2}{2}\nu_i^2 + \frac{f_3}{3!}\nu_i^3 + \frac{f_4}{4!}\nu_i^4 + \mathcal{O}\left(\nu_i^5\right). \tag{19}$$

Similarly, using the Taylor's series for $1/f'(y_i)$ around α, we obtain

$$\frac{1}{f'(y_i)} = f_1^{-1} - \frac{f_2\nu_i}{f_1^2} + \frac{\nu_i^2}{f_1}\left(-\frac{f_3}{2f_1} + \frac{f_2^2}{f_1^2}\right) + \frac{\nu_i^3}{f_1}\left(-\frac{f_4}{6f_1} + \frac{f_2f_3}{2f_1^2} + \frac{\left(f_3f_1 - 2f_2^2\right)f_2}{2f_1^3}\right) + \mathcal{O}\left(\nu_i^4\right). \tag{20}$$

Multiplying (19) and (20), we obtain

$$\frac{f(y_i)}{f'(y_i)} = -\left(\frac{\left(2f_4f_1^2 - 7f_3f_2f_1 + 6f_2^3\right)\nu_i^4}{12f_1^3}\right) - \left(\frac{\left(2f_3f_1 - 3f_2^2\right)\nu_i^3}{6f_1^2}\right) - \left(\frac{\nu_i^2 f_2}{2f_1}\right) + \nu_i. \tag{21}$$

Substituting (21) in the first step of (9), we obtain

$$\rho_i = \frac{\left(2f_4f_1^2 - 7f_3f_2f_1 + 6f_2^3\right)\nu_i^4}{12f_1^3} + \frac{\left(2f_3f_1 - 3f_2^2\right)\nu_i^3}{6f_1^2} + \frac{\nu_i^2 f_2}{2f_1}, \tag{22}$$

where $\rho_i = z_i - \alpha$. Using the Taylor's series for $f(z_i)$ around α, we obtain

$$f(z)_i = f_1\rho_i + \frac{f_2}{2!}\rho_i^2 + \frac{f_3}{3!}\rho_i^3 + \frac{f_4}{4!}\rho_i^4 + \mathcal{O}\left(\rho_i^5\right). \tag{23}$$

Substituting (19), (20), and (23) in the fourth step of (9), one obtains

$$\begin{aligned}\zeta_{i+1} = {} & \frac{\nu_i^3 f_3}{3f_1} + \frac{f_2^4\nu_i^5}{2f_1^4} + \frac{f_2^2\nu_i^5}{12f_1^2} - \frac{f_3^2\rho_i^2\nu_i^2}{2f_1^3} + \frac{f_4^2\rho_i^2\nu_i^3}{2f_1^4} - \frac{\nu_i^3 f_2^2}{2f_1^2} - \frac{f_2\rho_i^2}{2f_1} + \frac{\nu_i^2 f_2}{2f_1} \\ & + \frac{\nu_i^4 f_4}{6f_1} + \frac{\nu_i^4 f_2^3}{2f_1^3} + \frac{\rho_i\nu_i^3 f_2^3}{f_1^3} + \frac{f_2^2\rho_i^2\nu_i}{2f_1^2} - \frac{\rho_i\nu_i^2 f_2^2}{f_1^2} + \frac{\rho_i\nu_i^3 f_4}{6f_1} + \frac{f_3\nu_i^6 f_2^3}{6f_1^4} + \frac{\rho_i f_2\nu_i}{f_1} \\ & + \frac{\rho_i\nu_i^2 f_3}{2f_1} - \frac{2f_2^2\nu_i^5 f_3}{3f_1^2} + \frac{f_3\nu_i^6 f_4}{36f_1^2} - \frac{f_3^2\nu_i^6 f_2}{6f_1^2} - \frac{7\nu_i^4 f_2 f_3}{12f_1^2} + \frac{f_2\nu_i^5 f_4}{12f_1^2} + \frac{f_2\rho_i^2\nu_i^3 f_4}{12f_1^2} \\ & + \frac{f_2\rho_i^2\nu_i^2 f_3}{4f_1^2} - \frac{\rho_i\nu_i^3 f_2 f_3}{f_1^2} - \frac{f_2^2\rho_i^2\nu_i^3 f_3}{2f_1^3} - \rho_i.\end{aligned} \tag{24}$$

Finally, using , and (14) and (18), (22) for the above equation, we obtain

$$\zeta_{i+1} = 2\left(\frac{f_2}{2f_1}\right)^{11}\zeta_i^{12} + \mathcal{O}\left(\zeta_i^{13}\right). \tag{25}$$

Hence, the twelfth-order convergence of the proposed method P12 given by (9) for the nonlinear functions in single variable $(f(x) = 0)$ is proved. □

3.2. Convergence Theory with Vector Form.

$$\begin{aligned}\mathbf{w}_i &= \mathbf{x}_i - \mathbf{f}'(\mathbf{x}_i)^{-1}\mathbf{f}'(\mathbf{x}_i), \\ \mathbf{y}_i &= \mathbf{w}_i - \mathbf{f}'(\mathbf{w}_i)^{-1}\mathbf{f}'(\mathbf{w}_i), \\ \mathbf{z}_i &= \mathbf{y}_i - \mathbf{f}'(\mathbf{y}_i)^{-1}\mathbf{f}'(\mathbf{y}_i), \\ \mathbf{x}_{i+1} &= \mathbf{y}_i - \mathbf{f}'(\mathbf{y}_i)^{-1}[\mathbf{f}(\mathbf{y}_i) + \mathbf{f}(\mathbf{z}_i)]i\, i = 0, 1, 2, 3 \ldots.\end{aligned} \tag{26}$$

$\mathbf{f}_i = \mathbf{F}^{(i)}(\alpha)$, $i = 1, 2, \ldots$.

Proof. Suppose α be a simple root of $\mathbf{f}(\mathbf{x}_i) = 0$, where $\mathbf{x}_i$ be the i th approximation for the root by the proposed method (9), and $\zeta_i = \mathbf{x}_i - \alpha$ be the error term in variable $\mathbf{x}$ at the i th iteration step. Employing the multi variable Taylor's series given in the theorem [9] for $\mathbf{f}(\mathbf{x}_i)$ around α, we obtain

$$\mathbf{f}(\mathbf{x}_i) = \mathbf{f}_1\zeta_i + \frac{\mathbf{f}_2}{2!}\zeta_i^2 + \frac{\mathbf{f}_3}{3!}\zeta_i^3 + \frac{\mathbf{f}_4}{4!}\zeta_i^4 + \mathcal{O}\left(\zeta_i^5\right). \tag{27}$$

Again, using the Taylor's expansion for the inverted Jacobian matrix $\mathbf{f}'(\mathbf{x}_i)^{-1}$ around α, we obtain

$$f'(\mathbf{x}_i)^{-1} = \mathbf{f}_1^{-1} - \frac{\mathbf{f}_2\zeta_i}{\mathbf{f}_1^2} + \frac{\zeta_i^2}{\mathbf{f}_1}\left(-\frac{\mathbf{f}_3}{2\mathbf{f}_1} + \frac{\mathbf{f}_2^2}{\mathbf{f}_1^2}\right) + \frac{\zeta_i^3}{\mathbf{f}_1}\left(-\frac{\mathbf{f}_4}{6\mathbf{f}_1} + \frac{\mathbf{f}_2\mathbf{f}_3}{2\mathbf{f}_1^2} + \frac{\left(\mathbf{f}_3\mathbf{f}_1 - 2\mathbf{f}_i^2\right)\mathbf{f}_2}{2\mathbf{f}_1^3}\right) + \mathcal{O}\left(\zeta_i^4\right). \tag{28}$$

Multiplying (27) and (28), we obtain

$$f'(\mathbf{x}_i)^{-1}\mathbf{f}(\mathbf{x}_i) = -\frac{\left(2\mathbf{f}_4\mathbf{f}_1^2 - 7\mathbf{f}_3\mathbf{f}_2\mathbf{f}_1 + 6\mathbf{f}_2^3\right)\boldsymbol{\zeta}_i^4}{12\mathbf{f}_1^3} - \frac{\left(2\mathbf{f}_3\mathbf{f}_1 - 3\mathbf{f}_2^2\right)\boldsymbol{\zeta}_i^3}{6\mathbf{f}_1^2} - \frac{\boldsymbol{\zeta}_i^2\mathbf{f}_2}{2\mathbf{f}_1} + \boldsymbol{\zeta}_i. \tag{29}$$

Substituting (29) in the first step of (9), we obtain

$$\boldsymbol{\eta}_i = \frac{\left(2\mathbf{f}_4\mathbf{f}_1^2 - 7\mathbf{f}_3\mathbf{f}_2\mathbf{f}_1 + 6\mathbf{f}_2^3\right)\boldsymbol{\zeta}_i^4}{12\mathbf{f}_1^3} + \frac{\left(2\mathbf{f}_3\mathbf{f}_1 - 3\mathbf{f}_2^2\right)\boldsymbol{\zeta}_i^3}{6\mathbf{f}_1^2} + \frac{\boldsymbol{\zeta}_i^2\mathbf{f}_2}{2\mathbf{f}_1}, \tag{30}$$

where $\eta_i = \mathbf{w}_i - \alpha$. Using the Taylor's series for $\mathbf{f}(\mathbf{w}_i)$ around α, we obtain

$$\mathbf{f}(\mathbf{w}_i) = \mathbf{f}_1\boldsymbol{\eta}_i + \frac{\mathbf{f}_2}{2!}\boldsymbol{\eta}_i^2 + \frac{\mathbf{f}_3}{3!}\boldsymbol{\eta}_i^3 + \frac{\mathbf{f}_4}{4!}\boldsymbol{\eta}_i^4 + \mathcal{O}, \tag{31}$$

Again, using the Taylor's expansion for the inverted Jacobian matrix $\mathbf{f}'(\mathbf{w}_i)^{-1}$ around α, we obtain

$$f'(\mathbf{w}_i)^{-1} = \mathbf{f}_1^{-1} - \frac{\mathbf{f}_2\boldsymbol{\eta}_i}{\mathbf{f}_1^2} + \frac{\boldsymbol{\eta}_i^2}{\mathbf{f}_1}\left(-\frac{\mathbf{f}_3}{2\mathbf{f}_1} + \frac{\mathbf{f}_2^2}{\mathbf{f}_1^2}\right) + \frac{\boldsymbol{\eta}_i^3}{\mathbf{f}_1}\left(-\frac{\mathbf{f}_4}{6\mathbf{f}_1} + \frac{\mathbf{f}_2\mathbf{f}_3}{2\mathbf{f}_1^2} + \frac{\left(\mathbf{f}_3\mathbf{f}_1 - 2\mathbf{f}_2^2\right)\mathbf{f}_2}{2\mathbf{f}_1^3}\right) + \mathcal{O}\left(\boldsymbol{\eta}_i^4\right). \tag{32}$$

Multiplying (31) and (32), we obtain

$$f'(\mathbf{w}_i)^{-1}\mathbf{f}(\mathbf{w}_i) = -\frac{\left(2\mathbf{f}_4\mathbf{f}_1^2 - 7\mathbf{f}_3\mathbf{f}_2\mathbf{f}_1 + 6\mathbf{f}_i^3\right)\boldsymbol{\eta}_i^4}{12\mathbf{f}_1^3} - \frac{\left(2\mathbf{f}_3\mathbf{f}_1 - 3\mathbf{f}_2^2\right)\boldsymbol{\eta}_i^3}{6\mathbf{f}_1^2} - \frac{\boldsymbol{\eta}_i^2\mathbf{f}_2}{2\mathbf{f}_1} + \boldsymbol{\eta}_i. \tag{33}$$

Substituting (33) in the second step of (9), we obtain

$$\boldsymbol{\nu}_i = \frac{\left(2\mathbf{f}_4\mathbf{f}_1^2 - 7\mathbf{f}_3\mathbf{f}_2\mathbf{f}_1 + 6\mathbf{f}_2^3\right)\boldsymbol{\eta}_i^4}{12\mathbf{f}_1^3} + \frac{\left(2\mathbf{f}_3\mathbf{f}_1 - 3\mathbf{f}_2^2\right)\boldsymbol{\eta}_i^3}{6\mathbf{f}_1^2} + \frac{\boldsymbol{\eta}_i^2\mathbf{f}_2}{2\mathbf{f}_1}, \tag{34}$$

where $\nu_i = \mathbf{y}_i - \alpha$. Using the Taylor's expansion for $\mathbf{f}(\mathbf{y}_i)$ around α, we obtain

$$\mathbf{f}(\mathbf{y}_i) = \mathbf{f}_1\boldsymbol{\nu}_i + \frac{\mathbf{f}_2}{2}\boldsymbol{\nu}_i^2 + \frac{\mathbf{f}_3}{3!}\boldsymbol{\nu}_i^3 + \frac{\mathbf{f}_4}{4!}\boldsymbol{\nu}_i^4 + \mathcal{O}\left(\boldsymbol{\nu}_i^5\right). \tag{35}$$

Again, using the Taylor's expansion for the inverted Jacobian matrix $\mathbf{f}'(\mathbf{y}_i)^{-1}$ around α, we obtain

$$f'(\mathbf{y}_i)^{-1} = \mathbf{f}_1^{-1} - \frac{\mathbf{f}_2\boldsymbol{\nu}_i}{\mathbf{f}_1^2} + \frac{\boldsymbol{\nu}_i^2}{\mathbf{f}_1}\left(-\frac{\mathbf{f}_3}{2\mathbf{f}_1} + \frac{\mathbf{f}_2^2}{\mathbf{f}_1^2}\right) + \frac{\boldsymbol{\nu}_i^3}{\mathbf{f}_1}\left(-\frac{\mathbf{f}_4}{6\mathbf{f}_1} + \frac{\mathbf{f}_2\mathbf{f}_3}{2\mathbf{f}_1^2} + \frac{\left(\mathbf{f}_3\mathbf{f}_1 - 2\mathbf{f}_2^2\right)\mathbf{f}_2}{2\mathbf{f}_1^3}\right) + \mathcal{O}\left(\boldsymbol{\nu}_i^4\right). \tag{36}$$

Multiplying (35) and (36), we obtain

$$f'(\mathbf{y}_i)^{-1}\mathbf{f}(y_i) = -\frac{\left(2\mathbf{f}_4\mathbf{f}_1^2 - 7\mathbf{f}_3\mathbf{f}_2\mathbf{f}_1 + 6\mathbf{f}_2^3\right)\boldsymbol{\nu}_i^4}{12\mathbf{f}_1^3} - \frac{\left(2\mathbf{f}_3\mathbf{f}_1 - 3\mathbf{f}_2^2\right)\boldsymbol{\nu}_i^3}{6\mathbf{f}_1^2} - \frac{\boldsymbol{\nu}_i^2\mathbf{f}_2}{2\mathbf{f}_1} + \boldsymbol{\nu}_i. \tag{37}$$

Substituting (37) in the first step of (9), we obtain

$$\boldsymbol{\rho}_i = \frac{\left(2\mathbf{f}_4\mathbf{f}_1^2 - 7\mathbf{f}_3\mathbf{f}_2\mathbf{f}_1 + 6\mathbf{f}_2^3\right)\boldsymbol{\nu}_i^4}{12\mathbf{f}_1^3} + \frac{\left(2\mathbf{f}_3\mathbf{f}_1 - 3\mathbf{f}_2^2\right)\boldsymbol{\nu}_i^3}{6\mathbf{f}_1^2} + \frac{\boldsymbol{\nu}_i^2\mathbf{f}_2}{2\mathbf{f}_1}. \tag{38}$$

where $\rho_i = \mathbf{z}_i - \alpha$. Using the Taylor's series for $\mathbf{f}(\mathbf{z}_i)$ around α, we obtain

$$\mathbf{f}(z_i) = \mathbf{f}_1\boldsymbol{\rho}_i + \frac{\mathbf{f}_2}{2!}\boldsymbol{\rho}_i^2 + \frac{\mathbf{f}_3}{3!}\boldsymbol{\rho}_i^3 + \frac{\mathbf{f}_4}{4!}\boldsymbol{\rho}_i^4 + \mathcal{O}\left(\boldsymbol{\rho}_i^5\right). \tag{39}$$

Substituting (35), (36), and (39) in the fourth step of (9), one obtains

$$\begin{aligned}\boldsymbol{\zeta}_{i+1} = {} & \frac{\mathbf{v}_i^3\mathbf{f}_3}{3\mathbf{f}_1} + \frac{\mathbf{f}_2^4\mathbf{v}_i^5}{2\mathbf{f}_1^4} + \frac{\mathbf{f}_2^3\mathbf{v}_i^5}{12\mathbf{f}_1^2} - \frac{\mathbf{f}_3^2\boldsymbol{\rho}_i^2\mathbf{v}_i^2}{2\mathbf{f}_1^3} + \frac{\mathbf{f}_2^4\boldsymbol{\rho}_i^2\mathbf{v}_i^3}{2\mathbf{f}_1^4} - \frac{\mathbf{v}_i^3\mathbf{f}_2^2}{2\mathbf{f}_1^2} - \frac{\mathbf{f}_2\boldsymbol{\rho}_i^2}{2\mathbf{f}_1} + \frac{\mathbf{v}_i^2\mathbf{f}_2}{2\mathbf{f}_1} \\ & + \frac{\mathbf{v}_i^4\mathbf{f}_4}{6\mathbf{f}_1} + \frac{\mathbf{v}_i^4\mathbf{f}_2^3}{2\mathbf{f}_1^3} + \frac{\boldsymbol{\rho}_i\mathbf{v}_i^3\mathbf{f}_2^3}{\mathbf{f}_1^3} + \frac{\mathbf{f}_2^2\boldsymbol{\rho}_i^2\mathbf{v}_i}{2\mathbf{f}_1^2} - \frac{\boldsymbol{\rho}_i\mathbf{v}_i^2\mathbf{f}_2^2}{\mathbf{f}_1^2} + \frac{\boldsymbol{\rho}_i\mathbf{v}_i^3\mathbf{f}_4}{6\mathbf{f}_1} + \frac{\mathbf{f}_3\mathbf{v}_i^6\mathbf{f}_2^3}{6\mathbf{f}_1^4} + \frac{\boldsymbol{\rho}_i\mathbf{f}_2\mathbf{v}_i}{\mathbf{f}_1} \\ & + \frac{\boldsymbol{\rho}_i\mathbf{v}_i^2\mathbf{f}_3}{2\mathbf{f}_1} - \frac{2\mathbf{f}_2^2\mathbf{v}_i^5\mathbf{f}_3}{3\mathbf{f}_1^3} + \frac{\mathbf{f}_3\mathbf{v}_i^6\mathbf{f}_4}{36\mathbf{f}_1^2} - \frac{\mathbf{f}_2^3\mathbf{v}_i^6\mathbf{f}_2}{6\mathbf{f}_1^3} - \frac{7\mathbf{v}_i^4\mathbf{f}_2\mathbf{f}_3}{12\mathbf{f}_1^2} + \frac{\mathbf{f}_2\mathbf{v}_i^5\mathbf{f}_4}{12\mathbf{f}_1^2} + \frac{\mathbf{f}_2\boldsymbol{\rho}_i^2\mathbf{v}_i^3\mathbf{f}_4}{12\mathbf{f}_1^2} \\ & + \frac{\mathbf{f}_2\boldsymbol{\rho}_i^2\mathbf{v}_i^2\mathbf{f}_3}{4\mathbf{f}_1^2} - \frac{\boldsymbol{\rho}_i\mathbf{v}_i^3\mathbf{f}_2\mathbf{f}_3}{\mathbf{f}_1^2} - \frac{\mathbf{f}_2^2\boldsymbol{\rho}_i^2\mathbf{v}_i^3\mathbf{f}_3}{2\mathbf{f}_1^3} - \boldsymbol{\rho}_i\end{aligned} \tag{40}$$

Finally, using , and (30) and (34), (38) for the above equation, we obtain

$$\boldsymbol{\zeta}_{i+1} = 2\left(\frac{\mathbf{f}_2}{2\mathbf{f}_1}\right)^{11}\boldsymbol{\zeta}_i^{12} + \mathcal{O}\left(\boldsymbol{\zeta}_i^{13}\right). \tag{41}$$

Hence, the twelfth-order convergence of the proposed multi-step (four-step) hybrid method P12 mentioned by (9) for the nonlinear functions in multi-variable $(\mathbf{f}(\mathbf{x}) = 0)$ case is proved. □ □

4. Polynomiography

Polynomiography is a process that integrates mathematics and art to create a new type of visual art. The produced graphics result from algorithmic visualization of iterative approaches for solving a polynomial equation. This term was first introduced by Dr. Bahman Kalantari at the start of the 21st century [18]. Dr. Bahman Kalantari's study on polynomial root-finding, which is an old and traditional discipline that continues to find new implications with each generation of mathematicians and scientists, inspired the concepts of Polynomiography. Dr. Kalantari invented the term "polynomiography," which is a mixture of the word "polynomial" with the suffix "graphy." A "polynomiograph" is a separately produced picture resulting from Polynomiography. It is defined as "An iterative procedure for producing two-dimensional colored pictures (polynomiographs) that represent polynomials."

In recent years, researchers worked in the field of Polynomiography along with its implementations in other fields. In [19], the authors introduced a new mathematical art with the help of Newton–Ellipsoid method. Gdawiec et al. in [20], presented the visual analysis of Newton's method with fractional-order derivatives. The authors employed the techniques of coloring by roots and coloring via iterations to study the convergence and dynamical aspects of the processes visualized by polynomiographs.

Naseem et al. in [21] presented some new graphical art with the help of newly suggested ninth-order iteration schemes. Scot et al. in [22], presented the basin of attraction for several methods and examined its dependence on their convergence orders. In [23], the authors introduced a new family of eighth-order methods and then drew their basins of attractions by assuming different polynomials. Finally, in [24], the authors generated some new fractal patterns by combing two root-finding methods. The obtained fractal patterns were diverse and had many applications in the textile and ceramic industries.

We use a rectangle $R \in \mathbb{C}$ along with the dimension $[-2, 2] \times [-2, 2]$, accuracy $\varepsilon = 1 \times 10^{-3}$ and the max. no. of iterations $T = 20$ to create the polynomiographs over the complex plane C through the computer software by taking multiple complex polynomials. The color black is allocated to the spots where the method failed to converge. The partitioning of R determines the pixel density of the created visual representations; for example, if we partition the rectangle R into a grid of 2000×2000, the plotting polynomiographs will then have better resolution.

For drawing graphical objects in the complex plane, we use the four complex polynomials listed below:

$$\begin{aligned}&\mathfrak{q}_1(t) = t^3 - 1,\ \mathfrak{q}_2(t) = 3t^3 + 2t^2 - t + 1, \\ &\mathfrak{q}_3(t) = t^4 - 1,\ \mathfrak{q}_4(t) = \left(t^2 + 1\right)\left(t^2 - 2\right).\end{aligned} \tag{42}$$

For coloring the iterations, we employ the colormap given in Figure 3.

Problem 1. Polynomiographs for the Polynomial $q_1(t)$ Through Various Methods

In this example, we investigate and compare the dynamical results obtained through different iteration schemes with our presented method by considering the cubic

Figure 3: The colormap for drawing polynomiographs.

polynomial $t^3 - 1$ which possesses three distinct simple zeros:1, $-(1/2) - (\sqrt{3}/2)i$, $-(1/2) + (\sqrt{3}/2)i$. We executed all the methods to achieve the simple zeros of the considered polynomials and the results *can be visualized in* Figure 4.

Problem 2. Polynomiographs for the Polynomial $q_2(t)$ Through Various Methods

In this example, we investigate and compare the dynamical results obtained through different iteration schemes with our presented method by considering the 3rd-degree polynomial $3t^3 + 2t^2 - t + 1$ which possesses three distinct simple zeros*:*

$$-\frac{2003}{1690}, \frac{867}{3344} \pm \frac{1504}{3251}i. \tag{43}$$

We executed all methods to achieve the simple zeros of the considered polynomials and the results can be seen in Figure 5.

Problem 3. Polynomiographs for the Polynomial $q_3(t)$ Through Various Methods

In this example, we investigate and compare the dynamical results obtained through different methods with our presented method by considering the 4th-degree polynomial $t^4 - 1$ which possesses the following simple zeros:1, -1, i, and $-i$. We executed all the methods to achieve the simple zeros of the considered polynomials and the results are given in Figure 6.

Problem 4. Polynomiographs for the Polynomial $q_4(t)$ Through Various Methods

In this example, we investigate and compare the dynamical results obtained through different iteration methods with our presented method by considering 4th-degree polynomial $(t^2 - 1)(t^2 - 2)$ which possesses the simple zeros:1, -1, 2, and -2. We executed all methods to achieve the simple zeros of the considered polynomials and the results can be visualized in Figure 7.

In all given examples, a detailed graphical analysis of the designed algorithm has been provided via polynomigraphs. For plotting polynomiographs on the complex plane, we take two cubic-degree polynomials namely: $q_1(t)$, and $q_2(t)$ and two quatric-degree polynomials represented by $q_3(t)$, and $q_4(t)$ respectively. The plotted graphs tell us about the convergence speed and the iterations performed by the method for drawing these objects. The second characteristic is the dynamics of the iteration scheme. In each polynomiographs, the individual root has been denoted by the blue colored dot. The black colored zones denote the divergence area or deficiency of the method through which the polynomiographs has been plotted. The darker or brighter zones in the provided polynomiographs showing less iterations performed to approximate the solution. One can easily observe the superiority of the proposed method over the others by examining the more darker or brighter zones of the polynomiographs drawn by the suggested method.

5. Numerical Simulations: Real-world Scenarios

This section of the paper discusses the real-life applications by applying the newly proposed hybrid method. We also present a numerical comparison with other existing most frequently used methods: N2, N4, W8, N9, P10, N11, and N12, whose computational steps are shown in the introductory section above. In each applied model, we set the tolerance to be $\varepsilon = 10^{-100}$ as the stopping criterion of the iterative process of every method under consideration: $|x_N - x_e| < \varepsilon$. Two additional methods with fifth- and sixth-order of convergence are also included for the simulations of a six-dimensional model chosen from the field of neurophysiology based on the reason that some of the methods under discussion in the above introductory section did not prove to be valuable candidates when it comes to the simulations of the nonlinear models presented in the system or vector form.

Problem 5. The Plank's radiation law in physics explains the spectral density of radiation emitted by a black body in thermal equilibrium at the temperature T and the condition that there must not be a flow of energy between the body and its surroundings. In other words, the law is introduced to determine the amount of energy density in a black body based on isothermal properties. Moreover, it is sometimes used to estimate the maximal radiation's wavelength. As described in [25], the maximal wavelength of the radiation may be written in the form of the following nonlinear equation in scalar version:

$$f_1(x) = \exp(-x) + \frac{x}{5} - 1, \tag{44}$$

where x stands for the maximal wavelength. The exact solution of the above equation is as follows: 0.0.

The Plank's radiation model described in (44) is simulated with several numerical algorithms while assuming two different initial guesses. The maximum number of iterations in each case is set to be $N = 4$. It can be observed in Table 1 that the accuracy is maximum for P12 at the cost of a slightly higher amount of CPU time, regardless of the initial estimate's location. The eleventh-order method N11 did not converge with the initial estimate taken to be $x_0 = 0.49$ while it converges second to P12 when the initial guess $x_0 = 0.75$ is taken. With this second initial guess, the CPU time consumption also slightly increases for N4 and N11.

Problem 6. Fraction Conversion of Nitrogen-Hydrogen to Ammonia [26]. This nonlinear scalar problem depicts the fractional conversion of nitrogen-hydrogen to ammonia and has appeared in several research works conducted in the past and recent literature. In this experiment, we set the pressure value to be 250 atmospheric pressure while the temperature is set to 500 degrees Celsius. In terms of a nonlinear function,

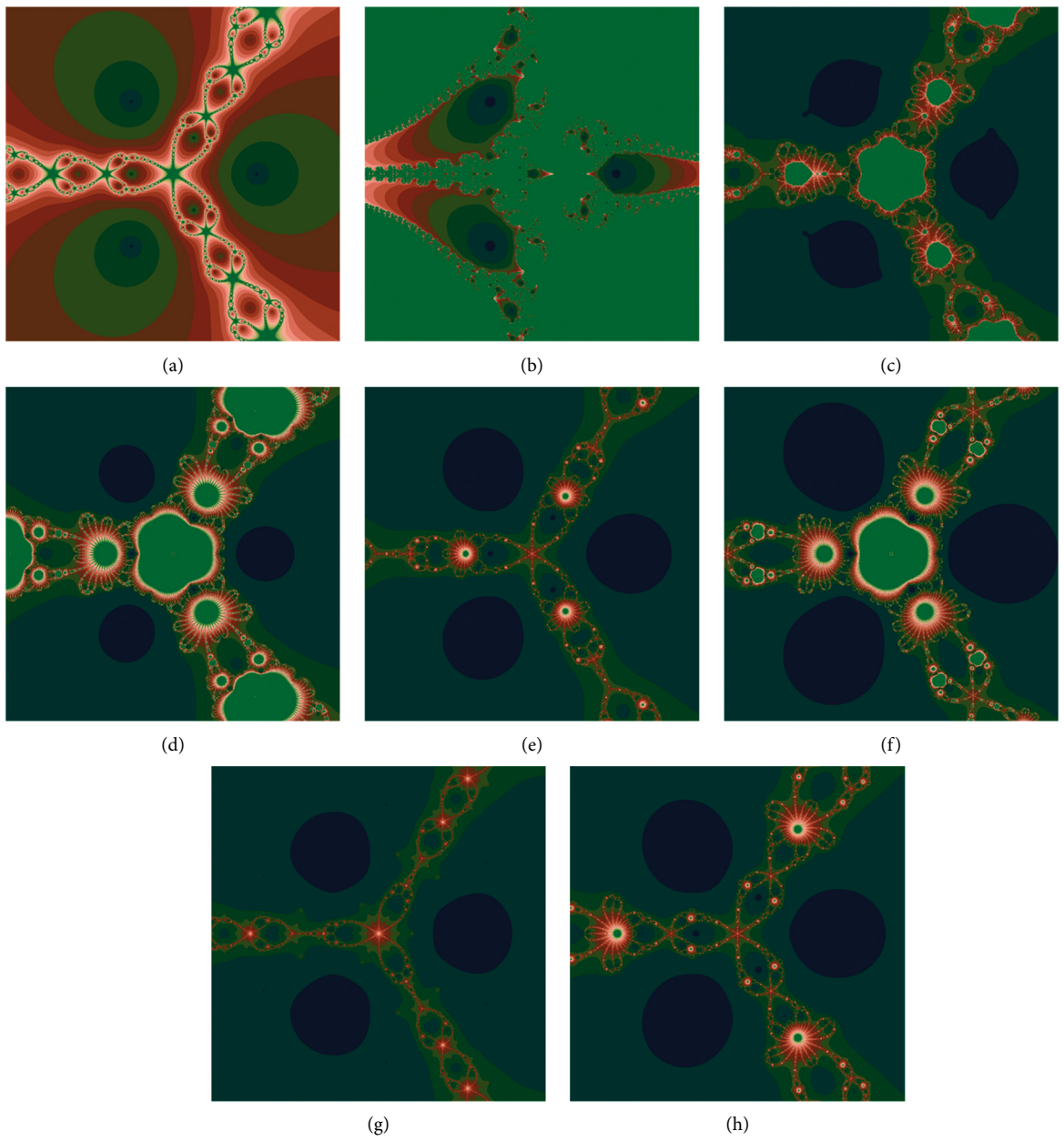

Figure 4: Polynomiographs for $q_1(t)$ using different methods.

the model mentioned above has the following polynomial form:

$$f_2(x) = x^4 - 7.79075x^3 + 14.744x^2 + 2.511x - 1.674. \tag{45}$$

It has been identified in the recent work [27] that one of its positive real roots lies in the open unit interval $(0, 1)$ which is estimated to be 0.2777595428.

For this nonlinear model, the numerical simulations are shown in Table 2 while the number of iterations for each method under consideration is set to be 7. Two different initial guesses, that is, $x_0 = 0.5$ (near to the exact solution) and $x_0 = 0.95$ (away from the exact solution), are chosen. It is seen that the fourth-order method N4 converges towards some other solution for the first initial guess while the method abbreviated as N11 failed after three iterations while the same is the case for the W8 method, but the method W8 produced the correct approximate solution till four iterations and failed after that. The Newton method N2 has the comparatively most significant absolute error at the fourth iteration compared to other methods. Nonetheless, the proposed hybrid method, in addition to a few more methods, always converged towards the required solution. More so, the proposed method has achieved the minor error tolerance with a reasonable amount of time. Hence, it can be concluded that the initial location of the estimate does not matter much when it comes to the proposed hybrid method devised in this article.

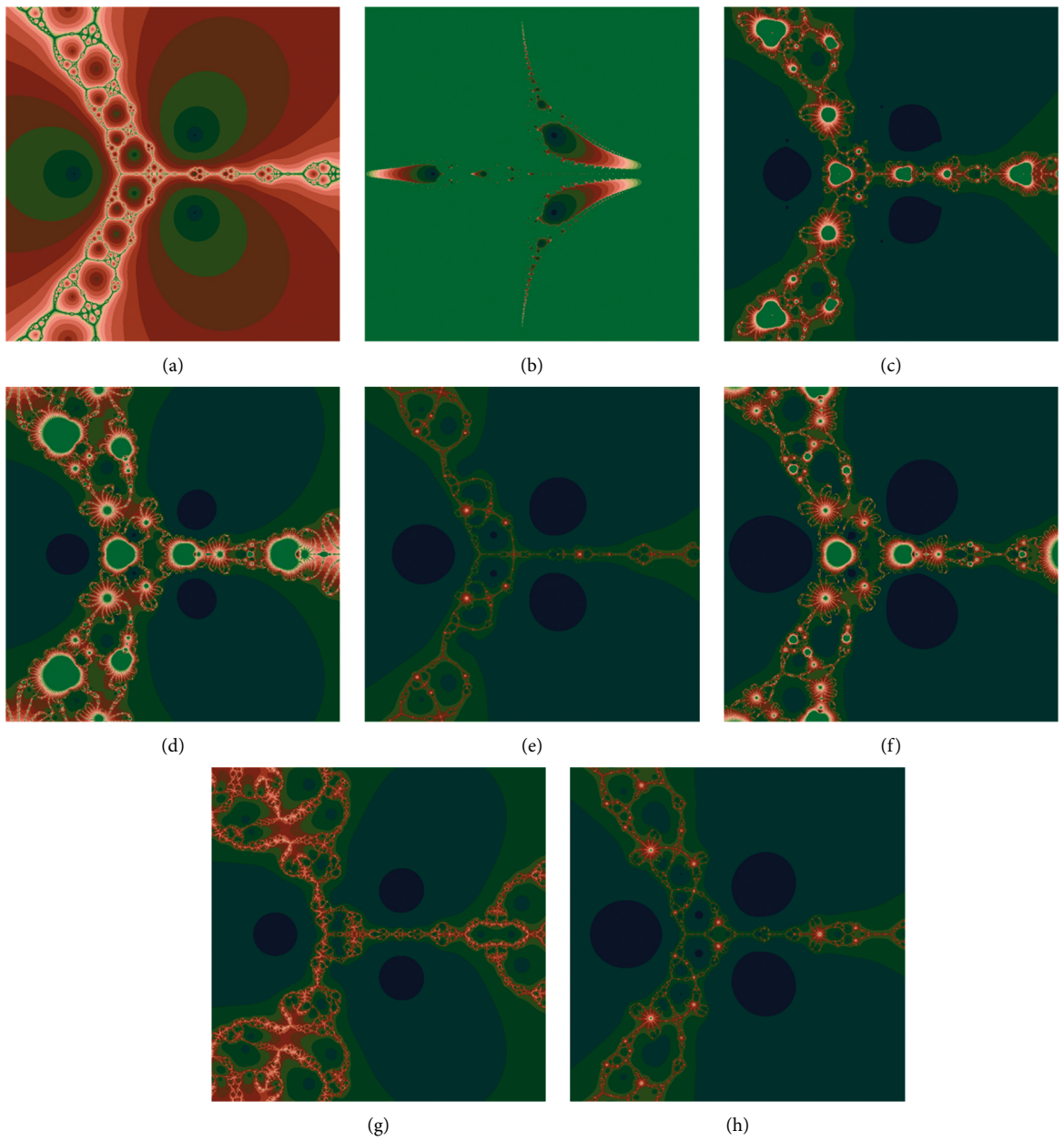

Figure 5: Polynomiographs for $q_2(t)$ using different methods.

Problem 7. Application of mechanical engineering [28]: There are several fields wherein the use of thermodynamics is extensively required. The particular areas include mechanical, civil, mechatronics, electronic, chemical engineering, and many others. The fourth-order polynomial is used to show a relation between the zero-pressure specific heat of dry air c_p (kJ/kgK) to temperature x:

$$f_3(x) = 1.9520 \times 10^{-14}x^4 - 9.5838 \times 10^{-11}x^3 + 9.721510^{-8}x^2 + 1.671 \times 10^{-4}x - 0.99403 - 1.2, \tag{46}$$

where $c_p = 1.2$ is used.

As described in [28], the above nonlinear model given in terms of fourth-order polynomial has two real distinct roots given as: $r_1 = 1126.009751$ and $r_2 = -1289.950382$. It can be observed in Table 3 that each method converges for the initial guesses chosen to determine the approximate solution of the above model. The eleventh-order method N11 performed better from an accuracy viewpoint, followed by the proposed hybrid method. Looking at the CPU values, it is clear that the methods N11 and P12 take the same amount of

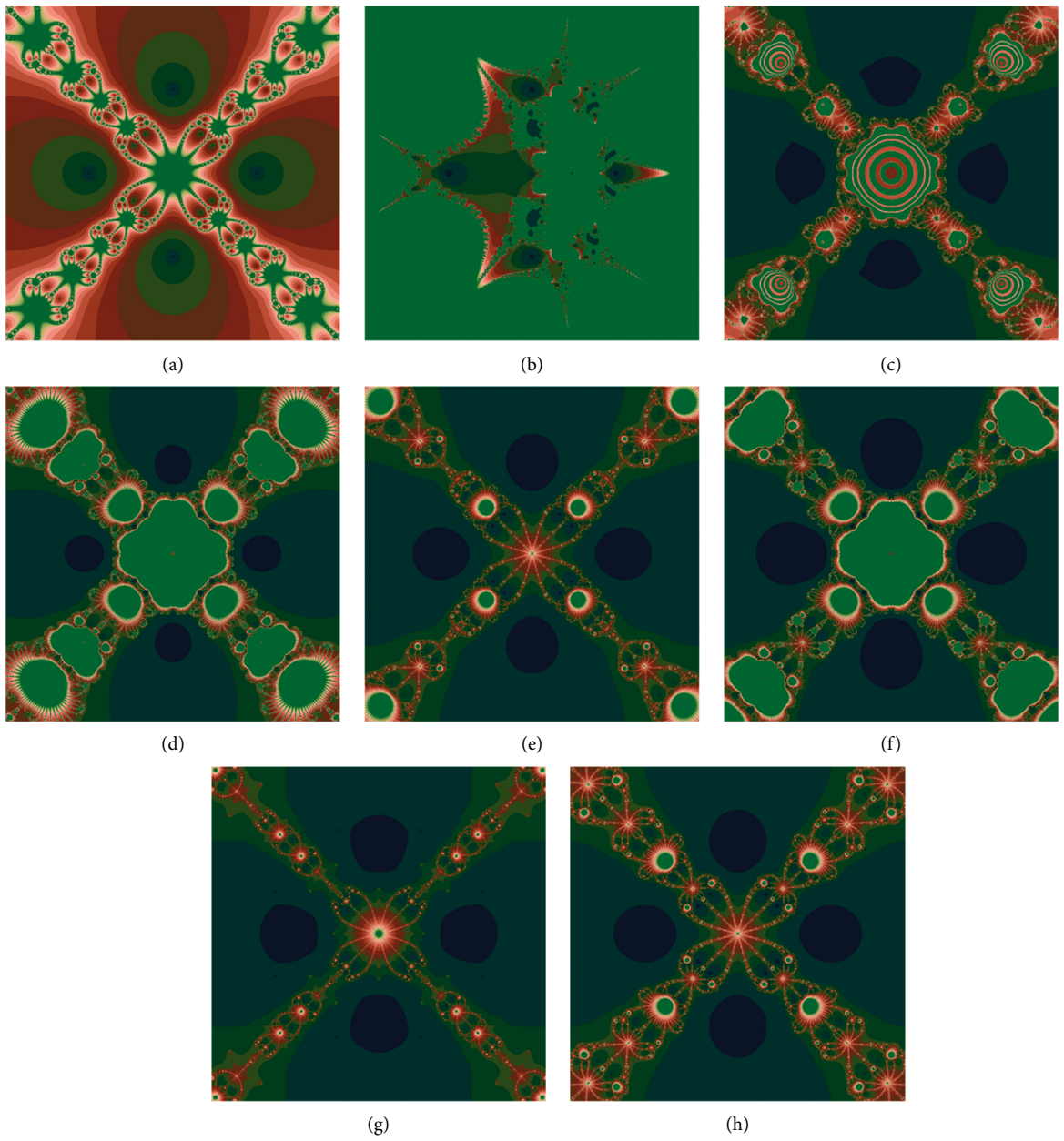

Figure 6: Polynomiograph for $q_3(t)$ using different methods.

time, thereby being equally time-efficient for this particular fourth-order polynomial. Moreover, the absolute functional values are identical for both methods, including others such as N9 and P10.

Problem 8. Neurophysiology Application: As a final experiment, we consider a six-dimensional nonlinear system first proposed in [29] and later was used by several researchers for the simulation purpose of their newly developed algorithms. See, for example, [30], and some cited references therein. The nonlinear model consists of the following six equations:

$$\begin{aligned} x_1^2 + x_3^2 &= 1, \\ x_2^2 + x_4^2 &= 1, \\ x_5 x_3^3 + x_6 x_4^3 &= c_1, \\ x_5 x_1^3 + x_6 x_2^3 &= c_2, \\ x_5 x_1 x_3^2 + x_6 x_4^2 x_2 &= c3, \\ x_5 x_1^2 x_3 + x_6 x_2^2 x_4 &= c_4. \end{aligned} \tag{47}$$

The constants c_i in the above model can be randomly chosen. In our experiment, we co*nsidered* $c_i = 0, i = 1, \ldots, 4$.

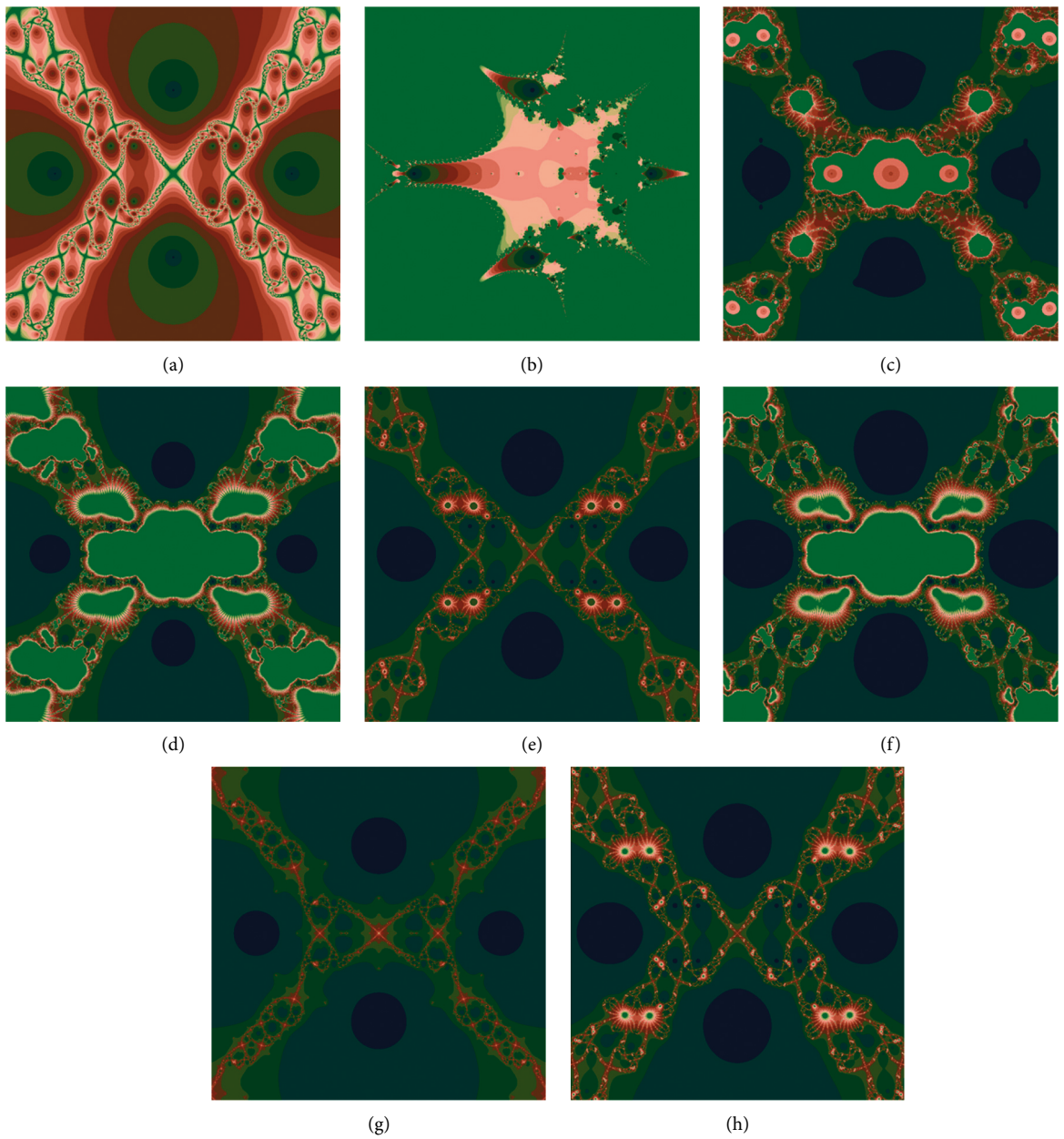

Figure 7: Polynomiograph for $q_4(t)$ using different methods.

Table 1: Comparison of several methods with the same number of iterations ($N = 4$) for the Plank's radiation model given in Problem 5.

Method	$\lvert x_N - x_e \rvert$	$\lvert f_1(x_N) \rvert$ $f_1(x), x_0 = 0.49$	Time	$\lvert x_N - x_e \rvert$	$\lvert f_1(x_N) \rvert$ $f_1(x), x_0 = 0.75$	Time
N2	3.80e-04	7.24e-08	4.70e-02	1.91e-02	1.85e-04	4.70e-02
N4	6.34e-52	1.25e-01	1.25e-01	9.98e-35	6.19e-139	9.40e-02
W8	4.32e-254	1.24e-2030	3.10e-02	2.98e-112	6.44e-896	6.30e-02
N9	1.67e-208	7.90e-1872	1.60e-02	2.82e-35	9.01e-313	4.60e-02
P10	7.38e-458	1.00e-3000	3.20e-02	2.18e-247	2.78e-2469	4.70e-02
N11	divergence	–	–	1.18e-305	1.00e-3000	4.70e-02
N12	5.05e-317	9.90e-2534	7.80e-02	1.12e-210	5.92e-1683	9.40e-02
P12	3.71e-737	0.00e+00	9.30e-02	1.34e-375	2.00e-3000	9.30e-02

Table 2: Comparison of several methods with the same number of iterations ($N = 4$) for the Problem 6.

Method	$\lvert x_N - x_e \rvert$	$\lvert f_2(x_N) \rvert$ $f_2(x), x_0 = 0.5$	Time	$\lvert x_N - x_e \rvert$	$\lvert f_2(x_N) \rvert$ $f_2(x), x_0 = 0.95$	Time
N2	2.75e-07	6.60e-13	1.60e-02	1.51e-06	1.99e-11	1.60e-02
N4	other sol.	–	–	1.29e-02	3.53e-04	9.30e-02
W8	5.37e-333	5.04e-2657	6.20e-02	9.41e-209	4.51e-1663	9.40e-02
N9	1.86e-488	0.00e+00	1.60e-02	7.91e-407	0.00e+00	3.10e-02
P10	3.21e-783	0.00e+00	3.10e-02	4.19e-691	0.00e+00	3.10e-02
N11	failed	–	–	failed	–	–
N12	8.40e-334	2.10e-2663	1.60e-02	2.04e-224	2.51e-1788	4.60e-02
P12	2.18e-1373	0.00e+00	1.50e-02	1.16e-1213	0.00e+00	7.80e-02

Table 3: Comparison of several methods with the same number of iterations ($N = 3$) for the Problem 7.

Method	$\lvert x_N - x_e \rvert$	$\lvert f_3(x_N) \rvert$ $f_3(x), x_0 = 1126.0$	Time	$\lvert x_N - x_e \rvert$	$\lvert f_3(x_N) \rvert$ $f_3(x), x_0 = -1286$	Time
N2	1.83e-18	2.61e-43	3.20e-02	1.84e-07	2.25e-20	3.10e-02
N4	2.44e-47	6.07e-194	7.80e-02	2.10e-07	8.04e-34	1.57e-01
W8	3.41e-331	9.35e-2671	6.30e-02	1.53e-172	7.94e-1402	7.80e-02
N9	2.22e-412	1.00e-3000	3.10e-02	3.22e-188	7.03e-1715	4.60e-02
P10	2.80e-519	1.00e-3000	3.10e-02	2.57e-241	4.58e-2437	3.20e-02
N11	5.53e-1659	1.00e-3000	1.60e-02	2.56e-761	3.00e-3000	4.70e-02
N12	2.42e-331	5.66e-2672	3.10e-02	3.37e-159	1.69e-1293	3.20e-02
P12	1.72e-748	1.00e-3000	1.60e-02	1.06e-345	3.00e-3000	4.70e-02

Table 4: Comparison of several methods with the same number of iterations ($N = 5$) while the initial guess is set to be $F(x_{10}, x_{20}, x_{30}, x_{40}, x_{50}, x_{60}) = (1.8, 2.6, 3.5, 1.3, 1.0, 1.1)$ for the Problem 8.

Method	$\varepsilon = \lvert x_N - x_e \rvert$	Time
N2	8.77e-02	4.70e-02
HM5	8.22e-94	2.34e-01
HM6	1.56e-242	1.57e-01
P10	2.37e-1667	2.03e-01
P12	5.02e-2823	1.57e-01

The simulations for the above neurophysiology application system are shown in Table 4 wherein the two columns represent the absolute error at the last iteration and the CPU time consumption. Two more methods, including fifth-order Halley's (HM5) in [6] and a sixth-order Hameer-Mujtaba method (HM6) in [17], is used for the simulations of the above system. It is evident from Table 4 that the accuracy is much higher for the proposed approach in comparison to other competitive methods, while the CPU time is also reasonable.

6. Concluding Remarks and Future Directions

A new four-step nonlinear method for solving $f(x) = 0$ type models is introduced in this research work with twelfth-order convergence, and seven function evaluations are required per iteration. The theoretical order of convergence for the proposed hybrid method is proved under both scalar and vector cases, along with an asymptotic error constant. Comparison with various existing numerical methods discloses the better performance of the proposed approach when the absolute errors, the absolute functional value computed at the last iteration, and the time of machine in seconds are taken into consideration. The proposed method brings out the slightest absolute error regardless of initial conditions chosen for the simulations of the nonlinear models that belong to real-world scenarios from science and engineering. The rapid convergence of the proposed hybrid method is confirmed with the aid of polynomiography when the method is applied to some complex-valued polynomials.

Declarations

Data Availability

All the data required for this paper is included within the paper.

Ethical Approval

We with this affirm that the contents of this article are original. Furthermore, it has been neither published elsewhere fully or partially in any language nor submitted for publication (fully or partially) elsewhere simultaneously. It contains no matter that is scandalous, obscene, fraud, plagiarism, libelous, or otherwise contrary to law.

Conflicts of Interest

The authors do not have any conflicts of interest.

Authors' Contributions

All authors contributed equally in this paper.

References

[1] H. Ramos and M. T. T. Monteiro, "A new approach based on the Newton's method to solve systems of nonlinear equations," *Journal of Computational and Applied Mathematics*, vol. 318, pp. 3–13, 2017.

[2] H. Ramos and J. Vigo-Aguiar, "The application of Newton's method in vector form for solving nonlinear scalar equations where the classical Newton method fails," *Journal of Computational and Applied Mathematics*, vol. 275, pp. 228–237, 2015.

[3] A. Cordero, H. Ramos, and J. R. Torregrosa, "Some variants of Halley's method with memory and their applications for solving several chemical problems," *Journal of Mathematical Chemistry*, vol. 58, no. 4, pp. 751–774, 2020.

[4] H. Ramos, "March). Some efficient one-point variants of Halley's method, with memory, for solving nonlinear equations," *AIP Conference Proceedings*, vol. 1648, no. 1, Article ID 810004, 2015.

[5] J. M. Ortega, *Numerical Analysis: A Second Course*, Society for Industrial and Applied Mathematics, Philadelphia, PA, USA, 1990.

[6] Y. Ham and C. Chun, "A fifth-order iterative method for solving nonlinear equations," *Applied Mathematics and Computation*, vol. 194, no. 1, pp. 287–290, 2007.

[7] X. Wang and L. Liu, "New eighth-order iterative methods for solving nonlinear equations," *Journal of Computational and Applied Mathematics*, vol. 234, no. 5, pp. 1611–1620, 2010.

[8] Z. Hu, L. Guocai, and L. Tian, "An iterative method with ninth-order convergence for solving nonlinear equations," *International Journal of Contemporary Mathematical Sciences*, vol. 6, no. 1, pp. 17–23, 2011.

[9] A. Tassaddiq, S. Qureshi, A. Soomro, E. Hincal, D. Baleanu, and A. A. Shaikh, "A new three-step root-finding numerical method and its fractal global behavior," *Fractal and Fractional*, vol. 5, no. 4, p. 204, 2021.

[10] M. Raza, "Eleventh-order convergent iterative method for solving nonlinear equations," *International Journal of Applied Mathematics*, vol. 25, no. 3, pp. 365–371, 2012.

[11] N. A. Mir and T. Zaman, "Some quadrature based three-step iterative methods for nonlinear equations," *Applied Mathematics and Computation*, vol. 193, no. 2, pp. 366–373, 2007.

[12] H. F. Ding, Y. X. Zhang, S. F. Wang, and X. Y. Yang, "A note on some quadrature based three-step iterative methods for nonlinear equations," *Applied Mathematics and Computation*, vol. 215, no. 1, pp. 53–57, 2009.

[13] M. A. Noor, K. I. Noor, E. Al-Said, and M. Waseem, "Some New Iterative Methods for Nonlinear Equations," *Mathematical Problems in Engineering*, vol. 2010, Article ID 198943, 12 pages, 2010.

[14] A. R. Alharbi, M. I. Faisal, F. A. Shah, M. Waseem, R. Ullah, and S. Sherbaz, "Higher order numerical approaches for nonlinear equations by decomposition technique," *IEEE Access*, vol. 7, pp. 44329–44337, 2019.

[15] F. Soleimani, F. Soleymani, and S. Shateyi, "Some iterative methods free from derivatives and their basins of attraction for nonlinear equations," *Discrete Dynamics in Nature and Society*, vol. 2013, Article ID 301718, 10 pages, 2013.

[16] T. Zhanlav, O. Chuluunbaatar, and G. Ankhbayar, "On Newton-type methods with fourth and fifth-order convergence," *Discrete and Continuous Models and Applied Computational Science*, vol. 2, no. 2, pp. 30–35, 2010.

[17] H. A. Abro and M. M. Shaikh, "A new time-efficient and convergent nonlinear solver," *Applied Mathematics and Computation*, vol. 355, pp. 516–536, 2019.

[18] B. Kalantari, "Polynomiography: from the fundamental theorem of algebra to art," *Leonardo*, vol. 38, no. 3, pp. 233–238, 2005.

[19] B. Kalantari and E. H. Lee, "Newton-Ellipsoid polynomiography," *Journal of Mathematics and the Arts*, vol. 13, no. 4, pp. 336–352, 2019.

[20] K. Gdawiec, W. Kotarski, and A. Lisowska, "Visual analysis of the Newton's method with fractional order derivatives," *Symmetry*, vol. 11, p. 1143, 2019.

[21] A. Naseem, M. A. Rehman, and T. Abdeljawad, "Some new iterative algorithms for solving one-dimensional non-linear equations and their graphical representation," *IEEE Access*, vol. 9, pp. 8615–8624, 2021.

[22] M. Scott, B. Neta, and C. Chun, "Basin attractors for various methods," *Applied Mathematics and Computation*, vol. 218, no. 6, pp. 2584–2599, 2011.

[23] D. Herceg and D. Herceg, "Eighth order family of iterative methods for nonlinear equations and their basins of attraction," *Journal of Computational and Applied Mathematics*, vol. 343, no. 1, pp. 458–480, 2018.

[24] K. Gdawiec, "Fractal patterns from the dynamics of combined polynomial root-finding methods," *Nonlinear Dynamics*, vol. 90, no. 4, pp. 2457–2479, 2017.

[25] S. Qureshi, H. Ramos, and A. K. Soomro, "A new nonlinear ninth-order root-finding method with error analysis and basins of attraction," *Mathematics*, vol. 9, no. 16, p. 1996, 2021.

[26] G. V. Balaji and J. D. Seader, "Application of interval Newton's method to chemical engineering problems," *Reliable Computing*, vol. 1, no. 3, pp. 215–223, 1995.

[27] M. A. Rehman, A. Naseem, and T. Abdeljawad, "Some novel sixth-order iteration schemes for computing zeros of nonlinear scalar equations and their applications in engineering," *Journal of Function Spaces*, vol. 2021, pp. 1–11, Article ID 5566379, 2021.

[28] M. Shams, N. Rafiq, N. Kausar, S. F. Ahmed, N. A. Mir, and S. Chandra Saha, "Inverse Family of Numerical Methods for Approximating All Simple and Roots with Multiplicity of Nonlinear Polynomial Equations with Engineering Applications," *Mathematical Problems in Engineering*, vol. 2021, Article ID 3124615, 9 pages, 2021.

[29] J. Verschelde, P. Verlinden, and R. Cools, "Homotopies exploiting Newton polytopes for solving sparse polynomial systems," *SIAM Journal on Numerical Analysis*, vol. 31, no. 3, pp. 915–930, 1994.

[30] C. Grosan and A. Abraham, "A new approach for solving nonlinear equations systems," *IEEE Transactions on Systems, Man, and Cybernetics - Part A: Systems and Humans*, vol. 38, no. 3, pp. 698–714, 2008.

Hindawi
Complexity
Volume 2022, Article ID 8406649, 8 pages
https://doi.org/10.1155/2022/8406649

WILEY | Hindawi

Research Article

Cost-Efficient Privacy-Preserving Authentication and Key Management Scheme for Internet of Vehicle Ecosystem

Tahir Ali Shah,[1] Fahad Algarni,[2] Insaf Ullah,[3] Ako Muhammad Abdullah,[4,5] Fazal Noor,[6] and Muhammad Asghar Khan[3]

[1]*School of Computer, Jiangsu University of Science and Technology, Zhenjiang, Jiangsu Province, China*
[2]*College of Computing and Information Technology, The University of Bisha, Bisha, Saudi Arabia*
[3]*Hamdard Institute of Engineering & Technology, Hamdard University, Islamabad 44000, Pakistan*
[4]*University of Sulaimani, College of Basic Education, Computer Science Department, Sulaimaniyah, Kurdistan Region, Iraq*
[5]*Department of Information Technology, University College of Goizha, Sulaimaniyah, Kurdistan Region, Iraq*
[6]*Department of Computer and Information Systems, Islamic University of Madinah, Madinah 400411, Saudi Arabia*

Correspondence should be addressed to Insaf Ullah; insafktk@gmail.com

Received 8 March 2022; Revised 21 April 2022; Accepted 25 April 2022; Published 3 June 2022

Academic Editor: Jawad Ahmad

Internet of vehicles (IoV) is an emerging area of advanced transportation systems, in which the functionality of traditional vehicular ad hoc networks (VANET) combined with the Internet of things (IoT). This technology allows vehicle users and drivers to interact in real time from anywhere and anytime. However, until recently, the major two problems that authentication and key management methods may solve are security and privacy. In this study, we offer a privacy-preserving authentication and key management scheme for the IoV environment that is computationally and communication cost-effective. We conducted a thorough security analysis, demonstrating that the proposed scheme is resistant to a variety of cryptographic attacks. We have included a cost analysis that indicates the proposed scheme is more efficient than IoV's current privacy-preserving authentication and key management schemes.

1. Introduction

Vehicular ad hoc network (VANET) has emerged as one of the most significant research fields in recent years, encompassing things such as vehicles, which include On-Board Units (OBU), Road-Side Units (RSU), and Trusted Authority (TA). An OBU is an electromagnetic device that is usually installed on a vehicle and used to send and receive data to and from the RSU [1]. It is made up of a resource command processor and resources, which store and restore data using a read/write memory [2]. RSUs are permanent communication gateways that feature an antenna, CPU, and read/write memory to enable wireless communication employing IEEE 802.11p radio technology between OBU and servers or the Internet [3]. The TA provides numerous premium Internet services to VANET subscribers through RSU, as well as protecting the entire vehicular network [4]. The Internet of things (IoT) allows smart connected objects to communicate with one another, expanding existing vehicular ad hoc networks (VANETs) into the Internet of vehicles (IoV) as a result of recent advancements in communication network technology [5].

The most essential services in IoV are traffic efficiency and road safety, which share real-time data through the Internet to reduce road accidents [6]. Figure 1 shows the usual flow diagram for IoV, which shows the communication process between entities such as the TA, OBU, and RSU.

Apart from standard IoV communication, the Fifth Generation (5G) cellular network is a viable choice for effectively delivering all of these services. The basic infrastructure for constructing a smart IoV environment will be provided by 5G, which will push vehicle network performance and capabilities needs to an acceptable level [7].

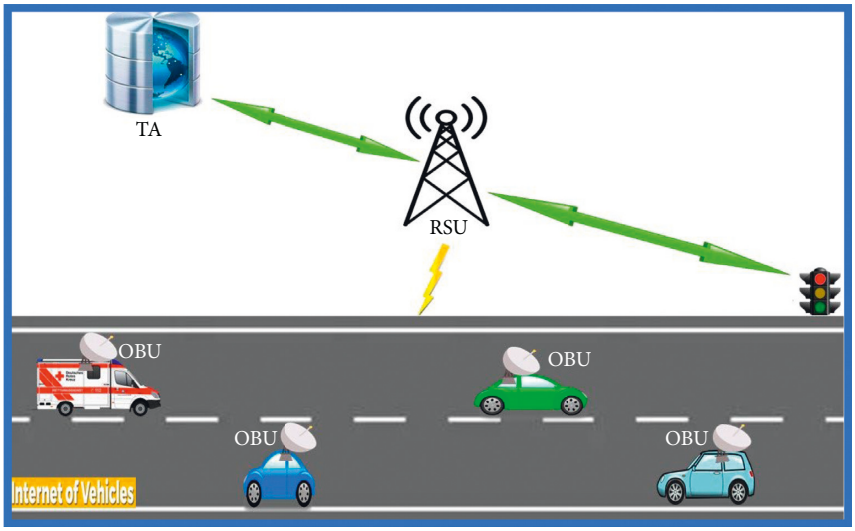

Figure 1: Basic flow of IoV.

Because the IoT is an open network, there are certain serious security risks that must be addressed. Indeed, users are growing increasingly concerned about the impact of modern technology on their privacy. For example, an attacker eavesdropping in on communications may exploit private information to trace down a specific vehicle and its driver's movements [8]. These malicious activities could jeopardize users' privacy as well as lead to robbery and physical injury [9]. Authentication and key agreement will be the most effective techniques for dealing with such attacks. Authentication is the process through which two or more participants in an IoV environment learn about each other before exchanging data [10]. Furthermore, before communicating with one another, the key management system allows all participants (e.g., OBU, RSU, and TA) to validate the messages by matching the generated keys [11].

Batch verifications [12] are a technique that, in addition to the two procedures mentioned above, provides for the authentication of numerous messages at once. The elliptic-curve cryptography (ECC) and Rivest Shamir Adleman (RSA) algorithms, which are well-known public-key methods and provide the same functions, are used in the majority of existing schemes, but the computation cost is still very high because key creation, signing, and decryption are all extremely slow, making them a little more difficult to implement securely.

To address the limitations of existing vehicle communication methods, this study uses hyperelliptic curve cryptography (HECC) to show a 5G vehicular network that is both safe and efficient while also lowering computational costs. As a result of the preceding debate, we have made the following contributions to this work:

(1) We propose an authentication and key management scheme with the help of HECC

(2) We conducted a thorough security study, which revealed that the proposed scheme is resistant to a variety of cyber-attacks

(3) We performed a computational cost study, comparing our proposed scheme to previously published approaches, and the findings demonstrate that the proposed scheme is more efficient.

1.1. Preliminaries. This section gives a short overview of the hyperelliptic curve idea and formal definition.

1.1.1. Hyperelliptic-Curve Cryptography. Hyperelliptic-curve cryptography was first developed by Miller and Koblitz, in 1988, which is the extent of an elliptic curve that depends on discrete logarithm problem in the Jacobian with genus two. Equation (1) represents the popular form of hyperelliptic curve of genus two on Jacobian group with finite field $\mathfrak{F}_q$:

$$B\colon a^2 + h(b)a = k(b)\mathrm{mod}q, \tag{1}$$

where $h(b) \in \mathfrak{F}[b]$ is a polynomial and degree $h(b) \le g$ and $k(b) \in \mathfrak{F}[b]$ is a monic polynomial and degree of $k(b) \le 2g + 1$.

1.1.2. Divisor. The finite formal sum of points on hyperelliptic curve is called divisor and represented in MumFord form as

$$R = (m(b), n(b)) = \left(\sum_{i=0}^{g} m_i b^i, \sum_{i=0}^{g-1} n_i b^i\right). \tag{2}$$

1.1.3. Jacobian Group. The divisors form an Abelian group which is called Jacobian group $J_c(\mathfrak{F}_q)$ and the order of the Jacobian group $o(J_c(\mathfrak{F}_q))$ is defined as

$$\left|(\sqrt{q} - 1)^{2g}\right| \le o\left(J_c\left(\mathfrak{F}_q\right)\right) \le \left|(\sqrt{q} + 1)^{2g}\right|. \tag{3}$$

1.1.4. Hyperelliptic-Curve Discrete Logarithm Problem (HECDLP). Let $Đ$ be divisor of order n in the Jacobian group $J_c(\mathfrak{F}_q)$; find an integer $b \in \mathfrak{F}_q$, such that

$$Đ_1 = b.Đ. \tag{4}$$

2. Related Work

Any entity in the IoV that receives relevant traffic messages must go through an authentication process to guarantee that the message's source is trustworthy and that the content is complete and legitimate. Many researchers have made contributions to the field of IoV network authentication methods in this regard. To assure vehicle legitimacy, Lu et al. [13] proposed a cost-effective conditional privacy-preserving (ECPP) authentication mechanism based on certificates. A vehicle can connect to other cars in the transmission range using its certificate in this scheme; however, if the certificate's time slot expires, the vehicle must visit an RSU to produce a new certificate. Zhang et al. [14] developed an identity-based batch verification (IBV) system, in which each vehicle stores crucial parameters and generates pseudonyms, allowing numerous messages to be evaluated at the same time using bilinear pairing characteristics.

Jiang et al. [15] used similar strategies to create an effective unidentified batch authentication methodology (ABAH) for effectively authenticating a large number of communications. Wang et al. [16] proposed a two-factor lightweight privacy-preserving authentication system (2FLIP), in which each On-Board Unit (OBU) is equipped with a perfect tamper-proof device (TPD) that stores a system key and generates a message authentication code (MAC) using the system key while signing a message. Each TPD's retention of the system key might result in a single point of failure. In DAPPA, each authorized vehicle gets two-member secrets from RSUs, and Zhang et al. [17] introduced a distributed aggregate privacy-preserving authentication approach (DAPPA) that can conduct batch verification without needing the use of an optimum TPD. Although their multiplications are the identical, these two-member secrets differ based on the vehicle. The discovered member secrets and the one-time identity-based aggregate signature may then be used by cars to do batch verification. However, because this DAPPA system includes several pairing operations, there is a significant verification delay when a large number of messages need to be validated.

Based on a registration list, Zhong et al. [18] developed a privacy-preserving conditional authentication approach (CPPARL). The proposed CPPARL allows RSU to collect and validate all messages sent by cars within its transmission range, after which it encrypts and sends out two bloom filters, one positive and one negative, using its secret key.

To mitigate failure of service (DoS) attacks, Liu et al. [19] proposed a puzzle-based pseudonymous authentication mechanism for a 5G vehicular network. In this scheme, each vehicle must solve a hash problem before transmitting a message. However, because messages are not sent at the proper moment, this approach has a significant communication cost. To achieve efficient message authentication, Huang et al. [3] suggested a safe and efficient privacy-preserving authentication strategy for automotive networks, which uses a registration list and elliptic-curve public-key cryptography. This solution, however, does not define the service profile identifier (SPID) validation time or the hash list update rate in order to enhance network performance.

Raja et al. [20] developed an RSU-based group authentication (RGA) system in which each vehicle in its range is assigned a group ID and group key pair, ensuring more secure communication while reducing network overhead. However, their technique has a high total computing cost. Hashem Eiza et al. [21] established secure video reporting services for 5G car networks, in which vehicles may quickly report a road accident by simply sending recorded video footage, while the reporter's identity and video data are kept private. However, because this technology is built for video transmission services, it is incompatible with other safety-related apps. Bouchelaghem and Omar [22] proposed a privacy-preserving pseudonym shifting technique for VANET; as a result, this scheme has certain security difficulties for OBU and traffic monitoring cameras-based tracking. Yao et al. [23] developed an enhanced mutual authentication strategy for VANETs that uses the ECC to provide forward secrecy; however, their proposed system has a significant computational cost and communication overhead owing to the usage of the elliptic curve.

3. Network Model

Figure 2 depicts our proposed IoV network system architecture, which includes three communication system partners: OBU, Trusted Authority (TA), and RSU, in that order. We used the substeps below to explain the function of each entity.

(1) OBU: it encrypts his identity and uses TA's public key to do a hash function. The hash values and the encrypted identifying text are subsequently transferred to TA. TA decrypts the encrypted text and applies the hash function to the decrypted text after receiving the encrypted text and hash value. It also analyses both hash values and, if they match, generates the public and private key for OBU and sends it via a secure channel. It produces the digital signature, secret key, and ciphertext of its identification and sends the authentication message to RSU after receiving the public and private key.

(2) TA: upon reception of encrypted text and hash value from OBU or RSU, TA first decrypts the encrypted text before applying the hash function to it. Furthermore, it compares both hash values and, if they match, generates the public and private key for OBU or RSU and delivered it via a secure route.

(3) RSU: it performs two execution processes on its identification, one of which is encryption using TA's public key and the other of which is a hash function. Then, it sends the encrypted text of identity along

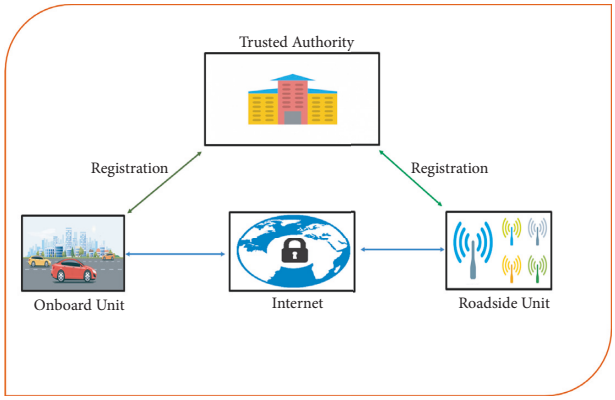

Figure 2: Network model for our proposed scheme.

with the hash values to TA. Upon reception of encrypted text and hash value, TA first decrypts the encrypted text and performs the hash function on the decrypted text. Furthermore, it compares both the hash values and, if it is matched, then produces the public and private key for OBU and dispatched it through a secure channel. When it is received, the public key and private key, further, received the authentication message from OBU, it performs the decryption process for cipher text and verification process for signature; if both the processes are performed successfully, then it set the secret key for further communications.

4. Proposed Mutual Authentication Scheme for IoV

Table 1 includes the symbols used in this scheme and the inclusive stages of our mutual authentication scheme for IoV explained as follows:

(i) Setup: here, the trusted authority (TA) computes $\chi = Đ.\mathscr{D}$ and sets χ as his public key and $Đ$ as his master private key, where $Đ$ has been choose randomly. Furthermore, it makes and publishes $\mathscr{F} = \{\chi, \text{HEC}, \mathscr{D}, F^Q, H\}$ as a global parameter set, where χ denotes the master public key of TA, HEC denotes a genus 2 hyperelliptic curve, $\mathscr{D}$ denotes a 80 bits devisor, F^Q denotes an order Q finite field and its value will be equal to 80 bits, and H represents a collision resistant and irreversible hash function.

(ii) Registrations: each Actor (A_i) with ID_{Ai} computes $\text{CID}_{Ai} = E_\chi(\text{ID}_{Ai})$ and $\text{HID}_{Ai} = H(\text{ID}_{Ai})$, where χ is the public key of TA and E_χ represent the encryption function that encrypts the value through the public key of TA. Then, A_i send $(\text{CID}_{Ai}, \text{HID}_{Ai})$ to TA. So, upon reception of $(\text{CID}_{Ai}, \text{HID}_{Ai})$, CA can compute $\text{ID}_{Ai} = D_Đ(\text{CID}_{Ai})$ and $\text{HID}_{Ai}/ = H(\text{ID}_{Ai})$, where $Đ$ is the private key of CA and $D_Đ$ represent the decryption function that decrypts the value through the private key of TA. Furthermore, CA compare $\text{HID}_{Ai}/ = \text{HID}_{Ai}$; if it is equal, then it computes $\ell_{Ai} = \beta_{Ai}.\mathscr{D}$, $\Omega_{Ai} = H(\text{ID}_{Ai}, \ell_{Ai})$, and $\varphi_{Ai} = \beta_{Ai} + \Omega_{Ai}.Đ$, where β_{Ai} denotes a random private number that is only know to CA, φ_{Ai} denotes the private key of A_i, and ℓ_{Ai} represents the public key of A_i. At the end, TA can delivers $(\varphi_{Ai}, \ell_{Ai})$ to A_i utilizing secure network.

(iii) Mutual authentication and secrete management: a sender Actor (A_s) with ID_{AS} computes $\mathfrak{S}_{A1_s} = \alpha_{A1_s}.\mathscr{D}$, $\mathfrak{S}_{A2_s} = \alpha_{A2_s}.\mathscr{D}$, $K = \alpha_{A1_s}(\ell_{Ar} + \Omega_{As}\chi)$, and $\text{SKC}_{As} = E_K(\text{ID}_{\text{AS}}, \text{ID}_{\text{AR}})$, where α_{A1_s} and α_{A2_s} represent the two private numbers which are randomly selected by A_s, ℓ_{Ar} denote the public key of receiver actor (A_r), φ_{As} denotes the private key of A_s, and E_K denotes the encryption function that encrypts the identity of A_s and A_r that are $(\text{ID}_{\text{AS}}, \text{ID}_{\text{AR}})$ through the secret key which is generated by A_s. Furthermore, A_s can compute $\xi_{As} = H(\text{ID}_{\text{AS}}, \text{ID}_{\text{AR}})$ and $S_{As} = \alpha_{A2_s} + \xi_{As}.\varphi_{As}$ and send $(\xi_{As}, S_{As}, \mathfrak{S}_{A1_s}, \mathfrak{S}_{A2_s}, \text{SKC}_{As})$ to A_r.

When A_r received $(\xi_{As}, S_{As}, \mathfrak{S}_{A1_s}, \mathfrak{S}_{A2_s}, \text{SKC}_{As})$, it can compute $K = \varphi_{As}.\mathfrak{S}_{A1_s}$, $\text{ID}_{\text{AS}}, \text{ID}_{\text{AR}} = D_K(\text{SKC}_{As})$, and $\xi_{As}/ = H(\text{ID}_{\text{AS}}, \text{ID}_{\text{AR}})$; it compares $\xi_{As}/ = \xi_{As}$; if it is equal, then the identities are not modified, and it is going for signature authentication as $S_{As}.\mathscr{D} = \mathfrak{S}_{A2_s} + \xi_{As}(\beta_{As} + \Omega_{As}.Đ)$ (Table 1).

4.1. Message Signing. A sender Actor (A_s), with ID_{AS}, can compute $\xi_{As} = H(\text{ID}_{\text{AS}}, \text{ID}_{\text{AR}})$ and $S_{As} = \alpha_{A2_s} + \xi_{As}.\varphi_{As}$; α_{A2_s} represents randomly selected by A_s and sends $(S_{As}, \mathfrak{S}_{A2_s})$ to A_r.

4.2. Message Verifications. When A_r received $(S_{As}, \mathfrak{S}_{A2_s})$, it can compute for signature authentication as $S_{As}.\mathscr{D} = \mathfrak{S}_{A2_s} + \xi_{As}(\beta_{As} + \Omega_{As}.Đ)$.

4.3. Correctness. Here, A_r can verify the received set $(\xi_{As}, S_{As}, \mathfrak{S}_{A1_s}, \mathfrak{S}_{A2_s}, \text{SKC}_{As})$ as follows:

$S_{As}.\mathscr{D} = \mathfrak{S}_{A2_s} + \xi_{As}(\ell_{Ai} + \Omega_{Ai}.\chi) = (\alpha_{A2_s} + \xi_{As}.\varphi_{As})\mathscr{D} = (\alpha_{A2_s}\mathscr{D} + \xi_{As}.\varphi_{As}\mathscr{D}) = \mathfrak{S}_{A2_s} + \xi_{As}.(\beta_{As} + \Omega_{As}.Đ)(\mathscr{D} = \mathfrak{S}_{A2_s} + \xi_{As}.(\beta_{As}\mathscr{D} + \Omega_{As}.Đ.\mathscr{D}) = \mathfrak{S}_{A2_s} + \xi_{As}.(\ell_{As} + \Omega_{As}.\chi)$. Hence, it is proved.

Also, it can generate a secret key as $K = \varphi_{As}.\mathfrak{S}_{A1_s} = K = \alpha_{A1_s}(\ell_{As} + \Omega_{As}\chi) = \alpha_{A1_s}(\beta_{As}.\mathscr{D} + \Omega_{As}Đ.\mathscr{D}) = \alpha_{A1_s}.\ \mathscr{D}(\beta_{As} + \Omega_{As}Đ) = \mathfrak{S}_{A1_s}\varphi_{As}$; hence, it is proved.

5. Security Analysis

Before we can describe the security aspects of our proposed scheme, we must first discuss some of the characteristics of an attacker who would represent a threat to it. We will explore the Dolev–Yao model, in which the attacker can conduct a variety of actions. It includes the properties such as mutual authentication, anonymity, confidentiality of identities, unforgeability of signature, forward secrecy, secrete key leakage, and identity authentication. We explain the above properties one by one using the following steps.

Table 1: Symbols used in the proposed algorithm.

Symbol	Used for
χ	Master public key of TA
$Đ$	Master private key of TA
$\mathcal{F}$	Global parameter set
HEC	A genus 2 hyperelliptic curve
A_i	Each actor
E_χ	Represent the encryption function that encrypt the value through the public key of TA
φ_{Ai}	Denotes the private key of A_i
A_s	Sender actor
α_{A1_s}, α_{A2_s}	Represents the two private number which is randomly selected by A_s
ℓ_{Ar}	Denotes the public key of receiver actor (A_r)
E_K	Denotes the encryption function that encrypt the identity of A_s and A_r that are ($\mathrm{ID_{AS}}, \mathrm{ID_{AR}}$) through the secret key which is generated by A_s
TA	Trusted authority
$\mathcal{D}$	A hyperelliptic-curve devisor
H	Collision resistant and one way hash function
F^Q	Denotes an order Q finite field and its value will be equal to 80 bits
ID_{Ai}	Identity of each actor
β_{Ai}	Denotes a random private number that is only know to TA
ℓ_{Ai}	Represents the public key of A_i
$\mathrm{ID_{AS}}$	Identity of sender actor
$\mathrm{ID_{AR}}$	Identity of receiver actor
φ_{As}	Denotes the private key of A_s
K	Common secret key

Table 2: The comparison of computation costs in terms of major operations between schemes in IoV.

Schemes	Message signing	Single message verification	Total
Ali and Li	3 Tmp-ECC + 2Th	Tp + Tmp-ECC + Th	Tp + 4Tmp-ECC + 3Th
Zhong et al.	3 Tmp-ECC + Tmtp + Th	3Tp + Tmtp + 2Tmp-ECC + Tmp-p + Th	3Tp + 2Tmtp + 5Tmp-ECC + Tmp-p + 2Th
Cui et al.	2 Tmp-ECC + 2 Th	Th	2 Tmp-ECC + 3 Th
M.Yao et al.	Tmp-ECC + Th	3Tmp-ECC + 2 Th	4Tmp-ECC + 3 Th
Our scheme	1 Tmp-HECC + Th	3 Tmp-HECC + Th	4Tmp-HECC+ 2Th

5.1. Mutual Authentication. In the proposed scheme, A_s generates a signature as $S_{As} = \alpha_{A2_s} + \xi_{As}.\varphi_{As}$ and sends this signature to A_r through unsecure network. When A_r received S_{As}, for verification, it can check the equality of the following equation $S_{As}.\mathcal{D} = \mathfrak{S}_{A2_s} + \xi_{As}(\beta_{As} + \Omega_{As}.Đ)$; if it is satisfied, then we can say that this scheme provide mutual authentication property. If we look into the correctness analysis section of this study, then we can see the equality of the above equation is hold.

5.2. Anonymity. If we look into the communicated parameter of our proposed scheme ($\xi_{As}, S_{As}, \mathfrak{S}_{A1_s}, \mathfrak{S}_{A2_s}, \mathrm{SKC}_{As}$), where $\xi_{As} = H(\mathrm{ID_{AS}}, \mathrm{ID_{AR}})$ is the hash value with the property of irreversibility, $S_{As} = \alpha_{A2_s} + \xi_{As}.\varphi_{As}$ is the hyperelliptic-curve point which does not contain any identity, $\mathfrak{S}_{A1_s}$ and $\mathfrak{S}_{A2_s}$ are also hyperelliptic-curve point, and $\mathrm{SKC}_{As} = E_K(\mathrm{ID_{AS}}, \mathrm{ID_{AR}})$ in which both the identity of A_s and A_r are protected through encryption function E_K with secret key K that is only known to A_s and A_r. The above discussion confirmed the existence of anonymity property in the proposed scheme.

5.3. Confidentiality of Identities. In the proposed scheme, A_s generate the ciphertext of both the identities is $\mathrm{SKC}_{As} = E_K(\mathrm{ID_{AS}}, \mathrm{ID_{AR}})$ and send it to through unsecure network, where secret key as $K = \alpha_{A1_s}(\ell_{Ar} + \Omega_{As}\chi)$, so if the attacker tries to decrypt the ciphertext, it is obligatory for him/her to make secret key first. However, we need α_{A1_s} from $\mathfrak{S}_{A1_s} = \alpha_{A1_s}.\mathcal{D}$ is equal to find the solution of hyperelliptic-curve discrete logarithm problem that can be infeasible for the attacker.

5.4. Unforgeability of Signature. In the proposed scheme, A_s generate a signature as $S_{As} = \alpha_{A2_s} + \xi_{As}.\varphi_{As}$ and send this signature to A_r through unsecure network. If the attacker tries to make a forge signature, then it will be completely failed because α_{A2_s} and φ_{As} are the two unknown value so that finding two unknown variables from the same equation is infeasible.

5.5. Forward Secrecy. In the proposed scheme, the secret key is renewed for every session so that if the attacker gets access to the previously communicated messages secret key, then it will not be able to extract the content of a currently dispatched message.

5.6. Secrete Key Leakage. When the attacker wants to generate the secret key as $K = \varphi_{As}.\mathfrak{S}_{A1_s}$, then it needs φ_{As} from $\varphi_{Ai} = \beta_{Ai} + \Omega_{Ai}.Đ$ so that it will be completely failed because

Table 3: The comparison of computation costs in terms of milliseconds between schemes in IoV.

Schemes	Message signing	Signature verification	Total
Ali and Li	$3^*12.4 + 2^*0.7 = 38.6$	$22.4 + 12.4 + 0.7 = 35.5$	$22.4 + 4^*12.4 + 3^*0.7 = 74.1$
Zhong et al.	$3^*12.4 + 30.6 + 0.7 = 68.5$	$3^*22.4 + 30.6 + 2^*12.4 + 3.1 + 0.7 = 126.4$	$3^*22.4 + 2^*30.6 + 5 * 12.4 + 3.1 + 2^*0.7 = 194.9$
Cui et al.	$2^*12.4 + 2^*0.7 = 26.2$	0.7	$2^*12.4 + 3^*0.7 = 26.9$
M.Yao et al.	$12.4 + 0.7 = 13.1$	$3^*12.4 + 2^*0.7 = 38.6$	$4^*12.4 + 3^*0.7 = 51.7$
Our scheme	$1^*6.2 + 0.7 = 6.9$	$3^*6.2 + 0.7 = 19.3$	$4^*6.2 + 2^*0.7 = 26.2$

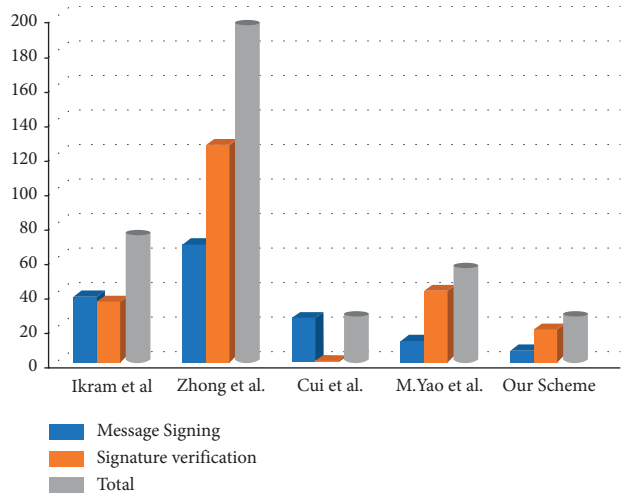

Figure 3: Computational cost comparison in milliseconds.

Table 4: Communicational cost comparisons with the help of major operations.

Schemes	Communication cost	Communication cost with bits
Ali and Li	$\|M\| + 2\|G\| + \|T\|$	$1200 + 2^*1024 + 34 = 3282$ bits
Zhong et al.	$\|M\| + 4\|G\| + \|T\|$	$1200 + 4^*1024 + 34 = 5330$ bits
Cui et al.	$\|M\| + 4\|q\|$	$1200 + 4^*160 = 1840$ bits
M.Yao et al.	$\|M\| + 4\|G\| + \|T\|$	$1200 + 4^*1024 + 34 = 5330$ bits
Our scheme	$\|M\| + 3\|n\|$	$1200 + 3^*80 = 1440$ bits

Note. We suppose $|M| = 1200$ bits, $|T| = 34$ bits, $|G| = 1024$ bits, $|q| = 160$ bits, and $|n| = 80$ bits.

β_{Ai} and $Đ$ are the two unknown values so that finding two unknown variables from the same equation is infeasible.

5.7. Identity Authentication. In the proposed scheme, A_s can encrypt $\mathrm{SKC}_{As} = E_K(\mathrm{ID}_{\mathrm{AS}}, \mathrm{ID}_{\mathrm{AR}})$ and generate a hash value as $\xi_{As} = H(\mathrm{ID}_{\mathrm{AS}}, \mathrm{ID}_{\mathrm{AR}})$; then, send SKC_{As} and ξ_{As} to A_r. When A_r received $(\xi_{As}, \mathrm{SKC}_{As})$, it can compute $\xi_{As}/ = H(\mathrm{ID}_{\mathrm{AS}}, \mathrm{ID}_{\mathrm{AR}})$ and then compare $\xi_{As}/ = \xi_{As}$; if it is equal, then the identities are not modified. So, in our scheme, we provide the identity authentication in this way.

6. Computational Cost Comparison

The computational cost is the key component in measuring the cryptographic scheme's performance. Here, we start by defining the notation for the time overhead of some cryptographic operations in the proposed scheme and other schemes that are Ali et al. [24], Zhong et al. [25], Cui et al. [26], and Yao et al. [23]. For this purpose, we then explain that Tℏ, T𝔭, T𝔐𝔭-𝔭, T𝔐𝔭-ECC, and T𝔐𝔱𝔭 can denote consuming time for a hash function, pairing operation, multiplication over pairing, multiplication over an elliptic curve, and map-to-point operation, respectively. Furthermore, according to [27–29], Tℏ, T𝔭, T𝔐𝔭-𝔭, T𝔐𝔭-ECC, and T𝔐𝔱𝔭 consume 0.7, 22.4, 3.1, 12.4, and 30.6, respectively. So, Tables 2 and 3 and Figure 3 are witnessed that the proposed scheme required fewer computational costs in the comparisons of Ali et al. [24], Zhong et al. [25], Cui et al. [26], and Yao et al. [23].

7. Communication Overhead

This section compares the proposed scheme's communication overhead efficiencies to those of Ali et al. [24], Zhong et al. [25], Cui et al. [26], and Yao et al. [23]. This comparison is based on extra parameters sent with the message, which are $|T|$, $|G|$, $|q|$, and $|n|$, which represent the current timestamp size, bilinear pairing parameter size, elliptic-curve point size, and hyperelliptic-curve divisor size, respectively.

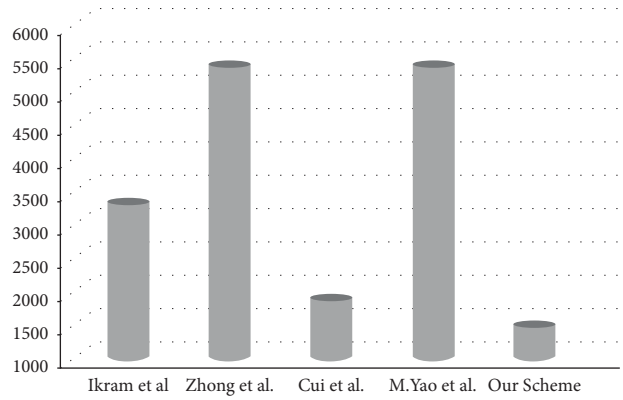

Figure 4: Communication cost comparison in bits.

We assume $|M| = 1200$ bits, $|T| = 34$ bits, $|G| = 1024$ bits, $|q| = 160$ bits, and $|n| = 80$ bits, and we have performed a comparative analysis in Table 4 using these assumed values, which include the extra parameters along with the message in design and Ali et al. [24], Zhong et al. [25], Cui et al. [26], and Yao et al. [23] schemes. We can conclude from Table 3 and Figure 4 that our proposed strategy clearly outperforms the other four designs in both characteristics.

8. Conclusion

This study proposed a low-cost, privacy-preserving authentication and key management strategy for the IoV ecosystem. The proposed solution makes use of the HECC mathematical concept. In terms of computation and communication costs, the proposed scheme is more cost-effective than existing privacy-preserving authentication solutions. Mutual authentication, anonymity, identity confidentiality, signature unforgeability, forward secrecy, secret key leakage, and identity authentication are among the security properties offered by the proposed approach. As a consequence, because the HECC has fewer parameters and delivers the same level of security as the elliptic curve and RSA, the proposed scheme may be a better alternative for IoV system.

Data Availability

All the data are used to support the findings of the study are included within the article.

Conflicts of Interest

The authors declare that they have no conflicts of interest regarding the present study.

References

[1] M. Umar, S. H. Islam, K. Mahmood, S. Ahmed, Z. Ghaffar, and M. A. Saleem, "Provable secure identity-based anonymous and privacy-preserving inter-vehicular authentication protocol for VANETS using PUF," *IEEE Transactions on Vehicular Technology*, vol. 70, no. 11, pp. 12158–12167, 2021.

[2] S. H. Islam, M. S. Obaidat, P. Vijayakumar, E. Abdulhay, F. Li, and M. K. C. Reddy, "A robust and efficient password-based conditional privacy preserving authentication and group-key agreement protocol for VANETs," *Future Generation Computer Systems*, vol. 84, pp. 216–227, 2018.

[3] Q. Mei, H. Xiong, J. Chen, M. Yang, S. Kumari, and M. K. Khan, "Efficient certificateless aggregate signature with conditional privacy preservation in IoV," *IEEE Systems Journal*, vol. 15, no. 1, pp. 245–256, 2021.

[4] M. Nikooghadam, H. Amintoosi, S. H. Islam, and M. F. Moghadam, "A provably secure and lightweight authentication scheme for Internet of Drones for smart city surveillance," *Journal of Systems Architecture*, vol. 115, Article ID 101955, 2021.

[5] I. Ullah, M. A. Khan, F. Khan et al., "An efficient and secure multi-message and multi-receiver signcryption scheme for edge enabled Internet of vehicles," *IEEE Internet of Things Journal*, vol. 9, pp. 2688–2697, 2021.

[6] M. N. Majeed, S. P. Chattha, A. Akram, and M. Zafrullah, "Vehicular ad hoc networks: history and future development arenas," *Int. J. Inf. Techno. Elect. Eng.*vol. 2, no. 2, pp. 25–29, 2013.

[7] D. Kombate, "December the Internet of vehicles based on 5G communications," in *Proceedings of the 2016 IEEE International Conference on Internet of Things (iThings) and IEEE Green Computing and Communications (GreenCom) and IEEE Cyber Physical and Social Computing (CPSCom) and IEEE Smart Data (SmartData)*, pp. 445–448, IEEE, Chengdu, China, December 2016.

[8] M. A. Ferrag, L. Maglaras, A. Argyriou, D. Kosmanos, and H. Janicke, "Security for 4G and 5G cellular networks: a survey of existing authentication and privacy-preserving schemes," *Journal of Network and Computer Applications*, vol. 101, pp. 55–82, 2018.

[9] N. Sharma, N. Chauhan, and N. Chand, "Security challenges in internet of vehicles (IoV) environment," in *Proceedings of the 2018 First International Conference on Secure Cyber Computing and Communication (ICSCCC)*, pp. 203–207, IEEE, Jalandhar, India, December 2018.

[10] Y. Liu, Y. Wang, and G. Chang, "Efficient privacy-preserving dual authentication and key agreement scheme for secure V2V communications in an IoV paradigm," *IEEE Transactions on Intelligent Transportation Systems*, vol. 18, no. 10, pp. 2740–2749, 2017.

[11] P. Bagga, A. K. Das, M. Wazid, J. J. P. C. Rodrigues, K. K. R. Choo, and Y. Park, "On the design of mutual authentication and key agreement protocol in internet of vehicles-enabled intelligent transportation system," *IEEE Transactions on Vehicular Technology*, vol. 70, no. 2, pp. 1736–1751, 2021.

[12] M. Zhang, J. Zhou, G. Zhang, M. Zou, and M. Chen, "EC-BAAS: elliptic curve-based batch anonymous authentication scheme for Internet of Vehicles," *Journal of Systems Architecture*, vol. 117, Article ID 102161, 2021.

[13] R. Lu, X. Lin, H. Zhu, P. H. Ho, and X. Shen, "ECPP: efficient conditional privacy preservation protocol for secure vehicular communications," in *Proceedings of the IEEE INFOCOM 2008-The 27th Conference on Computer Communications*, pp. 1229–1237, IEEE, Phoenix, AZ, USA, April 2008.

[14] C. Zhang, R. Lu, X. Lin, P. H. Ho, and X. Shen, "An efficient identity-based batch verification scheme for vehicular sensor networks," in *Proceedings of the IEEE INFOCOM 2008-The 27th Conference on Computer Communications*, pp. 246–250, IEEE, Phoenix, AZ, USA, April 2008.

[15] S. Jiang, X. Zhu, and L. Wang, "An efficient anonymous batch authentication scheme based on HMAC for VANETs," *IEEE*

Transactions on Intelligent Transportation Systems, vol. 17, no. 8, pp. 2193–2204, 2016.

[16] F. Wang, Y. Xu, H. Zhang, Y. Zhang, and L. Zhu, "2FLIP: a two-factor lightweight privacy-preserving authentication scheme for VANET," *IEEE Transactions on Vehicular Technology*, vol. 65, no. 2, pp. 896–911, 2016.

[17] L. Zhang, Q. Wu, J. Domingo-Ferrer, B. Qin, and C. Hu, "Distributed aggregate privacy-preserving authentication in VANETs," *IEEE Transactions on Intelligent Transportation Systems*, vol. 18, no. 3, pp. 516–526, 2017.

[18] H. Zhong, B. Huang, J. Cui, Y. Xu, and L. Liu, "Conditional privacy-preserving authentication using registration list in vehicular ad hoc networks," *IEEE Access*, vol. 6, pp. 2241–2250, 2018.

[19] P. Liu, B. Liu, Y. Sun, B. Zhao, and I. You, "Mitigating DoS attacks against pseudonymous authentication through puzzle-based co-authentication in 5G-VANET," *IEEE Access*, vol. 6, Article ID 20806, 2018.

[20] G. Raja, S. Anbalagan, G. Vijayaraghavan, P. Dhanasekaran, Y. D. Al-Otaibi, and A. K. Bashir, "Energy-efficient end-to-end security for software-defined vehicular networks," *IEEE Transactions on Industrial Informatics*, vol. 17, no. 8, pp. 5730–5737, 2021.

[21] M. Hashem Eiza, Q. Ni, and Q. Shi, "Secure and privacy-aware cloud-assisted video reporting service in 5G-enabled vehicular networks," *IEEE Transactions on Vehicular Technology*, vol. 65, no. 10, pp. 7868–7881, 2016.

[22] S. Bouchelaghem and M. Omar, "Secure and efficient pseudonymization for privacy-preserving vehicular communications in smart cities," *Computers & Electrical Engineering*, vol. 82, Article ID 106557, 2020.

[23] M. Yao, X. Wang, Q. Gan, Y. Lin, and C. Huang, "An Improved and Privacy-Preserving Mutual Authentication Scheme with Forward Secrecy in VANET," *Security and Communication Networks*, vol. 2021, Article ID 6698099, 12 pages, 2021.

[24] I. Ali, T. Lawrence, A. A. Omala, and F. Li, "An efficient hybrid signcryption scheme with conditional privacy-preservation for heterogeneous vehicular communication in VANETs," *IEEE Transactions on Vehicular Technology*, vol. 69, no. 10, Article ID 11280, 2020.

[25] H. Zhong, S. Han, J. Cui, J. Zhang, and Y. Xu, "Privacy-preserving authentication scheme with full aggregation in VANET," *Information Sciences*, vol. 476, pp. 211–221, 2019.

[26] J. Cui, W. Xu, Y. Han, J. Zhang, and H. Zhong, "Secure mutual authentication with privacy preservation in vehicular ad hoc networks," *Vehicular Communications*, vol. 21, Article ID 100200, 2020.

[27] M. A. Khan, I. Ullah, M. H. Alsharif, A. H. Alghtani, A. A. Aly, and C. M. Chen, "An Efficient Certificate-Based Aggregate Signature Scheme for Internet of Drones," *Security and Communication Networks*, vol. 2022, Article ID 9718580, 9 pages, 2022.

[28] M. A. Khan, H. Shah, S. U. Rehman et al., "Securing internet of drones with identity-based proxy signcryption," *IEEE Access*, vol. 9, Article ID 89142, 2021.

[29] I. Ullah, S. Zeadally, N. U. Amin, M. K. Asghar, and H. Khattak, "Lightweight and provable secure cross-domain access control scheme for internet of things (IoT) based wireless body area networks (WBAN)," *Microprocessors and Microsystems*, vol. 81, Article ID 103477, 2021.

Hindawi
Complexity
Volume 2022, Article ID 5715922, 19 pages
https://doi.org/10.1155/2022/5715922

Research Article

Qualitative Analysis of a Spatiotemporal Prey-Predator Model with Additive Allee Effect and Fear Effect

Changcheng Ke,[1] Ming Yi,[1] and Yanfeng Guo [1,2]

[1]*School of Mathematics and Physics, China University of Geosciences, Wuhan, Hubei 430074, China*
[2]*School of Science, Guangxi University of Science and Technology, Liuzhou, Guangxi 545006, China*

Correspondence should be addressed to Yanfeng Guo; guoyan_feng@163.com

Received 24 February 2022; Revised 18 March 2022; Accepted 3 May 2022; Published 2 June 2022

Academic Editor: Jawad Ahmad

A diffusive predator-prey system with both the additive Allee effect and the fear effect in the prey subject to Neumann boundary conditions is considered in this paper. Firstly, non-negative and non-trivial solution a priori estimations are shown. Furthermore, for specific parameter ranges, the absence of non-constant positive solutions is demonstrated. Secondly, we use the linearized theory to investigate the stability of non-negative constant solutions. The spatially homogeneous and non-homogeneous periodic solutions, as well as non-constant steady state solutions, are next investigated by using Allee effect parameters as the bifurcation parameter. Finally, numerical simulation is used to illustrate some theoretical results.

1. Introduction

The biodynamics of ecosystems are current hot issues in biology and ecology. The intense effort to understand the pattern formation and mechanisms of spatial diffusion during the late 20th century, especially in the context of biological and ecological contexts, has gradually raised more and more concerns. Especially, in biochemical reactions characterized by interactions of different species, the study on predator-prey types has been studied widely in [1–4].

Recently, Allee effect, which was initially introduced by Allee in 1931 [5], has been studied extensively [6–10]. With the development of the theory for reaction-diffusion equations, many scholars have done many mathematical research to better describe the relationship between different species. Especially, introducing the Allee effect into the model makes the dynamic behavior of the model closer to reality. The spatiotemporal complexity of a delayed predator-prey model with double Allee effect was given by [11]. In [12], P. J. Pal and S. Tapan consider a system with a double Allee effect in prey population growth, which are very sensitive to parameter perturbations and position of initial conditions. H. Molla and S. Sarwardi developed a predator-prey model that combines these phenomena, considering variable prey refuge with additive Allee effect on the prey species, and also investigated the appearance of Hopf bifurcations in a neighborhood of the unique interior equilibrium point of the dynamical system [13]. The rich behaviour of the dynamics suggests that both prey refuge and a strong Allee affect are important factors in ecological complexity. For a reaction-diffusion system with double Allee effect induced by fear factors subject to Neumann boundary conditions, for details, please refer to [2]. The dynamical behavior of a reaction-diffusion-advection model with weak Allee effect type growth has been studied in [9]. Han and Dai investigated the spatiotemporal pattern formation and selection driven by nonlinear cross-diffusion of a toxic-phytoplankton-zooplankton model with Allee effect. By taking cross-diffusion rate as bifurcation parameter, amplitude equations under nonlinear cross-diffusion are derived that describe the spatiotemporal dynamics [14].

Some researchers have indicated that predators can not only capture prey directly but also affect the behavior of prey, even that it could affect the prey more influential than predation [15, 16]. In fact, all animals show various kinds of antipredator responses, such as feeling of fear, habitat

changes, vigilance, foraging, and different physiological changes ([17–21]).

The cost of fear is objective, and it should be taken into consideration when establishing predation and predation models. For example, Jana et al. [22] have explored the influence of habitat complexity on a predator-prey system under fear effect by incorporating self-diffusion. Tiwari et al. analyzed a predator-prey interaction model with Beddington-DeAngelis functional response (BDFR) and incorporating the cost of fear into prey reproduction. For the spatial system, the Hopf bifurcation around the interior equilibrium, stability of homogeneous steady state, direction, and stability of spatially homogeneous periodic orbits have been established [23]. For a plankton-fish model with both the zooplankton refuge and the fear effect, the local and global dynamics of such a model have been investigated in [24]. Moreover, the investigation in [25] has revealed the threshold behavior of a stochastic predator-prey system with fear effect, prey refuge, and non-constant mortality rate. Sasmal and Takeuchi studied the dynamics of a prey-predator interaction model using Monod–Haldane type functional response and provided detailed mathematical results, including basic dynamical properties, existence of positive equilibria, asymptotic stability of all equilibria, Hopf bifurcation, direction, and stability of bifurcated periodic solutions [26]. Furthermore, they also investigated the role of predation fear and its carry-over effects in the prey-predator model. Basic dynamical properties, as well as the global stability of each equilibrium, have been discussed [27].

Allee effect comes in different forms, including multiplicative Allee effect and additive Allee effect. Furthermore, Dennis [6] first proposed the equation incorporating additive Allee effect:

$$\frac{\mathrm{du}}{\mathrm{dt}} = ru\left(1 - \frac{u}{k} - \frac{m}{u+a}\right), \tag{1}$$

where m and a are constants, which reflect the degree of Allee effect; $m/u + a$ denotes the additive Allee effect; r is the intrinsic growth rate of prey; k presents capacity. We note that if $0 < m < a$, then (1) has the weak Allee effect and if $m > a$, then it has the strong Allee effect.

Motivated by the previous works above, we further consider the following reaction-diffusion system with fear effect and additive Allee effect:

$$\begin{cases} \dfrac{\partial u}{\partial t} = d_1\Delta u + ru\left(1 - u - \dfrac{m}{u+a}\right)\dfrac{1}{1+fv} - buv, x \in \Omega, t > 0, \\ \dfrac{\partial v}{\partial t} = d_2\Delta v + cbuv - dv, x \in \Omega, t > 0, \\ \partial_\nu u = \partial_\nu v = 0, x \in \partial\Omega, t > 0, \\ u(x,0) = u_0(x) \geq 0, x \in \Omega, \\ v(x,0) = v_0(x) \geq 0, x \in \Omega, \end{cases} \tag{2}$$

where Δ is the Laplace operator on domains. $d_1 > 0, d_2 > 0$ meanss the diffusion coefficients. The homogeneous Neumann boundary condition is imposed so that there is no population flow across the boundary, ν denotes the outward normal to the boundary $\partial\Omega$. u, v stand for the density of the prey and predator, respectively; m and a are constants, which reflect the degree of Allee effect; f is a constant, which reflects the degree of fear effect; $1/1 + fv$ and $m/u + a$ denote the fear effect and additive Allee effect, respectively; b represents the modified capture rate; c is the conversion coefficient; r is the intrinsic growth rate of prey; d is the death rate of predator. Then, the steady-state system corresponding to (2) is

$$\begin{cases} d_1\Delta u + ru\left(1 - u - \dfrac{m}{u+a}\right)\dfrac{1}{1+fv} - buv = 0, x \in \Omega, \\ d_2\Delta v + cbuv - dv = 0, x \in \Omega, \\ \partial_\nu u = \partial_\nu v = 0, x \in \partial\Omega. \end{cases} \tag{3}$$

The remainder of the paper is structured as follows. In Section 2, we carry out a priori estimates for (3) and the requirements for the nonexistence of non-constant positive solutions. In Section 3, we consider the stability of non-negative constant steady state solutions for system (3). In Section 4, we demonstrate the existence of Hopf bifurcation and steady state bifurcation. In Section 5, we show how the parameters affect the dynamical behavior of the system. Furthermore, we verify the analysis results with the numerical simulation results. In section 6, the paper ends with some conclusions.

2. Preliminaries

In this section, we first present some properties of equilibrium solutions of (3) including a priori estimates. Then, we discuss the nonexistence of non-constant positive solutions for certain parameter range. It is an essential part for analysis of the existence of non-constant positive steady states and the global bifurcation. We first recall the maximum principle in [28].

Lemma 1 (see [28]). *We suppose that $F(x,w) \in C(\overline{\Omega} \times R)$. If $w \in C^2(\Omega) \cap C^1(\overline{\Omega})$ satisfies*

$$\begin{cases} \Delta w(x) + F(x, w(x)) \geq 0, x \in \Omega, \\ \dfrac{\partial w}{\partial \nu} \leq 0, x \in \partial\Omega, \end{cases} \tag{4}$$

and $w(x_0) = \max_{\overline{\Omega}} w$, then $F(x_0, w(x_0)) \geq 0$. Similarly, if the two inequalities are reversed and $w(x_0) = \min_{\overline{\Omega}} w$, then $F(x_0, w(x_0)) \leq 0$.

We note that Ω is a bounded domain in $\mathbf{R}^N$ with smooth boundary. Let $\lambda_i, i = 0, 1, 2, \ldots$ be the eigenvalues of $-\Delta$ under Neumann boundary condition.

By Lemma 1, we have a prior estimates as follows:

Theorem 1. *Let $(u(x)), v(x)$ be non-negative and non-trivial solution of (3); we assume that $cr/(1+a)d$ $(1+a)^4/4 - m + cd_1/d_2 > 0$. Then, $(u(x)), v(x)$satisfies*

$$0 < u(x) \le 1, 0 < v \le \frac{cr}{(1+a)d}\left(\frac{(1+a)^2}{4} - m\right) + \frac{cd_1}{d_2}, \tag{5}$$

where $d, r, c, d_1, d_2, a, m > 0$.

Proof. From the strong maximum principle, we have $u > 0$ and $v > 0$. Then, by Lemma 1, it follows $0 < u(x) \le 1$. The first equation of (3) is multiplied by c and adding the two equations of (3), we obtain

$$\begin{aligned} -(cd_1\Delta u + d_2\Delta v) &= cru\left(1 - u - \frac{m}{u+a}\right)\frac{1}{1+fv} - \mathrm{d}v \\ &= cr\frac{u}{u+a}\left((1-u)(u+a) - m\right)\frac{1}{1+fv} - \mathrm{d}v, \le cr\frac{u}{u+a}\left(\frac{(1+a)^2}{4} - m\right)\frac{1}{1+fv} - dv, \\ &\le \frac{cr}{1+a}\left(\frac{(1+a)^2}{4} - m\right) - dv, \le \frac{cr}{1+a}\left(\frac{(1+a)^2}{4} - m\right) + \frac{dd_1c}{d_2} - \frac{e}{d_2}(cd_1u + d_2v), \end{aligned} \tag{6}$$

which leads to

$$\begin{aligned} &\Delta(cd_1u + d_2v) + \frac{cr}{1+a}\left(\frac{(1+a)^2}{4} - m\right) + \frac{\mathrm{d}d_1c}{\mathrm{d}_2} \\ &\quad - \frac{\mathrm{d}}{\mathrm{d}_2}(cd_1u + d_2v) \ge 0, \end{aligned} \tag{7}$$

under the condition of $m \le a$. Then, by Lemma 1, we obtain

$$cd_1u + d_2v \le \frac{cr\mathrm{d}_2}{(1+a)\mathrm{d}}\left(\frac{(1+a)^2}{4} - m\right) + cd_1, \tag{8}$$

which implies

$$v \le \frac{cr}{(1+a)\mathrm{d}}\left(\frac{(1+a)^2}{4} - m\right) + \frac{c\mathrm{d}_1}{\mathrm{d}_2}. \tag{9}$$

□

Theorem 2. *For any fixed $d, r, a, b, c, f > 0$, there exists $d^*(r, b, c, d, m, a, f, \Omega)$ such that if $min\{d_1, d_2\} > d^*$, then (3) has no non-constant positive solution.*

Proof. Let (u, v) be a non-negative solution of (3). We denote (10) as

$$\begin{aligned} \overline{u} &= |\Omega|^{-1}\int_\Omega u dx, \\ \overline{v} &= |\Omega|^{-1}\int_\Omega v dx, \\ F(u) &= ru\left(1 - u - \frac{m}{u+a}\right). \end{aligned} \tag{10}$$

Then,

$$\int_\Omega (u - \overline{u})dx = \int_\Omega (v - \overline{v})dx = 0. \tag{11}$$

Multiplying the first equation of (3) by $u - \overline{u}$ and integrating on Ω , applying Theorem 1 that

$$\begin{aligned} d_1\int_\Omega |\nabla(u - \overline{u})|^2 dx &= \int_\Omega (u - \overline{u})F(u)\frac{1}{1+fv}dx - \int_\Omega buv(u - \overline{u})dx \\ &= \int_\Omega (u - \overline{u})\left(F(u)\frac{1}{1+fv} - F(\overline{u})\frac{1}{1+f\overline{v}}\right)dx - \int_\Omega bv(u - \overline{u})^2 dx - \int_\Omega bv\overline{u}(u - \overline{u})dx \\ &\le \int_\Omega (u - \overline{u})\left(F(u)\frac{1}{1+fv} - F(\overline{u})\frac{1}{1+fv} + F(\overline{u})\frac{1}{1+fv} - F(\overline{u})\frac{1}{1+f\overline{v}}\right) - \int_\Omega bv\overline{u}(u - \overline{u})dx \\ &\le r\left(1 + \frac{m}{a^2}\right)\int_\Omega (u - \overline{u})^2 dx + \int_\Omega fF(\overline{u})\frac{(u - \overline{u})(v - \overline{v})}{(1+fv)(1+f\overline{v})}dx - \int_\Omega bv\overline{u}(u - \overline{u})dx. \end{aligned} \tag{12}$$

Similarly, multiplying the second equation of (3) by $v - \overline{v}$, we obtain

$$\begin{aligned} d_2\int_\Omega |\nabla(v-\overline{v})|^2dx &= cb\int_\Omega uv(v-\overline{v})dx - \int_\Omega dv(v-\overline{v})dx \\ &= cb\int_\Omega uv(v-\overline{v})dx - \int_\Omega d(v-\overline{v})(v-\overline{v})dx \le cb\int_\Omega (uv(v-\overline{v}) - u\overline{v}(v-\overline{v}) + u\overline{v}(v-\overline{v}) - \overline{u}\overline{v}(v-\overline{v}))dx \\ &= cb\int_\Omega \left(u(v-\overline{v})^2 + (u-\overline{u})(v-\overline{v})\overline{v}\right)dx \le cb\int_\Omega (v-\overline{v})^2dx + cb\int_\Omega u\overline{v}(v-\overline{v})dx. \end{aligned} \tag{13}$$

Multiplying the first equation of (3) by c, added to the second equations of (3), and integrating on Ω, we obtain

$$-\int_\Omega (cd_1\Delta u + d_2\Delta v)dx = \int_\Omega \left(cru\left(1-u-\frac{m}{u+a}\right)\frac{1}{1+fv} - dv\right)dx. \tag{14}$$

Subject it to the boundary conditions, we have

$$d\int_\Omega vdx = \int_\Omega cru\left(1-u-\frac{m}{u+a}\right)\frac{1}{1+fv}\mathrm{d}x \le |\Omega|\frac{cr}{4}. \tag{15}$$

Hence,

$$\overline{v} = \frac{1}{|\Omega|}\int_\Omega vdx \le \frac{cr}{4\mathrm{d}}. \tag{16}$$

By and (16), it follows from Theorem 1 and Young inequality that

$$\begin{aligned} \int_\Omega u\overline{v}(v-\overline{v})dx &= \int_\Omega \overline{v}(u-\overline{u})(v-\overline{v}) \le \frac{cr}{4d}\int_\Omega |u-\overline{u}||v-\overline{v}|dx \\ &\le \frac{cr}{8d}\int_\Omega (u-\overline{u})^2dx + \frac{cr}{8d}\int_\Omega (v-\overline{v})^2dx. \end{aligned} \tag{17}$$

Similarly, we have

$$\int_\Omega -v\overline{u}(u-\overline{u})dx = \int_\Omega (\overline{v}-v)\overline{u}(u-\overline{u})dx \le \frac{1}{2}\int_\Omega (u-\overline{u})^2dx + \frac{1}{2}\int_\Omega (v-\overline{v})^2dx, \tag{18}$$

$$\begin{aligned} \int_\Omega fF(\overline{u})\frac{(u-\overline{u})(\overline{v}-v)}{(1+fv)(1+f\overline{v})}dx &= \int_\Omega fr\overline{u}\left(1-\overline{u}-\frac{m}{\overline{u}+a}\right)\frac{(u-\overline{u})(\overline{v}-v)}{(1+fv)(1+f\overline{v})}dx \le \left(\frac{rf}{8}+\frac{mrf}{2a}\right)\int_\Omega (u-\overline{u})^2dx \\ &+\left(\frac{rf}{8}+\frac{mrf}{2a}\right)\int_\Omega (v-\overline{v})^2dx. \end{aligned} \tag{19}$$

From (12), (13), (16)–(19) and the Poincaré inequality, we obtain that

$$\begin{aligned} &d_1\int_\Omega |\nabla(u-\overline{u})|^2dx + d_2\int_\Omega |\nabla(v-\overline{v})|^2dx \\ &\le \frac{1}{\lambda_1}\left(A\int_\Omega |\nabla(u-\overline{u})|^2dx + B\int_\Omega |\nabla(v-\overline{v})|^2\right)dx, \end{aligned} \tag{20}$$

where

$$\begin{aligned} A &= r\left(1+\frac{m}{a^2}\right) + \frac{bc^2r}{8\mathrm{d}} + \frac{rf}{8} + \frac{mrf}{2a} + \frac{1}{2}, \\ B &= \frac{bc^2r}{8\mathrm{d}} + \frac{rf}{8} + \frac{mrf}{2a} + \frac{1}{2} + cb. \end{aligned} \tag{21}$$

This shows that if

$$\min\{d_1, d_2\} > \frac{1}{\lambda_1}\max\{A, B\} := d^*, \tag{22}$$

then

$$\nabla(u-\overline{u}) = \nabla(v-\overline{v}) = 0. \tag{23}$$

and (u, v) must be a constant solution. □

3. Non-Negative Constant Steady-State Solutions

In this section, the stability of non-negative constant steady state solutions of (3) will be investigated by the standard linearization theory. By [17], under particular situations, (3) has the non-negative constant steady state solutions as follows.

(1) the trivial solution $E_0 = (0, 0)$ always exists.

(2) if $a \in (0, 1)$, there is no boundary constant solution when $a < (a+1)^2/4 < m$.

(3) if $a \in (0, 1)$, then $E_1(1-a/2, 0)$ is unique boundary equilibria when $a < m = (a+1)^2/4$.

(4) if $a \in (0, 1)$, there is two boundary constant solution $E_2(1-a-\sqrt{(a+1)^2-4m}/2, 0)$ and $E_3(1-a+\sqrt{(a+1)^2-4m}/2, 0)$ when $a < m < (a+1)^2/4$.

(5) if $a \in (0, 1)$, there is unique boundary constant solution E_3 under the condition of $0 < m \le a < (a+1)^2/4$.

(6) if $a = 1$, there is unique boundary constant solution $E_4(\sqrt{1-m}, 0)$ only when $0 < m < 1$.

(7) if $a > 1$, there is unique boundary constant solution $E_5(1 - a + \sqrt{(a+1)^2 - 4m}/2, 0)$ when $0 < m < a < (a+1)^2/4$.

(8) there is unique positive constant solution $E^*(d/cb, -b + \sqrt{\Delta}/2bf) = (u^*, v^*)$ with $\Delta = b^2 + 4bfr(1 - u^* - m/u^* + a)$ when $1 - u^* - m/u^* + a > 0$.

Under the no-flux boundary condition, $-\Delta$ has eigenvalues $0 = \lambda_0 < \lambda_1 \le \lambda_2 \le \ldots$ and $\lim_{i \longrightarrow \infty} \lambda_i = \infty$. Let $X(\lambda_i)$ be the eigenspace generated by the eigenfunctions corresponding to λ_i. Let m_i be the algebraic multiplicity of λ_i. Let $\phi_{ij}(i \ge 0, 1 \le j \le m_i)$ be the normalized eigenfunctions corresponding to λ_i. Then, the set $\{\phi_{ij}(1 \le j \le m_i)\}$ forms a complete orthonormal basis in $L^2(\Omega)$.

Next, we consider the stability of constant steady state solutions.

Theorem 3. *For all constants $a, b, c, d, r, f, d_1, d_2 > 0$, we have that*

(1) For trivial solution E_0, if $m > a$, then E_0 is locally asymptotically stable; if $m < a$, then E_0 is unstable

(2) If $0 < a < m = (a+1)^2/4 < 1$, then E_1 is unstable

(3) If $0 < a < m < (a+1)^2/4 < 1$, then E_2 is unstable

(4) If $cbu_j - d < 0$, $E_j(j = 3, 4, 5)$ is stable and if $cbu_j - d > 0$, E_j is unstable

(5) E^* exists if and only if $-m/a + u^* - u^* + 1 > 0$. If $a > \sqrt{m} - u^*$, then E^* is stable. If $a < \sqrt{m} - u^*$, then E^* is unstable

Proof. We rewrite (3) as

$$\begin{cases} d_1 \Delta u + F_1(u, v) = 0, x \in \Omega, \\ d_2 \Delta v + F_2(u, v) = 0, kx \in \Omega, \\ \partial_\nu u = \partial_\nu v = 0, x \in \partial\Omega. \end{cases} \tag{24}$$

The linearization matrix of (3) at a constant solution $E = (u_0, V_0)$ can be expressed by

$$J = \begin{pmatrix} \partial_u F_1(u_0, v_0) + d_1\Delta & \partial_v F_1(u_0, v_0) \\ \partial_u F_2(u_0, v_0) & \partial_v F_2(u_0, v_0) + d_2\Delta \end{pmatrix}. \tag{25}$$

where

$$\begin{aligned} \partial_u F_1(u_0, v_0) &= -bv + \frac{ru\left(-1 + m/(a+u)^2\right)}{1 + fv} \\ &\quad + \frac{r(1 - u - m/a + u)}{1 + fv}, \\ \partial_v F_1(u_0, v_0) &= -bu - \frac{fru(1 - u - m/a + u)}{(1 + fv)^2}, \\ \partial_u F_2(u_0, v_0) &= cbv, \\ \partial_v F_2(u_0, v_0) &= cbu - d. \end{aligned} \tag{26}$$

We define that $X_{ij} = \{a \cdot \phi_{ij} : a \in R^2\}$, $X_i = \oplus_{j=1}^{m_i} X_{ij}$, and $X = \oplus_{i=1}^{\infty} X_i$. Let $(\Phi(x), \Psi(x))$ be a pair of eigenfunction of J corresponding to an eigenvalue λ. Then, we have

$$J\begin{pmatrix} \Phi \\ \Psi \end{pmatrix} = \begin{pmatrix} f_u + d_1\Delta f_v \\ g_u g_v + d_2\Delta \end{pmatrix}\begin{pmatrix} \Phi \\ \Psi \end{pmatrix} = \lambda\begin{pmatrix} \Phi \\ \Psi \end{pmatrix}. \tag{27}$$

We set

$$\begin{aligned} \Phi &= \sum_{0 \le i \le \infty, 1 \le j \le m_i} a_{ij}\phi_{ij}, \\ \Psi &= \sum_{0 \le i \le \infty, 1 \le j \le m_i} b_{ij}\psi_{ij}. \end{aligned} \tag{28}$$

Then, we obtain

$$\begin{aligned} &\sum_{0 \le i \le \infty, 1 \le j \le m_i} \begin{pmatrix} f_u + d_1\lambda_i & f_v \\ g_u & g_v + d_2\lambda_i \end{pmatrix}\begin{pmatrix} a_{ij} \\ b_{ij} \end{pmatrix} \\ \phi_{ij} &= \sum_{0 \le i \le \infty, 1 \le j \le m_i} P_i\begin{pmatrix} a_{ij} \\ b_{ij} \end{pmatrix} \\ \phi_{ij} &= \lambda\begin{pmatrix} a_{ij} \\ b_{ij} \end{pmatrix}\phi_{ij}. \end{aligned} \tag{29}$$

From the chapter 5 of [29, 30], we know that if all the eigenvalues of J have negative real parts, then the constant solution E is locally asymptotically stable; J is unstable if there is an eigenvalue of J with positive real part; if all the eigenvalues have non-positive real parts while some eigenvalues have zero real parts, then the stability of E cannot be determined by the linearization. Furthermore, λ is an eigenvalue of J if and only if λ is an eigenvalue of the matrix $\lambda I - P_i$ for some $i \ge 0$. We have.

$$|\lambda I - P_i| = \lambda^2 - T_i\lambda + D_i, \tag{30}$$

where

$$\begin{aligned} T_i &= -(d_1 + d_2)\lambda_i + f_u + g_v, \\ D_i &= d_1 d_2 \lambda_i^2 - (d_2 f_u + d_1 g_v)\lambda_i + f_u g_v - f_v g_u. \end{aligned} \tag{31}$$

(1) For trival solution $E_0 = (0, 0)$,

$$\begin{aligned} T_i &= -(d_1 + d_2)\lambda_i + r\left(1 - \frac{m}{a}\right) - d, \\ D_i &= d_1 d_2 \lambda_i^2 + \left(dd_1 + r\left(\frac{m}{a} - 1\right)d_2\right)\lambda_i + dr\left(\frac{m}{a} - 1\right). \end{aligned} \tag{32}$$

If $m > a$, then for all eigenvalues λ, we have $T_i < 0$ and $D_i > 0$, which leads to $\mathrm{Re}\lambda < 0$. Hence, E_0 is locally asymptotically stable. If $m < a$, then for $i = 0$, there exists a positive eigenvalue $r(m/a - 1)$, which implies that E_0 is unstable. In addition, if $m = a = 1$, E_0 is stable, else if $m = a \ne 1$, E_0 is unstable.

(2) For $E_1(1 - a/2, 0)$, with $0 < a < m = (a+1)^2/4 < 1$,

$$T_i = -(d_1 + d_2)\lambda_i + \frac{cb(a-1)}{2} - d,$$
$$D_i = d_1 d_2 \lambda_i^2 + d_1\left(\mathrm{d} + \frac{bc(1-a)}{2}\right)\lambda_i. \tag{33}$$

For corresponding ordinary system, E_1 is unstable, so for any $d_1, d_2 > 0$, E_1 is unstable.

(3) For $E_2(1-a-\sqrt{(a+1)^2-4m}/2, 0) = (u_2, v_2)$, with $0 < a < m < (a+1)^2/4 < 1$,

$$T_i = -(d_1 + d_2)\lambda_i + ru_2\left(-1 + \frac{m}{(u_2+a)^2}\right) + cbu_2 - d,$$
$$D_i = d_1 d_2 \lambda_i^2 - \left(d_2 ru_2\left(-1 + \frac{m}{(u_2+a)^2}\right) + d_1(cbu_2 - d)\right)\lambda_i + d_1 d_2 (cbu_2 - d)\left(-ru_2 + \frac{mru_2}{(u_2+a)^2}\right). \tag{34}$$

For $i = 0$, there exists a positive eigenvalue $ru_2(-1 + m/(u_2+a)^2)$. So, E_2 is always unstable.

(4) For $j = 3, 4, 5$, E_j is stable when $cbu_j - d < 0$, and in this case, $T_i < 0, D_i > 0$ for any $i \geq 0$. Additionally, in other cases, E_j is unstable, so for any $d_1, d_2 > 0$, E_j is unstable.

$$T_i = -(d_1 + d_2)\lambda_i + ru_i\left(-1 + \frac{m}{(u_i+a)^2}\right) + cbu_i - d,$$
$$D_i = d_1 d_2 \lambda_i^2 - \left(d_2 ru_i\left(-1 + \frac{m}{(u_i+a)^2}\right) + d_1(cbu_i - d)\right)\lambda_i + ru_i\left(-1 + \frac{m}{(u_i+a)^2}\right)(cbu_i - d). \tag{35}$$

(5) For positive constant solution, $E^*(u^*, v^*) = (d/cb, 1/2bf(-b + \sqrt{b^2 + 4bfr(1 - u^* - m/u^* + a)}))$. The Jacobi matrix of (3) at E^* is

$$J(E^*) = \begin{pmatrix} \left(\frac{m}{(a+u^*)^2} - 1\right)\frac{ru^*}{fv^*+1} - \mathrm{d}_1\lambda_i & -\left(-\frac{m}{a+u^*} - u^* + 1\right)\frac{fru^*}{(fv^*+1)^2} - bu^* \\ cbv^* & -d_2\lambda_i \end{pmatrix}. \tag{36}$$

It is noted that

$$T_i = -(d_1 + d_2)\lambda_i + ru^*\left(\frac{m}{(a+u^*)^2} - 1\right)\frac{1}{fv^*+1},$$
$$D_i = d_1 d_2 \lambda_i^2 - \left(d_2 ru^*\left(\frac{m}{(a+u^*)^2} - 1\right)\frac{1}{fv^*+1}\right)\lambda_i + cbv^*\left(\left(-\frac{m}{a+u^*} - u^* + 1\right)\frac{fru^*}{(fv^*+1)^2} + bu^*\right). \tag{37}$$

For E^* exists if and only if $-m/a + u^* - u^* + 1 > 0$, so it is easy to conclude that $T_i < 0, D_i > 0$ if $m/(a+u^*)^2 - 1 < 0$ $(a > \sqrt{m} - u^*)$, which implies that E^* is stable. If $a < \sqrt{m} - u^*$, for $i = 0$, we obtain that $T_i > 0$ and $D_i > 0$, so it

follows that there exist two of the eigenvalues with positive real parts, which implies that E^* is unstable. □

4. Existence of Non-Constant Positive Solutions

In this section, we consider the existence of non-constant positive solutions to (3) in $\Omega = [0, l\pi]$. First, the existence of spatially homogeneous and non-homogeneous periodic solutions is studied by taking m as the bifurcation parameter. Then, the structure and the stability of the bifurcation solutions that bifurcate from (u^*, v^*) are shown. From Theorem 3, the stability of (u^*, v^*) is determined by the trace and determinant of J. Furthermore, we will restrict $-m/a + u^* - u^* + 1 > 0$. To put out our discussion into the context of the Hopf bifurcation, we convert (3) into the following system by $\tilde{u} = u - u^*$ and $\tilde{v} = v - v^*$ and drop " ~ " for simplicity. We have

$$\begin{cases} \dfrac{\partial u}{\partial t} = d_1 \dfrac{\partial^2 u}{\partial x^2} + r(u+u^*)\left(1 - (u+u^*) - \dfrac{m}{(u+u^*)+a}\right)\dfrac{1}{1+f(v+v^*)} \\ \quad - b(u+u^*)(v+v^*), x \in (0, l\pi), t > 0, \dfrac{\partial v}{\partial t} = d_2 \dfrac{\partial^2 v}{\partial x^2} + cb(u+u^*)(v+v^*) - d(v+v^*), x \in (0, l\pi), t > 0, \\ \partial_\nu u(0,t) = \partial_\nu u(l\pi, t) = \partial_\nu v(0,t) = \partial_\nu v(l\pi, t) = 0, t > 0. \end{cases} \tag{38}$$

Firstly, we define the real-valued Sobolev space

$$\mathcal{X} = \left\{(u,v) \in H^2([0,l\pi]) \times H^2([0,l\pi]): \frac{\partial u(0,t)}{\partial x} = \frac{\partial u(l\pi,t)}{\partial x} = \frac{\partial v(0,t)}{\partial x} = \frac{\partial v(l\pi,t)}{\partial x} = 0\right\}, \tag{39}$$

and the corresponding complexification space is given by $\mathcal{X}_C = \mathcal{X} \oplus i\mathcal{X} = \{a + ib: a, b \in \mathcal{X}\}$.

The linearized operator of the steady state system of (39) evaluated at $(m, 0, 0)$ is

$$L(m) = \begin{pmatrix} ru^*\left(m/(a+u^*)^2 - 1\right)1/fv^* + 1 + d_1\partial^2/\partial x^2 - fru^*\left(-m/a + u^* - u^* + 1\right)1/\left(fv^* + 1\right)^2 - bu^* \\ cbv^* d_2\partial^2/\partial x^2 \end{pmatrix}, \tag{40}$$

where $\mathcal{X}_C$ is the domain of $L(m)$.

The adjoint operator of $L(m)$ is defined by

$$L^*(m) = \begin{pmatrix} ru^*\left(m/(a+u^*)^2 - 1\right)1/fv^* + 1 + d_1\partial^2/\partial x^2 cbv^* \\ -fru^*\left(-m/a + u^* - u^* + 1\right)1/\left(fv^* + 1\right)^2 - bu^* d_2\partial^2/\partial x^2 \end{pmatrix}, \tag{41}$$

where the domain of $L^*(m)$ is $\mathcal{X}_C$.

The following condition in [31] is crucial to ensure that the Hopf bifurcation occurs.

(H1) There exists a neighborhood $\mathcal{O}$ of m_0 such that for $m \in \mathcal{O}$, $L(m)$ has a pair of complex, simple, conjugate eigenvalues $\alpha(m) \pm i\omega(m)$, continuously differentiable in m, with $\alpha(m_0) = 0, \omega(m_0) = \omega_0 > 0$, and $\alpha'(m_0) \neq 0$, all other eigenvalues of $L(m)$ have non-zero real parts for $m \in \mathcal{O}$.

Motived by [31], we apply the Hopf bifurcation theory to analyze our system. For the eigenvalue problem

$$\begin{aligned} -\varphi'' &= \lambda\varphi, x \in (0, l\pi), \\ \varphi'(0) &= \varphi'(l\pi) = 0, \end{aligned} \tag{42}$$

we know that the corresponding (42) eigenvalues are $\lambda_n = n^2/l^2$ $(n = 0, 1, \ldots)$, with corresponding eigenfunctions $\varphi_n(x) = \cos nx/l$. Let

$$\begin{pmatrix} \phi \\ \psi \end{pmatrix} = \sum_{n=0}^{\infty} \begin{pmatrix} a_n \\ b_n \end{pmatrix} \cos\frac{nx}{l}, \tag{43}$$

be a pair of eigenfunctions of $L(m)$ corresponding to an eigenvalue $\rho(m)$, that is, $L(m)(\phi,\psi)^T = \rho(m)(\phi,\psi)^T$. By a straightforward analysis, we have

$$L_n(m)\begin{pmatrix} a_n \\ b_n \end{pmatrix} = \rho(m)\begin{pmatrix} a_n \\ b_n \end{pmatrix}, n = 0, 1, \ldots, \tag{44}$$

where

$$L_n(m) = \begin{pmatrix} ru^*\left(m/(a+u^*)^2 - 1\right)1/fv^* + 1 - d_1n^2/l^2 - fru^*\left(-m/a + u^* - u^* + 1\right)1/\left(fv^* + 1\right)^2 - bu^* \\ cbv^* - d_2n^2/l^2 \end{pmatrix}. \tag{45}$$

Hence, the eigenvalues of $L(m)$ are given by the eigenvalues of $L_n(m)$, $(n = 0, 1, \ldots)$. The characteristic equation of $L_n(m)$ is

$$\begin{aligned} &\rho^2 - T_n(m)\rho + D_n(m) = 0, \\ &n = 0, 1, \ldots, \end{aligned} \tag{46}$$

where

$$\begin{cases} T_n(m) = -\dfrac{(d_1+d_2)n^2}{l^2} + ru^*\left(\dfrac{m}{(a+u^*)^2} - 1\right)\dfrac{1}{fv^*+1}, \\ D_n(m) = \dfrac{d_1d_2n^4}{l^4} - \left(d_2ru^*\left(\dfrac{m}{(a+u^*)^2} - 1\right)\dfrac{1}{fv^*+1}\right)\dfrac{n^2}{l^2} + cbv^*\left(fru^*\left(-\dfrac{m}{a+u^*} - u^* + 1\right)\dfrac{1}{(fv^*+1)^2} + bu^*\right). \end{cases} \tag{47}$$

$$\begin{aligned} T_0 &= ru^*\left(\frac{m}{(a+u^*)^2} - 1\right)\frac{1}{fv^*+1}, \\ D_0 &= cbv^*\left[fru^*\left(-\frac{m}{a+u^*} - u^* + 1\right)\frac{1}{(fv^*+1)^2} + bu^*\right] > 0. \end{aligned} \tag{48}$$

Therefore, the eigenvalues are determined by

$$\begin{aligned} &\rho(m) = \frac{T_n(m) \pm \sqrt{T_n^2(m) - 4D_n(m)}}{2}, \\ &n = 0, 1, \ldots \end{aligned} \tag{49}$$

If the condition (H1) holds, $L(a)$ has a pair of simple purely imaginary $\pm i\omega_0$ at $a = a_0$, if and only if there exists a unique $n \in N$ such that $\pm i\omega_0$ are the purely imaginary eigenvalues of $L_n(m)$. The related eigenvector is denoted by $q = q_n = (a_n, b_n)^T \cos nx/l$, with $a_n, b_n \in C$, such that $L(m_0)q = i\omega_0 q$.

We identify the Hopf bifurcation point m_0 which satisfies the condition (H1): there exists $n \in N$ such that

$$T_n(m_0) = 0, D_n(m_0) > 0, T_j(m_0) \neq 0, D_j(m_0) \neq 0 \text{for} j \neq n, \tag{50}$$

and for the unique pair of complex eigenvalues near the imaginary axis $\alpha(m) \pm i\omega(m)$

$$\alpha'(m_0) \neq 0. \tag{51}$$

It is easy to obtain $T_n(m) < 0$ and $D_n(m) > 0$ if $0 < m < (a+u^*)^2$, which implies that the steady state (u^*, v^*) is locally asymptotically stable. Hence, any potential bifurcation points must be in the interval $[(a+u^*)^2, (a+u^*)(1-u^*))$. This means that $u^* < 1 - a/2$ is essential for bifurcation condition. For any Hopf bifurcation point m_0 in $[(a+u^*)^2, (a+u^*)(1-u^*))$, $\alpha(m) \pm i\omega(m)$ are the eigenvalues of $L_n(m)$, where

$$\begin{aligned} &\alpha(m) = \frac{ru^*\left(m/(a+u^*)^2 - 1\right)1/fv^* + 1}{2} - \frac{(d_1+d_2)n^2}{2l^2}, \\ &\omega(m) = \sqrt{D_n(m) - \alpha^2(m)}, \end{aligned} \tag{52}$$

$$\alpha'(m) > 0, \tag{53}$$

for m in $[(a+u^*)^2, (a+u^*)(1-u^*))$. Hence, the transversality condition is always satisfied.

From the discussion above, the determination of Hopf bifurcation points reduces to describing the set

$$\Gamma := \left\{ m \in \left[(a+u^*)^2, (a+u^*)(1-u^*) \right) : \text{for some } n \in N, \text{which satisfies the condition } (H1) \right\}. \tag{54}$$

when a set of parameters $d_1, d_2, l, a, b, c, d, f, r$ are given.

In the following, for $d_1, d_2, a, b, c, d, f, r > 0$ and $0 < m < (a+u^*)(1-u^*)$ fixed, we choose l appropriately. $m^H = (a+u^*)^2$ is always an element of Γ for any $l > 0$ because of $T_0(m_0^H) = 0, T_j(m_0^H) < 0$ for any $j > 1$, and $D_k(m_0^H) > 0$ for any $k \in N$. This corresponds to the Hopf bifurcation of spatially homogeneous periodic solution. Apparently, m_0^H is also the unique value m for the Hopf bifurcation of spatially homogeneous periodic solution for any $l > 0$.

In the following, we search for spatially non-homogeneous Hopf bifurcation points for $n \geq 1$. As $T_0(m_0^H) = 0$ and $T_0'(m) > 0$ for $m \in [m_0^H, (a+u^*)(1-u^*))$, we obtain that $0 < T_0(m) < T_0((a+u^*)(1-u^*)) = ru^*(1-a-2u^*)/((a+u^*)(fv^*+1)) := M_*$ for $m \in (m_0^H, (a+u^*)(1-u^*))$. We define

$$l_n = n\sqrt{\frac{d_1+d_2}{M_*}}, n \in N^*. \tag{55}$$

Then for $l_n < l \leq l_{n+1}$, and $1 \leq j \leq n$, we derive the root of $T_0(m) = (d_1+d_2)j^2/l^2$ as m_j^H such that $m_0^H < m_j^H < (a+u^*)(1-u^*)$. Moreover, by $T_0'(m) > 0$ in $[m_0^H, (a+u^*)(1-u^*))$, we derive (56) and (57)

$$0 < m_0^H < m_1^H < m_2^H < \ldots < m_n^H < (a+u^*)(1-u^*) \tag{56}$$

$$T_j\left(m_j^H\right) = 0, T_i\left(m_j^H\right) \neq 0 \text{for} i \neq j. \tag{57}$$

Since $D_j(m_j^H) > 0$, now we discuss a condition to verify $D_n(m_j^H) \neq 0$ for $j \neq n$. For $m \in [m_0^H, (a+u^*)(1-u^*))$, we have

$$D_i(m) = \frac{d_1 d_2 i^4}{l^4} - d_2 T_0(m)\frac{i^2}{l^2} + D_0(m) := \tau\left(\frac{i^2}{l^2}\right). \tag{58}$$

The quadratic function $\tau(i^2/l^2)$ is positive for all $l \in R$ if the discriminant of $\tau(i^2/l^2) = 0$ is negative, which means that (60)

$$d_2^2 T_0^2(m) - 4d_1 d_2 D_0 = d_2^2\left(ru^*\left(\frac{m}{(a+u^*)^2} - 1\right)\frac{1}{fv^*+1}\right)^2, -4d_1 d_2 cbv^*\left(fru^*\left(-\frac{m}{a+u^*} - u^* + 1\right)\frac{1}{(fv^*+1)^2} + bu^*\right). \tag{59}$$

We note that

$$\overline{f} = \left(\frac{r^2 d_2^2 u^{*4}\left(m/(a+u^*)^2 - 1\right)^4}{16 d_1^2 c^2 (1 - u^* - m/u^* + a)^2} - b^2\right) \frac{1}{4br(1 - u^* - m/u^* + a)}. \tag{60}$$

For $(a+u^*)^2 \leq m < (a+u^*)(1-u^*)$, we can choose $f > \overline{f}$ such that the discriminant of $\tau(i^2/l^2) = 0$ is negative. Then, $\tau(i^2/l^2) > 0$ for $i \in N$ such that $D_i(m_j^H) > 0$.

We summarize our analysis above and apply Theorem 2 in [31]. The existence of both spatially homogeneous and non-homogeneous periodic solutions bifurcation from (u^*, v^*) can be obtained as follows:

Theorem 4. *For any l in $(l_n, l_{n+1}]$ and $f > \overline{f}$, system (2) undergoes Hopf bifurcation at each $m = m_j^H (1 \leq j \leq n)$. Moreover, the bifurcation periodic solutions near $(m, u, v) = (m_j^H, u^*, v^*)$ can be parameterized as $(m(s), u(s), v(s))$ so that $m(s) \in L^\infty$ in the form of $m(s) = m_j^H + o(s)$ for $s \in (0, \delta)$ for some small $\delta > 0$, (61) and (62)*

$$\begin{cases} u(s)(t,x) &= u^* + s\left(a_n e^{i2\pi t/T(s)} + \overline{a}_n e^{-i2\pi t/T(s)}\right)\cos\dfrac{nx}{l} + o\left(s^2\right), \\ v(s)(t,x) &= v^* + s\left(b_n e^{i2\pi t/T(s)} + \overline{b}_n e^{-i2\pi t/T(s)}\right)\cos\dfrac{nx}{l} + o\left(s^2\right), \end{cases} \tag{61}$$

where (a_n, b_n) is the corresponding eigenvector, and

$$T(s) = \frac{2\pi}{\omega_0}\left(1 + \tau_2 s^2\right) + o\left(s^4\right),$$
$$\tau_2 = -\frac{1}{\omega_0}\left(\mathrm{Im}\left(c_1\left(m_j^H\right)\right) - \frac{Re\left(c_1\left(m_j^H\right)\right)}{\alpha'\left(m_j^H\right)}\omega_0'\left(m_j^H\right)\right), \tag{62}$$
$$T''(0) = \frac{4\pi}{\omega_0}\tau_2 = -\frac{4\pi}{\omega_0^2}\left(\mathrm{Im}\left(c_1\left(m_j^H\right)\right) - \frac{Re\left(c_1\left(m_j^H\right)\right)}{\alpha'\left(m_j^H\right)}\omega_0'\left(m_j^H\right)\right). \tag{63}$$

Furthermore, we notice that

(1) The bifurcating periodic orbits from $m = m_0^H$ are spatially homogeneous, which coincide with the periodic orbits of the corresponding ODE system

(2) The bifurcating periodic orbits from $m = m_j^H$ are spatially non-homogeneous.

Then, we consider the direction and stability of spatially homogeneous Hopf bifurcation.

Theorem 5. *For system (2), if all other eigenvalues of $L_n(m_0^H)$ have negative real parts and $Re(c_1(m_0^H)) < 0$ (resp. > 0), the spatially homogeneous periodic solutions bifurcating from $m = m_0^H$ are locally asymptotically stable (resp. unstable). Moreover, the Hopf bifurcation at m_0^H is supercritical (resp. subcritical) if $1/\alpha'(m_0^H)Re(c_1(m_0^H)) < 0$ (resp. > 0).*

Proof. Here, the notations and calculations in [31] are used in the same way. For the sake of simplicity, we denote $1 - u^* - m/u^* + a$ by M. Then, we introduce

$$\begin{cases} q := \begin{pmatrix} a_0 \\ b_0 \end{pmatrix} = \begin{pmatrix} 1 \\ --cb + c\sqrt{b^2 + 4bfrM}/2f\omega_0 i \end{pmatrix}, \\ q^* := \begin{pmatrix} a_0^* \\ b_0^* \end{pmatrix} = \begin{pmatrix} 1/2\pi l \\ -\omega_0 f/\left(-cb + c\sqrt{b^2 + 4bfrM}\right)\pi l i \end{pmatrix}, \end{cases} \tag{64}$$

such that $\langle q^*, q\rangle = 1, \langle q^*, \overline{q}\rangle = 0$, $L(m_0^H)q = i\omega_0 q$ and $L^*(m_0^H)q^* = -i\omega_0 q^*$, where

$$\omega_0 = 2b\frac{\sqrt{u^* cM\sqrt{b^2 + 4bfrM}}}{b + \sqrt{b^2 + 4bfrM}}. \tag{65}$$

And $\langle u, v\rangle = \int_0^{l\pi} \overline{u}^T v dx$ denotes the inner product in $L^2(0, l\pi) \times L^2(0, l\pi)$. Then, we get the derivatives at (u^*, v^*, m_0^H) as follows:

$$\begin{aligned}
f_{uu} &= -\frac{2r\left(a^3 + 3a^2u^* - am + 3au^{*2} + u^{*3}\right)}{(a + u^*)^3(fv^* + 1)}, g_{uu} = 0, \\
f_{uv} &= \frac{fr\left(a^2(2u^* - 1) + a(m + 2u^*(2u^* - 1)) + u^{*2}(2u^* - 1)\right)}{(a + u^*)^2(fv^* + 1)^2} - b, g_{uv} = cb, \\
f_{vv} &= \frac{2f^2ru^*M}{(1 + fv^*)^3}, g_{vv} = 0, \\
f_{uuu} &= -\frac{6amr}{(a + u^*)^4(1 + fv^*)}, g_{uuu} = 0, \\
f_{uuv} &= \frac{2fr\left(a^3 + 3a^2u^* - am + 3au^{*2} + u^{*3}\right)}{(a + u^*)^3(fv^* + 1)^2}, g_{uuv} = 0, \\
f_{uvv} &= -\frac{2f^2r\left(a^2(2u^* - 1) + a(m + 2u^*(2u^* - 1)) + u^{*2}(2u^* - 1)\right)}{(a + u^*)^2(fv^* + 1)^3}, g_{uvv} = 0, \\
f_{vvv} &= -\frac{6f^3ru^*M}{(1 + fv^*)^4}, g_{vvv} = 0.
\end{aligned} \tag{66}$$

In addition, we note

$$Q_{qq} = \begin{pmatrix} c_n \\ d_n \end{pmatrix} \cos^2 \frac{nx}{l},$$
$$Q_{q\overline{q}} = \begin{pmatrix} e_n \\ f_n \end{pmatrix} \cos^2 \frac{nx}{l}, \tag{67}$$
$$Q_{qq\overline{q}} = \begin{pmatrix} g_n \\ h_n \end{pmatrix} \cos^3 \frac{nx}{l},$$

where $c_n, d_n, e_n, f_n, g_n, h_n$ are defined as the same with [31].

$$\begin{aligned}
c_n &= f_{uu} a_n^2 + 2 f_{uv} a_n b_n + f_{vv} b_n^2, \\
d_n &= g_{uu} a_n^2 + 2 g_{uv} a_n b_n + g_{vv} b_n^2, \\
e_n &= f_{uu} |a_n|^2 + f_{uv} \left(a_n \overline{b}_n + \overline{a}_n b_n \right) + f_{vv} |b_n|^2, \\
f_n &= g_{uu} |a_n|^2 + g_{uv} \left(a_n \overline{b}_n + \overline{a}_n b_n \right) + g_{vv} |b_n|^2, \\
g_n &= f_{uuu} |a_n|^2 a_n + f_{uuv} \left(2 |a_n|^2 b_n + a_n^2 \overline{b}_n \right) + f_{uvv} \left(2 |b_n|^2 a_n + b_n^2 \overline{a}_n \right) + f_{vvv} |b_n|^2 b_n, \\
h_n &= g_{uuu} |a_n|^2 a_n + g_{uuv} \left(2 |a_n|^2 b_n + a_n^2 \overline{b}_n \right) + g_{uvv} \left(2 |b_n|^2 a_n + b_n^2 \overline{a}_n \right) + g_{vvv} |b_n|^2 b_n.
\end{aligned} \tag{68}$$

For $n = 0$, by calculation, we derive (69)

$$\begin{aligned}
c_0 &= -\frac{2 c f^2 r^3 M^2}{\left(f v^* + 1 \right)^3 \sqrt{4 b f r M + b^2}} + \frac{2 r \left(m / \left(a + u^* \right)^2 - 1 \right)}{f v^* + 1} - \frac{2 m r u^*}{\left(a + u^* \right)^3 \left(f v^* + 1 \right)} \\
&\quad - \frac{i 2 c r M \left(- f r M / \left(f v^* + 1 \right)^2 - f r u^* \left(m / \left(a + u^* \right)^2 - 1 \right) / \left(f v^* + 1 \right)^2 - b \right)}{\sqrt{c u^* M \sqrt{4 b f r M + b^2}}}, \\
d_0 &= -\frac{i 2 c^2 b r M}{\sqrt{c u^* M \sqrt{b \left(4 f r M + b \right)}}}, \\
e_0 &= \frac{2 c f^2 r^3 M^2}{\left(f v^* + 1 \right)^3 \sqrt{4 b f r M + b^2}} - \frac{2 r m u^*}{\left(a + u^* \right)^3 \left(f v^* + 1 \right)} + \frac{2 r \left(m - \left(a + u^* \right)^2 \right)}{\left(a + u^* \right)^2 \left(1 + f v^* \right)}, \\
g_0 &= \frac{r}{32 \left(f v^* + 1 \right)^4} \left(\frac{192 i c^3 f^3 r^3 u^* M^4}{\left(c u^* M \sqrt{b^2 + 4 b f r M} \right)^{3/2}} + \frac{64 c f^2 r^2 M^2 \left(m a + \left(2 u^* - 1 \right) \left(a + u^* \right)^2 \right) \left(f v^* + 1 \right)}{u^* \left(a + u^* \right) \left(\left(a + u^* \right) \left(u^* - 1 \right) + m \right) \sqrt{b^2 + 4 b f r M}} \right. \\
&\quad \left. + \frac{64 i c f r M \left(\left(a + u^* \right)^3 - a m \right) \left(f v^* + 1 \right)^2}{\left(a + u^* \right)^3 \sqrt{c u^* M \sqrt{b^2 + 4 b f r M}}} + \frac{192 m u^* \left(f v^* + 1 \right)^3}{\left(a + u^* \right)^4} - \frac{192 m \left(f v^* + 1 \right)^3}{\left(a + u^* \right)^3} \right), \\
f_0 &= h_0 = 0.
\end{aligned} \tag{69}$$

Then, we can obtain (70)

$$\begin{aligned}
\langle q^*, Q_{qq}\rangle &= bc - \frac{cf^2r^3M^2}{(fv^*+1)^3\sqrt{b^2+4bfrM}} - \frac{mru^*}{(a+u^*)^3(fv^*+1)} + \frac{r\left(m-(a+u^*)^2\right)}{(a+u^*)^2(1+fv^*)} \\
&\quad + \frac{icrM\left(b-\left(fr\left((a+u^*)^2(2u^*-1)+am\right)/(a+u^*)^2(1+fv^*)^2\right)\right)}{\sqrt{cu^*M\sqrt{b^2+4bfrM}}}, \\
\langle q^*, Q_{q\overline{q}}\rangle &= \frac{cf^2r^3M^2}{(fv^*+1)^3\sqrt{b^2+4bfrM}} - \frac{mru^*}{(a+u^*)^3(fv^*+1)} + \frac{r\left(m-(a+u^*)^2\right)}{(a+u^*)^2(fv^*+1)}, \\
\langle \overline{q}^*, Q_{qq}\rangle &= -bc - \frac{cf^2r^3M^2}{(fv^*+1)^3\sqrt{b^2+4bfrM}} - \frac{mru^*}{(a+u^*)^3(fv^*+1)} + \frac{r\left(m-(a+u^*)^2\right)}{(a+u^*)^2(1+fv^*)} \\
&\quad + \frac{icrM\left(b-\left(fr\left((a+u^*)^2(2u^*-1)+am\right)/(a+u^*)^2(1+fv^*)^2\right)\right)}{\sqrt{cu^*M\sqrt{b^2+4bfrM}}}, \\
\langle \overline{q}^*, Q_{q\overline{q}}\rangle &= \frac{cf^2r^3M^2}{(fv^*+1)^3\sqrt{b^2+4bfrM}} - \frac{mru^*}{(a+u^*)^3(fv^*+1)} + \frac{r\left(m-(a+u^*)^2\right)}{(a+u^*)^2(fv^*+1)}. \\
\langle \overline{q}^*, C_{qq\overline{q}}\rangle &= \frac{r}{64(fv^*+1)^4}\left(\frac{192ic^3f^3r^3u^*M^4}{\left(cu^*M\sqrt{b^2+4bfrM}\right)^{3/2}} + \frac{64cf^2r^2M^2\left(ma+(2u^*-1)(a+u^*)^2\right)(fv^*+1)}{u^*(a+u^*)((a+u^*)(u^*-1)+m)\sqrt{b^2+4bfrM}}\right. \\
&\quad \left. + \frac{64icfrM\left((a+u^*)^3-am\right)(fv^*+1)^2}{(a+u^*)^3\sqrt{cu^*M\sqrt{b^2+4bfrM}}} + \frac{192mu^*(fv^*+1)^3}{(a+u^*)^4} - \frac{192m(fv^*+1)^3}{(a+u^*)^3}\right).
\end{aligned} \tag{70}$$

And, we note

$$\begin{aligned}
\omega_{20} &= \left[2i\omega_0 I - L\left(m_0^H\right)\right]^{-1} H_{20}, \\
\omega_{11} &= -\left[L\left(m_0^H\right)\right]^{-1} H_{11}, \\
H_{20} &= \begin{pmatrix} c_0 \\ d_0 \end{pmatrix} - \langle q^*, Q_{qq}\rangle \begin{pmatrix} a_0 \\ b_0 \end{pmatrix} - \langle \overline{q}^*, Q_{qq}\rangle \begin{pmatrix} \overline{a}_0 \\ \overline{b}_0 \end{pmatrix} = 0, \\
H_{11} &= \begin{pmatrix} e_0 \\ f_0 \end{pmatrix} - 0\langle q^*, Q_{q\overline{q}}\rangle \begin{pmatrix} a_0 \\ b_0 \end{pmatrix} - \langle \overline{q}^*, Q_{q\overline{q}}\rangle \begin{pmatrix} \overline{a}_0 \\ \overline{b}_0 \end{pmatrix} = 0.
\end{aligned} \tag{71}$$

Hence, $\omega_{20} = \omega_{11} = 0$, $\langle q^*, Q_{\omega_{20}\overline{q}}\rangle = \langle q^*, Q_{\omega_{11}q}\rangle = 0$. By further calculation, we obtain that

$$\begin{aligned}\mathrm{Re}\left(c_1\left(m_0^H\right)\right) &= \mathrm{Re}\left\{\frac{i}{2\omega_0}\langle q^*, Q_{qq}\rangle \cdot \langle q^*, Q_{q\bar{q}}\rangle + \frac{1}{2}\langle q^*, C_{qq\bar{q}}\rangle\right\} \\ &= -\frac{1}{2\omega_0}\left(\frac{crM\left(b - fr\left(\left(a+u^*\right)^2\left(2u^*-1\right)+am\right)/\left(a+u^*\right)^2\left(1+fv^*\right)^2\right)}{\sqrt{cu^*M\sqrt{b^2+4bfrM}}}\right. \\ &\quad \cdot\left(\frac{cf^2r^3M^2}{\left(fv^*+1\right)^3\sqrt{b^2+4bfrM}} - \frac{mru^*}{\left(a+u^*\right)^3\left(fv^*+1\right)} + \frac{r\left(m-\left(a+u^*\right)^2\right)}{\left(a+u^*\right)^2\left(fv^*+1\right)}\right) \\ &\quad \left. + \frac{1}{128\left(1+fv^*\right)^4}\left(\frac{64cf^2r^2M^2\left(ma+\left(2u^*-1\right)\left(a+u^*\right)^2\right)\left(fv^*+1\right)}{u^*\left(a+u^*\right)\left(\left(a+u^*\right)\left(u^*-1\right)+m\right)\sqrt{b^2+4bfrM}} + \frac{192mu^*\left(fv^*+1\right)^3}{\left(a+u^*\right)^4} - \frac{192m\left(fv^*+1\right)^3}{\left(a+u^*\right)^3}\right).\end{aligned} \tag{72}$$

From above analysis, we know that $\alpha'(m_0^H) > 0$. Hence, by Theorem 2 in [31], the bifurcating solutions bifurcated from (m_0^H, u^*, v^*) are locally asymptotically stable (resp. unstable) if $\mathrm{Re}(c_1(m_0^H)) < 0$ (resp. > 0) and $T_j(m_0^H) < 0$, $D_j(m_0^H) > 0$ for $j \geq 1$, and the Hopf bifurcation at m_0^H is supercritical (resp. subcritical) if $1/\alpha'(m_0^H)\mathrm{Re}(c_1(m_0^H)) < 0$ (resp. > 0). The proof is complete.

Inspired by [31, 32], we take m as the bifurcation parameter and also restrict $(a+u^*)^2 \leq m < (a+u^*)(1-u^*)$. We suppose that $\Omega = (0, l\pi)$. The non-negative steady state solutions of (72) satisfy the elliptic problem corresponding to

$$\begin{cases} d_1\dfrac{\partial^2 u}{\partial x^2} + r\left(u+u^*\right)\left(1-\left(u+u^*\right)-\dfrac{m}{\left(u+u^*\right)+a}\right)\dfrac{1}{1+f\left(v+v^*\right)} - b\left(u+u^*\right)\left(v+v^*\right) = 0, x \in (0, l\pi), t > 0, \\ d_2\dfrac{\partial^2 v}{\partial x^2} + cb\left(u+u^*\right)\left(v+v^*\right) - d\left(v+v^*\right) = 0, x \in (0, l\pi), t > 0, \partial_\nu u(0,t) = \partial_\nu u(l\pi,t) = \partial_\nu v(0,t) = \partial_\nu v(l\pi,t) = 0. \end{cases} \tag{73}$$

From Theorem 3, we know that (u^*, v^*) is locally asymptotically stable for $0 < m < (a+u^*)^2$ and unstable for $(a+u^*)^2 < m < (a+u^*)(1-u^*)$.

The steady state bifurcation point m_0 satisfies the steady state bifurcation condition (H2) in [31]:

$$\begin{aligned} &D_n(m_0) = 0, T_n(m_0) \neq 0, \text{and } T_j(m_0) \neq 0, D_j(m_0) \\ &\neq 0 \text{ for } j \neq n \in N_0. \end{aligned} \tag{74}$$

$$\frac{\mathrm{d}}{\mathrm{d}m}D_n(m_0) \neq 0. \tag{75}$$

It means that the potential steady state bifurcation points m shall satisfy conditions (74) and (75). Recall that for $m \in (0, m_0^H]$, $T_n(m) \leq 0$ and $D_n(m) > 0$. Then, any potential bifurcation point m_0 must be in the interval $(m_0^H, (a+u^*)(1-u^*))$. Hence, the steady state bifurcation points reduces to the set

$$\Lambda: = \left\{m \in \left(m_0^H, \left(a+u^*\right)\left(1-u^*\right)\right): \text{for some } n \in N, (74) \text{ and } (75) \text{are satisfied}\right\}, \tag{76}$$

when a set of parameters $(d_1, d_2, a, b, c, d, f, r, l)$ are fixed.

Recall that $D_n(m) = d_1d_2\rho^2 - d_2T_0(m)\rho + D_0$, where $\rho = n^2/l^2$. By solving $D_n(m) = 0$, we have

$$\rho = \rho_\pm(m): = \frac{\mathrm{d}_2T_0(m) \pm \sqrt{\mathrm{d}_2^2T_0^2(m) - 4\mathrm{d}_1\mathrm{d}_2D_0(m)}}{2\mathrm{d}_1\mathrm{d}_2}. \tag{77}$$

We define that

$$z(m) = d_2 r^2 u^{*2}\left(\frac{m}{(a+u^*)^2} - 1\right)^2 - 4d_1 cr\left(1 - u^* - \frac{m}{u^*+a}\right)\sqrt{b^2 + 4bfr\left(1 - u^* - \frac{m}{u^*+a}\right)},$$
$$B(m) = d_2^2 T_0^2(m) - 4d_1 d_2 D_0(m) = \frac{4b^2 \mathrm{d}_2 u^*}{\left(b + \sqrt{b^2 + 4bfr(1 - u^* - m/u^* + a)}\right)^2} z(m). \tag{78}$$

For $z(m)$, we have $z'(m) > 0$ and $z(a+u^*)^2 < 0$, $z((a+u^*)(1-u^*)) > 0$ for $(a+u^*)^2 \le m < (a+u^*)(1-u^*)$.

Hence, there exists a unique root of $z(m) = 0$ denoted by m^B, which implies that $B(m^B) = 0$ and $\rho_\pm(m) > 0$ exists only for $m^B \le m < (a+u^*)(1-u^*)$. Therefore, the potential steady state bifurcation points reduces to the set (79).

$$\Theta: = \left\{m \in \left[m^B, (a+u^*)(1-u^*)\right): \text{for some } n \in N, (74) \text{ and } (75) \text{are satisfied}\right\}. \tag{79}$$

Then, the properties of $\rho_\pm(m)$ can be summarized as follows: □

Lemma 2. *We assume that $d_1, d_2, f > 0, u^* < 1 - a/2$. Then, for any $m \in [m^B, (a+u^*)(1-u^*))$, $\rho_\pm(m)$ exists. Moreover, $\rho_+(m)$ is increasing and $\rho_-(m)$ is decreasing.*

$$\lim_{m \longrightarrow m^B} \rho_+(m) = \lim_{m \longrightarrow m^B} \rho_-(m) = \frac{T_0\left(m^B\right)}{2d_1},$$
$$\lim_{m \longrightarrow m^B} \rho_+'(m) = +\infty, \quad \lim_{m \longrightarrow m^B} \rho_-'(m) = -\infty,$$
$$\rho_+\left((a+u^*)(1-u^*)\right) = \frac{1}{d_1} ru^*\left(\frac{1-u^*}{a+u^*} - 1\right), \tag{80}$$
$$\rho_-\left((a+u^*)(1-u^*)\right) = 0.$$

Proof. The first limit equation is trivial, so we omit here. We mainly analyze the monotonicity result on $\rho_\pm((a+u^*)(1-u^*))$ with respect to m for $m \in (m^B, (a+u^*)(1-u^*)]$.

Differentiating $D_n(m)$ with respect to m, it follows that

$$2d_1 d_2 \rho_\pm(m)\rho_\pm'(m) - d_2 T_0(m)\rho_\pm(m) - d_2 T_0 \rho_\pm'(m) + D_0' = 0. \tag{81}$$

Hence, $\rho_\pm'(m) = d_2 T_0'(m)\rho_\pm(m) - D_0'(m)/2d_1 d_2 \rho_\pm - d_2 T_0(m)$. It is easy to get $2d_1 d_2 \rho_+(m) - d_2 T_0(m) > 0$ and $2d_1 d_2 \rho_-(m) - d_2 T_0(m) < 0$ from (77). In addition, by calculation, we obtain that for $m \in (m^B, (1-u^*)(a+u^*))$, $d_2 T_0'(m)\rho_\pm(m) - D_0'(m) > 0$. The proof is completed.

It follows from Lemma 1 that the curve $(m, \rho_\pm)$ forms a smooth connected curve which connects $(m, \rho) = (m^B, T_0(m^B)/2d_1)$, $((1-u^*)(a+u^*), 1/d_1 ru^*(1-u^*/a+u^*-1)$, and $(m, \rho) = (m, 0)$.

By the properties of $\rho_\pm$, if

$$0 < \frac{n^2}{l^2} < \frac{1}{d_1} ru^*\left(\frac{1-u^*}{a+u^*} - 1\right), \tag{82}$$

then there exists $m_n^B \in [m^B, (1-u^*)(a+u^*))$ such that $\rho_+(m_n^B) = n^2/l^2$ or $\rho_-(m_n^B) = n^2/l^2$, and thus $D_n(m_n^B) = 0$. We define $\bar{l} = n/\sqrt{1/d_1 ru^*(1-u^*/a+u^*-1)}$. Then, for any $l > \bar{l}$, there exists a m_n^B such that $D_n(m_n^B) = 0$.

Next, we verify $\mathrm{d}D_n(m_n^B)/\mathrm{d}m \ne 0$. We recall that $D_n'(m) = -d_2 n^2/l^2 T_0'(m) + D_0'(m)$. Moreover, we know that $T_0'(m) > 0$ and $D_0'(m) < 0$. It follows that $\mathrm{d}D_n(m_n^B)/\mathrm{d}m < 0$. □

5. Numerical Simulations

In this section, in order to reveal the influence of fear effect, Allee effect, and other factors on the predator-prey model, a numerical method is used to analyze the effect of parameters on the asymptotic behavior of system (2) so as to verify and supplement the theoretical results mentioned before.

In Figure 1, we choose $d_1 = 0.1, d_2 = 0.1, a = 0.5, b = 1, c = 1, d = 0.2, r = 1, f = 15$. Varying the parameter m and choosing the initial data near (u^*, v^*), we indicate the following numerical results on the effects of parameter m:

(1) Take $0 < m = 0.3 < a$. Since $m < (d/bc + a)^2$, $(u^*, v^*) \approx (0.2000, 0.1275)$ is locally asymptotically stable by Theorem 3. The simulation results indicate that system (2) converges to the equilibrium (see Figures 1(a) and 1(b)).

(2) Taking $m = 0$, there is no Allee effect on prey. Since $m < (d/bc + a)^2$, $(u^*, v^*) \approx (0.2000, 0.2000)$ is locally asymptotically stable by Theorem 3. The simulation results indicate that system (2) converges to the equilibrium (see Figures 1(c) and 1(d)).

(3) Taking $0 < (d/bc + a)^2 < m = 0.495 < a < (d/bc + a)(1 - d/bc)$, it satisfies the condition of the weak Allee effect and Hopf bifurcation condition by Theorem 4. The simulation results indicate that system (2) undergoes Hopf bifurcation (see Figures 1(e) and 1(f)).

(4) Taking $0 < (d/bc + a)^2 < a < m = 0.51 < (d/bc + a)(1 - d/bc)$, it satisfies the condition of the strong Allee effect and Hopf bifurcation condition by

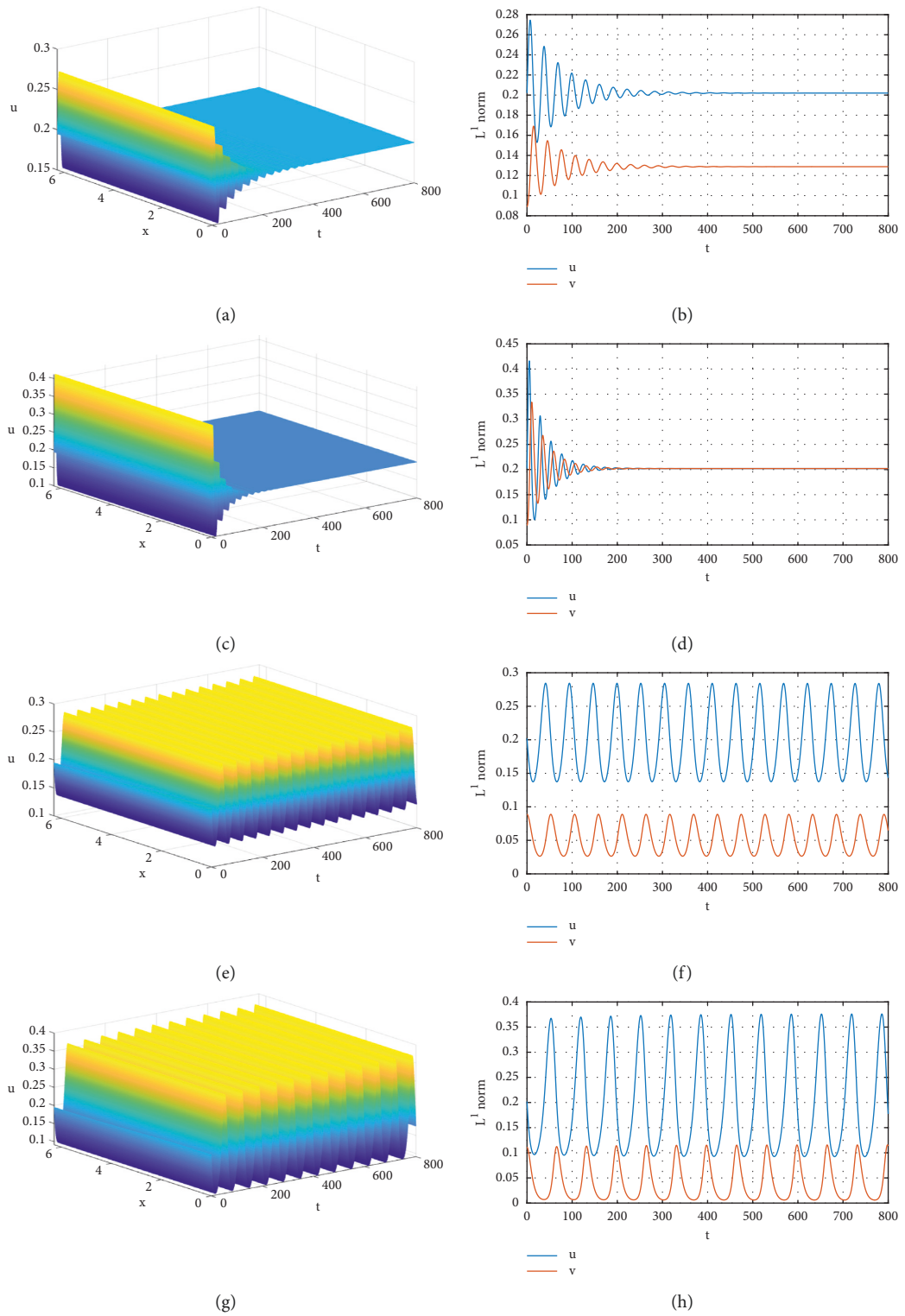

FIGURE 1: The effects of parameter m for $T = 800, l = 2$. The values of parameter m are as follows: (a, b) $m = 0.3$; (c, d) $m = 0$; (e, f) $m = 0.495$; (g, h) $m = 0.51$. The right column is the L^1 norm of u and v.

Theorem 4. The simulation results indicate that system (2) undergoes Hopf bifurcation (see Figure 1(g) and 1(h)).

In Figure 2, we choose $d_1 = 0.1, d_2 = 0.1, a = 0.5, b = 1, c = 1, d = 0.2, r = 1, m = 0.51$. Varying the parameter f and choosing the initial data near (u^*, v^*), it

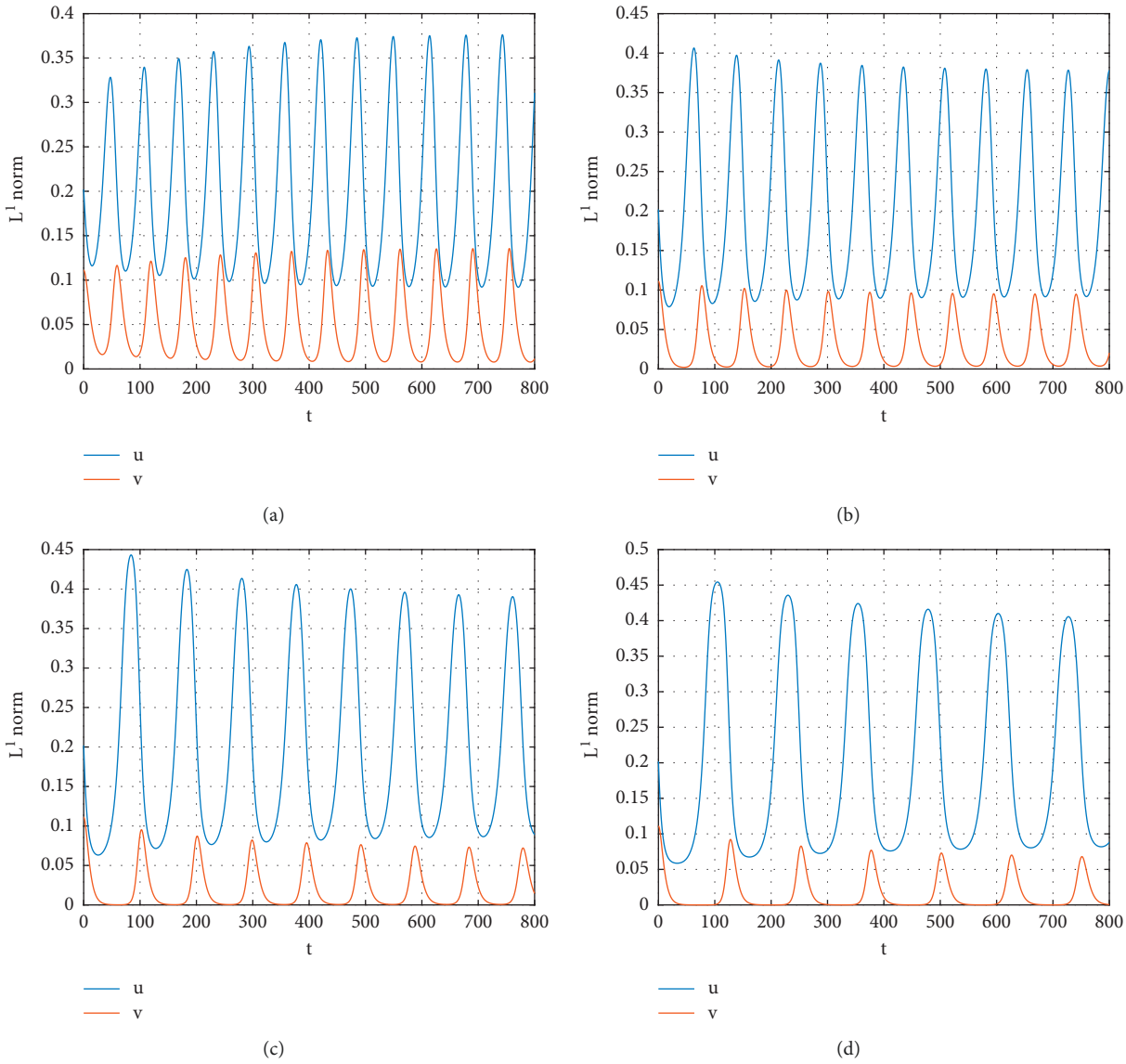

FIGURE 2: The effects of parameter f for $T = 800$, $l = 2$. The values of parameter f are as follows: (a) $f = 5$; (b) $f = 50$; (c) $f = 500$; (d) $f = 5000$.

shows that when f is small, system (2) has obviously periodic oscillation (see Figure 2(a)). When f increases, the maximum L^1 norms of u are almost the same. However, the maximum L^1 norms of v decrease with f increasing (see Figures 2(a)–2(d)). This means that the fear has a negative impact on predators. Moreover, the period of periodic solutions becomes larger as f increases. (see Figures 2(a)–2(d)).

In Figure 3, we choose $d_1 = 0.1, d_2 = 0.1, a = 0.5, b = 1$, $c = 1, r = 1$, $f = 15, m = 0.51$. Varying the parameter d and choosing the initial data near (u^*, v^*), it indicates that when d increases, the period of periodic solution is decreasing. Furthermore, with d increasing, the amplitude of periodic solutions is also decreasing. (see Figures 3(a)–3(c)). As d continues to increase, system (2) converges to an equilibrium (see Figure 3(d)).

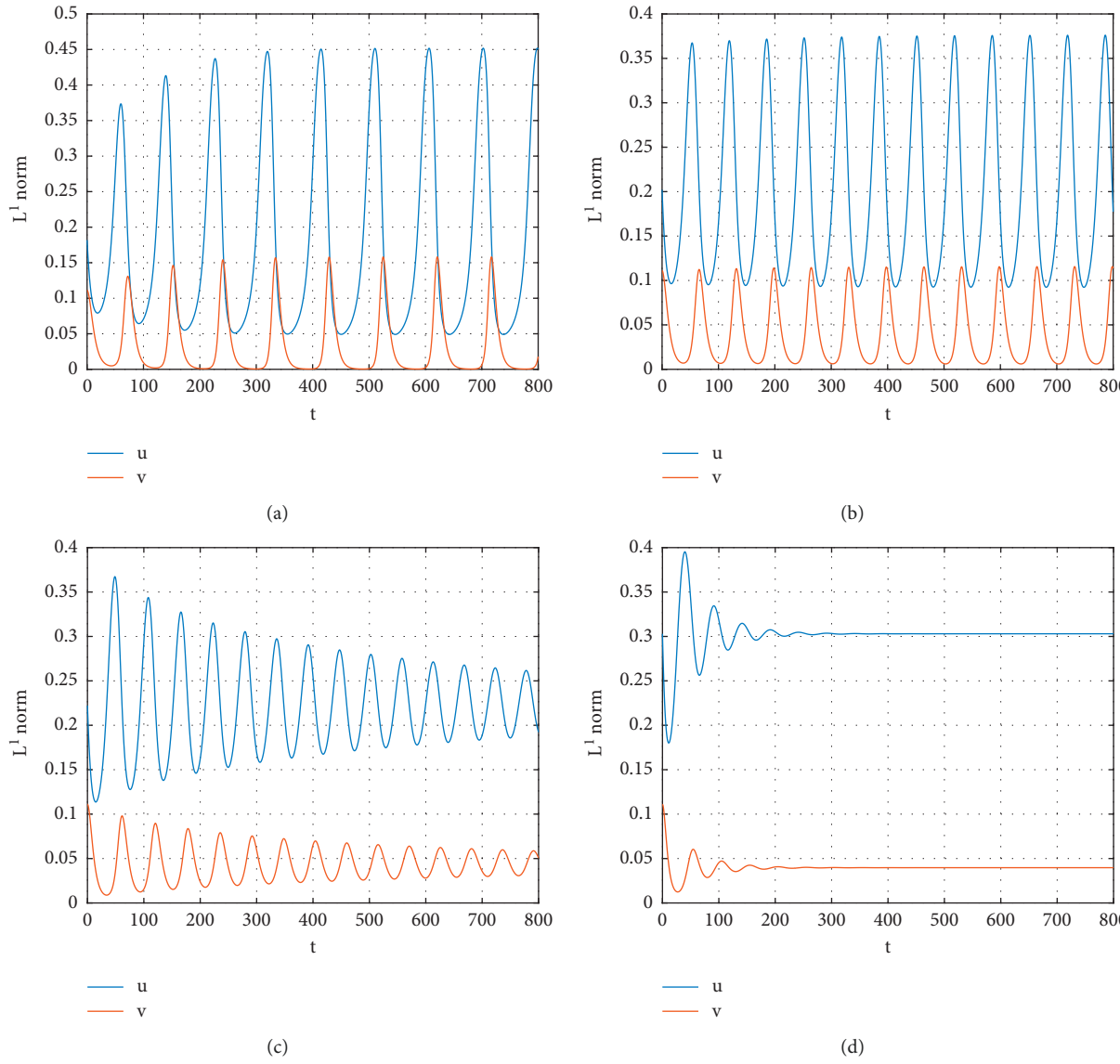

FIGURE 3: The effects of parameter d for $T = 800, l = 2$. The values of parameter d are as follows: (a) $d = 0.18$; (b) $d = 0.2$; (c) $d = 0.22$; (d) $d = 0.3$.

6. Conclusion

In this paper, a diffusive predator-prey model with additive Allee effects induced by fear factors is considered, in which prey can represent the antipredator behavior due to fear factors. Analytical results indicate that the upper bound of v depends on the diffusion rates d_1, d_2, the death rate of the predators d, the Allee effects parameters m, a, the conversion rate c, and the level of fear f. There exists d^*, which depends on $a, b, c, d, r, m, f, \Omega$, such that if $\min\{d_1, d_2\} > d^*$, the system have only constant positive solution. Furthermore, the dynamic behavior near $E^* = (u^*, v^*)$ is of more concerned. Then, we indicate the existence of non-constant positive solutions. Taking m as a bifurcation parameter, system undergoes Hopf bifurcation at each $m = m_j^H$ $(0 \le j \le n)$. Furthermore, for $d_1, d_2, a, b, c, d, r, f > 0$, $0 < m < (1 - d/bc)(d/bc + a)$ are fixed, and there is a smooth curve Γ_n of non-constant positive solutions bifurcating from (u^*, v^*).

We observe that the Allee effect is essential to the dynamical behavior of system (2) by numerical simulations. The amplitude in the strong Allee effect is increasing with m increasing. On the other hand, numerical simulations reveal that the fear effect have an impact on the dynamical behavior of system (2). With the fear effect increasing, the period of periodic solutions is increasing, but the maximum L_1 norm of u is almost the same. On the contrary, the maximum L_1 norm of v decreases with f increasing. From a biological standpoint, the prey survives by adopting antipredator behavior as a result of the fear effect, and the predator is impacted by the prey's antipredator behavior. At last, we show how the death rate d affects system (2) with the strong

Allee effect. As d increases, the amplitude of periodic solution is decreasing, and the period of periodic solution is also decreasing.

It is extremely important to construct animal interaction models in the incorporation of these different types of factors. Considering the different ways of introducing the Allee effect and the interaction with the fear effect, further analysis of the bifurcating solutions of (2) remains a challenging problem. From our discussion before, we conjecture that Turing-Hopf bifurcation, Hopf-Hopf bifurcation is likely to exist in the system, which reveals more complex dynamic behavior and potential biological significance.

Data Availability

The raw data supporting the conclusions of this article will be made available by the authors, without undue reservation, to any qualified researcher.

Conflicts of Interest

The authors declare that there are no conflicts of interest regarding the publication of this paper.

Acknowledgments

This paper was supported by National Natural Science Foundation of China (Nos. 11861013, 11771444), and the Fundamental Research Funds for the Central Universities, China University of Geosciences (Wuhan) (No. 2018061).

References

[1] Y. Dong, S. Li, and S. Zhang, "Hopf bifurcation in a reaction-diffusion model with Degn-Harrison reaction scheme," *Nonlinear Analysis: Real World Applications*, vol. 33, pp. 284–297, 2017.

[2] Y. Shi, J. Wu, and Q. Cao, "Analysis on a diffusive multiple Allee effects predator-prey model induced by fear factors," *Nonlinear Analysis: Real World Applications*, vol. 59, Article ID 103249, 2021.

[3] Y. e. Wang, J. Wu, and Y. Jia, "Steady-state bifurcation for a biological depletion model," *International Journal of Bifurcation and Chaos*, vol. 26, no. 04, Article ID 1650066, 2016.

[4] L. Yang and S. Zhong, "Dynamics of a diffusive predator-prey model with modified Leslie-Gower schemes and additive Allee effect," *Computational and Applied Mathematics*, vol. 34, no. 2, pp. 671–690, 2015.

[5] W. C. Allee, *Animal Aggregations: A Study in General Sociology*, University of Chicago Press, Chicago, Illinois, 1931.

[6] B. Dennis, "Allee effects: population growth, critical density, and the chance of extinction," *Natural Resource Modeling*, vol. 3, no. 4, pp. 481–538, 1989.

[7] M. J. Wittmann, H. Stuis, and D. Metzler, "Genetic Allee effects and their interaction with ecological Allee effects," *Journal of Animal Ecology*, vol. 87, no. 1, pp. 11–23, 2018.

[8] J. Jiao and C. Chen, "Bogdanov-Takens bifurcation analysis of a delayed predator-prey system with double Allee effect," *Nonlinear Dynamics*, vol. 104, no. 2, pp. 1697–1707, 2021.

[9] Y. Wang, J. Shi, and J. Wang, "Persistence and extinction of population in reaction-diffusion-advection model with strong Allee effect growth," *Journal of Mathematical Biology*, vol. 78, no. 7, pp. 2093–2140, 2019.

[10] C. Zhang and H. Yuan, "Pattern formation in a variable diffusion predator–prey model with additive Allee effect," *Mathematical Methods in the Applied Sciences*, vol. 43, no. 7, pp. 4023–4035, 2020.

[11] B. Xie, Z. Wang, Y. Xue, and Z. Zhang, "The dynamics of a delayed predator-prey model with double Allee effect," *Discrete Dynamics in Nature and Society*, vol. 2015, pp. 1–8, Article ID 102597, 2015.

[12] P. J. Pal and T. Saha, "Qualitative analysis of a predator-prey system with double Allee effect in prey," *Chaos, Solitons & Fractals*, vol. 73, pp. 36–63, 2015.

[13] H. Molla, S. Sarwardi, S. R. Smith, and M. Haque, "Dynamics of adding variable prey refuge and an Allee effect to a predator-prey model," *Alexandria Engineering Journal*, vol. 61, no. 6, pp. 4175–4188, 2022.

[14] R. Han and B. Dai, "Spatiotemporal pattern formation and selection induced by nonlinear cross-diffusion in a toxic-phytoplankton-zooplankton model with Allee effect," *Nonlinear Analysis: Real World Applications*, vol. 45, no. 6, pp. 822–853, 2019.

[15] S. Creel and D. Christianson, "Relationships between direct predation and risk effects," *Trends in Ecology & Evolution*, vol. 23, no. 4, pp. 194–201, 2008.

[16] W. Cresswell, "Predation in bird populations," *Journal of Ornithology*, vol. 152, no. S1, pp. 251–263, 2011.

[17] L. Lai, Z. Zhu, and F. Chen, "Stability and bifurcation in a predator-prey model with the additive allee effect and the fear effect," *Mathematics*, vol. 8, no. 8, 1280 pages, 2020.

[18] K. H. Elliott, G. S. Betini, and D. R. Norris, "Fear creates an Allee effect: experimental evidence from seasonal populations," *Proc Biol Sci*, vol. 284, no. 1857, Article ID 20170878, 2017.

[19] M. Clinchy, M. J. Sheriff, and L. Y. Zanette, "Predator-induced stress and the ecology of fear," *Functional Ecology*, vol. 27, no. 1, pp. 56–65, 2013.

[20] S. D. Peacor, B. L. Peckarsky, G. C. Trussell, and J. R. Vonesh, "Costs of predator-induced phenotypic plasticity: a graphical model for predicting the contribution of nonconsumptive and consumptive effects of predators on prey," *Oecologia*, vol. 171, no. 1, pp. 1–10, 2013.

[21] X. Wang, L. Zanette, and X. Zou, "Modelling the fear effect in predator-prey interactions," *Journal of Mathematical Biology*, vol. 73, no. 5, pp. 1179–1204, 2016.

[22] D. Jana, S. Batabyal, and M. Lakshmanan, "Self-diffusion-driven pattern formation in prey-predator system with complex habitat under fear effect," *The European Physical Journal Plus*, vol. 135, no. 11, pp. 884–942, 2020.

[23] V. Tiwari, J. P. Tripathi, S. Mishra, and R. K. Upadhyay, "Modeling the fear effect and stability of non-equilibrium patterns in mutually interfering predator-prey systems," *Applied Mathematics and Computation*, vol. 371, Article ID 124948, 2020.

[24] R. P. Kaur, A. Sharma, and A. K. Sharma, "Impact of fear effect on plankton-fish system dynamics incorporating zooplankton refuge," *Chaos, Solitons & Fractals*, vol. 143, Article ID 110563, 2021.

[25] H. Qi and X. Meng, "Threshold behavior of a stochastic predator-prey system with prey refuge and fear effect," *Applied Mathematics Letters*, vol. 113, Article ID 106846, 2021.

[26] S. K. Sasmal and Y. Takeuchi, "Dynamics of a predator-prey system with fear and group defense," *Journal of Mathematical*

Analysis and Applications, vol. 481, no. 1, Article ID 123471, 2020.

[27] S. K. Sasmal and Y. Takeuchi, "Modeling the Allee effects induced by cost of predation fear and its carry-over effects," *Journal of Mathematical Analysis and Applications*, vol. 505, no. 2, Article ID 125485, 2022.

[28] W. M. Ni and M. Tang, "Turing patterns in the Lengyel-Epstein system for the CIMA reaction," *Transactions of the American Mathematical Society*, vol. 357, no. 10, pp. 3953–3969, 2005.

[29] D. Henry, *Geometric Theory of Semilinear Parabolic Equations*Springer-Verlag, Berlin, NY, USA, 2006.

[30] B. D. Hassard, N. D. Kazarinoff, and Y. H. Wan, *Theory and Applications of Hopf Bifurcation*, Cambridge Press, England UK, 1981.

[31] F. Yi, J. Wei, and J. Shi, "Bifurcation and spatiotemporal patterns in a homogeneous diffusive predator-prey system," *Journal of Differential Equations*, vol. 246, no. 5, pp. 1944–1977, 2009.

[32] J. Wang, J. Shi, and J. Wei, "Dynamics and pattern formation in a diffusive predator-prey system with strong Allee effect in prey," *Journal of Differential Equations*, vol. 251, no. 4-5, pp. 1276–1304, 2011.

Hindawi
Complexity
Volume 2022, Article ID 7803798, 14 pages
https://doi.org/10.1155/2022/7803798

WILEY | Hindawi

Research Article

Some Novel Solutions to a Quadratically Damped Pendulum Oscillator: Analytical and Numerical Approximations

Alvaro H. Salas,[1] **Wedad Albalawi**,[2] **M. R. Alharthi**,[3] **and S. A. El-Tantawy**[4,5]

[1]*Department of Mathematics and Statistics, Universidad Nacional de Colombia, FIZMAKO Research Group, Bogota, Colombia*
[2]*Department of Mathematical Sciences, College of Science, Princess Nourah bint Abdulrahman University, P.O. Box 84428, Riyadh 11671, Saudi Arabia*
[3]*Department of Mathematics and Statistics, College of Science, Taif University, P.O. Box 11099, Taif 21944, Saudi Arabia*
[4]*Department of Physics, Faculty of Science, Port Said University, Port Said 42521, Egypt*
[5]*Research Center for Physics (RCP), Department of Physics, Faculty of Science and Arts, Al-Baha University, Al-Mikhwah, Saudi Arabia*

Correspondence should be addressed to Alvaro H. Salas; ahsalass@unal.edu.co

Received 4 January 2022; Accepted 21 April 2022; Published 28 May 2022

Academic Editor: Akif Akgul

In this paper, some novel analytical and numerical techniques are introduced for solving and analyzing nonlinear second-order ordinary differential equations (ODEs) that are associated to some strongly nonlinear oscillators such as a quadratically damped pendulum equation. Two different analytical approximations are obtained: for the first approximation, the ansatz method with the help of Chebyshev approximate polynomial is employed to derive an approximation in the form of trigonometric functions. For the second analytical approximation, a novel hybrid homotopy with Krylov–Bogoliubov–Mitropolsky method (HKBMM) is introduced for the first time for analyzing the evolution equation. For the numerical approximation, both the finite difference method (FDM) and Galerkin method (GM) are presented for analyzing the strong nonlinear quadratically damped pendulum equation that arises in real life, such as nonlinear phenomena in plasma physics, engineering, and so on. Several examples are discussed and compared to the Runge–Kutta (RK) numerical approximation to investigate and examine the accuracy of the obtained approximations. Moreover, the accuracy of all obtained approximations is checked by estimating the maximum residual and distance errors.

1. Introduction

Duffing-type equation is one of the most important second-degree differential equations that is used to describe many different phenomena [1–6]. The Duffing equation can be used for describing a nonlinear oscillator with a cubic nonlinearity, and the standard form of this equation reads as $\ddot{x}(t) + f(x) = 0$, with $f(x) = \sum_{i=1}^{\infty} \alpha_i x^i$ being the only odd polynomial where $i = 1, 3, 5, \ldots$. George Duffing, a German engineer, is the first person who did arrive at this equation and used it in the study of many different oscillators [3]. He also prepared a book in this regard and explained in it many applications that use this equation in the interpretation of many natural phenomena. Since then, there has been a tremendous amount of research works done about this equation of motion and some related equations, including (un)damped Duffing oscillator $\ddot{x}(t) + \beta\dot{x}(t) + f(x) = 0$, forced Duffing oscillator $\ddot{x}(t) + f(x) = F(t)$, forced damped Duffing oscillator $\ddot{x}(t) + \beta\dot{x}(t) + f(x) = F(t)$, and many other oscillators with odd polynomials and complicated damping term [7–10]. Moreover, there is another type of oscillator that combines both odd and even polynomials, which is called the Helmholtz–Duffing (HD) oscillator $\ddot{x}(t) + f(x) + g(x) = 0$ (here, $f(x) = \sum_{i=1}^{\infty} \alpha_i x^i$ is only odd polynomial where $i = 1, 3, 5, \ldots$ and $g(x) = \sum_{i=2}^{\infty} \gamma_i x^i$ is only even polynomial where $i = 2, 4, 6, \ldots$) and some related oscillators such as (un)damped HD oscillator $\ddot{x}(t) + \beta\dot{x}(t) + f(x) + g(x) = 0$, forced HD oscillator

$\ddot{x}(t) + f(x) + g(x) = F(t)$, forced damped HD oscillator $\ddot{x}(t) + \beta\dot{x}(t) + f(x) + g(x) = F(t)$ and many other HD oscillators with complicated damping term and complicated polynomials [11–15]. All these oscillations have several applications in various fields of science, e.g., oscillations in electronic circuits, oscillations in different plasma models, pendulum oscillator, etc. Due to the importance of these equations, many studies have been conducted to find some analytical and numerical solutions to accurately describe the engineering and physical systems associated with these oscillations [17–19].

As a contribution to the literature, in this article, we present some novel analytical and numerical solutions to the complicated damped HD-type oscillator for a given arbitrary initial conditions by means of both elliptic (exact solution) and trigonometric functions (approximate solution). First, we follow the work of Sugie [20] where the author obtained the equation of motion of underwater pendulum and studied the stability of this oscillator. This equation is called the quadratically damped pendulum equation [20]:

$$\ddot{\theta} + 2\varepsilon\,\dot{\theta}|\dot{\theta}| + \omega_0^2 \sin\,\theta = 0, \tag{1}$$

where ε represents the coefficient of the damping term and ω_0 indicates restoring coefficient per unit of the moment of inertia. For small θ, equation (1) can be approximated as follows:

$$\ddot{\theta} + 2\varepsilon\dot{\theta}|\dot{\theta}| + \omega_0^2\theta = 0. \tag{2}$$

Numerous oscillators with quadrature damping have been investigated over a wide range of different fields [21–26]. There are many methods for solving nonlinear differential equations. There are many analytical and numerical methods that dealt with solving different differential equations, and some of these methods can be found in Refs. [28–34]. In this paper, we will consider four different methods for solving and analyzing equation (1). First, we will solve this equation using the effective ansatz method in order to find some analytical approximations. In the second method, the hybrid homotopy Krylov–Bogoliubov–Mitropolsky method (HKBMM) will be employed to find an approximate solution with high accuracy. On the other hand, two highly accurate numerical schemes which are called the finite difference method (FDM) and Galerkin Hats method (GHM) will be introduced for analyzing evolution equation (1).

2. Analytical Approximations

In this section, two different approximations will be obtained. For the first approximation, the ansatz method with the help of Chebyshev approximate polynomial is employed to obtain an approximation in trigonometric form. For the second approximation, the new HKBMM is introduced.

2.1. First Approach: Ansatz Method and Trigonometric Solution. Let us rewrite evolution equation (1) in the form of the initial value problem (i.v.p.):

$$\begin{cases} \ddot{\theta} + 2\varepsilon\,\dot{\theta}|\dot{\theta}| + \omega_0^2 \sin\,\theta = 0, \\ \theta(0) = \theta_0 \text{ and } \theta'(0) = \dot{\theta}_0. \end{cases} \tag{3}$$

Based on Chebyshev polynomial approximation, the value of $\sin\,\theta$ can be expanded as

$$\begin{aligned} \sin\,\theta &\approx \theta - \lambda\theta^3, \\ \dot{\theta}|\dot{\theta}| &\approx r_0\dot{\theta} + r_1\dot{\theta}^3, \text{for} |\dot{\theta}| \le M, \end{aligned} \tag{4}$$

where

$$\begin{aligned} r_0 &= \frac{M}{2}\sqrt{1 - \frac{1}{\sqrt{2}}}, \\ r_1 &= \frac{1}{M}\sqrt{2 - \sqrt{2}}, \\ \lambda &= \frac{2}{13}. \end{aligned} \tag{5}$$

Other possible choices for (r_0, r_1, λ) can be considered as

$$\begin{aligned} r_0 &= \frac{5M}{16}, \\ r_1 &= \frac{3}{5}48M, \\ \lambda &= \frac{1}{6}. \end{aligned} \tag{6}$$

For $(\omega_0, \dot{\theta}_0) = (1, 0)$, the following approximation is obtained:

$$M = -0.900775\varepsilon\theta_0 + 0.240105\varepsilon + 0.905583\theta_0. \tag{7}$$

Next, we replace the original i.v.p. (3) by the following approximate i.v.p.

$$\begin{cases} \mathbb{R} \equiv \ddot{\theta} + 2\varepsilon\left(r_0\dot{\theta} + r_1\dot{\theta}^3\right) + \omega_0^2\left(\theta - \lambda\theta^3\right) = 0, \\ \theta(0) = \theta_0\theta'(0) = \dot{\theta}_0. \end{cases} \tag{8}$$

Assume that the solutions to the i.v.p. (8) have the following formulas:

$$\begin{aligned} \theta_{\text{Trigon}} &= c_0 \exp(-\rho t)\cos\left(f(t) + \cos^{-1}\left(\frac{\theta_0}{c_0}\right)\right), \\ \theta_{\text{Trigon}} &= c_0 \exp(-\rho t)\sin\left(f(t) + \sin^{-1}\left(\frac{\theta_0}{c_0}\right)\right), \end{aligned} \tag{9}$$

with the initial conditions (ICs)

$$\begin{aligned} f(0) &= 0, \\ \theta(0) &= \theta_0, \\ \theta'(0) &= \dot{\theta}_0, \end{aligned} \tag{10}$$

where the number ρ and the function $f \equiv f(t)$ are chosen in order to get the smallest possible residual error $R(t)$:

$$R(t) = \theta'' + 2\varepsilon\,\theta'\left|\theta'\right| + \omega_0^2\left(\theta - \lambda\theta^3\right). \tag{11}$$

Now by substituting ansatz (9) into the i.v.p. (8), we get

$$\begin{aligned}\mathbb{R} = {} & \mathsf{F}_1 \sin(\phi) + \mathsf{F}_2\cos(\phi) + \mathsf{F}_3\sin(3\phi) \\ & + \mathsf{F}_4\cos(3\phi),\ \sqrt{b^2 - 4ac},\end{aligned} \tag{12}$$

with

$$\begin{aligned}\mathsf{F}_1 &= \frac{1}{2}c_0 e^{-3\varepsilon\rho t}\left[-3c_0^2\varepsilon\left(f'\right)^3 r_1 - \left(3c_0^2\varepsilon^3\rho^2 r_1 + 4\varepsilon r_0 e^{2\varepsilon\rho t}\right.\right. \\ &\quad \left.\left. -4\varepsilon\rho e^{2\varepsilon\rho t}\right)f' - 2\mathrm{f}\prime\prime\mathrm{e}^{2\varepsilon\rho\mathrm{t}}\right], \\ \mathsf{F}_2 &= \frac{1}{4}c_0 e^{-3\varepsilon\rho t}\begin{bmatrix} -\left(6c_0^2\varepsilon^2\rho r_1 + 4e^{2\varepsilon\rho t}\right)\left(f'\right)^2 - 3c_0^2\lambda\omega_0^2 - 6c_0^2\varepsilon^4\rho^3 r_1 \\ -8\varepsilon^2\rho r_0 e^{2\varepsilon\rho t} + 4\varepsilon^2\rho^2 e^{2\varepsilon\rho t} + 4\omega_0^2 e^{2\varepsilon\rho t}\end{bmatrix}, \\ \mathsf{F}_3 &= -\frac{1}{2}c_0^3\varepsilon r_1 e^{-3\varepsilon\rho t}\left(3\varepsilon^2\rho^2 - \left(f'\right)^2\right)f', \\ \mathsf{F}_4 &= -\frac{1}{4}c_0^3 e^{-3\varepsilon\rho t}\left(-6\varepsilon^2\rho r_1\left(f'\right)^2 + \lambda\omega_0^2 + 2\varepsilon^4\rho^3 r_1\right),\end{aligned} \tag{13}$$

where $\phi = f(t) + \cos^{-1}(\theta_0/c_0)$.

For $\mathsf{F}_2 = 0$, we get

$$\begin{aligned}\left(f'\right)^2 &= \frac{4e^{2\varepsilon\rho t}\left(\varepsilon^2\,\rho\left(\rho - 2r_0\right) + \omega_0^2\right) - 3c_0^2\left(\lambda\omega_0^2 + 2\varepsilon^4\rho^3 r_1\right)}{6c_0^2\varepsilon^2\rho r_1 + 4e^{2\varepsilon\rho t}} \\ &= A + \frac{B}{1 + C\,\exp(2\rho\varepsilon t)},\end{aligned} \tag{14}$$

with

$$\begin{aligned}A &= \varepsilon^2\rho\left(\rho - 2r_0\right) + \omega_0^2, \\ B &= -2\varepsilon^2\rho^2 - \omega_0^2\left(\frac{\lambda}{2\varepsilon^2\rho r_1} + 1\right) + 2\varepsilon^2\rho r_0, \\ C &= \frac{2}{3c_0^2\varepsilon^2\rho r_1}.\end{aligned} \tag{15}$$

Integrating equation (14) leads to

$$f = F(t) - F(0), \tag{16}$$

with

$$\begin{aligned}F(t) = \frac{1}{\varepsilon\rho}\Bigg[&\sqrt{A}\tanh^{-1}\left(\frac{\sqrt{A + B/Ce^{2\varepsilon\rho t} + 1}}{\sqrt{A}}\right) \\ &-\sqrt{A + B}\tanh^{-1}\left(\frac{\sqrt{A + B/Ce^{2\varepsilon\rho t} + 1}}{\sqrt{A + B}}\right)\Bigg].\end{aligned} \tag{17}$$

Inserting the value of f given in equation (16) into ansatz (9) and applying the ICs $\theta'(0) = \dot{\theta}_0$, the value of c_0 can be determined from the following quartic equation:

$$\begin{aligned}&4\left(2\varepsilon^2\rho^2\theta_0^2 - 2\varepsilon^2\rho r_0\theta_0^2 + \theta_0^2\omega_0^2 + 2\varepsilon\rho\theta_0\dot{\theta}_0 + \dot{\theta}_0^2\right) \\ &\quad + \left(-4\varepsilon^2\rho^2 + 8\varepsilon^2\rho r_0 - 4\omega_0^2 - 3\lambda\theta_0^2\omega_0^2\right. \\ &\quad \left. + 12\varepsilon^3\rho^2 r_1\theta_0\dot{\theta}_0 + 6\varepsilon^2\rho r_1\dot{\theta}_0^2\right)c_0^2 \\ &\quad + 3\left(2\varepsilon^4\rho^3 r_1 + \lambda\omega_0^2\right)c_0^4 = 0.\end{aligned} \tag{18}$$

Solution (9) θ_{Trigon} is presented in Figures 1(a) and 1(b) for $\theta_0 = 0$ and $\theta_0 = \pi/6$ at $(\varepsilon, \omega_0, \dot{\theta}_0) = (0.2, 1, 0.1)$. Moreover, in the same figure, solution (9) is compared to the RK numerical approximation and the maximum distance error according to the following relation is calculated:

$$\text{Error} \equiv L_\infty = \max_{0\le t\le T}\left|\mathrm{RK} - \theta_{\mathrm{Trigon}}\right|. \tag{19}$$

The maximum distance error according to relation (19) for $\theta_0 = 0$ and $\theta_0 = \pi/6$ at $(\varepsilon, \omega_0, \dot{\theta}_0) = (0.2, 1, 0.1)$ is, respectively, estimated as

$$\begin{aligned}L_\infty|_{\theta_0=0} &= 0.00515945, \\ L_\infty|_{\theta_0=\frac{\pi}{6}} &= 0.0511852.\end{aligned} \tag{20}$$

It is noted that the accuracy of solution (9) becomes good and acceptable for small θ_0, but for large value of θ_0, the accuracy of solution (9) reduces as shown in Figure 1.

Also, the maximum residual error is defined as

$$E_T(\theta) = \max_{0\le t\le T}\left|\theta''(t) + 2\varepsilon\,\theta'(t)\left|\theta'(t)\right| + \omega_0^2\sin(\theta(t))\right|. \tag{21}$$

This is another form for the error to check the accuracy of the obtained approximations.

2.2. Second Approach: HKBMM. Let us consider the i.v.p.

$$\left\{\ddot{x} + \omega_0^2 x = F(t, x, \dot{x}), x(0) = x_0 \text{ and } x'(0) = \dot{x}_0 \text{ for } 0 \le t \le T.\right. \tag{22}$$

Suppose that the physical problem described by (22) involves some small parameters $\varepsilon_1, \varepsilon_2, \ldots, \varepsilon_r$. Let $x \equiv x(t)$ be the solution to the i.v.p. (22) and assume that

$$F(t, x, \dot{x}) \equiv 0 \text{ when } \varepsilon_1 = \varepsilon_2 = \ldots = \varepsilon_r = 0. \tag{23}$$

The solution $x \equiv x(t)$ depends not only on t but also on the parameters $\varepsilon_1, \varepsilon_2, \ldots, \varepsilon_r$, so that we can rewrite $x \equiv x(t)$ as

$$x = x\left(t; \varepsilon_1, \varepsilon_2, \ldots, \varepsilon_r\right). \tag{24}$$

Let us multiply each parameter by some other parameter p and consider the following p–parametric solution:

$$x_p = x_p\left(t; p\varepsilon_1, p\varepsilon_2, \ldots, p\varepsilon_r\right). \tag{25}$$

Accordingly, the function x_p may be written in a power series as follows:

$$x_p = u_0 + pu_1 + p^2u_2 + \cdots, \tag{26}$$

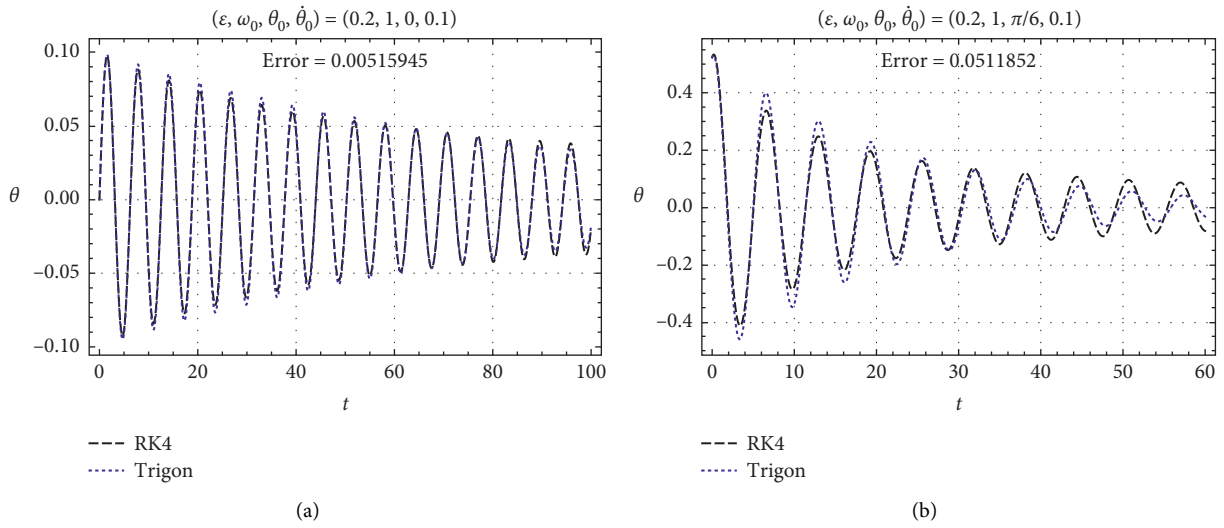

Figure 1: Both trigonometric solution (9) and RK numerical approximation are plotted in (θ, t)−plane.

where u_k depends on t only, say $u_k = u_k(t)$.

Based on Krylov–Bogoliubov–Mitropolsky method (KBMM), the solution of equation (22) is assumed to be

$$x_p = a\cos(\psi) + \sum_{n=1}^{N} p^n u_n(a,\psi) + O\left(p^{N+1}\right), \tag{27}$$

where each u_n is a periodic function of ψ and a and ψ are assumed to vary with time according to

$$\frac{da}{dt} \equiv \dot{a} = \sum_{n=1}^{N} p^n A_n(a) + O\left(p^{N+1}\right), \tag{28}$$

$$\frac{d\psi}{dt} \equiv \dot{\psi} = \omega_0 + \sum_{n=1}^{N} p^n \psi_n(a) + O\left(p^{N+1}\right), \tag{29}$$

where $a \equiv a(t)$ and $\psi \equiv \psi(t)$.

Moreover, the hybrid homotopy KBMM (HKBMM) is suggested to be

$$H\left(x_p, t\right) = \ddot{x}_p + \omega_0^2 x_p - pF\left(t, x_p, \dot{x}_p\right). \tag{30}$$

The next step is to write the residual $H_p(x,t)$ as a power series in p:

$$H\left(x_p, t\right) = \ddot{x}_p + \omega_0^2 x_p + p\Upsilon_1 + p^2\Upsilon_2 + p^3\Upsilon_3 + \cdots. \tag{31}$$

For the determination of the unknown functions u_n, ψ_n, A_n, and a, we equate to zero the coefficients Υ_n in equation (22) and then we can get a system of ODEs. To avoid the so-called secularity, we choose only the solutions that do not contain $\cos\psi$ nor $\sin\psi$. For $N = 2$ (the first approximation), we may use the following formulas (we neglected all terms containing p^j for $j \geq 2$):

$$\begin{aligned}
\dot{x} &= p\left(\omega_0 u_{1,\psi} - a\psi_1 \sin(\psi) + A_1\cos(\psi)\right) - a\omega_0\sin(\psi),\\
x &= p\left(\omega_0^2 u_{1,\psi,\psi} - 2a\psi_1\omega_0\cos(\psi)\right.\\
&\quad \left. -2A_1\omega_0\sin(\psi)\right) - a\omega_0^2\cos(\psi),\\
x^2 &= \frac{1}{2}a^2\cos(2\psi) + \frac{a^2}{2} + 2apu_1\cos(\psi),\\
x^3 &= \frac{3}{4}a^3\cos(\psi) + \frac{1}{4}a^3\cos(3\psi) + p\left(\frac{3}{2}a^2u_1\cos(2\psi) + \frac{3a^2u_1}{2}\right),\\
x^4 &= \frac{1}{2}a^4\cos(2\psi) + \frac{1}{8}a^4\cos(4\psi) + \frac{3a^4}{8}\\
&\quad + p\left(3a^3u_1\cos(\psi) + a^3u_1\cos(3\psi)\right),\\
x^5 &= \frac{5}{8}a^5\cos(\psi) + \frac{5}{16}a^5\cos(3\psi) + \frac{1}{16}a^5\cos(5\psi)\\
&\quad + p\left(\frac{5}{2}a^4u_1\cos(2\psi) + \frac{5}{8}a^4u_1\cos(4\psi) + \frac{15a^4u_1}{8}\right),
\end{aligned} \tag{32}$$

and

$$x\dot{x} = p\begin{pmatrix} a\omega_0\cos(\psi)u_{1,\psi} + a^2\psi_1\sin(\psi)(-\cos(\psi)) \\ \\ +\frac{1}{2}aA_1\cos(2\psi) + \frac{aA_1}{2} - au_1\omega_0\sin(\psi) \end{pmatrix}, -a^2\omega_0\sin(\psi)\cos(\psi),$$

$$\dot{x}^2 = p\begin{pmatrix} -2a\omega_0^2 \sin(\psi)u_{1,\psi} + a^2\psi_1\omega_0 \\ +a^2\psi_1\omega_0(-\cos(2\psi)) - aA_1\omega_0 \sin(2\psi) \end{pmatrix} - \frac{1}{2}a^2\omega_0^2 \cos(2\psi) + \frac{1}{2}a^2\omega_0^2,$$

$$\dot{x}^3 = p\begin{pmatrix} \frac{3}{2}a^2\omega_0^3 u_{1,\psi} - \frac{3}{2}a^2\omega_0^3 \cos(2\psi)u_{1,\psi} \\ -\frac{9}{4}a^3\psi_1\omega_0^2 \sin(\psi) + \frac{3}{4}a^3\psi_1\omega_0^2 \sin(3\psi) \\ +\frac{3}{4}a^2A_1\omega_0^2 \cos(\psi) - \frac{3}{4}a^2A_1\omega_0^2 \cos(3\psi) \end{pmatrix} - \frac{3}{4}a^3\omega_0^3 \sin(\psi) + \frac{1}{4}a^3\omega_0^3 \sin(3\psi),$$

$$x^2\dot{x} = p\begin{pmatrix} \frac{1}{2}a^2\omega_0 u_{1,\psi} + \frac{1}{2}a^2\omega_0 \cos(2\psi)u_{1,\psi} - \frac{1}{4}a^3\psi_1 \sin(\psi) \\ -\frac{1}{4}a^3\psi_1 \sin(3\psi) + \frac{3}{4}a^2A_1 \cos(\psi) \\ +\frac{1}{4}a^2A_1 \cos(3\psi) - a^2u_1\omega_0 \sin(2\psi) \end{pmatrix} - \frac{1}{4}a^3\omega_0 \sin(\psi) - \frac{1}{4}a^3\omega_0 \sin(3\psi), \tag{33}$$

with

$$\begin{aligned} u_{1,\psi,\psi} &= \partial_\psi^2 u_1, \\ u_{1,\psi} &= \partial_\psi u_1. \end{aligned} \tag{34}$$

The approximate analytical solution is obtained by putting $p = 1$. However, we may keep the parameter p and then we may use it as a residual minimization parameter. The optimal value to p will be near $p = 1$.

Now, the proposed method can be applied for investigating the i.v.p. (8):

$$\begin{cases} \ddot{\theta} + \omega_0^2\theta = F(t, \theta, \dot{\theta}), \\ \theta(0) = \theta_0 \text{ and } \theta'(0) = \dot{\theta}_0, \end{cases} \tag{35}$$

where in our case, $x = \theta$ and

$$F(t, \theta, \dot{\theta}) = -2\varepsilon\left(r_0\dot{\theta} + r_1\dot{\theta}^3\right) + \lambda\omega_0^2\theta^3. \tag{36}$$

Observe that when $\varepsilon_1 = \varepsilon \longrightarrow 0$ and $\varepsilon_2 = \lambda \longrightarrow 0$, we get $F = 0$.

In equations (27)–(29), for $N = 1$ and $\lambda = 2/13$, we have

$$\begin{aligned} x_p &= a\cos(\psi) + pu_1(a, \psi), \\ \dot{a} &= A_1(a), \\ \dot{\psi} &= \omega_0 + \psi_1(a). \end{aligned} \tag{37}$$

The homotopy to equation (35) is written as

$$H_p(\theta, t) = \ddot{\theta}_p + \omega_0^2\theta_p - p\left[-2\varepsilon\left(r_0\dot{\theta} + r_1\dot{\theta}^3\right) + \frac{2}{13}\omega_0^2\theta^3\right]. \tag{38}$$

The substitution of equation (37) into equation (38) leads to

$$\begin{aligned} H_p(\theta, t) = \Big[&\frac{1}{4}\left(4\omega_0^2u_{1,\psi,\psi} + 4u_1\omega_0^2\right) \\ &+ \frac{1}{4}\left(-3a^3\lambda\omega_0^2 - 8a\psi_1\omega_0\right)\cos(\psi) \\ &+ \frac{1}{4}\left(-6a^3\varepsilon r_1\omega_0^3 - 8a\varepsilon r_0\omega_0 - 8A_1\omega_0\right)\sin(\psi) \\ &- \frac{1}{4}a^3\lambda\omega_0^2 \cos(3\psi) + \frac{1}{2}a^3\varepsilon r_1\omega_0^3 \sin(3\psi)\Big]p + \cdots. \end{aligned} \tag{39}$$

We must have

$$\begin{aligned} &\frac{1}{4}\left(4\omega_0^2u_{1,\psi,\psi} + 4u_1\omega_0^2\right) \\ &+ \frac{1}{4}\left(-3a^3\lambda\omega_0^2 - 8a\psi_1\omega_0\right)\cos(\psi) \\ &+ \frac{1}{4}\left(-6a^3\varepsilon r_1\omega_0^3 - 8a\varepsilon r_0\omega_0 - 8A_1\omega_0\right)\sin(\psi) \\ &- \frac{1}{4}a^3\lambda\omega_0^2 \cos(3\psi) + \frac{1}{2}a^3\varepsilon r_1\omega_0^3 \sin(3\psi) = 0. \end{aligned} \tag{40}$$

The coefficients of $\cos(\psi)$ and $\sin(\psi)$ must be vanished to eliminate the secularity. Accordingly, we have

$$\begin{aligned} \psi_1(a) &= -\frac{3}{52}a^2\omega_0, \\ A_1(a) &= -\frac{3}{4}a^3\varepsilon r_1\omega_0^2 - a\varepsilon r_0. \end{aligned} \tag{41}$$

Thus, equation (40) reduces to

$$\begin{aligned} &\frac{1}{4}\left(4\omega_0^2u_{1,\psi,\psi} + 4u_1\omega_0^2\right) + \frac{1}{4}a^3\lambda\omega_0^2 \cos(3\psi) \\ &+ \frac{1}{2}a^3\varepsilon r_1\omega_0^3 \sin(3\psi) = 0. \end{aligned} \tag{42}$$

Solving equation (42), the following particular solution without any secularity terms is obtained:

$$u_1(a, \psi) = -\frac{1}{208}a^3\left(\cos(3\psi) - 13\varepsilon r_1\omega_0 \sin(3\psi)\right). \tag{43}$$

From equations (37) and (41), the functions $a \equiv a(t)$ and $\psi \equiv \psi(t)$ can be determined:

$$\begin{cases} \dot{a} = -\frac{3}{4}\varepsilon r_1 \omega_0^2 a^3 - \varepsilon r_0 a, \\ \dot{\psi} = \omega_0 - \frac{3}{52}\omega_0 a^2. \end{cases} \tag{44}$$

By solving system (44), we get

$$a = \frac{2\sqrt{r_0/3r_1}}{\sqrt{\left(1 + 4r_0/3A^2 r_1 \omega_0^2\right)e^{2t\varepsilon r_0} - 1} \cdot \omega_0}, \tag{45}$$

and

$$\psi = \left(\omega_0 + \frac{r_0}{13\omega_0 r_1}\right)t + B - \frac{1}{26\varepsilon r_1 \omega_0}\log \left(e^{2\varepsilon\rho r_0 t} + \frac{3A^2 r_1 \omega_0^2}{4r_0}\left(e^{2t\varepsilon r_0 t} - 1\right)\right). \tag{46}$$

We finally get the analytical approximation in its first approximation ($p = 1$).

$$\theta = a\cos(\psi) - \frac{1}{208}a^3\left(\cos(3\psi) - 13\varepsilon r_1 \omega_0 \sin(3\psi)\right). \tag{47}$$

We now introduce three optimization parameters by replacing $(\varepsilon, \psi) = (\rho\varepsilon, \kappa\psi)$ and then the approximation (47) can be modified to be

$$\theta(p, \rho, \kappa) = a_\rho \cos\left(\psi_{\rho,\kappa}\right) - \frac{p}{208}{a_\rho}^3 \left(\cos\left(3\psi_{\rho,\kappa}\right) - 13\varepsilon r_1 \omega_0 \sin\left(3\psi_{\rho,\kappa}\right)\right), \tag{48}$$

with

$$a_\rho = \frac{2\sqrt{r_0/3r_1}}{\sqrt{\left(1 + 4r_0/3A^2 r_1 \omega_0^2\right)e^{2t\varepsilon\rho r_0} - 1}\omega_0}, \tag{49}$$

and

$$\psi_{\rho,\kappa} = \kappa\left(\omega_0 t + B - \frac{\log\left(e^{2\varepsilon\rho r_0 t} + 3A^2 r_1 \omega_0^2/4r_0\left(e^{2t\varepsilon\rho r_0 t} - 1\right)\right) - 2\varepsilon\rho r_0 t}{26\varepsilon\rho r_1 \omega_0}\right). \tag{50}$$

The numbers ρ, κ, and p are free parameters that we choose in order to minimize the residual error

$$R(t) = \theta''(t) + 2\varepsilon\,\theta'(t)\left|\theta'(t)\right| + \omega_0^2 \sin\,\theta(t). \tag{51}$$

The default parameter values are $\rho = \kappa = p = 1$. The constants A and B are determined from the initial conditions (ICs) $\theta(0) = \theta_0$ and $\theta'(0) = \theta_0$.

Following the same procedure above, we can get some higher-order approximations. For example, for $N = 3$, the following solution is obtained:

$$\theta = a\cos(\psi) + S_1 a^3 + S_2 a^5 + S_3 a^7, \tag{52}$$

where the coefficients $S_{1,2,3}$ are defined in Appendix. The values of (a, ψ) associated to this solution can be determined from the following equations:

$$\dot{a} = -\varepsilon r_0 a - \frac{3}{52}\varepsilon\left(r_0 + 13r_1\omega_0^2\right)a^3 - \frac{3\varepsilon\left(5r_0 - 16r_1\omega_0^2 + 429\varepsilon^2 r_0 r_1^2 \omega_0^2\right)}{1664}a^5 - \frac{27\varepsilon r_1 \omega_0^2\left(21 + 2197\varepsilon^2 r_1^2 \omega_0^2\right)}{173056}a^7, \tag{53}$$

and

$$\dot{\psi} = \omega_0 - \frac{\varepsilon^2 r_0^2}{2\omega_0} + \frac{3\left(\varepsilon^2 r_0^2 - 2\omega_0^2\right)}{104\omega_0}a^2 + \frac{3\omega_0\left(494\varepsilon^2 r_0 r_1 + 507\varepsilon^2 r_1^2 \omega_0^2 - 5\right)}{10816}a^4 + \frac{3\omega_0\left(37687\varepsilon^2 r_1^2 \omega_0^2 - 41\right)}{2249728}a^6. \tag{54}$$

The approximate solution of the i.v.p. (35) using the HKBMM is introduced in Figures 2(a) and 2(b) for $\theta_0 = 0$ and $\theta_0 = \pi/6$. Also, the maximum distance error L_∞ is estimated for the two cases as follows:

$$\begin{aligned} L_\infty|_{\theta_0 = 0} &= 0.00145602, \\ L_\infty|_{\theta_0 = \frac{\pi}{6}} &= 0.0209098. \end{aligned} \tag{55}$$

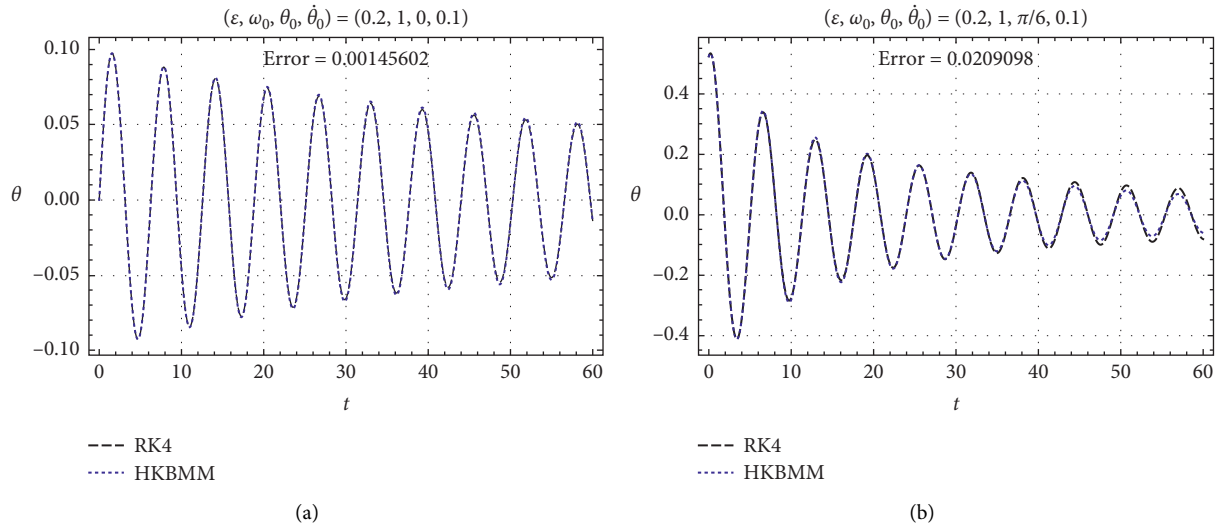

Figure 2: The approximate solutions using both HKBMM and RK numerical method are plotted in $(\theta, t)-$ plane.

It is observed that approximate solution of the i.v.p. (35) using the HKBMM is characterized by high accuracy and more stability for long time and for arbitrary values of θ_0. Also, this approximation is better than the trigonometric solution (9) θ_{Trigon} as shown from Figures 1 and 2 as well as from the values of the errors.

3. Numerical Solution

In this section, some effective and highly accurate numerical schemes will be introduced for analyzing evolution equation (3). Both the finite difference method (FDM) and Galerkin Hats method (GHM) are presented below.

3.1. Numerical Approximation via FDM. First, let us discuss and apply the FDM on the general second-order ODE. Thus, the following general second-order is introduced:

$$\left\{ \ddot{x} = F(t, x, \dot{x}), x(0) = x_0,\ x'(0) = \dot{x}_0 \text{ and } 0 \le t \le T. \right. \tag{56}$$

Choose some positive integer $n \ge 6$ and divide the interval $[0, T]$ into n-subintervals by means of the knots $t_i = ih$, where $h = T/n/(i = 0, 1, 2, \ldots, n)$. Then, the first and second-order derivatives can be approximated as follows:

$$x'(t_i) \approx \frac{-12x_{i-5} + 75x_{i-4} - 200x_{i-3} + 300x_{i-2} - 300x_{i-1} + 137x_i}{60h},$$
$$x''(t_i) \approx \frac{-10x_{i-5} + 61x_{i-4} - 156x_{i-3} + 214x_{i-2} - 154x_{i-1} + 45x_i}{12h^2}. \tag{57}$$

Consequently, the following discrete version to ODE (56) for $i = 5, 6, \ldots$ is obtained:

$$\frac{-10x_{i-5} + 61x_{i-4} - 156x_{i-3} + 214x_{i-2} - 154x_{i-1} + 45x_i}{12h^2} = F\left(t_i, x_i, \frac{-12x_{i-5} + 75x_{i-4} - 200x_{i-3} + 300x_{i-2} - 300x_{i-1} + 137x_i}{60h}\right). \tag{58}$$

The values of x_1, x_2, x_3, and x_4 are obtained from some numerical or approximate analytical solution to the i.v.p. (56). System (58) may be solved recursively.

The above algorithm can be applied for analyzing the i.v.p. (note here $\theta(t) \equiv x(t)$ without loss of generality):

$$\begin{cases} \ddot{\theta} = F(t, \theta, \dot{\theta}), \\ \theta(0) = \theta_0 \& \theta'(0) = \dot{\theta}_0, \end{cases} \tag{59}$$

with

$$F(t, \theta, \dot{\theta}) = -2\varepsilon\, \dot{\theta}|\dot{\theta}| - \omega_0^2 \sin\, \theta. \tag{60}$$

The numerical approximation using FDM is plotted in Figures 3 and 4 for different values of (n, θ_0). In Figures 3(a) and 3(b), the FDM numerical approximation is plotted against $n = 150$ and $n = 300$, respectively. Moreover, the effect of θ_0 on the numerical approximation is illustrated in Figures 4(a) and 4(b) for $\theta_0 = 0$ and $\theta_0 = \pi/6$, respectively. Furthermore, the maximum distance error is calculated for all mentioned cases as follows:

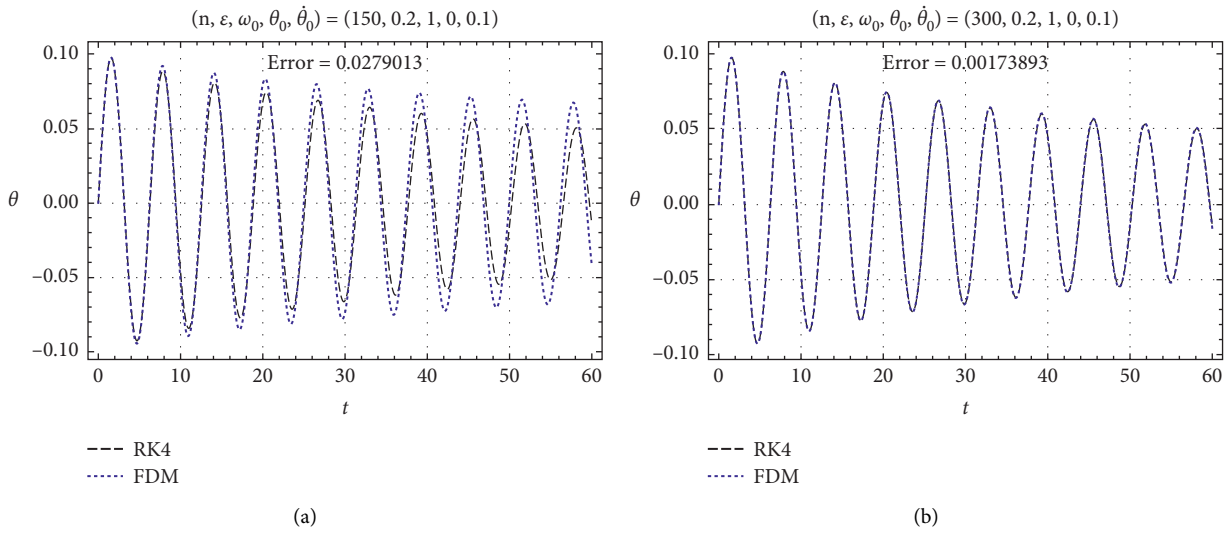

Figure 3: The approximate solutions using both FDM and RK numerical method are plotted in (θ, t)−plane for (a) $(n, \theta_0) = (150, 0)$ and (b) $(n, \theta_0) = (300, 0)$.

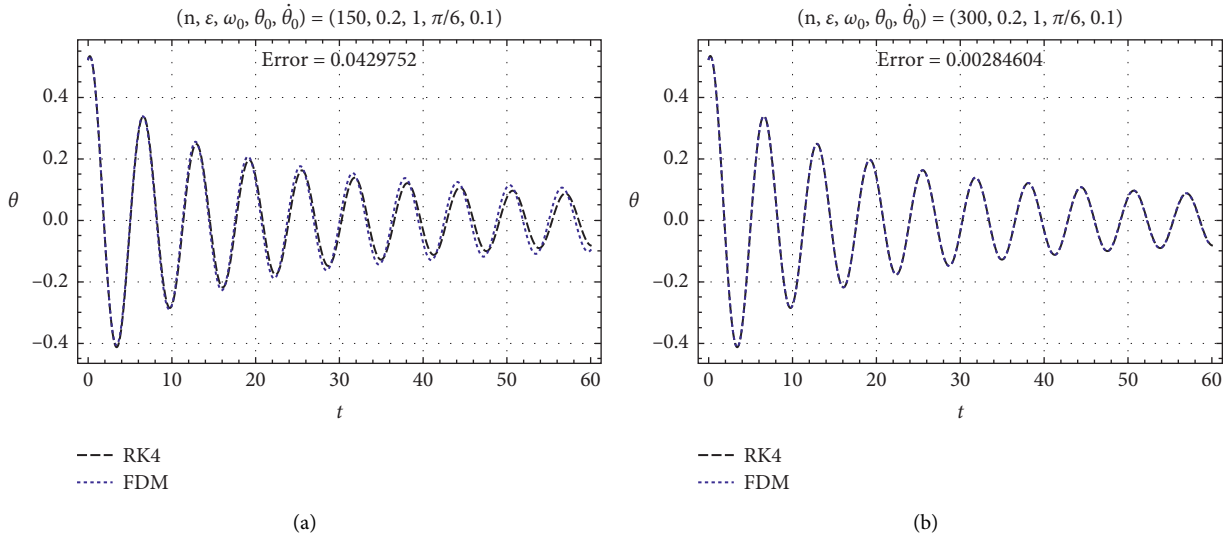

Figure 4: The approximate solutions using both FDM and RK numerical method are plotted in (θ, t)−plane for (a) $(n, \theta_0) = (150, \pi/6)$ and (b) $(n, \theta_0) = (300, \pi/6)$.

$$
\begin{aligned}
L_\infty &= 0.0279013, \text{for}\,(n, \theta_0) = (150, 0),\\
L_\infty &= 0.00173893, \text{for}\,(n, \theta_0) = (300, 0),\\
L_\infty &= 0.0429752, \text{for}\,(n, \theta_0) = \left(150, \frac{\pi}{6}\right),\\
L_\infty &= 0.00284604, \text{for}\,(n, \theta_0) = \left(300, \frac{\pi}{6}\right).
\end{aligned}
\tag{61}
$$

It is clear that the accuracy of the FDM numerical approximation increases with increasing n. Also, this approximation is stable against the long time intervals and arbitrary angle θ_0. Moreover, this approximation is better than the trigonometric solution (9) θ_{Trigon}.

3.2. Numerical Approximation via Galerkin Hats Method. First, let us consider a polynomial second-order forced damped i.v.p.

$$
\left\{ \ddot{x} + 2\varepsilon\dot{x} + P(x) = 0, x(0) = 0 \text{and}\, x'(0) = \dot{x}_0, \right. \tag{62}
$$

where $x \equiv x(t)$.

Let us consider the i.v.p.

$$\{\ddot{y} + 2\varepsilon\dot{y} + P(y) = 0, y(0) = y_0 \text{ and } y'(0) = \dot{y}_0. \quad (63)$$

Suppose that $x = x(t; c_1)$ is the solution to the i.v.p.

$$\{\ddot{x} + 2\varepsilon\dot{x} + P(x) = 0,\ x(0) = 0 \text{ and } x'(0) = c_1. \quad (64)$$

Define

$$y(t) = x(t + c_0; c_1). \quad (65)$$

The constants c_0 and c_1 are determined from the system

$$x(0 + c_0; c_1) = y_0 \text{ and } x'(0 + c_0; c_1) = \dot{y}_0. \quad (66)$$

Thus, problemproblem (61) reduces to (60) by problem (63) reduces to (62).

Some particular cases to the i.v.p. (62) are defined as

$$\{\ddot{x} + 2\varepsilon\dot{x} + n(t) + p(t)x = f(t), \ddot{x} + 2\varepsilon\dot{x} + n(t) + p(t)x + q(t)x^2 = f(t), \ddot{x} + 2\varepsilon\dot{x} + n(t) + p(t)x + q(t)x^2 + r(t)x^3 = f(t). \quad (67)$$

We will use the same idea for the linear case.

Here, we start to discuss the linear case in system (67):

$$\{\ddot{x} + 2\varepsilon\dot{x} + p(t)x = 0,\ x(0) = 0 \text{ and } x'(0) = \dot{x}_0. \quad (68)$$

An approximate solution to the i.v.p. (68) is assumed to be in the following ansatz form:

$$x = \sum_{k=1}^{n} c_k \varphi_k(t), \quad (69)$$

where the functions $\varphi_k(t)$ are the so-called linear Galerkin hats.

Let us investigate the present problem in the interval $0 \le t \le T$ and by choosing some positive integer $n \ge 2$ and define the step $h = T/n$ and let $\xi_j = jh = jT/n$ for $j = 0, 1, 2, \cdots$. The functions $\varphi_k(t)$ for $k = 1, 2, \ldots, n$ are defined as

$$\varphi_k(t) = \begin{cases} c\dfrac{t - \xi_{k-1}}{h}, & \text{if } \xi_{k-1} \le t \le \xi_k, \\ -\dfrac{t - \xi_{k+1}}{h}, & \text{if } \xi_k \le t \le \xi_{k+1}. \end{cases} \quad (70)$$

For an illustration, see Figure 1.

Figure 1 Galerkin hats for $n = 7$ and $T = 5$.

Some properties of these functions can be illustrated as follows:

$$\varphi_j(t)\varphi_k(t)dt = 0, \quad (71)$$

for $|j - k| \ge 2$ and $t \in [0, T]$, and

$$\int_0^T \varphi_j^p(t) = \frac{2T}{(p+1)n}, \quad (72)$$

for $j \ge 1$ and $p = 1, 2, 3, \ldots$.

In general, for $|j - k| = 1$ and $r, s = 0, 1, 2, 3, \cdots$, we have

$$\int_0^T \varphi_j^r(t)\varphi_k^s(t) = \frac{\mathrm{Tr!}s!}{n(r + s + 1)!}. \quad (73)$$

Using the formula

$$\int_0^T \varphi_j(t)x(t)^N dt = \frac{h}{(N+1)(N+2)} \left(\sum_{k=0}^{N-1} (k+1)\left(c_{j-1}^{N-k} + c_{j+1}^{N-k}\right)c_j^k + 2(N+1)c_j^N \right), \quad (74)$$

for any $N \ge 0$ and $c_0 = c_{n+1} = 0$, and assuming that $a_j(t) \equiv a_j = \text{const}$, we may evaluate easily the following integration:

$$\int_0^T P(x)\varphi_j(t)dt = \sum_{N=0}^{m} a_N \int_0^T \varphi_j(t)x(t)^N dt \text{ for any } j,$$

$$\int_0^T x\prime\prime(t)\varphi_j(t)dt = -\int_0^T x\prime(t)\varphi_j'(t)dt = \frac{c_{j-1} - 2c_j + c_{j+1}}{h} \text{ for any } j,$$

$$\int_0^T x'(t)|x'(t)|\varphi_j(t)dt = \frac{n}{2T}\left[\sqrt{\left(c_{j-1} - c_{j-2}\right)^2} + \sqrt{\left(c_j - c_{j-1}\right)^2}\right]. \quad (75)$$

Now, let us return to the original i.v.p. (3):

$$\begin{cases} \ddot{\theta} + 2\varepsilon\dot{\theta}|\dot{\theta}| + \omega_0^2 \sin\theta = 0, \\ \theta(0) = 0 \text{and } \theta'(0) = \dot{\theta}_0. \end{cases} \quad (76)$$

Using the Chebyshev approximation,

$$\sin\theta \approx \theta - \frac{4}{0}241\theta^3 + \frac{\theta^5}{131} \text{ for } |\theta| \le \frac{\pi}{2}. \quad (77)$$

Another approximation may be obtained by minimizing the integral

$$\int_{-\frac{\pi}{2}}^{\frac{\pi}{2}} \left(a\theta + b\theta^3 + c\theta^5 - \sin\theta\right)^2 d\theta \longrightarrow \min. \quad (78)$$

The minimization procedure yields the values

$$\min = \frac{\pi}{2} - \frac{3360\left(11975040 - 2661120\pi^2 + 171720\pi^4 - 2664\pi^6 + 13\pi^8\right)}{\pi^{11}} \approx 5.5 \times 10^{-9}, \quad (79)$$

with

$$a = \frac{105\left(23760 - 2592\pi^2 + 19\pi^4\right)}{\pi^7} = 0.99977,$$
$$b = -\frac{2520\left(18480 + 17\pi^2\left(\pi^2 - 120\right)\right)}{\pi^9} = -0.16583, \quad (80)$$
$$c = \frac{166320\left(1008 - 112\pi^2 + \pi^4\right)}{\pi^{11}} = 7.5742 \times 10^{-3},$$

$$\sin\theta \approx \theta - \frac{1}{6}\theta^3 + \frac{\theta^5}{132}.$$

Then, i.v.p. (76) can be reduced to the following approximate i.v.p.

$$\begin{cases} \ddot{\theta} + 2\varepsilon\dot{\theta}|\dot{\theta}| + \omega_0^2\left(\theta - \frac{4}{0}241\theta^3 + \frac{\theta^5}{131}\right) = 0, \\ \theta(0) = 0 \text{and} \theta'(0) = \dot{\theta}_0. \end{cases} \quad (81)$$

Assume that the solution to i.v.p. (81) is given by

$$\theta = \sum_{k=1}^{n} c_k \varphi_k(t). \quad (82)$$

The Galerkin method solves the following algebraic system of nonlinear equations:

$$\frac{n}{T}\left(c_{j-2} - 2c_{j-1} + c_j\right) + \frac{n}{T} \left(\sqrt{\left(c_{j-2} - c_{j-1}\right)^2} + \sqrt{\left(c_j - c_{j-1}\right)^2}\right)\varepsilon + \omega_0^2 S_j = 0, \quad (83)$$

with

$$\begin{aligned} S_j = {} & \frac{T\omega_0^2}{5544n}c_j^5 + \frac{T\omega_0^2 c_{j-1}}{2772n}c_j^4 + \frac{T\omega_0^2\left(5c_{j-1}^2 - 77\right)}{9240n}c_j^3 \\ & + \frac{T\omega_0^2 c_{j-1}\left(10c_{j-1}^2 - 231\right)}{13860n}c_j^2 + \frac{T\omega_0^2\left(25c_{j-1}^4 - 693c_{j-1}^2 + 4620\right)}{27720n}c_j \\ & + \frac{T\omega_0^2}{27720n}\begin{pmatrix} 5c_{j-2}^5 + 10c_{j-1}c_{j-2}^4 + 3\left(5c_{j-1}^2 - 77\right)c_{j-2}^3 \\ +\left(20c_{j-1}^3 - 462c_{j-1}\right)c_{j-2}^2 + \left(25c_{j-1}^4 - 693c_{j-1}^2 + 4620\right)c_{j-2} \\ +12c_{j-1}\left(5c_{j-1}^4 - 154c_{j-1}^2 + 1540\right) \end{pmatrix}, \end{aligned} \quad (84)$$

for $j = 2, 3, \ldots$, where $c_0 = 0$ and $c_1 = T/n\dot{\theta}_0$. System (83) can be solved recursively.

For $j = 2$, the value of c_2 can be determined from the following quintic equation:

$$\begin{aligned} & \frac{2310n^6\varepsilon\left|\dot{\theta}_0\right| - 4620n^6\dot{\theta}_0 \mp 2310n^6\varepsilon\dot{\theta}_0 + 1540n^4T^2\omega_0^2\dot{\theta}_0 - 154n^2T^4\omega_0^2\dot{\theta}_0^3 + 5T^6\omega_0^2\dot{\theta}_0^5}{2310n^6} \\ & + \frac{27720n^6 \pm 27720n^6\varepsilon + 4620n^4T^2\omega_0^2 - 693n^2T^4\omega_0^2\dot{\theta}_0^2 + 25T^6\omega_0^2\dot{\theta}_0^4}{27720n^5T}c_2 - \frac{T^2\omega_0^2\dot{\theta}_0\left(231n^2 - 10T^2\dot{\theta}_0^2\right)}{13860n^4}c_2^2 \\ & - \frac{T\omega_0^2\left(77n^2 - 5T^2\dot{\theta}_0^2\right)}{9240n^3}c_2^3 + \frac{T^2\omega_0^2\dot{\theta}_0}{2772n^2}c_2^4 + \frac{T\omega_0^2}{5544n}c_2^5 = 0. \end{aligned} \quad (85)$$

We choose the real root to equation (86) that is closest to c_1. Suppose we already found the values c_2, c_3,..., c_{k-1} for some $k \geq 2$. Then, the value of c_k is found by solving the quintic in equation (82) by letting $j = k$. However, since $\sqrt{(c_k - c_{k-1})^2} = \pm(c_k - c_{k-1})$, we must solve two quintics in c_k. We choose the real root to the two quintics that is closest to c_{k-1}. Let us introduce the quintic

$$\lambda_5 c_k^5 + \lambda_4 c_k^4 + \lambda_3 c_k^3 + \lambda_2 c_k^2 + \lambda_1 c_k + \lambda_0 = 0, \tag{86}$$

Any of the two quintics (82) for $j = k$. Then, for sufficiently large n, the value of c_k may be estimated by means of the formula

$$\begin{aligned} z \approx z_0 - & \frac{\left(\lambda_1 + 5\lambda_5 z_0^4 + 4\lambda_4 z_0^3 + 3\lambda_3 z_0^2 + 2\lambda_2 z_0\right)}{\lambda_1^2 - \lambda_0\lambda_2 + 15\lambda_5^2 z_0^8 + 24\lambda_4\lambda_5 z_0^7 + 10\lambda_4^2 z_0^6} \\ & \left(\lambda_0 + \lambda_5 z_0^5 + \lambda_4 z_0^4 + \lambda_3 z_0^3 + \lambda_2 z_0^2 + \lambda_1 z_0\right) \\ & +17\lambda_3\lambda_5 z_0^6 + 15\lambda_3\lambda_4 z_0^5 + 9\lambda_2\lambda_5 z_0^5 + 6\lambda_3^2 z_0^4 \\ & +9\lambda_2\lambda_4 z_0^4 + 8\lambda_2\lambda_3 z_0^3 + 2\lambda_1\lambda_4 z_0^3 \\ & -10\lambda_0\lambda_5 z_0^3 + 3\lambda_2^2 z_0^2 + 3\lambda_1\lambda_3 z_0^2 \\ & -6\lambda_0\lambda_4 z_0^2 + 3\lambda_1\lambda_2 z_0 - 3\lambda_0\lambda_3 z_0 \end{aligned} \tag{87}$$

where $z_0 = c_{k-1}$.

For arbitrary ICs, i.e., for any values to $(\theta_0, \dot{\theta}_0)$, the following ansatz is assumed:

$$\theta(t) = \theta_0\varphi_0(t) + \frac{T}{n}\dot{\theta}_0\varphi_2(t) + \sum_{k=2}^{n} c_k\varphi_k(t). \tag{88}$$

Then, we get

$$\int_0^T \varphi_j(t)\theta''(t)dt = \frac{n\left(c_{j-2} - 2c_{j-1} + c_j\right)}{T}, \tag{89}$$

and

$$\begin{aligned} 2\varepsilon\int_0^T \varphi_j(t)\theta'(t)\left|\theta'(t)\right|dt = \frac{\varepsilon n}{T}\Big(&\left(c_j - c_{j-1}\right)^2\operatorname{sgn}\left(c_j - c_{j-1}\right) \\ &-\left(c_{j-2} - c_{j-1}\right)^2\operatorname{sgn}\left(c_{j-2} - c_{j-1}\right)\Big). \end{aligned} \tag{90}$$

Using the approximation

$$\sin\theta \approx \theta - \frac{1}{6}\theta^3 + \frac{1}{132}\theta^5, \tag{91}$$

gives

$$\int_0^T \varphi_j(t)\sin(\theta(t))dt \approx \frac{T\omega_0^2}{27720n}\begin{pmatrix} 5c_{j-2}^5 - 231c_{j-2}^3 + 4620c_{j-2} + 60c_{j-1}^5 + 5c_j^5 - 231c_j^3 + 4620c_j + \\ 25c_{j-1}^4\left(c_{j-2} + c_j\right) + 4c_{j-1}^3\left(5c_{j-2}^2 + 5c_j^2 - 462\right) + \\ 3c_{j-1}^2\left(5c_{j-2}^3 - 231c_{j-2} + 5c_j^3 - 231c_j\right) + \\ 2c_{j-1}\left(5c_{j-2}^4 - 231c_{j-2}^2 + 5c_j^4 - 231c_j^2 + 9240\right) \end{pmatrix}. \tag{92}$$

The following definitions are used in our analysis:

$$\begin{aligned} c_0 &= \theta_0, \\ c_1 &= \theta_0 + \frac{T}{n}\dot{\theta}_0, \\ c_j &= 0 \text{for } j < 0 \text{or } j > n. \end{aligned} \tag{93}$$

The algebraic system to be solved for $j = 2, 3, \ldots, n$ reads as

$$\begin{aligned} &\frac{n\left(c_{j-2} - 2c_{j-1} + c_j\right)}{T} + \frac{\varepsilon n}{T}\left(\left(c_j - c_{j-1}\right)^2\operatorname{sgn}\left(c_j - c_{j-1}\right) - \left(c_{j-2} - c_{j-1}\right)^2\operatorname{sgn}\left(c_{j-2} - c_{j-1}\right)\right) \\ &+ \frac{T\omega_0^2}{27720n}\begin{pmatrix} 5c_{j-2}^5 - 231c_{j-2}^3 + 4620c_{j-2} + 60c_{j-1}^5 + 5c_j^5 - 231c_j^3 + 4620c_j + \\ 25c_{j-1}^4\left(c_{j-2} + c_j\right) + 4c_{j-1}^3\left(5c_{j-2}^2 + 5c_j^2 - 462\right) + \\ 3c_{j-1}^2\left(5c_{j-2}^3 - 231c_{j-2} + 5c_j^3 - 231c_j\right) + \\ 2c_{j-1}\left(5c_{j-2}^4 - 231c_{j-2}^2 + 5c_j^4 - 231c_j^2 + 9240\right) \end{pmatrix} = 0. \end{aligned} \tag{94}$$

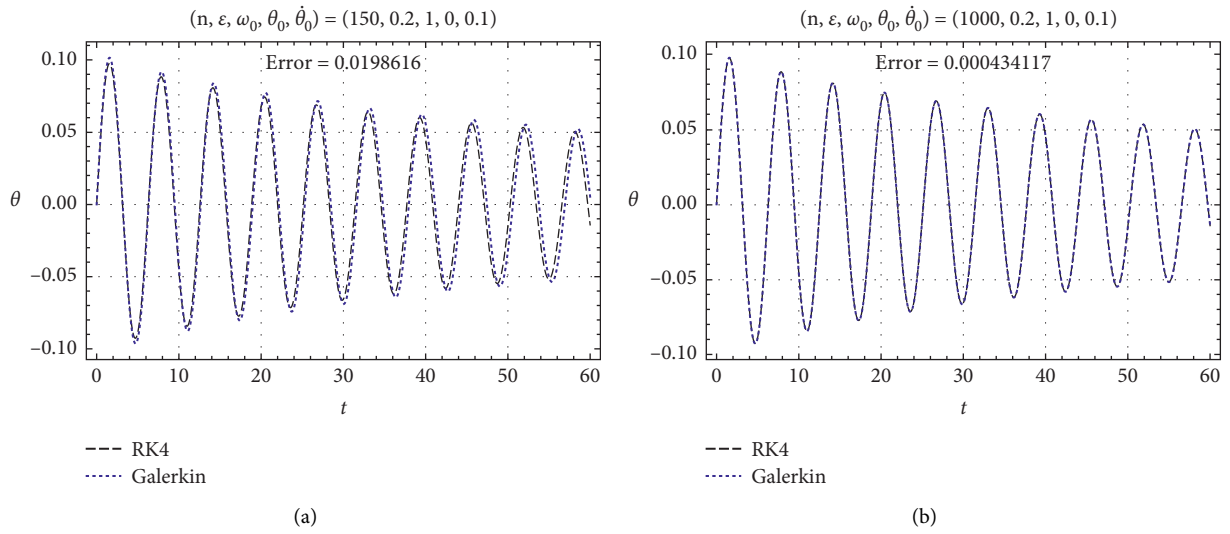

FIGURE 5: The approximate solutions using both GM and RK numerical method are plotted in (θ, t)−plane for (a) $(n, \theta_0) = (150, 0)$ and (b) $(n, \theta_0) = (1000, 0)$.

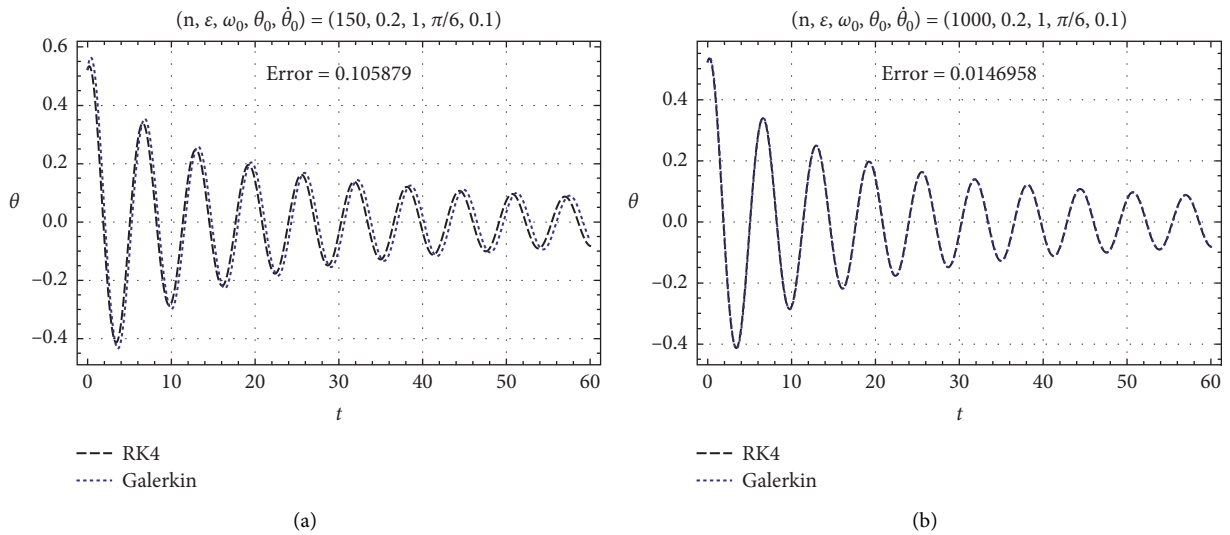

FIGURE 6: The approximate solutions using both GM and RK numerical method are plotted in (θ, t)−plane for (a) $(n, \theta_0) = (150, \pi/6)$ and (b) $(n, \theta_0) = (1000, \pi/6)$.

The Galerkin numerical approximation to i.v.p. (3) is introduced in Figures 5 and 6 for different values of $(n, \theta_0, \dot{\theta}_0)$. Also, the maximum distance error is estimated for different values of $(n, \theta_0, \dot{\theta}_0)$ as follows:

$$\begin{aligned} L_\infty &= 0.0198616, \quad \text{for } (n, \theta_0) = (150, 0), \\ L_\infty &= 0.000434117, \quad \text{for } (n, \theta_0) = (1000, 0), \\ L_\infty &= 0.105879, \quad \text{for } (n, \theta_0) = \left(150, \frac{\pi}{6}\right), \\ L_\infty &= 0.0146958, \quad \text{for } (n, \theta_0) = \left(1000, \frac{\pi}{6}\right). \end{aligned} \tag{95}$$

It is clear that increasing the number of hats n leads to the increase of approximation accuracy, i.e., the error shrinks with the enhancement of the number of hats n. Moreover, it is observed that the Galerkin numerical approximation is characterized by high accuracy compared to RK numerical approximation.

4. Conclusion

In this paper, the quadratically damped pendulum equation with strong nonlinearity has been solved and analyzed using some novel and effective analytical and numerical techniques. In the beginning, the ansatz method was devoted to

find an analytical approximation to the mentioned equation in the form of trigonometric functions. Also, in this study, for the first time, a new hybrid homotopy with Krylov–Bogoliubov–Mitropolsky method (HKBMM) was applied for analyzing the evolution equation and deriving an analytical approximation with high accuracy. Moreover, both the finite difference method (FDM) and Galerkin method (GM) were employed for analyzing the present evolution equation as well as some related oscillators. The obtained approximations were graphically compared with each other. Furthermore, the maximum residual error for each approximation was estimated. In the GM, we derived the iterative schemes for finding the coefficients that appear in the linear Galerkin hat combination in the ansatz form solution for the evolution equation. These coefficients may be found iteratively. It was found that the numerical approximations are more accurate than analytical ones, but both give good accuracy. Also, it was observed that the obtained results become reasonably good for small initial speed. One of the most important features of Galerkin method is that it gives more stable approximations for any values to the physical parameters and for long time. Thus, this method can be devoted for studying and investigating different pendulum oscillators for any nonlinearity [16, 27].

4.1. Future Work. There are many oscillators that may be solved using the proposed method. Examples include

$$\begin{aligned}
&\ddot{x} + 2\varepsilon\dot{x} + \alpha x + \beta x^2 + \gamma x^3 = F\cos(\Omega t),\\
&x + 2\varepsilon\dot{x} + \alpha x + \beta x + \gamma x^5 = F\cos(\Omega t),\\
&x - \varepsilon\left(1 - x^2\right)\dot{x} + \alpha x + \beta x^2 + \gamma x^3 = F\cos(\Omega t),\\
&x + 2\varepsilon\dot{x} + \left(\alpha - Q_0\cos(\gamma t)\right)\sin(x) = F\cos(\Omega t).
\end{aligned} \tag{96}$$

Appendix

The coefficients $S_{1,2,3}$ of solution (46):

$$\begin{aligned}
S_1 &= -\frac{1}{208}\left(\cos(3\psi) - 13\varepsilon\sin(3\psi)r_1\omega_0\right) + \frac{312\varepsilon r_0}{43264\omega_0}\left(-\sin(3\psi) + 13\varepsilon\cos(3\psi)r_1\omega_0\right)\\
&\quad - \frac{97344\varepsilon^2 r_0^2}{26996736\omega_0^2}\left(-\cos(3\psi) + 13\varepsilon\sin(3\psi)r_1\omega_0\right),\\
S_2 &= \frac{1}{43264}\begin{pmatrix} -52\varepsilon(6\sin(3\psi) + \sin(5\psi))r_1\omega_0 \\ +\cos(5\psi)\left(1 - 507\varepsilon^2 r_1^2\omega_0^2\right) \\ +3\cos(3\psi)\left(-7 + 1521\varepsilon^2 r_1^2\omega_0^2\right)\end{pmatrix} + \frac{104\varepsilon r_0}{26996736\omega_0}\begin{pmatrix} -567\sin(3\psi) + 19\sin(5\psi) \\ +5616\varepsilon\cos(3\psi)r_1\omega_0 + 52\varepsilon\cos(5\psi)r_1\omega_0 \\ +31941\varepsilon^2\sin(3\psi)r_1^2\omega_0^2 + 8619\varepsilon^2\sin(5\psi)r_1^2\omega_0^2\end{pmatrix},\\
S_3 &= \frac{3}{26996736}\begin{pmatrix} -\cos(7\psi) - 10647\varepsilon\sin(3\psi)r_1\omega_0 - 195\varepsilon\sin(5\psi)r_1\omega_0 \\ +130\varepsilon\sin(7\psi)r_1\omega_0 + 3549\varepsilon^2\cos(7\psi)r_1^2\omega_0^2 \\ +731601\varepsilon^3\sin(3\psi)r_1^3\omega_0^3 + 336141\varepsilon^3\sin(5\psi)r_1^3\omega_0^3 \\ -26364\varepsilon^3\sin(7\psi)r_1^3\omega_0^3 + \cos(5\psi)\left(43 + 3211\varepsilon^2 r_1^2\omega_0^2\right) \\ +3\cos(3\psi)\left(-139 + 8957\varepsilon^2 r_1^2\omega_0^2\right)\end{pmatrix}.
\end{aligned} \tag{A.1}$$

Data Availability

No data were used to support this study.

Conflicts of Interest

The authors declare that they have no conflicts of interest.

Authors' Contributions

All authors contributed equally and approved the final version of the manuscript.

Acknowledgments

The authors express their gratitude to Princess Nourah bint Abdulrahman University Researchers Supporting Project number (PNURSP2022R157), Princess Nourah bint Abdulrahman University, Riyadh, Saudi Arabia. Taif University Researchers Supporting Project No. (TURSP-2020/275), Taif University, Taif, Saudi Arabia.

References

[1] N. Nayfeth and D. T. Mook, *Non-linear Oscillations*, John Wiley, New York, NY, USA, 1973.

[2] I. Kovacic and M. J. Brennan, *The Duffing Equation: Nonlinear Oscillators and Their Behaviour*, John Wiley & Sons, New Jersey, NJ, USA, 2011.

[3] G. Duffing, *Erzwungene Schwingungen bei veranderlicher Eigenfrequenz und ihre technische Bedeutung*, Vieweg & Sohn, Braunschweig, Germany, 1918.

[4] A. H. Salas, S. A. El-Tantawy, and J. H Castillo, "Analytical solution to the damped cubic-quintic duffing equation,"

International Journal of Mathematics and Computer Science, vol. 17, no. 1, pp. 425–430, 2022.

[5] A. H. Salas, S. A. El-Tantawy, and E. C. H. Jairo, "On the approximate and analytical solutions to the fifth-order Duffing oscillator and its physical applications," *Waves in Random and Complex Media*, pp. 1–21, 2021.

[6] A. H. Salas and A. E. El-Tantawy, "Analytical solutions of some strong nonlinear oscillators," *Optimization Problems in Engineering [Working Title]*, Springer, Berlin, Germnay, 2021.

[7] S. A. E. Tantawy, A. H. Salas, and M. R. Alharthi, "On the analytical solutions of the forced damping duffing equation in the form of weierstrass elliptic function and its applications," *Mathematical Problems in Engineering*, vol. 2021, Article ID 6678102, 9 pages, 2021.

[8] N. H. Aljahdaly and S. A. El-Tantawy, "On the multistage differential transformation method for analyzing damping Duffing oscillator and its applications to plasma physics," *Mathematics*, vol. 9, no. 4, p. 432, 2021.

[9] S. Nourazar and A. Mirzabeigy, "Approximate solution for nonlinear Duffing oscillator with damping effect using the modified differential transform method," *Scientia Iranica B*, vol. 20, pp. 364–368, 2013.

[10] R. E. Mickens, "Mathematical and numerical study of the Duffing-harmonic oscillator," *Journal of Sound and Vibration*, vol. 244, no. 3, pp. 563–567, 2001.

[11] H. S. Alvaro, S. A. El-Tantawy, and M. R. Alharthi, "Novel solutions to the (un) damped Helmholtz-Duffing oscillator and its application to plasma physics: moving boundary method," *Physica Scripta*, vol. 96, Article ID 104003, 2021.

[12] H. S. Alvaro, S. A. El-Tantawy, and M. R. Alharthi, "A new approach for modelling the damped Helmholtz oscillator: applications to plasma physics and electronic circuits," *Communications in Theoretical Physics*, vol. 73, Article ID 035501, 2021.

[13] M. A. Hosen and M. S. H. Chowdhury, "Analytical approximate solutions for the helmholtz-duffing oscillator," *ARPN J. Eng. App. Sci.*vol. 10, Article ID 17363, 2015.

[14] Y. Geng, "Exact solutions for the quadratic mixed-parity Helmholtz-Duffing oscillator by bifurcation theory of dynamical systems," *Chaos, Solitons & Fractals*, vol. 81, pp. 68–77, 2015.

[15] D.-Q. Wei, X.-S. Luo, and S.-Y. Zeng, "Noise-triggered escapes in Helmholtz oscillator," *Modern Physics Letters B*, vol. 28, Article ID 1450047, 2014.

[16] J. A. Almendral, "Integrability and symmetries for the Helmholtz oscillator with friction," *Journal of physics a general physics*, vol. 36, 2033.

[17] W. Albalawi, A. H. Salas, S. A. El-Tantawy, and A. A. A.-R. Youssef, "Approximate analytical and numerical solutions to the damped pendulum oscillator: Newton–Raphson and moving boundary methods," *Journal of Taibah University for Science*, vol. 15, pp. 479–485, 2021.

[18] E. Gluskin, "A nonlinear resistor and nonlinear inductor using a nonlinear capacitor," *Journal of the Franklin Institute*, vol. 336, pp. 1035–1047, 1999.

[19] A. H. Salas and S. A. El-Tantawy, "On the approximate solutions to a damped harmonic oscillator with higher-order nonlinearities and its application to plasma physics: semi-analytical solution and moving boundary method," *Eur. Phys. J. Plus*, vol. 135, 2020.

[20] J. Sugie, "Asymptotic stability of a pendulum with quadratic damping," *Zeitschrift für Angewandte Mathematik und Physik*, vol. 65, pp. 865–884, 2014.

[21] D. W. Bass and M. R. Haddara, "Nonlinear models of ship roll damping," *International Shipbuilding Progress*, vol. 38, pp. 51–71, 1991.

[22] A. Cardo, A. Francescutto, and R. Nabergoj, "On damping models in free and forced rolling motion," *Ocean Engineering*, vol. 9, pp. 171–179, 1982.

[23] L. Cvetićanin, "Oscillator with strong quadratic damping force," *Publications de l'Institut Mathématique*, vol. 85, no. 99, pp. 119–130, 2009.

[24] I. Kovacic and Z. Rakaric, "Study of oscillators with a non-negative real-power restoring force and quadratic damping," *Nonlinear Dynamics*, vol. 64, pp. 293–304, 2011.

[25] M. A. S. Neves, N. A. Pérez, and L. Valerio, "Stability of small fishing vessels in longitudinal waves," *Ocean Engineering*, vol. 26, pp. 1389–1419, 1999.

[26] M. Taylan, "The effect of nonlinear damping and restoring in ship rolling," *Ocean Engineering*, vol. 27, pp. 921–932, 2000.

[27] A. H. Salas, J. E. Castillo, and J. G. E. Lugo, "Exact solutions for a nonlinear model," *Applied Mathematics and Computation*, vol. 217, pp. 1646–1651, 2010.

[28] P. J. Jolmes, "A nonlinear oscillator with a strange attractor," *Proc. R. Sot.*vol. 292, pp. 419–448, 1979.

[29] S. A. Khuri and S. S. Xie, "On the numerical verification of the asymptotic expansion of Duffing 's equation," *International Journal of Computer*, vol. 72, pp. 325–330, 1999.

[30] F. Mirzaee and N. Samadyar, "Combination of nite difference method and meshless method based on radial basis functions to solve fractional stochastic advection diffusion equations," *Engineering with Computers*, vol. 36, 2019.

[31] N. Samadyar and F. Mirzaee, "Numerical solution of two-dimensional weakly singular stochastic integral equations on non-rectangular domains via radial basis functions," *Engineering Analysis with Boundary Elements*, vol. 101, pp. 27–36, 2019.

[32] F. Mirzaee and N. Samadyar, "Numerical solution based on two-dimensional orthonormal Bernstein polynomials for solving some classes of two-dimensional nonlinear integral equations of fractional order," *Applied Mathematics and Computation*, vol. 344, pp. 191–203, 2019.

[33] Y. F. Liu and R. L. Guo, "Matter wave soliton solution of the cubic-quintic nonlinear Schrodinger equation with an anharmonic potential," *Applied Mathematics and Computation*, vol. 219, pp. 4847–4852, 2013.

[34] Y. Geng, J. Li, and L. Zhang, "Exact explicit traveling wave solutions for two nonlinear Schrodinger type equatios," *Applied Mathematics and Computation*, vol. 217, pp. 1509–1521, 2010.

Hindawi
Complexity
Volume 2022, Article ID 3629416, 16 pages
https://doi.org/10.1155/2022/3629416

Research Article

Magnetic Field Effect on Heat and Momentum of Fractional Maxwell Nanofluid within a Channel by Power Law Kernel Using Finite Difference Method

Maha M. A. Lashin,[1] Muhammad Usman,[2] Muhammad Imran Asjad,[3] Arfan Ali,[3] Fahd Jarad,[4,5,6] and Taseer Muhammad[7]

[1]*Electrical Engineering Department, College of Engineering, Princess Nourah bint Abdulrahman University, P.O. Box 84428, Riyadh 11671, Saudi Arabia*
[2]*Department of Mathematics, National University of Modern Languages (NUML), Islamabad 44000, Pakistan*
[3]*Department of Mathematics, University of Management and Technology Lahore, Lahore, Pakistan*
[4]*Department of Mathematics, Cankaya University, Etimesgut, Ankara, Turkey*
[5]*Department of Mathematics, King Abdulaziz University, Jeddah, Saudi Arabia*
[6]*Department of Medical Research, China Medical University Hospital, China Medical University, Taichung, Taiwan*
[7]*Department of Mathematics, College of Sciences, King Khalid University, Abha 61413, Saudi Arabia*

Correspondence should be addressed to Fahd Jarad; fahd@cankaya.edu.tr

Received 11 January 2022; Revised 2 March 2022; Accepted 7 March 2022; Published 23 May 2022

Academic Editor: Jawad Ahmad

The mathematical model of physical problems interprets physical phenomena closely. This research work is focused on numerical solution of a nonlinear mathematical model of fractional Maxwell nanofluid with the finite difference element method. Addition of nanoparticles in base fluids such as water, sodium alginate, kerosene oil, and engine oil is observed, and velocity profile and heat transfer energy profile of solutions are investigated. The finite difference method involving the discretization of time and distance parameters is applied for numerical results by using the Caputo time fractional operator. These results are plotted against different physical parameters under the effects of magnetic field. These results depicts that a slight decrease occurs for velocity for a high value of Reynolds number, while a small value of Re provides more dominant effects on velocity and temperature profile. It is observed that fractional parameters α and β show inverse behavior against $u(y,t)$ and $\theta(y,t)$. An increase in volumetric fraction of nanoparticles in base fluids decreases the temperature profile of fractional Maxwell nanofluids. Using mathematical software of MAPLE, codes are developed and executed to obtain these results.

1. Introduction

Partial differential equations (PDEs) are the best way to express physical phenomena mathematically. PDEs are widely used in many fields of engineering like bioengineering, chemical engineering, and oceanography. Few years earlier, the main focus of researchers was the integral order of these PDEs. But, for the last few decades, the fractional order of PDEs is a hot topic among scientists. This is because the fractional modeling of natural phenomena gave a new direction to solutions of real-world problems, including diffusion, chaos, chemical reactions, dynamics, and viscoelasticity [1–3]. Approximately, all the polymeric matters have a viscoelastic behavior and conventional derivatives do not interpret such trend. Most of the fractional fluid problems are solved analytically due to the linearity of the problems. But, for the nonlinear problem, analytical techniques are complex to use. Fractional modeling of such physical problems can describe the heredity aspects and memory effect of problems. Nowadays, this idea of fractional

modeling has been published in several articles of applied mathematics, fluid dynamics, and thermal engineering. These models are formulated by using various differentiation operators such as Caputo, Caputo-Fabrizio, and Atangana–Baleanu derivatives [4, 5]. An analytical solution has been obtained via Laplace transformation, and it is concluded that fractional results are better rather than using classical derivation for temperature and velocity profile [6, 7]. These operators are used to investigate mass concentration, heat flow, and momentum along different geometries. These theories have been applied to various fluids including Cassin fluids, Brickman type fluids, Oldroyd-B fluids, and Maxwell fluids as well [8, 9]. Recently, the Maxwell models have gained much attention from researchers as it is the first and one of the simplest rate type models (RTMs). The Maxwell model is widely used to represent the response of polymeric liquids. But, this model does not express the typical relation between shear strain and shear stress [10, 11]. The research work which has already been done for fractional Maxwell fluid (FMF) modeling (particularly on analytical side) has various bounds for momentum transfer only [12–17]. An investigation has been done for FMF flow, by introducing some suitable variables to make the irregular boundary of the stretching sheet and the regular one in [18]. It can be seen [19] that Brownian motion, mass concentration, and temperature profile as well are studied for FMF flow near a moving plate by using L1-algorithm i.e., numerically. By applying Laplace and Henkel transformation jointly, flow of FMF was investigated in [20]. The recent development in modeling of FMF rather than that of simple Maxwell fluids may be seen in [21–23]. In recent days, fractional modeling of Maxwell fluids with nanomaterials is the hot issue in nanotechnology. Nanomaterials are the nanoparticles of size range from 1 nm to 100 nm. These nanosized particles are helpful to enhance the thermal conductivity of base fluids (water, sodium alginate, kerosene oil, engine oil, etc.). This idea was given for the first time by Choi and Eastman in [24], and later on, the size and shapes of different nanoparticles were investigated in a square cavity in [25]. Since the addition of nanoparticles in base fluids increases the surface area of the fluid, it consequently enhances the heat conduction of the system, .i.e., control the entropy generation of heat. Analytical study has been done using Laplace transform for Caputo time derivatives of convective flow. Under the effects of magnetic field, exact solutions were obtained in [26]. Shamushuddin and Eid [27] examined heat transfer in water-based nanofluids containing ferromagnetic nanoparticles flowing between parallel stretchable spinning discs with variable viscosity influences and variable conductivities through the Chebyshev spectral collocation procedure. Unsteady flow was investigated under the effect of pressure gradient and magnetic field by using Laplace transformation as in [28]. Developing a fractional, coupled but linear PDEs model, the results were plotted against different physical parameters in [29, 30]. Similarly, it can be seen that solutions of many PDEs models are obtained analytically. After many assumptions, the models are turned into linear ones for simplicity of the problems. In [31–33], the analytical approach is used to find the solutions of mathematical models. Also, mostly results are driven by analytical technique by many assumptions to make the model a linear one for simplicity.

The research work which has already been discussed has various research gaps in the field of nanofluids. As numerical study had not been performed, fractional behavior of mathematical models was not discussed properly with the basic tensor form. Therefore, this article deals with numerical solutions of unsteady flow of MHD-based fractional Maxwell nanofluids. This will provide the basis for further in-depth study while investigating the dynamics of FMF within a bounded channel instead of other geometric properties. Rather than the analytical technique, the strong numerical technique of the finite difference method FDM is applied to obtain solution of the FMF which involves discretization of spatial and time derivatives. The velocity profile and temperature profile have been plotted against various physical parameters by using MAPLE software. By developing and executing MAPLE coding against different physical parameters, results are obtained graphically.

2. Mathematical Modeling

The boundary layer flow within a channel is considered in this article, taking water-based nanofluids (Cu and Al_2O_3) in a vertical channel. Both the plates are separated by a distance d. One of the plates is fixed along the x-axis, vertically upward, i.e., x-axis is parallel to the plates and y-axis is normal to the plates, with B_0 strength of magnetic field. At the start, for $t = 0$, plates as well as fluids are supposed to have temperature θ_d. For some time $t > 0$, the temperature is raised to θ_0, causing the free convection flow as illustrated in Figure 1.

Hence, the velocity field is of the form $\mathbf{V}(x, y, t) = \mathbf{V}[u(y, t), 0, 0]$. Considering the unsteady flow of water-based nanofluid in this vertical channel, the assumptions for the mathematical formulation of PDEs of the coupled and nonlinear fractional Maxwell nanofluid model is as follows:

(i) Flow is incompressible, viscoelastic, and nonlinear

(ii) Flow is unsteady

(iii) Pressure gradient is neglected, i.e., $\partial P/\partial x = 0$

(iv) A uniform magnetic field is applied along the vertical direction (along y – direction), neglecting induced magnetic field

(v) Viscous dissipation is absent

We know that the tensor for the Maxwell fluid given in [34] is

$$\mathbf{T} = -p\mathbf{I} + \mathbf{S},$$
$$\mathbf{S} + \lambda_1 \frac{\delta \mathbf{S}}{\delta t} = \mu \mathbf{A}_1, \tag{1}$$

where $\mathbf{S}, \mathbf{I}, p, \mathbf{T}, \lambda_1$, and $\mathbf{A}_1$ are the extra stress tensor, identity tensor (matrix tensor), dynamic pressure, Cauchy stress tensor, time relaxation, and first Rivlin–Ericksen tensor, respectively. And, D$\mathbf{S}$/Dt is given in [35] and defined as

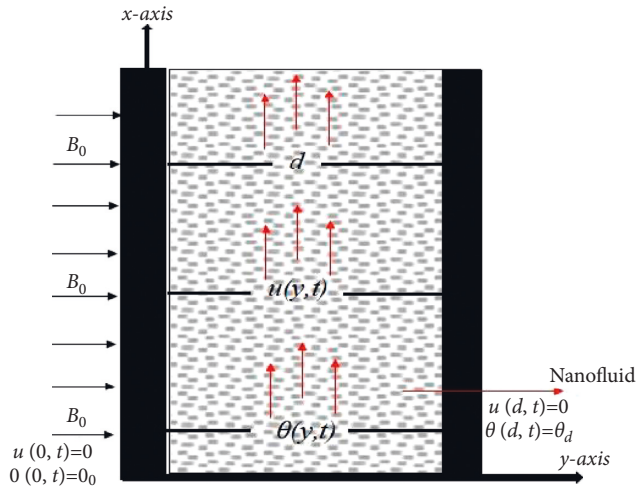

Figure 1: Geometry of the problem.

$$\frac{\delta \mathbf{S}}{\delta t} = \frac{\mathrm{D}\mathbf{S}}{\mathrm{D}t} - \mathbf{LS} - \mathbf{SL}^T, \tag{2}$$

where D/Dt is the material time derivative and $\mathbf{A}_1$ is the first Rivlin–Ericksen tensor defined as

$$\mathbf{A}_1 = \mathrm{grad}\mathbf{V} + (\mathrm{grad}\mathbf{V})^T. \tag{3}$$

Using all of the above-discussed results, the constitutive relation for Maxwell fluid model is obtained [15].

$$\left(1 + \lambda_1^{\alpha} D_t^{\alpha}\right)\mathbf{S}_{xy} = \mu \frac{\partial u}{\partial y} \quad \text{with } 0 < \alpha < 1, \tag{4}$$

where $\mathbf{S}_{xy}$ is the nonzero component of extra stress tensor, μ is the coefficient of viscosity, λ_1 is the time relaxation, and D_t^{α} is Caputo time fractional differentiation operator of order α, defined in [36].

$${}_0^C D_t^{\alpha} f(t) = \frac{1}{\Gamma(1-\alpha)} \int_0^t (t-\eta)^{-\alpha} \frac{\partial f(\eta)}{\partial \eta} \mathrm{d}\eta, \quad 0 < \alpha < 1, \tag{5}$$

where $\Gamma(.)$ is the Gamma function defined in [36].

$$\Gamma(z) = \int \eta^{z-1} e^{-\eta} \mathrm{d}\eta, \quad z \epsilon \mathbb{C}, \ \mathbb{R}e(z) > 0. \tag{6}$$

Under the aforementioned assumptions, the mathematical model of this problem is as follows. The equation of continuity [37] is

$$\frac{\partial \rho}{\partial t} + \rho(\nabla . \mathbf{V}) = 0, \tag{7}$$

where ρ is the density, ∇ is the gradient operator, and $\mathbf{V}$ is a velocity field.

Here, we neglect v component of velocity along y – direction, in both momentum and energy equations. Also, taking into account the Boussinesq approximation, the momentum equation is given as in [38]

$$\rho_{nf} \frac{\partial u}{\partial t} = \frac{\partial \mathbf{S}_{xy}}{\partial y} + g(\rho\beta_\theta)_{nf}(\theta - \theta_0) - \sigma_{nf} B_0^2 u, \tag{8}$$

where ρ_{nf} is the dynamic viscosity of the nanofluid and g, $(\beta_\theta)_{nf}$, σ_{nf}, and B_0 are acceleration due to gravity, coefficient of thermal expansion of nanofluid, and coefficient of electrical conductivity for nanofluids, and magnetic field strength, respectively.

Multiplying $(1 + \lambda_1^{\alpha} D_t^{\alpha})$ on both sides of (7),

$$\left(1 + \lambda_1^{\alpha} D_t^{\alpha}\right)\rho_{nf} \frac{\partial u}{\partial t} = \left(1 + \lambda_1^{\alpha} D_t^{\alpha}\right) \frac{\partial \mathbf{S}_{xy}}{\partial y} + g(\rho\beta_\theta)_{nf}\left(1 + \lambda_1^{\alpha} D_t^{\alpha}\right)(\theta - \theta_0) - \sigma_{nf} B_0^2 \left(1 + \lambda_1^{\alpha} D_t^{\alpha}\right) u. \tag{9}$$

Using $(1 + \lambda_1^{\alpha} D_t^{\alpha})\mathbf{S}_{xy} = \mu_{nf} \partial u / \partial y$, the constitutive relation for Maxwell fluid in [39] is

$$\left(1 + \lambda_1^{\alpha} D_t^{\alpha}\right)\rho_{nf} \frac{\partial u}{\partial t} = \mu_{nf} \frac{\partial^2 u}{\partial y^2} + \left(1 + \lambda_1^{\alpha} D_t^{\alpha}\right) g(\rho\beta_\theta)_{nf}(\theta - \theta_0) - \left(1 + \lambda_1^{\alpha} D_t^{\alpha}\right)\sigma_{nf} B_0^2 u. \tag{10}$$

Also, the energy equation in the presence of Joule's heating effect in [38] is

$$\left(\rho C_p\right)_{nf}\left(\frac{\partial \theta}{\partial t}\right) = -\frac{\partial q}{\partial y} + \sigma_{nf} B_0^2 u^2. \tag{11}$$

Applying $(1 + \lambda_2^\beta D_t^\beta)$ on both sides of (10),

$$\left(1 + \lambda_2^\beta D_t^\beta\right)\left(\rho C_p\right)_{nf}\left(\frac{\partial \theta}{\partial t}\right) = -\frac{\partial}{\partial y}\left(1 + \lambda_2^\beta D_t^\beta\right)q + \sigma_{nf} B_0^2\left(1 + \lambda_2^\beta D_t^\beta\right)u^2. \tag{12}$$

But, by fractional Cattaneo's Law [40],

$$\left(1 + \lambda_2^\beta D_t^\beta\right)q = -k_{nf}\frac{\partial \theta}{\partial y}. \tag{13}$$

Hence, (11) becomes

$$\left(1 + \lambda_2^\beta D_t^\beta\right)\left(\rho C_p\right)_{nf}\left(\frac{\partial \theta}{\partial t}\right) = k_{nf}\frac{\partial \theta^2}{\partial y^2} + \sigma_{nf} B_0^2\left(1 + \lambda_2^\beta D_t^\beta\right)u^2. \tag{14}$$

It has the following initial and boundary conditions:

$$\begin{aligned} u(y,0) &= 0,\\ u(0,t) &= 0,\\ u(d,t) &= 0,\\ \theta(y,0) &= \theta_0,\\ \theta(0,t) &= \theta_0,\\ \theta(d,t) &= \theta_{\mathrm{d}}. \end{aligned} \tag{15}$$

Employ the following transformation for the channel flow:

$$\begin{aligned} u^* &= \frac{d}{\nu_f}u,\\ x^* &= \frac{x}{d},\\ t^* &= \frac{\nu_f}{d^2}t,\\ \theta^* &= \frac{\theta - \theta_0}{\theta_d - \theta_0},\\ \lambda_1^* &= \frac{\nu_f}{d^2}\lambda_1,\\ \lambda_2^* &= \frac{\nu_f}{d^2}\lambda_2,\\ y^* &= \frac{y}{d},\\ M^* &= \frac{\sigma_f B_0^2 \nu_f}{\left(\rho C_p\right)_f(\theta_d - \theta_0)},\\ Ha^2 = M &= \frac{d^2 \sigma_f B_0^2}{\mu_f},\\ Pr &= \frac{\left(\mu C_p\right)_f}{K_f},\\ Gr &= \frac{d^3 g(\beta_\theta)_f(\theta_d - \theta_0)}{\nu_f^2},\\ \frac{1}{\mathrm{Re}} &= \frac{\mu}{\rho U_0 d}. \end{aligned} \tag{16}$$

Here, $Ha = M, Pr, M^*$, and Gr given in [41] are the square of Hartmann number, Prandtl number, Joule's heating parameter, and Grashof number, respectively. The following governing equations for velocity and temperature profile are obtained after omitting "*" notation for the sack of brevity of mathematical modeling:

$$\left(1 + \lambda_1^\alpha D_t^\alpha\right)\left(\frac{\partial u}{\partial t}\right) = b_1\frac{\partial^2 u}{\partial y^2} + \left(1 + \lambda_1^\alpha D_t^\alpha\right)b_2 Gr\theta - b_3 M\left(1 + \lambda_1^\alpha D_t^\alpha\right)u, \tag{17}$$

$$\left(1 + \lambda_2^\beta D_t^\beta\right)\left(\frac{\partial \theta}{\partial t}\right) = b_4\frac{1}{Pr}\frac{\partial^2 \theta}{\partial y^2} + b_5 M^*\left(1 + \lambda_2^\beta D_t^\beta\right)u^2. \tag{18}$$

Here, $b_1 = a_3/a_1$, $b_2 = a_2/a_1$, $b_3 = a_6/a_1$, $b_4 = a_5/a_4$, and $b_5 = a_6/a_4$. But, thermophysical properties for nanofluids in [42, 43] are known.

$$\left.\begin{aligned} &\frac{\rho_{nf}}{\rho_f} = a_1 = \left[(1-\phi) + \phi\frac{\rho_s}{\rho_f}\right], && \frac{(\rho\beta_\theta)_{nf}}{(\rho\beta_\theta)_f} = a_2 = \left[(1-\phi) + \phi\left(\frac{(\rho\beta_\theta)_s}{(\rho\beta_\theta)_f}\right)\right] \\ &\frac{\mu_{nf}}{\mu_f} = a_3 = \frac{1}{(1-\phi)^{2.5}}, && \frac{(\rho C_p)_{nf}}{(\rho C_p)_f} = a_4 = \left[(1-\phi) + \phi\left(\frac{(\rho C_p)_s}{(\rho C_p)_f}\right)\right] \\ &\frac{k_{nf}}{k_f} = a_5 = \frac{(k_s+2k_f) - 2\phi(k_f-k_s)}{(k_s+2k_f) + \phi(k_f-k_s)}, && \frac{(\sigma)_{nf}}{(\sigma)_f} = a_6 = 1 + \frac{3(\sigma_s/\sigma_f - 1)\phi}{(\sigma_s/\sigma_f - 2) - (\sigma_s/\sigma_f - 1)\phi} \end{aligned}\right\}. \tag{19}$$

By using nondimensional parameters, the initial and boundary conditions are as follows:

$$\begin{aligned} u(y,0) &= 0, \\ u(0,t) &= 0, \\ u(1,t) &= 0, \end{aligned} \tag{20}$$

$$\begin{aligned} \theta(y,0) &= 0, \\ \theta(0,t) &= 0, \\ \theta(1,t) &= 1. \end{aligned} \tag{21}$$

Thus, governing equations (17) and (18) for the velocity and temperature profile of fractional Maxwell nanofluid with initial and boundary conditions represented in (20)-(21) express the physical phenomena of the coupled nonlinear model. Also, physical properties of nanoparticles presented in (17) with some thermophysical properties of base fluids and nanoparticles given in Table 1 are used for numerical results.

3. Skin Friction and Nusselt Number

For measuring shear stress and heat transfer effects in an ordinary integer order system, local skin friction and Nusselt number are defined in [44] as follows:

$$\begin{aligned} C_f &= \frac{\mu}{\rho U_0^2}\left(\frac{\partial u}{\partial y}\right)_{y=0}, \\ Nu &= \frac{-k\mathrm{d}}{\theta_w - \theta_0}\left(\frac{\partial \theta}{\partial y}\right)_{y=0}. \end{aligned} \tag{22}$$

The skin friction coefficient and local Nusselt number for (FMF) can be written by using (3) that is the fractional stress tensor for Maxwell fluid on the plate with fractional time Caputo derivative (details can be seen in [45]).

$$C_f + \lambda_1^\alpha \frac{\partial^\alpha S_f}{\partial t^\alpha} = \frac{\mu}{\rho U_0^2}\left(\frac{\partial u}{\partial y}\right)_{y=0}, \tag{23}$$

$$Nu + \lambda_1^\beta \frac{\partial^\beta Nu}{\partial t^\beta} = -\frac{k\mathrm{d}}{\theta_d - \theta_0}\left(\frac{\partial \theta}{\partial y}\right)_{y=0}. \tag{24}$$

The nondimensional form of (23)-(24) is given as

$$C_f + \lambda_1^\alpha \frac{\partial^\alpha S_f}{\partial t^\alpha} = \frac{1}{Re^2}\left(\frac{\partial u}{\partial y}\right)_{y=0}. \tag{25}$$

$$Nu + \lambda_1^\beta \frac{\partial^\beta Nu}{\partial t^\beta} = -\frac{k_{nf}}{k_f}\left(\frac{\partial \theta}{\partial y}\right)_{y=0}. \tag{26}$$

4. Numerical Procedure

The discretization of the method for fractional-order model, ${}_0^C D_t^\alpha u, {}_0^C D_t^{1+\alpha} u$ when $0 < \alpha \le 1, u_t$ and u_{yy}, is specified as follows:

$${}_0^C D_{t_{j+1}}^\alpha u(y_i, t_{j+1}) = \frac{\lambda_1^\alpha t^{-\alpha}}{\Gamma(2-\alpha)}\left[u_i^{j+1} - u_i^j\right] + \frac{\lambda_1^\alpha t^{-\alpha}}{\Gamma(2-\alpha)}\sum_{l=1}^{j}\left(u_i^{j-l+1} - u_i^{j-l}\right)\mathrm{d}_l^\alpha, \tag{27}$$

$${}_0^C D_{t_{j+1}}^{1+\alpha} u(y_i, t_{j+1}) = \frac{\lambda_1^\alpha t^{-(1+\alpha)}}{\Gamma(2-\alpha)}\left[u_i^{j+1} - 2u_i^j + u_i^{j-1}\right] + \frac{\lambda_1^\alpha t^{-(1+\alpha)}}{\Gamma(2-\alpha)} \times \sum_{l=1}^{j}\left(u_i^{j-l+1} - 2u_i^{j-l} + u_i^{j-l-1}\right)\mathrm{d}_l^\alpha, \tag{28}$$

Table 1: Thermophysical properties of some base fluids and nanoparticles.

Materials	$\rho(\mathrm{kgm}^{-3})$	$C_p(\mathrm{Jkg}^{-1}\mathrm{k}^{-1})$	$k(\mathrm{Wm}^{-1}\mathrm{k}^{-1})$	$\beta * 10^{-5}(\mathrm{k}^{-1})$	$\sigma(\Omega\mathrm{m})^{-1}$
Water	997	4197	0.613	21	0.05
Copper	8933	385	400	1.67	$5.96 * 10^7$
Alumina	3970	765	40	0.85	$2.6 * 10^6$

$$\begin{aligned}\frac{\partial}{\partial t}u\left(y_i,t_{j+1}\right)|_{t=t_{j+1}} &= \frac{1}{\Delta t}\left[u_i^{j+1}-u_i^j\right],\\ \frac{\partial^2}{\partial y^2}u\left(y_{i+1},t_j\right)|_{y=y_{i+1}} &= \frac{1}{\Delta y^2}\left[u_{i+1}^{j+1}-2u_i^{j+1}+u_{i-1}^{j+1}\right].\end{aligned} \tag{29}$$

The nonlinear term is approximated by means of the following concept:

$$u^2\left(y_i,t_j\right)=u\left(y_i,t_{j+1}\right)u\left(y_i,t_j\right). \tag{30}$$

In (27)-(28), $\mathrm{d}_l^\alpha=-l^{1-\alpha}+(1+l)^{1-\alpha}$ when $l=1,2,3,\ldots,j$. A rectilinear grid is considered for investigating the numerical solution of the deliberated fluid model through grid spacing $\Delta t>0$ and $\Delta y>0$ in time and space directions separately; here, $\Delta y=L/M$ and $\Delta t=T/N$ where $\Delta y,\Delta t\in\mathbb{Z}^+$. The inner grid points (y_i,t_j) in the considered domain $\Omega=[0,T]\times[0,L]$ are defined as $i\Delta y=y_i$ and $j\Delta t=t_j$. Discretization of the discussed problem at each inner grid point is given as

$$\begin{aligned}&1/\Delta t\left(u_i^{j+1}-u_i^j\right)+\frac{\lambda_1^\alpha\Delta t^{-(1+\alpha)}}{\Gamma(2-\alpha)}\left(u_i^{j+1}-2u_i^j+u_i^{j-1}\right)+\frac{\lambda_1^\alpha\Delta t^{-(1+\alpha)}}{\Gamma(2-\alpha)}\\ &\times\sum_{l=1}^{j}\left(u_i^{j-l+1}-2u_i^{j-l}+u_i^{j-l-1}\right)b_l^\alpha=\frac{b_1}{\Delta y^2}\left(u_{i+1}^{j+1}-2u_i^{j+1}+u_{i-1}^{j+1}\right)+b_2Gr\theta_i^{j+1}\\ &+\frac{b_2Gr\Delta t^{-\alpha}}{\Gamma(2-\alpha)}\left(\theta_i^{j+1}-\theta_i^j\right)+\frac{b_2Gr\Delta t^{-\alpha}}{\Gamma(2-\alpha)}\sum_{l=1}^{j}\left(\theta_i^{j-l+1}-\theta_i^{j-l}\right)b_l^\alpha\\ &-\frac{b_3Ha^2\Delta t^{-\alpha}}{\Gamma(2-\alpha)}\left(u_i^{j+1}-u_i^j\right)+\frac{b_3Ha^2\Delta t^{-\alpha}}{\Gamma(2-\alpha)}\sum_{l=1}^{j}\left(u_i^{j-l+1}-u_i^{j-l}\right)b_l^\alpha.\end{aligned} \tag{31}$$

Also,

$$\begin{aligned}&\frac{1}{\Delta t}\left(\theta_i^{j+1}-\theta_i^j\right)+\frac{\lambda_1^\beta\Delta t^{-(1+\beta)}}{\Gamma(2-\beta)}\left(\theta_i^{j+1}-2\theta_i^j+\theta_i^{j-1}\right)\\ &+\frac{\lambda_1^\beta\Delta t^{-(1+\beta)}}{\Gamma(2-\beta)}\sum_{l=1}^{j}\left(\theta_i^{j-l+1}-2\theta_i^{j-l}+\theta_i^{j-l-1}\right)b_l^\beta=\frac{b_4}{\mathrm{Pr}\Delta y^2}\left(\theta_{i+1}^{j+1}-2\theta_i^{j+1}+\theta_{i-1}^{j+1}\right)\\ &+b_5M^*u_i^j\left(u_i^{j+1}+\frac{\lambda_1^\beta\Delta t^{-\beta}}{\Gamma(2-\beta)}\left(u_i^{j+1}-u_i^j-\sum_{l=1}^{j}\left(u_i^{j-l+1}-u_i^{j-l}\right)b_l^\alpha\right)\right),\end{aligned} \tag{32}$$

for $j=1,2,3,\ldots,N-1$ and $i=1,2,3,\ldots,N-1$.

The simplest form of the above discretization is given as

$$
\begin{aligned}
&-\frac{b_1}{\Delta y^2}u_{i+1}^{j+1}+\left(\frac{1}{\Delta t}-\frac{\lambda_1^{\alpha}\Delta t^{-1-\alpha}}{\Gamma(2-\alpha)}+\frac{2b_1}{\Delta y^2}+\frac{b_3Ha^2\Delta t^{-\alpha}}{\Gamma(2-\alpha)}\right)u_i^{j+1}-\frac{b_1}{\Delta y^2}u_{i-1}^{j+1}\\
&-b_2Gr\left(1+\frac{\Delta t^{-\alpha}}{\Gamma(2-\alpha)}\right)\theta_i^{j+1}=\left(\frac{1}{\Delta t}+\frac{2\lambda_1^{\alpha}\Delta t^{-1-\alpha}}{\Gamma(2-\alpha)}+\frac{b_3Ha^2\Delta t^{-\alpha}}{\Gamma(2-\alpha)}\right)u_i^{j}-\frac{b_2Gr\Delta t^{-\alpha}}{\Gamma(2-\alpha)}\theta_i^{j}\\
&-\frac{\lambda_1^{\alpha}\Delta t^{-1-\alpha}}{\Gamma(2-\alpha)}u_i^{j-1}=F_{i,j},\\
&-\frac{b_4}{\mathrm{Pr}\Delta y^2}\theta_{i+1}^{j+1}+\left(\frac{1}{\Delta t}+\frac{\lambda_1^{\beta}\Delta t^{-1-\beta}}{\Gamma(2-\beta)}+\frac{2b_4}{\mathrm{Pr}\Delta y^2}\right)\theta_i^{j+1}-\frac{b_4}{\mathrm{Pr}\Delta y^2}\theta_{i-1}^{j+1}=\left(1/\Delta t-\frac{2\lambda_1^{\beta}\Delta t^{-1-\beta}}{\Gamma(2-\beta)}\right)\theta_i^{j}\\
&-\frac{\lambda_1^{\beta}\Delta t^{-1-\beta}}{\Gamma(2-\beta)}\theta_i^{j-1}+G_{i,j}+N_{i,j},
\end{aligned}
\tag{33}
$$

with the following initial and boundary conditions

$$
\begin{aligned}
u_i^0&=0,\\
u_i^1&=u_i^{-1},\\
\theta_i^0&=0,\\
\theta_i^1&=\theta_i^{-1},\quad \text{for } i=0,1,2,3,\ldots,M,\\
u_0^j&=0,\\
u_M^j&=0,\\
\theta_0^j&=0,\\
\theta_M^j&=1,\quad \text{for } j=0,1,2,3,\ldots,N-1,
\end{aligned}
\tag{34}
$$

where

$$
\begin{aligned}
F_{i,j}&=-\frac{\lambda_1^{\alpha}\Delta t^{-(1+\alpha)}}{\Gamma(2-\alpha)}\sum_{l=1}^{j}\left(u_i^{j-l+1}-2u_i^{j-l}+u_i^{j-l-1}\right)b_l^{\alpha}+\frac{b_2Gr\Delta t^{-\alpha}}{\Gamma(2-\alpha)}\sum_{l=1}^{j}\left(\theta_i^{j-l+1}-\theta_i^{j-l}\right)b_l^{\alpha}+\frac{b_3Ha^2\Delta t^{-\alpha}}{\Gamma(2-\alpha)}\sum_{l=1}^{j}\left(u_i^{j-l+1}-u_i^{j-l}\right)b_l^{\alpha},\\
G_{i,j}&=-\frac{\lambda_1^{\beta}\Delta t^{-(1+\beta)}}{\Gamma(2-\beta)}\sum_{l=1}^{j}\left(\theta_i^{j-l+1}-2\theta_i^{j-l}+\theta_i^{j-l-1}\right)b_l^{\beta},\\
N_{i,j}&=b_5M^*u_i^j\left(u_i^{j+1}+\frac{\lambda_1^{\beta}\Delta t^{-\beta}}{\Gamma(2-\beta)}\left(u_i^{j+1}-u_i^j-\sum_{l=1}^{j}\left(u_i^{j-l+1}-u_i^{j-l}\right)b_l^{\alpha}\right)\right).
\end{aligned}
\tag{35}
$$

5. Numerical Analysis and Discussion

5.1. Test Problem. Consider the following problem:

$$
{}_0^{C}D_t^{\alpha}U(y,t)=\frac{\partial^2}{\partial y^2}U(y,t)-\frac{\partial}{\partial y}U(y,t)+h(y,t).
\tag{36}
$$

Here, the conditions are given as follows and source term can be selected against the choice of fractional-order derivative:

$$
U(y,0)=U(0,t)=U(\mathrm{d},t)=0.
\tag{37}
$$

The exact solution of this problem is $U(y,t)=y(y-t)t^2$. Various simulations have been performed to check the accuracy of the proposed scheme. Figures 1(a) and 1(b) are plotted for maximum absolute error (MAE) and computational order of convergence (COC) given as follows when $N=10, 20, 40, 80, 160, 320, 640$:

$$\text{MAE} = \max_{\substack{1\le i\le M\\ 1\le j\le N}} \left|U\left(y_i, t_j\right) - U_i^j\right|,$$
$$\text{COC} = \log \frac{(\text{MAE}(k)/\text{MAE}(k+1))}{\log(N(k+1)/N(k))}. \tag{38}$$

It is noted that the scheme is convergent against the selection of each fractional-order derivative and its convergence order increases as $\alpha \longrightarrow 1$. Figures 2(c) and 2(b) contain the L_∞-norm between consecutive solutions, i.e., $|U^{j+1} - U^j|_\infty$ and $|U_{i+1} - U_i|_\infty$ when $0 \le i,\ j \le N$, and $M = 500$. Again, it is found that the proposed scheme is very efficient, accurate, and reliable for this problem. It is also demonstrated that the solution is stable against the selection of fractional-order parameters and mesh parameters.

6. Results and Discussion

This section of our research work deals with a detailed overview of the key numerical findings and physical interpretations of different emerging parameters such as $Pr, M, \alpha, \beta, M^*$, and$\phi$ which are the Prandtl number, magnetic field parameter, fractional parameters, Joule's heating parameter, and volumetric fraction of nanoparticles, respectively. The behavior of the velocity profile $u(y,t)$ and temperature profile $\theta(y,t)$ and the effects of aforementioned physical parameters are deliberated, as well as graphical illustration is made via MAPLE. Discretization of time and spatial derivatives is done using finite difference methods. The coupled, nonlinear, and fractional model has been solved numerically by using finite difference method (FDM) which is a dominant tool to deal with such kind of problems.

Results are obtained by solving (17)-(18) with initial and boundary conditions illustrated in (20)-(21) and physical properties of nanoparticle in (17) and Table 1. Various suitable ranges of physical parameters $(0.01 \le \lambda_1^\alpha \le 0.5)$, $(0 \le Ha = M \le 5)$, $(1 \le Gr \le 5)$, $(0.01 \le \phi \le 0.2)$, and $(0.2 \le \nu \le 1)$ for dimensionless velocity profile and $(0.01 \le \lambda_1^\beta \le 0.2)$, $(0 \le M^* \le 2)$, $(6.2 \le Pr \le 35)$, $(0.01 \le \phi \le 0.2)$, and $(0.2 \le \nu \le 1)$ for heat transport are considered, and also particular exertion has been given on the effects of these parameters on the velocity and temperature profile.

Figure 3 depicts the impact of time relaxation parameter λ_1^α on momentum $u(y,t)$ of the fractional Maxwell fluids. With increase in fractional parameter α, momentum and thermal boundary layers decrease and even become their thinnest for $\alpha = 1$. Therefore, increasing relaxation parameters with range $(0.01 \le \lambda_1^\alpha \le 0.5)$ has inverse impact on the velocity profile of the system, i.e., decrease occurs in the velocity profile.

Figure 4 shows the influence of magnetic field $Ha = M$ (the square of Hartmann Number) parameters on velocity profile $u(y,t)$. Both are inversely related, i.e., increasing value of Hartmann number Ha decreases the velocity profile. Since the increase in magnetic field parameter (Ha) gives hype to a well-known Lorentz force as this is the resistive force which works against the flow direction, consequently it shows decrease in all the velocity components.

Figure 5 displays the behavior of Grashof number Gr on velocity profile $u(y,t)$ of fractional Maxwell fluids (FMFs) under the effects of magnetic field. Since Grashof number Gr is the ratio of buoyancy force to viscous force and is alsoknown as buoyancy parameter, motion is resisted by the viscous force. So it was expected that an increase in Gr leads to an increase in the velocity profile of the bounded system, specifically near the wall of the bounded channel.

In Figure 6, results are drawn for volumetric fraction of nanoparticles against flow of fractional Maxwell fluids (FMFs). Addition of nanoparticles in base fluids increases their thickness (viscosity) which causes the internal resistance between the layers of flowing fluids, consequently decreasing the velocity $u(y,t)$ of the fluid. This is clearly deliberated in Figure 6.

Finally, the velocity profile against $\alpha = \beta = \nu$ (fractional parameters) is plotted in Figure 7, and results are verified as expected. The consequences of fractional order on fluid motion have an inverse relation. That is, for increasing values of fractional parameter α, the velocity profile decreases. However, $u(y,t)$ decreases for increasing values of α and attains its peak at $\alpha = 1$.

The heat transfer capability of the coupled and nonlinear model is illustrated in Figure 8. Here, the results for the temperature profile against time relaxation parameter λ_2^β are drawn and found as expected. Time relaxation is the key parameter used for characterization of the viscoelastic fluids, and it is the time in which a system relaxes under certain external conditions. Therefore, by the increase in λ_2^β, there results a decrease in the collision of particles within the fluids. This decreases the temperature profile $\theta(y,t)$ of fractional Maxwell nanofluids.

Figure 9 displays that magnetic field parameter impacts directly the temperature of the system because the enhancement in magnetic field parameter $Ha = M^*$ gives rise to a Lorentz force. This results in increase in the temperature profile $\theta(y,t)$ of the system.

Since Prandtl number Pr is the dimensionless number and is the ratio of momentum to thermal diffusivity. Since it is a fluid property, it does not have any dependence on flow type, as viscous forces exert a uniform effect on heat transfer for the whole of location of the channel. So, increase in Pr means heat transfer is favored to occur by momentum, not conduction. Therefore, increase in Pr decreases the temperature profile $\theta(y,t)$ of fractional Maxwell fluids (FMFs) as expressed in Figure 10.

Figure 11 gives the graphical results for influence of volume fraction of nanoparticles in base fluids on heat transfer capability of the system. Addition of nanoparticles in base fluids has a direct impact on enthalpy of the system. This results in entropy control of fluids during flow that is enhancement of thermal conductivity of fluids. The figure shows that increasing volume fraction ϕ enhances the thermal conductivity of the FMF with decrease in the temperature profile $\theta(y,t)$.

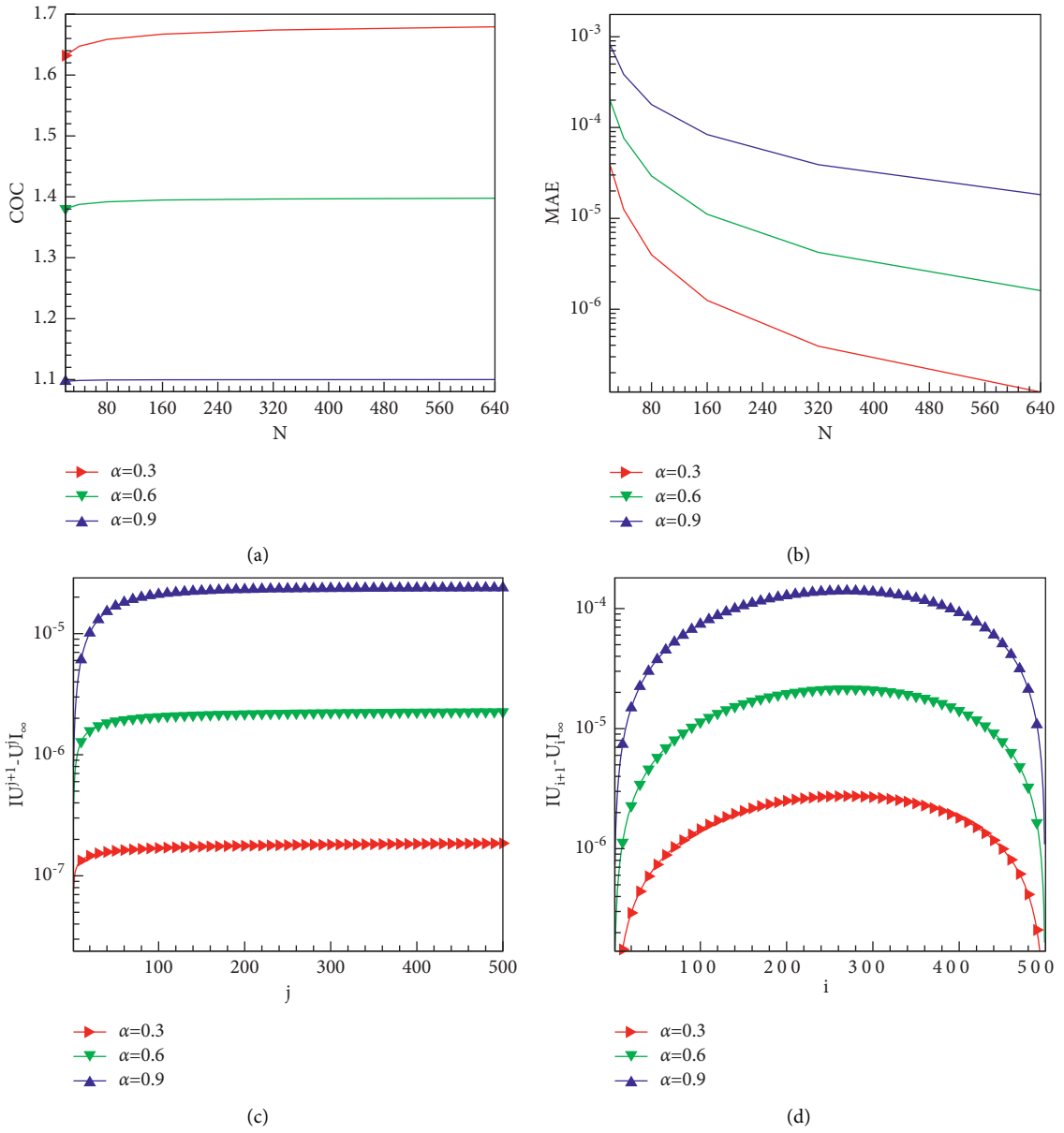

FIGURE 2: Code validation of the proposed scheme and varying time mesh sizes against (a) computational order of convergence (COC) and (b) maximum absolute error (MAE) and varying mesh sizes for (c) time and (d) space against L_∞-norm between consecutive solutions.

Finally, Figure 12 depicts the effect of $(\alpha = \beta = \nu)$ on the temperature profile of the fractional Maxwell fluids. The fractional-order parameter and temperature profile are inversely proportional. It was expected and we obtained that increase in $(\alpha = \beta = \nu)$ decreases the heat transfer capability of the system.

The variations of skin friction coefficient and local Nusselt number are deliberated in Tables 2 and 3. It is noted that the coefficient of skin friction increases with the increase in the physical parameters Gr, λ_1^α, and ϕ . The reverse behavior is observed against the variation of Hartmann number. Nusselt number impact against Pr, M$*$, λ_2^β, and ϕ seems increasing. On the other hand, dominant impact of the fractional-order parameters $\alpha = \beta = \nu$ can be seen in Tables 2 and 3.

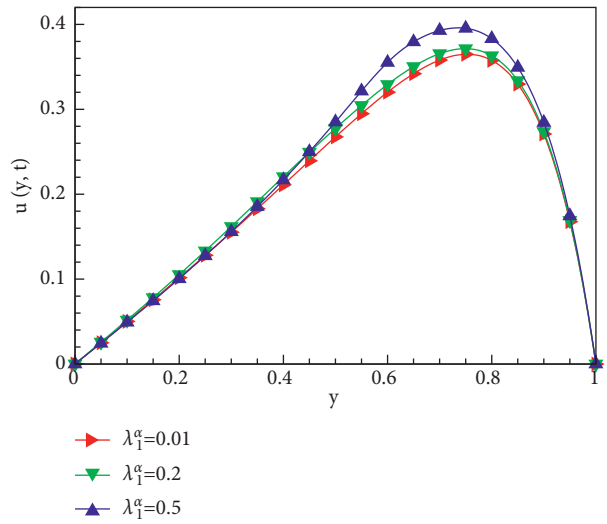

Figure 3: Influence of λ_1^α on u when $\alpha = \beta = 1$, $Gr = 5$, $Ha = 5$, $\lambda_2^\beta = 0.1$, Pr = 6.2, $M^* = 0.5$, and $\phi = 0.1$.

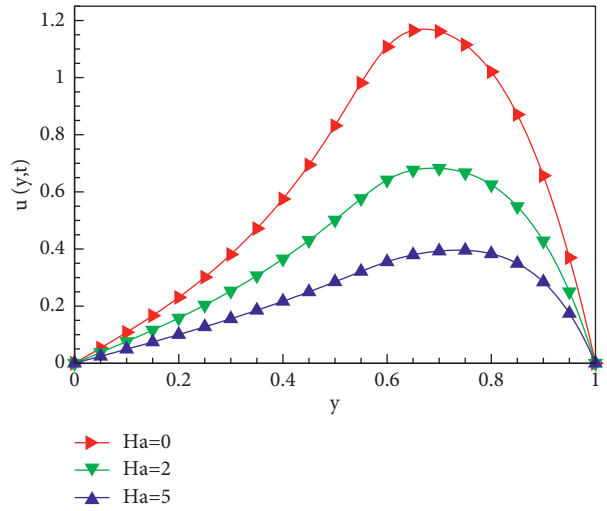

Figure 4: Influence of Ha on u when $\alpha = \beta = 1$, $\lambda_1^\alpha = 0.5$, $Gr = 5$, $\lambda_2^\beta = 0.1$, Pr = 6.2, $M^* = 0.5$, and $\phi = 0.1$.

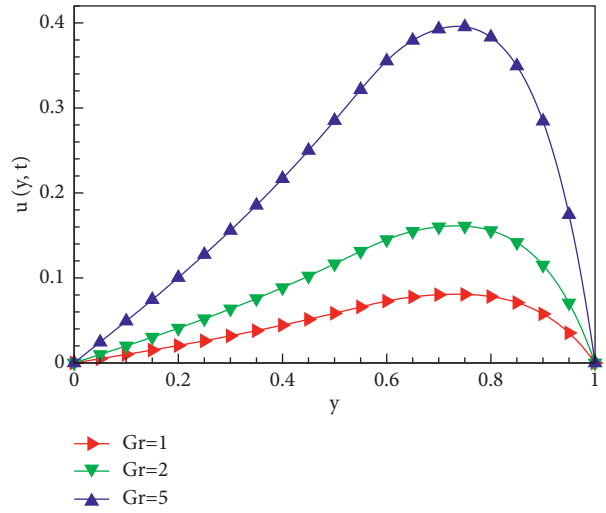

Figure 5: Influence of Gr on u when $\alpha = \beta = 1$, $\lambda_1^\alpha = 0.5$, $Ha = 5$, $\lambda_2^\beta = 0.1$, Pr = 6.2, $M^* = 0.5$, and $\phi = 0.1$.

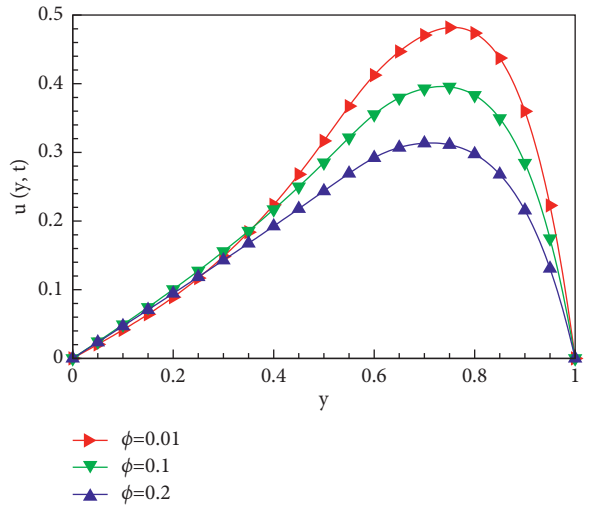

Figure 6: Influence of ϕ on u when $\alpha = \beta = 1$, $\lambda_1^{\alpha} = 0.5$, $Gr = 5$, $Ha = 5$, $\lambda_2^{\beta} = 0.1$, Pr = 6.2, and $M^* = 0.5$.

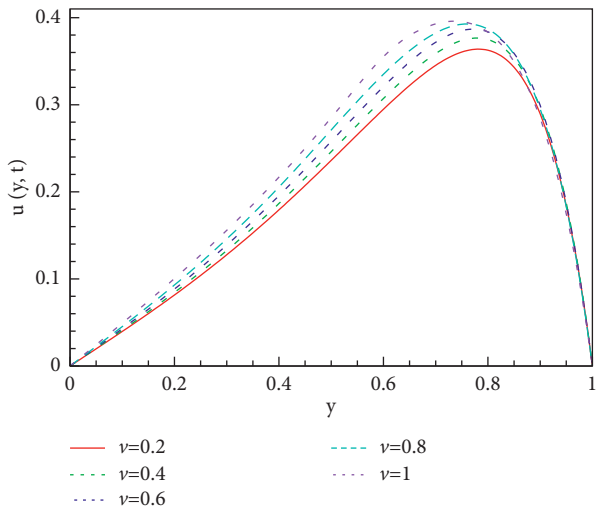

Figure 7: Influence of $\alpha = \beta = \nu$ on u when $\lambda_1^{\alpha} = 0.5$, $Gr = 5$, $Ha = 5$, $\lambda_2^{\beta} = 0.1$, Pr = 6.2, $M^* = 0.5$, and $\phi = 0.1$.

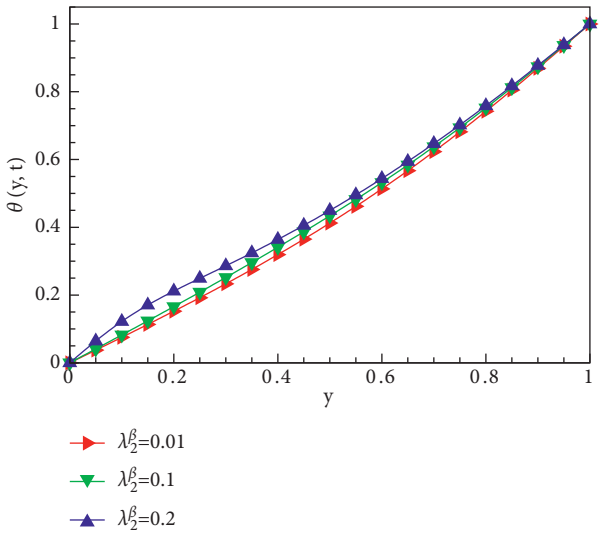

Figure 8: Influence of λ_2^{β} on θ when $\alpha = \beta = 1$, $\lambda_1^{\alpha} = 0.5$, $Gr = 5$, $Ha = 5$, Pr = 6.2, $M^* = 0.5$, and $\phi = 0.1$.

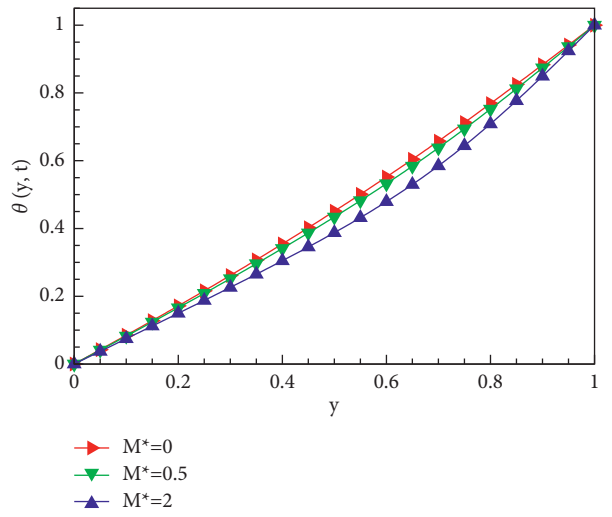

Figure 9: Influence of M^* on θ when $\alpha = \beta = 1$, $\lambda_1^\alpha = 0.5$, $Gr = 5$, $Ha = 5$, $\lambda_2^\beta = 0.1$, Pr = 6.2, and $\phi = 0.1$.

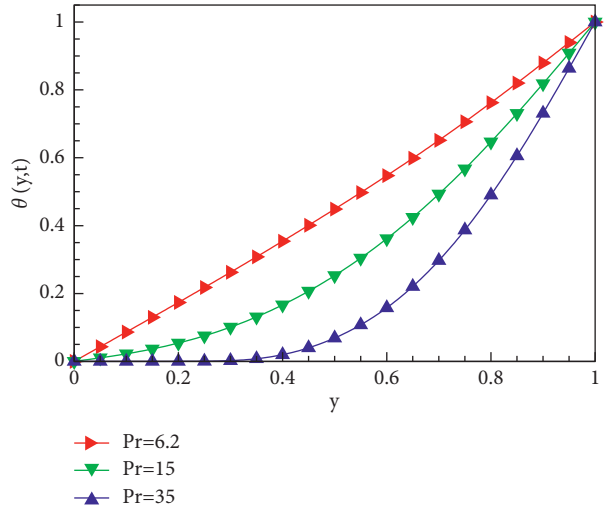

Figure 10: Influence of Pr on θ when $\alpha = \beta = 1$, $\lambda_1^\alpha = 0.5$, $Gr = 5$, $Ha = 5$, $\lambda_2^\beta = 0.1$, $M^* = 0.5$, and $\phi = 0.1$.

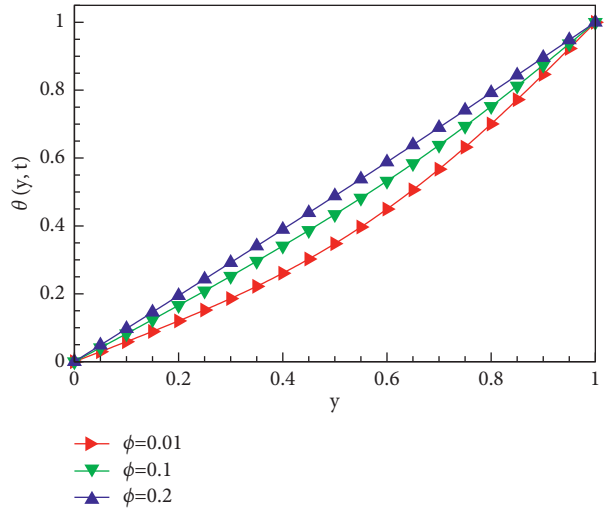

Figure 11: Influence of ϕ on θ when $\alpha = \beta = 1$, $\lambda_1^\alpha = 0.5$, $Gr = 5$, $Ha = 5$, $\lambda_2^\beta = 0.1$, Pr = 6.2, and $M^* = 0.5$.

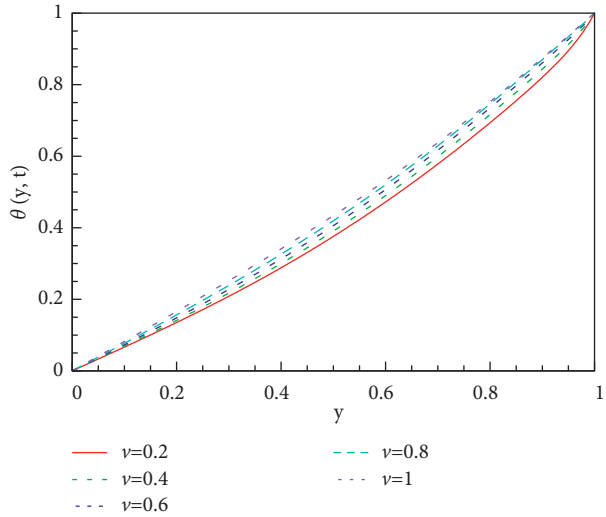

Figure 12: Influence of $\alpha = \beta = \nu$ on θ when $\lambda_1^{\alpha} = 0.5$, $Gr = 5$, $Ha = 5$, $\lambda_2^{\beta} = 0.1$, Pr = 6.2, $M^* = 0.5$, and $\phi = 0.1$.

Table 2: Skin friction analysis against different physical parameters when $\lambda_2^{\beta} = 0.1$, Pr = 6.8, $M^* = 0.5$, and $Re = 10$.

Gr	M	λ_1^{α}	ϕ	$\nu = 0.4$	$\nu = 0.7$	$\nu = 1$
0.1	10	0.5	0.1	0.0047	0.0051	0.0058
2				0.0934	0.1016	0.1160
5				0.2316	0.2519	0.2877
	0			1.0966	0.6819	0.4058
	2			1.0730	0.7047	0.4348
	5			1.0600	0.7500	0.4882
		0.1		0.4177	0.4119	0.4058
		0.3		0.4513	0.4445	0.4348
		0.5		0.5166	0.5044	0.4882
			0.01	0.3642	0.4105	0.3778
			0.15	0.3753	0.4429	0.4049
			0.25	0.4063	0.4910	0.4304

Table 3: Nusselt number analysis against different physical parameters when $\lambda_1^{\alpha} = 0.5, M = 10, Gr = 5$, and $Re = 10$.

Pr	M^*	λ_2^{β}	ϕ	$\nu = 0.4$	$\nu = 0.7$	$\nu = 1$
3.94	0.5	0.1	0.1	0.9142	0.7511	0.2134
6.2				0.9710	0.8129	0.2105
15				0.9999	0.8817	0.2038
3.94	0.1			0.7087	0.6799	0.6384
	2			0.7687	0.7363	0.6894
	5			0.8458	0.8070	0.7505
	0.5	0.01		0.7543	0.7024	0.6552
		0.1		0.7601	0.7617	0.7558
		0.2		0.7672	0.8374	1.3188
			0.01	0.4582	0.7967	0.9335
			0.15	0.4928	0.8582	0.9823
			0.25	0.5854	0.9140	0.9957

7. Conclusion

An unsteady flow and heat transfer for the coupled and nonlinear model of fractional Maxwell fluids is solved by using power law kernel. Findings are done under the effects of magnetic fields within a channel. Codes are developed and executed to obtain the numerical results by applying the finite difference method for discretization of spatial and time derivatives. Some key finding are illustrated as follows:

(a) Fractional-order parameters α and β have a direct impact on velocity profile and inverse impact on temperature profile.

(b) The velocity and temperature are enhanced for a high value of the unsteadiness parameter. Velocity is slightly decreasing for higher values of Reynolds number *Re*, while a smaller value of Reynolds number has more prominent impact on velocity and temperature.

(c) Addition of the nanoparticles to base fluids enhances the thermal conductivity by increasing the surface. Consequently, volumetric concentration of nanoparticles ϕ in base fluids results in decrease in the temperature profile of the FMF.

(d) Finally, the chosen numerical technique of the finite difference method shows stable results and gives new direction to such investigation.

(e) This method can be extended for more numerous types of physical sciences with complex geometries.

This simplified research problem can be generalized to express the effects of viscosity (viscous dissipation), variable thermal conductivity, and multidimensional MHD flow regime and temperature profile of non-Newtonian nanofluids. Many opportunities for further investigation exist in this direction for detailed study.

Abbreviations

$u\,(m/s)$: Velocity
$\theta\,(K)$: Temperature
$\rho_{nf}\,(\mathrm{kg/m^3})$: Density
$\mu_{nf}\,(\mathrm{kg/ms})$: Dynamic viscosity
$k_{nf}\,(W/mK)$: Thermal conductivity of nanofluid
$\beta_\theta\,(K^{-1})$: Volumetric thermal expansion coefficient
$g\,(m/s^2)$: Gravitational acceleration
$(C_p)_{nf}$: Heat capacity of nanoparticles
$\sigma_{nf}\,(S/m)$: Electrical conductivity of nanoparticles
$\nu_{nf}\,(m^2/s)$: Kinematic viscosity of nanoparticles
ϕ: Volume fraction of nanoparticles.

Data Availability

No data were used to support this study.

Conflicts of Interest

The authors declare that they have no conflicts of interest.

Acknowledgments

This research was funded by the Princess Nourah bint Abdulrahman University Researchers Supporting Project number (PNURSP2022R152), Princess Nourah bint Abdulrahman University, Riyadh, Saudi Arabia. Also, the authors extend their appreciation to the Deanship of Scientific Research at King Khalid University, Abha, Saudi Arabia for funding this work through research groups program under grant number R.G.P-2/135/42.

References

[1] M. Saqib, F. Ali, I. Khan, N. A. Sheikh, S. A. A. Jan, and U. H. Sami, "Exact solutions for free convection flow of generalized Jeffrey fluid: a Caputo-Fabrizio fractional model," *Alexandria Engineering Journal*, vol. 57, no. 3, pp. 1849–1858, 2018.

[2] M. Saqib, S. Shafie, I. Khan, Y.-M. Chu, and K. S. Nisar, "Symmetric MHD channel flow of nonlocal fractional model of BTF containing hybrid nanoparticles," *Symmetry*, vol. 12, no. 4, p. 663, 2020.

[3] M. Saqib, A. R. K. Mohd, N. F. Mohammad, D. L. C. Chuan, and S. Shafie, "Application of fractional derivative without singular and local kernel to enhanced heat transfer in CNTs nanofluid over an inclined plate," *Symmetry*, vol. 12, no. 5, p. 768, 2020.

[4] F. Ali, M. Saqib, I. Khan, and N. A. Sheikh, "Application of Caputo-Fabrizio derivatives to MHD free convection flow of generalized Walters'-B fluid model," *The European Physical Journal Plus*, vol. 131, no. 10, pp. 1–10, 2016.

[5] N. A. Sheikh, F. Ali, M. Saqib et al., "Comparison and analysis of the Atangana-Baleanu and Caputo-Fabrizio fractional derivatives for generalized Casson fluid model with heat generation and chemical reaction," *Results in Physics*, vol. 7, pp. 789–800, 2017.

[6] M. I. Asjad, M. D. Ikram, and R. Ali, "New analytical solutions of heat transfer flow of clay-water base nanoparticles with the application of novel hybrid fractional derivative," *Thermal Science*, vol. 24, no. Suppl. 1, pp. 343–350, 2020.

[7] Y.-M. Chu, M. D. Ikram, M. I. Asjad, A. Ahmadian, and F. Ghaemi, "Influence of hybrid nanofluids and heat generation on coupled heat and mass transfer flow of a viscous fluid with novel fractional derivative," *Journal of Thermal Analysis and Calorimetry*, vol. 144, no. 6, pp. 2057–2077, 2021.

[8] T. Hayat, A. Inayatullah, A. Alsaedi, and B. Ahmad, "Thermo diffusion and diffusion thermo impacts on bioconvection Walter-B nanomaterial involving gyrotactic microorganisms," *Alexandria Engineering Journal*, vol. 60, no. 6, pp. 5537–5545, 2021.

[9] A. Tassaddiq, I. Khan, K. Sooppy Nisar, and J. Singh, "MHD flow of a generalized Casson fluid with Newtonian heating: a fractional model with Mittag-Leffler memory," *Alexandria Engineering Journal*, vol. 59, no. 5, pp. 3049–3059, 2020.

[10] J. C. Maxwell, "On the dynamical theory of gases," *Proceedings of the Royal Society of London*, vol. 15, pp. 167–171, 1866.

[11] M. Takashima, "The effect of a magnetic field on thermal instability in a layer of Maxwell fluid," *Physics Letters A*, vol. 33, no. 6, pp. 371-372, 1970.

[12] J. Choi, Z. Rusak, and J. Tichy, "Maxwell fluid suction flow in a channel," *Journal of Non-newtonian Fluid Mechanics*, vol. 85, no. 2-3, pp. 165–187, 1999.

[13] C. Fetecau and C. Fetecau, "A new exact solution for the flow of a Maxwell fluid past an infinite plate," *International Journal of Non-linear Mechanics*, vol. 38, no. 3, pp. 423–427, 2003.

[14] C. Fetecau and C. Fetecau, "The Rayleigh-Stokes-Problem for a fluid of Maxwellian type," *International Journal of Non-linear Mechanics*, vol. 38, no. 4, pp. 603–607, 2003.

[15] C. Friedrich, "Relaxation and retardation functions of the Maxwell model with fractional derivatives," *Rheologica Acta*, vol. 30, no. 2, pp. 151–158, 1991.

[16] P. M. Jordan, A. Puri, and G. Boros, "On a new exact solution to Stokes' first problem for Maxwell fluids," *International Journal of Non-linear Mechanics*, vol. 39, no. 8, pp. 1371–1377, 2004.

[17] F. Olsson and J. Yström, "Some properties of the upper convected Maxwell model for viscoelastic fluid flow," *Journal of Non-newtonian Fluid Mechanics*, vol. 48, no. 1-2, pp. 125–145, 1993.

[18] L. Liu and F. Liu, "Boundary layer flow of fractional Maxwell fluid over a stretching sheet with variable thickness," *Applied Mathematics Letters*, vol. 79, pp. 92–99, 2018.

[19] M. Zhang, M. Shen, F. Liu, and H. Zhang, "A new time and spatial fractional heat conduction model for Maxwell nanofluid in porous medium," *Computers & Mathematics with Applications*, vol. 78, no. 5, pp. 1621–1636, 2019.

[20] N. Sadiq, M. Imran, C. Fetecau, and N. Ahmed, "Rotational motion of fractional Maxwell fluids in a circular duct due to a time-dependent couple," *Boundary Value Problems*, vol. 2019, no. 1, pp. 1–11, 2019.

[21] Y. Bai, L. Huo, Y. Zhang, and Y. Jiang, "Flow, heat and mass transfer of three-dimensional fractional Maxwell fluid over a bidirectional stretching plate with fractional Fourier's law and fractional Fick's law," *Computers & Mathematics with Applications*, vol. 78, no. 8, pp. 2831–2846, 2019.

[22] X. Chen, W. Yang, X. Zhang, and F. Liu, "Unsteady boundary layer flow of viscoelastic MHD fluid with a double fractional Maxwell model," *Applied Mathematics Letters*, vol. 95, pp. 143–149, 2019.

[23] N. Raza and M. A. Ullah, "A comparative study of heat transfer analysis of fractional Maxwell fluid by using Caputo and Caputo-Fabrizio derivatives," *Canadian Journal of Physics*, vol. 98, no. 1, pp. 89–101, 2020.

[24] S. U. Choi and J. A. Eastman, *Enhancing thermal Conductivity of Fluids with Nanoparticles*, Argonne National Lab., IL, USA, 1995.

[25] R. K. Tiwari and M. K. Das, "Heat transfer augmentation in a two-sided lid-driven differentially heated square cavity utilizing nanofluids," *International Journal of Heat and Mass Transfer*, vol. 50, no. 9-10, pp. 2002–2018, 2007.

[26] M. Saqib, I. Khan, and S. Shafie, "Application of Atangana-Baleanu fractional derivative to MHD channel flow of CMC-based-CNT's nanofluid through a porous medium," *Chaos, Solitons & Fractals*, vol. 116, pp. 79–85, 2018.

[27] M. Shamshuddin and M. R. Eid, "Magnetized nanofluid flow of ferromagnetic nanoparticles from parallel stretchable rotating disk with variable viscosity and thermal conductivity," *Chinese Journal of Physics*, vol. 74, pp. 20–37, 2021.

[28] M. Aleem, M. Imran Asjad, M. S. R. Chowdhury, and A. Hussanan, "Analysis of mathematical model of fractional viscous fluid through a vertical rectangular channel," *Chinese Journal of Physics*, vol. 61, pp. 336–350, 2019.

[29] W. Jamshed, C. Şirin, F. Selimefendigil, M. Shamshuddin, Y. Altowairqi, and M. R. Eid, "Thermal characterization of coolant maxwell type nanofluid flowing in parabolic trough solar collector (PTSC) used inside solar powered ship application," *Coatings*, vol. 11, no. 12, p. 1552, 2021.

[30] M. Shamshuddin, S. R. Mishra, O. A. Bég, T. A. Bég, and K. Ali, "Computation of radiative Marangoni (thermocapillary) magnetohydrodynamic convection in a Cu-water based nanofluid flow from a disk in porous media: smart coating simulation," *Heat Transfer*, vol. 50, no. 3, pp. 1931–1950, 2021.

[31] T. Hayat, T. Muhammad, S. A. Shehzad, G. Q. Chen, and I. A. Abbas, "Interaction of magnetic field in flow of Maxwell nanofluid with convective effect," *Journal of Magnetism and Magnetic Materials*, vol. 389, pp. 48–55, 2015.

[32] A. Jafarimoghaddam, "On the homotopy analysis method (HAM) and homotopy perturbation method (HPM) for a nonlinearly stretching sheet flow of Eyring-Powell fluids," *Engineering Science and Technology, an International Journal*, vol. 22, no. 2, pp. 439–451, 2019.

[33] C. Sravanthi and R. Gorla, "Effects of heat source/sink and chemical reaction on MHD Maxwell nanofluid flow over a convectively heated exponentially stretching sheet using homotopy analysis method," *International Journal of Applied Mechanics and Engineering*, vol. 23, no. 1, 2018.

[34] T. Anwar, P. Kumam, I. Khan, and W. Watthayu, "Heat transfer enhancement in unsteady MHD natural convective flow of CNTs Oldroyd-B nanofluid under ramped wall velocity and ramped wall temperature," *Entropy*, vol. 22, no. 4, p. 401, 2020.

[35] A. Q. Khan and A. Rasheed, "Numerical simulation of fractional Maxwell fluid flow through forchheimer medium," *International Communications in Heat and Mass Transfer*, vol. 119, Article ID 104872, 2020.

[36] N. A. Sheikh, F. Ali, I. Khan, M. Gohar, and M. Saqib, "On the applications of nanofluids to enhance the performance of solar collectors: a comparative analysis of Atangana-Baleanu and Caputo-Fabrizio fractional models," *The European Physical Journal Plus*, vol. 132, no. 12, pp. 1–11, 2017.

[37] C.-C. Wang, "Mathematical principles of mechanics and electromagnetism: Part A: Analytical and continuum mechanics," *Springer Science & Business Media*, vol. 16, 2013.

[38] M. Saqib, I. Khan, and S. Shafie, "Application of fractional differential equations to heat transfer in hybrid nanofluid: modeling and solution via integral transforms," *Advances in Difference Equations*, vol. 2019, no. 1, pp. 1–18, 2019.

[39] J. Zhao, L. Zheng, X. Zhang, and F. Liu, "Convection heat and mass transfer of fractional MHD Maxwell fluid in a porous medium with Soret and Dufour effects," *International Journal of Heat and Mass Transfer*, vol. 103, pp. 203–210, 2016.

[40] C. Cattaneo, "A form of heat-conduction equations which eliminates the paradox of instantaneous propagation," *Comptes Rendus*, vol. 247, p. 431, 1958.

[41] L. Liu, L. Zheng, and F. Liu, "Time fractional Cattaneo-Christov anomalous diffusion in comb frame with finite length of fingers," *Journal of Molecular Liquids*, vol. 233, pp. 326–333, 2017.

[42] T. A. Yusuf, F. Mabood, W. A. Khan, and J. A. Gbadeyan, "Irreversibility analysis of Cu-TiO2-H2O hybrid-nanofluid impinging on a 3-D stretching sheet in a porous medium with nonlinear radiation: Darcy-Forchhiemer's model," *Alexandria Engineering Journal*, vol. 59, no. 6, pp. 5247–5261, 2020.

[43] S. Hazarika, S. Ahmed, and A. J. Chamkha, "Investigation of nanoparticles Cu, Ag and Fe3O4 on thermophoresis and viscous dissipation of MHD nanofluid over a stretching sheet in a porous regime: a numerical modeling," *Mathematics and Computers in Simulation*, vol. 182, pp. 819–837, 2021.

[44] J. Zhao, L. Zheng, X. Zhang, and F. Liu, "Unsteady natural convection boundary layer heat transfer of fractional Maxwell viscoelastic fluid over a vertical plate," *International Journal of Heat and Mass Transfer*, vol. 97, pp. 760–766, 2016.

[45] A. Q. Khan and A. Rasheed, "Mixed convection magneto-hydrodynamics flow of a nanofluid with heat transfer: a numerical study," *Mathematical Problems in Engineering*, vol. 2019, Article ID 8129564, 14 pages, 2019.

Hindawi
Complexity
Volume 2022, Article ID 8362836, 12 pages
https://doi.org/10.1155/2022/8362836

Review Article

A Three-Dimensional Autonomous System with a Parabolic Equilibrium: Dynamical Analysis, Adaptive Synchronization via Relay Coupling, and Applications to Steganography and Chaos Encryption

Janarthanan Ramadoss,[1] Romanic Kengne,[2] Dianorré Tokoue Ngatcha,[3] Victor Kamdoum Tamba,[4] Karthikeyan Rajagopal,[5] and Marceline Motchongom Tingue[6]

[1]*Center for Artificial Intelligence, Chennai Institute of Technology, Chennai 600069, Tamilnadu, India*
[2]*Research Unit of Condensed Matter of Electronics and Signal Processing, Department of Physics, Faculty of Sciences, University of Dschang, P.O. Box 67, Dschang, Cameroon*
[3]*Department of Automotive and Mechatronics Engineering, National Advanced School of Engineering, University of Douala, P.O. Box 24, 2701, Douala, Cameroon*
[4]*Department of Telecommunication and Network Engineering, IUT-Fotso Victor of Bandjoun, University of Dschang, P.O. Box 134, Bandjoun, Cameroon*
[5]*Center for Nonlinear Systems, Chennai Institute of Technology, Chennai 600069, Tamilnadu, India*
[6]*Higher Technical Teachers Training College, University of Bamenda, P.O. Box 39, Bambili, Bamenda, Cameroon*

Correspondence should be addressed to Romanic Kengne; kengneromaric@gmail.com

Received 18 February 2022; Revised 16 April 2022; Accepted 23 April 2022; Published 16 May 2022

Academic Editor: Mustafa Cagri Kutlu

This paper is reporting on electronic implementation of a three-dimensional autonomous system with infinite equilibrium point belonging to a parabola. Performance analysis of an adaptive synchronization via relay coupling and a hybrid steganography chaos encryption application are provided. Besides striking parabolic equilibrium, the proposed three-dimensional autonomous system also exhibits hidden chaotic oscillations as well as hidden chaotic bursting oscillations. Electronic implementation of the hidden chaotic behaviors is done to confirm their physical existence. A good qualitative agreement is shown between numerical simulations and OrCAD-PSpice results. Moreover, adaptive synchronization via relay coupling of three three-dimensional autonomous systems with a parabolic equilibrium is analysed by using time histories. Numerical results demonstrate that global synchronization is achieved between the three units. Finally, chaotic behavior found is exploited to provide a suitable text encryption scheme by hidden secret message inside an image using steganography and chaos encryption.

1. Introduction

It is widely recognized that mathematically simple systems of nonlinear differential equations can exhibit chaos. With the advent of fast computers, it is now possible to explore the entire parameter space of these systems with the goal of finding parameters that result in some desired characteristics [1].

Recent research has involved categorizing periodic and chaotic attractors as either self-excited or hidden [2–10]. A self-excited attractor has a basin of attraction that is associated with an unstable equilibrium, whereas a hidden attractor has a basin of attraction that does not intersect with small neighbourhoods of any equilibrium points. The classical attractors of Lorenz, Rössler, Chua, Chen, and Sprott systems (cases B to S) and other widely known

attractors are those excited from an unstable equilibrium. From a computational point of view, this allows one to use a numerical method in which a trajectory started from a point on the unstable manifold in the neighbourhood of an unstable equilibrium and reaches an attractor, to identify it [2]. Hidden attractors cannot be found by this method and are important in engineering applications because they allow unexpected and potentially disastrous responses to perturbations in structures like a bridge or an airplane wing.

The chaotic attractors in dynamical systems without any equilibrium points, with only stable equilibria, or with infinite number of equilibria are hidden attractors. That is the reason why such systems are rarely found. However, recently, such systems have been reported in literatures [11–47]. Especially, systems with infinite number of equilibria are rare and challenging to find. There are three families of chaotic systems with infinite number of equilibria: systems with line equilibria [33–37], systems with closed-curve equilibria [38–41], and systems with open-curve equilibria [42, 43]. Recently, systems with infinite number of equilibria have been studied as an exciting research subject [26, 30, 44, 45]. However, there is still a necessity and challenge to discover new chaotic systems with different opened-curve equilibria [23, 46].

A three-dimensional autonomous system with hidden attractors and a parabolic curve of equilibria is introduced in this paper. The proposed chaotic system has one positive control parameter and six terms among which four are nonlinear. Its simplicity is remarkable while it is capable of displaying chaotic oscillations and chaotic bursting oscillations depending solely on the control parameter. It is worth noting that chaotic bursting oscillations are usually found in systems with self-excited attractors [47–52]. To the best of our knowledge, there is no three-dimensional system with hidden attractors exhibiting chaotic oscillations and chaotic bursting oscillations. However, some questions arise: Can the three-dimensional autonomous system with parabolic curve of equilibria synchronize? Can chaotic behavior found in the three-dimensional autonomous system with parabolic curve of equilibria be exploited to provide suitable steganography and chaos encryption?

The rest of this paper is organized as follows. In Section 2, fundamental properties of the proposed three-dimensional system are investigated by means of equilibrium points, eigenvalue structures, phase portrait, time series, basin of attraction, bifurcation diagram, and Lyapunov exponents. The physical existence of the chaotic behavior found in the proposed system is verified using electronic implementation in Section 3. An adaptive synchronization via relay coupling of three three-dimensional autonomous systems with parabolic curve of equilibria is investigated in Section 4. An application to steganography and chaos encryption is performed in Section 5. Finally, the paper is concluded in Section 6.

2. Analysis of the Three-Dimensional Autonomous System with a Parabolic Equilibrium

Inspired by the method and structure proposed in [41], a three-dimensional autonomous system with a parabolic equilibrium is introduced in this section:

$$\begin{aligned}\frac{\mathrm{d}x}{\mathrm{d}t} &= -z,\\ \frac{\mathrm{d}y}{\mathrm{d}t} &= xz^2,\\ \frac{\mathrm{d}z}{\mathrm{d}t} &= x - y^2 + z\left(ay^2 - z^2\right),\end{aligned} \tag{1}$$

where x, y, and z are state variables, t is the time, and a is a positive parameter. System (1) has only one parameter a. System (1) has a parabolic equilibrium given by

$$E = \left\{ \frac{(x, y, z) \in R^3}{x = \left(y^*\right)^2}, y = y^*, z = 0 \right\}. \tag{2}$$

The characteristic equation of system (1) evaluated at the parabolic equilibrium is

$$\lambda\left(\lambda^2 - a\left(y^*\right)^2\lambda + 1\right) = 0. \tag{3}$$

The roots of equation (3) depend on the sign of $a^2(y^*)^4 - 4$. If $a^2(y^*)^4 - 4 > 0$, the roots of equation (3) are $\lambda_1 = 0$ and $\lambda_{2,3} = (a(y^*)^2 \pm \sqrt{a^2(y^*)^4 - 4})/2$. The characteristic equations have at least a positive real root; therefore, E is unstable. For $a^2(y^*)^4 - 4 < 0$, the roots of equation (3) are $\lambda_1 = 0$ and $\lambda_{2,3} = (a(y^*)^2 \pm i\sqrt{|a^2(y^*)^4 - 4|})/2$. Since $a > 0$, equation (3) has a pair of complex conjugate eigenvalues with positive real root, so E is unstable. Thus, E is always unstable for $a > 0$.

To investigate the dynamical behaviors of system (1), Lyapunov exponents (LEs) and bifurcation diagram depicting maxima of $x(t)$ versus the parameter a for the initial conditions *(x(0), y(0), z(0)) = (0, 0.1, 0.2)* are plotted in Figure 1.

By increasing the parameter a from 3.0 to 3.5, system (1) exhibits chaotic behavior followed by a reverse period-doubling leading to period-1-oscillation as shown in Figure 1(c). Depending on the value of the amplitude of the output $x(t)$, the chaotic region can be divided into two regions: chaotic bursting oscillations for $3.0 \le a \le 3.127$ and chaotic oscillations for $3.127 < a < 3.198$. Chaotic behavior is confirmed by the LE shown in Figure 1(b). Chaotic behaviors found in the bifurcation diagram of Figure 1(a) are further detailed in Figure 2 which presents the time series of $x(t)$, $y(t)$, and $z(t)$ and the corresponding phase portraits for specific values of parameter a.

In the left panel of Figure 2, we can see that the variables *x(t)* and *z(t)* show a fast changing processes, while the variable *y(t)* describes a relatively slowly changing quantity.

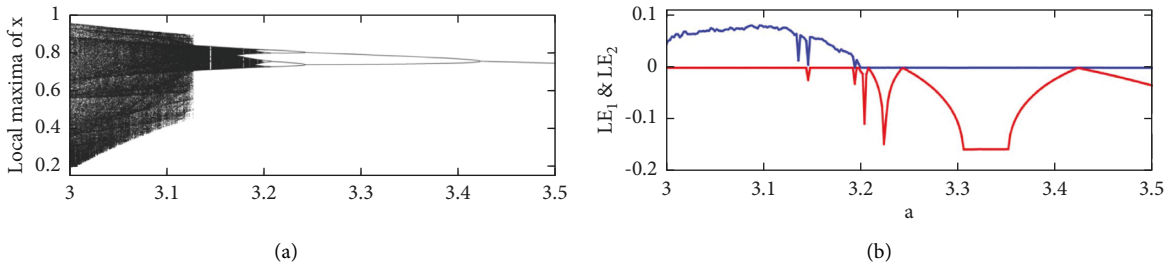

Figure 1: (a) Local maxima of (x) showing a typical reverse period-doubling route to chaos and (b) LE.

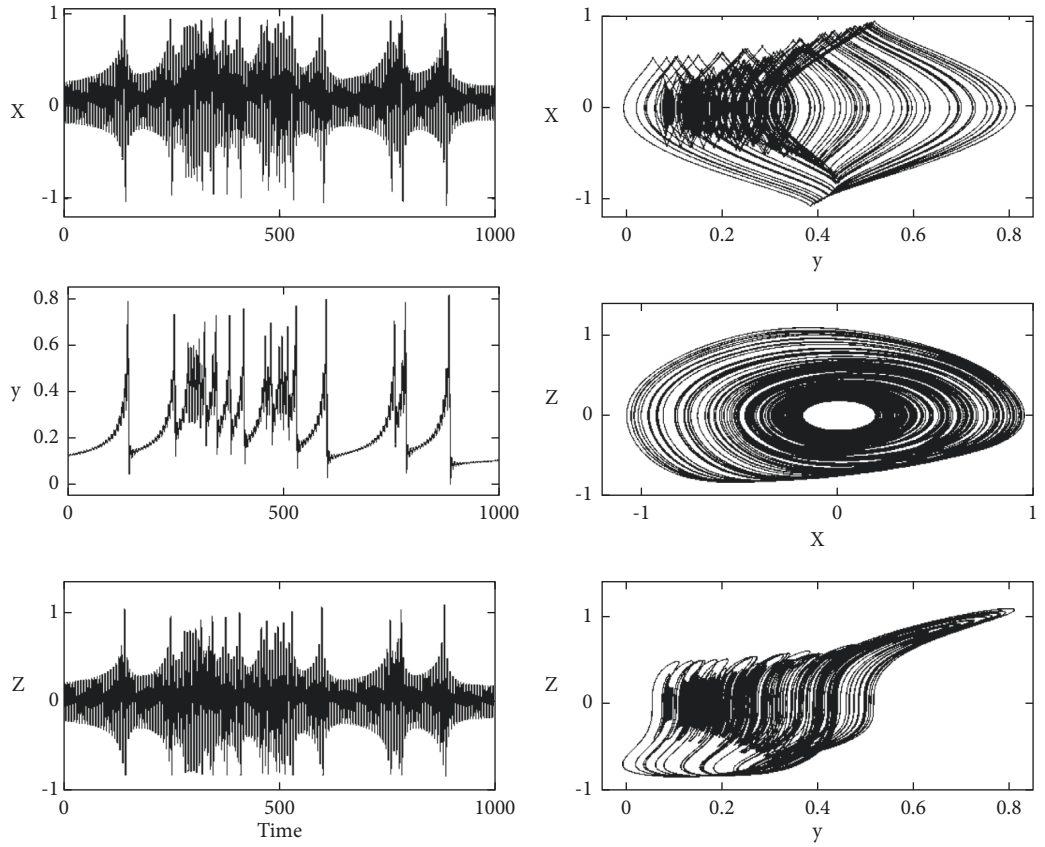

Figure 2: (a) Time series of $x(t)$, $y(t)$, and $z(t)$, while the (b) phase portraits in the different planes for $a = 3$.

The fast-slow variables are confirmed by the corresponding phase portraits in the right panel of Figure 2. The signals *x(t)* and *z(t)* alternate between a silent and an active phase. These latter are thus called chaotic bursting oscillations. Chaotic behaviors found in Figure 1 for $3.127 < a < 3.198$ are depicted in Figure 3.

In the time domain, Figure 3(a) shows chaotic oscillations, and in Figure 3(b), the phase portraits display chaotic attractors. The basin of attraction of system (1) in the plane $z = 0$ for $a = 3.0$ is shown in Figure 4.

In Figure 4, the initial conditions in the white region lead to unbounded orbits, those in the light blue region lead to the strange attractor, and those on the red curve are the parabolic equilibrium. From Figure 4, one can notice that the proposed three-dimensional autonomous system with a parabolic equilibrium belongs to chaotic systems with hidden attractors [2–6, 9, 47] since the basin of attraction of the strange attractor intersects only a limited portion of the curve of equilibria.

3. Electronic Circuit Simulation of the Three-Dimensional Autonomous System with a Parabolic Equilibrium

Three state variables x, y, and z of system (1) are rescaled to overcome the difficulties in realization [53–55]. Therefore, system (1) is rewritten as

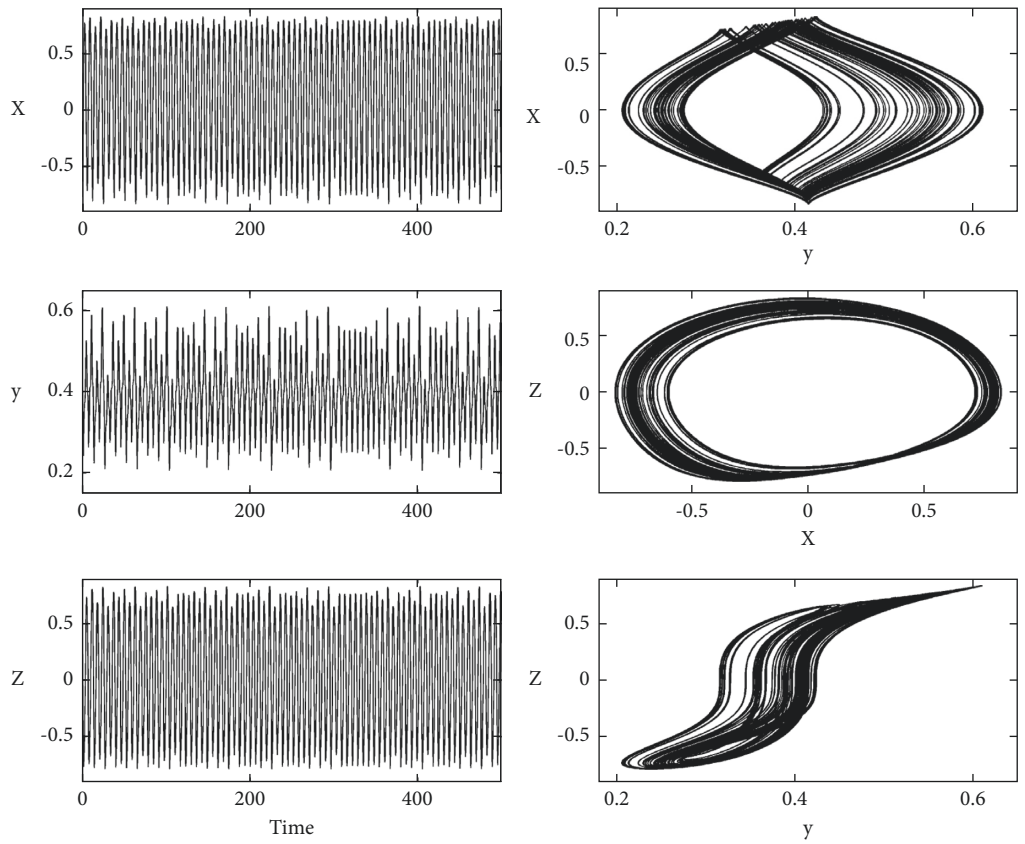

Figure 3: (a) Time series of $x(t)$, $y(t)$, and $z(t)$ while the (b) phase portraits in the different planes for $a = 3.16$.

$$\frac{dX}{dt} = -Z,$$

$$\frac{dY}{dt} = \frac{XZ^2}{10^2}, \tag{4}$$

$$\frac{dZ}{dt} = X - \frac{Y^2}{10} + a\frac{Y^2Z}{10^2} - \frac{Z^3}{10^2},$$

where $X = 10x$, $Y = 10y$, and $Z = 10z$. The circuit in Figure 5 is designed to realize system (4). This circuit has been designed using a multiplier's inherent characteristics [56, 57].

The circuit of Figure 5 consists of resistors, operational amplifiers, analogue multipliers, and capacitors. From Figure 5, the circuital equations are derived as

$$\frac{dV_X}{dt} = -\frac{1}{R_1C_1}V_Z,$$

$$\frac{dV_Y}{dt} = \frac{1}{R_2C_2k_m^2}V_XV_Z^2, \tag{5}$$

$$\frac{dV_Z}{dt} = \frac{1}{R_3C_3}V_X - \frac{1}{R_4C_3k_m}V_Y^2 + \frac{1}{R_5C_3k_m^2}V_Y^2V_Z - \frac{1}{R_6C_3k_m^2}V_Z^3,$$

where V_X, V_Y, and V_Z are the output voltages of the operational amplifiers (see Figure 5). The fixed constant of the multipliers is denoted as k_m, and $k_m = 10\,\mathrm{V}$. Normalizing circuital equations (5) by using the dimensionless states variables

$$X = \frac{V_X}{1.0\mathrm{V}}, Y = \frac{V_Y}{1.0\mathrm{V}}, Z = \frac{V_Z}{1.0\mathrm{V}}, t\prime = \tau t = 100\mu s \cdot t, \tag{6}$$

and inserting equations (6) in (5), the following system is obtained:

$$\frac{dX}{dt\prime} = \frac{\tau}{C_1}\left(-\frac{1}{R_1}Z\right),$$

$$\frac{dY}{dt\prime} = \frac{\tau}{C_2}\left(\frac{1}{R_2k_m^2}\right)XZ^2, \tag{7}$$

$$\frac{dZ}{dt\prime} = \frac{\tau}{C_3}\left(\frac{1}{R_3}X - \frac{1}{R_4k_m}Y^2 + \frac{1}{R_5k_m^2}Y^2Z - \frac{1}{R_6k_m^2}Z^3\right).$$

Obviously, system (7) is equivalent to system (4) with the following conditions:

$$\frac{\tau}{R_1C_1} = \frac{\tau}{R_2C_2} = \frac{\tau}{R_3C_3} = \frac{\tau}{R_4C_3} = \frac{\tau}{R_6C_3} = 1, \frac{\tau}{R_5C_3} = a. \tag{8}$$

The resistor R_5 is used to vary the value of the parameter a. As a result, the values of circuit components are selected as $R_1 = R_2 = R_3 = R_4 = R_6 = R = 10\,\mathrm{k\Omega}$, $C_1 = C_2 = C_3 = C = 10\,\mathrm{nF}$, and $R_5 = 3.333\,\mathrm{k\Omega}$ (for $a = 3$) or $R_5 = 3.165\,\mathrm{k\Omega}$ (for $a = 3.16$).

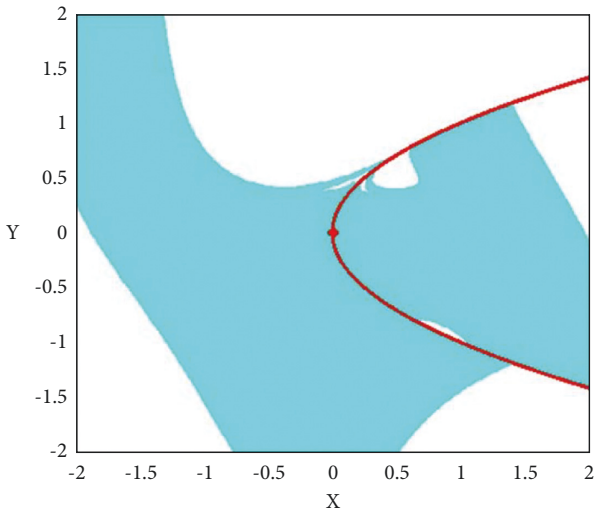

Figure 4: Cross section of the basins of attraction of the two attractors in the xy-plane at $z=0$. Initial conditions in the white region lead to unbounded orbits, those in the red region are exactly on the curve equilibrium (it can be seen that there is no basin for the curve of equilibria which proves that the equilibrium is unstable), and those in the light blue region lead to the strange attractor shown in cross section as black dots.

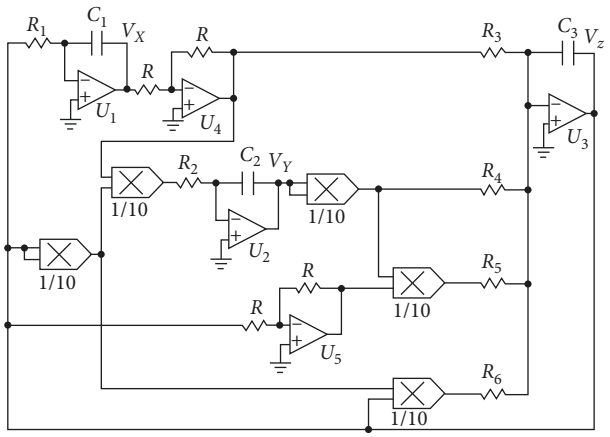

Figure 5: Schematic diagram of the designed circuit for system (4).

Phase portraits in Figure 6 are obtained by using the electronic simulation package OrCAD-PSpice.

There is a good agreement between the numerical simulations and OrCAD-PSpice results when comparing the phase portraits of Figures 2 and 3 with Figure 6.

4. Adaptive Synchronization between the Relay Coupling of Three Three-Dimensional Autonomous Systems with a Parabolic Equilibrium

The relay coupling topology of three three-dimensional autonomous systems with a parabolic equilibrium used in this paper is represented in Figure 7.

In Figure 7, outer 1 is defined by the state variables (x_m, y_m, z_m), outer 2 by the state variables (x_s, y_s, z_s), and relay by the state variables (x_r, y_r, z_r). The variables u_1 and u_2 are the control signals between outer 1 and relay whereas u_3 and u_4 are the control signals between outer 2 and relay. Based on Figure 7, the rate-equations describing the three units coupled in relay are given by the following.

Outer 1 oscillator:

$$\begin{aligned}\dot{x}_m &= -z_m\\ \dot{y}_m &= x_m z_m^2 + u_1\\ \dot{z}_m &= x_m - y_m^2 + z_m\left(a y_m^2 - z_m^2\right) + u_2.\end{aligned} \tag{9}$$

Outer 2 oscillator:

$$\begin{aligned}\dot{x}_s &= -z_s\\ \dot{y}_s &= x_s z_s^2 + u_3\\ \dot{z}_s &= x_s - y_s^2 + z_s\left(a y_s^2 - z_s^2\right) + u_4,\end{aligned} \tag{10}$$

and relay oscillator:

$$\begin{aligned}\dot{x}_r &= -z_r,\\ \dot{y}_r &= x_r z_r^2 + u_5,\\ \dot{z}_r &= x_r - y_r^2 + z_r\left(a y_r^2 - z_r^2\right) + u_6,\end{aligned} \tag{11}$$

where $u_i (i = 1, \ldots, 6)$ are the controller law defined as follows:

$$\begin{aligned}u_1 &= -k(t)(y_m - y_r)\\ u_2 &= -k(t)(z_m - z_r)\\ u_3 &= -k(t)(y_s - y_r)\\ u_4 &= -k(t)(z_s - z_r)\\ u_5 &= -(u_1 + u_3) = -k(t)(2y_r - y_m - y_s),\\ u_6 &= -(u_2 + u_4) = -k(t)(2z_r - z_m - z_s).\end{aligned} \tag{12}$$

The coupling strength $k(t)$ is updated with the law as follows:

$$\dot{k}(t) = \gamma\left[(2y_r - y_m - y_s)^2 + (2z_r - z_m - z_s)^2\right] \tag{13}$$

The global error states are defined as follows:

$$\begin{aligned}e_1(t) &= x_m + x_s - 2x_r,\\ e_2(t) &= y_m + y_s - 2y_r,\\ e_3(t) &= z_m + z_s - 2z_r.\end{aligned} \tag{14}$$

After some mathematical simplifications, the dynamical error system is given by

$$\begin{aligned}\dot{e}_1(t) &= -e_3,\\ \dot{e}_2(t) &= f(x, y, z) - 3k(t)e_2,\\ \dot{e}_3(t) &= e_1 + g(x, y, z) - 3k(t)e_3,\\ \dot{k}(t) &= \gamma\left(e_2^2 + e_3^2\right),\end{aligned} \tag{15}$$

where $f(x, y, z) = x_m z_m^2 + x_s z_s^2 - 2x_r z_r^2$ and $g(x, y, z) = -(y_m^2 + y_s^2 - 2y_r^2) + z_m(a y_m^2 - z_m^2) + z_s(a y_s^2 - z_s^2) - 2z_r(a y_r^2 - z_r^2)$.

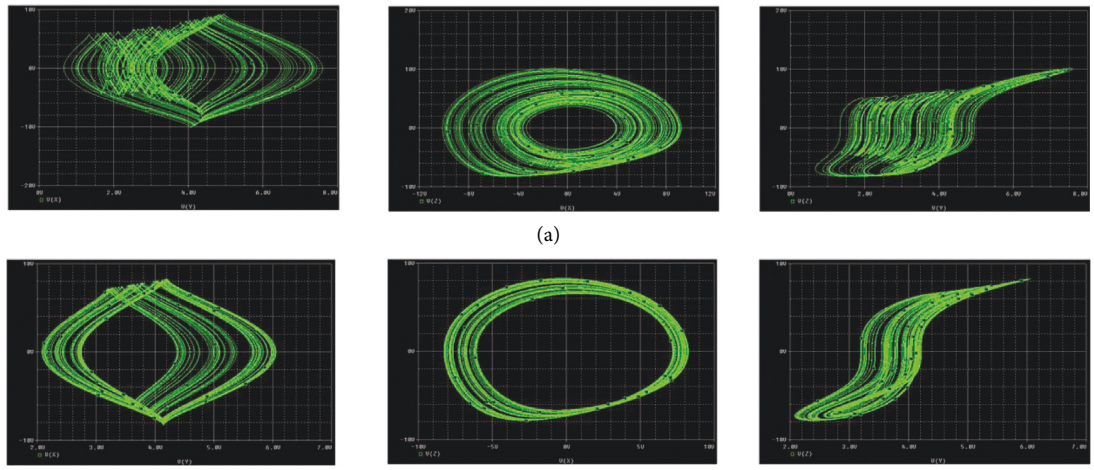

(a)

(b)

Figure 6: Phase portraits of the designed circuit obtained by using OrCAD-PSpice for (a) chaotic bursting oscillations and (b) chaotic oscillations.

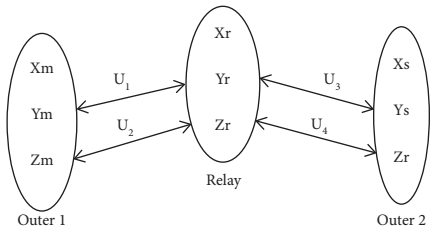

Figure 7: Schematic diagram of the relay coupling of the three three-dimensional autonomous systems with a parabolic equilibrium.

Assumption. . Since systems (9) to (11) exhibit chaotic behavior, the nonlinear functions $f(x, y, z)$ and $g(x, y, z)$ are bounded, so we can set $\|f(x, y, z)\| \leq \eta_1 \|e_2\|$ and $\|g(x, y, z)\| \leq \eta_2 \|e_3\|$ where η_1 and η_2 are positive parameters.

Theorem. . *Systems (9) to (11) achieve the global synchronization under the controller $u_i (i = 1, \ldots, 6)$ and the update law (13) of the coupling strength if the following condition is satisfied:*

$$\overline{k} \geq \frac{\max(\eta_1, \eta_2)}{3}. \tag{16}$$

Proof. The candidate Lyapunov function is chosen:

$$V = 0.5\left(e_1^2 + e_2^2 + e_3^2\right) + \frac{3}{2\gamma}(k(t) - \overline{k})^2. \tag{17}$$

The derivation of this Lyapunov function along the trajectories of system (15) gives

$$\begin{aligned} \dot{V} = e_1\dot{e}_1 + e_2\dot{e}_2 + e_3\dot{e}_3 + \frac{3\dot{k}(t)}{\gamma}(k(t) - \overline{k}) = f(x, y, z)e_2 \\ + g(x, y, z)e_3 - 3\overline{k}\left(e_2^2 + e_3^2\right). \end{aligned} \tag{18}$$

By using the above assumption, equation (18) becomes

$$\dot{V} \leq -\left(3\overline{k} - \eta_1\right)e_2^2 - \left(3\overline{k} - \eta_2\right)e_3^2. \tag{19}$$

From equation (19), one can conclude that systems (9) to (11) achieve global synchronization if and only if $\overline{k} \geq \max(\eta_1, \eta_2)/3$. This completes the proof.

Figure 8 depicts the global errors of synchronization between the three coupled oscillators (Figures 8(a)–8(c)) and the update law of coupling strength (Figure 8(d)). The initial condition of the adaptive law is $k(0) = 0$. The initial conditions of the coupled systems are set at values other than the equilibrium points. The synchronization between the three coupled oscillators is shown in Figure 9 which plots the times series of outer1 oscillator (in red) and those of outer 2 oscillator (in blue).

Figure 8 shows that the global errors described by equation (15) converge at zero from $t = 450$; at this time, the updated law stabilizes around a value $\overline{k} = 0.097$. It is noted that this result is not enough to guarantee the synchronization between the outer 1 and outer 2 because $X + Y - 2Z = 0$ does not necessarily lead to $X = Z$ and $Y = Z$, i.e., $X = Y$. The time series of the states variables of outer 1 and outer 2 is illustrated in Figure 9.

From Figure 9, when $t = 450$, the outer 1 oscillator (in red) and outer 2 oscillator (in blue) converge to the same dynamic. This last result confirms the global synchronization between the three coupled oscillators outer 1, outer 2, and relay. By comparison with results found in the litterature on relay coupled oscillators [58–64], this result is more interesting because the coupling strength is not manual but it is adapted as a function of the changes in the environment [65]. □

5. Application to Steganography and Chaos Encryption

The flowchart of steganography and chaos encryptions is depicted in Figure 10.

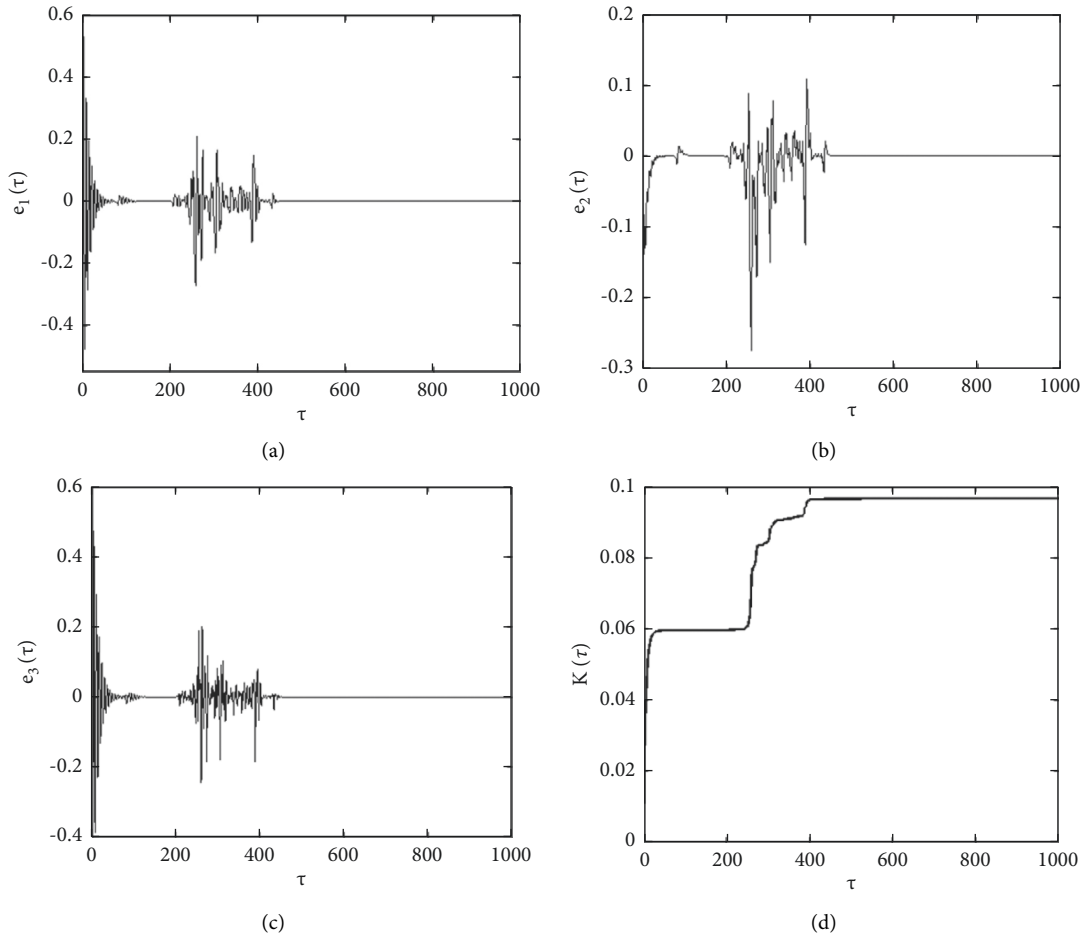

Figure 8: Global synchronization errors (a) to (c) and adaptive coupling strength (d) for $\gamma = 0.035$ and $a = 3$. The initial conditions are $(0, 0.1, 0.2)$, $(0, 0.15, 0.25)$, and $(0.3, 0.2, 0.4)$, respectively, for the outer 1, outer 2, and relay oscillators.

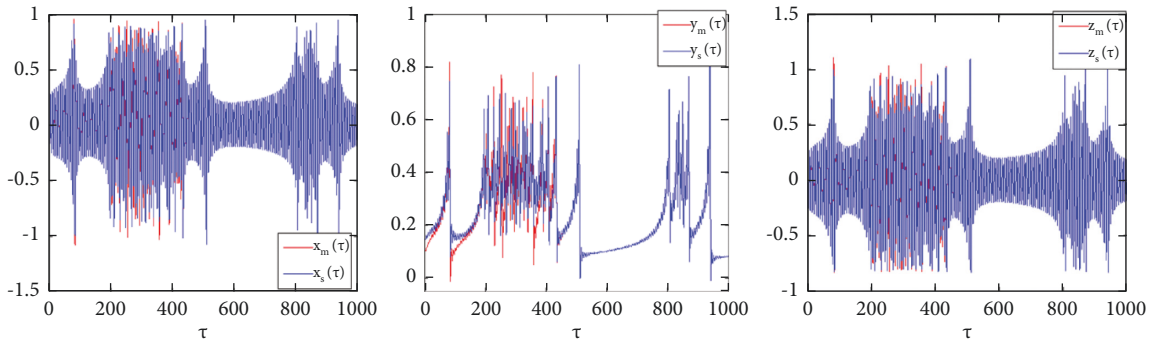

Figure 9: Time series of the state variables of outer 1 and outer 2 for $\gamma = 0.035$ and $a = 3$. The initial conditions are $(0, 0.1, 0.2)$, $(0, 0.15, 0.25)$, and $(0.3, 0.2, 0.4)$, respectively, for the outer 1, outer 2, and relay oscillators.

A cover image and text file secret image are used in Figure 10. The text file secret message is firstly encrypted by using an affine cipher based on adaptive synchronization between the relay coupled three three-dimensional autonomous systems with a parabolic equilibrium with the support of the date of birth (DOB) keys. The DOB keys enable to construct a key by using birth day, month, and year of the sender (S) and receiver (R), respectively. Then, the least significant bit (LSB) algorithm is applied to hide the encrypted text file secret message in the cover image file by embedding the encrypted text file in the LSB of pixel values of the cover image. The color image considered is decomposed into 3 subimages component (red, green, and blue). Each pixel of components assumes a value between [0, 255] and represented with 8 bit. The LSB of some pixels of components is replaced by each bits of the text file secret message.

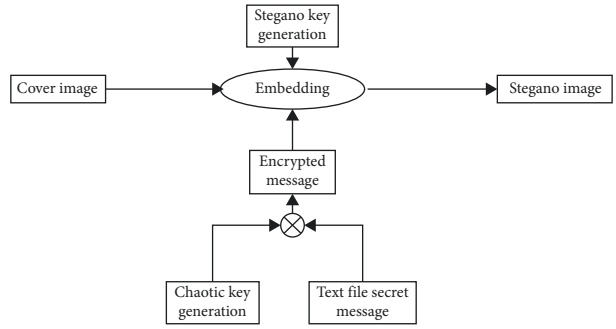

Figure 10: Schematic diagram of the proposed steganography and chaos encryption process.

The encryption *E(.)* and decryption *D(.)* processes of affine cipher for a given text file secret message M are expressed [66] as follows:

$$\begin{aligned} E(M) &= (l \times M) + m \,(\mathrm{mod}\ p), \\ D(M) &= l' \times (E(M) - m) \,(\mathrm{mod}\ p), \end{aligned} \tag{20}$$

where l and m are parameters of affine cypher key k (k=(l, m)) and l' is inverse of l modulo p and p is a positive integer. To exchange the text file secret message M, S and R have to generate their own secret key pair by using the DOB and three-dimensional chaotic autonomous system with a parabolic equilibrium. The DOB of S is $D_1 = DD - MM - YY$, and the DOB of R is $D_2 = dd - mm - yy$ where $D = (D_1, D_2)$ is a pair of the DOB of S and R.

5.1. S and R Key Generation.

(i) S solves the outer 1 of system (9) at time t and generates equations (21) and (22):

$$\begin{aligned} K_1 = DD \times x_m(t) + MM \times y_m(t) \\ + YY(i) \times z_m(t) \,(\mathrm{mod}\ p), \end{aligned} \tag{21}$$

$$\begin{aligned} K_2 = dd \times x_m(t) + mm \times y_m(t) \\ + yy(i) \times z_m(t) \,(\mathrm{mod}\ p), \end{aligned} \tag{22}$$

with $i = 1, \ldots, 4$ and $j = 3, \ldots, 6$.

(ii) R solves the outer 2 of system (10) at time t and generates equations (23) and (24):

$$\begin{aligned} L_1 = DD \times x_s(t) + MM \times y_s(t) \\ + YY(i) \times z_s(t) \,(\mathrm{mod}\ p), \end{aligned} \tag{23}$$

$$\begin{aligned} L_2 = dd \times x_s(t) + mm \times y_s(t) \\ + yy(i) \times z_s(t) \,(\mathrm{mod}\ p). \end{aligned} \tag{24}$$

5.2. Encryption and Decryption Message.

(i) S sends the text file secret message M to R secretly, and it encrypts M using *E(.)* function as follows:

$$E(M) = \left(M \times K_1\right) + K_2 \,(\mathrm{mod}\ p). \tag{25}$$

(ii) When the R receives the text file secret message M from S and recovers an original message M, it uses the decryption function *D(.)*:

$$D(M) = \left(E(M) - L_2\right) \times L_1^{-1} \,(\mathrm{mod}\ p). \tag{26}$$

Figure 11 presents the 2 covers images with size [512 × 512] used to hide the secret message encrypted and the stegano images. The secret message is chosen as M = **MY NAME IS STEGANO**. By applying the encryption *E(.)* to the message M with the following parameters: $DD = 10; MM = 06; YY = [1, 9, 9, 0]; dd = 22; MM = 10; YY = [1, 9, 8, 4]; p = 128; x_m = -24.67; y_m = -75.42; z_m = -4.381; x_s = -24.67; y_s = -75.42; z_s = -4.381$, the encrypted message obtained is M' = 刮儇□□"□≢璟.

From Figure 11, it is noted that the flower and Lena cover images have the same visual aspect with flower and Lena stegano images. Thanks to the Peak Signal to Noise Ratio (PSNR), the difference between cover and stegano images is expressed [67, 68] as follows:

$$\mathrm{PSNR} = 10 \log_{10}\left(\frac{255^2}{\mathrm{MSE}}\right), \tag{27}$$

where MSE is the mean squared error. By using the chosen text file secret message M, the PSNR of Lena and flower is 59.28 dB and 62.01 dB, respectively. Figure 12 shows the evolution of PSNR between cover and stegano images versus the length of the text file secret message M.

In Figure 12, the PSNR increases with the increase in the message length and it reaches a maximum at the message length of 150. By further increasing the message length, the PSNR decreases slowly. These results unveil the practicability and superiority of the proposed steganography and

Figure 11: (a) Cover and (b) stegano images.

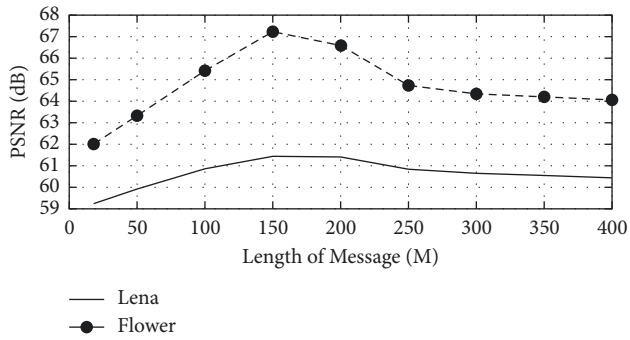

Figure 12: Variation of the PSNR of Lena and flower versus the length of message M.

chaos encryption algorithms. Note that, implementing such an encryption system may also be designed with a discrete chaotic/hyperchaotic card [69].

6. Conclusion

This paper was devoted to the dynamical analysis, adaptive synchronization via relay coupling, and applications to steganography and chaos encryption of a three-dimensional autonomous system with a parabolic equilibrium. The dynamical behaviors of the three-dimensional chaotic autonomous system with a parabolic equilibrium were analysed both analytically and numerically, and it was found that the proposed system can generate chaotic oscillations and chaotic bursting oscillations. Then, an analog circuit was designed to realize the differential equations of the chaotic system under study. The designed circuit was implemented and tested using the OrCAD-PSpice software to verify the

numerical simulations results. Comparison of the results obtained from the analog circuit and numerical simulations showed good qualitative agreement. Furthermore, it was demonstrated analytically and numerically that it is possible to achieve a global synchronization between a relay coupled three three-dimensional chaotic autonomous systems with parabolic equilibrium through an adaptive synchronization. Finally, a text message hidden inside an image was successfully realized by using steganography and chaos encryption.

Conflicts of Interest

The authors declare that there are no conflicts of interest regarding the publication of this paper.

Acknowledgments

This work was partially funded by the Center for Nonlinear Systems, Chennai Institute of Technology, India, via funding number CIT/CNS/2021/RD/064.

References

[1] J. C. Sprott, *Elegant Chaos: Algebraically Simple Chaotic Flows*, World Scientific, Singapore, 2010.

[2] G. A. Leonov, N. V. Kuznetsov, and V. I. Vagaitsev, "Localization of hidden Chua's attractors," *Physics Letters A*, vol. 375, no. 23, pp. 2230–2233, 2011.

[3] G. A. Leonov, N. V. Kuznetsov, and V. I. Vagaitsev, "Hidden attractor in smooth Chua systems," *Physica D: Nonlinear Phenomena*, vol. 241, no. 18, pp. 1482–1486, 2012.

[4] G. A. Leonov and N. V. Kuznetsov, "Hidden attractors in dynamical systems. From hidden oscillations in hilbert-Kolmogorov, aizerman, and kalman problems to hidden chaotic attractor in Chua circuits," *International Journal of Bifurcation and Chaos*, vol. 23, no. 01, Article ID 1330002, 2013.

[5] G. A. Leonov, N. V. Kuznetsov, M. A. Kiseleva, E. P. Solovyeva, and A. M. Zaretskiy, "Hidden oscillations in mathematical model of drilling system actuated by induction motor with a wound rotor," *Nonlinear Dynamics*, vol. 77, no. 1-2, pp. 277–288, 2014.

[6] G. A. Leonov, N. V. Kuznetsov, and T. N. Mokaev, "Hidden attractor and homoclinic orbit in Lorenz-like system describing convective fluid motion in rotating cavity," *Communications in Nonlinear Science and Numerical Simulation*, vol. 28, no. 1-3, pp. 166–174, 2015.

[7] B. A. Mezatio, M. Motchongom Tingue, R. Kengne, A. Tchagna Kouanou, T. Fozin Fonzin, and R. Tchitnga, "Complex dynamics from a novel memristive 6D hyperchaotic autonomous system," *International Journal of Dynamics and Control*, vol. 8, no. 1, pp. 70–90, 2020.

[8] B. A. Mezatio, M. T. Motchongom, B. R. Wafo Tekam, R. Kengne, R. Tchitnga, and A. Fomethe, "A novel memristive 6D hyperchaotic autonomous system with hidden extreme multistability," *Chaos, Solitons & Fractals*, vol. 120, pp. 100–115, 2019.

[9] D. Dudkowski, S. Jafari, T. Kapitaniak, N. V. Kuznetsov, G. A. Leonov, and A. Prasad, "Hidden attractors in dynamical systems," *Physics Reports*, vol. 637, pp. 1–50, 2016.

[10] C. Li, Y. Peng, Z. Tao, J. C. Sprott, and S. Jafari, "Coexisting infinite equilibria and chaos," *International Journal of Bifurcation and Chaos*, vol. 31, no. 05, Article ID 2130014, 2021.

[11] M. Molaie, S. Jafari, J. C. Sprott, and S. M. R. H. Golpayegani, "Simple chaotic flows with one stable equilibrium," *International Journal of Bifurcation and Chaos*, vol. 23, no. 11, Article ID 1350188, 2013.

[12] S. Jafari, J. C. Sprott, V.-T. Pham, S. M. R. H. Golpayegani, and A. H. Jafari, "A new cost function for parameter estimation of chaotic systems using return maps as fingerprints," *International Journal of Bifurcation and Chaos*, vol. 24, no. 10, Article ID 1450134, 2014.

[13] S. T. Kingni, S. Jafari, H. Simo, and P. Woafo, "Three-dimensional chaotic autonomous system with only one stable equilibrium: analysis, circuit design, parameter estimation, control, synchronization and its fractional-order form," *The European Physical Journal Plus*, vol. 129, pp. 1–16, 2014.

[14] S.-K. Lao, Y. Shekofteh, S. Jafari, and J. C. Sprott, "Cost function based on Gaussian mixture model for parameter estimation of a chaotic circuit with a hidden attractor," *International Journal of Bifurcation and Chaos*, vol. 24, no. 01, Article ID 1450010, 2014.

[15] V.-T. Pham, S. Jafari, C. Volos, X. Wang, and S. M. R. H. Golpayegani, "Is that really hidden? The presence of complex fixed-points in chaotic flows with no equilibria," *International Journal of Bifurcation and Chaos*, vol. 24, no. 11, Article ID 1450146, 2014.

[16] V.-T. Pham, C. Volos, S. Jafari, and X. Wang, "Generating a novel hyperchaotic system out of equilibrium," *Optoelectronics and Advanced Materials-Rapid Communications*, vol. 8, pp. 535–539, 2014.

[17] S. Jafari, J. C. Sprott, and F. Nazarimehr, "Recent new examples of hidden attractors," *The European Physical Journal - Special Topics*, vol. 224, no. 8, pp. 1469–1476, 2015.

[18] M. Shahzad, V.-T. Pham, M. A. Ahmad, S. Jafari, and F. Hadaeghi, "Synchronization and circuit design of a chaotic system with coexisting hidden attractors," *The European Physical Journal - Special Topics*, vol. 224, no. 8, pp. 1637–1652, 2015.

[19] J. C. Sprott, S. Jafari, V.-T. Pham, and Z. S. Hosseini, "A chaotic system with a single unstable node," *Physics Letters A*, vol. 379, no. 36, pp. 2030–2036, 2015.

[20] S. Jafari, V.-T. Pham, S. M. R. H. Golpayegani, M. Moghtadaei, and S. T. Kingni, "The relationship between chaotic maps and some chaotic systems with hidden attractors," *International Journal of Bifurcation and Chaos*, vol. 26, no. 13, Article ID 1650211, 2016.

[21] S. Jafari, V.-T. Pham, and T. Kapitaniak, "Multiscroll chaotic sea obtained from a simple 3D system without equilibrium," *International Journal of Bifurcation and Chaos*, vol. 26, no. 02, Article ID 1650031, 2016.

[22] S. Jafari, J. C. Sprott, and M. Molaie, "A simple chaotic flow with a plane of equilibria," *International Journal of Bifurcation and Chaos*, vol. 26, no. 06, Article ID 1650098, 2016.

[23] V.-T. Pham, S. Jafari, X. Wang, and J. Ma, "A chaotic system with different shapes of equilibria," *International Journal of Bifurcation and Chaos*, vol. 26, no. 04, Article ID 1650069, 2016.

[24] Z. Wei, "Dynamical behaviors of a chaotic system with no equilibria," *Physics Letters A*, vol. 376, no. 2, pp. 102–108, 2011.

[25] X. Wang and G. Chen, "Constructing a chaotic system with any number of equilibria," *Nonlinear Dynamics*, vol. 71, no. 3, pp. 429–436, 2013.

[26] S. T. Kingni, V.-T. Pham, S. Jafari, and P. Woafo, "A chaotic system with an infinite number of equilibrium points located on a line and on a hyperbola and its fractional-order form," *Chaos, Solitons & Fractals*, vol. 99, pp. 209–218, 2017.

[27] V.-T. Pham, S. Jafari, and T. Kapitaniak, "Constructing a chaotic system with an infinite number of equilibrium points," *International Journal of Bifurcation and Chaos*, vol. 26, no. 13, Article ID 1650225, 2016.

[28] V.-T. Pham, C. Volos, S. Jafari, and T. Kapitaniak, "A novel cubic-equilibrium chaotic system with coexisting hidden attractors: analysis, and circuit implementation," *Journal of Circuits, Systems, and Computers*, vol. 27, no. 04, Article ID 1850066, 2018.

[29] V.-T. Pham, F. Rahma, M. Frasca, and L. Fortuna, "Dynamics and synchronization of a novel hyperchaotic system without equilibrium," *International Journal of Bifurcation and Chaos*, vol. 24, no. 06, Article ID 1450087, 2014.

[30] V. T. Pham, S. Jafari, C. Volos, and T. Kapitaniak, "A gallery of chaotic systems with an infinite number of equilibrium points," *Chaos, Solitons & Fractals*, vol. 93, pp. 58–63, 2016.

[31] X. Wang, A. Akgul, S. Cicek, V.-T. Pham, and D. V. Hoang, "A chaotic system with two stable equilibrium points: dynamics, circuit realization and communication application," *International Journal of Bifurcation and Chaos*, vol. 27, no. 08, Article ID 1750130, 2017.

[32] A. T. Azar, "A novel chaotic system without equilibrium: dynamics, synchronization, and circuit realization," *Complexity*, Hindawi Publishing Corporation, vol. 2017, , p. 11, Article ID 7871467, 2017.

[33] J. P. Singh and B. K. Roy, "The simplest 4-D chaotic system with line of equilibria, chaotic 2-torus and 3-torus behaviour," *Nonlinear Dynamics*, vol. 89, no. 3, pp. 1845–1862, 2017.

[34] E. Chen, L. Min, and G. Chen, "Discrete chaotic systems with one-line equilibria and their application to image encryption," *International Journal of Bifurcation and Chaos*, vol. 27, no. 03, Article ID 1750046, 2017.

[35] S. Jafari and J. C. Sprott, "Simple chaotic flows with a line equilibrium," *Chaos, Solitons & Fractals*, vol. 57, pp. 79–84, 2013.

[36] C. Li, J. C. Sprott, and W. Thio, "Bistability in a hyperchaotic system with a line equilibrium," *Journal of Experimental and Theoretical Physics*, vol. 118, no. 3, pp. 494–500, 2014.

[37] J. Ma, Z. Chen, Z. Wang, and Q. Zhang, "A four-wing hyperchaotic attractor generated from a 4-D memristive system with a line equilibrium," *Nonlinear Dynamics*, vol. 81, no. 3, pp. 1275–1288, 2015.

[38] X. Wang, V.-T. Pham, and C. Volos, "Dynamics, circuit design, and synchronization of a new chaotic system with closed curve equilibrium," *Complexity*, Hindawi Publishing Corporation, vol. 2017, , p. 9, Article ID 7138971, 2017.

[39] T. Gotthans and J. Petržela, "New class of chaotic systems with circular equilibrium," *Nonlinear Dynamics*, vol. 81, no. 3, pp. 1143–1149, 2015.

[40] T. Gotthans, J. C. Sprott, and J. Petrzela, "Simple chaotic flow with circle and square equilibrium," *International Journal of Bifurcation and Chaos*, vol. 26, no. 08, Article ID 1650137, 2016.

[41] S. Mobayen, C. K. Volos, S. Kaçar, and Ü. Çavuşoğlu, "New class of chaotic systems with equilibrium points like a three-leaved clover," *Nonlinear Dynamics*, vol. 91, no. 2, pp. 939–956, 2018.

[42] V.-T. Pham, S. Jafari, C. Volos, S. Vaidyanathan, and T. Kapitaniak, "A chaotic system with infinite equilibria located on a piecewise linear curve," *Optik*, vol. 127, no. 20, pp. 9111–9117, 2016.

[43] Y. Chen and Q. Yang, "A new Lorenz-type hyperchaotic system with a curve of equilibria," *Mathematics and Computers in Simulation*, vol. 112, pp. 40–55, 2015.

[44] E. Tlelo-Cuautle, L. G. de la Fraga, V.-T. Pham, C. Volos, S. Jafari, and A. d. J. Quintas-Valles, "Dynamics, FPGA realization and application of a chaotic system with an infinite number of equilibrium points," *Nonlinear Dynamics*, vol. 89, no. 2, pp. 1129–1139, 2017.

[45] V.-T. Pham, C. Volos, S. Vaidyanathan, and X. Wang, "A Chaotic system with an infinite number of equilibrium points: dynamics, horseshoe, and synchronization," *Adv. Math. Phys.*vol. 2016, p. 8, Article ID 4024836, 2016.

[46] K. Barati, S. Jafari, J. C. Sprott, and V.-T. Pham, "Simple chaotic flows with a curve of equilibria," *International Journal of Bifurcation and Chaos*, vol. 26, no. 12, Article ID 1630034, 2016.

[47] Y. Ji and Q. Bi, "Bursting behavior in a non-smooth electric circuit," *Physics Letters A*, vol. 374, no. 13-14, pp. 1434–1439, 2010.

[48] X. Han, B. Jiang, and Q. Bi, "3-torus, quasi-periodic bursting, symmetric subHopf/fold-cycle bursting, subHopf/fold-cycle bursting and their relation," *Nonlinear Dynamics*, vol. 61, no. 4, pp. 667–676, 2010.

[49] Q. Bi and Z. Zhang, "Bursting phenomena as well as the bifurcation mechanism in controlled Lorenz oscillator with two time scales," *Physics Letters A*, vol. 375, no. 8, pp. 1183–1190, 2011.

[50] S. T. Kingni, B. Nana, G. S. Mbouna Ngueuteu, P. Woafo, and J. Danckaert, "Bursting oscillations in a 3D system with asymmetrically distributed equilibria: mechanism, electronic implementation and fractional derivation effect," *Chaos, Solitons & Fractals*, vol. 71, pp. 29–40, 2015.

[51] S. T. Kingni, L. Keuninckx, P. Woafo, G. Van der Sande, and J. Danckaert, "Dissipative chaos, Shilnikov chaos and bursting oscillations in a three-dimensional autonomous system: theory and electronic implementation," *Nonlinear Dynamics*, vol. 73, no. 1-2, pp. 1111–1123, 2013.

[52] S. T. Kingni, G. S. Mbouna Ngueuteu, and P. Woafo, "Bursting generation mechanism in a three-dimensional autonomous system, chaos control and synchronization in its fractional-order form," *Nonlinear Dynamics*, vol. 76, pp. 1169–1183, 2010.

[53] J. Lü and G. Chen, "Generating multiscroll chaotic attractors: theories, methods and applications," *International Journal of Bifurcation and Chaos*, vol. 16, pp. 775–858, 2006.

[54] S. Yu, W. K. S. Tang, J. Lü, and G. Chen, "Design and implementation of multi-wing butterfly chaotic attractors via Lorenz-type systems," *International Journal of Bifurcation and Chaos*, vol. 20, no. 01, pp. 29–41, 2010.

[55] S. Yu, J. Lu, X. Yu, and G. Chen, "Design and implementation of grid multiwing hyperchaotic Lorenz system family via switching control and constructing super-heteroclinic loops," *IEEE Transactions on Circuits and Systems I: Regular Papers*, vol. 59, no. 5, pp. 1015–1028, 2012.

[56] J. Wu, C. Li, X. Ma, T. Lei, and G. Chen, "Simplification of chaotic circuits with quadratic nonlinearity," *IEEE Transactions on Circuits and Systems II: Express Briefs*, vol. 69, 2021.

[57] R. Kengne, M. Motchongom Tingue, A. Kammogne Souop Tewa, G. Djuidjé Kenmoé, and T. C. Kofane, "Optimal phase control in a Remoissenet–Peyrard substrate potential: numerical and analogical investigations," *Indian Journal of Physics*, 2022.

[58] I. Fischer, R. Vicente, J. M. Buldú et al., "Zero-lag long-range synchronization via dynamical relaying," *Physical Review Letters*, vol. 97, no. 12, Article ID 123902, 2006.

[59] R. Gutiérrez, R. Sevilla-Escoboza, P. Piedrahita et al., "Generalized synchronization in relay systems with instantaneous coupling," *Physical review. E, Statistical, nonlinear, and soft matter physics*, vol. 88, Article ID 052908, 2013.

[60] A. Sharma, M. D. Shrimali, A. Prasad, R. Ramaswamy, and U. Feudel, "Phase-flip transition in relay-coupled nonlinear oscillators," *Physical review. E, Statistical, nonlinear, and soft matter physics*, vol. 84, Article ID 016226, 2011.

[61] I. G. Da Silva, J. M. Buldú, C. R. Mirasso, and J. García-Ojalvo, "Synchronization by dynamical relaying in electronic circuit arrays," *Chaos: An Interdisciplinary Journal of Nonlinear Science*, vol. 16, no. 4, Article ID 043113, 2006.

[62] B. Nana and P. Woafo, "Chaotic masking of communication in an emitter-relay-receiver electronic setup," *Nonlinear Dynamics*, vol. 82, no. 1-2, pp. 899–908, 2015.

[63] R. Kengne, R. Tchitnga, S. Mabekou, B. R. W. Tekam, G. B. Soh, and A. Fomethe, "On the relay coupling of three fractional-order oscillators with time-delay consideration: global and cluster synchronizations," *Chaos, Solitons & Fractals*, vol. 111, pp. 6–17, 2018.

[64] M. Motchongom Tingue, H. L. Ndassi, A. R. Tchamda, E. R. Mache Kengne, R. Tchitnga, and M. Tchoffo, "Bursting mechanism in a memristive Lorenz based system and function projective synchronization in its-fractional-order form: digital implementation under ATmega328P microcontroller," *Physica Scripta*, vol. 96, no. 12, Article ID 125229, 2021.

[65] R. Kengne, R. Tchitnga, A. Mezatio, A. Fomethe, and G. Litak, "Finite-time synchronization of fractional-order simplest two-component chaotic oscillators," *The European Physical Journal B*, vol. 90, no. 5, p. 88, 2017.

[66] P. Muthukumar, P. Balasubramaniam, K. Ratnavelu, P. Balasubramaniam, and K. Ratnavelu, Fast projective synchronization of fractional order chaotic and reverse chaotic systems with its application to an affine cipher using date of birth (DOB)," in *Nonlinear Dyn*vol. 80, no. 4, , pp. 1883–1897, Springer, 2015.

[67] A. Saleema and T. Amarunnishad, "A new steganography algorithm using hybrid fuzzy neural networks," *Procedia Technology*, vol. 24, pp. 1566–1574, 2016.

[68] N. H. Alombah, A. E. T. Tchendjeu, A. E. T. Tchendjeu, K. Romanic, F. C. Talla, and H. B. Fotsin, "FPGA implementation of a novel two-internal-state memristor and its two component chaotic circuit," *Indian Journal of Science and Technology*, vol. 14, no. 27, pp. 2257–2271, 2021.

[69] Y. Li, C. Li, S. Zhang, G. R. Chen, and Z. Zeng, "A self-reproduction hyperchaotic map with compound lattice dynamics," *IEEE Transactions on Industrial Electronics*, 2022.

Hindawi
Complexity
Volume 2022, Article ID 8093696, 13 pages
https://doi.org/10.1155/2022/8093696

Research Article

Nonlinear Stochastic SIS Epidemic Model Incorporating Lévy Process

Amine El Koufi

Laboratory of Analysis, Modeling and Simulation (LAMS), Faculty of Sciences Ben M'sik, Hassan II University, P. O Box 7955 Sidi Othman, Casablanca, Morocco

Correspondence should be addressed to Amine El Koufi; elkoufiamine1@gmail.com

Received 16 February 2022; Accepted 24 March 2022; Published 22 April 2022

Academic Editor: Chun-Biao Li

In this work, we study a stochastic SIS epidemic model with Lévy jumps and nonlinear incidence rates. Firstly, we present our proposed model and its parameters. We establish sufficient conditions for the extinction and persistence of the disease in the population using some stochastic analysis background. We illustrate our theoretical results by numerical simulations. We conclude that the white noise and Lévy jump influence the transmission of the epidemic.

1. Introduction and Preliminary

For a long time, infectious diseases have been the cause of disappointment of many people in the world, and only very few of these diseases have disappeared, despite the development of medicine and the change in the lifestyle of human beings. Therefore, several scientists have concentrated their research on the study of the transmission mechanisms of these diseases and have proposed relevant solutions in order to reduce the contamination by these infectious diseases. Also, several mathematical epidemic models are proposed to describe the dynamics of infectious diseases in human populations and to study the complex behavior of these diseases. Among the models proposed, the classic SIR epidemic model of Kermack and McKendrick is widely used [1] which divides the population into three classes, namely, susceptible (S), infected (I), and recovered (R). As a result, other works have generalized the Kermack–McKendrick (see, for example, [2–8]) model. On the other hand, for some diseases such as bacterial diseases and some sexually transmitted diseases, the SIR model is not suitable because the individuals infected with these diseases start to be susceptible, at a certain stage get the disease, and after a short infectious period become susceptible again [9, 10]. Therefore, the SIS epidemic model [11–13] is often used to model the dynamics of these specific diseases. Then, the SIS epidemic model is represented by the following ordinary differential equations:

$$\begin{cases} \dfrac{\mathrm{d}S(t)}{\mathrm{d}t} = A - \rho S - \beta SI + \delta I, \\ \dfrac{\mathrm{d}I(t)}{\mathrm{d}t} = \beta SI - (\rho + \theta + \delta)I, \end{cases} \tag{1}$$

where $S(t)$ and $I(t)$ represent the number of susceptible and infected individuals, respectively. A represents the recruitment rate of susceptible, β denotes the transmission coefficient of diseases, ρ represents the natural death rate for susceptible and infected classes, θ is the disease-related death rate, and δ denotes the recovery rate.

The quantity βSI is the disease incidence rate, which represents the number of new cases per unit of time. Many authors have used the bilinear incidence to model disease transmission. But, in many cases, the bilinear incidence is not preferable (for example, when the population is saturated [14]). So, the nonlinear incidence can better model the nonlinear transmission of epidemics. Swati in [15] proposed a fractional-order epidemic model and modeled the transmission of disease by the Beddington–DeAngelis incidence rate. In [16], Lu et al. introduced a nonmonotone incidence

rate into an epidemic model composed of three classes of individuals (susceptible, infectious, and recovered). Rajasekar and Zhu [17] examined the impact of media coverage on a SIRS epidemic model with relapse. Therefore, several nonlinear incidences have been proposed (see Table 1). In the present paper, we model the disease transmission by a nonlinear incidence $\beta\phi(S,I)$, where ϕ satisfies the following conditions.

$(C)\phi(S,I)$ is two-order continuously differentiable for any $S(t)$, $I(t)\geq 0$. For each fixed $I\geq 0$, $\phi(S,I)$ is increasing for $S>0$ and for each fixed $S\geq 0$, $\phi(S,I)/I$ is decreasing for $I>0$. $\phi(S,0)=\phi(0,I)=0$ for any $S,I>0$, and $\partial\phi(S_0,0)/\partial I>0$, with $S_0=A/\rho$.

In mathematical modeling, the stochastic systems show more precisely the reality by including the environmental effects, which are an essential aspect in biological environments. So, epidemic models are often subject to random noises (see [4]). For this reason, many works have studied the effect of white noise on deterministic systems. Tornatore et al. in [22] studied the effect of white noise on the SIR epidemic model, and they presented the model by a stochastic differential system. In [23], the author has examined the effect of environmental fluctuations on an epidemic model by affecting some parameters in the model by the white noise. Hussain et al. [24] investigated a stochastic epidemic model with white noise for the transmission of coronavirus. They showed sufficient conditions for the extinction and existence of stationary distribution by employing some stochastic calculus background. To reasonably measure the influence of environmental noise on disease transmission, we assume that parameter β is perturbed by the white noise as follows:

$$\beta\longrightarrow\beta+\sigma\dot{M}_B(t), \tag{2}$$

where $M_B(t)$ is a standard Brownian motion and σ represent the intensities of white noise. Then, we represent the stochastic model corresponding to deterministic model (1) by the following stochastic differential equation system:

$$\begin{cases} \mathrm{d}S(t)=(A-\rho S-\beta\phi(S,I)+\delta I)\mathrm{d}t-\sigma\phi(S,I)\mathrm{d}M_B(t),\\ \mathrm{d}I(t)=(\beta\phi(S,I)-(\rho+\theta+\delta)I)\mathrm{d}t+\sigma\phi(S,I)\mathrm{d}M_B(t). \end{cases} \tag{3}$$

Stochastic differential equations with white noise represent many advantages in modeling infectious diseases. But, in reality, the biological systems are frequently attacked by abrupt and massive disturbances such as natural disasters: volcanoes, tsunamis, earthquakes, and pandemics (SARS, COVID-19, Ebola, and so on). These events may break the continuity of the solution [4, 25, 26]. Then, to describe these events, it is necessary to integrate a jump process [27] in the stochastic system (3).

Thus, to properly describe the reality, we use the Lévy jump process which can well model the sudden and massive fluctuations; also, we perturb the parameter β by two environmental noises (white noise and Lévy noise) as follows:

$$\beta\longrightarrow\beta+\sigma\dot{M}_B(t)+\dot{\mathscr{Y}}(t), \tag{4}$$

where $M_B(t)$ is an independent standard Brownian motion, σ is the intensity of $M_B(t)$, and $\dot{\mathscr{Y}}(t)=\int_0^t\int_{\mathbb{E}}\eta(t)\tilde{N}(\mathrm{d}t,\mathrm{d}l)$. Then, we present the stochastic version corresponding to model (3) by the following stochastic differential equation system driven with Lévy jumps:

$$\begin{cases} \mathrm{d}S(t)=(A-\rho S-\beta\phi(S,I)+\delta I)\mathrm{d}t-\sigma\phi(S,I)\mathrm{d}M_B(t)-\displaystyle\int_{\mathbb{E}}\eta(l)\phi(S((t-),I(t-)\tilde{N}(\mathrm{d}t,\mathrm{d}l)),\\ \mathrm{d}I(t)=(\beta\phi(S,I)-(\rho+\theta+\delta)I)\mathrm{d}t+\sigma\phi(S,I)\mathrm{d}M_B(t)+\displaystyle\int_{\mathbb{E}}\eta(l)\phi(S(t-),I((t-))\tilde{N}(\mathrm{d}t,\mathrm{d}l), \end{cases} \tag{5}$$

where $S(t-)$ and $I(t-)$ are the left limits of $S(t)$ and $I(t)$, respectively. $\tilde{N}(\mathrm{d}t,\mathrm{d}l)=N(\mathrm{d}t,\mathrm{d}l)-\nu(l)\mathrm{d}t$, N is a Poisson counting measure with characteristic measure ν on measurable subset $\mathbb{E}$ of $[0,\infty)$, with $\nu(\mathbb{E})<\infty$, and $\eta\colon\mathbb{E}\times\Omega\longrightarrow R$ represents the effect of random jumps; it is bounded and continuous with respect to ν and $\mathfrak{B}(\mathbb{E})\times\mathscr{F}_t$-measurable.

Throughout this paper, let $(\Omega,\mathscr{F},\{\mathscr{F}\}_{t\geq 0},\mathbb{P})$ be a complete probability space with a filtration $\{\mathscr{F}\}_{t\geq 0}$ satisfying the usual conditions (i.e., it is right continuous and $\mathscr{F}_0$ contains all $\mathbb{P}$-null sets), and we suppose that the Brownian motion $M_B(t)$ is defined on the complete probability space $(\Omega,\mathscr{F},\{\mathscr{F}\}_{t\geq 0},\mathbb{P})$.

For equation (5) to admit a unique global solution, it must satisfy the linear growth condition and the local Lipschitz condition [28]. In effect, equation (5) satisfies the local Lipschitz condition and not the linear growth condition. Therefore, the solution of system (3) will explode in finite time. So, to ensure the global existence and uniqueness of the solution, we propose as in [4] the following assumptions:

$(\mathbf{C}_1)$ For each $N>0$, there exists $L_N>0$ such that

$$\int_{\mathbb{E}}|K(x,\alpha)-K(y,\alpha)|^2\nu(dl)\leq L_N|x-y|^2, \tag{6}$$

and $|x|\vee|y|\leq N$, with $K(x',l)=\eta(l)x'$ for $x'=S(t-)I(t-)$.

$(\mathbf{C}_2)$ $0\leq A/\rho\eta(l)<1$, for $l\in\mathbb{E}$.

The following region:

$$\mathscr{I}=\left\{(S,I)\in\mathbb{R}_+^2\colon S+I\leq\frac{A}{\rho}\right\}, \tag{7}$$

is almost surely positively invariant by stochastic system (3), namely, if $(S(0),I(0))\in\mathscr{I}$, then $(S(t),I(t))\in\mathscr{I}\ \forall t\geq 0\ a.s.$

Table 1: Some nonlinear incidence rates.

Incidence name	Expression	Reference
Standard incidence rate	$\beta SI/N$	[18]
Saturated incidence rate	$\beta SI/1+kI$	[14]
Beddington–DeAngelis functional response	$\beta SI/1+k_1S+k_2I$	[19]
Crowley–Martin functional response	$\beta SI/1+k_1S+k_2I+k_1k_2SI$	[20]
Incidence with media coverage effect	$\beta_1-\beta_2 I/I+m$	[21]

Theorem 1. *For any initial condition $(S(0),I(0))\in\mathcal{I}$, there exists a unique positive solution $(S(t),I(t))\in\mathcal{I}\forall t\geq 0$ a.s.*

Let $V_m=\inf_{(S,I)\in\mathcal{T}}\phi(S,I)/I$.

Definition 1. System (3) is said to be persistent in the mean, if

$$\liminf_{t\longrightarrow\infty}\frac{1}{t}\int_0^t I(r)\mathrm{d}r>0\ a.s. \tag{8}$$

Lemma 1. *Let $f\in\mathcal{C}([0,\infty)\times t\Omega n;q(0,\infty))$. If there exist positive constants m_1, m_2, and T, such that*

$$\ln f(t)\geq m_1t-m_2\int_0^t f(x)\mathrm{d}x+F(t)\ a.s.\quad for all\ t\geq T, \tag{9}$$

where $F\in([0,\infty)\times\Omega;\mathbb{R})$ and $\lim_{t\longrightarrow\infty}F(t)/t=0$ a.s., then $\liminf_{t\longrightarrow\infty}\langle f(t)\rangle\geq m_1/m_2$ a.s.

Lemma 2 (see [29]). *Suppose that (**C**) hold. For all $s>z>0$, define*

$$\mathbb{H}=\left\{(S,I)\in\mathbb{R}_+^2|z\leq S+I\leq s\right\}. \tag{10}$$

Then,

$$\begin{aligned}&\max_{(S,I)\in\mathbb{H}}\left\{\frac{\phi((S,I))}{S},\frac{\phi((S,I))}{I}\right\}<\infty,\\&\max_{(S,I)\in\mathbb{H}}\left\{\left|\frac{1}{I}\frac{\partial\phi(S,I)}{\partial I}-\frac{\phi(S,I)}{I^2}\right|,\left|\frac{1}{I}\frac{\partial\phi(S,I)}{\partial S}\right|\right\}<\infty.\end{aligned} \tag{11}$$

The differential operator $\mathscr{L}$ (see [30]) associated with the following stochastic differential equation with Lévy process:

$$\mathrm{d}x(t)=f(x(t),t)\mathrm{d}t+g(x(t),t)\mathrm{d}M_B(t)+\int_{\mathbb{E}}h(x(t-),l)\widetilde{N}(\mathrm{d}t,\mathrm{d}l), \tag{12}$$

is defined by

$$\begin{aligned}\mathscr{L}x(t-)=&\frac{\partial x(t-)}{\partial t}+\sum_{i=1}^n\frac{\partial x(t-)}{\partial x_i}f_i(x,t)+\frac{1}{2}\sum_{i,j=1}^n\frac{\partial^2x(t-)}{\partial x_i\partial x_j}\left[g^T(x,t)g(x,t)\right]_{ij}\\&+\int_{\mathbb{E}}\left[(x(t-)+h(x(t-),l))-x(t-)-\frac{\partial x(t-)}{\partial x_i}h(x(t-),l)\right]\nu(\mathrm{d}l).\end{aligned} \tag{13}$$

If $\mathscr{L}$ acts on a function $F\in\mathcal{C}^{1,2}(\mathbb{R}^n\times\mathbb{R}_+;\mathbb{R}_+)$, then

$$\begin{aligned}\mathscr{L}F(x(t))=&F_t(x(t-))+F_x(x(t-))f(x(t-),t)\\&+\frac{1}{2}\mathrm{trace}\left[g^T(x(t-),t)F_{xx}(x(t-))g(x(t-),t)\right]_{ij}\\&+\int_{\mathbb{E}}\left[F(x(t-)+h(x(t-),l)-F(x(t-))-F_x(x(t-))h(x(t-),l)\right]\nu(\mathrm{d}l),\end{aligned} \tag{14}$$

where $F_t=\partial F/\partial t$, $F_x=(\partial F/\partial x_1,\ldots,\partial F/\partial x_n)$, $F_{xx}=(\partial^2F/\partial x_i\partial x_j)_{nn}$.

Then, generalized Itô's formula (for more details, see [31]) is presented by

$$dH(x(t)) = \mathscr{L}F(x(t-))dt + F_x(x(t-)g(x(t),t)dM_B(t) + \int_Z [F(x(t-) + h(x(t-),l)) - F(x(t-))]\tilde{N}(dt,dl). \tag{15}$$

The goal of this work is the proposition of conditions for the extinction and persistence of diseases. For this, we define a threshold number that coincides with the basic reproduction number of the deterministic model when the stochastic terms are absent and determine the extinction or persistence of disease. Moreover, it is important to note that our system (3) generalizes many models existing in the literature (for example, see [32–34]). In addition, our model (3) represents the impact of massive events on the transmission of disease and gives an additional degree of realism compared with the deterministic model and stochastic model with white noise. The organization of this paper is as follows. In Section 2, we give sufficient conditions for the extinction of the disease. Persistence in mean results is explored in Section 3. In Section 4, the analytical results are illustrated with the support of numerical examples. Finally, we close the article with a conclusion.

2. Extinction

In this section, we show sufficient conditions for the extinction of the disease of system (3) with the Lévy process.

We know that for deterministic systems, we should determine the extinction or persistence of disease according to the value of $\mathscr{R}_0$ (basic reproduction number). That is, if $\mathscr{R}_0$ is less than one, the disease dies out. In contrast, if $\mathscr{R}_0$ is greater than one, the disease persists. Likewise, we express the following threshold of our stochastic SIS epidemic model (3) with Lévy jumps as follows:

$$\mathscr{R}_{lj} = \beta\frac{\partial\phi(S_0,0)}{\partial I}\frac{1}{(\rho+\theta+\delta)} - \overline{\eta}\left(\frac{\partial\phi(S_0,0)}{\partial I}\right)^2\frac{1}{(\rho+\theta+\delta)} = \mathscr{R}_0 - \overline{\eta}\left(\frac{\partial\phi(S_0,0)}{\partial I}\right)^2\frac{1}{(\rho+\theta+\delta)}, \tag{16}$$

where $\overline{\eta} = (\sigma^2/2 + \int_{\mathbb{E}}\eta^2(l)/2(1+\eta(l)\partial\phi(S_0,0)/\partial I)^2\nu(dl))$.

Remark 1. The threshold $\mathscr{R}_{lj}$ coincides with the basic reproduction number $\mathscr{R}_0$ of the corresponding deterministic system in the absence of the noise coefficient.

Theorem 2. *Under the assumptions* (**C**). *Let* $(S(t),I(t))$ *be the solution of model (3) with any initial value* $(S(0),I(0)) \in \mathscr{I}$:

(i) If $\mathscr{R}_{lj} < 1$ *and* $\partial\phi(S_0,0)/\partial I \le \beta/\overline{\eta}$, *then*

$$\limsup_{t\longrightarrow\infty}\frac{\log I(t)}{t} \le (\rho+\theta+\delta)\left[\mathscr{R}_{lj}-1\right] < 0 \ a.s. \tag{17}$$

(ii) If $\sigma^2/2 + \int_{\mathbb{E}}\eta^2(l)/2(1+\eta(l)\partial\phi(S_0,0)/\partial I)^2\nu(dl) > \beta^2/2(\rho+\theta+\delta)$, *then*

$$\limsup_{t\longrightarrow\infty}\frac{\log I(t)}{t} \le \frac{\beta^2}{2}\left(\frac{\sigma^2}{2} + \int_{\mathbb{E}}\frac{\eta^2(l)}{2(1+\eta(l)\partial\phi(S_0,0)/\partial I)^2}\nu(dl)\right)^{-1} - (\rho+\theta+\delta) < 0 \ a.s. \tag{18}$$

In others word, $I(t)$ will go to zero almost surely. That is, the disease will be extinct almost surely.

Proof

(i) Using generalized Itô's formula, one can see that

$$d\log I = \left[\beta\frac{\phi(S,I)}{I} - (\rho+\theta+\delta) - \frac{\sigma^2}{2}\left(\frac{\phi(S,I)}{I}\right)^2\right]dt + \int_{\mathbb{E}}\left[\log\left(1+\eta(l)\frac{\phi(S,I)}{I}\right) - \eta(l)\frac{\phi(S,I)}{I}\right]\nu(dl) + \sigma\frac{\phi(S,I)}{I}dM_B(t) + \int_{\mathbb{E}}\log\left(1+\eta(l)\frac{\phi(S,I)}{I}\right)\tilde{N}(dt,dl). \tag{19}$$

Integrating both *sides* from 0 to t and dividing by t, we get

$$\frac{\log I(t)}{t} = \frac{\log I(0)}{t} + \frac{1}{t}\int_0^t\left[\beta\frac{\phi(S(r),I(r))}{I(r)} - (\rho+\theta+\delta) - \frac{\sigma^2}{2}\left(\frac{\phi(S(r),I(r))}{I(r)}\right)^2\right]dr + \frac{1}{t}\int_0^t\int_{\mathbb{E}}\left[log\left(1+\eta(l)\frac{\phi(S(r-),I(r-))}{I(r-)}\right) - \eta(l)\frac{\phi(S(r-),I(r-))}{I(r-)}\right]\nu(dl)dr + \frac{1}{t}\int_0^t\int_{\mathbb{E}}\log\left(1+\eta(l)\frac{\phi(S(r-),I(r-))}{I(r-)}\right)\tilde{N}(dr,dl) + \frac{1}{t}\int_0^t\sigma\frac{\phi(S(r),I(r))}{I(r)}dM_B(r). \tag{20}$$

Using the Taylor–Lagrange formula, one can see that

$$\begin{aligned}\log\left(1+\eta(l)\frac{\phi(S,I)}{I}\right)-\eta(l)\frac{\phi(S,I)}{I}&=-\frac{\eta^2(l)(\phi(S,I)/I)^2}{2(1+\eta(l)\phi(S,I)/I)^2}\\&\le-\frac{\eta^2(l)}{2\left(1+\eta(l)\partial\phi(S_0,0)/\partial I\right)^2}\left(\frac{\phi(S,I)}{I}\right)^2.\end{aligned}\tag{21}$$

Therefore,

$$\begin{aligned}\frac{\log I(t)}{t}\le\frac{\log I(0)}{t}+\frac{1}{t}\int_0^t\Bigg[\beta\frac{\phi(S(r),I(r))}{I(r)}-(\rho+\theta+\delta)\\-\left(\frac{\sigma^2}{2}+\int_{\mathbb{E}}\frac{\eta^2(l)}{2\left(1+\eta(0)\partial\phi(S_0,0)/\partial I\right)^2}\nu(\mathrm{d}l)\right)\left(\frac{\phi(S(r),I(r))}{I(r)}\right)^2\Bigg]\mathrm{d}r\\+\frac{1}{t}\int_0^t\int_{\mathbb{E}}\log\left(1+\eta(l)\frac{\phi(S(r-),I(r-))}{I(r-)}\right)\tilde{N}(\mathrm{d}r,\mathrm{d}l)\\+\frac{1}{t}\int_0^t\sigma\frac{\phi(S(r),I(r))}{I(r)}\mathrm{d}M_B(r).\end{aligned}\tag{22}$$

Since the function

$$h(z)=-(\rho+\theta+\delta)+\beta z-\left(\frac{\sigma^2}{2}+\int_{\mathbb{E}}\frac{\eta^2(l)}{2\left(1+\eta(l)\partial\phi(S_0,0)/\partial I\right)^2}\nu(\mathrm{d}l)\right)z^2,\tag{23}$$

is monotone *increasing* for all $z\in[0,\beta/(\sigma^2/2+\int_{\mathbb{E}}\eta^2(l)/2(1+\eta(l)\partial\phi(S_0,0)/\partial I)^2\nu(dl))]$, employing condition (i) and the inequality $\phi(S,I)/I\le\partial\phi(S_0,0)/\partial I$, we obtain

$$\begin{aligned}\frac{\log I(t)}{t}\le\frac{\log I(0)}{t}+\frac{1}{t}\int_0^t\Bigg[\beta\frac{\partial\phi(S_0,0)}{\partial I}-(\rho+\theta+\delta)\\-\left(\frac{\sigma^2}{2}+\int_{\mathbb{E}}\frac{\eta^2(l)}{2\left(1+\eta(l)\partial\phi(S_0,0)/\partial I\right)^2}\nu(\mathrm{d}l)\right)\left(\frac{\partial\phi(S_0,0)}{\partial I}\right)^2\Bigg]\mathrm{d}r\\+\frac{\mathscr{M}(t)}{t}+\frac{\mathscr{G}(t)}{t},\end{aligned}\tag{24}$$

where

$$\begin{aligned}\mathscr{M}(t)&=\int_0^t\int_{\mathbb{E}}\log\left(1+\eta((l))\frac{\phi(S(r-),I(r-))}{I(r-)}\right)\tilde{N}(\mathrm{d}r,\mathrm{d}l),\\\mathscr{G}(t)&=\int_0^t\sigma\frac{\phi(S(r-),I(r-))}{I(r-)}\mathrm{d}M_B(r).\end{aligned}\tag{25}$$

Then,

$$\begin{aligned}\langle\mathscr{M}(t),\mathscr{M}(t)\rangle&=\int_0^t\int_{\mathbb{E}}\left[\log\left(1+\eta(l)\frac{\phi(S(r-),I(r-))}{I(r-)}\right)\right]^2\nu(\mathrm{d}l)\mathrm{d}r\\&\le t\left[\log\left(1+\eta(l)\frac{\partial\phi(S_0,0)}{\partial I}\right)\right]^2\nu(\mathbb{E})<\infty,\end{aligned}\tag{26}$$

and

$$\langle \mathcal{G}(t), \mathcal{G}(t) \rangle = \int_0^t \left[\sigma \frac{\phi(S(r), I(r))}{I(r)} \right]^2 \mathrm{d}r \leq t \left[\sigma \frac{\partial \phi(S_0, 0)}{\partial I} \right]^2 < \infty. \tag{27}$$

According to the strong law of large numbers for martingales [28], we have

$$\begin{aligned} \lim_{t \longrightarrow \infty} \frac{\mathcal{M}(t)}{t} &= 0, \\ \lim_{t \longrightarrow \infty} \frac{\mathcal{G}(t)}{t} &= 0 \, a.s. \end{aligned} \tag{28}$$

Taking the limit superior on the both sides of (24) and combining with (28), we get

$$\begin{aligned} &\operatorname*{limsup}_{\mathrm{t} \longrightarrow \infty} \frac{\log \mathrm{I}(\mathrm{t})}{\mathrm{t}} \\ &\leq \beta \frac{\partial \phi(\mathrm{S}_0, 0)}{\partial \mathrm{I}} - (\rho + \theta + \delta) - \left(\frac{\sigma^2}{2} + \int_{\mathbb{E}} \frac{\eta^2(\mathrm{l})}{2(1 + \eta(\mathrm{l}) \partial \phi(\mathrm{S}_0, 0)/\partial \mathrm{I})^2} \nu(\mathrm{dl}) \right) \left(\frac{\partial \phi((\mathrm{S}_0, 0))}{\partial \mathrm{I}} \right)^2 \\ &\triangleq (\rho + \theta + \delta) \left[\mathscr{R}_{\mathrm{lj}} - 1 \right] < 0 \, a.s, \end{aligned} \tag{29}$$

which implies that

$$\lim_{t \longrightarrow \infty} I(t) = 0 \, a.s. \tag{30}$$

(ii) Using (4), we have

$$\begin{aligned} \frac{\log I(t)}{t} \leq & \frac{\log I(0)}{t} + \frac{1}{t} \int_0^t \left[\beta \frac{\phi(S(r), I(r))}{I(r)} - (\rho + \theta + \delta) \right. \\ & \left. - \left(\frac{\sigma^2}{2} + \int_{\mathbb{E}} \frac{\eta^2(l)}{2(1 + \eta(l) \partial \phi(S_0, 0)/\partial I)^2} \nu(dl) \right) \left(\frac{\phi(S(r), I(r))}{I(r)} \right)^2 \right] \mathrm{d}r \\ & + \frac{1}{t} \int_0^t \int_{\mathbb{E}} \log \left(1 + \eta(l) \frac{\phi(S(r-), I(r-))}{I(r-)} \right) \tilde{N}(\mathrm{d}r, \mathrm{d}l) \\ & + \frac{1}{t} \int_0^t \sigma \frac{\phi(S(r), I(r))}{I(r)} \mathrm{d}M_B(r) \\ = & \frac{\log I(0)}{t} + \frac{1}{t} \int_0^t \left[-\frac{1}{2} \xi \left(Z - \frac{\beta}{\xi} \right)^2 + \frac{\beta^2}{2\xi} - (\rho + \theta + \delta) \right] \mathrm{d}r, \end{aligned} \tag{31}$$

where $\xi = (\sigma^2/2 + \int_{\mathbb{E}} \eta^2(l)/2(1 + \eta(l) \partial \phi(S_0, 0)/\partial I)^2 \nu(\mathrm{d}l))$ and $Z = \phi(S, I)/I$. Then,

$$\frac{\log I(t)}{t} \leq \frac{\log I(0)}{t} + \frac{\beta^2}{2\xi} - (\rho + \theta + \delta) + \frac{1}{t}\int_0^t \int_{\mathbb{E}} \log\left(1 + \eta(l)\frac{\phi((S(r-), I(r-))}{I(r-)}\right)\widetilde{N}(\mathrm{d}r, \mathrm{d}l) + \frac{1}{t}\int_0^t \sigma \frac{\phi(S(r), I(r))}{I(r)}\mathrm{d}M_B(r). \tag{32}$$

By taking the superior on both sides of (32), we obtain

$$\operatorname{limsup}_{t \longrightarrow \infty} \frac{\log I(t)}{t} \leq \frac{\beta^2}{2}\left(\frac{\sigma^2}{2} + \int_{\mathbb{E}} \frac{\eta^2(l)}{2\left(1 + \eta(l)\partial\phi(S_0, 0)/\partial I\right)^2}\nu(\mathrm{d}l)\right)^{-1} - (\rho + \theta + \delta)\ a.s. \tag{33}$$

This completes the proof of the theorem. □

3. Persistence

In this section, we present sufficient conditions for the persistence in mean of disease in model (3). So, we have the following result.

Theorem 3. *Assume that* (**C**) *hold. If* $\mathscr{R}_{I'j} > 1$, *then for any given initial value* $(S(0), I(0)) \in \mathscr{F}$, *the solution of (3) satisfies*

$$\liminf_{t \longrightarrow \infty} \frac{1}{t}\int_0^t I(r)\mathrm{d}r \geq K_3^{-1}(\rho + \theta + \delta)\left[\mathscr{R}_{I'j} - 1\right] > 0\ a.s., \tag{34}$$

where K_3 *is a positive constant.*

Proof. From system (3), we have

$$\frac{A}{\rho} - \frac{1}{t}\int_0^t S(r)\mathrm{d}r = \frac{(\rho + \theta)}{\rho}\frac{1}{t}\int_0^t I(r)\mathrm{d}r + \frac{\varpi((t))}{\rho}, \tag{35}$$

where $\varpi(t) = S(t) - S(0)/t + I(t) - I(0)/t$. Using Itô's formula and the fact that $\phi(S, I)/I \leq \partial\phi(S_0, 0)/\partial I$, we get

$$\begin{aligned} d\log I &\geq \left[\beta\frac{\phi(S, I)}{I} - (\rho + \theta + \delta) - \left(\frac{\sigma^2}{2} + \int_{\mathbb{E}} \frac{\eta^2(l)}{2\left(1 + \eta(l)V_m\right)^2}\nu(\mathrm{d}l)\right)\left(\frac{\partial\phi(S_0, 0)}{\partial I}\right)^2\right]\mathrm{d}t \\ &\quad + \sigma\frac{\phi(S, I)}{I}\mathrm{d}M_B(t) + \int_{\mathbb{E}} \log\left(1 + \eta(l)\frac{\phi(S, I)}{I}\right)\widetilde{N}(\mathrm{d}t, \mathrm{d}l) \\ &= \left[\beta\frac{\partial\phi(S_0, 0)}{\partial I} - (\rho + \theta + \delta) - \left(\frac{\sigma^2}{2} + \int_{\mathbb{E}} \frac{\eta^2(l)}{2\left(1 + \eta(l)V_m\right)^2}\nu(dl)\right)\left(\frac{\partial\phi(S_0, 0)}{\partial I}\right)^2\right]\mathrm{d}t \\ &\quad + \left[\beta\frac{\phi(S, I)}{I} - \beta\frac{\partial\phi(S_0, 0)}{\partial I}\right]\mathrm{d}t + \sigma\frac{\phi(S, I)}{I}\mathrm{d}M_B(t) \\ &\quad + \int_{\mathbb{E}} \log\left(1 + \eta(l)\frac{\phi(S, I)}{I}\right)\widetilde{N}(\mathrm{d}t, \mathrm{d}l). \end{aligned} \tag{36}$$

Using Lagrange's mean value *theorem*, we obtain

$$\frac{\phi(S(t),I(t))}{I(t)}-\frac{\partial\phi(S_0,0)}{\partial I}=\left[\frac{1}{\Lambda_2(t)}\frac{\partial\phi(\Lambda_1(t),\Lambda_2(t))}{\partial I}-\frac{\phi(\Lambda_1(t),\Lambda_2(t))}{\Lambda_2^2(t)}\right]I(t)+\frac{1}{\Lambda_2(t)}\frac{\partial\phi(\Lambda_1(t),\Lambda_2(t))}{\partial S}(S(t)-S_0),\tag{37}$$

with $\Lambda_1(t)\in(S(t),S_0)$ and $\Lambda_2(t)\in(0,I(t))$. *Consequently*, from (37), one can derive that

$$\begin{aligned}\mathrm{dlog}\ I\geq\Bigg[&\beta\frac{\partial\phi(S_0,0)}{\partial I}-(\rho+\theta+\delta)-\left(\frac{\sigma^2}{2}+\int_{\mathbb{E}}\frac{\eta^2(l)}{2(1+\eta(l)V_m)^2}\nu(\mathrm{dl})\right)\left(\frac{\partial\phi(S_0,0)}{\partial I}\right)^2\\&+\beta\left(\frac{1}{\Lambda_2(t)}\frac{\partial\phi(\Lambda_1(t),\Lambda_2(t))}{\partial I}-\frac{\phi(\Lambda_1(t),\Lambda_2(t))}{\Lambda_2^2(t)}\right)I(t)\\&+\beta\frac{1}{\Lambda_2(t)}\frac{\partial\phi(\Lambda_1(t),\Lambda_2(t))}{\partial S}(S(t)-S_0)\Bigg]\mathrm{d}t+\sigma\frac{\phi(S,I)}{I}\mathrm{d}M_B(t)\\&+\int_{\mathbb{E}}\log\left(1+\eta(l)\frac{\phi(S,I)}{I}\right)\widetilde{N}(\mathrm{d}t,\mathrm{d}l).\end{aligned}\tag{38}$$

According to Lemma 2 and *since* $(\Lambda_1(t),\Lambda_2(t))\in\mathcal{F}$ *a.s.*, then

$$\begin{aligned}\frac{1}{\Lambda_2(t)}\frac{\partial\phi(\Lambda_1(t),\Lambda_2(t))}{\partial I}-\frac{\phi(\Lambda_1(t),\Lambda_2(t))}{\Lambda_2^2(t)}&\geq-K_1,\\\frac{1}{\Lambda_2(t)}\frac{\partial\phi(\Lambda_1(t),\Lambda_2(t))}{\partial S}(S(t)-S_0)&\leq K_2,\end{aligned}\tag{39}$$

with

$$\max_{(S,I)\in\mathbb{L}}\left\{\left|\frac{1}{I}\frac{\partial\phi(S,I)}{\partial I}-\frac{\phi(S,I)}{I}\right|\right\}=K_1,\tag{40}$$

and

$$\max_{(S,I)\in\mathbb{L}}\left\{\left|\frac{1}{I}\frac{\partial\phi(S,I)}{\partial S}\right|\right\}=K_2.\tag{41}$$

Injecting (11) in (10), we get

$$\begin{aligned}\mathrm{dlog}\ I\geq\Bigg\{&\beta\frac{\partial\phi(S_0,0)}{\partial I}-(\rho+\theta+\delta)-\left(\frac{\sigma^2}{2}+\int_{\mathbb{E}}\frac{\eta^2(l)}{2(1+\eta(l)V_m)^2}\nu(\mathrm{dl})\right)\left(\frac{\partial\phi(S_0,0)}{\partial I}\right)^2\\&-\beta[K_1I(t)+K_2(S_0-S(t))]\Bigg\}\mathrm{d}t+\sigma\frac{\phi(S,I)}{I}\mathrm{d}M_B(t)\\&+\int_{\mathbb{E}}\log\left(1+\eta(l)\frac{\phi(S,I)}{I}\right)\widetilde{N}(\mathrm{d}t,\mathrm{d}l).\end{aligned}\tag{42}$$

Integrating both sides of the *above* inequality from 0 to t and dividing by t, we have

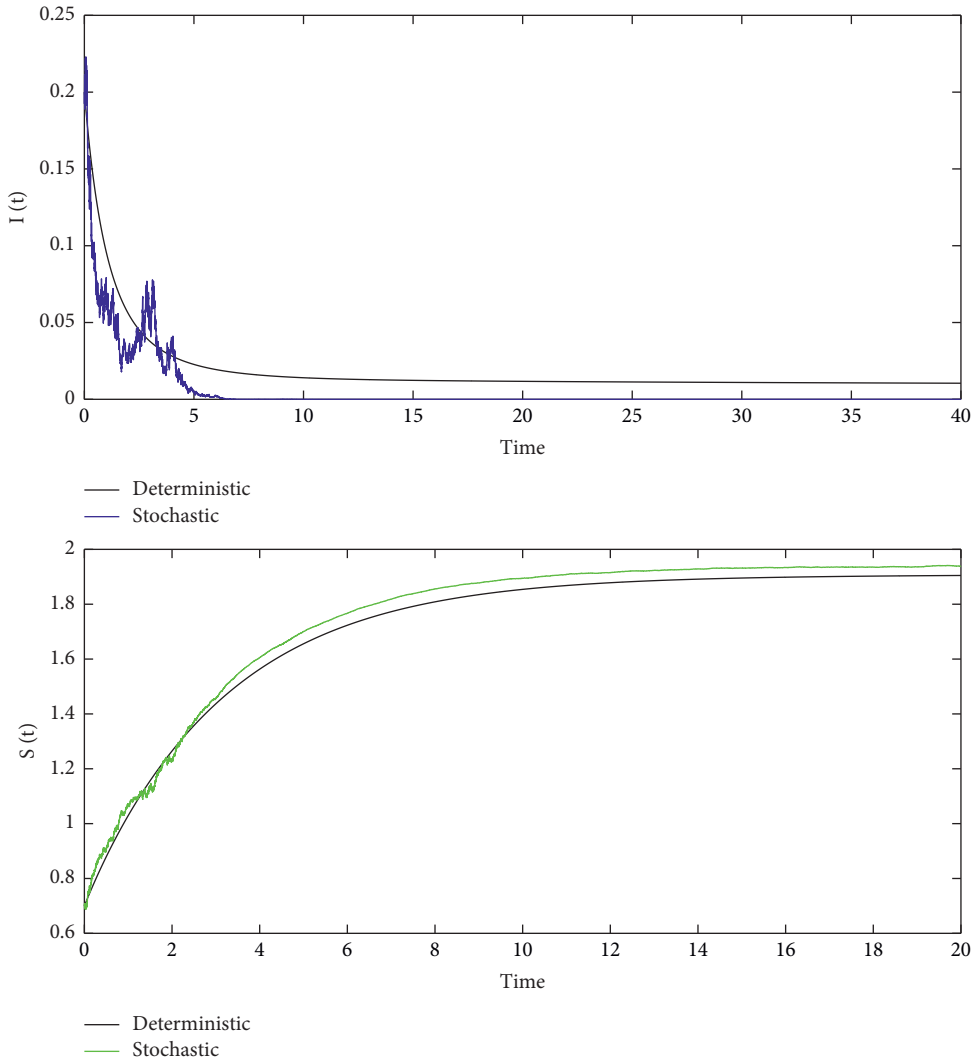

FIGURE 1: Comparison of the trajectory in stochastic system (3) ($I(t)$: blue graph and $S(t)$: green graph) and deterministic system (1) ($I(t)$: black graph and $S(t)$: black graph) for the extinction case.

$$\begin{aligned}\frac{\log I(t)}{t}-\frac{\log I(0)}{t}\geq\beta\frac{\partial\phi(S_0,0)}{\partial I}-(\rho+\theta+\delta)\\-\left(\frac{\sigma^2}{2}+\int_{\mathbb{E}}\frac{\eta^2(l)}{2(1+\eta(l)V_m)^2}\nu(\mathrm{d}l)\right)\left(\frac{\partial\phi(S_0,0)}{\partial I}\right)^2\\-\beta\left[K_1\frac{1}{t}\int_0^t I(r)\mathrm{d}r+K_2\left(S_0-\frac{1}{t}\int_0^t S(r)dr\right)\right]\\+\frac{1}{t}\int_0^t\sigma\frac{\phi(S,I)}{I}\mathrm{d}M_B(r)+\frac{1}{t}\int_0^t\\\int_{\mathbb{E}}\log\left(1+\eta(l)\frac{\phi(S,I)}{I}\right)\widetilde{N}(\mathrm{d}r,\mathrm{d}l).\end{aligned}\tag{43}$$

In view of (35), we obtain

$$\begin{aligned}\frac{\log I(t)}{t}\geq\beta\frac{\partial\phi(S_0,0)}{\partial I}-(\rho+\theta+\delta)\\-\left(\frac{\sigma^2}{2}+\int_{\mathbb{E}}\frac{\eta^2(l)}{2(1+\eta(l)V_m)^2}\nu(\mathrm{d}l)\right)\left(\frac{\partial\phi(S_0,0)}{\partial I}\right)^2\\-\beta\left[K_1+K_2\frac{\rho+\theta}{\rho}\right]\frac{1}{t}\int_0^t I(r)\mathrm{d}r+\pi(t),\end{aligned}\tag{44}$$

where

$$\begin{aligned}\pi(t)=-\frac{\beta K_2}{\rho}\varpi(t)+\frac{\log I(0)}{t}+\frac{1}{t}\int_0^t\sigma\frac{\phi(S,I)}{I}\mathrm{d}M_B(r)\\+\frac{1}{t}\int_0^t\int_{\mathbb{E}}\log\left(1+\eta(l)\frac{\phi(S,I)}{I}\right)\widetilde{N}(\mathrm{d}r,\mathrm{d}l).\end{aligned}\tag{45}$$

According to the large number theorem for local martingales [28] and the fact that $S, I\in\mathcal{I}$, we have

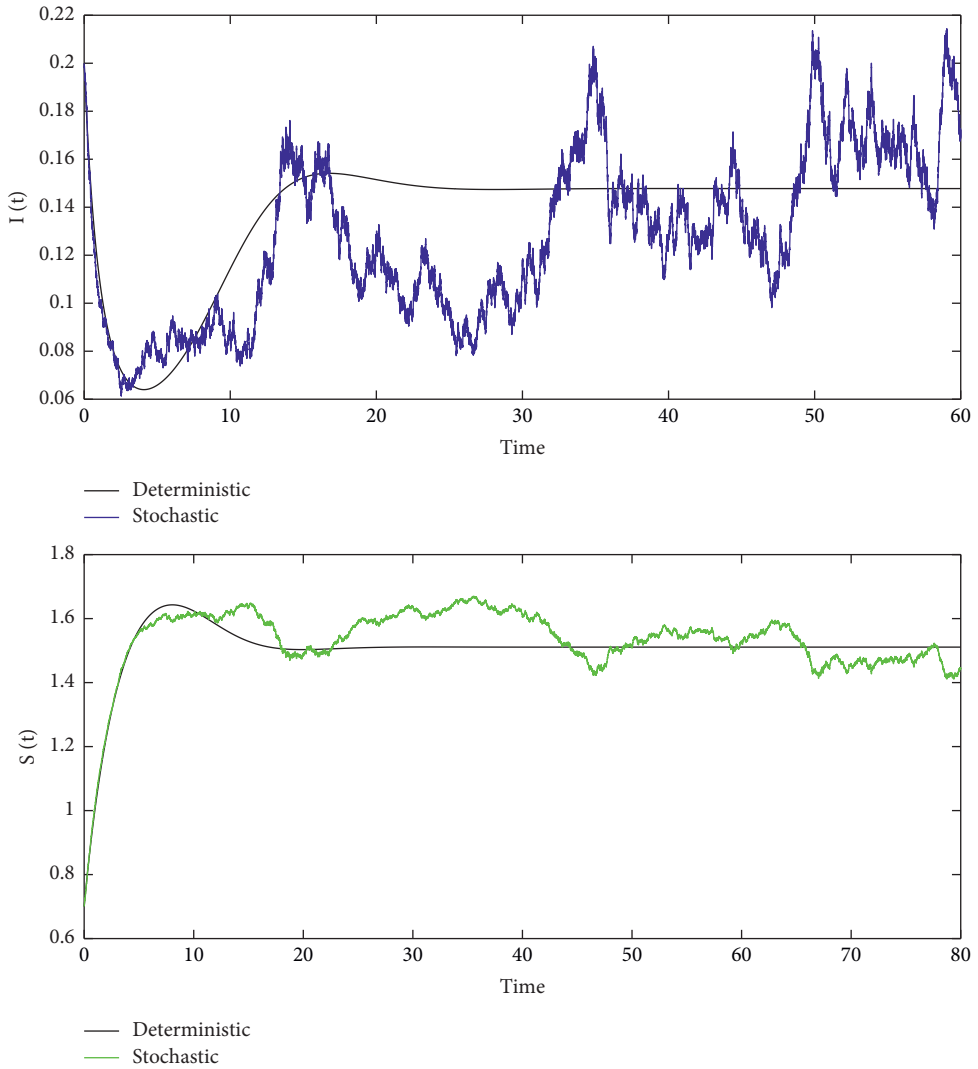

Figure 2: Comparison of the trajectory in stochastic system (3) ($I(t)$: blue graph and $S(t)$: green graph) and deterministic system (1) ($I(t)$: black graph and $S(t)$: black graph) for the persistence case.

$$\lim_{t\longrightarrow\infty} \pi(t) = 0 \; a.s. \tag{46}$$

According to Lemma 1, we obtain the following inequality:

$$\begin{aligned}\liminf_{t\longrightarrow\infty} \frac{1}{t}\int_0^t I(r)dr \geq K_3^{-1}\left[\beta\frac{\partial\phi(S_0,0)}{\partial I} - (\rho+\theta+\delta)\right.\\ \left.-\left(\frac{\sigma^2}{2} + \int_{\mathbb{E}} \frac{\eta^2(l)}{2(1+\eta(l)V_m)^2}\nu(dl)\right)\left(\frac{\partial\phi(S_0,0)}{\partial I}\right)^2\right],\end{aligned} \tag{47}$$

where $K_3 = \beta[K_1 + K_2\rho + \theta/\rho]$. Hence,

$$\liminf_{t\longrightarrow\infty} \frac{1}{t}\int_0^t I(r)dr \geq K_3^{-1}(\rho+\theta+\delta)\left[\mathscr{R}_{1'j} - 1\right] > 0 \; a.s. \tag{48}$$

□

Remark 2. The condition $\mathscr{R}_{1'j} > 1$ implies that the reproduction number is also greater than one, and this means that when the disease in stochastic system (3) persists, it can also persist in deterministic system (1).

4. Numerical Application

In this section, we give some simulations to support the theoretical results presented in this paper. For this, we use the Euler scheme described in [35]. In the figures, the black lines represent solutions of a deterministic system (1), the blue lines are the paths of $S(t)$ for stochastic system (3) with Lévy jumps, and the green lines are the paths of $I(t)$ for stochastic system (3) with Lévy jumps. In model (3), we take $\phi(S, I) = \beta SI/1 + kI$, which is the saturated incidence rate introduced by Capasso and Serio [14]. We can easily show that ϕ satisfies the assumptions (**C**). Then, we have

$$\mathscr{R}_{lj} = \frac{\beta S_0}{(\rho+\theta+\delta)} - \overline{\eta} S_0^2 \frac{1}{(\rho+\theta+\delta)} = \mathscr{R}_0 - \overline{\eta} S_0^2 \frac{1}{(\rho+\theta+\delta)}. \tag{49}$$

Hence, we have the following corollary of Theorem 3.

Corollary 1. *Under the assumptions* (**C**)*, let* $(S(t), I(t))$ *be the solution of model (3) with any initial value* $(S(0), I(0)) \in$*:*

(i) If $\mathscr{R}_{lj} < 1$ *and* $\partial\phi(S_0, 0)/\partial I \le \beta/\overline{\eta}$*, then*

$$\limsup_{t\longrightarrow\infty} \frac{\log I(t)}{t} \le (\rho+\theta+\delta)\left[\mathscr{R}_{lj} - 1\right] < 0 \; a.s. \tag{50}$$

(ii) If $\sigma^2/2 + \int_{\mathbb{E}} \eta^2(l)/2(1+\eta(l)\partial\phi(S_0,0)/\partial I)^2 \nu(dl) > \beta^2/2(\rho+\theta+\delta)$*, then*

$$\limsup_{t\longrightarrow\infty} \frac{\log I(t)}{t} \le \frac{\beta^2}{2}\left(\frac{\sigma^2}{2} + \int_{\mathbb{E}} \frac{\eta^2(l)}{2\left(1+\eta(l)\partial\phi(S_0,0)/\partial I\right)^2}\nu(dl)\right)^{-1} - (\rho+\theta+\delta) < 0 \; a.s. \tag{51}$$

In others word, $I(t)$ will go to zero almost surely. That is, the disease will be extinct almost surely.

4.1. Extinction Case. Take the parameters in stochastic system (3) as follows: $A = 0.66$, $\rho = 0.34$, $\beta = 0.7$, $k = 0.1$, $\theta = 0.65$, $\delta = 0.35$, $\sigma = 0.7$, and $\eta(l) = 0.05$. By simple computation, we obtain $\mathscr{R}_{lj} = 0.8295 < 1$ and $\mathscr{R}_0 = 1.0140$. Then, the condition of Theorem 2 holds. Hence, one can observe that disease is extinct. Figure 1 demonstrates this result. From a comparative point of view, we remark that in Figure 1, epidemic I tends to zero for the stochastic system (blue graph) and not for the deterministic system (black graph). Thus, the epidemic does not disappear from the population if there is no Lévy process effect. Deduce that Lévy jumps can significantly influence the properties of the system and can drive the disease to disappear (see Figure 1).

4.2. Persistence Case. In this case, we save the same parameter values employed in the extinction case. Also, we choose the noise values as follows: $\sigma = 0.1$ and $\eta(l) = 0.02$. By calculation, we get $\mathscr{R}_{l'j} = 1.2998 > 1$. Therefore, it follows from Theorem 3 that disease $I(t)$ persists in the mean with probability one. Figure 2 shows this result. So, the disease disappears when the values of the noise terms are not interesting.

Finally, the numerical simulation in Figures 1 and 2 clarifies the dynamics of the diseases as a function of time for two different values of the noise parameters. Then, you can see that the large value of noises parameters can remove the disease from the population.

5. Conclusion

This paper studies a stochastic SIS epidemic model with nonlinear incidence rate and Lévy jumps. Under assumption (**C**), we prove the following results:

(1) If $\mathscr{R}_{lj} < 1$ and $\partial\phi(S_0, 0)/\partial I \le \beta/\overline{\eta}$, then

$$\limsup_{t\longrightarrow\infty} \frac{\log I(t)}{t} \le (\rho+\theta+\delta)\left[\mathscr{R}_{lj} - 1\right] < 0 \; a.s. \tag{52}$$

Thus, the disease$I$ dies out with probability one.

(2) If $\sigma^2/2 + \int_{\mathbb{E}} \eta^2(l)/2(1+\eta(l)\partial\phi(S_0,0)/\partial I)^2 \nu(dl) > \beta^2/2(\rho+\theta+\delta)$, then

$$\limsup_{t\longrightarrow\infty} \frac{\log I(t)}{t} \le \frac{\beta^2}{2}\left(\frac{\sigma^2}{2} + \int_{\mathbb{E}} \frac{\eta^2(l)}{2\left(1+\eta(l)\partial\phi(S_0,0)/\partial I\right)^2}\nu(dl)\right)^{-1} - (\rho+\theta+\delta) < 0 \; a.s. \tag{53}$$

Thus, the disease I dies out with probability one.

(3) If $\mathscr{R}_{l'j} > 1$, then the disease persists in mean.

For our epidemic model (3), we have established the generalized basic reproduction number noted $\mathscr{R}_{lj}$ and concluded that the noise coefficient can eliminate the disease, that is, if the white noise value is large and $\eta(l) > 0$, the disease goes extinct. On the other hand, if the value of the noise parameters is very low, the disease persists in the population. So, white noise and Lévy noise can control the spread of disease in the population.

Data Availability

The data used to support the findings of this study are included within the article.

Conflicts of Interest

The author declares that there are no conflicts of interest.

References

[1] M. Kermark and A. Mckendrick, "Contributions to the mathematical theory of epidemics. Part I," *Proc. r. soc. a*, vol. 115, no. 5, pp. 700–721, 1927.

[2] J. Satsuma, R. Willox, A. Ramani, B. Grammaticos, and A. S. Carstea, "Extending the SIR epidemic model," *Physica A: Statistical Mechanics and Its Applications*, vol. 336, no. 3-4, pp. 369–375, 2004.

[3] G. Zaman, Y. Han Kang, and I. H. Jung, "Stability analysis and optimal vaccination of an SIR epidemic model," *Biosystems*, vol. 93, no. 3, pp. 240–249, 2008.

[4] A. El Koufi, J. Adnani, A. Bennar, and N. Yousfi, "Dynamics of a stochastic SIR epidemic model driven by Lévy jumps with saturated incidence rate and saturated treatment function," *Stochastic Analysis and Applications*, pp. 1–19, 2021.

[5] A. El Koufi, J. Adnani, A. Bennar, and N. Yousfi, "Analysis of a stochastic SIR model with vaccination and nonlinear incidence rate," *International Journal of differential equations*, vol. 2019, Article ID 9275051, 9 pages, 2019.

[6] A. El Koufi, A. Bennar, and N. Yousfi, "Dynamics behaviors of a hybrid switching epidemic model with levy noise," *Applied Mathematics*, vol. 15, no. 2, p. 131, 2021.

[7] R. M. Jena, S. Chakraverty, and D. Baleanu, "SIR epidemic model of childhood diseases through fractional operators with Mittag-Leffler and exponential kernels," *Mathematics and Computers in Simulation*, vol. 182, pp. 514–534, 2021.

[8] A. El Koufi, "The Power of Delay on a Stochastic Epidemic Model in a Switching Environment," *Complexity*, vol. 2022, Article ID 5121636, 9 pages, 2022.

[9] H. W. Hethcote and J. A. Yorke, *Gonorrhea transmission dynamics and control*, Springer, NY, USA, 2014.

[10] K. E. Lamb, D. Greenhalgh, and C. Robertson, "A simple mathematical model for genetic effects in pneumococcal carriage and transmission," *Journal of Computational and Applied Mathematics*, vol. 235, no. 7, pp. 1812–1818, 2011.

[11] X.-Z. Li, W.-S. Li, and M. Ghosh, "Stability and bifurcation of an SIS epidemic model with treatment," *Chaos, Solitons & Fractals*, vol. 42, no. 5, pp. 2822–2832, 2009.

[12] H. Kang and S. Ruan, "Mathematical analysis on an age-structured SIS epidemic model with nonlocal diffusion," *Journal of Mathematical Biology*, vol. 83, no. 1, pp. 5–30, 2021.

[13] S. Jana, M. Mandal, S. K. Nandi, and T. K. Kar, "Analysis of a fractional-order SIS epidemic model with saturated treatment," *International Journal of Modeling, Simulation, and Scientific Computing*, vol. 12, no. 1, Article ID 2150004, 2021.

[14] V. Capasso and G. Serio, "A generalization of the kermack-mckendrick deterministic epidemic model," *Mathematical Biosciences*, vol. 42, no. 1-2, pp. 43–61, 1978.

[15] N. Swati, "Fractional order SIR epidemic model with Beddington-De Angelis incidence and Holling type II treatment rate for COVID-19," *Journal of Applied Mathematics Computing*, vol. 1, 2022.

[16] M. Lu, J. Huang, S. Ruan, and P. Yu, "Global dynamics of a susceptible-infectious-recovered epidemic model with a generalized nonmonotone incidence rate," *Journal of Dynamics and Differential Equations*, vol. 33, no. 4, pp. 1625–1661, 2021.

[17] S. P. Rajasekar and Q. Zhu, "Higher order stochastically perturbed SIRS epidemic model with relapse and media impact," *Mathematical Methods in the Applied Sciences*, vol. 45, no. 2, pp. 843–863, 2022.

[18] M. C. M. De Jong, O. Diekmann, and H. Heesterbeek, "How does transmission of infection depend on population size," in *Epidemic Models: Their Structure and Relation to Data*, D. Mollison, Ed., Cambridge University Press, New York, NY, 1995.

[19] J. R. Beddington, "Mutual interference between parasites or predators and its effect on searching efficiency," *Journal of Animal Ecology*, vol. 44, no. 1, pp. 331–340, 1975.

[20] P. H. Crowley and E. K. Martin, "Functional responses and interference within and between year classes of a dragonfly population," *Journal of the North American Benthological Society*, vol. 8, no. 3, pp. 211–221, 1989.

[21] Y. Liu and J.-A. Cui, "The impact of media coverage on the dynamics of infectious disease," *International Journal of Biomathematics*, vol. 01, no. 01, pp. 65–74, 2008.

[22] E. Tornatore, S. Maria Buccellato, and P. Vetro, "Stability of a stochastic SIR system," *Physica A: Statistical Mechanics and Its Applications*, vol. 354, pp. 111–126, 2005.

[23] R. M. May, *Stability and Complexity in Model Ecosystems*, Princeton university press, Princeton, NJ, USA, 2019.

[24] G. Hussain, T. Khan, A. Khan et al., "Modeling the dynamics of novel coronavirus (COVID-19) via stochastic epidemic model," *Alexandria Engineering Journal*, vol. 60, no. 4, pp. 4121–4130, 2021.

[25] M. Liu and C. Bai, "Dynamics of a stochastic one-prey two-predator model with Lévy jumps," *Applied Mathematics and Computation*, vol. 284, pp. 308–321, 2016.

[26] H. Qiu and Y. Huo, "Persistence and extinction of a stochastic AIDS model driven by Lévy jumps," *Journal of Applied Mathematics and Computing*, vol. 1-14, 2022.

[27] A. El Koufi, A. Bennar, and N. Yousfi, "A stochastic analysis for a triple delayed SIR epidemic model with vaccination incorporating Lévy noise," *International Journal of Biomathematics*, p. 2250038, 2022.

[28] X. Mao, *Stochastic Differential Equations and Applications*, Elsevier, Amsterdam, Netherlands, 2007.

[29] A. El Koufi, A. Bennar, N. Yousfi, and M. Pitchaimani, "Threshold dynamics for a class of stochastic SIRS epidemic models with nonlinear incidence and Markovian switching," *Mathematical Modelling of Natural Phenomena*, vol. 16, p. 55, 2021.

[30] D. Applebaum, *Lévy Processes and Stochastic Calculus*, Cambridge Press, New York, NY, 2009.

[31] B. K. Øksendal and A. Sulem, *Applied Stochastic Control of Jump Diffusions*, Springer, Berlin, 2007.

[32] A. Gray, D. Greenhalgh, L. Hu, X. Mao, and J. Pan, "A stochastic differential equation SIS epidemic model," *SIAM Journal on Applied Mathematics*, vol. 71, no. 3, pp. 876–902, 2011.

[33] Z. Teng and L. Wang, "Persistence and extinction for a class of stochastic SIS epidemic models with nonlinear incidence rate," *Physica A: Statistical Mechanics and Its Applications*, vol. 451, pp. 507–518, 2016.

[34] N. Gao, Y. Song, X. Wang, and J. Liu, "Dynamics of a stochastic SIS epidemic model with nonlinear incidence rates," *Advances in Difference Equations*, vol. 2019, no. 1, pp. 1–19, 2019.

[35] P. Protter and D. Talay, "The Euler scheme for Lévy driven stochastic differential equations," *Annals of Probability*, vol. 25, no. 1, pp. 393–423, 1997.

Hindawi
Complexity
Volume 2022, Article ID 6627409, 19 pages
https://doi.org/10.1155/2022/6627409

WILEY | Hindawi

Research Article

Chaotic Fruit Fly Algorithm for Solving Engineering Design Problems

M. A. El-Shorbagy [1,2]

[1]*Department of Mathematics, College of Science and Humanities in Al-Kharj, Prince Sattam Bin Abdulaziz University, Al-Kharj 11942, Saudi Arabia*
[2]*Department of Basic Engineering Science, Faculty of Engineering, Menoufia University, Shebin El-Kom 32511, Egypt*

Correspondence should be addressed to M. A. El-Shorbagy; mohammed_shorbagy@yahoo.com

Received 12 February 2022; Revised 16 March 2022; Accepted 1 April 2022; Published 21 April 2022

Academic Editor: Akif Akgul

The aim of this article is to present a chaotic fruit fly algorithm (CFFA) as an optimization approach for solving engineering design problems (EDPs). In CFFA, the fruit fly algorithm (FFA), which is recognized for its durability and efficiency in addressing optimization problems, was paired with the chaotic local search (CLS) method, which allows for local exploitation. CFFA will be set up to work in two phases: in the first, FFA will be used to discover an approximate solution, and in the second, chaotic local search (CLS) will be used to locate the optimal solution. As a result, CFFA can address difficulties associated with the basic FFA such as falling into local optima, an imbalance between exploitation and exploration, and a lack of optimum solution acquisition (i.e., overcoming the drawback of premature convergence and increasing the local exploitation capability). The chaotic logistic map is employed in the CLS because it has been demonstrated to be effective in improving the quality of solutions and giving the best performance by many studies. The proposed algorithm is tested by the set of CEC'2005 special sessions on real parameter optimization and many EDPs from the most recent test suite CEC'2020. The results have demonstrated the superiority of the proposed approach to finding the global optimal solution. Finally, CFFA′s results were compared to those of earlier research, and statistical analysis using Friedman and Wilcoxon's tests revealed its superiority and capacity to tackle this type of problem.

1. Introduction

The engineering design problems (EDPs) are extremely significant from both the manufacturing and scientific perspective, where it is a very important and challenging area, especially in the field of engineering for getting designs that have efficient form and are more accurate. Generally, these problems are treated as nonlinear constrained optimization problems (NCOPs). NCOPs are very difficult, and the problem feasible region may be a thin subset of the search domain [1].

Traditionally, NCOPs are solved by some efficient methods such as recursive quadratic programming, projection method, generalized reduced gradient method, penalty method, and a multiplier method [2]. These methods are not efficient since they may only compute local optima, and it is very hard to apply these methods to problems as its feasible region is not convex or the objective function is not differentiable [3].

Because of the drawbacks of traditional optimization approaches, the meta-heuristic optimization algorithm for tackling NCOPs emerged. Meta-heuristic algorithms are considered the best optimization algorithms, where they have several advantages such as resilience, performance reliability, simplicity, ease of implementation, and so on. Meta-heuristic algorithms are divided into several categories, including:

(1) Evolutionary-based algorithms: These algorithms are based on evolutionary theory.

(2) Swarm-based algorithms: These algorithms mimic the social behavior and collective decision-making of different social groups. The reason for achieving a specific goal in these algorithms is typically based on bio-community intelligence and collective action.

(3) The rules of natural physics have been used for the emergence of physics-based algorithms.

(4) Algorithms influenced by human social behavior: Recently, optimization algorithms inspired by human social behavior have been suggested in the literature.

Table 1 contains examples of several classifications offered in the literature.

Swarm intelligence-based algorithms are regarded as one of the most essential types of meta-heuristic algorithms. These algorithms emulated the behavior and features of swarms' systems, for which Gerardo Beni and Jing Wang coined the term "swarm intelligence" (SI) in 1989 [62], the notion of which is critical in computer science and artificial intelligence. As a result, they have been dubbed swarm intelligence algorithms (SIAs). Swarm intelligence algorithms (SIAs) are connected to the study of swarms, or colonies of social creatures, where studies of social behavior in swarms of organisms influenced the development of many effective optimization algorithms. The simulation of bird flocks, for example, resulted in the particle swarm optimization (PSO) method, while studies of ant behavior in the construction of the ant colony optimization (ACO) algorithm [62]. SIAs, on the other hand, are simple in concepts, have a low probability to fall into local optima, and require simple information about the optimization problem without requiring that the objective function or the constraints are derivable or continuous [63]. Due to the drawbacks of traditional approaches, SIAs were commonly employed to solve engineering design problems (EDPs).

Many SIAs are presented today to tackle complex optimization problems. Although they can find promising solutions to optimization problems, they frequently become caught in local optima when the problem is complicated and contains several local optima. Creating hybrid SIAs has the potential to dramatically improve this issue. Most of the time, hybrid SIAs are more resilient and efficient than the basic versions since they may benefit from the advantages of different algorithms that are used in hybrid SIAs [64, 65]. Many researchers sought to design hybrid SIAs to produce more efficient global optimization algorithms. The most popular hybrid SIAs are hybrid cultural-trajectory-based search [66], hybrid of the ant colony and firefly algorithms (HAFA) [67], hybrid harmony search-cuckoo search (HS/CS) algorithm [68], hybrid particle swarm optimization-genetic algorithm (PSO/GA) [69], hybrid krill herd-biogeography-based optimization (KHBBO) algorithm [70], hybrid cat swarm optimization (CSO) [71], hybrid tissue membrane systems (TMS) and the evolution strategy with covariance matrix adaptation (CMA-ES) [72], hybrid grasshopper optimization algorithm-local search (GOA/LS) [73], krill herd-differential evolution (KHDE) [74], hybrid grasshopper optimization algorithm-genetic algorithm (GOA/GA) [75], hybrid bat algorithm with harmony search (BHS) [76], etc.

Recently, hybrid SIAs have become the most widely used method for solving EDPs such as a penalty-guided artificial bee colony (ABC) algorithm [77], hybrid Nelder–Mead simplex search and particle swarm optimization [78], Gaussian quantum-behaved particle swarm optimization [79], hybrid Lévy flight-chaotic local search-whale optimization algorithm (LF-CLS-WOA) [80], self-adaptive strategy-based firefly algorithm [81], hybrid genetic algorithm-particle swarm optimization-sequential quadratic programming (GA-PSO-SQP) [82], sine-cosine grey wolf optimizer [83], and improved moth-flame optimization algorithm (IMFO) [84]. It is now obvious that engineering design problems are a significant problem that scholars are focusing on to offer new hybrid methods for solving it and determining the best solutions.

Fruit fly algorithm (FFA) is a novel SI approach based on the foraging behaviors of fruit flies that competes with current swarm algorithms like particle swarm optimization (PSO). However, the FFA still has certain drawbacks, such as its necessitating long CPU times, which are impractical from an engineering standpoint, and limited convergence accuracy, which makes it easy to get stuck at a local optimal value during the evolution process [85]. As a result, the application of chaos theory to overcome these shortcomings is being researched. In recent years, the chaos theory has been applied to several fields of optimization science. As a new method of global optimization, chaos algorithms have garnered a lot of attention. The characteristics inherent in chaos can enhance algorithms of optimization by avoiding local solutions and enhancing convergence to reach a global solution.

Many researchers [86–97] proposed merging chaos theory and optimization algorithms to overcome these limitations, increase solution quality, and reach the ideal solution. For example, in [86], the chaos algorithm was included in the evolutionary process of the fundamental FFA to tackle the difficulties of poor convergence accuracy and quickly relapsing into the local extremum in the fundamental FFA. That is, in the case of local convergence, the chaos algorithm was used to search for the global optimum in the convergent area's outer space, leap out of the local extremum, and continue to optimize. Also, in [88], the conventional FFA was improved by including a new parameter that was integrated by chaotic to solve global optimization; overall study findings reveal that FFA with Chebyshev map outperforms FFA without Chebyshev map in terms of global optimality reliability and algorithm success rate. In addition, a novel version of FFA with Gaussian mutation operator and chaotic local search strategy (MCFFA) was proposed in [90]. To avoid premature convergence and enhance the algorithm's exploitative tendencies, the Gaussian mutation operator was first included in the basic FFA (MFFA). The chaotic local search approach was then used to improve the swarm of agents′ capacity to search locally (CFFA). MCFFA was used to handle issues involving benchmark functions with various properties and feature selection. MCFFA effectively increased FFA's performance and achieves optimal classification accuracy, according to the findings. Furthermore, chaotic fruit fly optimization [92] was presented as a novel learning technique for early detection and effective evaluation of sepsis, where two new mechanisms, chaotic population initiation

Table 1: Meta-heuristic algorithms classification [4].

Category	Algorithm name	References
Evolutionary-based algorithms [5–8]	Genetic algorithm (GA)	[5, 6]
	Differential evolution (DE)	[7]
	Evolutionary strategy (ES)	[8]
Swarm-based algorithms [9–41]	Particle swarm optimization (PSO)	[9–11]
	Ant colony optimization (ACO)	[12]
	Fruit fly algorithm (FFA)	[13]
	Bacterial foraging (BF)	[14]
	Glowworm swarm optimization (GSO)	[15]
	Grey wolf optimizer (GWO)	[16]
	Whale optimization algorithm (WOA)	[17]
	Firefly algorithm (FA)	[18]
	Moth-flame optimization (MFO)	[19]
	Salp swarm optimization (SSA)	[20]
	Grasshopper optimization algorithm (Goa)	[21]
	Artificial bee colony algorithm (ABCA)	[22]
	Bat algorithm (BA)	[23]
	Monkey algorithm (MA)	[24]
	Cuckoo search algorithm (CSA)	[25]
	Spherical search algorithm (SSA)	[26]
	Social spider optimization (SSO)	[27]
	Marine predators algorithm (MPA)	[28]
	Crow search algorithm (CSA)	[29]
	Krill herd algorithm (KHA)	[30]
	Chimp optimization algorithm (COA)	[31]
	Squirrel search algorithm (SCA)	[32]
	Flower pollination algorithm (FPA)	[33]
	Manta ray foraging optimization (MRFO)	[34]
	Sailfish optimizer (SO)	[35]
	Emperor penguin optimizer (EPO)	[36]
	Spotted hyena optimizer (SHO)	[37]
	Slime mould algorithm (SMA)	[38]
	Coyote optimization algorithm	[39]
	Harris hawks optimization (HHO)	[40]
	Colony predation algorithm (CPA)	[41]
Human behavior-based algorithms [42–48]	Group teaching optimization (GTO)	[42]
	Imperialist competitive algorithm (ICA)	[43]
	Teaching-learning based optimization (TLBO)	[44]
	League champion algorithm (LCA)	[45]
	Political optimizer (PO)	[46]
	Poor and rich optimization (PRO)	[47]
	Hunger games search (HGS)	[48]
Physics-based algorithms [49–61]	Gravitational search algorithm (GSA)	[49]
	Simulated annealing (SA)	[50]
	Artificial electric field optimization (AEFO)	[51]
	Sine-cosine algorithm (SCA)	[52, 53]
	Magnetic optimization algorithm (MOA)	[54]
	Turbulent flow of water-based optimization (TFWBO)	[55]
	Henry gas solubility optimization (HGSO)	[56]
	Archimedes optimization algorithm (AOA)	[57]
	Fireworks algorithm (FA)	[58]
	Mine blast algorithm (MBA)	[59]
	weIghted meaN oF vectOrs (INFO)	[60]
	RUNge Kutta optimizer (RUN)	[61]

and chaotic local search strategy, were added to the original FFA. The positive results showed that the approach developed may be a valuable diagnostic tool for clinical decision assistance. A novel support vector machine (SVM) optimization approach, on the other hand, was given in [95], that is based on an upgraded chaotic fruit fly algorithm (FFA) with a mutation strategy to execute SVM parameter setting turning and feature selection simultaneously. The chaotic particle in the enhanced FFA initializes the fruit fly swarm location and substitutes the distance expression for the fruit fly to find the food source. This strategy has been proved to be more resilient and successful than other well-known

optimization methods, especially when it comes to tackling medical diagnosis and credit card problems. Finally, in [97], a new method for parameter identification of a bidirectional inductive power transfer (BIPT) system was proposed utilizing a chaotic-enhanced FFA, which used a chaotic sequence to improve the original FFA′s global optimization capabilities. Simulations demonstrated that the suggested approach is efficient for measuring noise and changes in operating conditions, making it ideal for practical use.

From the above, it is clear that introducing chaos to improve FFA has received wide attention from many researchers. From this motivation, this paper proposed a chaotic fruit fly algorithm (CFFA). CFFA combines the fruit fly algorithm (FFA) with a chaotic local search (CLS) method to expedite optimum seeking and find the optimal solution. In addition, combining FFA global search and procedures of CLS offers the benefits of both methods of optimization, while compensating for their disadvantages to ensure the proposed algorithm's robustness. The main contributions to this paper are:

(1) For solving EDPs, a new algorithm called chaotic fruit fly algorithm (CFFA) is presented and tested.

(2) Demonstrating that combining the fruit fly algorithm (FFA) with a chaotic local search (CLS) strategy in CFFA accelerates optimum seeking and finds the EDPs' best solutions.

(3) Testing the robustness and reliability of CFFA and the ability for finding global solutions by using the test suite (CEC'2005) and many EDPs from the most recent test suite (CEC'2020).

(4) Validating by the numerical analysis results that the proposed algorithm has high performance and prove that statistically.

The following is how this paper is structured: the formulation of the nonlinear constrained optimization problem is discussed in Section 2. The proposed methodology is presented in Section 3. The computational experiment is shown in Section 4. Finally, the conclusion is provided in Section 5.

2. Nonlinear Constrained Optimization Problem

Mathematically, the generic nonlinear constrained optimization problem (NCOP) is expressed as:

Minimize/maximize: $f(x)$.

Subject to:

$$\begin{aligned} g_j &\le 0 \text{ for } j = 1, \ldots, m, \\ h_e &\le 0 \text{ for } e = 1, \ldots, l, \end{aligned} \tag{1}$$

where $f, g_1, \ldots, g_j, h_1, \ldots, h_e$ are functions defined on $\mathbb{R}^n$, x is a subset of $\mathbb{R}^n$, and is a vector of n components $x_1, \ldots, x_n$. The above problem must be solved for the values of the variables $x_1, \ldots, x_n$ that satisfy the restrictions and minimize or maximize the function f. The function f is the objective function or criterion function. An unconstrained problem is one in which there are no constraints. If there are constraints, the problem is called a constrained problem, and each of the constraints $g_j \le 0 \quad \forall j = 1, \ldots, m$ is called an inequality constraint, and each of the constraints $h_e \le 0 \quad \forall e = 1, \ldots, l$ is called equality constrain [98].

At solving the optimization problem, we are looking for a global solution and not stock on a local solution. An optimal solution (either maximum or minimum) within a neighboring set of candidate solutions is referred to as a local solution of an optimization problem. A global optimum solution is the best solution among all feasible solutions, not simply those within a neighboring set of candidate solutions [98]. Definition 1 introduces the difference between a local solution and a global solution. Figure 1 illustrates this definition.

Definition 1. Let $x = (x_1, x_2, \ldots, x_n)$ be a feasible solution to a minimization problem with objective function $f(x)$ [98]. Then, x is:

(i) A global minimum if $f(X) \le f(Y)$ for every feasible point $y = (y_1, y_2, \ldots, y_n)$.

(ii) A local minimum if $f(X) \le f(Y)$ for all feasible points $y = (y_1, y_2, \ldots, y_n)$ sufficiently close to x.

3. The Proposed Methodology

In this section, we provide a brief overview of both the fruit fly algorithm (FFA) and the chaos theory. The proposed algorithm is then thoroughly described.

3.1. Fruit fly Algorithm. The FFA [99] is a fruit fly-inspired swarm-based intelligence approach that mimics the fruit fly′s foraging behavior. Fruit flies use their keen sense of smell and eyesight to locate food sources. During foraging, fruit flies can detect the aromas of food sources from a long distance away, and swarms fly towards the food source with the highest concentration of the scent. When the fruit fly gets near enough to the food source, it may use its better vision to pinpoint the exact position of the food supply.

The procedure of foraging is emulated in the FFA by exploring the solution space iteratively. The search technique is divided into two parts: smell-based search and vision-based search. The FFA technique may be characterized as follows, according to the fruit fly′s characteristics:

Step 1: The algorithm′s parameters are set, as well as the swarms′ center position.

Step 2: Smell-based search.

Step 2.1: Determine a suitable position for the food supply towards the center of the swarms at random for each fruit fly.
Step 2.2: The concentration of smell at each site of the fruit fly is determined.

Step 3: Search-based vision.

Step 3.1: With the greatest concentration of smell, the most likely location is determined.

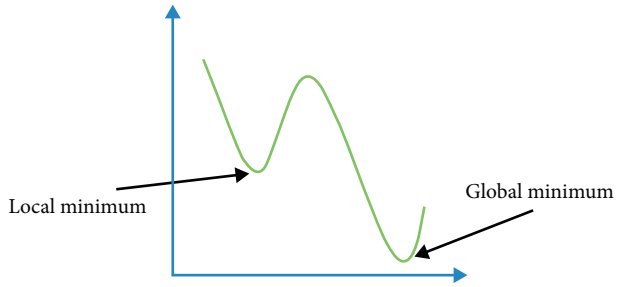

Figure 1: Global minimum and local minimum.

Step 3.2: The fruit fly swarms flock to this location, and the location of the swarm centers is updated.

Step 4: The algorithm is terminated if the stopping condition is fulfilled; otherwise, repeat steps 2 and 3.

3.2. Chaos Theory. By employing extremely unpredictable chaotical sequences, chaos theory (CS) enhances swarm intelligence algorithms [100] and increases convergence and variety of solutions. CS is seen as irregular behavior in nonlinear systems. These maps are meant to represent particles moving in a restricted range of nonlinear dynamic systems, with no knowledge of how the particles move.

To improve solution quality, many researchers proposed combining the CS and optimization algorithms, such as hybrid chaos-PSO [101, 102], chaotic genetic algorithm [103], the combined evolutionary algorithm with chaos [104], chaotic differential bee colony optimization algorithm [105], chaotic DE algorithm [106], chaotic WOA [107], chaotic artificial bee colony (ABC) [108], chaotic harmony search algorithm [109], and chaotic artificial neural networks [110]. There are many well-known chaotic maps, such as the sinusoidal map, Chebyshev map, singer map, tent map, sine map, circle map, Gauss map, logistic map, to be found in the literature [94].

3.3. Chaotic Fruit fly Algorithm. In this section, the chaotic fruit fly algorithm (CFFA) is proposed, which is an integration between the fruit fly algorithm (FFA) and chaos local search (CLS) strategy. The suggested approach is divided into two parts. In the first, FFA is used to discover an approximate solution. Then, in the second stage, CLS is used to speed up convergence, increase solution quality, and reach the optimal solution. The description of the essential idea of the suggested method is as follows:

3.3.1. Phase I: FFA.

Step 1 **(Initialization).** Define the fly group population size $i = 1, \ldots, N$, the iteration termination condition $T_{\max}$, and the starting fruit fly swarm center position $(X_{\text{axis}}, Y_{\text{axis}})$.

Step 2 **(Determination of individual locations).** The position of each fruit fly (X_i, Y_i) is assigned at random as:

$$\begin{aligned} X_i &= X_{\text{axis}} + \text{Random Value}, \\ Y_i &= Y_{\text{axis}} + \text{Random Value}. \end{aligned} \tag{2}$$

Step 3. The judgment value of smell concentration S_i is set as the reciprocal of the distance between the fruit fly and the origin (Dist_i):

$$\begin{aligned} S_i &= \frac{1}{\text{Dist}_i} \\ &= \frac{1}{\sqrt{X_i^2 + Y_i^2}}, \end{aligned} \tag{3}$$

Step 4 **(Repairing infeasible solutions).** A repair approach [111] will be used to deal with the constraint violation at each generation and before the solutions $S_i \forall i = 1, \ldots, N$ are assessed, which will segregate and repair any infeasible solution in the population. The proposed algorithm′s repairing procedure provides a new feasible solution y instead of an infeasible one q on a segment defined by two points: an initial feasible reference point R and any infeasible solution q. A user-specified parameter $\mu \in [0, 1]$ can be used to expand this segment equally on both sides. Therefore, the new feasible solution is produced as:

$$y_1 = \gamma q + (1 - \gamma) R. \tag{4}$$

If y_1 is infeasible, the feasible individual is produced by:

$$y_2 = \gamma R + (1 - \gamma) q. \tag{5}$$

where $\gamma = (1 + 2\mu)\delta - \mu$ and $\delta \in [0, 1]$ is a random number. Figure 2 depicts a schematic representation of a probable sample location for the produced solution.

Step 5 **(Evaluation).** The judgment function of smell concentration (fitness function) of the corresponding position is determined by substituting S_i in the objective function as:

$$\text{Smell}_i = \text{function}(S_i). \tag{6}$$

Step 6 **(Determine the best).** Calculate the minimal concentration of smell and its corresponding location as follows:

$$[\text{best Smell}, \text{best Index}] = \min(\text{Smell}) \quad \forall i. \tag{7}$$

Step 7**(Update swarm center location).** The swarm center position is replaced with the minimum smell location:

$$\begin{aligned} \text{Smell best} &= \text{best Smell}, \\ X_{\text{axis}} &= X(\text{best Index}), \\ Y_{\text{axis}} &= Y(\text{best Index}). \end{aligned} \tag{8}$$

Step 8. Do optimization by repeating Steps 2–6 to determine if the current smell concentration is better

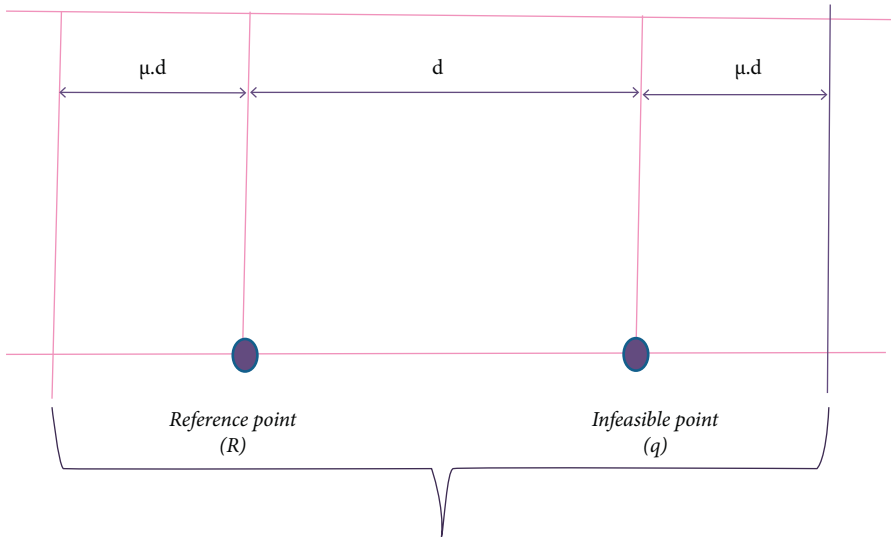

Figure 2: Probable sample location for the produced solution by repairing infeasible solutions.

than the previous smell concentration; if so, go to Step 7. Otherwise, proceed to Step 2 and iterate again.

Step 9. If the stopping criteria are met, the proposed algorithm is stopped. Otherwise, do optimization, and repeat Steps 2 to 8.

For either of the following two conditions, the proposed algorithm is stopped:

(i) Reaching the full predetermined number of generations $T_{\max}$.

(ii) When the individuals of the population converge, i.e., when solutions in the population are identical.

3.3.2. Phase II: Chaotic Local Search. Optimization by using the above-formulated FFA yields an approximate solution $x^* = (x_1^*, x_2^*, \ldots, x_n^*)$. To discover the optimal solution, chaotic local search (CLS) can disturb and explore the local region of the solution x^*. The following is a more extensive description of CLS:

Step 1 **(Determine the boundary range of CLS).** The range of CLS $[a_d, b_d]$, $d = 1, 2, \ldots, n$ for x^* is determined by $x_d^* - \varepsilon < a_d, x_d^* + \varepsilon > b_d \quad \forall d = 1, \ldots, n$, where ε is a specified radius of CLS and set $m = 1$, where m is the CLS iterations $m = 1, 2, \ldots, M$.

Step 2. **Create chaotic variables:** A chaotic number σ^m is generated by the logistic map as:

$$\sigma^m = 4 \times \sigma^{m-1} \times \left(1 - \sigma^{m-1}\right), \sigma^0 \in (0, 1), \sigma^0 \notin \{0, 0.25, 0.5, 0.75, 1\}. \tag{9}$$

According to the findings in [94], the logistic map increases the quality of solutions and delivers the best performance. Therefore, it was employed in this study.

Step 3. **Generate a new solution:** By using the chaos variable σ^m and the variance range $[a_d, b_d]$, the new solution is generated as:

$$\left(x_d^*\right)^m = a_d + \left(b_d - a_d\right)\sigma^m \quad \forall d = 1, \ldots, n. \tag{10}$$

Step 4. **Check feasibility:** If the new solution $(x^*)^m$ is feasible, update the approximate solution x^* as follows: if $f(x^*)^m < f(x^*)$, then set $x^* = (x^*)^m$, otherwise, set $m = m + 1$ and go to Step 2.

Step 5. Stopping CLS: If $m = M$, stop the CLS and put out x^* as the optimal solution. Otherwise, go to Step 2. Figure 3 depicts the suggested algorithm's flowchart.

4. Computational Experiment

In this section, CFFA is evaluated by the set of CEC'2005 special sessions on real parameter optimization to evaluate the performance of the proposed method for global optimization [112]. In addition, the CFFA′s applicability in real-world applications is evaluated in this section using three constrained engineering design problems from the most current test suite CEC'2020 [113]. These problems are common challenges that have been explored by other researchers. The suggested approach is compared to current meta-heuristic algorithms such as simulated annealing (SA) [114], continuous genetic algorithm (CGA) [115], grey wolf optimizer (GWO) [116], moth-flame optimization (MFO) [19], whale optimization algorithm (WOA) [117], Lévy-flight moth-flame optimization (LMFO) [118], water-cycle moth-flame optimization (WCMFO) [119], chimp optimization algorithm (ChOA) [31], arithmetic

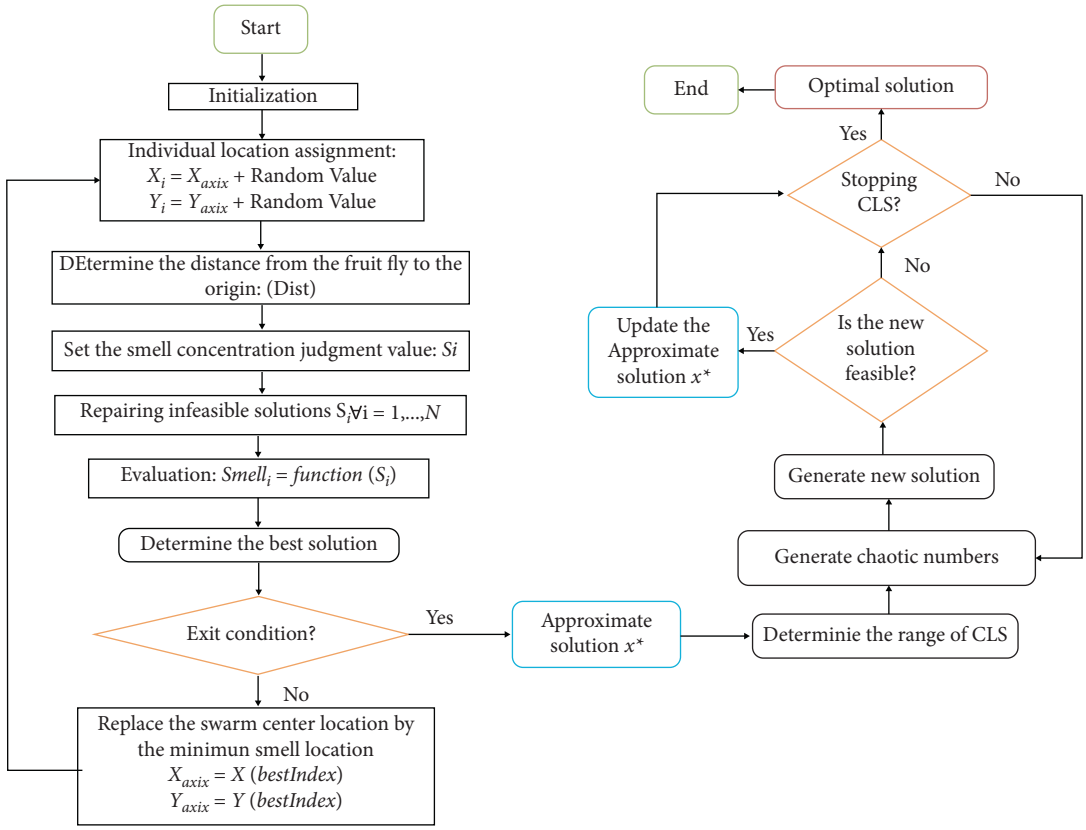

Figure 3: The suggested algorithm′s flowchart.

optimization algorithm (AOA) [120], sine-cosine moth-flame optimization (SMFO) [121], and improved moth-flame optimization (IMFO) [122].

The suggested method was coded in MATLAB (R2012b) and tested on a PC with an Intel(R) Core(TM) i7-6600U processor running at 2.60 GHz, 16 GB of RAM, and a Windows 10 operating system. Table 2 shows the parameter settings of comparing algorithms as they were in their original articles. The algorithms were running 20 times with the population size (N) 20 and maximum iterations $T_{\max} = (D \times 10^4)/N$ to ensure a fair comparison. The nonparametric Friedman test, on the other hand, is used to analyze the results statistically. Also, the Wilcoxon signed-rank test is employed to ensure that valid comparisons between all algorithms are made.

4.1. Computational Experiment for CEC'2005. In this part, 25 unconstrained test problems of dimension 10 from the CEC'2005 special session on real parameter optimization are used to evaluate CFFA. The following are the specifics of these functions:

(i) 5 unimodal functions:

F_1: Shifted sphere, F_2: Shifted Schwefel's, F_3: Shifted rotated high conditioned elliptic, F_4: Shifted Schwefel's with noise in fitness, and F_5: Schwefel's with global optimum on bounds.

(ii) 20 multimodal functions:

7 basic functions ⟶ F_6: Shifted Rosenbrock's, F_7: Shifted rotated Griewank without bounds, F_8: Shifted rotated Ackley's with global optimum on bounds, F_9: Shifted Rastrigin's, F_{10}: Shifted rotated Rastrigin's, F_{11}: Shifted rotated Weierstrass, and F_{12}: Schwefel's.

2 expanded functions ⟶ F_{13}: Expanded extended Griewank's plus Rosenbrock's (F_8F_2) and F_{14}: Shifted rotated expanded Scaffers F_6.

11 hybrid functions. Each one (F_{15} to F_{25}) is created by combining ten of the fourteen preceding functions (different in each case).

All functions are displaced to guarantee that their optimum is never discovered in the search space′s center. Furthermore, the optima cannot be identified inside the initialization range in two functions, and the search scope is not limited.

These test functions are solved by PSO [123], IPOP-CMA-ES [124], CHC [125], SSGA [126], SS-BLX [127], SS-Arit [128], DE-Bin [129], DE-Exp [129], SaDE [130], and the proposed algorithm CFFA. For each test function, all of the algorithms were performed 50 times. Each run ends when the obtained error is less than 10^{-8} or at the maximum number of evaluations (10^{-5}), whichever comes first. Table 3 presents a comparison of the average error achieved by CFFA and 9 continuous optimization techniques. Table 3 confirms that, on average, CFFA produces better solutions than all nine continuous optimization techniques.

Table 2: The CFFA and other competing algorithms′ parameter settings.

Parameter Settings for Algorithms	
SA	$T_0 = 10$.
CGA	$IPMut = 0.9$, $PX\text{cross} = 0.5$.
GWO	The parameter a is linearly decreased from 2 to 0.
MFO	$b = 1$, a is decreased linearly from −1 to −2.
WOA	α variable decreases linearly from 2 to 0, $b = 1$.
LMFO	$\beta = 1.5$, μ and v are normal distributions, Γ is the gamma function
WCMFO	The number of rivers and sea = 4.
ChOA	f decreases linearly from 2 to 0.
AOA	$\mu = 0.5$, $\alpha = 5$.
SMFO	r_4 = random number between interval (0, 1).
I-MFO	$\delta_1 = 2.02$, $\delta_2 = 1.08$, NF = random number between 1 and D.
CFFA	The specified radius ε is 0.1, $\sigma^0 = 0.001$, and $M = 100$

Table 3: The average error of the 25 CEC'2005 benchmark functions as determined by CFFA and comparing algorithms.

Function	PSO	IPOP-CMA-ES	CHC	SSGA	SS-BLX	SS-Arit	DE-Bin	DE-Exp	SaDE	CFFA
F_1	1.234E-4	0	2.464	8.420E-9	34.02	1.064	7.716E-9	8.260E-9	8.416E-9	0
F_2	0.02595	0	0.0118	8.719E-5	1.730	5.282	8.342E-9	8.181E-9	8.208E-9	0
F_3	51740	0	269900	79480	184400	253500	42.33	99.35	6560	20.8036
F_4	2.488	2932	91.9	2.585E-3	6.228	5.755	7.686E-9	8.350E-9	8.087E-9	0
F_5	409.5	8.104E-10	264.1	134.3	2.185	14.43	8.608E-9	8.514E-9	8.640E-9	2.600E-5
F_6	731	0	1416000	6.171	114.5	494.5	7.956E-9	8.391E-9	0.01612	0.635
F_7	26.78	1267	1269	1271	1966	1908	1266	1265	1263	4.831
F_8	20.43	20.01	20.34	20.37	20.35	20.36	20.33	20.38	20.32	14.54
F_9	14.38	28.41	5.886	7.286E-9	4.195	5.960	4.546	8.151E-9	8.330E-9	0.000
F_{10}	14.04	23.27	7.123	17.12	12.39	21.79	12.28	11.18	15.48	4.541
F_{11}	5.590	1.343	1.599	3.255	2.929	2.858	2.434	2.067	6.796	3.094
F_{12}	636.2	212.7	706.2	279.4	150.6	241.1	106.1	63.09	56.34	5.732
F_{13}	1.503	1.134	82.97	67.13	32.45	54.79	1.573	64.03	70.70	1.052
F_{14}	3.304	3.775	2.073	2.264	2.796	2.970	3.073	3.158	3.415	2.501
F_{15}	339.8	193.4	275.1	292	113.6	128.8	372.2	294	84.23	0
F_{16}	133.3	117	97.29	105.3	104.1	113.4	111.7	112.5	122.7	83.85
F_{17}	149.7	338.9	104.5	118.5	118.3	127.9	142.1	131.2	138.7	107.3
F_{18}	851.2	557	879.9	806.3	766.8	657.8	509.7	448.2	532	479.2
F_{19}	849.7	529.2	879.8	889.9	755.5	701	501.2	434.1	519.5	458.1
F_{20}	850.9	526.4	896	889.3	746.3	641.1	492.8	418.8	476.7	335.1
F_{21}	913.8	442	815.8	852.2	485.1	500.5	524	542	514	394.5
F_{22}	807.1	764.7	774.2	751.9	682.8	694.1	771.5	772	765.5	632.7
F_{23}	1028	853.9	1075	1004	574	582.8	633.7	582.4	650.9	594.7
F_{24}	412	610.1	295900	236	251.3	201.1	206	202	200	210.5
F_{25}	509.9	1818	1764	1747	1794	1804	1744	1742	1738	274.3

4.1.1. The Nonparametric Friedman Test for CEC′2005 Results. The Friedman test is used to statistically rank the significance of algorithms [131]. Table 4 summarizes the outcomes obtained by this test. According to this statistical analysis, the CFFA ranks top, and because the obtained P value is less than 0.05 ($\alpha = 0.000$), there are substantial variations in the performances of the CFFA and the other algorithms tested. Figure 4 includes the chart that depicts the ranking of the CFFA and competitor algorithms. The smallest bar on the graph represents the best algorithm, while the largest represents the worst. The chart reveals that the CFFA obtained the shortest bar with a mean rank equal to 2.12, while PSO obtained the largest bar with a mean rank equal to 7.76. As a result, the chart reveals that the CFFA beats other algorithms by obtaining the first rank (shortest bar).

4.1.2. The Nonparametric Wilcoxon Signed-Rank Test for CEC'2005 Results. To demonstrate the substantial differences between the CFFA and the other algorithms, the Wilcoxon signed-rank test is performed [132]. The Wilcoxon signed-rank test results are shown in Table 5. $R+$ is the sum of positive ranks, whereas R− is the sum of negative ranks. Table 5 shows that CFFA beats other algorithms by achieving $R+$ values larger than R− values in all comparisons. As a consequence, we may conclude that the suggested CFFA is a significant algorithm that outperforms the others.

4.2. Computational Experiment for Engineering Design Problems. The proposed method and rival algorithms compete in this evaluation to solve three different problems: a gas transmission compressor design problem, a three-bar

Table 4: Friedman test results for the 25 CEC′2005 benchmark functions.

Test Statistics	
N	25
Chi-square	66.126
df	9
Asymp. Sig.	0.000
Ranks	
Algorithm	Mean rank
PSO	7.76
IPOP-CMA-ES	5.36
CHC	7.20
SSGA	6.60
SS-BLX	5.80
SS-Arit	6.40
DE-Bin	4.60
DE-Exp	4.28
SaDE	4.88
CFFA	2.12

truss design problem, and a tension/compression spring design problem.

(1) P_1: Design of gas transmission compressor problem. The basic purpose of the gas transmission compressor design challenge is to minimize the objective function utilizing four design variables which are length between compressor stations $L = x_1$, compression ratio that denotes the inlet pressure to the compressor $r = x_2$, and inner diameter of the pipe $D = x_3$. Figure 5 and (11) depict and formulate this problem.

$$\begin{aligned} &\text{Min } f(x) = 8.61 \times 10^5 x_1^{0.5} x_2 x_3^{-2/3} x_4^{-0.5} + 3.69 \times 10^4 x_3 + \frac{7.72 \times 10^8 x_2^{0.219}}{x_1} - \frac{765.43 \times 10^6}{x_1}, \\ &\text{Subject to: } x_4 x_2^{-2} + x_2^{-2} - 1 \le 0, 20 \le x_1 \le 50,\ 1 \le x_2 \le 10, 20 \le x_3 \le 45, 0.1 \le x_4 \le 60. \end{aligned} \tag{11}$$

(2) P_2: Three-bar truss problem. The three-bar truss design is an engineering optimization problem to evaluate the optimal cross-sectional areas $A_1 = A_3 = x_1$ and $A_2 = x_2$ such that the volume of the statically loaded truss structure $f(x)$ is minimized while stress constraints σ are taken into consideration. The mathematical model of this problem is formulated using three constraints and two variables. Figure 6 and (12) show the formulation and schematic of this problem.

$$\begin{aligned} &\text{Min } f(x) = H\left(x_2 + 2\sqrt{2}\, x_1\right), \\ &\text{Subject to: } \frac{x_2}{2x_1x_2 + \sqrt{2}x_1^2} P - \sigma \le 0, \frac{x_2 + \sqrt{2}x_1}{2x_1x_2 + \sqrt{2}x_1^2} P - \sigma \le 0, \frac{1}{x_1 + \sqrt{2}x_2} P - \sigma \le 0, \\ &H = 100cm, P = \frac{2KN}{cm^2}, \sigma = \frac{2KN}{cm^2}, 0 \le x_1, x_2 \le 1. \end{aligned} \tag{12}$$

(3) P_3: Tension/compression spring design problem. The tension/compression spring design challenge′s purpose is to lower the tension/compression spring′s weight by considering three variables and four constraints. Wire diameter ($d = x_1$), mean coil diameter ($D = x_2$), and the number of active coils ($N = x_3$) are the variables (as indicated in Figure 7). (13) describes the problem and its constraints.

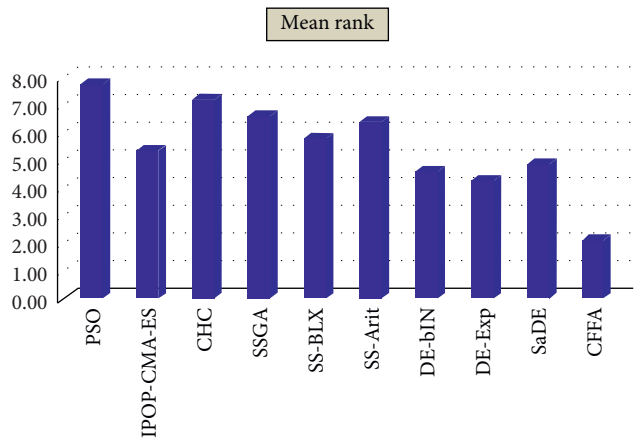

Figure 4: The Friedman test′s mean -ranking on CFFA and its 9 competitors.

Table 5: The results of Wilcoxon′s signed-rank test for the 25 CEC′2005 benchmark functions.

Test Statistics				Ranks		
				N	Mean Rank	Sum of Ranks
SaDE – CFFA		R^-	3^a	7.00	21.00	a. SaDE < CFFA
Z	-3.807^{ab}	**R^+**	22^b	13.82	304.00	b. SaDE > CFFA
Asymp. Sig. (2-Tailed)	0.000	**Ties**	0^c			c. SaDE = CFFA
ab. Based on negative ranks.		**Total**	25			
DE-Exp - CFFA		**R^-**	7^d	10.29	72.00	d. DE-Exp < CFFA
Z	-2.435^{ab}	**R^+**	18^e	14.06	253.00	e. DE-Exp > CFFA
Asymp. Sig. (2-Tailed)	0.015	**Ties**	0^f			f. DE-Exp = CFFA
ab. Based on negative ranks.		**Total**	25			
DE-Bin - CFFA		**R^-**	4^g	7.00	28.00	g. DE-Bin < CFFA
Z	-3.619^{ab}	**R^+**	21^h	14.14		h. DE-Bin > CFFA
Asymp. Sig. (2-Tailed)	0.000	**Ties**	0^i			i. DE-Bin = CFFA
ab. Based on negative ranks.		**Total**	25			
SS-Arit - CFFA		**R^-**	3^j	6.00	18.00	j. SS-Arit < CFFA
Z	-3.888^{ab}	**R^+**	22^k	13.95	307.00	k. SS-Arit > CFFA
Asymp. Sig. (2-Tailed)	0.000	**Ties**	0^l			l. SS-Arit = CFFA
ab. Based on negative ranks.		**Total**	25			
SS-BLX - CFFA		**R^-**	2^m	6.00	12.00	m. SS-BLX < CFFA
Z	-4.049^{ab}	**R^+**	23^n	13.61	313.00	n. SS-BLX > CFFA
Asymp. Sig. (2-Tailed)	0.000	**Ties**	0^0			o. SS-BLX = CFFA
ab. Based on negative ranks.		**Total**	25			
SSGA - CFFA		**R^-**	1^p	6.00	6.00	p. SSGA < CFFA
Z	-4.211^{ab}	**R^+**	24^q	13.29	319.00	q. SSGA > CFFA
Asymp. Sig. (2-Tailed)	0.000	**Ties**	0^r			r. SSGA = CFFA
ab. Based on negative ranks.		**Total**	25			
CHC - CFFA		**R^-**	3^s	3.67	11.00	s. CHC < CFFA
Z	-4.076^{ab}	**R^+**	22^t	14.27	314.00	t. CHC > CFFA
Asymp. Sig. (2-Tailed)	0.000	**Ties**	0^u			u. CHC = CFFA
ab. Based on negative ranks.		**Total**	25			
IPOP-CMA-ES - CFFA		**R^-**	4^v	4.25	17.00	v. IPOP-CMA-ES < CFFA
Z	-3.680^{ab}	**R^+**	19^w	13.63	259.00	w. IPOP-CMA-ES > CFFA
Asymp. Sig. (2-Tailed)	0.000	**Ties**	2^x			x. IPOP-CMA-ES = CFFA
ab. Based on negative ranks.		**Total**	25			
PSO - CFFA		**R^-**	0^y	0.00	0.00	y. PSO < CFFA
Z	-4.372^{ab}	**R^+**	25^z	13.00	325.00	z. PSO > CFFA
Asymp. Sig. (2-Tailed)	0.000	**Ties**	0^{aa}			aa. PSO = CFFA
ab. Based on negative ranks.		**Total**	25			

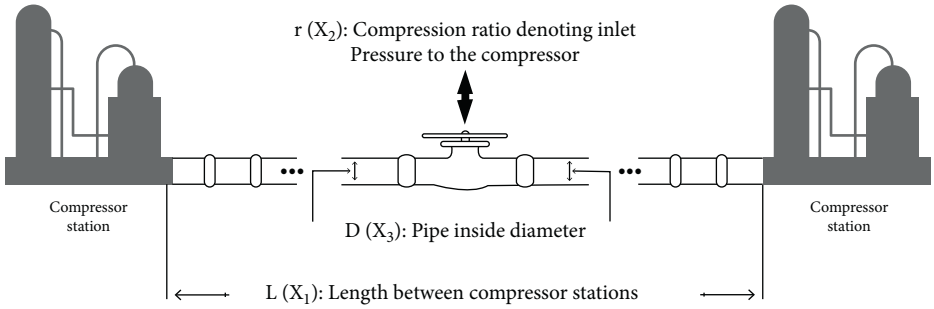

Figure 5: Gas transmission compressor problem design.

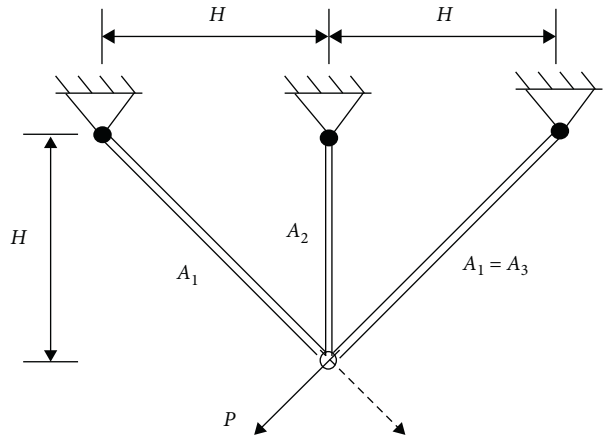

Figure 6: Three-bar truss problem design.

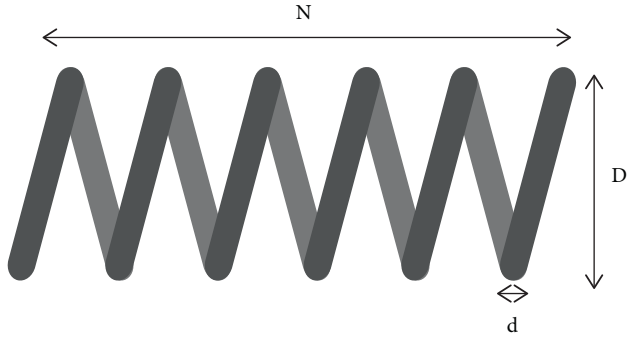

Figure 7: Design of tension/compression spring problem.

$$\text{Subject to: } 1-\frac{x_2^3x_3}{71785x_1^4}\le 0\,\frac{4x_2^2-x_1x_2}{12566\left(x_1^3x_2-x_1^4\right)}+\frac{1}{5108x_1^2}-1\le 01-\frac{140.45x_1}{x_2^2x_3}\le 0,\frac{x_1+x_2}{1.5}-1\le 0, \tag{13}$$

$$0.05\le x_1\le 2, 0.25\le x_2\le 1.3, 2\le x_3\le 15.$$

4.2.1. Engineering Design Problems Results. The suggested CFFA and comparative algorithms are compared. The results of these experiments are summarized in Table 6, which demonstrates that the CFFA technique outperforms other algorithms in obtaining a good approximation to the best values for low-weight variables.

Figures 8–10 also illustrate the convergence curves of the best function values obtained by CFFA before and after CLS for the gas transmission compressor design problem, the three-bar truss design problem, and the tension/compression spring design problem, respectively. Figures 8–10 show

Table 6: Results of the engineering design problems.

Algorithms	Gas transmission compressor: $\mathbf{T_{max}} = 2000$					Three-bar truss problem: $\mathbf{T_{max}} = 1000$			Tension/compression spring: $\mathbf{T_{max}} = 1500$			
	Optimal values				Optimal weight	Optimal values		Optimal weight	Optimal values			Optimal weight
	$\mathbf{x}_1$	$\mathbf{x}_2$	$\mathbf{x}_3$	$\mathbf{x}_4$		$\mathbf{x}_1$	$\mathbf{x}_2$		d	D	N	
SA	46.76	1.62	25.79	0.55	4390311	0.768630	0.474232	264.82456	0.075935	0.993094	3.879891	0.033670
CGA	49.97	20.01	31.47	49.83	17350230	0.792428	0.397752	263.90770	0.071031	1.019975	1.726076	0.019749
GWO	20.00	7.81	20.00	60.00	2964974	0.787771	0.410872	263.89619	0.051231	0.345699	11.970135	0.012676
MFO	50.00	1.18	24.57	0.39	2964902	0.789186	0.406806	263.89603	0.053064	0.390718	9.542437	0.012699
WOA	50.00	1.18	24.86	0.39	2965002	0.787713	0.410977	263.89653	0.050451	0.327675	13.219341	0.012694
LMFO	49.46	1.18	24.64	0.39	2965456	0.791713	0.399909	263.92114	0.050000	0.317154	14.107156	0.012771
WCMFO	50.00	1.18	24.61	0.39	2964897	0.788472	0.408822	263.89589	0.051509	0.352411	11.545969	0.012666
ChOA	50.00	1.19	24.24	0.41	2966828	0.787802	0.410724	263.89653	0.051069	0.341746	12.251078	0.012702
AOA	50.00	1.23	20.00	0.51	3014615	0.792789	0.396906	263.92526	0.050000	0.310475	15.000000	0.013195
SMFO	23.66	1.09	23.66	0.19	3052254	0.792044	0.398859	263.90973	0.050000	0.314692	14.696505	0.013136
I-MFO	50.00	1.18	24.60	0.39	2964896	0.788792	0.407919	263.89585	0.051710	0.357217	11.259785	0.012665
FFA	49.8660	1.1832	23.5344	0.3999	**2966272**	0.779348	0.435289	**263.96190**	0.0538558	0.405526	10.106720	**0.014240**
CFFA	49.9999	1.1782	24.5936	0.3882	**2964895**	0.788661	0.408286	**263.89584**	0.051813	0.359726	11.114753	**0.012665**

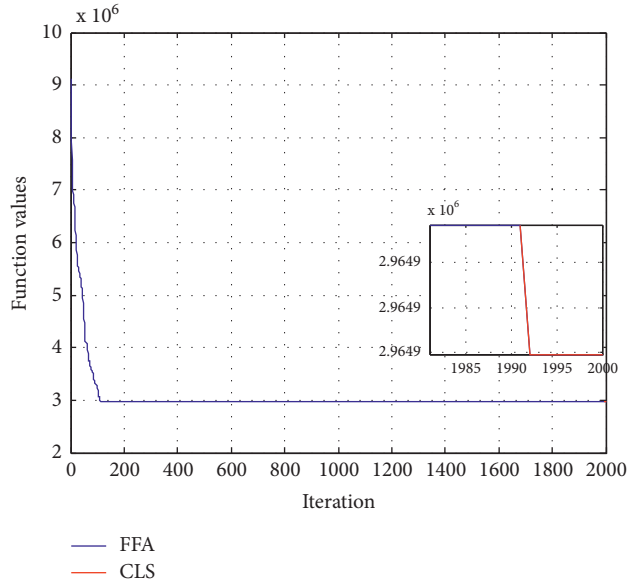

Figure 8: CFFA′s convergence curve of gas transmission compressor design problem before and after CLS.

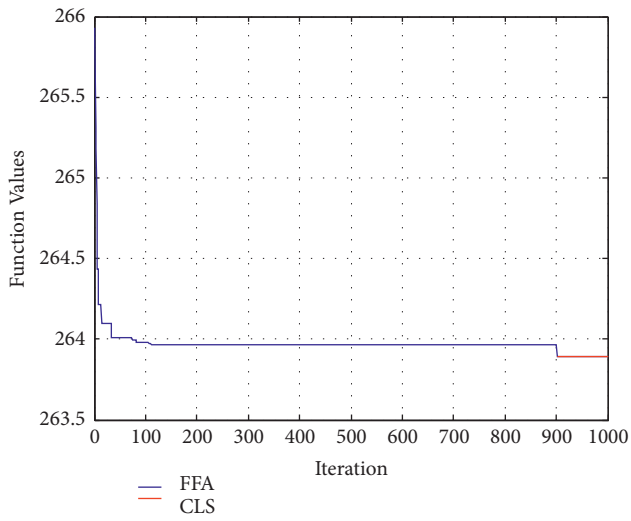

Figure 9: CFFA′s convergence curve of the three-bar truss design problem before and after CLS.

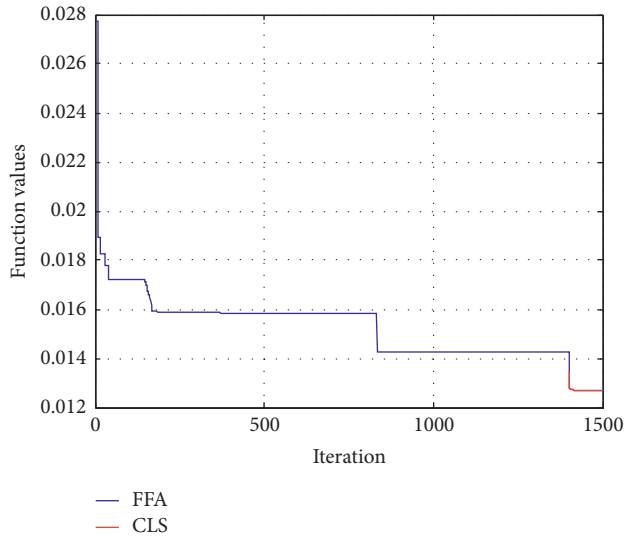

Figure 10: CFFA's convergence curve of tension/compression spring design problem before and after CLS.

how the basic FFA (before CLS/blue line) stuck in the local minimum for a long time. Figures, on the other hand, show how CLS disturbs and explore the local region of the approximate solution obtained by FFA and how it accelerates convergence, enhances solution quality, and finds the optimal solution (after CLS/red line). So, we can conclude that the convergence curves showed the importance of the introduction of the chaotic local search (CLS) on fruit fly algorithm (FFA) which improves the FFA results of FFA and help it to exit from the local optimal solution (blue line) and access to the globally optimal solution (red line).

(1) The nonparametric (Friedman & Wilcoxon signed-rank) tests for engineering design problems results. The findings of the Friedman test for engineering design problems are displayed in Table 7. The CFFA ranks top in this statistical study, and because the calculated p -value is less than 0.05 ($\alpha = 0.001$), there are significant differences between the CFFA and the other comparing algorithms. Figure 11 also shows a chart that shows the CFFA and rival algorithms' rankings. As previously stated, the best algorithm is represented by the shortest bar on the graph, while the poorest is represented by the biggest bar. The CFFA has the smallest bar, with a mean rank of 1.17, while SA has the largest bar, with a mean rank of 11.67. The basic FFA, on the other hand, obtains the 10^{th} rank among all algorithms. As a consequence, the chart shows that the CFFA outperforms other algorithms by having the first rank (shortest bar).

The Wilcoxon signed-rank test findings for engineering design problems, on the other hand, are presented in Table 8. In all comparisons, CFFA outperforms other algorithms, as shown in Table 8, by reaching R^+ values greater than R^- values. We can see that the statistical results of engineering design problems do not differ from the results of problems CEC'2005, as the presented method CFFA outperformed the rest of the other algorithms. As a consequence, we may conclude that the suggested CEGA is a significant algorithm that outperforms the others in the computational experiment.

Table 7: Friedman test′ results for the engineering design problems.

Test Statistics			
N		3	
Chi-square		31.25	
df		11	
Asymp. Sig.		**0.001**	
Ranks			
Method	**Mean rank**	**Method**	**Mean rank**
SA	12.67	**CGA**	11.00
GWO	4.67	**MFO**	4.67
WOA	5.83	**LMFO**	8.33
WCMFO	3.00	**ChOA**	7.50
AOA	10.33	**SMFO**	9.67
I-MFO	1.83	**FFA**	10.33
CFFA	1.17		

4.3. Discussions. Table 3 displayed the average error for all algorithms for the CEC′2005 benchmark functions, whereas Table 6 showed the best solution for all algorithms for the engineering design issues. Tables 3 and 6 indicated that CFFA beat other algorithms in terms of producing better results. Statistically, the Fridman test, as shown in Tables 4 and 7, demonstrated that the Asymp. Sig. (P value) is less than 0.05, suggesting that there are differences in the results obtained by all algorithms. Furthermore, as demonstrated in Tables 4 and 7 and Figures 4 and 11, CFFA beat the other algorithms by obtaining the lower mean rank. Tables 5 and 8, on the other hand, presented the Wilcoxon signed-rank test findings to investigate the major differences between the comparison methods. They proved that CFFA outperformed other algorithms by achieving more positive rank values (R^+) than negative rank values (R^-) in each of CEC'2005 benchmark functions and engineering design problems. The convergence curves also showed the importance of the proposed method, as the introduction of the chaotic local search (CLS) on fruit fly algorithm (FFA) proved its importance and the ability of the CLS to improve the results of

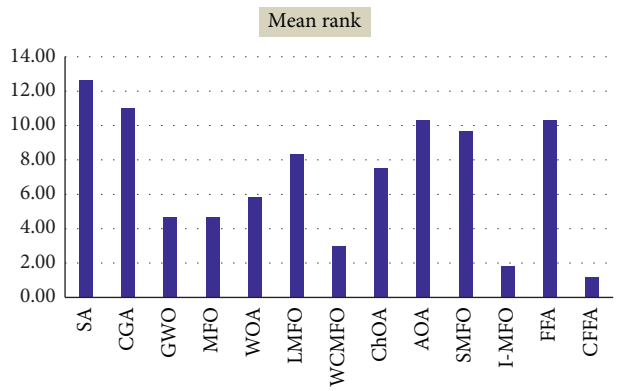

Figure 11: The Friedman test's mean-ranking on CFFA and its 11 competitors.

Table 8: The results of Wilcoxon's signed-rank test for the engineering design problems.

Test statistics				Ranks		
				N	Mean rank	Sum of ranks
SA - CFFA		R^-	0^a	0.00	0.00	a. SA < CFFA
Z	-1.604^{ak}	**R^+**	3^b	2.00	6.00	b. SA > CFFA
Asymp. Sig. (2-Tailed)	0.109	**Ties**	0^c			c. SA = CFFA
ak. Based on negative ranks		**Total**	3			
CGA - CFFA		**R^-**	0^d	0.00	0.00	d. CGA < CFFA
Z	-1.604^{ak}	**R^+**	3^e	2.00	6.00	e. CGA > CFFA
Asymp. Sig. (2-Tailed)	0.109	**Ties**	0^f			f. CGA = CFFA
ak. Based on negative ranks		**Total**	3			
GWO - CFFA		**R^-**	0^g	0.00	0.00	g. GWO < CFFA
Z	-1.604^{ak}	**R^+**	3^h	2.00	6.00	h. GWO > CFFA
Asymp. Sig. (2-Tailed)	0.109	**Ties**	0^i			i. GWO = CFFA
ak. Based on negative ranks		**Total**	3			
MFO - CFFA		**R^-**	0^j	0.00	0.00	j. MFO < CFFA
Z	-1.604^{ak}	**R^+**	3^k	2.00		6.00
Asymp. Sig. (2-Tailed)	0.109	**Ties**	0^l			l. MFO = CFFA
ak. Based on negative ranks		**Total**	3			
WOA - CFFA		**R^-**	0^m	0.00	0.00	m. WOA < CFFA
Z	-1.604^{ak}	**R^+**	3^n	2.00	6.00	n. WOA > CFFA
Asymp. Sig. (2-Tailed)	0.109	**Ties**	0^o			o. WOA = CFFA
ak. Based on negative ranks		**Total**	3			
LMFO - CFFA		**R^-**	0^p	0.00	0.00	p. LMFO < CFFA
Z	-1.604^{ak}	**R^+**	3^q	2.00	6.00	q. LMFO > CFFA
Asymp. Sig. (2-Tailed)	0.109	**Ties**	0^r			r. LMFO = CFFA
ak. Based on negative ranks		**Total**	3			
WCMFO - CFFA		**R^-**	0^s	0.00	0.00	s. WCMFO < CFFA
Z	-1.604^{ak}	**R^+**	3^t	2.00	6.00	t. WCMFO > CFFA
Asymp. Sig. (2-Tailed)	0.109	**Ties**	0^u			u. WCMFO = CFFA
ak. Based on negative ranks		**Total**	3			
ChOA - CFFA		**R^-**	0^v	0.00	0.00	v. ChOA < CFFA
Z	-1.604^{ak}	**R^+**	3^w	2.00	6.00	w. ChOA > CFFA
Asymp. Sig. (2-Tailed)		0.109	**Ties**			x. ChOA = CFFA
ak. Based on negative ranks		**Total**	3			
AOA - CFFA		**R^-**	0^y	0.00	0.00	y. AOA < CFFA
Z	-1.604^{ak}	**R^+**	3^z	2.00	6.00	z. AOA > CFFA
Asymp. Sig. (2-Tailed)	0.109	**Ties**	0^{aa}			aa. AOA = CFFA
ak. Based on negative ranks		**Total**	3			
SMFO - CFFA		**R^-**	0^{ab}	0.00	0.00	ab. SMFO < CFFA
Z	-1.604^{ak}	**R^+**	3^{ac}	2.00	6.00	ac. SMFO > CFFA
Asymp. Sig. (2-Tailed)	0.109	**Ties**	0^{ad}			ad. SMFO = CFFA
ak. Based on negative ranks		**Total**	3			

Table 8: Continued.

Test statistics		Ranks				
				N	Mean rank	Sum of ranks
I-MFO - CFFA		**R⁻**	0[ae]	0.00	0.00	ae. I-MFO < CFFA
Z	−1.342[ak]	**R⁺**	2[af]	1.50	3.00	af. I-MFO > CFFA
Asymp. Sig. (2-Tailed)	0.180	**Ties**	1[ag]			ag. I-MFO = CFFA
ak. Based on negative ranks		**Total**	3			
FFA - CFFA		**R⁻**	0[ah]	0.00	0.00	ah. FFA < CFFA
Z	−1.604[ak]	**R⁺**	3[ai]	1.50	3.00	ai. FFA > CFFA
Asymp. Sig. (2-Tailed)	0.109	**Ties**	0[aj]			aj. FFA = CFFA
ak. Based on negative ranks		**Total**	3			

FFA and help it to exit from the local optimal solution (blue line) and access to the globally optimal solution (red line).

From the above, CFFA showed several advantages, which we mention as follows:

(i) CFFA is a versatile and adaptable strategy for solving a broad variety of optimization issues.

(ii) Due to the combination of the advantages of the CLS and FFA, CFFA has a good solution quality.

(iii) Unlike traditional approaches, CFFA searches across a population of points to find the globally optimal solution.

(iv) Because CFFA only employs objective function information, it can handle any realistic optimization issue, including noncontinues, nonsmooth, and nondifferentiable functions.

(v) Computational trials have demonstrated the superiority of CFFA above those published in the literature where it outperforms other comparison approaches substantially.

(vi) The importance of the CFFA findings was demonstrated using Wilcoxon and Friedman tests.

(vii) Finally, the results of the engineering design problems show that the proposed CFFA is suitable for addressing real-world issues such as problems of cost-effective load transfer, resource allocation, wind farm turbine optimization, unit commitment, and real-time applications.

Finally, without prejudice, the proposed technique CFFA, like previous meta-heuristics algorithms, has the potential drawback of not ensuring an increase in computing speed or accuracy when addressing any optimization problem. Because meta-heuristics methods are random approaches, the CFFA's computational efficacy and solution quality are dependent on the problem's nature and complexity.

5. Conclusion

A chaotic fruit fly algorithm (CFFA) to solve engineering design problems (EDPs) was proposed in this paper. The fruit fly algorithm (FFA), recognized for its resilience and efficacy in addressing optimization problems, was merged with the chaotic local search (CLS) method, which is known for its ability to identify the global optimal solution. CFFA was used in two stages. In the first, FFA was used to get an approximate solution. The optimal solution was then found using chaotic local search (CLS) in the second phase. The proposed approach was tested utilizing a set of CEC'2005 special sessions on actual parameter optimization as well as, three restricted engineering design problems from the most recent test suite, CEC'2020. The experimental outcomes demonstrated the superiority of the proposed technique to finding the global optimal solution and reveal that the suggested CFFA may be utilized to address real-world engineering problems. Furthermore, the convergence curves of the best function values obtained by CFFA before and after CLS showed how CLS disturbed and explored the local region of the approximate solution and how it was utilized to speed convergence, improve solution quality, and find the ideal solution. Finally, the statistical efficiency of the CFFA was investigated by the Friedman test and Wilcoxon signed-rank test, which revealed that the proposed CFFA outperformed other algorithms.

A multi-objective version of CFFA can be developed in future works to solve continuous multi-objective issues. Furthermore, adapting CFFA to a discrete version for handling discrete optimization challenges like the community discovery problem is a promising direction.

Data Availability

All data used to support the findings of this study are included in the article.

Conflicts of Interest

The authors declare that this article′s content has no conflicts of interest.

Acknowledgments

The authors extend their appreciation to the Deputyship for Research and Innovation, Ministry of Education in Saudi Arabia, for funding this research work through the project number (IF-PSAU-2021/01/18049).

References

[1] B.-B. Michael, *Nonlinear Optimization with Engineering Applications*, Springer Optimization and Its Applications, Springer-Verlag, Switzerland, 2008.

[2] M. A. El-Shorbagy, *Hybrid Particle Swarm Algorithm for Multi-Objective Optimization, Master of Engineering Thesis*, Menoufia Univ, Egypt, 2010.

[3] Z. Michalewicz, "Evolutionary computation techniques for nonlinear programming problems," *International Transactions in Operational Research*, vol. 1, no. 2, pp. 223–240, 1994.

[4] T. L. Ayyarao, N. S. S. RamaKrishna, R. M. Elavarasam et al., "War Strategy Optimization Algorithm: A New Effective Metaheuristic Algorithm for Global Optimization," *IEEE Access*, vol. 10, 2022.

[5] I. M. El-Desoky, M. A. El-Shorbagy, S. M. Nasr, Z. M. Hendawy, and A. A. Mousa, "A hybrid genetic algorithm for job shop scheduling problems," *Int. J. Adv. Eng. Technol. Comput. Sci*, vol. 3, no. no. 1, pp. 6–17, 2016.

[6] M. A. El-Shorbagy, A. Y. Ayoub, I. M. El-Desoky, A. A. Mousa, and A. A. Mousa, "A novel genetic algorithm based k-means algorithm for cluster analysis," in *The International Conference on Advanced Machine Learning Technologies and Applications (AMLTA2018)*, pp. 92–101, Springer, Cham, NY, USA, 2018.

[7] R. Storn and K. Price, "Differential evolution-a simple and efficient heuristic for global optimization over continuous spaces," *Journal of Global Optimization*, vol. 11, no. 4, pp. 341–359, 1997.

[8] D. Simon, *Evolutionary Optimization Algorithms*, John Wiley & Sons, Hoboken, New Jersey, 2013.

[9] M. A. El-Shorbagy and A. E. Hassanien, "Particle swarm optimization from theory to applications," *International Journal of Rough Sets and Data Analysis*, vol. 5, no. 2, pp. 1–24, 2018.

[10] M. A. El-Shorbagy, "Weighted method based trust region-particle swarm optimization for multi-objective optimization," *American Journal of Applied Mathematics*, vol. 3, no. 3, p. 81, 2015.

[11] A. M. Abd Allah and M. A. El-Shorbagy, "Enhanced Particle Swarm Optimization Based Local Search for Reactive Power Compensation Problem," *Applied Mathematics*, vol. 3, 2012.

[12] M. Dorigo and T. Stutzle, *Ant Colony Optimization*, MIT Press, Cambridge, MA, 2004.

[13] W. T. Pan, *Fruit Fly Optimization Algorithm*, Tsang Hai publishing, Taibei, China, 2011.

[14] W. Zhao and L. Wang, "An effective bacterial foraging optimizer for global optimization," *Information Sciences*, vol. 329, pp. 719–735, 2016.

[15] M. Marinaki and Y. Marinakis, "A glowworm swarm optimization algorithm for the vehicle routing problem with stochastic demands," *Expert Systems with Applications*, vol. 46, pp. 145–163, 2016.

[16] H. Xu, X. Liu, and J. Su, "An improved grey wolf optimizer algorithm integrated with Cuckoo Search," in *Proceedings of the 2017 9th IEEE international conference on intelligent data acquisition and advanced computing systems: technology and applications (IDAACS)*, September 2017.

[17] F. S. Gharehchopogh and H. Gholizadeh, "A comprehensive survey: whale Optimization Algorithm and its applications," *Swarm and Evolutionary Computation*, vol. 48, pp. 1–24, 2019.

[18] M. Elsisy, D. Hammad, and M. El-Shorbagy, "Solving interval quadratic programming problems by using the numerical method and swarm algorithms," *Complexity*, vol. 2020, 11 pages, Article ID 6105952, 2020.

[19] S. Mirjalili, "Moth-flame optimization algorithm: a novel nature-inspired heuristic paradigm," *Knowledge-Based Systems*, vol. 89, pp. 228–249, 2015.

[20] S. Mirjalili, A. H. Gandomi, S. Z. Mirjalili, S. Saremi, H. Faris, and S. M. Mirjalili, "Salp Swarm Algorithm: a bio-inspired optimizer for engineering design problems," *Advances in Engineering Software*, vol. 114, pp. 163–191, 2017.

[21] M. A. El-Shorbagy and A. M. El-Refaey, "COVID-19: mathematical growth vs. precautionary measures in China, KSA, and the USA," *Informatics in Medicine Unlocked*, vol. 28, Article ID 100834, 2022.

[22] D. Karaboga and B. Basturk, "On the performance of artificial bee colony (ABC) algorithm," *Applied Soft Computing*, vol. 8, no. 1, pp. 687–697, 2008.

[23] X.-S. Yang, "A new metaheuristic bat-inspired algorithm," *Nature Inspired Cooperative Strategies for Optimization (NICSO 2010)*, vol. 284, pp. 65–74, 2010.

[24] Y. Zhou, X. Chen, and G. Zhou, "An improved monkey algorithm for a 0-1 knapsack problem," *Applied Soft Computing*, vol. 38, pp. 817–830, 2016.

[25] M. Shehab, A. T. Khader, M. Laouchedi, and O. A. Alomari, "Hybridizing cuckoo search algorithm with bat algorithm for global numerical optimization," *The Journal of Supercomputing*, vol. 75, no. 5, pp. 2395–2422, 2019.

[26] A. Kumar, R. K. Misra, D. Singh, S. Mishra, and S. Das, "The spherical search algorithm for bound-constrained global optimization problems," *Applied Soft Computing*, vol. 85, Article ID 105734, 2019.

[27] E. Cuevas, M. Cienfuegos, D. Zaldívar, and M. Pérez-Cisneros, "A swarm optimization algorithm inspired in the behavior of the social-spider," *Expert Systems with Applications*, vol. 40, no. 16, pp. 6374–6384, 2013.

[28] A. Faramarzi, M. Heidarinejad, S. Mirjalili, and A. H. Gandomi, "Marine predators algorithm: a nature-inspired metaheuristic," *Expert Systems with Applications*, vol. 152, p. 113377, 2020.

[29] A. Askarzadeh, "A novel metaheuristic method for solving constrained engineering optimization problems: crow search algorithm," *Computers & Structures*, vol. 169, pp. 1–12, 2016.

[30] A. L. a. Bolaji, M. A. Al-Betar, M. A. Awadallah, A. T. Khader, and L. M. Abualigah, "A comprehensive review: krill Herd algorithm (KH) and its applications," *Applied Soft Computing*, vol. 49, pp. 437–446, 2016.

[31] M. Khishe and M. R. Mosavi, "Chimp optimization algorithm," *Expert Systems with Applications*, vol. 149, Article ID 113338, 2020.

[32] M. Jain, V. Singh, and A. Rani, "A novel nature-inspired algorithm for optimization: squirrel search algorithm," *Swarm and Evolutionary Computation*, vol. 44, pp. 148–175, 2019.

[33] X.-S. Yang, "Flower pollination algorithm for global optimization," *Unconventional Computation and Natural Computation*, vol. 7445, pp. 240–249, 2012.

[34] W. Zhao, Z. Zhang, and L. Wang, "Manta ray foraging optimization: an effective bio-inspired optimizer for engineering applications," *Engineering Applications of Artificial Intelligence*, vol. 87, Article ID 103300, 2020.

[35] S. Shadravan, H. R. Naji, and V. K. Bardsiri, "The Sailfish Optimizer: a novel nature-inspired metaheuristic algorithm for solving constrained engineering optimization problems," *Engineering Applications of Artificial Intelligence*, vol. 80, pp. 20–34, 2019.

[36] G. Dhiman and V. Kumar, "Emperor penguin optimizer: a bio-inspired algorithm for engineering problems," *Knowledge-Based Systems*, vol. 159, pp. 20–50, 2018.

[37] G. Dhiman and V. Kumar, "Spotted hyena optimizer: a novel bio-inspired based metaheuristic technique for engineering

applications," *Advances in Engineering Software*, vol. 114, pp. 48–70, 2017.

[38] S. Li, H. Chen, M. Wang, A. A. Heidari, and S. Mirjalili, "Slime mould algorithm: a new method for stochastic optimization," *Future Generation Computer Systems*, vol. 111, pp. 300–323, 2020.

[39] J. Pierezan and L. Dos Santos Coelho, "Coyote optimization algorithm: a new metaheuristic for global optimization problems," in *Proceedings of the 2018 IEEE Congress on Evolutionary Computation (CEC)*, pp. 1–8, Rio de Janeiro, Brazil, July 2018.

[40] A. A. Heidari, S. Mirjalili, H. Faris, I. Aljarah, M. Mafarja, and H. Chen, "Harris hawks optimization: algorithm and applications," *Future Generation Computer Systems*, vol. 97, pp. 849–872, 2019.

[41] J. Tu, H. Chen, M. Wang, A. H. Gandomi, and Gandomi, "The colony predation algorithm," *Journal of Bionics Engineering*, vol. 18, no. 3, pp. 674–710, 2021.

[42] Y. Zhang and Z. Jin, "Group teaching optimization algorithm: a novel metaheuristic method for solving global optimization problems," *Expert Systems with Applications*, vol. 148, Article ID 113246, 2020.

[43] E. Atashpaz-Gargari and C. Lucas, "Imperialist competitive algorithm: an algorithm for optimization inspired by imperialistic competition," in *Proceedings of the 2007 IEEE Congress on Evolutionary Computation*, pp. 4661–4667, Singapore, September 2007.

[44] R. V. Rao, V. J. Savsani, and D. P. Vakharia, "Teaching-Learning-Based Optimization: an optimization method for continuous non-linear large scale problems," *Information Sciences*, vol. 183, no. 1, pp. 1–15, 2012.

[45] A. Husseinzadeh Kashan, "An efficient algorithm for constrained global optimization and application to mechanical engineering design: league championship algorithm (LCA)," *Computer-Aided Design*, vol. 43, no. 12, pp. 1769–1792, 2011.

[46] Q. Askari, I. Younas, and M. Saeed, "Political Optimizer: a novel socio-inspired meta-heuristic for global optimization," *Knowledge-Based Systems*, vol. 195, Article ID 105709, 2020.

[47] S. H. Samareh Moosavi and V. K. Bardsiri, "Poor and rich optimization algorithm: a new human-based and multi populations algorithm," *Engineering Applications of Artificial Intelligence*, vol. 86, pp. 165–181, 2019.

[48] Y. Yang, H. Chen, A. A. Heidari, and A. H. Gandomi, "Hunger games search: visions, conception, implementation, deep analysis, perspectives, and towards performance shifts," *Expert Systems with Applications*, vol. 177, Article ID 114864, 2021.

[49] E. Rashedi, H. Nezamabadi-pour, and S. Saryazdi, "GSA: a gravitational search algorithm," *Information Sciences*, vol. 179, no. 13, pp. 2232–2248, 2009.

[50] P. J. M. van Laarhoven and E. H. L. Aarts, "Simulated annealing," in *Simulated Annealing: Theory and Applications*, pp. 7–15, Springer Netherlands, Dordrecht, 1987.

[51] Anita and A. Yadav, "AEFA: artificial electric field algorithm for global optimization," *Swarm and Evolutionary Computation*, vol. 48, pp. 93–108, 2019.

[52] Y. Abo-Elnaga and M. A. El-Shorbagy, "Multi-sine cosine algorithm for solving nonlinear bilevel programming problems," *International Journal of Computational Intelligence Systems*, vol. 13, no. 1, p. 421, 2020.

[53] M. A. El-Shorbagy, M. A. Farag, A. A. Mousa, and I. M. El-Desoky, "A hybridization of sine cosine algorithm with steady state genetic algorithm for engineering design problems," in *Proceedings of the International Conference on Advanced Machine Learning Technologies and Applications*, A. E. Hassanien, A. Azar, T. Gaber, R. Bhatnagar, and M. F. Tolba, Eds., vol. 921, pp. 1–13, AMLTA 2019, AISC 921, Springer, Berlin, Germany, 2020.

[54] M. H. Tayarani-N and M. R. Akbarzadeh-T, "Magnetic optimization algorithms a new synthesis," in *Proceedings of the 2008 IEEE Congress on Evolutionary Computation (IEEE World Congress on Computational Intelligence)*, pp. 2659–2664, 2008.

[55] M. Ghasemi, I. F. Davoudkhani, E. Akbari, A. Rahimnejad, S. Ghavidel, and L. Li, "A novel and effective optimization algorithm for global optimization and its engineering applications: turbulent Flow of Water-based Optimization (TFWO)," *Engineering Applications of Artificial Intelligence*, vol. 92, Article ID 103666, 2020.

[56] F. A. Hashim, E. H. Houssein, M. S. Mabrouk, W. Al-Atabany, and S. Mirjalili, "Henry gas solubility optimization: a novel physics-based algorithm," *Future Generation Computer Systems*, vol. 101, pp. 646–667, 2019.

[57] F. A. Hashim, K. Hussain, E. H. Houssein, M. S. Mabrouk, and W. Al-Atabany, "Archimedes optimization algorithm: a new metaheuristic algorithm for solving optimization problems," *Applied Intelligence*, vol. 51, no. 3, pp. 1531–1551, 2021.

[58] Y. Tan and Y. Zhu, "Fireworks algorithm for optimization," *Lecture Notes in Computer Science*, vol. 6145, pp. 355–364, 2010.

[59] A. Sadollah, A. Bahreininejad, H. Eskandar, and M. Hamdi, "Mine blast algorithm: a new population based algorithm for solving constrained engineering optimization problems," *Applied Soft Computing*, vol. 13, no. 5, pp. 2592–2612, 2013.

[60] I. Ahmadianfar, A. A. Heidari, S. Noshadian, H. Chen, A. H. Gandomi, and Gandomi, "INFO: an efficient optimization algorithm based on weighted mean of vectors," *Expert Systems with Applications*, vol. 195, Article ID 116516, 2022.

[61] I. Ahmadianfar, A. A. Heidari, A. H. Gandomi, X. Chu, and H. Chen, "RUN beyond the metaphor: an efficient optimization algorithm based on Runge Kutta method," *Expert Systems with Applications*, vol. 181, Article ID 115079, 2021.

[62] G. Beni and J. Wang, *Swarm Intelligence in Cellular Robotic Systems". Proceed. NATO Advanced Workshop on Robots and Biological Systems, Tuscany, Italy*, pp. 703–712, Springer, Berlin, Heidelberg, 1993.

[63] G. C. Onwubolu and B. V. Babu, *New Optimization Techniques in Engineering*, p. 141, Springer Science & Business Media, Berlin/Heidelberg, Germany, 2004.

[64] X. Z. Gao, X. Wang, T. Jokinen, S. J. Ovaska, A. Arkkio, and K. Zenger, "A hybrid optimization method for wind generator design," *Int J Innov Comput Inf Control*, vol. 8, pp. 4347–4373, 2012.

[65] S. Khalilpourazari and S. Khalilpourazary, "Optimization of production time in the multi-pass milling process via a Robust Grey Wolf Optimizer," *Neural Computing & Applications*, vol. 29, 2016.

[66] M. Z. Ali, N. H. Awad, P. N. Suganthan, R. M. Duwairi, and R. G. Reynolds, "A novel hybrid Cultural Algorithms framework with trajectory-based search for global numerical optimization," *Information Sciences*, vol. 334-335, pp. 219–249, 2016.

[67] R. Goel and R. Maini, "A hybrid of ant colony and firefly algorithms (HAFA) for solving vehicle routing problems," *Journal of Computational Science*, vol. 25, pp. 28–37, 2018, þ.

[68] G.-G. Wang, A. H. Gandomi, X. Zhao, and H. C. E. Chu, "Hybridizing harmony search algorithm with cuckoo search for global numerical optimization," *Soft Computing*, vol. 20, no. 1, pp. 273–285, 2016.

[69] W. F. Abd-El-Wahed, A. A. Mousa, and M. A. El-Shorbagy, "Integrating particle swarm optimization with genetic algorithms for solving nonlinear optimization problems," *Journal of Computational and Applied Mathematics*, vol. 235, no. 5, pp. 1446–1453, 2011.

[70] G.-G. Wang, A. H. Gandomi, and A. H. Alavi, "An effective krill herd algorithm with migration operator in biogeography-based optimization," *Applied Mathematical Modelling*, vol. 38, no. 9-10, pp. 2454–2462, 2014b.

[71] V. I. Skoullis, I. x. Tassopoulos, and G. N. Beligiannis, "Solving the high school timetabling problem using a hybrid cat swarm optimization based algorithm," *Applied Soft Computing*, vol. 52, pp. 277–289, 2017.

[72] C. Liu and L. Fan, "A hybrid evolutionary algorithm based on tissue membrane systems and CMA-ES for solving numerical optimization problems," *Knowledge-Based Systems*, vol. 105, pp. 38–47, 2016.

[73] M. A. El-Shorbagy and A. Y. Ayoub, "Integrating grasshopper optimization algorithm with local search for solving data clustering problems," *International Journal of Computational Intelligence Systems*, vol. 14, no. 1, pp. 783–793, 2021.

[74] G.-G. Wang, A. H. Gandomi, A. H. Alavi, and G.-S. Hao, "Hybrid krill herd algorithm with differential evolution for global numerical optimization," *Neural Computing & Applications*, vol. 25, no. 2, pp. 297–308, 2014.

[75] M. A. El-Shorbagy and A. M. El-Refaey, "Hybridization of grasshopper optimization algorithm with genetic algorithm for solving system of non-linear equations," *IEEE Access*, vol. 8, pp. 220944–220961, 2020.

[76] G. Wang and L. Guo, "A novel hybrid bat algorithm with harmony search for global numerical optimization," *Journal of Applied Mathematics*, vol. 2013, 21 pages, Article ID 696491, 2013.

[77] H. Garg, "Solving structural engineering design optimization problems using an artificial bee colony algorithm," *Journal of Industrial and Management Optimization*, vol. 10, no. 3, pp. 777–794, 2014.

[78] E. Zahara and Y.-T. Kao, "Hybrid Nelder-Mead simplex search and particle swarm optimization for constrained engineering design problems," *Expert Systems with Applications*, vol. 36, no. 2, pp. 3880–3886, 2009.

[79] L. d. S. Coelho, "Gaussian quantum-behaved particle swarm optimization approaches for constrained engineering design problems," *Expert Systems with Applications*, vol. 37, no. 2, pp. 1676–1683, 2010.

[80] H. Chen, Y. Xu, M. Wang, and X. Zhao, "A balanced whale optimization algorithm for constrained engineering design problems," *Applied Mathematical Modelling*, vol. 71, pp. 45–59, 2019.

[81] R. Tao, Z. Meng, and H. Zhou, "A self-adaptive strategy based firefly algorithm for constrained engineering design problems," *Applied Soft Computing*, vol. 107, Article ID 107417, 2021.

[82] Y. Belkourchia, L. Azrar, and M. Z. Es-Sadek, "A hybrid optimization algorithm for solving constrained engineering design problems," in *Proceedings of the 2019 5th International Conference on Optimization and Applications (ICOA)*, pp. 1–7, IEEE, Kenitra, Morocco, April 2019.

[83] S. Gupta, K. Deep, H. Moayedi, L. K. Foong, and A. Assad, "Sine cosine grey wolf optimizer to solve engineering design problems," *Engineering with Computers*, vol. 37, no. 4, pp. 3123–3149, 2021.

[84] Y. Li, X. Zhu, and J. Liu, "An improved moth-flame optimization algorithm for engineering problems," *Symmetry*, vol. 12, no. 8, p. 1234, 2020.

[85] C. Xiao, K. Hao, and Y. Ding, "An improved fruit fly optimization algorithm inspired from cell communication mechanism," *Mathematical Problems in Engineering*, vol. 2015, 15 pages, Article ID 492195, 2015.

[86] H. Chengzhong and L. Junying, "Adaptive chaos fruit fly optimization algorithm," *Journal of Computer Applications*, vol. 33, no. 05, p. 1313, 2013.

[87] A. A. Mousa, M. A. El-Shorbagy, I. Mustafa, and H. Alotaibi, "Chaotic search based equilibrium optimizer for dealing with nonlinear programming and petrochemical application," *Processes*, vol. 9, no. 2, 2021.

[88] M. Mitić, N. Vuković, M. Petrović, and Z. Miljković, "Chaotic fruit fly optimization algorithm," *Knowledge-Based Systems*, vol. 89, pp. 446–458, 2015.

[89] M.-Y. Cheng and K.-Yu Huang, "Genetic algorithm-based chaos clustering approach for nonlinear optimization," *Journal of Marine Science and Technology*, vol. 18, no. 3, p. 15, 2010.

[90] X. Wang, Z. Wang, J. Weng, C. Wen, H. Chen, and X. Wang, "A new effective machine learning framework for sepsis diagnosis," *IEEE Access*, vol. 6, Article ID 48300, 2018.

[91] S. Gao, Yu Yang, Y. Wang, J. Wang, J. Cheng, and M. C. Zhou, "Chaotic local search-based differential evolution algorithms for optimization," *IEEE Transactions on Systems, Man, and Cybernetics: Systems*, vol. 51, no. 6, pp. 3954–3967, 2019.

[92] X. Zhang, Y. Xu, C. Yu et al., "Gaussian mutational chaotic fruit fly-built optimization and feature selection," *Expert Systems with Applications*, vol. 141, Article ID 112976, 2020.

[93] A. Baykasoğlu and B. O. Fehmi, "Adaptive firefly algorithm with chaos for mechanical design optimization problems," *Applied Soft Computing*, vol. 36, pp. 152–164, 2015.

[94] M. A. El-Shorbagy, A. A. Mousa, and S. M. Nasr, "A chaos-based evolutionary algorithm for general nonlinear programming problems," *Chaos, Solitons & Fractals*, vol. 85, pp. 8–21, 2016.

[95] F. Ye, X. Y. Lou, and L. F. Sun, "An improved chaotic fruit fly optimization based on a mutation strategy for simultaneous feature selection and parameter optimization for SVM and its applications," *PLoS One*, vol. 12, no. 4, Article ID e0173516, 2017.

[96] A. A. Mousa, M. A. El-Shorbagy, and M. A. Farag, "Steady-state sine cosine genetic algorithm based chaotic search for nonlinear programming and engineering applications," *IEEE Access*, vol. 8, Article ID 212036, 2020.

[97] X. Yuan, Y. Liu, Y. Xiang, and X. Yan, "Parameter identification of BIPT system using chaotic-enhanced fruit fly optimization algorithm," *Applied Mathematics and Computation*, vol. 268, pp. 1267–1281, 2015.

[98] S. S. Rao, *Engineering Optimization: Theory and Practice*, A Wiley-Interscience publication, New Jersey, fourth edition, 2009.

[99] W. T. Pan, "A new fruit fly optimization algorithm: taking the financial distress model as an example," *Knowl.-Based Syst.*vol. 26, pp. 69–74, 2013.

[100] D. Yang, G. Li, and G. Cheng, "On the efficiency of chaos optimization algorithms for global optimization," *Chaos, Solitons & Fractals*, vol. 34, no. 4, pp. 1366–1375, 2007.

[101] M. A. E. Shorbagy and A. A. Mousa, "Chaotic particle swarm optimization for imprecise combined economic and emission dispatch problem," *Review of Information Engineering and Applications*, vol. 4, no. 1, pp. 20–35, 2017.

[102] B. Alatas, E. Akin, and A. B. Ozer, "Chaos embedded particle swarm optimization algorithms," *Chaos, Solitons & Fractals*, vol. 40, no. 4, pp. 1715–1734, 2009.

[103] M. Jampour, "Chaotic genetic algorithm based on lorenz chaotic system for optimization problems," *Intelligent Systems and Applications*, vol. 5, no. 5, pp. 19–24, 2013.

[104] J. Xiao, "Improved quantum evolutionary algorithm combined with chaos and its application," *Advances in Neural Networks - ISNN 2009*, vol. 5553, pp. 704–713, 2009.

[105] P. Lu, J. Zhou, H. Zhang, R. Zhang, and C. Wang, "Chaotic differential bee colony optimization algorithm for dynamic economic dispatch problem with valve-point effects," *International Journal of Electrical Power & Energy Systems*, vol. 62, pp. 130–143, 2014.

[106] L. d. S. Coelho, H. V. H. Ayala, and V. C. Mariani, "A self-adaptive chaotic differential evolution algorithm using gamma distribution for unconstrained global optimization," *Applied Mathematics and Computation*, vol. 234, pp. 452–459, 2014.

[107] D. Oliva, M. Abd El Aziz, and A. Ella Hassanien, "Parameter estimation of photovoltaic cells using an improved chaotic whale optimization algorithm," *Applied Energy*, vol. 200, pp. 141–154, 2017.

[108] B. Alatas, "Chaotic bee colony algorithms for global numerical optimization," *Expert Systems with Applications*, vol. 37, no. 8, pp. 5682–5687, 2010.

[109] B. Alatas, "Chaotic harmony search algorithms," *Applied Mathematics and Computation*, vol. 216, no. 9, pp. 2687–2699, 2010.

[110] Z. Aram, S. Jafari, J. Ma, J. C. Sprott, S. Zendehrouh, and V.-T. Pham, "Using chaotic artificial neural networks to model memory in the brain," *Communications in Nonlinear Science and Numerical Simulation*, vol. 44, pp. 449–459, 2017.

[111] A. A. Mousa, M. A. El-Shorbagy, W. Abd-El-Wahed, and F. Abd-El-Wahed, "Local search based hybrid particle swarm optimization algorithm for multiobjective optimization," *Swarm and Evolutionary Computation*, vol. 3, pp. 1–14, 2012.

[112] P. Suganthan, N. Hansen, J. Liang et al., "Problem Definitions and Evaluation Criteria for the CEC'2005 Special Sessionon Real Parameter Optimization," Nanyang Technological University, Tech. Rep, 2005, http://www.ntu.edu.sg/home/epnsugan/index_files/cec-%2005/Tech-Report-May-30-05.pdf.

[113] A. Kumar, G. Wu, M. Z. Ali, R. Mallipeddi, P. N. Suganthan, and S. Das, "A test-suite of non-convex constrained optimization problems from the real-world and some baseline results," *Swarm and Evolutionary Computation*, vol. 56, Article ID 100693, 2020.

[114] S. Kirkpatrick, C. D. Gelatt, and M. P. Vecchi, "Optimization by simulated annealing," *Science*, vol. 220, no. 4598, pp. 671–680, 1983.

[115] R. Chelouah and P. Siarry, "A continuous genetic algorithm designed for the global optimization of multimodal functions," *Journal of Heuristics*, vol. 6, no. 2, pp. 191–213, 2000.

[116] S. Mirjalili, S. M. Mirjalili, and A. Lewis, "Grey wolf optimizer," *Advances in Engineering Software*, vol. 69, pp. 46–61, 2014.

[117] S. Mirjalili and A. Lewis, "The whale optimization algorithm," *Advances in Engineering Software*, vol. 95, pp. 51–67, 2016.

[118] Z. Li, Y. Zhou, S. Zhang, and J. Song, "Lévy-flight moth-flame algorithm for function optimization and engineering design problems," *Mathematical Problems in Engineering*, vol. 2016, 22 pages, Article ID 1423930, 2016.

[119] S. Khalilpourazari and S. Khalilpourazary, "An efficient hybrid algorithm based on Water Cycle and Moth-Flame Optimization algorithms for solving numerical and constrained engineering optimization problems," *Soft Computing*, vol. 23, no. 5, pp. 1699–1722, 2019.

[120] L. Abualigah, A. Diabat, S. Mirjalili, M. Abd Elaziz, and A. H. Gandomi, "The arithmetic optimization algorithm," *Computer Methods in Applied Mechanics and Engineering*, vol. 376, Article ID 113609, 2021.

[121] C. Chen, X. Wang, H. Yu, M. Wang, and H. Chen, "Dealing with multi-modality using synthesis of Moth-flame optimizer with sine cosine mechanisms," *Mathematics and Computers in Simulation*, vol. 188, pp. 291–318, 2021.

[122] M. H. Nadimi-Shahraki, A. Fatahi, H. Zamani, S. Mirjalili, and L. Abualigah, "An improved moth-flame optimization algorithm with adaptation mechanism to solve numerical and mechanical engineering problems," *Entropy*, vol. 23, no. 12, p. 1637, 2021.

[123] J. Kennedy and R. Eberhart, "Particle swarm optimization," in *Proceedings of the 4th IEEE International Conference on Neural Networks*, Piscataway, New Jersey, December 1995.

[124] A. Auger and N. Hansen, "A restart CMA evolution strategy with increasing population size," in *Proceedings of the 2005 IEEE Congress on Evolutionary Computation*, pp. 1769–1776, Edinburgh, UK, September 2005.

[125] L. J. Eshelman, "The CHC adaptive search algorithm: how to have safe search when engaging in nontraditional genetic recombination," in *Foundations of Genetic Algorithms, Morgan Kaufmann*, G. J. E. Rawlins, Ed., pp. 265–283, San Mateo, California, 1991.

[126] C. Fernandes and A. Rosa, "A study of non-random matching and varying population size in genetic algorithm using a royal road function," in *Proceedings of the 2001 Congress on Evolutionary Computation*, pp. 60–66, Piscataway, New Jersey, 2001.

[127] F. Herrera, M. Lozano, and D. Molina, "Continuous scatter search: an analysis of the integration of some combination methods and improvement strategies," *European Journal of Operational Research*, vol. 169, no. 2, pp. 450–476, 2006.

[128] M. Laguna, R. Marti, and R. C Martí, *Scatter Search. Methodology and Implementation in C*, Springer Science & Business Media, Berlin, Germany, 2003.

[129] K. V. Price, M. Rainer, and J. A. Lampinen, *Differential Evolution: A Practical Approach to Global Optimization*, Springer-Verlag, NY, USA, 2005.

[130] A. K. Qin and P. N. Suganthan, "Self-adaptive differential evolution algorithm for numerical optimization," *Proceedings of the 2005 IEEE Congress on Evolutionary Computation*, vol. 2pp. 1785–1791, Edinburgh, UK, September 2005.

[131] J. Derrac, S. García, D. Molina, and F. Herrera, "A practical tutorial on the use of nonparametric statistical tests as a methodology for comparing evolutionary and swarm intelligence algorithms," *Swarm and Evolutionary Computation*, vol. 1, no. 1, pp. 3–18, 2011.

[132] S. García, A. Fernández, J. Luengo, and F. Herrera, "Advanced nonparametric tests for multiple comparisons in the design of experiments in computational intelligence and data mining: experimental analysis of power," *Information Sciences*, vol. 180, no. 10, 2010.

Hindawi
Complexity
Volume 2022, Article ID 7047282, 15 pages
https://doi.org/10.1155/2022/7047282

Research Article

A New Multistage Encryption Scheme Using Linear Feedback Register and Chaos-Based Quantum Map

Adel R. Alharbi,[1] Jawad Ahmad,[2] Arshad,[3] Sajjad Shaukat Jamal,[4] Fawad Masood,[2,5] Yazeed Yasin Ghadi,[6] Nikolaos Pitropakis,[2] and William J Buchanan[2]

[1]*College of Computing and Information Technology, University of Tabuk, Tabuk 71491, Saudi Arabia*
[2]*School of Computing, Edinburgh Napier University, Edinburgh EH105DT, UK*
[3]*Institute for Energy and Environment, University of Strathclyde, Glasgow G11XQ, UK*
[4]*Department of Mathematics, College of Science, King Khalid University, Abha 61413, Saudi Arabia*
[5]*College of Information Engineering, Yangzhou University, Yangzhou 225009, China*
[6]*Department of Computer Science and Software Engineering, Al Ain University, Abu Dhabi 122612, UAE*

Correspondence should be addressed to Jawad Ahmad; j.ahmad@napier.ac.uk

Received 20 December 2021; Revised 10 February 2022; Accepted 2 March 2022; Published 18 April 2022

Academic Editor: Atila Bueno

With the increasing volume of data transmission through insecure communication channels, big data security has become one of the important concerns in the cybersecurity domain. To address these concerns and keep data safe, a robust privacy-preserving cryptosystem is necessary. Such a solution relies on chaos encryption algorithms over standard cryptographic methods that possess multistage encryption levels, including high speed, high security, low compute overheads, and procedural power, among other characteristics. In this work, a secure image encryption scheme is proposed using linear feedback shift register (LFSR) and chaos-based quantum chaotic map. The focus of the scheme is mainly dependent on the secret keys from the input of the algorithm. The threat landscape, the statistical test analysis, along critical comparisons with other schemes indicate that the presented algorithm is significantly secure and is resistant to a wide range of different attacks such as differential and statistical attacks. The proposed method has sufficiently higher sensitivity and security when compared to existing encryption algorithms. Several security parameters validated the security of proposed work such as correlation coefficient analyses among the neighboring pixels, entropy, the number of pixels change rate (NPCR), unified average change intensity (UACI), mean square error (MSE), brute force, key sensitivity, and peak signal to noise ratio (PSNR) analyses. The randomness of the ciphers produced by the proposed technique is also passed through NIST-800-22. The results of NIST indicate that the ciphers are highly random and do not produce any type of periodicity or pattern.

1. Introduction

With the fast progression of data technology, a high volume of multimedia data, comprising digital images, video, and audio, is produced and distributed across various networks. Multimedia data, particularly digital images, is one of the most extensively used data formats in modern times. Since digital images contain information that can be sensitive at times, unauthorized access to a secret image can result in serious information security incidents. As a result, it is critical to add a security layer to protect sensitive digital images. Researchers in this area have recently established numerous methodologies to securely communicate digital images, such as information hiding, data encryption, steganography, and digital watermarking. Contents in an image can be protected via image encryption algorithms. An image data encryption algorithm converts meaningful information into cipher data that is unrecognizable, thus preventing the potential intruders from extracting the original information. The original data can be fully retrieved by using the proper

key. The sensitive data cannot be retrieved by using the wrong key. Among all image encryption techniques, chaos theory is the most extensively utilized and operational technique that provides security to the data without introducing considerable overheads. This is because chaos theory shares many properties with image encryption principles [1–3].

On the other hand, chaos deprivation occurs due to precision limitations when a chaotic system is employed in a digital stage. As a result, image encryption methodologies that rely solely on chaotic schemes have numerous security flaws. Combining chaotic systems with other techniques is one effective way to solve this problem. Furthermore, several image encryption procedures based on other methodologies, such as frequency domain transformation and compressive sensing, have been suggested in the literature [2, 3].

Encrypted multimedia information such as chaos-based image security plays an essential role in the upcoming quantum computers era. With the introduction of quantum systems, concerns regarding chaos-based classical systems have drawn the attention of the cyber security community. As time passes, the classical chaos-based dynamical system becomes quantized; thus, researchers need to study the combined effect of quantum and chaotic systems. The quantum chaotic map with the bifurcation explanation was initially proposed in [4]. After that, the quantized baker's transformation was studied in [5]. The structure of the trace formula for quantum maps on a compact phase space was analyzed in [6]. Many other aspects of quantum chaos were discussed in [7–10]. The new version of the study is known as the quantum version of the classical chaotic system. The innovative quantized version of the chaos-based system using chaotic quantum system possesses better properties and provides deep insight into the nature of quantum chaos. The sensitive dependence of chaotic systems gives rise to chaos for some specific initial conditions. The new map, the quantized version (chaotic quantum map), is based on canonical transformation; however, there is no proper technique for quantizing the classical map. Many cryptographers and researchers are working on using quantum maps for image encryption in the context of quantum chaos combination.

Numerous image data encryption technique has been examined and concluded that symmetric cipher-based encryption systems require limited options and have larger bandwidth, making them appropriate for multimedia data security. Chai et al. proposed an image encryption technique based on DNA encryption and chaos [11]. Praveen et al. developed a new cryptosystem for medical image Trans receiving based on the chaos [12]. Kadir et al. utilized the concept of a hyperchaotic system of 6^{th} order CNN and skew tent map for color image encryption [13]. Masood et al. employed the combination of chaos and DNA genetic encoding for the construction of a secure encryption scheme [14]. Fawad et al. offered a secure medical encryption algorithm based on Brownian motion, Henon chaotic map, and Chen's chaotic system with elevated security [15]. Shah et al. proposed a privacy-preserving mechanism using Dynamic Newton Leipnik and Modified logistic maps [16]. Butt et al. applied the combination of Lucas series and Pseudo Quantum map to offer a digital image confidentiality scheme [17]. Private key ciphers are further categorized into two types: stream ciphers and block ciphers. Numerous existing block and stream ciphers produce high randomness that might be resistant to different classical attacks. However, it has been discovered that stream ciphers are slow as they encrypt one bit or one byte at a time. The stream cipher's basic operation is to yield a high-quality long pseudorandom keystream, which is then used to encode the image data. The output from several Linear Feedback Shift Register (LFSRs) can be fed into an appropriate nonlinear Boolean function to create a stream cipher. Furthermore, the utilization of bit-positioned operations in the LFSR-based algorithm, this image encryption has higher bandwidth. Because of its high throughput and low computational resource requirements, arbitrary number initiation may be a promising method for data encryption. Moreover, current workstations support the word process, and the price of creating a one bit is the equivalent as that of producing a w-bit word, where w is the machine processor's word size [18, 19]. The block size of a processor can range from 16 to 64 bits. The current review encourages us to use word-LFSR based on nonlinear functions for data encryption. Many encryption schemes based on the quantum chaotic map along with some other structures have been proposed in the literature [20–22]. But the key generation procedures in the recent quantum-based chaotic structures are independent of the plaintext which makes it vulnerable against the differential and classical attacks. Therefore, our proposed encryption structure includes the key generation based on plaintext and changes concerning the change in the input.

In this work, the combination of LFSR and quantum chaotic map has been utilized to offer an efficient image encryption approach. The suggested system is completely key-dependent. The input of the algorithm generates the initial seeds to LFSR and quantum chaotic map. The proposed encryption technique comprises confusion-diffusion architecture. Some cryptographic analysis ensures the security of the offered system. The simulation results of performance analysis indicate that the suggested encryption technique yields ciphers with high randomness and low correlation. Therefore, the proposed encryption structure is robust and secure for data transmission. The contributions of this work can be summarized as follows:

(i) A novel multistage encryption scheme using a linear feedback register and a chaos-based quantum map is proposed

(ii) Security of the proposed methodology against known attacks is extensively analyzed

(iii) A comparison of the proposed methodology against competing approaches found in the literature is conducted

This manuscript is structured as follows: Section 2 offers basic concepts about cryptosystem; Structure of offered approach is defined in Section 3; In Section 4, security analyses are performed; Section 5 presents comparative

analysis; Finally, Section 6 concludes our work while giving some pointers for future work.

2. Some Basic Concepts

2.1. Linear Feedback Shift Register. LFSR is based on a logic circuit that works in a sequential order used in digital circuits to store digital data. It is built up in a linear form with inputs/outputs coupled. The process of data starts once the circuit is triggered. The input bit of LFSR yields a linear function of two or further of its preceding states, also known as taps. An LFSR of size n is made up of n stages as, $0, 1, \ldots, n-1$, each of which may store one bit, and a clock that controls data interchange. The shift register would be initialized with a vector containing elements $p_0, \ldots, p_{n-1}$. The following operations are carried out at time i.

(i) The output includes p_i (the content of stage 0)

(ii) The data of stage i is relocated to phase $i-1$, for $1 \le i \le n-1$

(iii) The new data (the feedback bit) of stage $n-1$ is acquired by XORing a subsection of the n stages' data

An LFSR's initial input is referred to as a seed. Because any register can only have a restricted number of taps, it must ultimately become periodic. An LFSR with a carefully designed feedback function and seed, on the other hand, can generate a structure of bits that seems random (and has strong statistical features) and has a long period. Pseudorandom numbers, rapid digital counters, pseudo-noise sequences, cryptography, whitening sequences, and other applications can all benefit from LFSRs, which can be employed in hardware and software. There are many alternative setups such as Figure 1 illustrates a simple setup that starts with an input of all 1's and is very simple to employ in hardware and software. An LFSR of this category will never encompass only 0's and will stop if a binary string containing only 0's is input into it. Only certain tap combinations (i.e., the nonzero coefficients ci described below) will result in a maximum sequence with a period of $2^n - 1$ series. If the initial (left) 4 bits are given to the LFSR, the subsequent sequence will be generated:

1, 1, 1, 1, 0, 1, 0, 0, 1, 1, 1, 0, 1, 0, 0, 1, 1, 1, 0, 1, 0, 0, 1, 1, 1, 0, 1, 0, 0, 1.

If the content of the phase p_i is p_i, $0 \le i \le m-1$, then $[p_{m-1}, \ldots, p_1, p_0]$ is known as the initial state of the LFSR. From the description of an LFSR, the yielded sequence $p_0, p_1, \ldots$ will satisfy the subsequent recursion

$$p_j = \sum_{i=1}^{m} c_i p_{j-i}, \quad j \ge m. \tag{1}$$

The polynomial $C(x) = 1 + c_1 x + \cdots + c_m x^m$ is the feedback (or connection) polynomial of the sequence $\{c_j\}_j = \{p_j : j = 0, 1, \ldots\}$. The LFSR is nonsingular if $c_m = 0$, that is, the degree of its feedback polynomial is m .

As the powers in the linear feedback function are 16, 14, 13, 11, the bits at these situations are XORed. The bits are shifted by 1, and then the XORed value is maintained as the first bit. The pseudoalgorithm explaining the general scenario of the linear feedback shift register is presented in Algorithm 1.

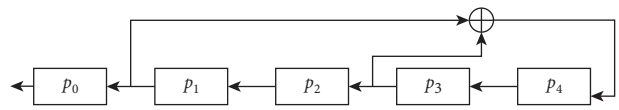

Figure 1: LFSR with five stages p_i, and feedback bit $p_4 = p_1 \oplus p_3$.

2.2. Quantum Chaotic Map. This section presents a high-level summary of the quantum logistic map. The logistic map is discussed in [23] when the dissipation parameter is increased. Goggin et al., [24] developed a chaos-based quantum map that was dissipative by attaching a harmonic oscillator (quantum kicked) and observing the resulting dissipation. They write $p = p + \delta p$ to explore the properties of quantum corrections, where δp signifies a quantum fluctuation about p [24], and p represents a quantum correction. The following differential equations govern this map with the lower order quantum corrections:

$$\begin{cases} a_{i+1} = r\left(a_i - |a_i|^2\right) - r b_i, \\ b_{i+1} = -b_i e^{-2\beta} + e^{-\beta} r\left[(2 - a_i - a_i^*) b_i - a_i c_i^* - a_i^* b_i\right], \\ c_{i+1} = -c_i e^{-2\beta} + e^{-\beta} r\left[2(1 - a_i^*) c_i - 2 a_i b_i - a_i\right], \end{cases} \tag{2}$$

where $a = p$, $b = \delta a^\dagger \delta a$, $c = \delta a \delta a$, and β, r are bifurcation parameters. In general, a_{i+1}, b_{i+1}, and c_{i+1} are all complex numbers, with a_i^* signifying the complex conjugate of a_i and c_i^* symbolizing the complex conjugate of $\mathbf{c_i}$, respectively. If it is established that the initial values are real numbers, it can be concluded that all following values will also be real numbers. The logistic map with additive noise has the same shape as in equation (1) a. It should be mentioned that the noise is generated entirely by the computer system. The noise in this circumstance serves as a gauge for the strength of quantum correlations. The quantum corrections $b_i$and $c_i \longrightarrow \infty$reduce equation (1) to the classical, one-dimensional logistic map in the presence of the quantum corrections. The resilient dissipation limit $\beta \longrightarrow \infty$ of the quantum logistic map also provides the classical logistic map, which is a further benefit. The quantum map depicts a road to chaos that doubles in length every period. When using an unsigned binary representation, the fixed point at 1 can be avoided by rounding down, whereas the fixed point at 0 is more difficult to avoid. Options include reseeding the circuit with a new randomly chosen initial condition (which must be coordinated with synchronized circuits), adding a constant value (which leads to known state conditions to any source that knows the constant and arithmetic precision), or limiting the valid range of chaotic parameter values so that the mapping cannot generate a value less than LSB/2 [25]. Figure 2 shows the bifurcation diagram of equation (1).

Input: key
Output: pseudorandom numbers sequence
(1)**while** value! = 0 and value is not reiterating,
Do
(2)**Bin** ⟵ attain the binary configuration of the Value.
(3)Pad until bin has 16 bits with leading zeros.
(4)**XOR** the bits at situations respective to LF function and save it in m.
(5)**Bin** ← shift the bin by one toward the right.
(6)Pad until bin has 16 bits with leading zeros.
(7)The first bit is replaced with m in the bin.
(8)**Value** ← attain the decimal value of the obtained binary configuration.
(9) **End**

Algorithm 1: Algorithm of Linear Feedback Shift Register.

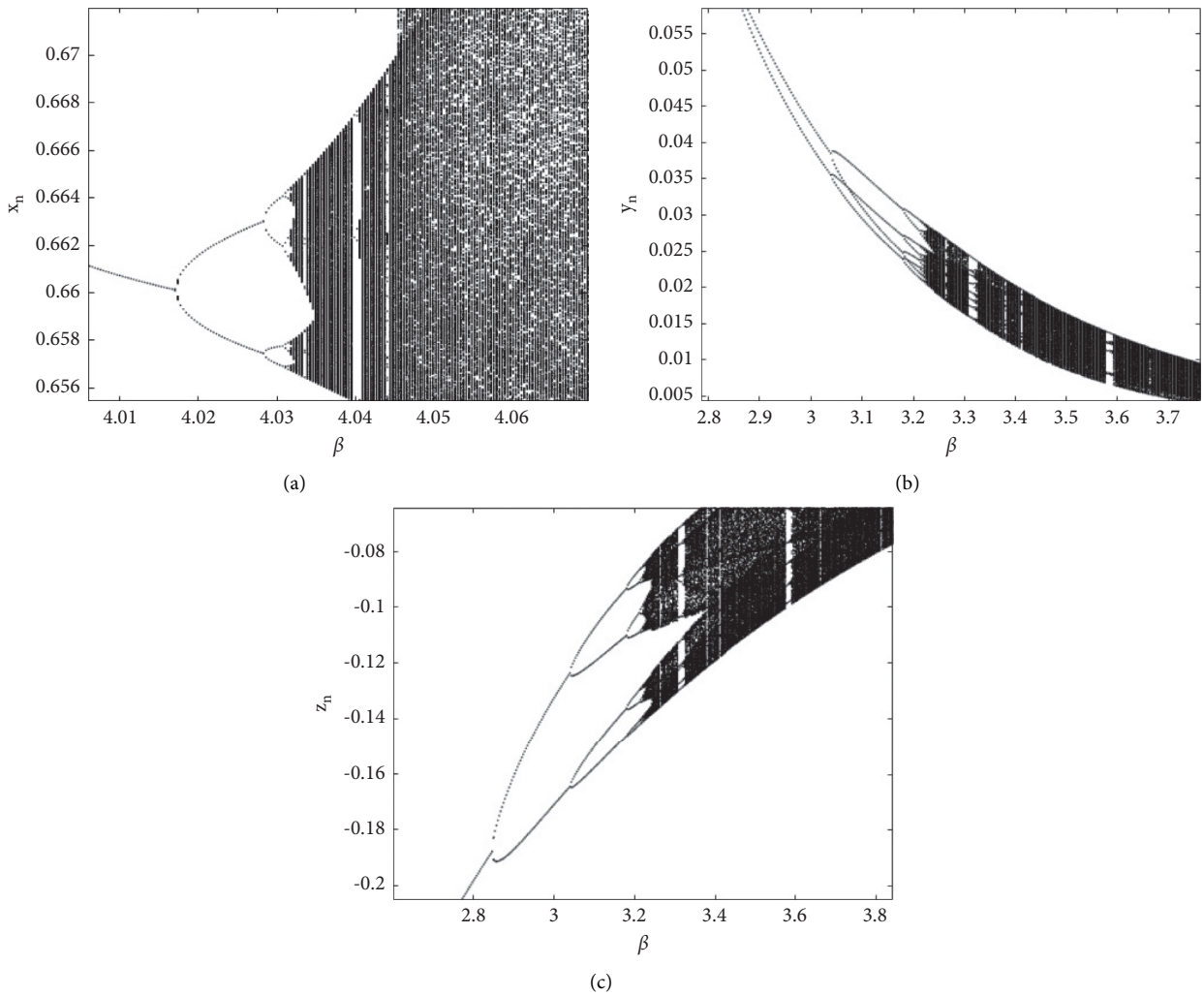

Figure 2: Bifurcation diagram of parameters β at r = 3.88 in (a) x-direction; (b) y-direction; (c) z-direction.

3. Proposed Encryption Algorithm

The combination of quantum chaotic map and LFSR is created for use in the encryption system that is being suggested. Using this function in combination with word-based LFSR, it is possible to generate extremely high-quality pseudorandom numbers. In cryptography, developing a robust LFSR with extraordinary periodicity and great cryptological characteristics is a current research topic. This function can preserve a wide range of cryptographic

characteristics. The secret key generation, with the addition presented technique using encryption and decryption, is structured as follows:

3.1. Key Generation. The key generation of the proposed cryptosystem is completely dependent on the input of the encryption technique. The private key's dependency on plaintext makes it secure against chosen-plaintext attack, chosen-ciphertext attack, and known-plaintext attack. The two parts of encryption diffusion and key-based substitution depend on the plaintext-based key. The first part is the generation of the LFSR sequence for which the plaintext provides seed value. The produced LFSR sequences are diffused with the original image. The second part is the production of a quantum chaotic map-based key for key-based substitution. The chaotic map key is also plaintext dependent because the initial values of the differential equation set are induced by using input values.

Consider the size of the input image M is $P \times Q \times 3$. After separating the image into three layers, R, G, B, we get each layer of size $P \times Q$. The seed value for LFSR and initial conditions for the chaotic map is generated by

$$I = \frac{\sum_{i=1}^{P} \sum_{j=1}^{Q} p_i q_j}{P \times Q}. \tag{3}$$

After inserting this value of I for image M the keys K_1 and K_2 are obtained by the LFSR and chaotic quantum map.

3.2. Encryption and Decryption. The encryption process of the presented structure follows the confusion and diffusion properties. Corresponding to Shannon's theory [26], a resilient cryptosystem must contain confusion and diffusion effects. To achieve robust security, the system is subjected to input-dependent key and confusion-diffusion strategies. The encryption strides are defined as follows:

Step 1. Read an image input M of size $P \times Q \times 3$ and convert it into a red, green, and blue layer.

Step 2. Diffuse the original image layers secret key K_1 obtained by seeding input image to LFSR.

Step 3. The image layers obtained in Step 2 are stored as diffused image $D^I, I = R, G, B$.

Step 4. The key K_2 obtained by chaotic quantum map by using the original image based initial conditions is utilized for substitution as follows:

Rule 1: if $0 \le k_2(ij) \le 150$ then put $c_{ij}^I = d_{ij}^I \oplus k_2(ij)$

Rule 2: if $151 \le k_2(ij) \le 255$ then put $c_{ij}^I = d_{ij}^I \oplus k_2(ij) \oplus a$

Here, $a \in \mathbb{Z}_{256}$, is any fixed constant selected randomly, $d_{ij}^I \in D_{ij}^I$ is the pixel value of diffused image D^I, $k_2(ij)$ is the value of K_2 and $c_{ij}^I \in C_{ij}^I$ is the pixel value of the final cipher image $C^I, I = R, G, B$, and position i and j, respectively.

The image $C^I, I = R, G, B$ is the diffusion-substitution-based cipher obtained from the presented strategy.

A clear description of the presented encryption is defined in Figure 3.

The decryption of the presented structure is based on a similar strategy in a reverse manner. The same key K_1 is first diffused with the encrypted image. After that, the key K_2 is utilized for the process of inverse substitution. The substitution rules are defined in a reverse manner as:

Rule 1: if $0 \le k_2(ij) \le 150$ then put $d_{ij}^I = c_{ij}^I \oplus k_2(ij)$

Rule 2: if $151 \le k_2(ij) \le 255$ then put $d_{ij}^I = c_{ij}^I \oplus k_2(ij) \oplus a$

Where $a \in \mathbb{Z}_{256}$, is any fixed constant selected randomly, $d_{ij}^I \in D_{ij}^I$ is the pixel value of diffused image D^I, $k_2(ij)$ is the value of K_2 and $c_{ij}^I \in C_{ij}^I$ is the pixel value of the final cipher image $C^I, I = R, G, B$, and position i and j, respectively.

The inverse of the diffusion process is computed by the following way:

$$M = D_{ij}^I \oplus K_1, \tag{4}$$

where M is the decrypted plain image.

4. Statistical Analysis of Recovered Image

Good encryption procedures should be resistant to a wide range of different attacks such as the differential, statistical attacks, and brute force attacks. We carried out a security analysis of our proposed scheme. The enciphered images yielded by the presented encryption structure are illustrated in Figure 4.

4.1. Entropy. Entropy analysis was performed to examine the randomness that can be used to define image texture and information content. It refers to the pixel's ability to detect various gray levels. Entropy is high if image pixels are uniformly scattered, while entropy is low in the case of the plain image. Scientifically it can be inscribed as

$$H(S) = -\sum_{i=0}^{255} p(s_i) \log_2 (p(s_i)). \tag{5}$$

The numerical outcomes of the information entropy are displayed in Table 1. The results were calculated for plain and encrypted layers of some standard images with sizes. $512 \times 512 \times 3$ From the listed results, it can be perceived that the entropies for enciphered images are near enough to the epitome value that is 8 compared to the original ones. Therefore, the presented scheme produces uniform ciphers with a higher value of entropy.

The entropy calculated above in Table 2 is the global entropy. The global Shannon entropy does not always measure actual randomness. Unlike global Shannon entropy, local Shannon entropy $H_{(k,TB)}$ can capture local image block unpredictability, while global Shannon entropy cannot. The local entropy $E_{(k,TB)}$ can be calculated as

$$\overline{H_{(k,TB)}}(S) = \sum_{i=1}^{k} \frac{H(S_i)}{k}, \tag{6}$$

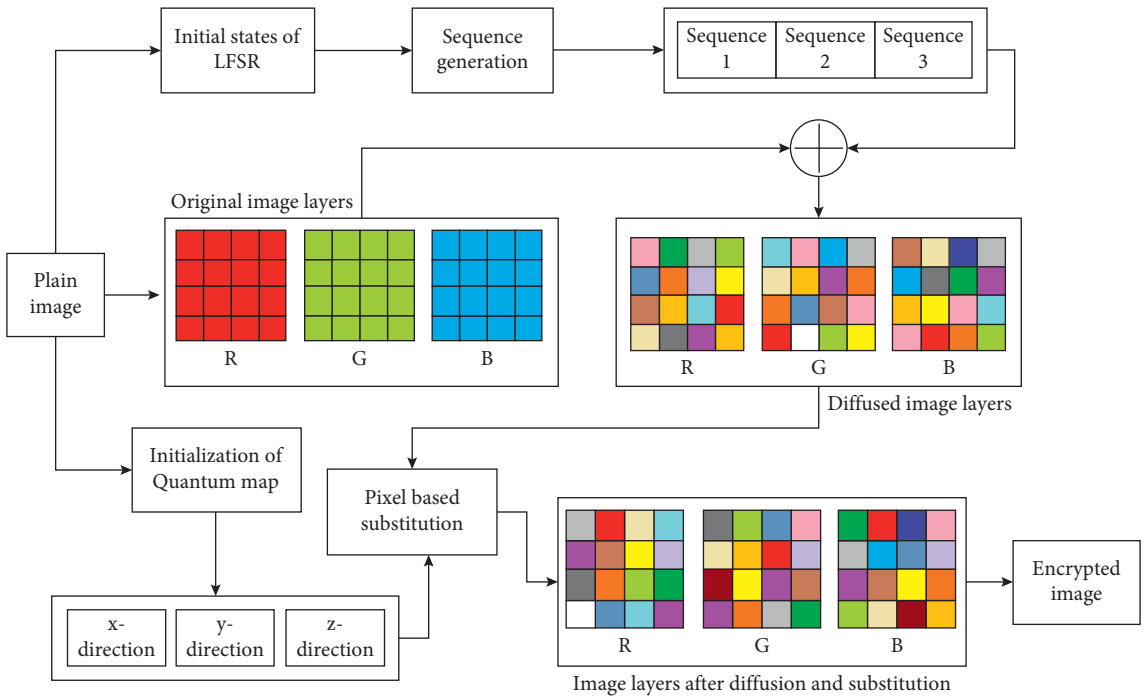

Figure 3: Design of presented encryption scheme.

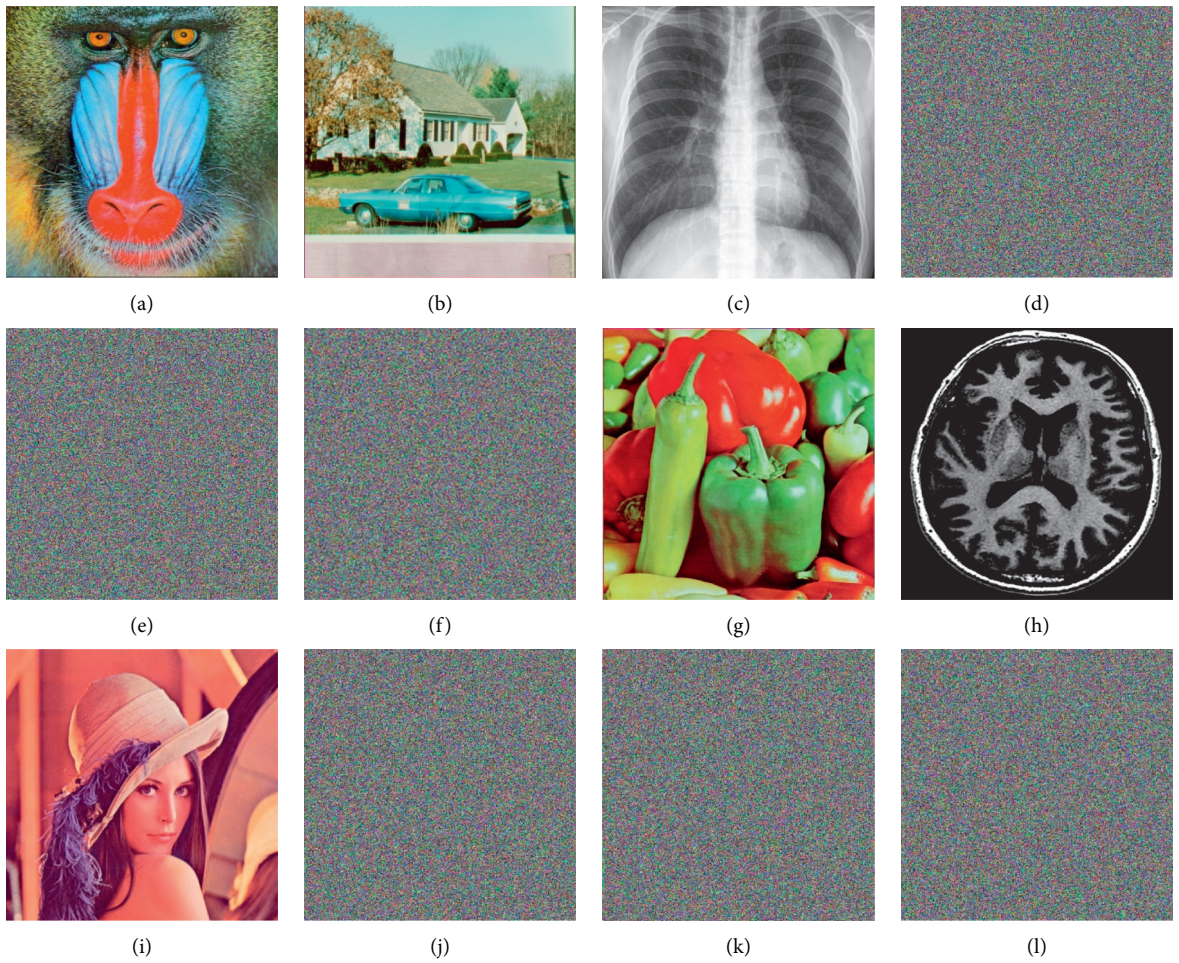

Figure 4: (a-c), (g-i) Original standard images of size 512×512; (d-f), (j-k) Respective cipher images.

Table 1: Entropy measures for different images.

Image	Original image				Enciphered image			
	Color	R	G	B	Color	R	G	B
Baboon	7.7624	7.7067	7.4744	7.7522	7.9996	7.9992	7.9995	7.9991
Peppers	7.6698	7.3388	7.4963	7.0583	7.9998	7.9991	7.9983	7.9994
House	7.0686	6.4311	6.5389	6.2320	7.9986	7.9972	7.9986	7.9983
Brain	7.0156	7.0156	7.0156	7.0156	7.9991	7.9986	7.9989	7.9989
X-ray	7.2369	7.2369	7.2369	7.2369	7.9993	7.9993	7.9989	7.9996
Lena	7.7562	7.5889	7.1060	6.8147	7.9995	7.9990	7.9992	7.9993

Table 2: Local entropy measures for different sizes of Lena image.

Lena image		Entropy value		
k	TB	R	G	B
16	32×32	5.9635	5.8740	5.9954
32	64×64	6.8951	6.0147	6.5214
64	128×128	6.0589	5.9959	56.0028
128	256×256	6.5230	6.5024	6.5804
256	512×512	7.8111	7.8047	7.9852
512	1024×1024	7.8974	7.9632	7.9841

where S_i denotes the nonoverlapping blocks of image S, k shows the number of blocks, TB represents the total size of the image, and L shows the intensity of the pixels.

The calculation of local entropy of Lena image for different sizes of the image is shown in Table 2 which depicts the maximum randomness of the ciphers produced from the proposed algorithm.

4.2. Histogram Analysis. The distribution of pixel numerical information within any image can be revealed using histogram analysis. If the image histogram after the encryption is distributed uniformly, this is considered a robust encryption system. Featured image histograms show complete similarity and differ from the dynamic histograms of explicit images, which is important in resisting any cryptographic assault. The similarity to the grayscale of the embedded image proves that no practical information can be obtained when performing any mathematical attack on the compiled image. 3D color histograms for Brain images of size $512 \times 512 \times 3$are depicted in Figure 5. From Figures 5(a)–5(d), we can perceive the pattern of original data in histogram distribution, and in the case of encrypted ones Figures 5(e)–5(h), the distribution is uniform. Therefore, the presented encryption design is robust against all the linear and differential attacks due to the ideal uniformity in the encrypted data.

In addition to the visual examination of the encrypted image histogram distribution, we perform the chi-square test (χ^2) to prove that the encrypted image has a uniform histogram distribution more precisely. The p value of the chi-square test is a real number in the range [0, 1]. For a test image to pass, the p value must be larger than a significant level α. Table 3 shows the p values for some standard cipher images encrypted by the proposed algorithm, using an a priori of 0.05. The cipher image has a uniform histogram distribution based on the results of the chi-square test in Table 3. The depicted results show that the proposed approach accepts null hypotheses and confirms the uniformity of histograms.

4.3. Correlation Analysis. Pixel correlation is a frequent approach for measuring the picture encryption algorithm's performance. In the image, a secure encryption algorithm requires a reduction in the correlation of contiguous pixels. The subsequent formula is utilized to quantify the correlation between two neighboring pixels:

$$\gamma_{xy} = \frac{E\left(\left(x - \mu_x\right)\left(y - \mu_y\right)\right)}{\sqrt{\delta_x \delta_y}}, \tag{7}$$

where μ is the expected value and δ shows variance, the results obtained from correlation analysis are presented in Table 4. The values between two neighboring pixels are significantly lowered. The results show that the presented technique is resilient against different assaults as the correlation value is close to zero, so the scheme meets the standard criteria.

Figure 6(a)–6(f) depicts the scattering of neighboring pixels in various directions. The Lena image in Figures 6(a)–6(c) displays a substantial correlation among neighboring pixels for horizontal, vertical, and diagonal of the plain image. The correlation diagrams of the enciphered image are displayed in Figures 6(d)–6(f). The dots in the encrypted image are dispersed randomly, with no evident distribution features.

4.4. Randomness Analysis

4.4.1. NIST Test. The NIST-800-22 trial was designed to test the pseudorandom number generator (PRNG). It can be examined that a complex binary sequence is appropriate for

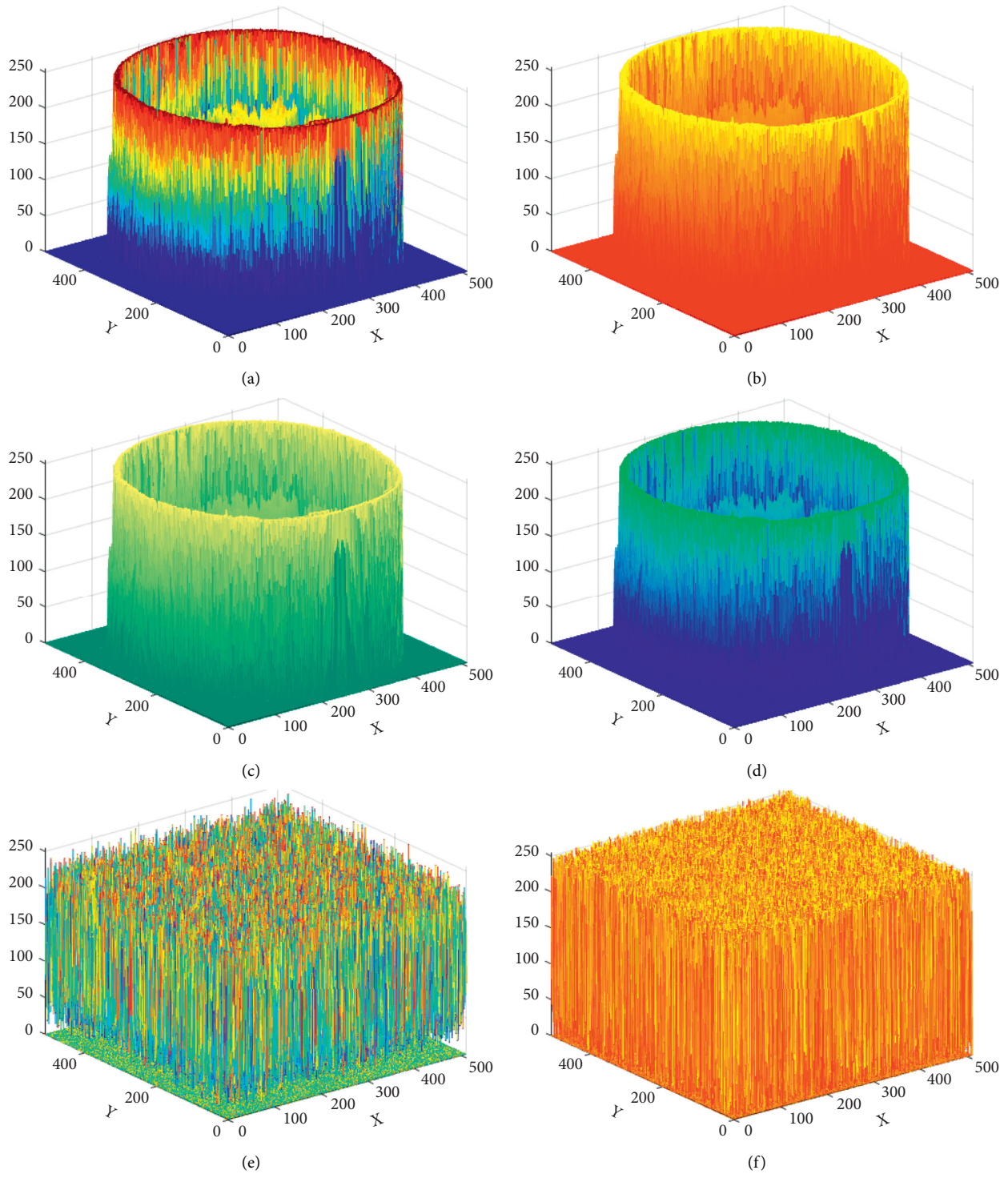

Figure 5: Continued.

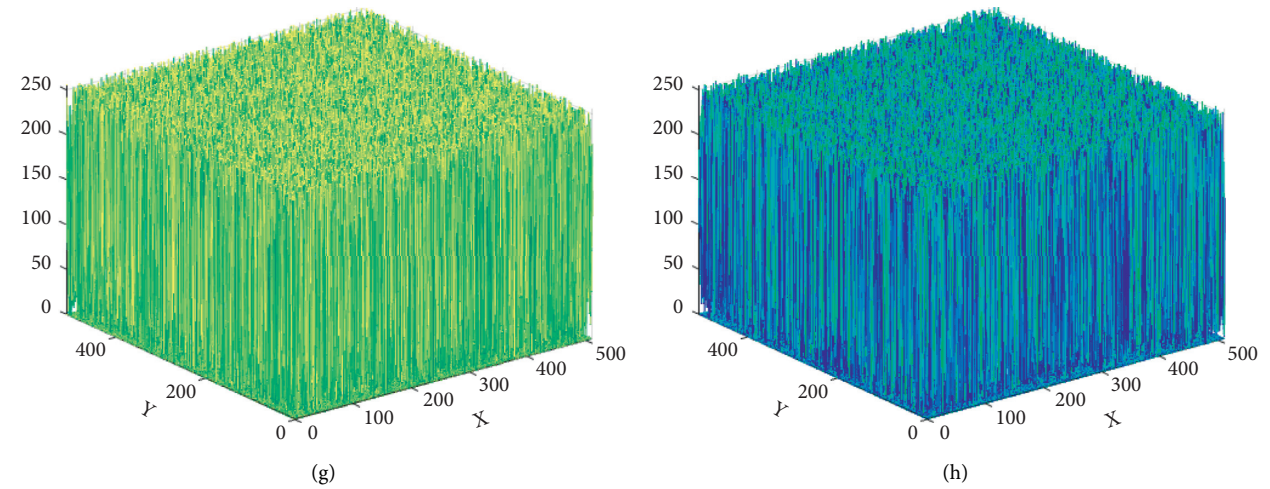

Figure 5: (a–d) 3D histogram of brain original image layers; (e–h) 3D histograms of brain encrypted image layers, respectively.

Table 3: Chi-square test measures for different images.

Image	Color	R	G	B
Baboon	0.4561	0.3698	0.4157	0.3687
Peppers	0.5151	0.9002	0.6958	0.2589
House	0.5102	0.0947	0.5179	0.4763
Brain	0.5089	0.8962	0.6527	0.6215
X-ray	0.4011	0.0940	0.8526	0.1258
Lena	0.0647	0.0871	0.9654	0.7521

Table 4: Correlation coefficient measures for enciphered images.

Image	Orientation	Encrypted		
		R	G	B
Baboon	Diagonal	−0.0001	−0.0009	0.0007
	Vertical	0.0002	0.0010	0.0010
	Horizontal	−0.0003	−0.0011	0.0001
Peppers	Diagonal	0.0043	0.0001	−0.0005
	Vertical	0.0013	−0.0003	−0.0004
	Horizontal	−0.0005	0.0002	0.0090
House	Diagonal	0.0014	−0.0015	0.0012
	Vertical	−0.0043	0.0014	−0.0054
	Horizontal	0.0015	−0.0002	0.0003
Brain	Diagonal	0.0032	0.0003	−0.0020
	Vertical	0.0011	−0.0002	−0.0010
	Horizontal	−0.0021	−0.0002	0.0003
X-ray	Diagonal	0.0004	0.0030	−0.0011
	Vertical	−0.0012	−0.0011	0.0040
	Horizontal	−0.0007	0.0012	−0.0056
Lena	Diagonal	0.0001	−0.0021	0.0003
	Vertical	−0.0001	0.0031	−0.0019
	Horizontal	−0.0031	−0.0011	0.0003

a cryptosystem based on the outcomes of the NIST test. The NIST-800-22 trial comprises 15 test approaches, comprising frequency test, run test, cumulative test, longest run test, etc. The number of p can measure the random sequence of the test sequence. If $P \geq 0.01$, the sequence is random. If $P < 0.01$, the sequence is nonrandom and predictable. If $P = 1$, the structure is completely set. If $p = 0$, the structure is by no means random. In addition, the greater the p value; the better the random sequence. The results of NIST for chaotic sequences and some standard images are presented in Table 5. The depicted results reflect that the sequence generated from the chaotic map is highly random and ideal for encryption. The results can be scrutinized using the presented encryption algorithm that helps to generate highly random ciphers with $P \geq 0.01$.

4.5. Differential Attack. In the plain image, some pixels are faintly modified to attain the respective enciphered image. The opponent recurrently makes the connection between the encrypted images and the plain ones. If a small modification in the pixels of the image can significantly disturb the cipher image, it indicates that the structure has a resilient capability to withstand differential assaults. Differential attacks are usually inspected by the number of pixels change rate (NPCR) and unified average changing intensity (UACI) values [27, 28]. These two gauges are examined as follows:

NPCR is employed to enumerate plaintext sensitivity, i.e., the outcome of converting a lone pixel in the plain image into an encrypted image. It also describes the arbitrariness and modification among the original image and its respective cipher and can be written as

$$\text{NPCR} = \frac{\sum_{i=1}^{M} \sum_{j=1}^{N} D(i,j)}{w \times h}. \tag{8}$$

The larger the value of NPCR, is better the original image sensitivity offered by the encryption algorithm. The UACI is defined as

$$\text{UACI} = \left[\frac{\sum_{i=1}^{w} \sum_{j=1}^{h} \left| C_1(i,j) - C_2(i,j) \right|}{\left(2^8 - 1\right) \times w \times h} \right] \times 100\%, \tag{9}$$

where C_1 is the first encrypted image and C_2 is the second encrypted image, and w and h are the width and height of

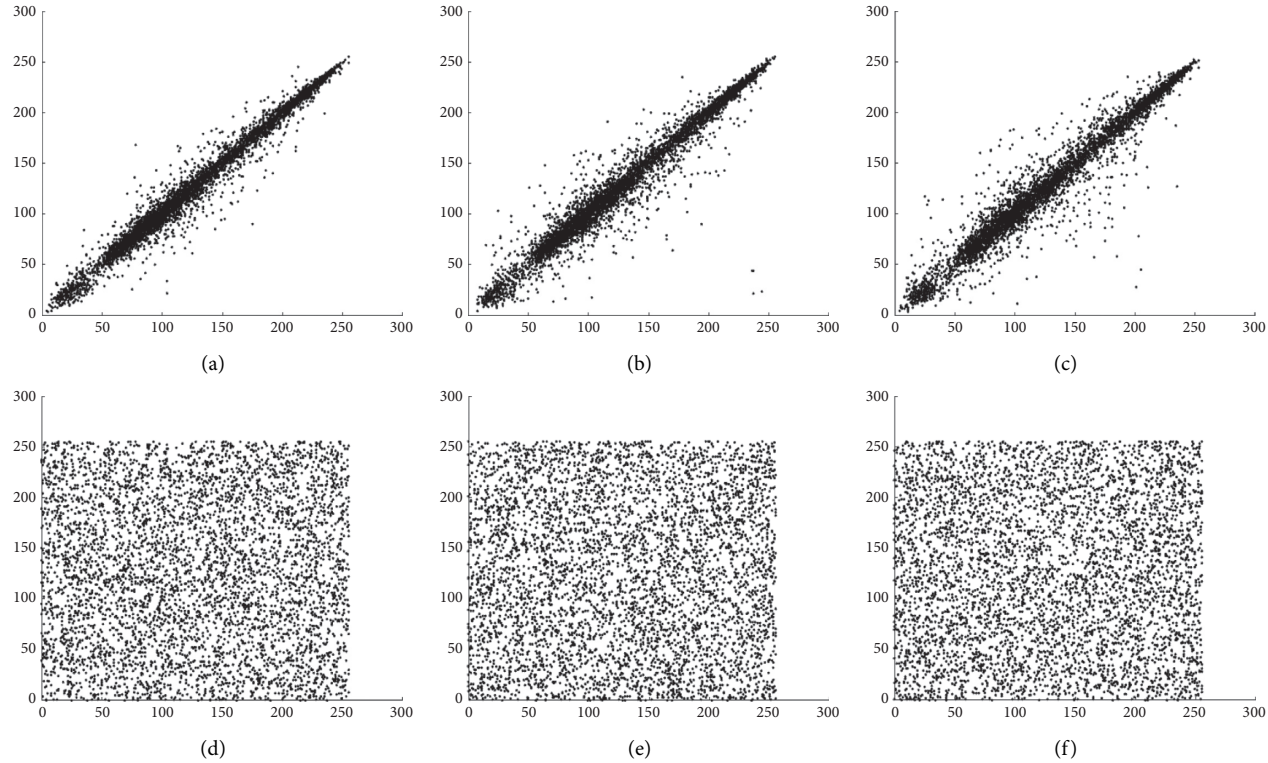

Figure 6: Correlation diagram of Lena original image in (a) horizontal direction; (b) diagonal direction; (c) vertical direction; correlation diagram of Lena encrypted image in (d) horizontal direction; (e) diagonal direction; (f) vertical direction.

cipher images C_1 and C_2. 2^8 represents the number of bits in one pixel of red, green, and blue layers in a color image.

It can be observed from Table 6 that the results for NPCR and UACI are designated as over 99% and 33%, respectively. These results indicate that the suggested scheme can withstand differential attacks.

The strength of the algorithm against differential attack varies concerning the change in the size of input data [29]. Therefore, we have performed NPCR and UACI measures for different sizes of images to check the deviation of results. The results of NPCR and UACI for various sizes of Lena images are depicted in Table 7. The key generation of the offered encryption algorithm entirely depends on the input data. Therefore, a minor change in input refers to a large change in output. The data in Table 7 indicates that the algorithm resists differential attacks for various sizes of input data.

4.6. Key Analysis

4.6.1. Key Sensitivity Test. In the encryption-decryption process, an ideal cryptographic algorithm must be sensitive to the private keys. To inspect the key sensitivity test, an enciphered image is deciphered using the different keys, which are one bit different from the correct key. Lena's standard color image of size $512 \times 512 \times 3$ is evaluated for the test. Figure 7 depicts the results of this test and one can see that when the decryption key was only one bit different, the output (Figures 7(a), 7(b), and 7(c)) shows that it does not reveal the contents of the original information. Figure 7(d) shows that decryption is possible only with the correct key.

4.6.2. Brute Force Attack. Space support is critical in countering a brute force attack. The authors of [1] proposed that the private keys of a cryptographic algorithm be greater than 2^{100} to avoid Brute force attacks. To encrypt the plain image, a chaotic map seed value and a 256 bit key/seed value of a special LFSR to yield pseudorandom numbers are utilized. The proposed encryption system has a key space greater than 2^{256} that is sufficient to withstand a Brute force attack. The integer value of the chaotic map when computing key space is not considered.

4.7. Known and Chosen Plain Text Attacks. Any cryptosystem with an excellent diffusion property is capable to withstand chosen and known-plaintext attacks. Overall, the opponent selects a distinct set of plaintexts consisting of sequential 0 and 1 data to demonstrate the algorithm's uncertainty. In the aforementioned attacks, plaintext and their corresponding ciphertext are selected. It permits our cryptosystem to produce enciphered images that are highly random.

The first step of the generation of encryption/decryption keys depends upon plaintext. The dependency of the algorithm on plaintext increases its security in contrast to chosen-plaintext attacks and chosen-ciphertext attacks. The substitution part of the suggested algorithm is also sensitive

Table 5: NIST measures for chaotic map and different standard color images.

Test name		P value				Status
		Chaotic sequence	Baboon	Peppers	House	
Frequency		0.5632	0.7412	0.8191	0.8421	Pass
Block frequency		0.0125	0.2156	0.0182	0.1355	Pass
Runs		0.9523	0.1534	0.9542	0.9018	Pass
Longest run		0.0357	0.0357	0.0357	0.0357	Pass
Rank		0.2919	0.2919	0.2919	0.2919	Pass
Serial 1		0.9635	0.8261	0.1144	0.6021	Pass
Serial 2		0.8852	0.5963	0.7344	0.3740	Pass
Cumulative sums		0.3562	0.3110	0.5810	0.5520	Pass
Overlapping template		0.8899	0.9568	0.8625	0.8752	Pass
Universal		0.7616	0.9981	0.9987	0.9986	Pass
Approximate entropy		0.9523	0.2082	0.1342	0.7566	Pass
Nonoverlapping template		0.8536	0.9989	0.9685	0.9452	Pass
Random excursions	$X = -4$	1	0.9971	0.0114	0.1526	Pass
	$X = -3$	0.0563	0.2251	0.2586	0.3698	Pass
	$X = -2$	0.6677	0.3698	0.2589	0.0058	Pass
	$X = -1$	0.5147	0.9962	0.4411	0.6398	Pass
	$X = 1$	0.2431	0.8144	0.6325	0.9990	Pass
	$X = 2$	0.8891	0.0007	0.0081	0.5858	Pass
	$X = 3$	0.6974	0.5222	0.0014	0.0025	Pass
	$X = 4$	0.2547	0.0258	0.9981	0.0097	Pass
Random excursions variants	$X = -7$	0.0145	0.1184	0.8894	0.0001	Pass
	$X = -6$	0.0021	0.0215	0.6235	0.0147	Pass
	$X = -5$	0.5449	0.0523	0.7412	0.9638	Pass
	$X = -4$	0.1254	0.9632	0.9632	0.9965	Pass
	$X = -3$	0.8025	1	0.5258	0.1963	Pass
	$X = -2$	0.3698	0.0639	0.0258	0.6687	Pass
	$X = -1$	0.2250	0.0259	0.2649	0.2991	Pass
	$X = 1$	0.5896	0.9417	0.3258	0.3447	Pass
	$X = 2$	0.1569	0.2698	0.0143	0.7319	Pass
	$X = 3$	0.0147	0.6943	0.0984	0.7982	Pass
	$X = 4$	0.2589	0.5861	0.9584	0.9963	Pass
	$X = 5$	0.1267	0.9974	0.7463	0.2210	Pass
	$X = 6$	0.0145	0.2255	0.8847	0.0009	Pass
	$X = 7$	0.0012	0.0006	0.3698	0.1717	Pass

Table 6: NPCR and UACI measures for standard images.

Image	NPCR			UACI		
	R	G	B	R	G	B
Baboon	99.57	99.64	99.60	34.46	33.42	33.14
Peppers	99.62	99.69	99.63	33.43	32.44	33.32
House	99.63	99.64	99.62	32.50	33.43	34.52
Brain	99.74	99.70	99.63	33.49	33.47	33.37
X-ray	98.82	98.64	98.72	32.45	34.03	34.12
Lena	99.60	99.62	99.58	33.49	33.48	34.62

Table 7: NPCR and UACI measures for different sizes of Lena images.

Image	NPCR			UACI		
	R	G	B	R	G	B
$128 \times 128 \times 3$	99.01	98.90	99.30	32.21	32.95	32.01
$256 \times 256 \times 3$	99.70	99.60	99.80	33.36	33.58	33.44
$512 \times 512 \times 3$	99.66	99.54	99.64	33.40	33.49	33.61
$1024 \times 1024 \times 3$	99.67	99.63	99.63	33.95	33.60	33.69

to initial conditions because it changes with the respective plaintext. Therefore, in the presented structure, the chosen-plaintext and the chosen-ciphertext attack do not give any information about the secret keys of the system. As a result, the presented cryptosystem can efficiently endure chosen and known-plaintext attacks.

4.8. Robustness Analysis. While encrypted images are transported across the public network, one must take care of the noise issue. The noise enhancement may seem in modification, damage, and a condensed procedure of image data. The high level of noise creates it meaningfully tricky to retrieve the original images from the enciphered images. Therefore, repelling noise is an important benchmark to examine the strength of the cryptosystem.

To examine the strength of the presented encryption scheme two types of noises are added. The decrypted images are understandable though different types of noises were provided. From the decrypted image maximum information

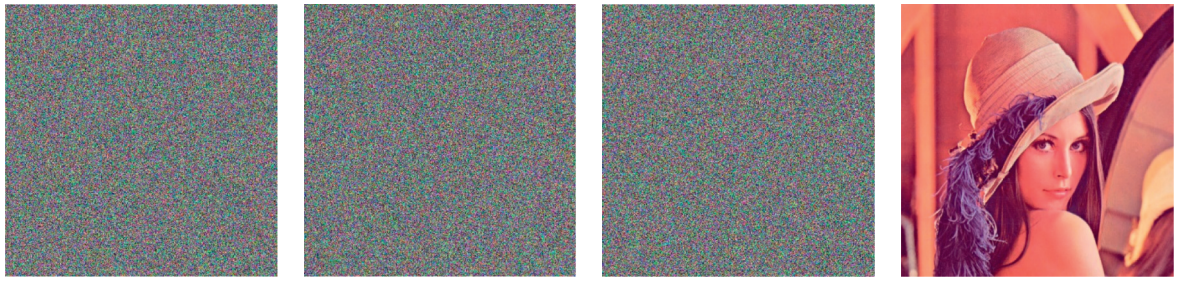

(a) (b) (c) (d)

Figure 7: (a–c) Images decrypted from one-bit change key; (d) Image decrypted from the original key.

can be recovered. To check the quality of decrypted images, various tests are carried out such as peak signal-to-noise ratio (PSNR), mean-square error (MSE), homogeneity, and contrast.

4.8.1. Mean Square Error (MSE). MSE is a square measure of the error (pixel difference) of two images, obtained by taking a square root of a square error dispersed by the number of pixels in the image. Mathematically, it can be written as

$$\mathrm{MSE} = \left[\frac{1}{H * W}\sum_{y=0}^{H-1}\sum_{x=0}^{W-1}\left(f(x,y) - f'(x,y)\right)^2\right]^{1/2}, \quad (10)$$

where MSE is the mean square error, in image cryptography that means a larger number of MSE possess better image encryption capability. Average MSE values greater than 6000 for each channel are shown in Table 5 which depicts that the presented scheme is highly secure.

4.8.2. Peak Signal to Noise Ratio (PSNR). PNSR is defined as

$$\mathrm{PSNR} = 10\ \log_{10}\left(\frac{(255)^2}{\mathrm{MSE}}\right), \quad (11)$$

a larger number of PSNR means better-deciphered images, and a smaller number means better image encryption.

The results of PSNR consequences of decrypted images with dissimilar levels of alterations are presented in Table 8. After incorporating numerous levels of noise concentrations in the encrypted image, it is perceived that the PSNR value reduces when noise concentration rises. The graphic excellence of the decrypted image is abridged, but the content is still noticeably predictable.

The PSNR value increases the fidelity of the encrypted picture to the original plain image [27]. When the PSNR is above 30 dB, it becomes difficult to distinguish between the original and decrypted pictures. The original Elaine test picture is encrypted twice. The resulting cipher pictures are then subjected to 33% data block loss, 99% data block loss, 0.005% Salt and Pepper noise, and 0.025% Salt and Pepper noise. Figures 8 show the outcomes for PSNR after including noise. In the 3×3 data block loss test, the proposed method provides a PSNR of slightly under 35 dB (excellent quality).

Table 8: MSE and PSNR measures for different standard images.

Image	MSE			PSNR		
	R	G	B	R	G	B
Baboon	9231.2	8911.0	8952.3	39.6011	36.7412	39.3691
Peppers	9742.2	10356.1	11652.1	37.0031	48.8523	39.0001
House	7763.2	9954.1	7633.11	38.3737	29.5698	47.1102
Brain	6953.1	7836.2	8951.9	47.0186	37.8142	29.0997
X-ray	8642.2	9214.2	8686.1	39.1796	48.6981	59.1475
Lena	6651.4	9961.0	10029.2	39.7865	49.1345	39.1239

PSNR lowers to around 21 dB when testing for 9×9 data block loss. A PSNR approaching 30 dB is achieved for the cipher image damaged by 0.005% Salt and Pepper noise. When the degradation reaches 0.02 percent, the PSNR nears 20 dB. Overall, the findings show that the suggested approach is somewhat robust to data loss and noise.

4.9. Execution Time Analysis. The speed at which an encryption-decryption method is executed is one of the most important quantifiable parameters. To determine the time for the presented system, three important processes are taken into consideration: parameter initialization, diffusion, and key-based substitution operation. Section 4 of this document contains a description of the presented system specification. Table 9 depicts the time requirements (in seconds) for encryption and decryption in this case. The demand for encryption and decryption time implies that the suggested algorithm is well-suited to dealing with a huge capacity of image data as compared to the existing results [30, 31].

Both the approximation of rounds as well as operations are required to achieve the enciphering and deciphering mechanism which is necessary to determine the computation difficulty. To estimate the computational complexity, the plain image had a dimension of $M \times M$ is assumed. Initially, the pixel-level scrambling technique requires $O(M \times M)$ time to complete. Following that, the keystream size is like the image size, $M \times M$, and $O(M \times M)$ is known as the complexity of generation in nature. Finally, the diffusion operation requires $O(M \times M)$. As a result, the encryption approach has a total time complexity $O(M^2)$.

Figure 8: Data loss and noise attacks on encrypted images. (a) The untouched encrypted image and (b) its decrypted image; (c) the encrypted image with 3×3 data block loss and (d) its decrypted image; (e) the encrypted image with 9×9 data block loss and (f) its decrypted image; (g) the encrypted image deteriorated with 0.005% Salt and Pepper noise and (h) its decrypted image; (i) the encrypted image deteriorated with 0.02% Salt and Pepper noise and (j) its decrypted image.

Table 9: Time complexity analysis (in seconds) of offered structure.

Image size	Parameter initialization	Diffusion	Key-based substitution	Encryption	Decryption
$128 \times 128 \times 3$	0.050	0.198	0.311	0.559	0.418
$256 \times 256 \times 3$	0.191	0.224	0.298	0.713	0.691
$512 \times 512 \times 3$	0.283	0.356	0.489	1.128	0.918
$1024 \times 1024 \times 3$	0.412	0.517	0.511	1.440	1.3111

5. Comparison Analysis

Some of the critical performance measures, including key space analysis, the NPCR and UACI analysis, the correlation coefficient test for adjacent pixel analysis, and information entropy, are used to compare the performance of the suggested encryption scheme to that of current works in this section. Table 10 illustrates the comparison results between the given performance metrics of a Lena picture size $256 \times 256 \times 3$ based on the suggested technique and the comparison results between existing methods. According to the tabulated results, the presented strategy outperforms the competition by a significant margin. One can see from Table 7 that the correlation in diagonal, horizontal, and vertical directions shows that the proposed scheme has significantly low correction values when compared to other state-of-the-art encryption schemes. Therefore, our proposed algorithm is perfect because it comprises ideal

Table 10: Comparison of statistical results of the suggested scheme with existing work.

Features	Proposed	Ref. [32]	Ref. [11]	Ref. [12]	Ref. [13]
Key space	2^{256}	2^{512}	2^{617}	2^{104}	2^{393}
Diagonal correlation					
R	0.0001	−0.0060	−0.0026	0.0091	0.0167
G	−0.0021	0.0127	−0.0039	−0.0012	0.0171
B	0.0003	−0.0041	0.0012	0.0089	0.0170
Horizontal correlation					
R	−0.0031	−0.0033	−0.0029	0.0681	0.0021
G	−0.0011	−0.0067	−0.0032	0.0682	0.0023
B	0.0003	−0.0005	0.0040	0.0683	0.0024
Vertical correlation					
R	−0.0001	0.0055	0.0013	−0.0081	0.0017
G	0.0031	−0.0048	−0.0032	0.0040	0.0013
B	−00019	−0.0016	−0.0018	−0.0039	0.0011
NPCR					
R	99.60	99.51	99.60	99.87	99.57
G	99.62	99.53	99.61	99.88	99.56
B	99.58	99.54	99.61	99.89	99.57
UACI					
R	33.49	33.37	33.56	33.47	33.81
G	33.48	33.39	33.45	33.49	33.83
B	34.62	33.37	33.49	33.48	33.81
Information entropy					
R	7.9990	7.9992	7.9973	7.9953	7.9874
G	7.9992	7.9992	7.9969	7.9953	7.9871
B	7.9993	7.9992	7.9971	7.9953	7.9866

correlation values. NPCR and UACI of the proposed scheme are greater than 99.6 and 34, respectively. Our offered algorithm possesses perfect values of NPCR and UACI measures as compared to recently proposed work. The information entropy of the proposed scheme is near to the ideal value of 8 and it is also greater than other schemes. The greater value of information entropy as compared to other schemes indicates the robustness of the offered encryption algorithm. Through the comparison table, it is evident that the proposed scheme security is higher. However, the key space of the proposed scheme is lower than Reference [32], Reference [11], and Reference [13]. In the future, we will use coupled multi-chaotic maps for the higher key space.

6. Conclusion

Ensuring data security during the processes of communication and storage is mandatory these days as potential information leakage might have unwanted consequences. In this work, LFSR and chaos-based quantum map image encryption algorithm is presented. Both confusion and diffusion steps are utilized in the presented encryption. The proposed methodology can be used to encrypt images of different sizes. The entropy values of the encrypted images are significantly high when compared to the entropy values of original images. The presented scheme provides a security layer for images, and its effectiveness was validated through various experimental results such as key space and key sensitivity analysis. Furthermore, the proposed scheme has low correlation values and higher NPCR, and UACI test results. The algorithm is resistant to most known attacks such as differential and statistical attacks etc. These security metrics prove that the proposed scheme achieved a higher security level, and it is well suited for digital image encryption for robust communications. The suggested technique has a low computing overhead and produces a secure ciphertext image within a few seconds. Our work can be further improved and modified to encrypt sensor data, biomedical data [33, 34] in the future. Furthermore, the system can be improved using the concept of parallelism to encrypt massive amounts of multimedia data.

Data Availability

The data used to support the findings of this study are available from the corresponding author upon request.

Consent

Not Applicable.

Conflicts of Interest

The authors declare no conflict of interest.

Authors' Contributions

Institutional Review Board Statement: not applicable. *Human and Animals' rights*. This article does not contain any studies with human participants or animals performed by any of the authors.

Acknowledgments

One of the authors, Sajjad Shaukat Jamal, extends his gratitude to the Deanship of Scientific Research at King Khalid University for funding this work through a research group program under grant number R. G. P. 1/399/42.

References

[1] A. Churcher, R. Ullah, J. Ahmad et al., "An experimental analysis of attack classification using machine learning in IoT networks," *Sensors*, vol. 21, no. 2, p. 446, 2021.

[2] A. Qayyum, J. Ahmad, W. Boulila et al., "Chaos-based confusion and diffusion of image pixels using dynamic substitution," *IEEE Access*, vol. 8, Article ID 140876, 2020.

[3] F. Masood, J. Ahmad, S. A. Shah, S. S. Jamal, and I. Hussain, "A novel hybrid secure image encryption based on julia set of fractals and 3D Lorenz chaotic map," *Entropy*, vol. 22, no. 3, p. 274, 2020.

[4] M. V. Berry, N. L. Balazs, M. Tabor, and A. Voros, "Quantum maps," *Annals of Physics*, vol. 122, no. 1, pp. 26–63, 1979.

[5] N. L. Balazs and A. Voros, "The quantized Baker's transformation," *Annals of Physics*, vol. 190, no. 1, pp. 1–31, 1989.

[6] M. Saraceno, "Classical structures in the quantized baker transformation," *Annals of Physics*, vol. 199, no. 1, pp. 37–60, 1990.

[7] R. X. D. Schack and C. M. Caves, "Shifts on a finite qubit string: a class of quantum baker's maps," *Applicable Algebra in Engineering, Communication and Computing*, vol. 10, no. 4-5, pp. 305–310, 2000.

[8] N. Meenakshisundaram, *Studies in Quantum Chaos: From an Almost Exactly Solvable Model to Hypersensitive Operators*, Ph.D. thesis, Indian Institute of Technology Madras, Chennai, 2010.

[9] S. Graffi and M. Degli Esposti, "The mathematical aspects of quantum maps," *Lecture Notes in Physics*, Springer, vol. 618, , 2003.

[10] F. Haake, *Quantum Signatures of Chaos*, Springer, NewYork, NY, USA, 2000.

[11] X. Chai, X. Fu, Z. Gan, Y. Lu, and Y. Chen, "A color image cryptosystem based on dynamic DNA encryption and chaos," *Signal Processing*, vol. 155, pp. 44–62, 2019.

[12] P. Praveenkumar, N. Kerthana Devi, D. Ravichandran et al., "Transreceiving of encrypted medical image - a cognitive approach," *Multimedia Tools and Applications*, vol. 77, no. 7, pp. 8393–8418, 2018.

[13] A. Kadir, A. Hamdulla, and W.-Q. Guo, "Color image encryption using skew tent map and hyper chaotic system of 6th-order CNN," *Optik*, vol. 125, no. 5, pp. 1671–1675, 2014.

[14] F. Masood, W. Boulila, J. Ahmad et al., "A novel privacy approach of digital aerial images based on mersenne twister method with DNA genetic encoding and chaos," *Remote Sensing*, vol. 12, no. 11, p. 1893, 2020.

[15] F. Masood, M. Driss, W. Boulila et al., "A lightweight chaos-based medical image encryption scheme using random shuffling and XOR operations," *Wireless Personal Communications*, pp. 1–29, 2021.

[16] S. A. Shah, J. Ahmad, F. Masood et al., "Privacy-preserving wandering behavior sensing in dementia patients using modified logistic and dynamic Newton Leipnik maps," *IEEE Sensors Journal*, vol. 21, no. 3, pp. 3669–3679, 2021.

[17] K. K. Butt, G. Li, F. Masood, and S. Khan, "A digital image confidentiality scheme based on pseudo-quantum chaos and Lucas sequence," *Entropy*, vol. 22, no. 11, p. 1276, 2020.

[18] S. K. Bishoi, H. K. Haran, and S. U. Hasan, "A note on the multiple-recursive matrix method for generating pseudo-random vectors," *Discrete Applied Mathematics*, vol. 222, pp. 67–75, 2017.

[19] G. Zeng, W. Han, and K. He, "High Efficiency Feedback Shift Register: σ–LFSR," 2007, https://eprint.iacr.org/2007/114. Cryptology ePrint Archive, Report 2007/114.

[20] J. Zhang and D. Huo, "Image encryption algorithm based on quantum chaotic map and DNA coding," *Multimedia Tools and Applications*, vol. 78, no. 11, pp. 15605–15621, 2019.

[21] Y. Dong, X. Huang, Q. Mei, and Y. Gan, "Self-Adaptive Image Encryption Algorithm Based on Quantum Logistic Map," *Security and Communication Networks*, vol. 2021, Article ID 6674948, 12 pages, 2021.

[22] A. Ahmed, L. Abd El, L. Li, N. Wang, H. Qi, and X. Niu, A new approach to chaotic image encryption based on quantum chaotic system, exploiting color spaces," *Signal Processing*, vol. 93, no. 11, pp. 2986–3000, 2013.

[23] R. Graham, T. Tel, and S. Isermann, "Quantization of Hanon's map with dissipation," *Zeitschrift for Physik B Condensed Matter*, vol. 60, no. 2-4, pp. 127–136, 1985.

[24] M. E. Goggin, B. Sundaram, and P. W. Milonni, "Quantum logistic map," *Physical Review A*, vol. 41, no. 10, pp. 5705–5708, 1990.

[25] A. J. Michaels, "Quantitative comparisons of digital chaotic circuits for use in communications," *Proceedings of the Joint INDS'11 & ISTET'11*, vol. 11, pp. 1–8, 2011.

[26] C. E. Shannon, "Communication theory of secrecy systems," *Bell System Technical Journal*, vol. 28, no. 4, pp. 656–715, 1949.

[27] E. Yavuz, "A novel chaotic image encryption algorithm based on content-sensitive dynamic function switching scheme," *Optics & Laser Technology*, vol. 114, pp. 224–239, 2019.

[28] Z. Hua, F. Jin, B. Xu, and H. Huang, "2D Logistic-Sine-coupling map for image encryption," *Signal Processing*, vol. 149, pp. 148–161, 2018.

[29] Y. Wu, "NPCR and UACI randomness tests for image encryption," *Cyber Journals: Journal of Selected Areas in Telecommunications*, pp. 31–38, 2011.

[30] S. Amina and F. K. Mohamed, "An efficient and secure chaotic cipher algorithm for image content preservation," *Communications in Nonlinear Science and Numerical Simulation*, vol. 60, pp. 12–32, 2018.

[31] E. Yavuz, "A new parallel processing architecture for accelerating image encryption based on chaos," *Journal of Information Security and Applications*, vol. 63, Article ID 103056, 2021.

[32] D. S. Laiphrakpam and M. S. Khumanthem, "A robust image encryption scheme based on chaotic system and elliptic curve over finite field," *Multimedia Tools and Applications*, vol. 77, no. 7, pp. 8629–8652, 2018.

[33] J. Masood, M. Shahzad, Z. A. Khan et al., "Effective classification algorithms and feature selection for bio-medical data using IoT," in *Proceedings of the 2020 Seventh International Conference on Information Technology Trends (ITT)*, pp. 42–47, IEEE, Abu Dhabi, UAE, November 2020.

[34] K. Driss, W. Boulila, A. Batool, and J. Ahmad, "A novel approach for classifying diabetes' patients based on imputation and machine learning," in *Proceedings of the 2020 International Conference on UK-China Emerging Technologies (UCET)*, pp. 1–4, IEEE, Glasgow, UK, August 2020.

Hindawi
Complexity
Volume 2022, Article ID 2078372, 18 pages
https://doi.org/10.1155/2022/2078372

Research Article

Finite Difference Computation of *Au-Cu*/Magneto-Bio-Hybrid Nanofluid Flow in an Inclined Uneven Stenosis Artery

H. Thameem Basha,[1] **Karthikeyan Rajagopal**,[1] **N. Ameer Ahammad**,[2] **S. Sathish**,[3] **and Sreedhara Rao Gunakala**[4]

[1]*Centre for Nonlinear Systems, Chennai Institute of Technology, Chennai, India*
[2]*Department of Mathematics, University of Tabuk, Tabuk 71491, Saudi Arabia*
[3]*School of Mathematics and Statistics, MIT-WPU, Pune, India*
[4]*Department of Mathematics and Statistics, The University of the West Indies, St.Augustine, Kingston, Jamaica*

Correspondence should be addressed to H. Thameem Basha; thameembashah@citchennai.net

Received 21 December 2021; Accepted 8 March 2022; Published 12 April 2022

Academic Editor: Mustafa Cagri Kutlu

The present study addresses the fluid transport behaviour of the flow of gold (*Au*)-copper (*Cu*)/biomagnetic blood hybrid nanofluid in an inclined irregular stenosis artery as a consequence of varying viscosity and Lorentz force. The nonlinear flow equations are transformed into dimensionless form by using nonsimilar variables. The finite-difference technique (FTCS) is involved in computing the nonlinear transport dimensionless equations. The significant parameters like angle parameter, the Hartmann number, changing viscosity, constant heat source, the Reynolds number, and nanoparticle volume fraction on the flow field are exhibited through figures. Present results disclose that the Lorentz force strongly lessens the hybrid nanofluid velocity. Elevating the Grashof number values enhances the rate of blood flow. Growing values of the angle parameter cause to reduce the resistance impedance on the wall. Hybrid nanoparticles have a superior wall shear stress than copper nanoparticles. The heat transfer rate is amplifying at the axial direction with the growing values of nanoparticles concentration. The applied Lorentz force significantly reduces the hybrid and unitary nanofluid flow rate in the axial direction. The hybrid nanoparticles expose a supreme rate of heat transfer than the copper nanoparticles in a blood base fluid. Compared to hybrid and copper nanofluid, the blood base fluid has a lower temperature.

1. Introduction

In the physiology system, the heart is the primary organ that plays a vital role in circulating the oxygenated blood to other organs via arteries. The active and proper functioning of the heart is essential for a healthy life cycle. Improper blood transportation in the circulatory system and cardiac-related issues have been the cause of most physical illnesses and death in recent times. Based on the World Health Organization (WHO) report, 30% of deaths in 2008 were related to cardiac disease [1–3]. Most cardiac diseases are caused by cellular waste products, deposits of cholesterol, fibrin, calcium, and buildup of fatty substances in the lumen of the arteries or the formation of plaques. Such plaque formation in the arteries contributes to obstructing blood circulation flow, and this cardiac disease is perceived as stenosis. Besides, the accumulation of fatty substances on the blood vessels walls leads to heart attacks, blood clots, impeding the blood supply, myocardial infarction, and cerebral strokes. Changdar and De [4] scrutinized the impact of inclination on three different nanoparticles (silver, copper, and gold) cases in blood nanofluid flow in a multiple stenosis artery and observed that the wall exhibits low shear stress in the absence of angle parameter. Zaman et al. [5] reported the transport behaviour of silver and aluminium oxide hybrid blood nanofluid flow in a vertical stenotic artery and showed that the unity nanofluid has a higher temperature than the hybrid nanofluid. Tripathi et al. [6] utilized the explicit

forward time step approach to scrutinize the flow of gold (Ag)-silver (Au)/blood hybrid nanofluid in irregular stenosis with the variable viscosity and noted that the variable viscosity parameter promotes the hybrid nanofluid axial velocity. Das et al. [7] explained the impacts of Hall current and inclination on hybrid blood nanofluid flow in a mild stenosis artery and reported that the growing values of the Grashof number elevate the blood velocity. Some studies about the blood fluid flow can be found in references [8–17].

The physiological fluids that are affected by the external magnetic field and magnetization are dubbed biomagnetic fluids. In recent times, researchers give much attention to the examination of biomagnetic fluid because it has significant applications in biomedical and bioengineering, including targeted drug delivery, cell separation, magnetic wound treatment, reduction of bleeding during surgeries, medical devices (magnetic tracers and blood pumps), and magnetic hyperthermia. It is noticed that the blood is one of the relevant examples of a biomagnetic fluid because it have the cell membrane, haemoglobin compound interface, and intercellular protein. Besides, the unadulterated blood is experienced less impact with the magnetic field. Therefore, in such cases, notable magnetic fields strength is essential to influence its flow. It is observed that artificially suspending nanoparticles with magnetic behaviour can greatly promote the magnetization of the blood. Further, blood containing such magnetic nanoparticles refuses the diamagnetic material or discarding paramagnetic and leads to behaving as a ferromagnetic fluid; as a result, fluid velocity rises gradually. Misra and Shit [18] addressed the influence of magnetic dipole on the flow of viscoelastic biomagnetic fluid past an extending surface and observed that the ferromagnetic interaction parameter diminishes the biomagnetic axial velocity. Murtaza et al. [19] performed a numerical study with the aim to express fluid transport behaviour of maxwell biomagnetic fluid flow over an extending surface and pointed out the rate of heat transfer is reduced with the rising values of magnetic field. Maiti et al. [20] employed the Caputo-Fabrizio (CF) derivative model to examine the biomagnetic blood fluid flow in a porous vessel and found that the thermal radiation and the Schmidt number decline the blood concentration. The flow of biomagnetic fluid through a normal duct in the presence of magnetic dipole and Lorentz force was scrutinized by Mousavi et al. [21] and noticed that the Lorentz force near the constricted zone lessens the wall shear stress. Some notable studies on blood flow with the impact of the magnetic field are exposed through Refs. [22–29].

Numerous researchers and engineers have paid significant attention to nanotechnology because it is used in several practical situations, for instance, biochemical engineering and medical industries. Several nanoparticles like silver, copper, gold, and ferrite particles are utilized in proteins, delivery of drugs, nucleic acids, vaccines, and genes [30–33]. Because these nanoparticles exhibit high biocompatibility, magnetic, chemical, unique mechanical, and thermal effects. It is observed that gold (atomic number = 79) nanoparticles have much popularity in biomedical applications for RNA quantification (via optical biosensors) and treating malignant tumours owing to unique quenching efficiencies, targeting ligands, significant surface modifiability, and imaging probes when comparing with other nanoparticles [34–38]. Besides, the gold nanoparticles exhibit a nontoxic behaviour in biological media. Gold nanoparticles have a unique optical behavior, which is more relevant for several therapeutic applications (photothermal and radiotherapy for eradicating cancer cells) and diagnostic approaches (cell imaging, computed tomography, and optical imaging). It is important to mention that the gold nanoparticles can be remarkably functionalized with DNA, proteins, antibodies, polyelectrolyte, and ligands. Koriko et al. [39] examined the heat transfer behaviour of gold-blood Carreau nanofluid flow with the influence of partial slip and that the elevating gold nanoparticle concentration tends to diminish the rate of heat transfer. Kumar and Srinivas [40] employed the Maxwell Garnett and Brinkman models (thermophysical property model) to analyze the flow of gold blood nanofluid in a channel and found that the gold nanoparticles have a less temperature in the blood than the aluminium oxide. Khan et al. [41] conducted a numerical study to determine the impact of nonlinear radiation on Casson gold–blood nanofluid flow over an extending spinning disk and noticed that the blood temperature rises by elevating nanoparticle volume fraction. Bhatti [42] explored the Jeffrey-gold intrauterine nanofluid flow through an asymmetric channel by means of linear thermal radiation and showed that thermal radiation maximizes Jeffrey blood temperature. Most science and engineering problems are usually in the form of nonlinear boundary value problems (BVPs). The solution of such nonlinear problems plays a significant role in understanding science and engineering systems. It is noticed that most of the nonlinear BVPs are partial differential equations (PDEs). Numerous numerical and analytical approaches are available in the literature to solve such PDEs. In that, the explicit finite-difference FTCS method is one of the notable approaches, and it is described in Hoffmann's book [43]. It is essential to mention that many researchers extensively used FTCS in fluid mechanical and biomechanical problems [44, 45]. Further, it is revealed that this scheme is stable, rapidly convergent, and easy to program.

The motivation of this current analysis is that for the applications in targeted nano-drug delivery systems. Besides, this numerical simulation's primary purpose is to effectively carry out the decision-making process during arterial disease treatment. In recent times, targeting the nano-drugs at the stenosis region is the trending and influential approach compared to the conventional treatment method. The nano-drug delivery improves the stenosis throat's clotting formation; further, this computational simulation can also predict the effects of post-treatment processes. It is witnessed from the above literature that several studies explore the blood flow in different types of stenosis arteries with numerous physical aspects. However, no study has focused on the gold and copper/blood nanofluid flow in an uneven inclined stenosis artery in the presence of a magnetic field, viscous dissipation, and heat generation. Further, the gold and copper [46, 47] nanoparticles have predominant

applications in drug targeting, wound treatment, cancer diagnosis, cardiovascular treatment, and chemotherapy. With these enthused, the current framework focuses on biomagnetic gold-copper blood hybrid nanofluid flow in an irregular inclined stenosis artery utilizing varying viscosity and Lorentz force. By means of nonsimilar variables, the dimensional flow equations are reduced in dimensionless form. The finite-difference approach is executed to compute the reduced flow equations. The physical parameters that arise from the regime equations are projected through graphs.

2. Mathematical Formulation

This model considers time-dependent two-dimensional biomagnetic gold-copper hybrid nanofluid flow in an inclined irregular stenosis artery, and the schematic model is exhibited in Figure 1. The nanoparticle volume fraction model is utilized to scrutinize the biomagnetic blood flow. It is noted that the gold and copper nanoparticles are suspended in the biomagnetic blood fluid, and the thermophysical properties of the base fluid (blood) and nanomaterial (gold and copper) are provided in Table 1. The strength of Lorentz force is executed in the transverse to the blood flow direction. For this modelling, the two-dimensional cylindrical coordinate (r, θ, z) system is employed, and r and z are represented as the artery radial and axial coordinates (Tripathi et al. [6]).

$$R(z) = \begin{cases} R_0 - 2\delta\left[\cos\left(\left(\frac{z-d}{2} - \frac{l_0}{4}\right)2\pi\right) - \frac{7}{100}\cos\left(\left(z - d - \frac{l_0}{2}\right)32\pi\right)\right], & d < z < d + l_0 \\ R_0, \quad \text{otherwise} \end{cases}, \tag{1}$$

where δ is the stenosis depth, d is the stenosis distance from origin, z is the axial co-ordinate, and l_0 is the stenosis length.

In this model, the blood nanofluid flowing is unsteady and bidirectionally; the velocity and temperature can be expressed as

$$\begin{aligned} &\text{Velocity: } V = [\overline{u}(r,z,t), 0, \overline{w}(r,z,t)], \\ &\text{Temperature: } T = T(r,z,t). \end{aligned}, \tag{2}$$

where $\overline{u}$ and $\overline{w}$ have denoted the of components radial and axial velocities. With these frameworks, the governing flow equations are written as follows (Zaman et al. [5], Tripathi et al. [6, 45], Das et al. [7], and Rathore and Srikanth [16]):

$$\frac{\partial \overline{u}}{\partial \overline{r}} + \frac{\overline{u}}{\overline{r}} + \frac{\partial \overline{w}}{\partial \overline{z}} = 0. \tag{3}$$

$$\begin{aligned} (\rho_{\text{hnf}})\left(\frac{\partial \overline{u}}{\partial \overline{t}} + \overline{u}\frac{\partial \overline{u}}{\partial \overline{r}} + \overline{w}\frac{\partial \overline{u}}{\partial \overline{z}}\right) = &-\frac{\partial \overline{p}}{\partial \overline{r}} + \frac{1}{\overline{r}}\left[\frac{\partial}{\partial \overline{r}}\left(\mu_{\text{hnf}}(T)\frac{\partial \overline{u}}{\partial \overline{r}}\right) - 2\mu_{\text{hnf}}(T)\frac{\overline{u}}{\overline{r}}\right] \\ &+ \frac{\partial}{\partial \overline{z}}\left(\mu_{\text{hnf}}(T)\left(\frac{\partial \overline{u}}{\partial \overline{z}} + \frac{\partial \overline{w}}{\partial \overline{r}}\right)\right) - g(\gamma\rho)_{\text{hnf}}(T - T_1)\cos(\alpha). \end{aligned} \tag{4}$$

$$\begin{aligned} (\rho_{\text{hnf}})\left(\frac{\partial \overline{w}}{\partial \overline{t}} + \overline{u}\frac{\partial \overline{w}}{\partial \overline{r}} + \overline{w}\frac{\partial \overline{w}}{\partial \overline{z}}\right) = &-\frac{\partial \overline{p}}{\partial \overline{z}} + \frac{1}{\overline{r}}\frac{\partial}{\partial \overline{r}}\left(r\mu_{\text{hnf}}(T)\left(\frac{\partial \overline{u}}{\partial \overline{z}} + \frac{\partial \overline{w}}{\partial \overline{r}}\right)\right) \\ &+ \frac{\partial}{\partial \overline{z}}\left(2\mu_{\text{hnf}}(T)\frac{\partial \overline{w}}{\partial \overline{z}}\right) + g(\gamma\rho)_{\text{hnf}}(T - T_1)\sin(\alpha) - \sigma_{\text{hnf}}B_0^2 w. \end{aligned} \tag{5}$$

$$\left(\rho C_p\right)_{\text{hnf}}\left(\frac{\partial T}{\partial \overline{t}} + \overline{u}\frac{\partial T}{\partial \overline{r}} + \overline{w}\frac{\partial T}{\partial \overline{z}}\right) = k_{\text{hnf}}\left(\frac{\partial^2 T}{\partial \overline{r}^2} + \frac{1}{\overline{r}}\frac{\partial T}{\partial \overline{r}} + \frac{\partial^2 T}{\partial \overline{z}^2}\right) + Q_0. \tag{6}$$

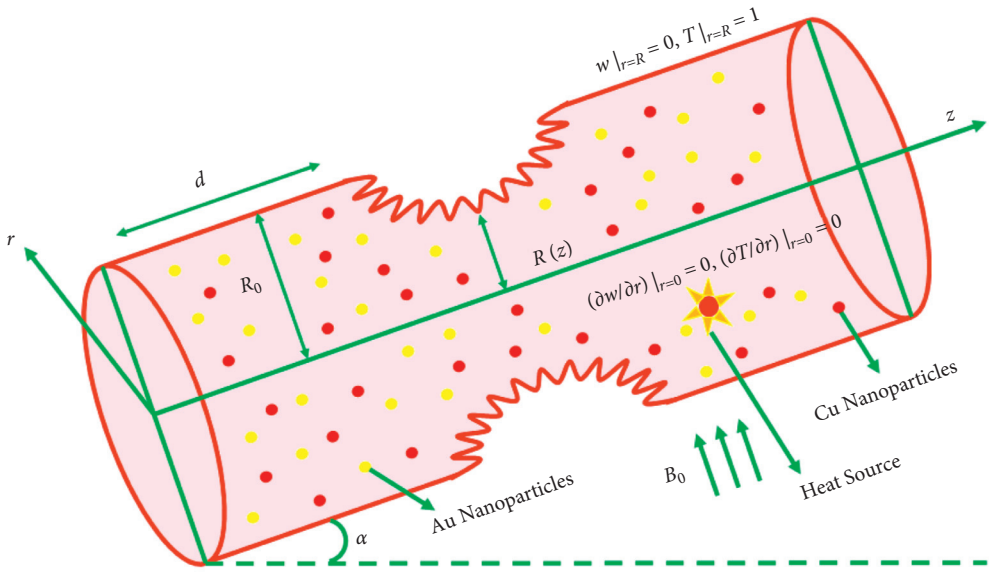

Figure 1: Physical configuration of the problem.

Table 1: Values of the various physical parameters (blood, gold and copper) (Das et al. [7], Koriko [39], and Kumar and Srinivas [40]).

Physical properties	Blood	Gold (Au)	Copper (Cu)
ρ (kg/m^3)	1063	19320	8933
C_p (J/kgK)	3594	129	385
$\gamma \times 10^{-5}$ (K^{-1})	0.18	1.4	1.67
k (W/mK)	0.492	314	401
σ (S/m)	6.67×10^{-1}	4.10×10^{7}	59.6×10^{6}

In the foregoing equation, α is the angle parameter, Q_0 is the constant heat source parameter, B_0 is the uniform magnetic field, ρ_{hnf} is the density, $\overline{t}$ is the time, $\overline{p}$ is the pressure, $\overline{r}$ is the radial coordinate, k_{hnf} is the thermal conductive, μ_{hnf} is the dynamic viscosity, T is the temperature, γ_{hnf} is the thermal expansion, g is the gravitational acceleration, σ_{hnf} is the electrical conductivity, $(C_p)_{\mathrm{hnf}}$ is the specific heat capacity, and subscript hnf is the hybrid nanofluid.

The relevant limiting conditions are expressed as follows:

$$\left.\begin{aligned} w(R,t) = 0, \frac{\partial w(0,t)}{\partial r} = 0, w(r,0) = 0, \\ T(R,t) = 1, \frac{\partial T(0,t)}{\partial r} = 0, T(r,0) = 0. \end{aligned}\right\}. \tag{7}$$

The governing nonlinear flow equations are transformed by suitable nonsimilar variables, which are shown as follows (Zaman et al. [5] and Tripathi et al. [6, 45]):

$$\begin{aligned} r &= \frac{\overline{r}}{R_0}, \\ z &= \frac{\overline{z}}{l_0}, \\ \overline{p} &= \frac{R_0^2 P}{U_0 l_0 \mu_f}, \\ u &= \frac{l_0 \overline{u}}{\delta^* U_0}, \\ \theta &= \frac{T - T_1}{T_w - T_1}, \\ w &= \frac{\overline{w}}{U_0}, \\ R &= \frac{\overline{R}}{R_0}, \\ t &= \frac{U_0 \overline{t}}{R_0}, \\ d &= \frac{\overline{d}}{l_0}. \end{aligned} \tag{8}$$

Here, U_0 is the reference velocity, $G_r = g\rho_f R_0^2 \gamma_f (T_w - T_1)/U_0\mu_f$ is the Grashof number, T_w is the wall temperature, $M_a = \sqrt{\sigma_f/\mu_f} B_0 R_0$ is the Hartmann number, $\varepsilon = R_0/l_0$ is the vessel aspect ratio, $\Pr = (C_p)_f \mu_f / k_f$ is the Prandtl number, $\delta = \delta^*/R_0$ is the stenosis height parameter, and $R_e = U_0\rho_f R_0/\mu_f$ is the Reynolds number.

By employing the above variables in equations (3)–(6), the transformed equations are as follows:

$$
\begin{aligned}
&\delta\left(\frac{\partial u}{\partial r} + \frac{u}{r}\right) + \frac{\partial w}{\partial z} = 0,\\
&R_e\left(\frac{\rho_{\mathrm{hnf}}}{\rho_f}\right)\delta\varepsilon^2\left(\frac{\partial u}{\partial t} + (\delta\varepsilon)u\frac{\partial u}{\partial r} + \varepsilon w\frac{\partial u}{\partial z}\right) = -\frac{\partial p}{\partial r} + \left(\frac{\delta R_0}{l_0^2\mu_0}\right)\frac{1}{r}\frac{\partial}{\partial r}\left(\mu_{\mathrm{hnf}}(\theta)\frac{\partial u}{\partial r}\right)\\
&+\left(\frac{\varepsilon^2 R_0}{\mu_0}\right)\frac{\partial}{\partial z}\left(\mu_{\mathrm{hnf}}(\theta)\left(\frac{\delta\varepsilon}{l_0}\frac{\partial u}{\partial z} + \frac{1}{R_0}\frac{\partial w}{\partial r}\right)\right)\\
&-2\left(\frac{\delta\varepsilon^2}{\mu_0}\right)\mu_{\mathrm{hnf}}(\theta)\left(\frac{u}{r^2}\right) - \left(\frac{(\rho\gamma)_{\mathrm{hnf}}}{(\rho\gamma)_f}\right)\varepsilon\cos(\alpha)G_r\theta,\\
&R_e\left(\frac{\rho_{\mathrm{hnf}}}{\rho_f}\right)\left(\frac{\partial w}{\partial t} + (\delta\varepsilon)u\frac{\partial w}{\partial r} + \varepsilon w\frac{\partial w}{\partial z}\right) = -\frac{\partial p}{\partial z} + \frac{1}{r}\frac{\partial}{\partial r}\left(\frac{r\mu_{\mathrm{hnf}}(\theta)}{\mu_0}\left\{\delta\varepsilon^2\frac{\partial u}{\partial z} + \frac{\partial w}{\partial r}\right\}\right)\\
&+\varepsilon^2\frac{\partial}{\partial z}\left(\frac{2\mu_{\mathrm{hnf}}(\theta)}{\mu_0}\frac{\partial w}{\partial z}\right) + \left(\frac{(\rho\gamma)_{\mathrm{hnf}}}{(\rho\gamma)_f}\right)G_r\theta\sin(\alpha) - \frac{\sigma_{\mathrm{hnf}}}{\sigma_f}M_a^2 w,\\
&R_e\Pr\left(\frac{k_f}{k_{\mathrm{hnf}}}\right)\left(\frac{\left(\rho C_p\right)_{\mathrm{hnf}}}{\left(\rho C_p\right)_f}\right)\left(\frac{\partial\theta}{\partial t} + (\delta\varepsilon)u\frac{\partial\theta}{\partial r} + \varepsilon w\frac{\partial\theta}{\partial z}\right)\\
&=\left(\frac{\partial^2\theta}{\partial r^2} + \frac{1}{r}\frac{\partial\theta}{\partial r} + \varepsilon^2\frac{\partial^2\theta}{\partial z^2}\right) + \left(\frac{k_f}{k_{\mathrm{hnf}}}\right)\beta.
\end{aligned}
\tag{9}
$$

Usually, in a biological system, the viscosity of blood is not constant in all cases since it varies due to several factors such as hematocrit ratio, vessel width, temperature, and axial or radial coordinates. Such a viscosity variation causes several reality cases, including decreasing blood thickness, rising of blood circulation, lowering coagulation factors, and maximizing blood flow. To capture these behaviours, in this model, the blood nanofluid viscosity is considered dependent on fluid temperature, which is given as (Zaman et al. [5])

$$
\mu_f(\theta) = \mu_0 e^{-\eta_0\theta}, \quad \text{where } e^{-\eta_0\theta} = 1 - \eta_0\theta, \quad \eta_0 \ll 1, \tag{10}
$$

where η_0 is the viscosity constant.

The density, thermal conductivity, electrical conductivity, thermal expansion, dynamic viscosity, and specific heat capacity of the nanofluid and hybrid nanofluid are (Tripathi et al. [6] and Das et al. [7])

$$
\left.
\begin{aligned}
&\rho_{\mathrm{nf}} = \phi\rho_s + (1-\phi)\rho_f, \sigma_{\mathrm{nf}} = \sigma_f\left(\frac{3\left(\sigma_s/\sigma_f - 1\right)\phi}{\left(\sigma_s/\sigma_f + 2\right) - \phi\left(\sigma_s/\sigma_f - 1\right)} + 1\right),\\
&\left(\rho C_p\right)_{\mathrm{nf}} = \phi\left(\rho C_p\right)_s + (1-\phi)\left(\rho C_p\right)_f, \mu_{\mathrm{nf}} = \frac{\mu_f}{(1-\phi)^{2.5}},\\
&k_{\mathrm{nf}} = k_f\left(\frac{k_s + 2k_f - 2\phi\left(k_f - k_s\right)}{k_s + 2k_f + \phi\left(k_f - k_s\right)}\right), (\rho\gamma)_{\mathrm{nf}} = \phi(\rho\gamma)_s + (1-\phi)(\rho\gamma)_f.
\end{aligned}
\right\},
$$

$$\left.\begin{aligned}
&\rho_{\mathrm{hnf}} = \left(\phi_1\rho_{s_1} + (1-\phi_1)\rho_f\right)(1-\phi_2) + \phi_2\rho_{s_2}, \mu_{\mathrm{hnf}} = \frac{\mu_f(\theta)}{(1-\phi_1)^{2.5}(1-\phi_2)^{2.5}},\\
&\frac{\sigma_{\mathrm{hnf}}}{\sigma_{\mathrm{bf}}} = \frac{\sigma_{s_2} + 2\sigma_{\mathrm{bf}} - 2\phi_2\left(\sigma_{\mathrm{bf}} - \sigma_{s_2}\right)}{\sigma_{s_2} + 2\sigma_{\mathrm{bf}} + \phi_2\left(\sigma_{\mathrm{bf}} - \sigma_{s_2}\right)}, \frac{k_{\mathrm{hnf}}}{k_{\mathrm{bf}}} = \frac{k_{s_2} + 2k_{\mathrm{bf}} - 2\phi_2\left(k_{\mathrm{bf}} - k_{s_2}\right)}{k_{s_2} + 2k_{\mathrm{bf}} + \phi_2\left(k_{\mathrm{bf}} - k_{s_2}\right)},\\
&\left(\rho C_p\right)_{\mathrm{hnf}} = \left(\phi_1\left(\rho C_p\right)_{s_1} + (1-\phi_1)\left(\rho C_p\right)_f\right)(1-\phi_2) + \phi_2\left(\rho C_p\right)_{s_2},\\
&(\rho\gamma)_{\mathrm{hnf}} = \left(\phi_1(\rho\gamma)_{s_1} + (1-\phi_1)(\rho\gamma)_f\right)(1-\phi_2) + \phi_2(\rho\gamma)_{s_2},\\
&\text{where } \frac{\sigma_{\mathrm{bf}}}{\sigma_f} = \frac{\sigma_{s_1} + 2\sigma_f - 2\phi_1\left(\sigma_f - \sigma_{s_1}\right)}{\sigma_{s_1} + 2\sigma_f + \phi_1\left(\sigma_f - \sigma_{s_1}\right)}, \frac{k_{\mathrm{bf}}}{k_f} = \frac{k_{s_1} + 2k_f - 2\phi_1\left(k_f - k_{s_1}\right)}{k_{s_1} + 2k_f + \phi_1\left(k_f - k_{s_1}\right)}.
\end{aligned}\right\}, \tag{11}$$

where μ_f, σ_f, $(C_p)_f$, ρ_f, γ_f, and k_f are the viscosity, electrical conductivity, specific heat capacity, density, thermal expansion, and thermal conductivity of the base fluid, (ϕ_1, ϕ_2) is the nanoparticle volume fraction, subscript s_1, bf, and s_2 are the first solid particle, base fluid, and second solid particle.

It is observed that compared with the artery radius, the stenosis maximum height is small, and the further length of the stenotic region and artery radius is of comparable magnitude. Therefore, the dimensionless flow equations are minimized with the following hypothesis $\delta \ll 1$ and $\varepsilon = \mathrm{O}(1)$. By employing these hypotheses, the reduced equations are

$$\frac{\partial w}{\partial z} = 0,$$

$$\frac{\partial p}{\partial r} = 0,$$

$$R_e\left(\frac{\rho_{\mathrm{hnf}}}{\rho_f}\right)\left(\frac{\partial w}{\partial t}\right) = -\left(\frac{\partial p}{\partial z}\right) + \frac{1}{r}\frac{\partial}{\partial r}\left(\frac{r\mu_{\mathrm{hnf}}(\theta)}{\mu_0}\left(\frac{\partial w}{\partial r}\right)\right)$$

$$+\left(\frac{(\rho\gamma)_{\mathrm{hnf}}}{(\rho\gamma)_f}\right)G_r\theta\,\sin(\alpha) - \frac{\sigma_{\mathrm{hnf}}}{\sigma_f}M_a^2 w, \tag{12}$$

$$R_e\left(\frac{\left(\rho C_p\right)_{\mathrm{hnf}}}{\left(\rho C_p\right)_f}\right)\left(\frac{k_f}{k_{\mathrm{hnf}}}\right)\mathrm{Pr}\left(\frac{\partial\theta}{\partial t}\right) = \left(\frac{\partial^2\theta}{\partial r^2} + \frac{1}{r}\frac{\partial\theta}{\partial r}\right) + \left(\frac{k_f}{k_{\mathrm{hnf}}}\right)\beta,$$

$$R(z) = \left\{\begin{array}{ll} 1 - 2\delta^*\left[\cos\left(\left(\frac{(z-d)}{2} - \frac{1}{4}\right)2\pi\right) - \cos\left(\left(z - d - \frac{1}{2}\right)32\pi\right)\left(\frac{7}{100}\right)\right], & d < \overline{z} < d+1 \\ 1, & \text{otherwise} \end{array}\right\}.$$

According to Burton [48], the pulsatile pressure gradient is denoted as

$$-\frac{\partial p}{\partial z} = A_0 + A_1 t\,\cos\left(2\pi\omega_p\right), \quad t > 0, \tag{13}$$

where A_0 represents the mean pressure gradient and A_1 represents the amplitude of the pulsatile component that controls systolic and diastolic pressures.

By employing (8) in (13), the simplified equation is

$$-\frac{\partial p}{\partial z} = B_1\left(1 + e\,\cos\left(c_1 t\right)\right), \tag{14}$$

where $e = A_1/A_0, B_1 = A_0 a^2/\mu_0 U_0$ and $c_1 = 2\pi\,\mathrm{aw}_p/U_0$.

Incorporating the (14) in the blood hybrid nanofluid axial velocity, one can get:

$$R_e\left(\frac{\rho_{\mathrm{hnf}}}{\rho_f}\right)\left(\frac{\partial w}{\partial t}\right) = B_1\left(1 + e\,\cos\left(c_1 t\right)\right) + \frac{1}{r}\frac{\partial}{\partial r}\left(\frac{r\mu_{\mathrm{hnf}}(\theta)}{\mu_0}\left(\frac{\partial w}{\partial r}\right)\right) + \left(\frac{(\rho\gamma)_{\mathrm{hnf}}}{(\rho\gamma)_f}\right)G_r\theta\,\sin(\alpha) - \frac{\sigma_{\mathrm{hnf}}}{\sigma_f}M_a^2 w. \tag{15}$$

The set of equations are transformed in the radial coordinate $(x = r/R(z))$ form since the governing flow equations are incorporated with limiting conditions:

$$\begin{aligned} &R_e\left(\frac{\rho_{\mathrm{hnf}}}{\rho_f}\right)\left(\frac{\partial w}{\partial t}\right) = B_1\left(1 + e\,\cos\left(c_1 t\right)\right) + \left(\frac{\mu_{\mathrm{hnf}}(\theta)}{\mu_0}\right)\\ &\frac{1}{R^2}\left(\frac{\partial^2 w}{\partial x^2} + \frac{1}{x}\frac{\partial w}{\partial x}\right) + \left(\frac{(\rho\gamma)_{\mathrm{hnf}}}{(\rho\gamma)_f}\right)\\ &G_r\theta\,\sin(\alpha) - \frac{\sigma_{\mathrm{hnf}}}{\sigma_f}M_a^2 w,\\ &\left(\frac{\left(\rho C_p\right)_{\mathrm{hnf}}}{\left(\rho C_p\right)_f}\right)\left(\frac{k_f}{k_{\mathrm{hnf}}}\right)R_e\mathrm{Pr}\left(\frac{\partial\theta}{\partial t}\right)\\ &= \frac{1}{R^2}\left(\frac{\partial^2\theta}{\partial x^2} + \frac{1}{x}\frac{\partial\theta}{\partial x}\right) + \left(\frac{k_f}{k_{\mathrm{hnf}}}\right)\beta. \end{aligned} \tag{16}$$

The radial coordinate form of boundary conditions are

$$\begin{aligned} &x = 0\colon \frac{\partial w(0,t)}{\partial x} = 0, \frac{\partial\theta(0,t)}{\partial x} = 0,\\ &x = 1\colon w(1,t) = 0, \theta(1,t) = 1,\\ &t = 0\colon w(x,0) = 0, \theta(x,0) = 0. \end{aligned} \tag{17}$$

Wall shear stress (τ_s), the Nusselt number (Nu^*), volumetric flow rate (Q_F), and resistance impedance (λ) of the present model are written as

$$\left.\begin{aligned} &\tau_s = -\frac{1}{R(z)}\left(\frac{\partial w}{\partial x}\right)_{x=1},\\ &\mathrm{Nu}^* = -\frac{1}{R(z)}\left(\frac{\partial\theta}{\partial x}\right)_{x=1},\\ &Q_F = (R(z))^2 2\pi\left(\int_0^1 \mathrm{wx}\,\mathrm{d}x\right),\\ &\lambda = L\left[\frac{(\partial p/\partial z)}{Q_F}\right] = L\left[\frac{B_1\left(1 + e\,\cos(2\pi t)\right)}{(R(z))^2 2\pi\left(\int_0^1 \mathrm{wx}\,\mathrm{d}x\right)}\right]. \end{aligned}\right\} \tag{18}$$

3. Numerical Method

The FTCS (forward time central space) finite-difference technique is employed to solve the present mathematical model's nonlinear coupled dimensionless flow equations subject to the appropriate initial and boundary condition. A rectangular region of the flow field is chosen in the explicit approach. The region is divided into a grid of lines parallel to axes, and it is displayed in Figure 2. The spatial domain is first discretized in this approach and after that the velocity and temperature values are obtained from each node x_j. Besides, instant step t^i is found over the time. The first derivative is discretized by forward differencing and the second derivative for central differencing. The $N + 1$ steps are used to discretize the spatial variable with the $\Delta x/N + 1$ step size. t^i expresses the time change, and $t^i = \Delta t\,(i - 1)$ finds its value. It is noticed that the Δt is a small difference in time. The blood velocity and the temperature are calculated in a different time step.

$$\left.\begin{aligned} &\frac{\partial w}{\partial t} \cong \frac{w_j^{i+1} - w_j^i}{\Delta t}; \frac{\partial\theta}{\partial t} \cong \frac{\theta_j^{i+1} - \theta_j^i}{\Delta t}\\ &\frac{\partial w}{\partial x} \cong \frac{w_{j+1}^i - w_{j-1}^i}{2\Delta x}; \frac{\partial\theta}{\partial x} \cong \frac{\theta_{j+1}^i - \theta_{j-1}^i}{2\Delta x}\\ &\frac{\partial^2 w}{\partial x^2} \cong \frac{w_{j+1}^i - 2w_j^i + w_{j-1}^i}{2\Delta x}; \frac{\partial^2\theta}{\partial x^2} \cong \frac{\theta_{j+1}^i - 2\theta_j^i + \theta_{j-1}^i}{2\Delta x} \end{aligned}\right\} \tag{19}$$

By employing the above expression, the discretized form of equations is written as follows:

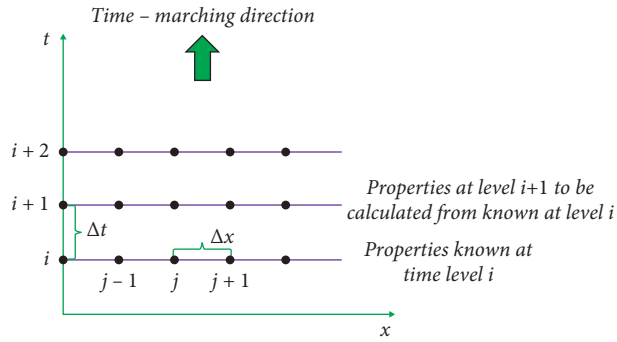

Figure 2: Finite difference space grid.

$$w_j^{i+1} = w_j^i + \frac{\Delta t}{R_e\left(1-\phi_2\left[(1-\phi_1)+\phi_1\left(\rho_{s_1}/\rho_f\right)\right]+\phi_2\rho_{s_2}/\rho_f\right)}\left[\begin{array}{c} B_1\left(1+e\,\cos\left(c_1 t^i\right)\right)+\dfrac{\left(1-\eta_0\theta_j^i\right)}{\left(1-\phi_1\right)^{2.5}\left(1-\phi_2\right)^{2.5}} \\ \left(\dfrac{1}{R^2}\right)\left(\dfrac{\partial^2 w}{\partial x^2}+\dfrac{1}{x}\dfrac{\partial w}{\partial x}\right) \\ +\left(1-\phi_2\left[(1-\phi_1)+\phi_1\left(\dfrac{(\rho\gamma)_{s_1}}{(\rho\gamma)_f}\right)\right]+\phi_2\dfrac{(\rho\gamma)_{s_2}}{(\rho\gamma)_f}\right) \\ G_r\theta_j^i\sin(\alpha)-\dfrac{\sigma_{\mathrm{hnf}}}{\sigma_f}M_a^2 w_j^i \end{array}\right], \tag{20}$$

$$\theta_j^{i+1} = \theta_j^i + \frac{\left(k_{\mathrm{hnf}}/k_f\right)\Delta t}{R_e\mathrm{Pr}\left(1-\phi_2\left[(1-\phi_1)+\phi_1\left(\left(\rho C_p\right)_{s_1}/\left(\rho C_p\right)_f\right)\right]+\phi_2\left(\rho C_p\right)_{s_2}/\left(\rho C_p\right)_f\right)}$$
$$\left\{\frac{1}{R^2}\left(\frac{\partial^2\theta}{\partial x^2}+\frac{1}{x}\frac{\partial\theta}{\partial x}\right)+\left(\frac{k_f}{k_{\mathrm{hnf}}}\right)\beta\right\}.$$

With the boundary conditions are

$$\left.\begin{array}{ll} w_j^1=\theta_j^1=0, & \text{at } t=0, \\ w_{j+1}^i=w_j^i,\ \theta_{j+1}^i=\theta_j^i, & \text{at } x=0, \\ w_{N+1}^i=0,\ \theta_{N+1}^i=1, & \text{at } x=1. \end{array}\right\}. \tag{21}$$

The stability of this scheme completely depends on time increment (Δt) and step size (Δx); thus, $\Delta t = 0.0001$ and $\Delta x = 0.025$ are fixed to tackle the stability condition. Several studies [5, 6, 43, 45, 46] proved that these values are suitable for stability and convergence of the FTCS approach. Further, Hoffmann's book [43] exposed that the above-used time and spatial values confirm this scheme's stability and convergence. Figure 3 (*a*) and Figure 3 (*b*) shows the local error and sum of time and space error on the dimensionless radius, respectively. From these figures, it is observed that the velocity and temperature of blood maintain 10^{-10} error at each spatial node. As similar, the sum of time and space error is 10^{-6}. This is evidence that the current numerical approach provides efficient results. The FTCS approach has been employed in numerous previous simulations, including heat transfer enhancement for solar energy absorber in a permeable annular [49], the blood flow of viscoelastic fluid in tapered overlapping even stenosed artery [50], and the exploration of nano-Bingham-Papanastasiou fluid in a diseased curved artery [51]. The studies manifest above have extensively validated that the FTCS approach is efficient for blood flow computation in complex geometries.

4. Results and Discussion

This section affords the physical aspects of emerging parameters like variable viscosity ($\eta_0 = 0, 0.1, 0.3, 0.5$), constant heat source ($\beta = 0, 0.3, 0.6, 0.9$), angle parameter ($\alpha = 0, \pi/6, \pi/4, \pi/2$), the Hartmann number

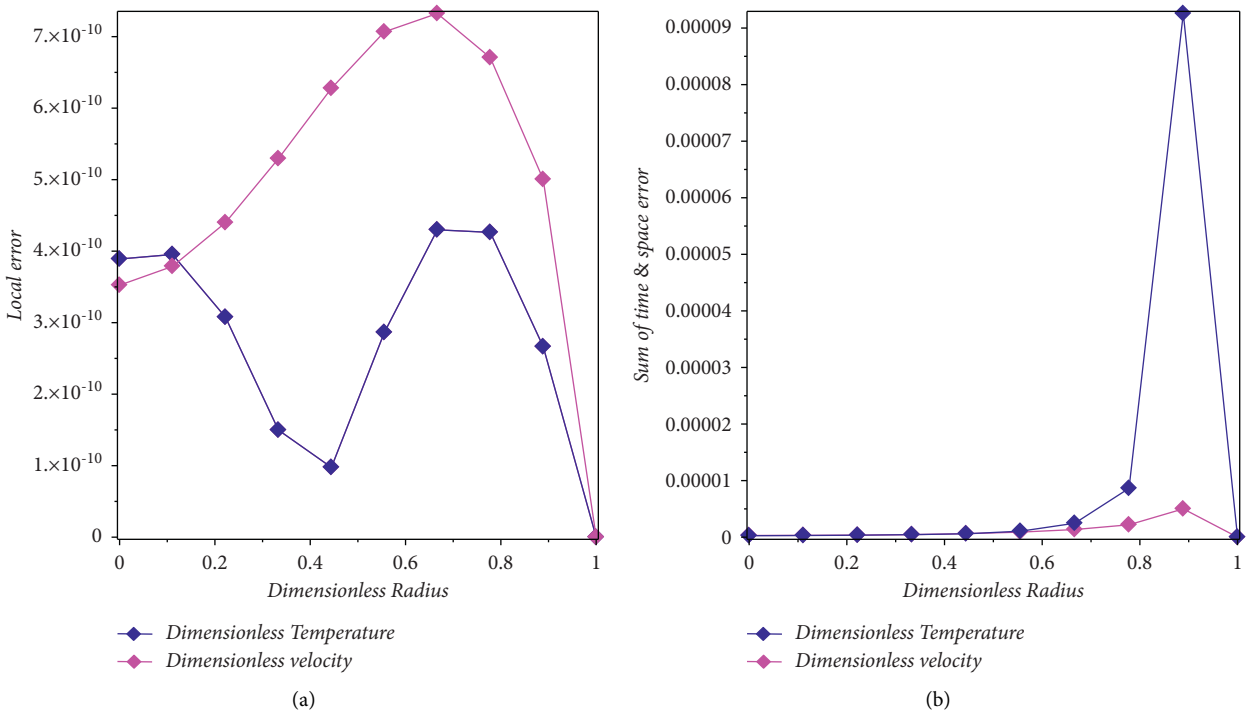

Figure 3: (a) Local error on w and θ. (b) Sum of time and space error on w and θ.

($M_a = 1, 2, 3, 4$), the Grashof number ($G_r = 0, 0.1, 0.3, 0.5$), the Reynolds number ($R_e = 2, 3, 4, 5$), and nanoparticle volume fraction ($\phi_1 + \phi_2 = 0.01, 0.02, 0.03, 0.05$) on the biomagnetic blood hybrid nanofluid velocity (w), temperature (θ), resistance impedance (λ), wall shear stress (τ_s), the Nusselt number (Nu^*), and volumetric flow rate (Q_F). The parametric values [4, 5, 6, 46] such as $B_1 = 1.41$, $d = 0.5$, $\delta^* = 0.1$, $e = 0.5$, $\mathrm{Pr} = 14$, $c_1 = 1$, $\beta = 0.1$, $G_r = 0.5$, $R_e = 2$, $M_a = 0.5$, $\alpha = \pi/2$, $\eta_0 = 0.2$, $\phi_1 = 0.025$, and $\phi_2 = 0.025$ are considered for computation. In this model, the significance of gold-copper hybrid nanofluid and copper nanofluid characteristics is analyzed via graphs. The system of equations is reduced with the help of nonsimilar variables, and FTCS obtains the solution. For obtaining scheme validation, the present result is compared with earlier results in Table 2. It is witnessed that the present results are in valid agreement. It is essential to note that the hybrid nanofluid turns into a mono nanofluid in the absence of gold nanoparticles ($\phi_1 = 0$). To show the variation in figures, the solid line is used for the hybrid nanofluid case, and the dashed line is used for the nanofluid case. The behaviour of the base fluid, nanofluid, and hybrid nanofluid on temperature is compared in Table 3. This table shows that the blood base fluid generates a lower temperature than the nanofluid and hybrid nanofluid cases.

Variation of the Reynolds number (R_e) on biomagnetic blood hybrid nanofluid axial velocity and temperature is visualised for hybrid nanofluid and Cu nanofluid cases in Figures 4 and 5, respectively. In this study, due to the laminar flow case, meagre Reynolds numbers are assumed, so the viscosity is dominant in the regime. It is clear from these figures that the biomagnetic blood axial velocity significantly

Table 2: Validation of biomagnetic blood axial velocity with Zaman et al. [5] and Tripathi et al. [6].

R	Zaman et al. [5]	Tripathi et al. [6]	Present result
0	0.5859	0.5881	0.58900
0.1	0.5829	0.5845	0.58289
0.2	0.5725	0.5725	0.57170
0.3	0.5540	0.5518	0.55339
0.4	0.5261	0.5215	0.52593
0.5	0.4864	0.4802	0.48727
0.6	0.4323	0.4257	0.43843
0.7	0.3605	0.3549	0.37083
0.8	0.2671	0.2637	0.27891
0.9	0.1483	0.1473	0.15715
1.0	0	0	0

Table 3: Comparison of base fluid, nanofluid, and hybrid nanofluid on temperature.

R	Temperature		
	Blood basefluid	*Cu*/blood nanofluid	*Au-Cu*/blood hybrid nanofluid
0	0.060607	0.092054	0.093989
0.1	0.067032	0.099859	0.101855
0.2	0.087374	0.124016	0.126176
0.3	0.124622	0.166525	0.168902
0.4	0.182908	0.229936	0.232505
0.5	0.266231	0.316289	0.318937
0.6	0.376797	0.425898	0.428428
0.7	0.513356	0.556286	0.558456
0.8	0.670114	0.701653	0.703227
0.9	0.836782	0.853146	0.853959
1.0	1	1	1

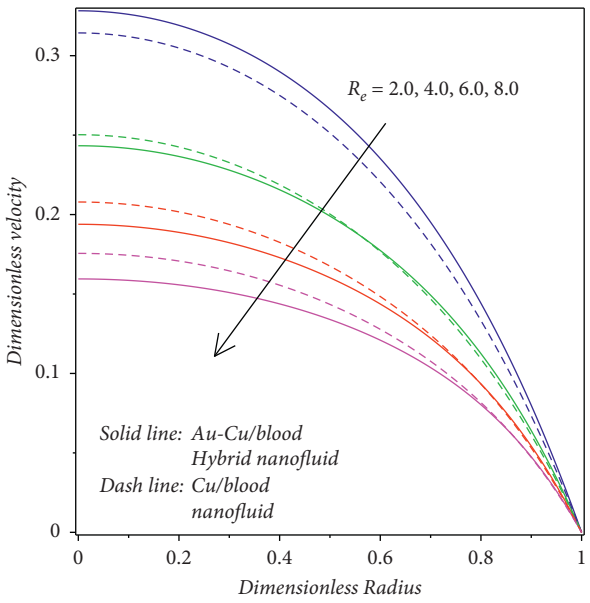

Figure 4: Behaviour of R_e on w.

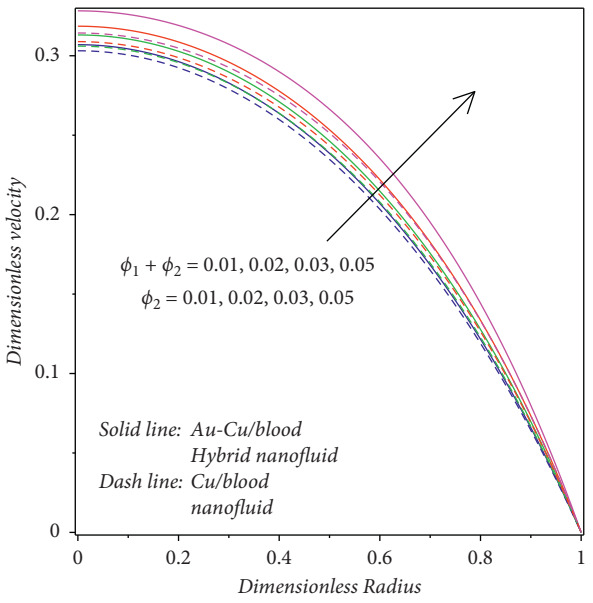

Figure 6: Behaviour of $\phi_1 + \phi_2$ and ϕ_2 on w.

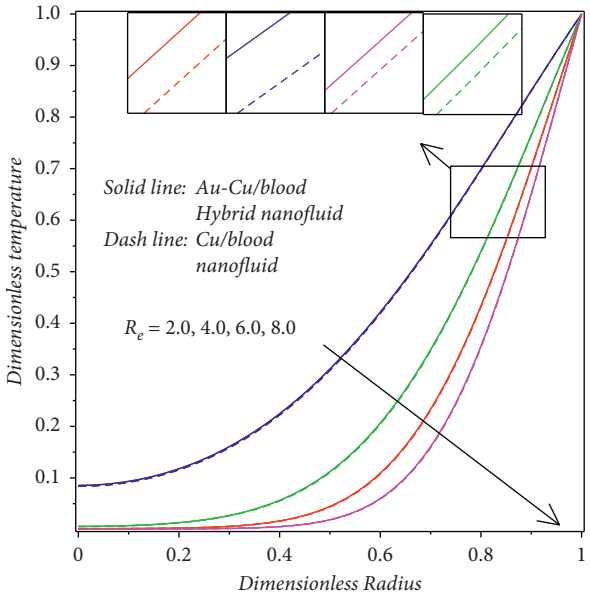

Figure 5: Behaviour of R_e on θ.

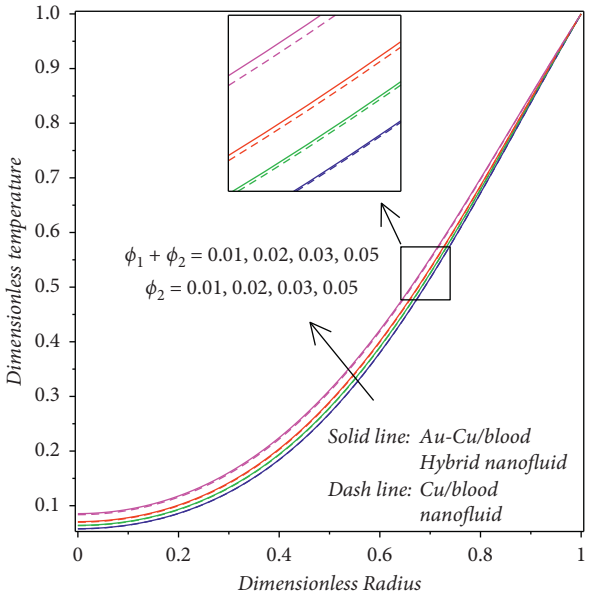

Figure 7: Behaviour of $\phi_1 + \phi_2$ and ϕ_2 on θ.

reduces while growing values of R_e. Further, blood temperature experiences a similar nature. The lower value of R_e ($R_e = 2$) exhibits less impact on the blood velocity and temperature; however, its magnitudes variation is higher by growing R_e ($R_e = 4, 6, 8$). Due to stenosis prohibition and nanoparticles, blood flow reduction occurs in the channel, even though the Reynolds number promotes the inertial force. Due to this reason, biomagnetic blood velocity and temperature are behaving with the impact of R_e.

Figures 6 and 7 demonstrate the characteristics of nanoparticles volume fraction $(\phi_1 + \phi_2)$ on blood velocity and temperature in hybrid nanofluid and nanofluid cases. It is seen from Figure 6 that the augmentation of gold-copper $(\phi_1 + \phi_2)$ nanoparticle concentration and copper (ϕ_2) nanoparticle concentration from 0.01 to 0.05 tends to promote the blood velocity in the artery. This characteristic of hybrid nanofluid is predominant to clinicians because it may help to promote the blood flow in the capillary tubes and stenosis during surgery. Figure 7 is drawn to discuss the behaviour of nanoparticles volume fraction $(\phi_1 + \phi_2)$ on blood temperature. An increment in nanoparticles

volume fraction remarkably elevates the blood temperature. Further, coupling the gold nanoparticle (ϕ_1) with copper nanoparticles (ϕ_2) highly contributes to blood temperature growth than copper nanoparticles suspension in the blood. It is revealed from this figure that the thermal diffusion of blood rises with nanoparticles in the stenotic vessel, which leads to elevating the transport process. These results show that the hybrid nanoparticles and copper nanoparticles help to accelerate the blood flow in the regular and irregular stenosis artery region.

Figure 8 is plotted to exhibit the influence of the Hartmann number (M_a) on blood velocity. In the case of $M_a = 0$, the biomagnetic blood nanofluid behave as a nonmagnetic blood nanofluid. It is found that the fluid momentum has a higher magnitude difference for M_a values 1–5. The gold and copper nanoparticles are highly dragged with the strength of Lorentz force in the artery. This creates a resistive behaviour in the blood flow. Due to this reason, blood velocity declines. Further, it is noticed that the present outcome accords with the results of Das et al. [7]. The greater diffusion of nanoparticles is the prime objective in medical applications, so that this characteristic of M_a is remarkable in synthesising bio-nanomaterials. Also, due to the characteristic of the magnetic field, it is employed to control the blood flow in the artery. It can be used to treat several cardiovascular diseases as an effective tool. In particular, this may be useful in wound treatments and pharmacological, for instance, healing skin contusions and burns.

Figure 9 explores the changes of the Grashof number (G_r) on blood hybrid nanofluid axial velocity. An increase in G_r causes to lift the blood velocity for both the hybrid and unitary nanofluid cases. It is noted that G_r is the ratio between buoyancy force and viscous force. The concentration differences of nanoparticles tend to grow the diffusion of nanoparticle species in the blood. Thus, the thermal buoyancy force increases in the channel, whereas viscous force decreases. As a result, the blood velocity rises. Figures 10 and 11 demonstrate the nature of constant heat source (β) on blood velocity and temperature. In the channel, the generation of energy takes place as a result of the increase of β. The gold and copper nanoparticles are energized with the impact of β. Besides, the heat slightly triggers the buoyancy force. Therefore, the blood nanofluid and hybrid nanofluid velocity and temperature increases. Figure 12 displays the influence of changing viscosity parameter (η_0) on blood velocity. It is observed that it has the same characteristic as G_r on fluid velocity. Physically, the viscosity of the blood lessens owing to the rising values of η_0. As a consequence, blood velocity is accelerated. Numerous values of angle parameter (α) on biomagnetic blood nanofluid velocity is displayed in Figure 13. It is evident that the blood velocity augments with the increasing values of α. In this model, α is incorporated with the thermal buoyancy term in the momentum equation. Therefore, when α is absent, it eliminates the thermal buoyancy effect in the regime. Further, rising the α highly enhances the buoyancy effect, and it accelerates the blood velocity.

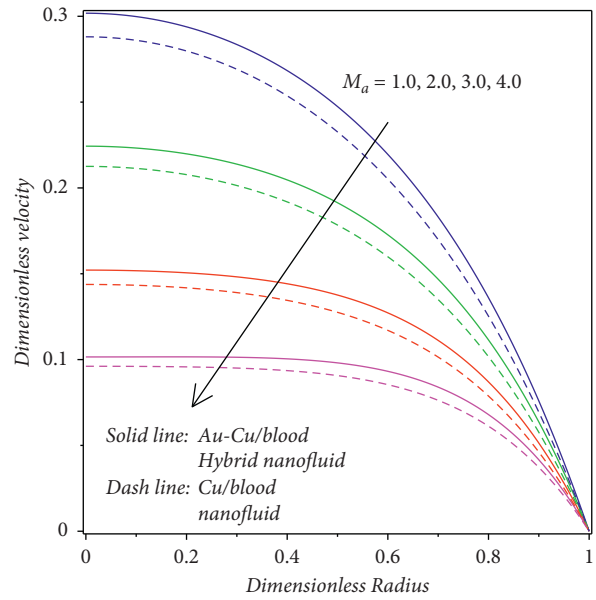

Figure 8: Behaviour of M_a on w.

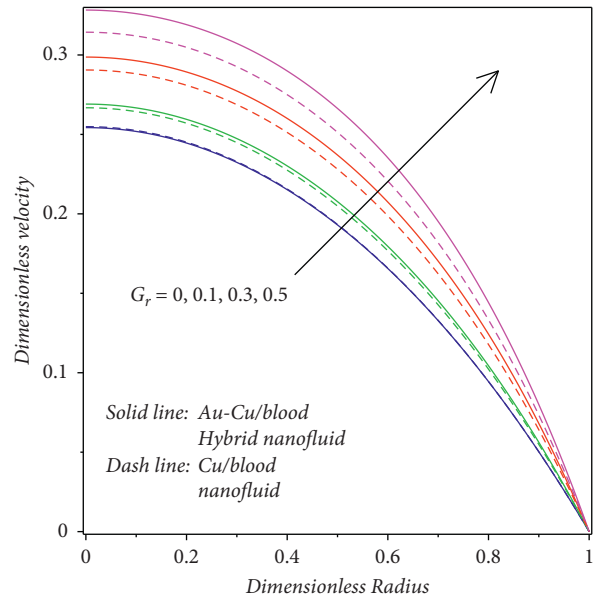

Figure 9: Behaviour of G_r on w.

Figures 14–17 depict the influences of the Grashof number (G_r), angle parameter (α), the Reynolds number (R_e), and the Hartmann number (M_a) on volumetric flow rate (Q_F) for hybrid and single nanofluid cases. It is cleared that the integration of variable blood velocity concerning the channel radial direction is known as volumetric flow rate. Besides, the volumetric flow rate reveals the nature of the axis velocity. The impacts of M_a and R_e on volumetric flow rate are illustrated in Figures 14 and 15. It is confirmed that M_a and R_e highly reduce the axial blood velocity (see

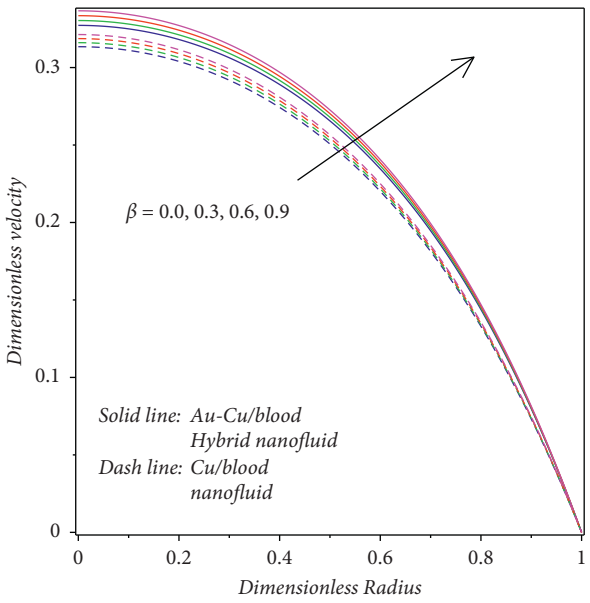

Figure 10: Behaviour of β on w.

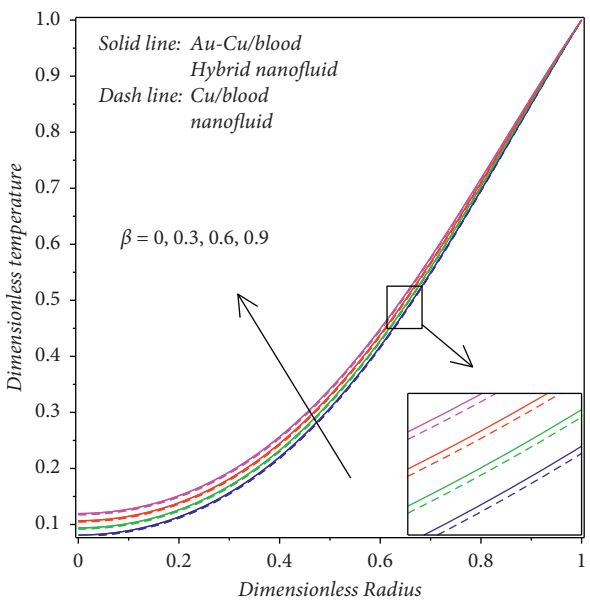

Figure 11: Behaviour of β on θ.

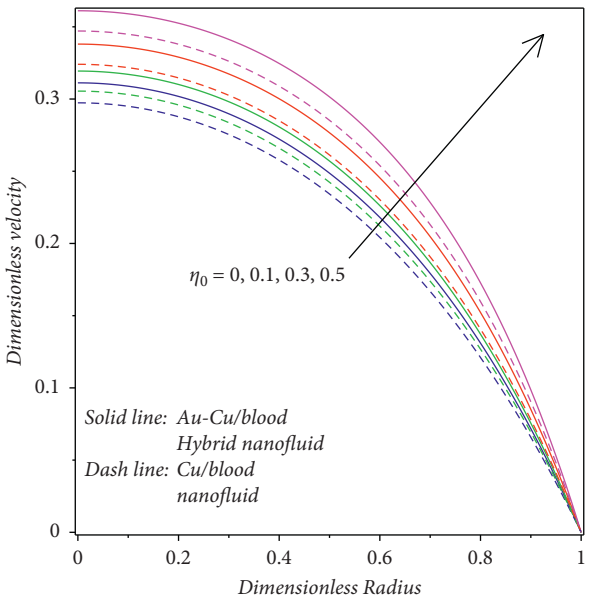

Figure 12: Behaviour of η_0 on w.

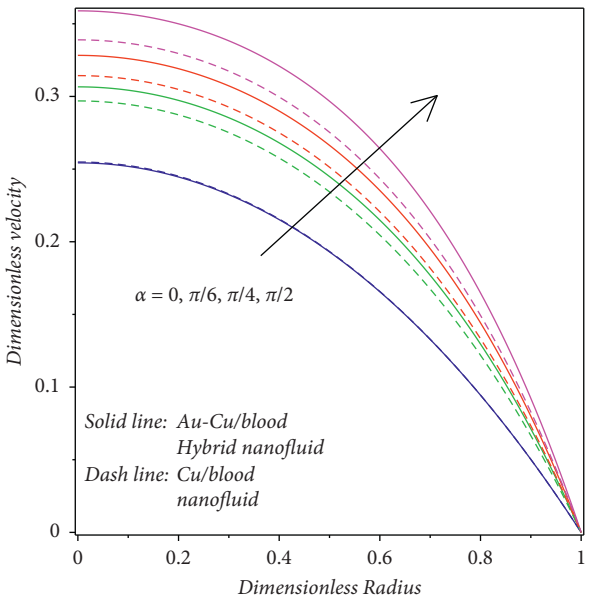

Figure 13: Behaviour of α on w.

Figures 4 and 8). M_a and R_e follow the same behaviour expressed in axial blood velocity on the volumetric flow rate. The response in volumetric flow rate to G_r and α parameters is provided in Figures 16 and 17. From these figures, it is clear that both the parameters have a similar trend. The amplification in G_r and α tends to enhance Q_F. Further, the absence of G_r and α expresses a lower Q_F; however, magnifying these parameters manifests a greater Q_F in the artery.

The behaviours of the Grashof number (G_r), angle parameter (α), changing viscosity parameter (η_0), and the Hartmann number (M_a) on the wall shear stress (τ_s) are sketched in Figures 18–21. It is evident that endothelial proliferation and turbulent flow happen in the system when low shear stress occurs. Besides, laminar flow happens with high shear stress. Figure 18 shows the impact of M_a on wall shear stress. When this term is magnified, the wall shear

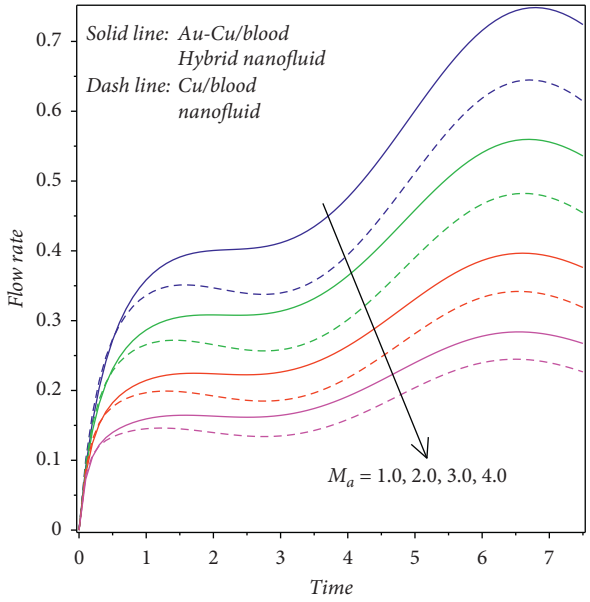

Figure 14: Behaviour of M_a on Q_F.

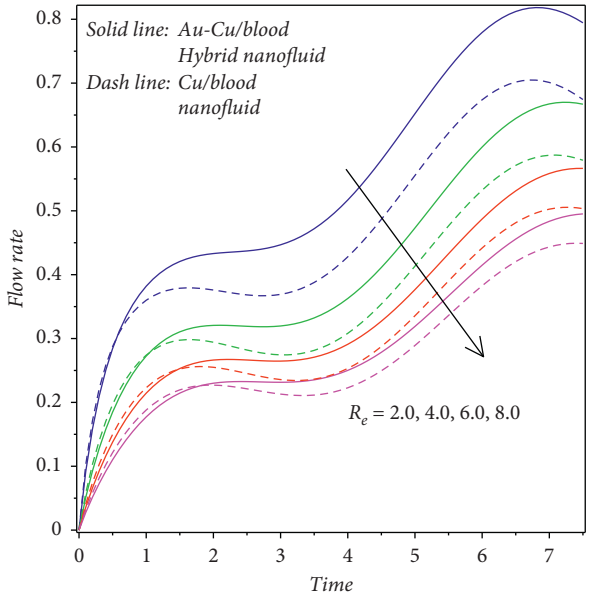

Figure 15: Behaviour of R_e on Q_F.

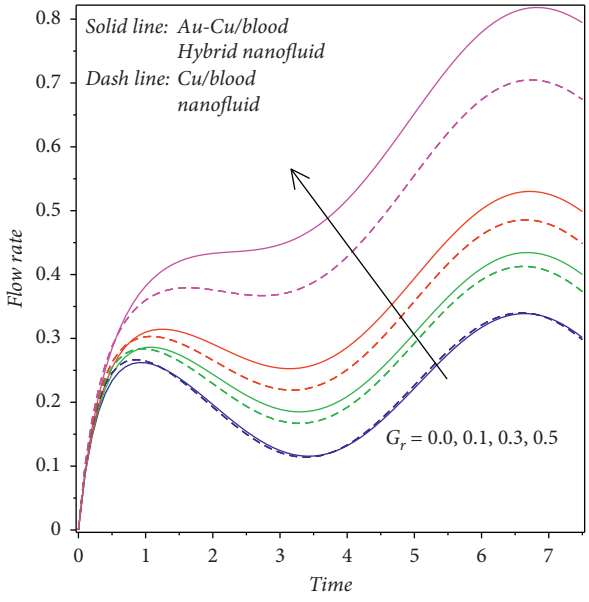

Figure 16: Behaviour of G_r on Q_F.

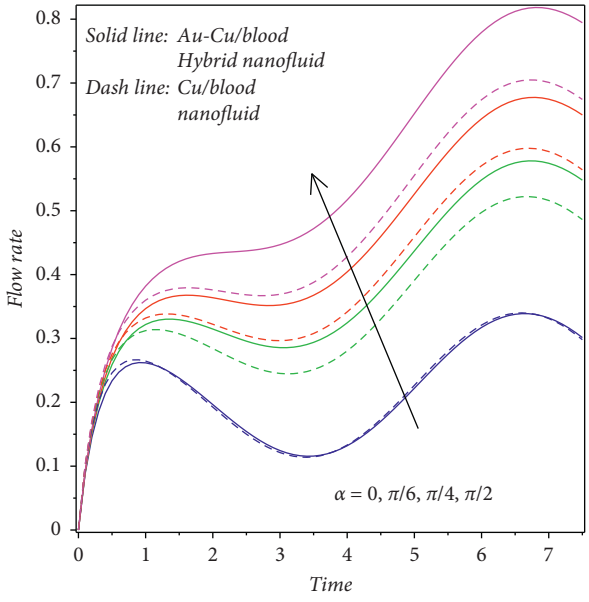

Figure 17: Behaviour of α on Q_F.

stress is reduced. It is revealed that the magnetic field plays a major role to maintain a laminar flow in the system. Figures 19–21 are drawn to explore the influences of G_r, α, and η_0 on wall shear stress. These figures show that higher values of G_r, α, and η_0 result in increasing the wall shear stress for nanofluid and hybrid nanofluid cases. It is cleared from these figures that wall shear stress (τ_s) is highly sensitive to copper (ϕ_2) nanoparticles rather than gold-copper ($\phi_1 + \phi_2$) hybrid nanoparticles.

Figures 22 and 23 present the effects of the Hartmann number (M_a) and angle parameter (α) on resistance impedance. The resistance impedance is inversely related

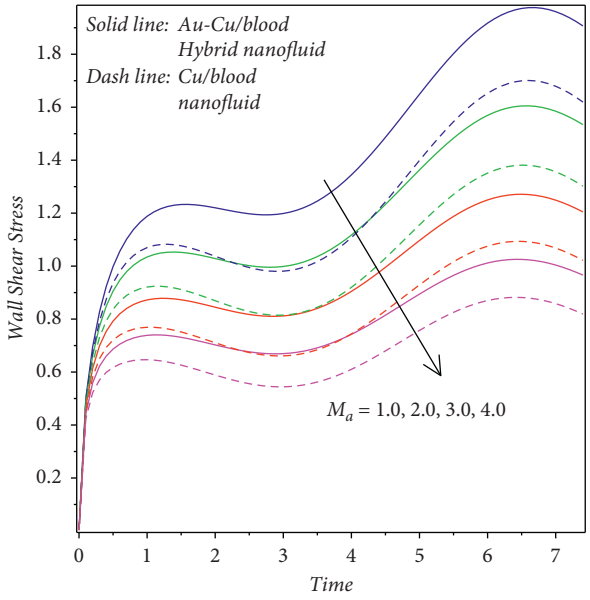

Figure 18: Behaviour of M_a on τ_s.

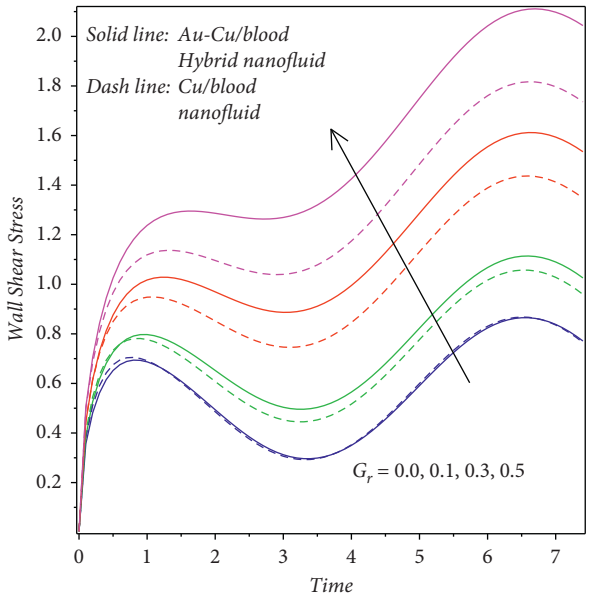

Figure 19: Behaviour of G_r on τ_s.

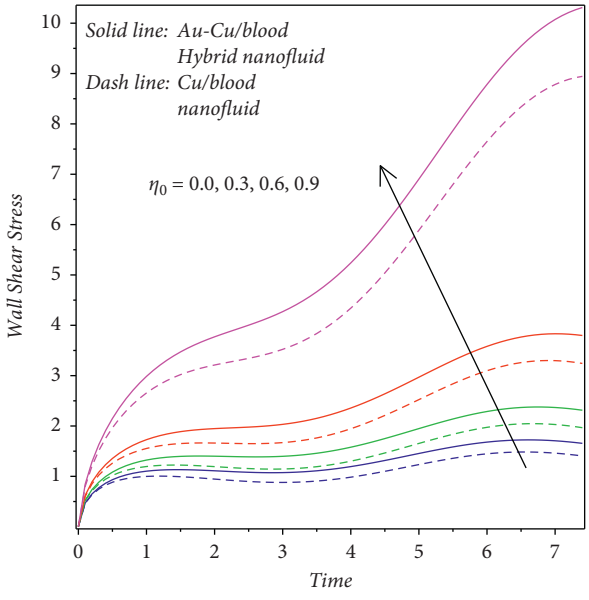

Figure 20: Behaviour of η_0 on τ_s.

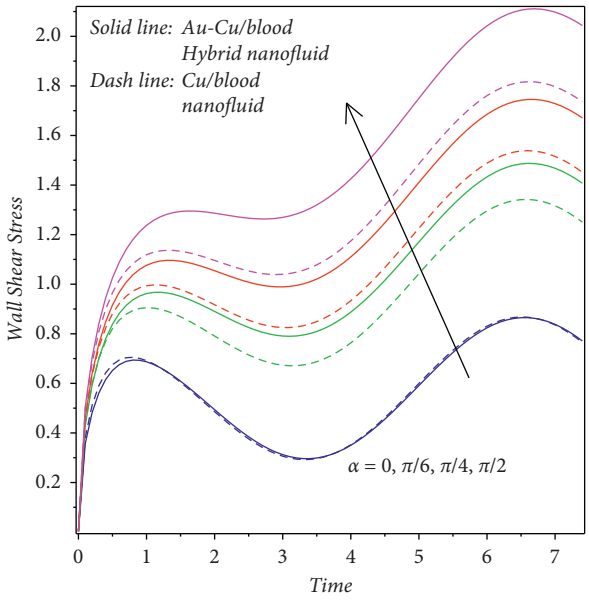

Figure 21: Behaviour of α on τ_s.

to the flow rate, which is exhibited in (18). Magnifying the magnetic field (M_a) slowdown the resistance impedance in the artery, whereas the opposite trend is found for α. This flow pattern exhibits that the growing magnetic field declines the impedance of the blood rheology. Further, the magnetic field behaves like a controlling parameter to tune the impedance effects. This result shows that controlling the blood movement in the artery thus help to stabilize the patients instantly. Figures 24 and 25 exhibit the changes in blood flow rate for several values of the

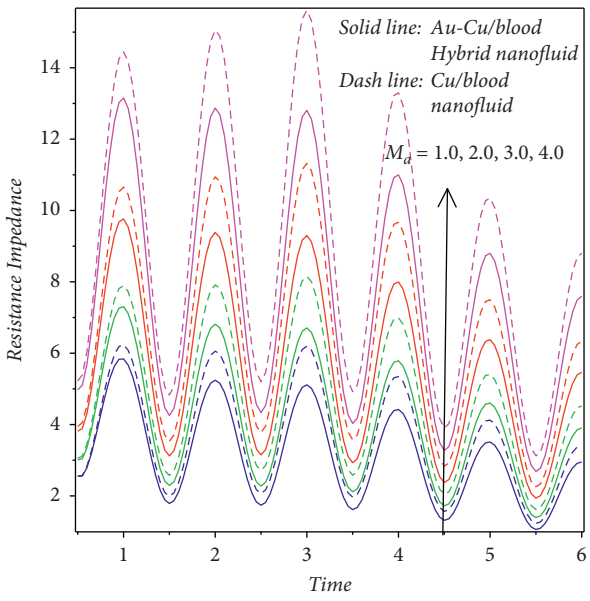

Figure 22: Behaviour of M_a on λ.

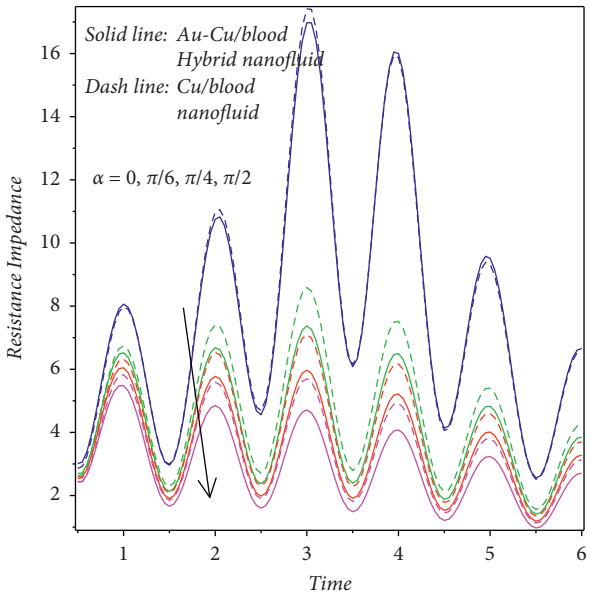

Figure 23: Behaviour of α on λ.

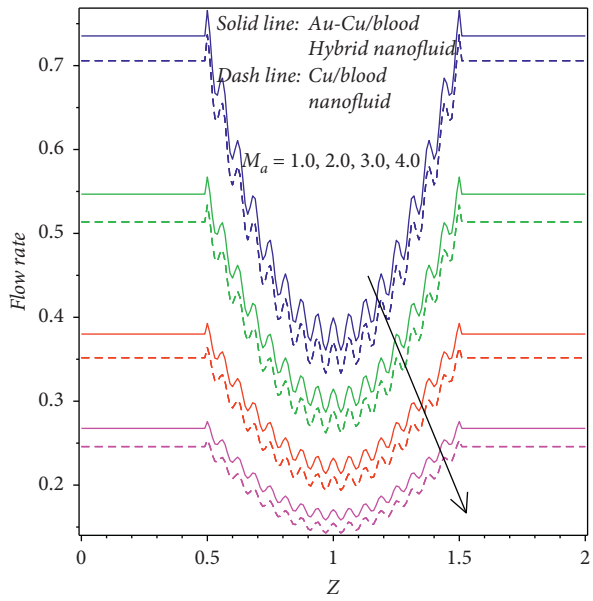

Figure 24: Behaviour of M_a on Q_F at Z.

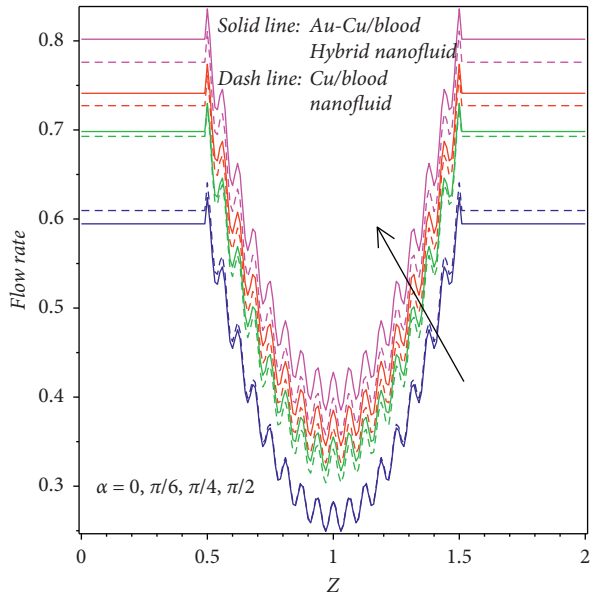

Figure 25: Behaviour of α on Q_F at Z.

Hartmann number (M_a) and angle parameter (α). It is cleared that the flow rate in the axial coordinate is elevated with the increasing values of α, whereas a reverse trend is found for M_a. The influences of ϕ_1, ϕ_2, and β on the Nusselt number (Nu^*) are depicted in Figures 26 and 27, respectively. It is ascertained that the Nusselt number is highly improved with the impacts of ϕ_1, ϕ_2, and β . Further, it is clear that the hybrid nanofluid has a supreme heat transfer rate than the copper nanofluid case.

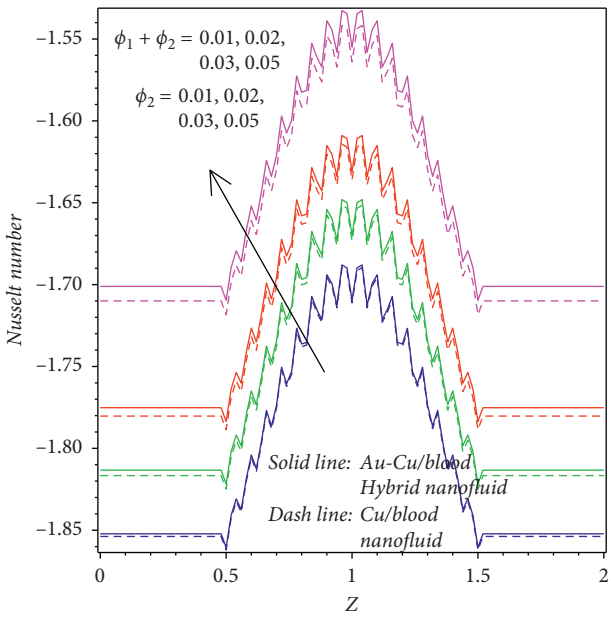

Figure 26: Behaviour of $\phi_1 + \phi_2$ and ϕ_2 on Nu* at Z .

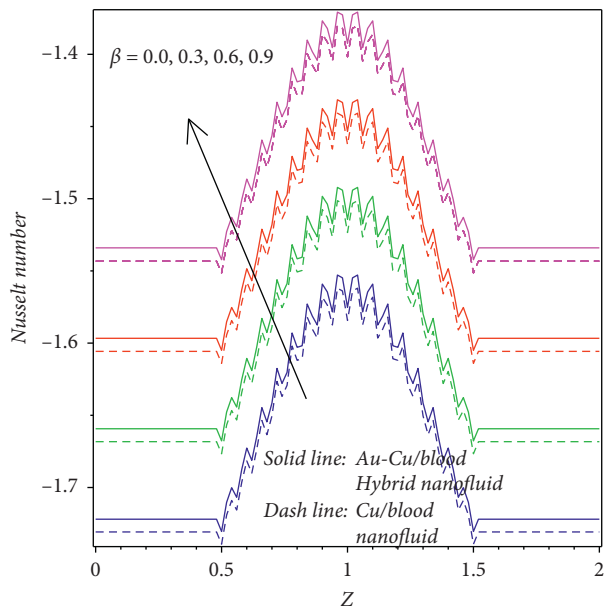

Figure 27: Behaviour of β on Nu* at Z.

5. Conclusions

The impacts of changing viscosity and Lorentz force on the biomagnetic hybrid nanofluid flow through an inclined irregular stenosis artery have been scrutinized in this study. To exhibit the characteristics of hybrid nanofluid, the volume fraction model is adopted. The mild stenosis approximation is considered to simplify governing flow equations. The nondimensionalized flow equations are solved by deploying a finite-difference approach. The present numerical solution is validated with Zaman et al. [5] and Tripathi et al. [6] for various axial velocity values, which is portrayed in Table 2. From this Table 2, it is evident that the adopted numerical method has a decent agreement. Variations caused by the influences of growing parameters on blood hybrid nanofluid velocity, temperature, and physical quantities (wall shear stress, resistance impedance, flow rate) are shown through graphs. The preeminent findings of the present analysis are itemized as follows:

(I) It is cleared that the hybrid nanoparticles have a better fluid flow and heat transfer than the unitary nanoparticles

(II) The hybrid nanoparticle and copper nanoparticle volume fraction promote the axial velocity and temperature of the blood

(III) The hybrid nanoparticles express a supreme flow rate than the copper nanoparticles

(IV) In the absence of the Grashof number and angle parameter, the wall shear stress and flow rate have similar trends for hybrid nanofluid and copper nanofluid cases

(V) The variable viscosity parameter exhibits the peak magnitude on wall shear stress by magnifying values

(VI) In the 2.5-to-3.5-time region, the Hartmann number and angle parameter manifest a greater resistance impedance on the blood hybrid nanofluid flow

(VII) Variable viscosity, heat source/sink, and angle parameter cause to enhance the blood hybrid nanofluid velocity

(VIII) The blood axial velocity in the stenosis artery decreases by means of the growing Reynolds number

Data Availability

The data used in the study are provided in the respective text part, and no additional data are employed for these outcomes.

Conflicts of Interest

The authors declare that they have no conflicts of interest.

Acknowledgments

This work was funded by the Chennai Institute of Technology, India, vide funding number CIT/CNS/2021/RD/064.

References

[1] M. N. Krishnan, "Coronary heart disease and risk factors in India - on the brink of an epidemic?" *Indian Heart Journal*, vol. 64, no. 4, pp. 364–367, 2012.

[2] R. Gupta, I. Mohan, and J. Narula, "Trends in coronary heart disease epidemiology in India," *Annals of Global Health*, vol. 82, no. 2, pp. 307–15, 2016.

[3] J. V. Ramana Reddy, D. Srikanth, and S. K. Das, "Modelling and simulation of temperature and concentration dispersion

in a couple stress nanofluid flow through stenotic tapered arteries," *The European Physical Journal Plus*, vol. 132, no. 8, p. 365, 2017.

[4] S. Changdar and S. De, "Investigation of nanoparticle as a drug carrier suspended in a blood flowing through an inclined multiple stenosed artery," *BioNanoScience*, vol. 8, no. 1, pp. 166–178, 2018.

[5] A. Zaman, N. Ali, and A. A. Khan, "Computational biomedical simulations of hybrid nanoparticles on unsteady blood hemodynamics in a stenotic artery," *Mathematics and Computers in Simulation*, vol. 169, pp. 117–132, 2020.

[6] J. Tripathi, B. Vasu, and O. A. Bég, "Computational simulations of hybrid mediated nano- hemodynamics (Ag-Au/Blood) through an irregular symmetric stenosis," *Computers in Biology and Medicine*, vol. 130, Article ID 104213, 2021.

[7] S. Das, T. K. Pal, R. N. Jana, and B. Giri, "Significance of Hall currents on hybrid nano-blood flow through an inclined artery having mild stenosis: homotopy perturbation approach," *Microvascular Research*, vol. 137, Article ID 104192, 2021.

[8] J. Prakash and O. D. Makinde, "Radiative heat transfer to blood flow through a stenotic artery in the presence of magnetic field," *Latin American Applied Research*, vol. 41, no. 3, pp. 273–277, 2011.

[9] M. M. Rashidi, M. Keimanesh, O. A. Bég, and T. K. Hung, "Magnetohydrodynamic biorheological transport phenomena in a porous medium: a simulation of magnetic blood flow control and filtration," *International Journal for Numerical Methods in Biomedical Engineering*, vol. 27, no. 6, pp. 805–821, 2011.

[10] M. Rashidi, M. Bhatti, M. Abbas, and M. Ali, "Entropy generation on MHD blood flow of nanofluid due to peristaltic waves," *Entropy*, vol. 18, no. 4, p. 117, 2016.

[11] R. Ponalagusamy and S. Priyadharshini, "Numerical modelling on pulsatile flow of Casson nanofluid through an inclined artery with stenosis and tapering under the influence of magnetic field and periodic body acceleration," *Korea-Australia Rheology Journal*, vol. 29, no. 4, pp. 303–316, 2017.

[12] S. Noreen, M. M. Rashidi, and M. Qasim, "Blood flow analysis with considering nanofluid effects in vertical channel," *Applied Nanoscience*, vol. 7, no. 5, pp. 193–199, 2017.

[13] H. T. Basha and R. Sivaraj, "Numerical simulation of blood nanofluid flow over three different geometries by means of gyrotactic microorganisms: applications to the flow in a circulatory system," *Proceedings of the Institution of Mechanical Engineers - Part C: Journal of Mechanical Engineering Science*, vol. 235, no. 2, pp. 441–460, 2020.

[14] M. U. Ashraf, M. Qasim, A. Wakif, M. I. Afridi, and I. L. Animasaun, "A generalized differential quadrature algorithm for simulating magnetohydrodynamic peristaltic flow of blood-based nanofluid containing magnetite nanoparticles: a physiological application," *Numerical Methods for Partial Differential Equations*, pp. 1–27, 2020.

[15] H. T. Basha and R. Sivaraj, "Exploring the heat transfer and entropy generation of Ag/Fe$$_3$$O$$_4$$-blood nanofluid flow in a porous tube: a collocation solution," *The European Physical Journal E*, vol. 44, no. 3, p. 31, 2021.

[16] S. Rathore and D. Srikanth, "Mathematical study of transport phenomena of blood nanofluid in a diseased artery subject to catheterization," *Indian Journal of Physics*, vol. 106, 2021.

[17] H. Basha and R. Sivaraj, "Entropy generation of peristaltic Eyring-Powell nanofluid flow in a vertical divergent channel for biomedical applications," *Proceedings of the Institution of Mechanical Engineers - Part E: Journal of Process Mechanical Engineering*, vol. 235, no. 5, pp. 1575–1586, 2021.

[18] J. C. Misra, "Biomagnetic viscoelastic fluid flow over a stretching sheet," *Applied Mathematics and Computation*, vol. 210, no. 2, pp. 350–361, 2009.

[19] M. G. Murtaza, M. Ferdows, J. C. Misra, and E. E. Tzirtzilakis, "Three-dimensional biomagnetic Maxwell fluid flow over a stretching surface in presence of heat source/sink," *International Journal of Biomathematics*, vol. 12, no. 3, Article ID 1950036, 2019.

[20] S. Maiti and S. Shaw, "Caputo-Fabrizio fractional order model on MHD blood flow with heat and mass transfer through a porous vessel in the presence of thermal radiation," *Physica A: Statistical Mechanics and Its Applications*, vol. 540, Article ID 123149, 2019.

[21] S. M. Mousavi, A. A. R. Darzi, O. a. Akbari, D. Toghraie, and A. Marzban, "Numerical study of biomagnetic fluid flow in a duct with a constriction affected by a magnetic field," *Journal of Magnetism and Magnetic Materials*, vol. 473, pp. 42–50, 2019.

[22] S. R. El Koumy, E. S. I. Barakat, and S. I. Abdelsalam, "Hall and porous boundaries effects on peristaltic transport through porous medium of a maxwell model," *Transport in Porous Media*, vol. 94, no. 3, pp. 643–658, 2012.

[23] S. Changdar and S. De, "Analytical investigation of nanoparticle as a drug carrier suspended in a MHD blood flowing through an irregular shape stenosed artery," *Iranian Journal of Science and Technology*, vol. 43, no. 1, pp. 1259–1272, 2017.

[24] Y. A. Elmaboud and S. I. Abdelsalam, "DC/AC magneto-hydrodynamic-micropump of a generalized Burger's fluid in an annulus," *Physica Scripta*, vol. 94, no. 11, Article ID 115209, 2019.

[25] M. M. Bhatti, S. Z. Alamri, R. Ellahi, and S. I. Abdelsalam, "Intra-uterine particle-fluid motion through a compliant asymmetric tapered channel with heat transfer," *Journal of Thermal Analysis and Calorimetry*, vol. 144, no. 6, pp. 2259–2267, 2020.

[26] S. I. Abdelsalam, J. X. Velasco-Hernández, and A. Z. Zaher, "Electro-magnetically modulated self-propulsion of swimming sperms via cervical canal," *Biomechanics and Modeling in Mechanobiology*, vol. 20, pp. 861–878, 2020.

[27] A. Chatterjee, S. Changdar, and S. De, "Study of nanoparticle as a drug carrier through stenosed arteries using Bernstein polynomials," *International Journal for Computational Methods in Engineering Science and Mechanics*, vol. 21, no. 5, pp. 243–251, 2020.

[28] B. Bhaumik, S. Changdar, and S. De, "Combined impact of Brownian motion and thermophoresis on nanoparticle distribution in peristaltic nanofluid flow in an asymmetric channel," *International Journal of Ambient Energy*, pp. 1–12, 2021.

[29] K. S. Mekheimer, R. E. Abo-Elkhair, S. I. Abdelsalam, K. K. Ali, and A. M. A. Moawad, "Biomedical simulations of nanoparticles drug delivery to blood hemodynamics in diseased organs: synovitis problem," *International Communications in Heat and Mass Transfer*, vol. 130, p. 105756, 2022.

[30] M. A. Abbas, Y. Q. Bai, M. M. Rashidi, and M. M. Bhatti, "Application of drug delivery in magnetohydrodynamics peristaltic blood flow of nanofluid in a non-uniform channel," *Journal of Mechanics in Medicine and Biology*, vol. 16, no. 4, Article ID 1650052, 2016.

[31] H. Thameem Basha, R. Sivaraj, A. Subramanyam Reddy, and A. J Chamkha, "SWCNH/diamond-ethylene glycol nanofluid flow over a wedge, plate and stagnation point with induced

magnetic field and nonlinear radiation - solar energy application," *The European Physical Journal - Special Topics*, vol. 228, no. 12, pp. 2531–2551, 2019.

[32] H. Shojaie Chahregh and S. Dinarvand, "TiO2-Ag/blood hybrid nanofluid flow through an artery with applications of drug delivery and blood circulation in the respiratory system," *International Journal of Numerical Methods for Heat and Fluid Flow*, vol. 30, no. 11, pp. 4775–4796, 2020.

[33] P. B. A. Reddy, "Biomedical aspects of entropy generation on electromagnetohydrodynamic blood flow of hybrid nanofluid with nonlinear thermal radiation and non-uniform heat source/sink," *The European Physical Journal Plus*, vol. 135, no. 10, p. 852, 2020.

[34] E. H. Jeong, G. Jung, C. A. Hong, and H. Lee, "Gold nanoparticle (AuNP)-based drug delivery and molecular imaging for biomedical applications," *Archives of Pharmacal Research*, vol. 37, no. 1, pp. 53–59, 2014.

[35] M. Sengani, A. M. Grumezescu, and V. D. Rajeswari, "Recent trends and methodologies in gold nanoparticle synthesis - a prospective review on drug delivery aspect," *Open*, vol. 2, pp. 37–46, 2017.

[36] N. S. Aminabad, M. Farshbaf, and A. Akbarzadeh, "Recent advances of gold nanoparticles in biomedical applications: state of the art," *Cell Biochemistry and Biophysics*, vol. 77, no. 2, pp. 123–137, 2019.

[37] M. Vairavel, E. Devaraj, and R. Shanmugam, "An eco-friendly synthesis of Enterococcus sp.-mediated gold nanoparticle induces cytotoxicity in human colorectal cancer cells," *Environmental Science and Pollution Research*, vol. 27, no. 8, pp. 8166–8175, 2020.

[38] X. Chen, X. Zhao, and G. Wang, "Review on marine carbohydrate-based gold nanoparticles represented by alginate and chitosan for biomedical application," *Carbohydrate Polymers*, vol. 244, Article ID 116311, 2020.

[39] O. K. Koriko, I. L. Animasaun, B. Mahanthesh, S. Saleem, G. Sarojamma, and R. Sivaraj, "Heat transfer in the flow of blood-gold Carreau nanofluid induced by partial slip and buoyancy," *Heat Transfer - Asian Research*, vol. 9, no. 6, pp. 1–18, 2018.

[40] P. Bharath Kumar and S. Srinivas, "Pulsating flow of a non-Newtonian nanofluid in a porous channel with magnetic field," *Materials Today Proceedings*, vol. 9, no. 2, pp. 320–332, 2019.

[41] U. Khan, S. Bilal, A. Zaib, O. D. Makinde, and A. Wakif, "Numerical simulation of a nonlinear coupled differential system describing a convective flow of Casson gold–blood nanofluid through a stretched rotating rigid disk in the presence of Lorentz forces and nonlinear thermal radiation," *Numerical Methods for Partial Differential Equations*, pp. 1–21, 2020.

[42] M. M. Bhatti, "Biologically inspired intra-uterine nanofluid flow under the suspension of magnetized gold (Au) nanoparticles: applications in nanomedicine," *Inventions*, vol. 6, no. 2, p. 28, 2021.

[43] K. A. Hoffman and S. T. Chiang, "Computational fluid dynamics. Engineering education system," *Kansas*, vol. 1, p. 486, 2000.

[44] O. A. Bég, M. S. Khan, I. Karim, M. M. Alam, and M. Ferdows, "Explicit numerical study of unsteady hydromagnetic mixed convective nanofluid flow from an exponentially stretching sheet in porous media," *Applied Nanoscience*, vol. 4, no. 8, pp. 943–957, 2014.

[45] J. Tripathi, B. Vasu, O. A. Bég, R. S. R. Gorla, and P. K. Kameswaran, "Computational simulation of rheological blood flow containing hybrid nanoparticles in an inclined catheterized artery with stenotic, aneurysmal and slip effects," *Computers in Biology and Medicine*, vol. 139, Article ID 105009, 2021.

[46] A. Zaman, N. Ali, and N. Kousar, "Nanoparticles (Cu, TiO2, Al2O3) analysis on unsteady blood flow through an artery with a combination of stenosis and aneurysm," *Computers & Mathematics with Applications*, vol. 76, no. 9, pp. 2179–2191, 2018.

[47] K. S. Mekheimer, B. M. Shankar, S. F. Ramadan, H. E. Mallik, and M. S. Mohamed, "On the stability of convection in a non-Newtonian vertical fluid layer in the presence of gold nanoparticles: drug agent for thermotherapy," *Mathematics*, vol. 9, no. 11, p. 1302, 2021.

[48] A. C. Burton, "Physiology and biophysics of the circulation," *Introductory Text*, Year Book Medical Publisher, Chicago, 1966.

[49] O. A. Bég, N. Ali, A. Zaman, E. T. A. Bég, and A. Sohail, "Computational modeling of heat transfer in an annular porous medium solar energy absorber with the P1-radiative differential approximation," *Journal of the Taiwan Institute of Chemical Engineers*, vol. 66, pp. 258–268, 2016.

[50] A. Zaman, N. Ali, O. Anwar Bég, and M. Sajid, "Heat and mass transfer to blood flowing through a tapered overlapping stenosed artery," *International Journal of Heat and Mass Transfer*, vol. 95, pp. 1084–1095, 2016.

[51] F. Sultan, N. A. Khan, and M. I. Afridi, "Investigation of biological mechanisms during flow of nano-Bingham-Papanastasiou fluid through a diseased curved artery," *Part N: Journal of Nanomaterials, Nanoengineering and Nanosystems*, vol. 234, no. 3, pp. 69–81, 2020.

Hindawi
Complexity
Volume 2022, Article ID 3086747, 11 pages
https://doi.org/10.1155/2022/3086747

Research Article

A Hidden Chaotic Attractor with an Independent Amplitude-Frequency Controller

Yousuf Islam,[1,2] Chunbiao Li,[1,2] Yicheng Jiang,[1,2] Xu Ma,[1,2] and Akif Akgul[3]

[1]*School of Electronic Information Engineering, Nanjing University of Information Science & Technology, Nanjing 210044, China*
[2]*Jiangsu Collaborative Innovation Center of Atmospheric Environment and Equipment Technology (CICAEET), Nanjing University of Information Science & Technology, Nanjing 210044, China*
[3]*Department of Computer Engineering, Faculty of Engineering, Hitit University, Corum 19030, Turkey*

Correspondence should be addressed to Akif Akgul; akifakgul@hitit.edu.tr

Received 10 January 2022; Accepted 11 February 2022; Published 6 March 2022

Academic Editor: M. De Aguiar

In this paper, a three-dimensional chaotic system with a line equilibrium is studied, in which a single nonbifurcation parameter is used to control the amplitude and frequency. A variety of chaotic signals can be modified using the amplitude-frequency control switch. The realization of circuit simulation based on multisim further verifies the theoretical analysis. Finally, the method for encrypting color images is tested, and the process performance is valued. It shows that the novel chaotic oscillation has a promising application prospect in image encryption.

1. Introduction

Since chaos was first modeled by Edward Norton Lorenz in 1963 [1], great attention has been attracted for the reason that in such deterministic systems, chaos refers to the presence of seemingly random irregular motion [2]. In fact, chaos is a universal phenomenon in nonlinear systems and an inherent property of nonlinear dynamic systems. Chaos is a fundamental concept in nonlinear systems, and it is frequently used to characterize phenomena including bifurcation and periodic motion [3, 4]. It is found that a chaotic system will display bifurcation under specific parameters and that periodic and aperiodic motion can become entangled. Many famous 3-D chaotic systems have been proposed, including Arneodo systems, Sprott systems, Chen systems, Lv-Chen systems, Cai systems, and T systems [5–8]. A chaotic circuit is a significant research topic and an important representation of chaos. Chua proposed the first chaotic circuit in 1984 [9–12], trying to bridge the gap between chaos theory and chaotic circuits. People have performed significant research on chaos theory and produced numerous novel breakthroughs in recent years as a result of the wide application of chaos [13–17]. For information encryption, chaotic sequence signals have a significant application value. Chaos has been extensively applied for many aspects due to the intricate relationship between chaos and cryptography, and significant advancement has been performed in this area. Because of the irregularities and unpredictability of chaotic signals, chaos and corresponding fundamental systems have received a lot of attention [18–24]. A high-dimensional system's chaotic dynamics seem to be more complex, and sometimes, they show hyperchaos for more than two positive Lyapunov exponents [25, 26]. Therefore, it has been proven that chaotic signals can contribute to enhancing the security of chaos-based communication as well as digital encryption. Furthermore, a hidden chaotic attractor is an important phenomenon found ten years ago. The hidden oscillation has received a lot of attention because of its potential threat and possible applications. Finding hidden chaotic attractors in nonlinear dynamical systems has become a major issue in nonlinear dynamical system research [27–29]. Many hidden attractors have been found in memristive systems [30] and hyperchaotic systems [31]. However, there is not much attention on hidden attractors with amplitude-frequency control. Recently, Wang et al. [32]

studied the amplitude control and encryption application of chaotic signal, and they found that modular circuit cells with systematically configured parameters are useful for implementing multipiecewise Chua's diode. Wang et al. [33, 34] also studied the hidden oscillations in Chua's circuit and modified Sprott-A systems, where all the basins of attraction are not intersected with any equilibrium point indicating hidden attractor.

In this paper, a chaotic system with a line of equilibrium points is focused on, where the attractor stands in the region with negative y, and thus, the basin of attraction does not intersect with all equilibrium points indicating hidden attractor. Furthermore, the amplitude and frequency of hidden oscillation can be controlled by a single knob. Circuit implementation shows the convenience of amplitude-frequency control of the chaotic signal. Image encryption proves the merits of this system. The remaining of this paper is organized as follows. In Section 2, the system model is elaborated. In Section 3, the dynamics of the system are analyzed. In Section 4, the system is implemented in a simulated circuit. Finally, a chaotic system is applied to image encryption. The conclusions are presented in the last section.

2. A Novel Hidden Attractor

In reference [35], the 3-dimensional chaotic system is articulated as

$$\begin{cases} \dot{x} = cy + y^2 - ayz, \\ \dot{y} = -z^2 + byz, \\ \dot{z} = xy. \end{cases} \tag{1}$$

The system state variables are x, y, and z, while the constants a, b, and c are the real coefficients, with dots representing a derivative of time t. When $a = 0.9$, $b = 1$, $c = 1$, and IC = (2, −2, 2), the system (1) exhibits chaos in the region with negative y, as shown in Figure 1. There are six terms in this new system, with two nonlinear items. The Lyapunov exponents are $L_1 = 0.1314$, $L_2 = 0$, and $L_3 = -0.8453$.

3. Dynamical Analysis

3.1. Equilibrium Points. Let $\dot{x} = \dot{y} = \dot{z} = 0$. The equilibrium points of the system can be calculated as

$$\begin{cases} cy + y^2 - ayz = 0, \\ -z^2 + byz = 0, \\ xy = 0, \end{cases} \tag{2}$$

$$\begin{cases} E_O = x, 0, 0, \\ E_1 = 0, -c, 0, \\ E_2 = 0, \dfrac{c}{ab-1}, \dfrac{bc}{ab-1}, \end{cases} \tag{3}$$

where $a = 0.9$, $b = 1$, and $c = 1$. Solving this equation, the dynamical system (1) has three nontrivial equilibrium points in (2) which is independent of the value of the parameters a, b, and c.

$$J = \begin{vmatrix} 0 & c + 2y - az & -ay \\ 0 & bz & by - 2z \\ y & x & 0 \end{vmatrix}. \tag{4}$$

As $|J - \lambda I| = 0$, the characteristic equation is

$$\det(J - \lambda I) = -a\lambda y^2 + 2ayz^2 + bcy^2 + b\lambda^2 z + b\lambda xy + 2by^3 - 2cyz - \lambda^3 - 2\lambda xz - 4y^2 z = 0. \tag{5}$$

In the Jacobian matrix of system (1), the equilibrium point E is defined as

$$J(E_O) = J(E_1) = J(E_2) = \begin{pmatrix} 0 & c + 2y - az & -ay \\ 0 & bz & by - 2z \\ y & x & 0 \end{pmatrix}. \tag{6}$$

The eigenvalues of the matrix at the equilibrium point can be determined as follows:

$$\begin{cases} E_O\colon \lambda_1 = 0; \lambda_2 = 0; \lambda_3 = 0, \\ E_1\colon \lambda_1 = -0.7113; \lambda_2 = 0.3556 + 1.1311i; \lambda_3 = 0.3556 - 1.1311i, \\ E_2\colon \lambda_1 = 0.9911; \lambda_2 = -5.4956 + 8.4079i, \lambda_3 = -5.4956 - 8.4079i. \end{cases} \tag{7}$$

The eigenvalues of the system are obtained while $a = 0.9$, $b = 1$, and $c = 1$. The obtained all eigenvalues are given in Equation (7). The equilibrium $E_1(0, -c, 0)$ is a saddle-focus point of index-2; therefore, this equilibrium point E_1 is unstable, and we can see in E_2 that λ_1 is a positive real number, and λ_2 and λ_3 are a pair of complex conjugate

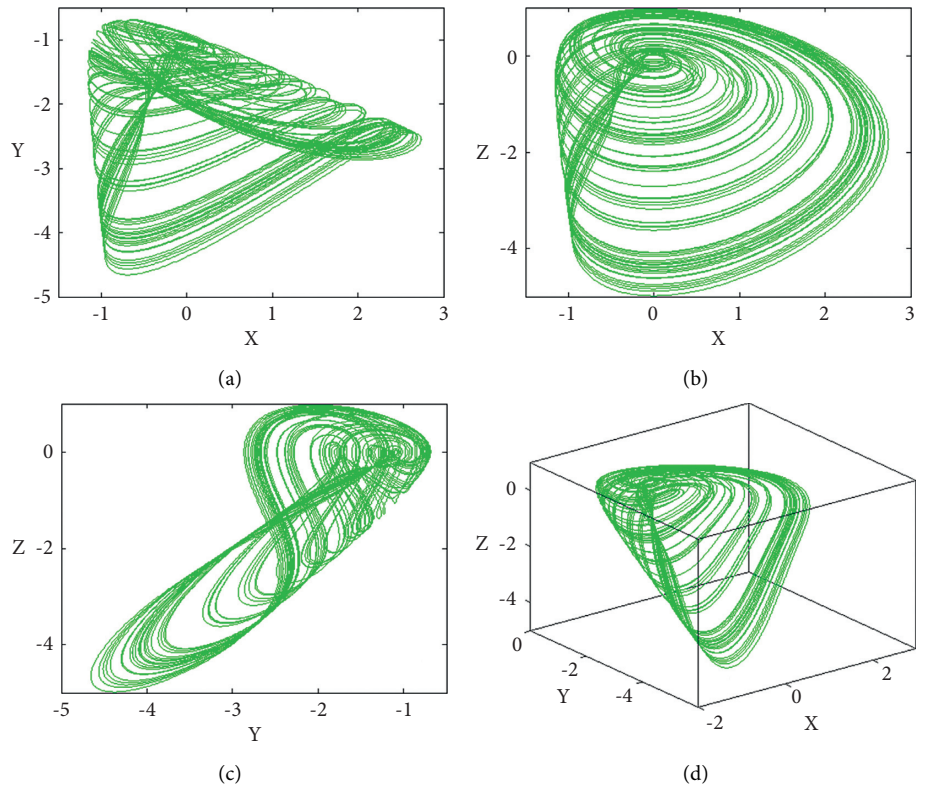

FIGURE 1: Chaotic attractor of system (1) with $a = 0.9$, $b = 1$, and $c = 1$ under initial condition IC = (2, − 2, 2): (a) (x)-(y), (b) (x)-(z), (c) (y)-(z), and (d) (x)-(y)-(z).

eigenvalues with a negative real number. The equilibrium $E_2(0, c/ab - 1, bc/ab - 1)$ is a saddle-focus point of index-1; therefore, this equilibrium point E_2 is also unstable.

3.2. Dissipativity Analysis. Inference μ is a region in the horizontal surface A^3, and $V(t)$ is set to be the volume of $\mu(t)$.

Here, we obtain

$$\dot{V}(t) = \int_{\mu(t)}^{\infty} (\nabla \times F) \mathrm{d}x\mathrm{d}y\mathrm{d}z. \tag{8}$$

Therefore, the dissipativity of the proposed chaotic system is

$$\begin{aligned} \nabla \times F &= \frac{\partial \dot{x}}{x} + \frac{\partial \dot{y}}{y} + \frac{\partial \dot{z}}{z}, \\ &= \frac{\partial\left(cy + y^2 - ayz\right)}{x} + \frac{\partial\left(-z^2 + byz\right)}{y} + \frac{\partial(xy)}{z} \\ &= 0 + bz + 0 = z = \gamma, \end{aligned} \tag{9}$$

where F is the 3-dimensional chaotic system, and b and z are the real parameters. The above equation is rewritten as

$$\dot{V}(t) = \int_{\mu(t)}^{\infty} \gamma \mathrm{d}x\mathrm{d}y\mathrm{d}z = \gamma V(t). \tag{10}$$

Therefore, we can obtain $V(t) = e^{\gamma} V(0)$; if $\nabla \times F < 0$, then system (1) is dissipative and the state of the system is bounded by the state of the system (when a = 0.9, b = 1, and c = 1).

3.3. Amplitude and Frequent Control. In system (1), parameter c is a single knob for amplitude and frequency control. Let $x \longrightarrow mx$, $y \longrightarrow my$, $z \longrightarrow mz$, $t \longrightarrow t/m$ $(m > 0)$; then, system (1) turns to be

$$\begin{cases} \dot{x} = \dfrac{c}{m} y + y^2 - ayz, \\ \dot{y} = -z^2 + byz, \\ \dot{z} = xy, \end{cases} \tag{11}$$

indicating that the parameter c can control the amplitude and frequency of all variables x, y, and z, as shown in Figure 2. In Figure 3(a), when the linear coefficient c is increased, system (1) keeps the chaotic state of all the time and the chaotic area continue to increase. The rescaled amplitude and frequency can also be proved by Lyapunov exponents, as shown in Figure 3(b).

4. Circuit Implementation

Circuit verification is also an essential step in the implementation of the proposed chaotic system to ensure its

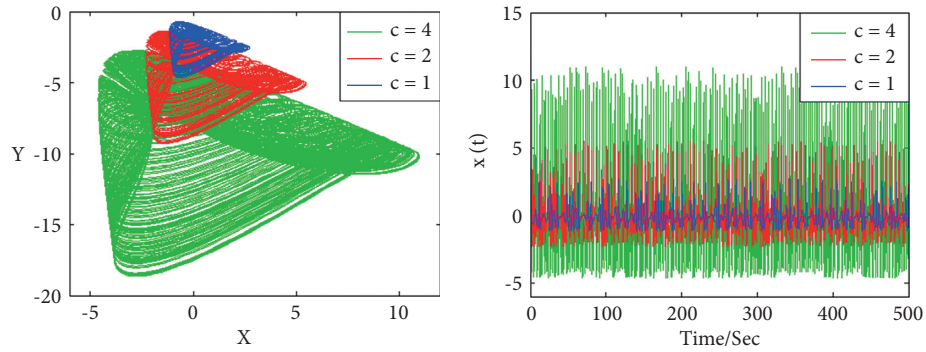

Figure 2: Rescaled attractor of system (1) with $a = 0.9$, $b = 1$, and initial values (2, −2, 2) under the parameter c: (a) (x)-(y) and (b) signal $x(t)$.

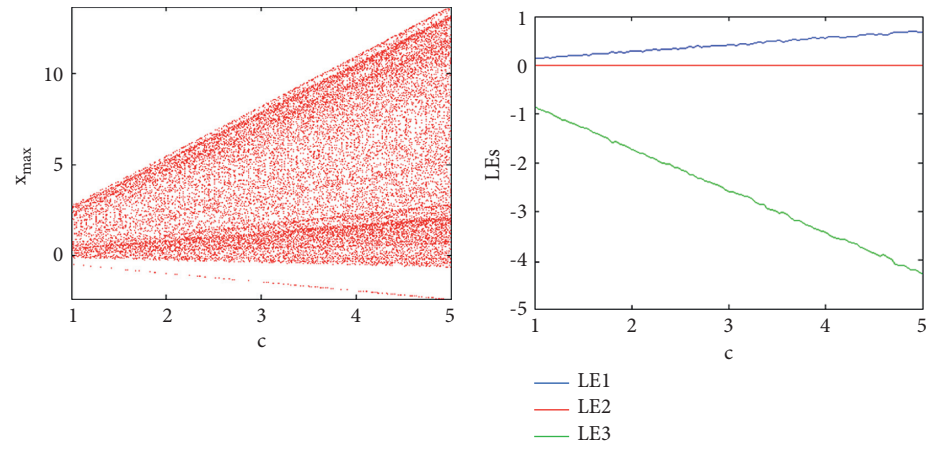

Figure 3: Dynamical evolution of system (1) with $a = 0.9$, $b = 1$, and initial values (2, − 2, 2) when c is in [1, 5]: (a) bifurcation diagram and (b) Lyapunov exponents.

correctness. Meanwhile, the key issue in the circuit is how to implement a circuit expression for a 3D chaotic system by converting and transforming it into a realistic circuit using electronic devices such as capacitors and resistors. To authenticate the efficiency of our proposed 3-dimensional chaotic system, the circuit implementation is designed and simulated with the NI multisim circuit simulation software, and the simulation results are detailed in this section.

For this circuit construction, it is transformed to be

$$\begin{cases} \dot{x} = \dfrac{1}{R_1 C_1} y + \dfrac{1}{R_2 C_1} y^2 - \dfrac{1}{R_3 C_1} yz, \\ \dot{y} = -\dfrac{1}{R_4 C_2} z^2 + \dfrac{1}{R_5 C_2} yz, \\ \dot{z} = \dfrac{1}{R_8 C_3} xy. \end{cases} \tag{12}$$

A chaotic system is defined as a system that has several causes and multiplication, addition, and differentiation, and differentiation exists in the system equations, and a realistic expression of this system is obtained utilizing a summation, an integrator, and a transformer. The relevant circuit implementation is depicted in Figure 4 based on the above explanations. The state variables x, y, and z in the system (1) correspond to the state voltages of the capacitors C_1, C_1, and C_3 in the simplified circuit, and the corresponding circuit components can be selected as follows: $V_1 = V_2 = 15V$, $C_1 = C_2 = C_3 = 10nF$, $R_1 = R_2 = R_4 = R_5 = R_6 = R_7 = R_8 = 100k\Omega$, $R_3 = 106k\Omega$; LM741CN is selected as an operational amplifier; there is a general time scale 1000 for better displaying in the oscilloscope.

Figure 5 shows the phase trajectory of the system (1) in the analog oscilloscope. The area of the phase track will change with the organization of the resistance R_1, as shown in Figure 5(d).

5. Application in Image Encryption

The chaotic system with a linear equilibrium in this section has a higher level of unpredictability, a larger keyspace, and a higher level of complexity, all of which make the encryption stronger secure in concept.

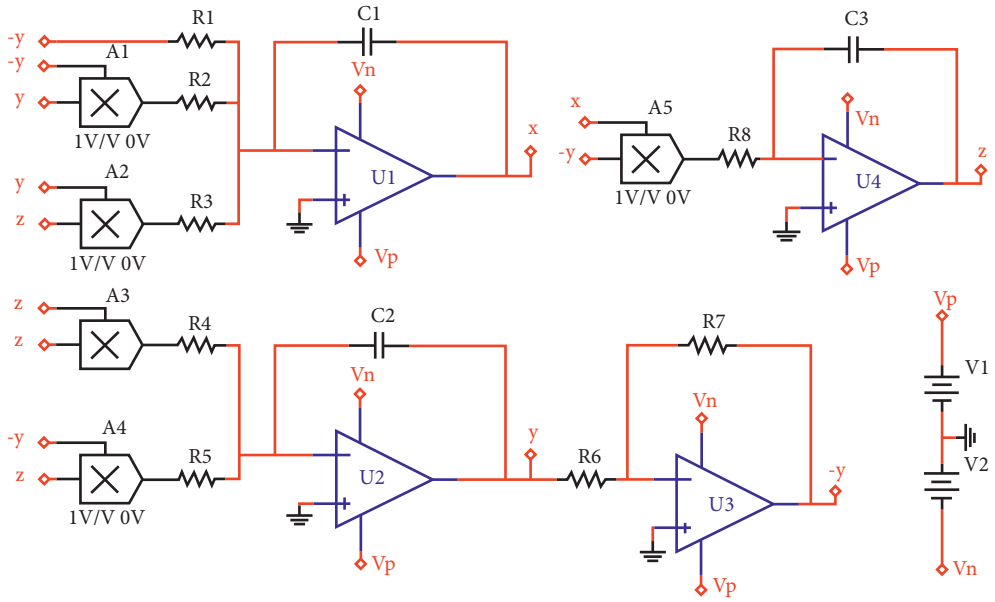

Figure 4: Circuit realization of the system (1).

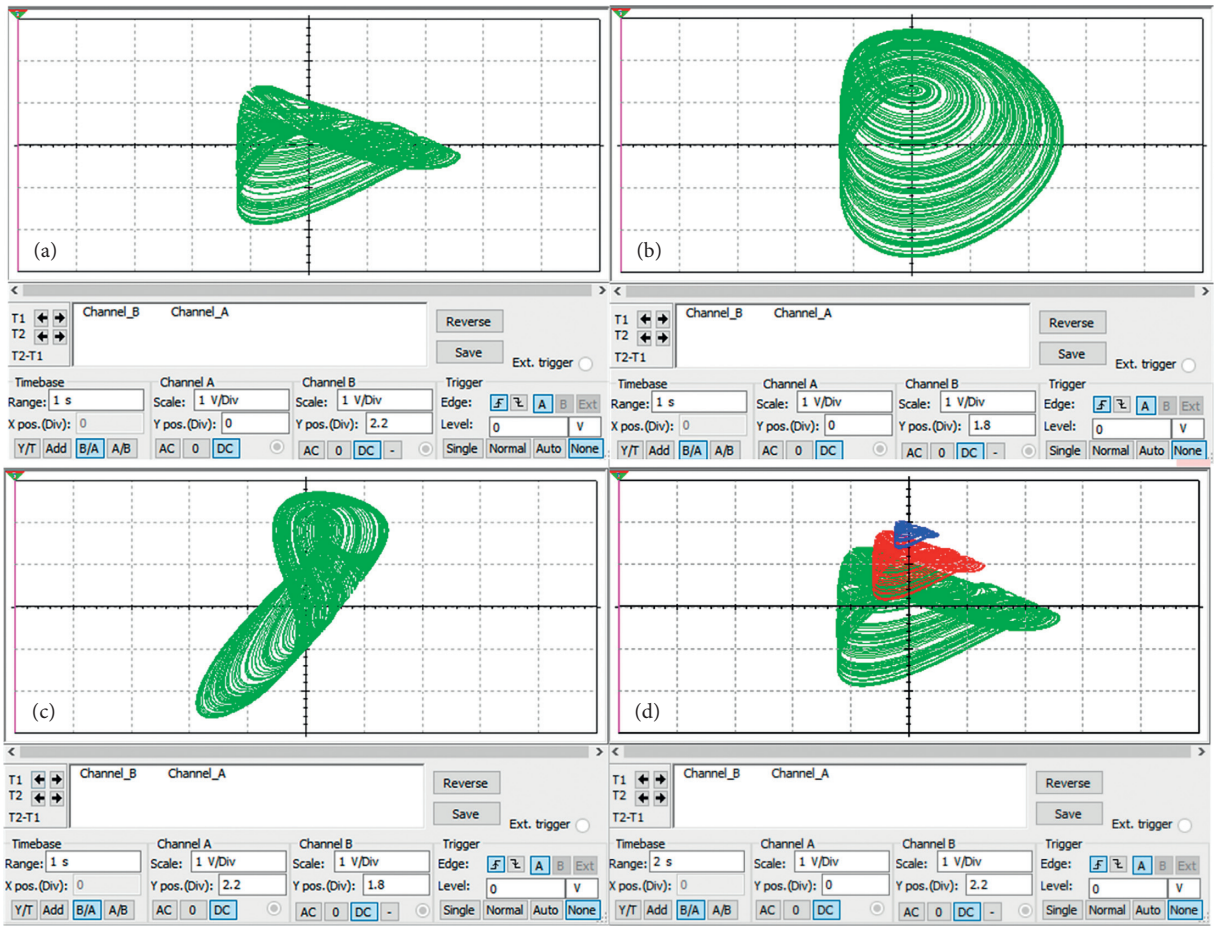

Figure 5: Chaotic attractor of system (1): (a) (x)-(y), (b) (x)-(z), (c) (y)-(z), and (d) the attractor changes due to the difference of R_1 resistance.

5.1. Encryption Application with a Chaotic System. The control parameters and initial conditions of the system are (Table 1) $\mu = 3.9999$ and $x_0 = 0.6209$, respectively, and a standard color image is chosen for testing, as illustrated in Figure 6. The new chaotic system parameters are $a = 0.9$, $b = 1$, and $c = 1$. The initial conditions are set as $X_0 = 0.7361, Y_0 = 0.4663, Z_0 = 0.1501$, and $U_0 = 0.7653$. Table 2 describes the selected keys that were chosen. M_1 and N_1 are the zeroing parameters used throughout encryption; k_1 is the average gray level of G in the original image, and the original image k_2 is the average gray level of B. Figure 6(b) shows the encrypted image after simulation. The image after encryption is chaotic and fundamentally different from the image before processing, as it can be observed. The properly decrypted image, which can be seen in Figure 6(c), is identical to the original image (Table 2).

5.2. Security Analysis. Secure analysis is the most essential and fundamental requirement for an encrypted system. In general, a chaotic image encryption algorithm requires a substantial keyspace, reversible encryption and decryption, strong antiattack characteristics, and the other performances, and then the performance of chaos-based encryption is the next to determine by using the following eligibility requirements: keyspace analysis, histogram analysis, information entropy analysis, and correlation analysis.

5.3. Keyspace Analysis. The keyspace can approach $(10^{16})^{10} = 10^{160}$, satisfying the security level of the keyspace (greater than 2^{128}) using a 64-bit processor, floating-point precision up to 10^{-16}. The modified system can be observed to be more resistant to the attacker's comprehensive attack. The decrypted image cannot be acquired accurately when the algorithm key is changed slightly, as shown in Figure 7. As a result, the new system has a high level of key sensitivity. The images used throughout the investigations are 256×256 conventional images with a $2^3 = 8$-bit grayscale.

5.4. Histogram Analysis. The distribution of pixel intensity values within an image is represented by a histogram. It can be utilized to defend against statistical attacks. The frequency distribution of each gray level pixel can be visually displayed using a gray histogram, which is a statistical analytical method. The histogram of the image becomes smooth even after encryption, compared to the fluctuation before encryption, thus preventing the attacker from accessing the original image information through statistical analysis, resulting in information leakage, and ensuring information. Figures 8(a)–8(c) are the histograms of the original image, and Figures 8(d)–8(f) are the histograms of the encrypted images. It is clear that the new system can withstand a more powerful onslaught.

5.5. Information Analysis for Entropy. The image's information entropy can be used to evaluate the level of uncertainty and randomness in the image distribution of its pixel gray value. Typically, the higher the image's entropy, the more consistent the image's gray distribution. In a grayscale image, each pixel is coded in 8 bits. As a result, an image's maximum entropy value is 8. The information entropy of the encrypted image should be near 8, which indicates the best amount of uncertainty, owing to a decent encryption process. To compute the information entropy, many users use the method as follows:

$$\text{entropy}H(m) = -\sum_{i=1}^{H} p(x_i)\log_2\ p(x_i), \tag{13}$$

where $p(x_i)$ represents the probability of the occurrence of the gray value x_i and H indicates the gray level of the image. Theoretically, for a completely random digital image with a grayscale of 256 has an evenly distributed pixel value in [0, 255], then $p(x_i) = 1/256$ $(i \in \in [0, 255])$, and the estimated information entropy is 8 bits. If the image is encrypted, the closer the image's information entropy is near 8, the better the encryption features.

5.6. Correlation Statistical Analysis. On the one hand, the correlation level of adjacent pixels is larger when the correlation coefficient degree of adjacent pixels is higher. On the other hand, the lower the correlation, the smaller the coefficient. As a result, calculating the correlation coefficient can be justified the algorithm's security. The lower the correlation and the advanced security, the smaller the coefficient. The correlation coefficients were calculated from the three channels (R, G, and B) with three directions: horizontal, vertical, and diagonal, to measure the correlation between the original image and adjacent pixels of the ciphertext image; N pairs of adjacent pixels were selected from the image, and the correlation coefficients were calculated from the three channels (R, G, B) with three directions: horizontal, vertical, and diagonal. To equivalence the autocorrelation of an unadorned and encrypted image, we have calculated the correlation coefficient r of each pair of pixels by using the following formula:

$$\begin{aligned} r_{XY} &= \frac{\text{cov}(X,Y)}{\sqrt{D(X)D(Y)}}, \\ E(X) &= \frac{1}{N}\sum_{i=1}^{N}(x_i), \\ D(X) &= \frac{1}{N}\sum_{i=1}^{N}(x_i - E(X)), \\ \text{cov}(X,Y) &= \frac{1}{N}\sum_{i=1}^{N}(x_i - E(X))(y_i - E(Y)), \end{aligned} \tag{14}$$

where $\text{cov}(X,Y)$ represents the correlation and autocorrelation function, X and Y are the grayscale values of two adjacent pixels in the image, and N denotes the sample. E is the expected value operator, and $D(X)$ represents the variance of the variable x. The values of r_{XY} lie in the range

Table 1: Algorithm key.

Key	μ	x_0	X_0	Y_0	Z_0	U_0	M_1	N_1	k_1	k_2
Value	3.9999	0.6209	0.7361	0.4663	0.1501	0.7653	0	0	0.4761	0.1255.

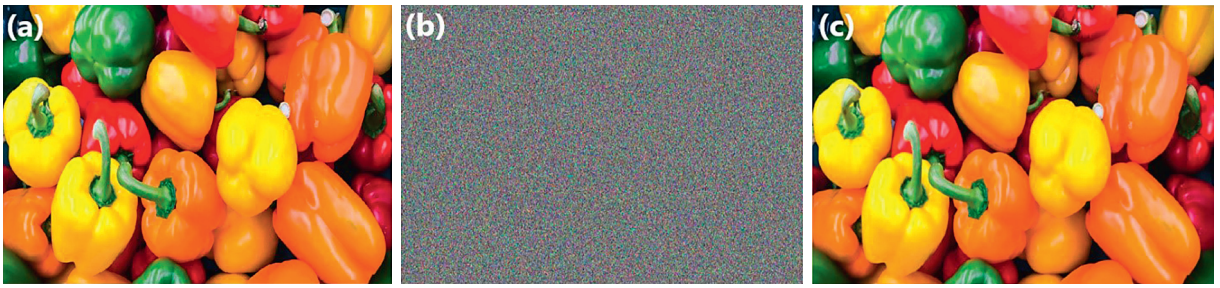

Figure 6: Encryption images: (a) original pepper image; (b) encryption pepper image; (c) decryption pepper image.

Table 2: The information entropy of the three channels in the original and encrypted on the pepper image.

Image	R channel entropy	G channel entropy	B channel entropy
Original picture	5.6871	7.6856	4.686
Encrypted image	7.9997	7.9997	7.9998

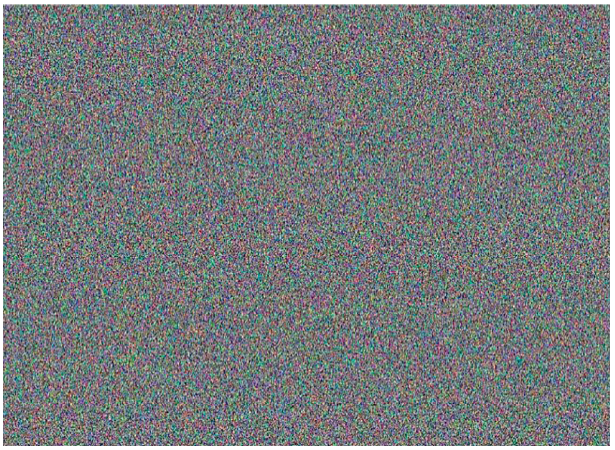

Figure 7: Initial condition perturbation ciphertext.

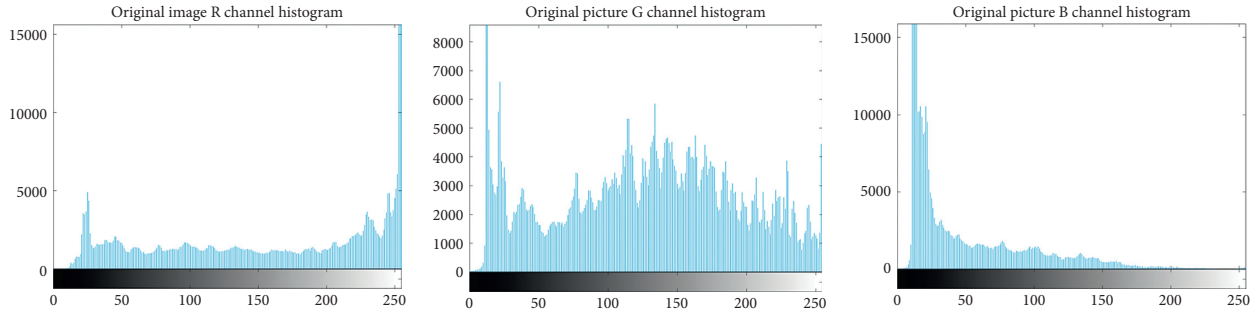

(a) (b) (c)

Figure 8: Continued.

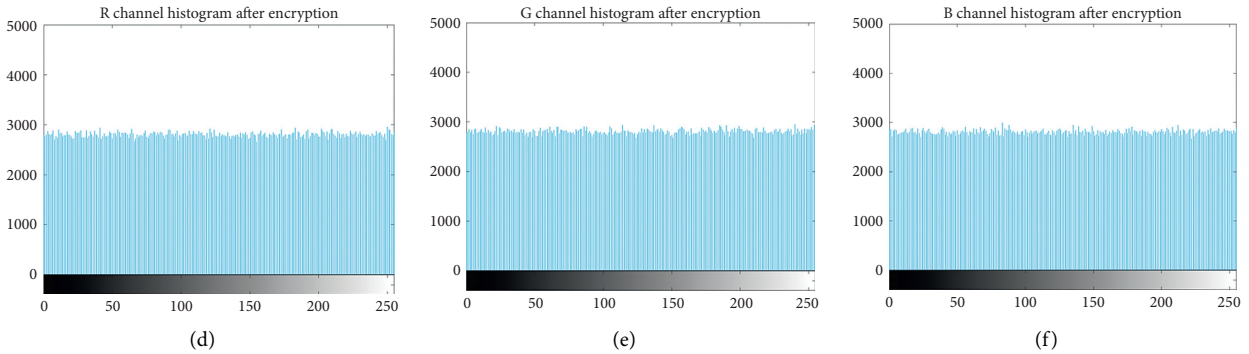

Figure 8: Histogram experiment images. (a–c) Histogram of the original image. (d–f) Histogram of the encrypted image.

Table 3: A correlation coefficient of two adjacent pixels in the original and encrypted on the pepper image.

Image	Channel	Horizontal	Vertical	Diagonal
Original image	B	0.98645	0.98782	0.97851
	G	0.99529	0.99282	0.98965
	R	0.99428	0.99168	0.98792
Encrypted image	B	0.00494	−0.02531	0.00540
	G	−0.01262	−0.01606	0.00444
	R	−0.00282	−0.01656	0.00919

Table 4: Correlation coefficient test result [36].

Image	Channel	Horizontal	Vertical	Diagonal
Original image	Red	0.97489	0.98660	0.96227
	Green	0.97532	0.98731	0.96377
	Blue	0.95167	0.97112	0.92931
Encrypted image	Red	0.00070	0.01175	0.01539
	Green	0.00855	−0.01537	−0.01660
	Blue	0.00122	0.00135	0.01235

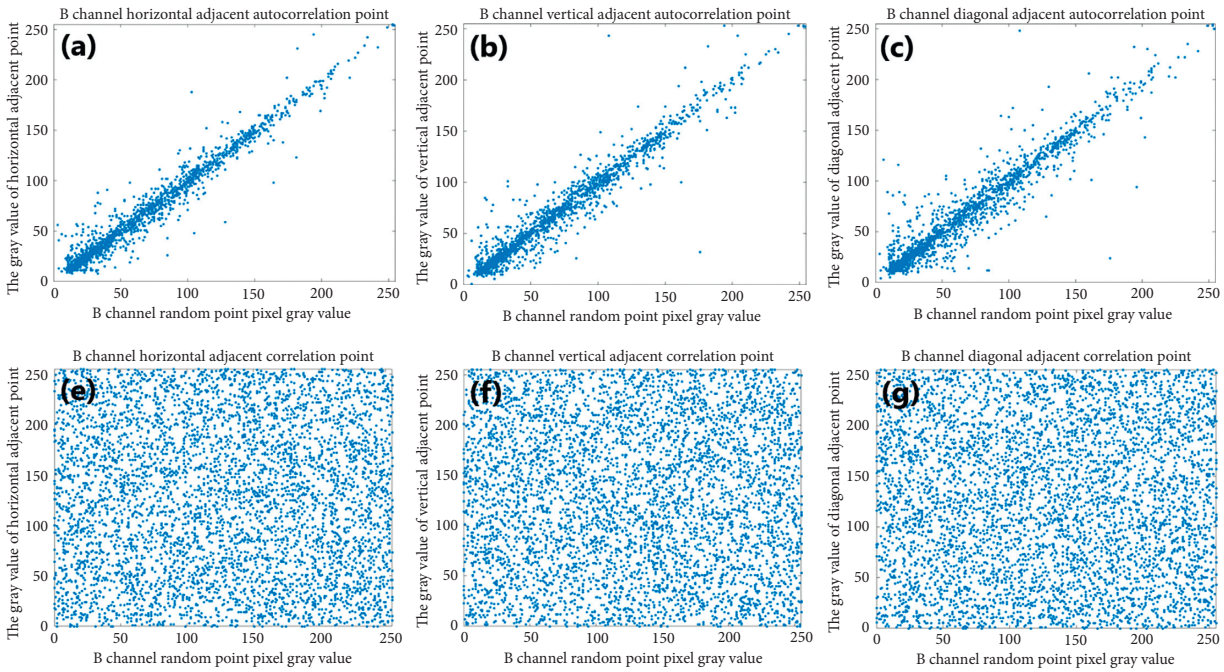

Figure 9: Correlation and autocorrelation of R channel adjacent pixels of the pepper image and its ciphered image: (a) horizontal direction of the pepper image; (b) vertical direction of the pepper image; (c) diagonal direction of the pepper image; (d) horizontal direction of the pepper ciphered image; (e) vertical direction of the pepper ciphered image; (f) diagonal direction of the pepper ciphered image.

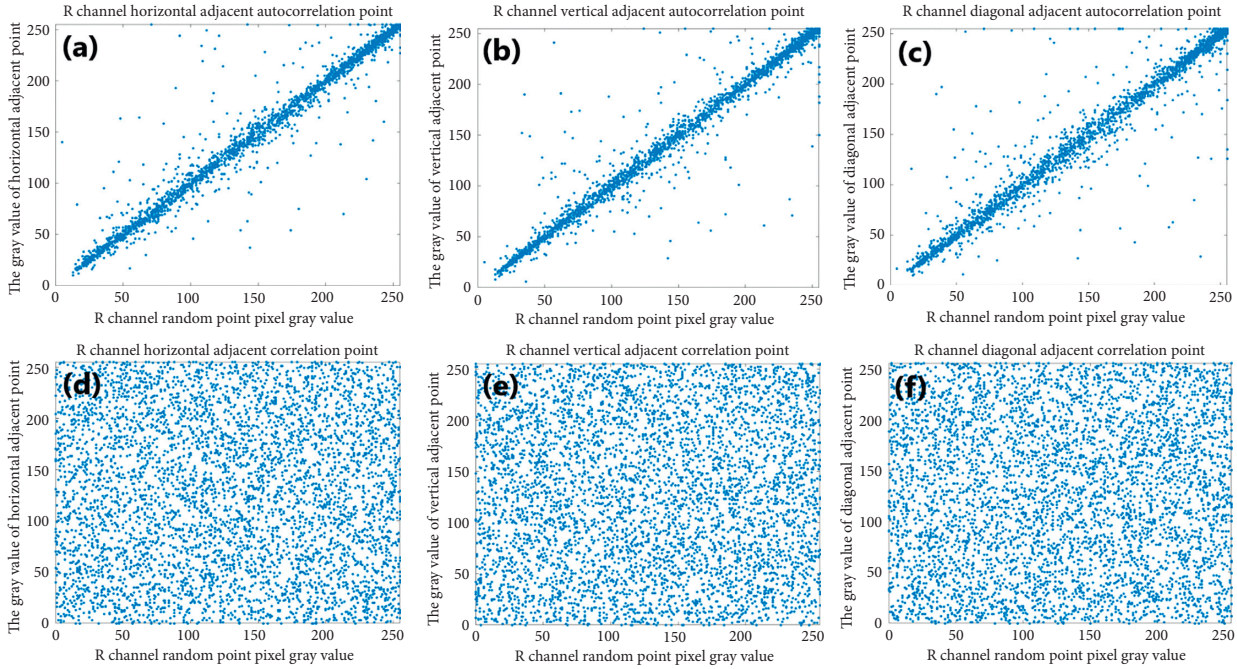

Figure 10: Correlation and autocorrelation of G channel adjacent pixels of the pepper image and its ciphered image: (a) horizontal direction of the pepper image; (b) vertical direction of the pepper image; (c) diagonal direction of the pepper image; (d) horizontal direction of the pepper ciphered image; (e) vertical direction of the pepper ciphered image; (f) diagonal direction of the pepper ciphered image.

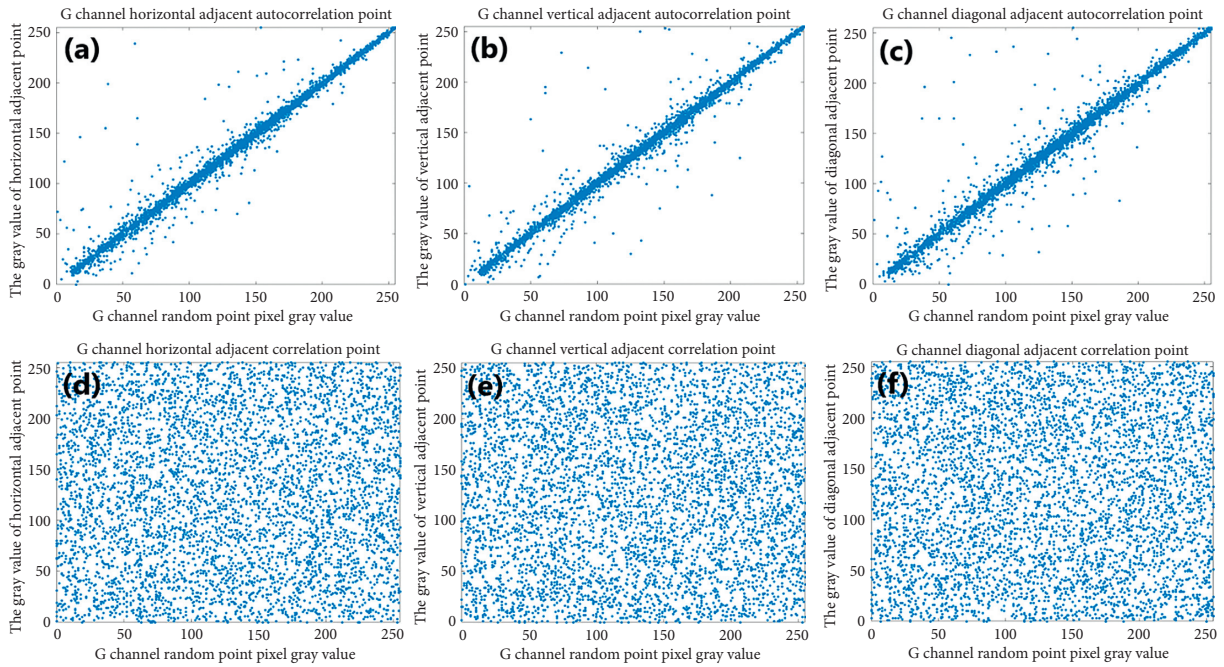

Figure 11: Correlation and autocorrelation of B channel adjacent pixels of the pepper image and its ciphered image: (a) horizontal direction of the pepper image; (b) vertical direction of the pepper image; (c) diagonal direction of the pepper image; (d) horizontal direction of the pepper ciphered image; (e) vertical direction of the pepper ciphered image; (f) diagonal direction of the pepper ciphered image.

[−1, 1], with 1 indicating perfect correlation, −1 indicating anticorrelation, and 0 representing no correlation.

Here, we can see from Table 3 that the correlation coefficients of the original image are all very close to 1, whereas the correlation coefficients of the encrypted image are all very close to 0, indicating that the encrypted image's pixel point distribution is very highly discrete.

If we compare Tables 3 and 4 with each other, we can see some different points. In Table 3, the original correlation coefficient values are average horizontal 99.2%, vertical

99.07%, and diagonal 98.54%, and in Table 4, the original correlation coefficient values are average horizontal 96.72%, vertical 98.17%, and diagonal 95.18%, that is, the original points in Table 3 are closer to 1 and the encrypted points are also closer to 0 than Table 4. So, Table 3 indicates that the encrypted points of distribution are highly discrete.

The correlation and autocorrelation plots for each image are shown in Figures 9–11. In Table 3, horizontal, vertical, and diagonal directions provide their correlation and autocorrelation coefficients. Table 3 also includes significant data from references for comparison.

6. Conclusion

The single nonbifurcation parameter of the system can effectively modify the amplitude and frequency of the demonstrated three-dimensional chaotic system. Numerical simulation and circuit experiment based on multisim agree to each other by proving the phenomenon. As a typical application, the property of image encryption is exhaustively analyzed. With the chaotic signal from the new system, a color image is well encrypted and decrypted in the keyspace. Histogram and correlation of adjacent pixels are used for showing the high encryption performance.

Data Availability

The data used to support the findings of this study are available from the corresponding author upon reasonable request.

Conflicts of Interest

The authors declare that there are no conflicts of interest regarding the publication of this paper.

References

[1] E. N. Lorenz, "Deterministic nonperiodic flow," *J. Atoms*, vol. 20, pp. 25–36, 1963.

[2] W. Yu, J. Wang, J. Wang et al., "Design of a new seven-dimensional hyperchaotic circuit and its application in secure communication," *IEEE Access*, vol. 7, pp. 125586–125608, 2019.

[3] C. Li, J. C. Sprott, W. Hu, and Y. Xu, "Infinite multistability in a self-reproducing chaotic system," *International Journal of Bifurcation and Chaos*, vol. 27, no. 10, Article ID 1750160, 2017.

[4] C. Li, W. Li, J. Zhang, Y. Xie, and Y. Zhao, "Amplitude-phase modulation, topological horseshoe and scaling attractor of a dynamical system," *Communications in Theoretical Physics*, vol. 66, no. 9, pp. 297–305, 2016.

[5] G. Chen and T. Ueta, "Yet another chaotic attractor," *International Journal of Bifurcation and Chaos*, vol. 9, no. 7, pp. 1465-1466, 1999.

[6] J. Lü and G. Chen, "A new chaotic attractor coined," *International Journal of Bifurcation and Chaos*, vol. 12, no. 3, pp. 659–661, 2002.

[7] J. Lü, G. Chen, D. Cheng, and S. Celikovsky, "Bridge the gap between the lorenz system and the chen system," *International Journal of Bifurcation and Chaos*, vol. 12, no. 12, pp. 2917–2926, 2002.

[8] Q. Yang, G. Chen, and T. Zhou, "A unified Lorenz-Type system and its canonical form," *International Journal of Bifurcation and Chaos*, vol. 16, no. 10, pp. 2855–2871, 2006.

[9] L. O. Chua, T. Matsumoto, and M. Komuro, "The double scroll family. 2. rigorous analysis of bifurcation phenomena," *IEEE Transactions on Circuits and Systems*, vol. 33, no. 11, pp. 1097–1118, 1986.

[10] Z. Wei, P. Yu, W. Zhang, and M. Yao, "Study of hidden attractors, multiple limit cycles from Hopf bifurcation and boundedness of motion in the generalized hyperchaotic Rabinovich system," *Nonlinear Dynamics*, vol. 82, no. 1-2, pp. 131–141, 2015.

[11] A. Akgul, S. Hussain, and I. Pehlivan, "A new three-dimensional chaotic system, its dynamical analysis and electronic circuit applications," *Optik*, vol. 127, no. 18, pp. 7062–7071, 2016.

[12] Z. Wei, V.-T. Pham, T. Kapitaniak, and Z. Wang, "Bifurcation analysis and circuit realization for multiple-delayed Wang-Chen system with hidden chaotic attractors," *Nonlinear Dynamics*, vol. 85, no. 3, pp. 1635–1650, 2016.

[13] S. M. Tabatabaie Nezhad, M. Nazari, and E. A. Gharavol, "A novel dos and ddos attacks detection algorithm using arima time series model and chaotic system in computer networks," *IEEE Communications Letters*, vol. 20, no. 4, pp. 700–703, 2016.

[14] Z. Wei, I. Moroz, J. C. Sprott, Z. Wang, and W. Zhang, "Detecting hidden chaotic regions and complex dynamics in the self-exciting homopolar disc dynamo," *International Journal of Bifurcation and Chaos*, vol. 27, no. 2, Article ID 1730008, 2017.

[15] J. P. Singh and B. K. Roy, "The simplest 4-D chaotic system with line of equilibria, chaotic 2-torus and 3-torus behaviour," *Nonlinear Dynamics*, vol. 89, no. 3, pp. 1845–1862, 2017.

[16] Z. Wang, A. Akgul, V. T. Pham, and S. Jafari, "Chaos-based application of a novel no-equilibrium chaotic system with coexisting attractors," *Nonlinear Dynamics*, vol. 89, no. 46, pp. 1877–1887, 2017.

[17] J. P. Singh and B. K. Roy, "Second order adaptive time varying sliding mode control for synchronization of hidden chaotic orbits in a new uncertain 4-D conservative chaotic system," *Transactions of the Institute of Measurement and Control*, vol. 40, no. 13, pp. 3573–3586, 2018.

[18] J. P. Singh, K. Lochan, N. V. Kuznetsov, and B. K. Roy, "Coexistence of single- and multi-scroll chaotic orbits in a single-link flexible joint robot manipulator with stable spiral and index-4 spiral repellor types of equilibria," *Nonlinear Dynamics*, vol. 90, no. 2, pp. 1277–1299, 2017.

[19] Z. Wei, I. Moroz, J. C. Sprott, A. Akgul, and W. Zhang, "Hidden hyperchaos and electronic circuit application in a 5d self-exciting homopolar disc dynamo," *Chaos: An Interdisciplinary Journal of Nonlinear Science*, vol. 27, no. 3, Article ID 033101, 2017.

[20] V. R. F. Signing and J. Kengne, "Coexistence of hidden attractors, 2-torus and 3-torus in a new simple 4-D chaotic system with hyperbolic cosine nonlinearity," *International Journal of Dynamics and Control*, vol. 6, pp. 421–1428, 2018.

[21] S. Vaidyanathan, A. Sambas, S. Kacar, and Ü. Çavuşoğlu, "A new three-dimensional chaotic system with a cloud-shaped curve of equilibrium points, its circuit implementation and sound encryption," *International Journal of Modelling, Identification and Control*, vol. 30, no. 3, pp. 184–196, 2018.

[22] Z. Wei, V. T. Pham, A. J. M. Khalaf, J. Kengne, and S. Jafari, "A modified multistable chaotic oscillator," *International Journal*

of Bifurcation and Chaos in Applied Sciences and Engineering, vol. 28, no. 7, Article ID 1850085, 2018.

[23] A. Akgül, S. Kaçar, B. Arıcıoğlu, and I. Pehlivan, "Text encryption by using one-dimensional chaos generators and nonlinear equations," in *Proceedings of the 2013 8th International Conference on Electrical and Electronics Engineering (ELECO)*, pp. 320–323, IEEE, Bursa, Turkey, November 2013.

[24] K. Rajagopal, V. T. Pham, F. R. Tahir, A. Akgul, H. R. Abdolmohammadi, and S. Jafari, "A chaotic jerk system with non-hyperbolic equilibrium: dynamics, effect of time delay and circuit realisation," *Pramana*, vol. 90, no. 4, pp. 1–8, 2018.

[25] X. Zhang, C. Li, Y. Chen, H. H. C. Iu, and T. Lei, "A memristive chaotic oscillator with controllable amplitude and frequency," *Chaos, Solitons & Fractals*, vol. 139, Article ID 110000, 2020.

[26] C. Li, J. C. Sprott, A. Akgul, H. H. C. Iu, and Y. Zhao, "A new chaotic oscillator with free control," *Chaos: An Interdisciplinary Journal of Nonlinear Science*, vol. 27, no. 8, Article ID 083101, 2017.

[27] G. A. Leonov, N. V. Kuznetsov, and V. I. Vagaitsev, "Localization of hidden Chua's attractors," *Physics Letters A*, vol. 375, no. 23, pp. 2230–2233, 2011.

[28] G. A. Leonov, N. V. Kuznetsov, and V. I. Vagaitsev, "Hidden attractor in smooth Chua systems," *Physica D: Nonlinear Phenomena*, vol. 241, no. 18, pp. 1482–1486, 2012.

[29] S. Vaidyanathan, A. T. Azar, A. Akgul, C. H. Lien, S. Kacar, and U. Cavusoglu, "A memristor-based system with hidden hyperchaotic attractors, its circuit design, synchronisation via integral sliding mode control and an application to voice encryption," *International Journal of Automation and Control*, vol. 13, no. 6, pp. 644–667, 2019.

[30] S. Zhang, J. Zheng, X. Wang, and Z. Zeng, "Multi-scroll hidden attractor in memristive HR neuron model under electromagnetic radiation and its applications," *Chaos: An Interdisciplinary Journal of Nonlinear Science*, vol. 31, no. 1, Article ID 011101, 2021.

[31] Q. Yang, L. Yang, and B. Ou, "Hidden hyperchaotic attractors in a new 5D system based on chaotic system with two stable node-foci," *International Journal of Bifurcation and Chaos*, vol. 29, no. 7, Article ID 1950092, 2019.

[32] N. Wang, C. Li, H. Bao, M. Chen, and B. Bao, "Generating multi-scroll chua's attractors via simplified piecewise-linear chua's diode," *IEEE Transactions on Circuits and Systems I: Regular Papers*, vol. 66, no. 12, pp. 4767–4779, 2019.

[33] N. Wang, G. Zhang, N. V. Kuznetsov, and H. Bao, "Hidden attractors and multistability in a modified Chua's circuit," *Communications in Nonlinear Science and Numerical Simulation*, vol. 92, Article ID 105494, 2021.

[34] N. Wang, G. Zhang, N. V. Kuznetsov, and H. Li, "Generating grid chaotic sea from system without equilibrium point," *Communications in Nonlinear Science and Numerical Simulation*, vol. 107, Article ID 106194, 2022.

[35] C. Li and J. C. Sprott, "Chaotic flows with a single nonquadratic term," *Physics Letters A*, vol. 378, no. 3, pp. 178–183, 2014.

[36] J. Sun, C. Li, T. Lu, A. Akgul, and F. Min, "A memristive chaotic system with hypermultistability and its application in image encryption," *IEEE Access*, vol. 8, pp. 139289–139298, 2020.

Hindawi
Complexity
Volume 2022, Article ID 4510236, 14 pages
https://doi.org/10.1155/2022/4510236

Research Article

Josephson Junction Model: FPGA Implementation and Chaos-Based Encryption of sEMG Signal through Image Encryption Technique

Colince Welba,[1] **Dhanagopal Ramachandran**,[2] **Alexendre Noura**,[3] **Victor Kamdoum Tamba**,[4] **Sifeu Takougang Kingni**,[5] **Pascal Eloundou Ntsama**,[3] **and Pierre Ele**[6]

[1]*Department of Fundamental Sciences, National Advanced School of Mines and Petroleum Industries, University of Maroua, P. O. Box 46, Maroua, Cameroon*
[2]*Center for Systems Design, Chennai Institute of Technology, Chennai 600069, Tamilnadu, India*
[3]*Department of Physics, Faculty of Science, University of Ngaoundere, P.O. Box: 454, Ngaoundere, Cameroon*
[4]*Department of Telecommunication and Network Engineering, IUT-Fotso Victor of Bandjoun, University of Dschang, P. O. Box: 134, Bandjoun, Cameroon*
[5]*Department of Mechanical, Petroleum and Gas Engineering, National Advanced School of Mines and Petroleum Industries, University of Maroua, P. O. Box 46, Maroua, Cameroon*
[6]*Electrical and Engineering, Telecommunications Department, National Advanced School of Engineering, University of Yaoundé I, P.O. Box 812, Yaoundé, Cameroon*

Correspondence should be addressed to Colince Welba; welbacolince@yahoo.fr

Received 12 November 2021; Revised 28 December 2021; Accepted 7 January 2022; Published 28 February 2022

Academic Editor: Akif Akgul

The field programmable gate array (FPGA) implementation of the nonlinear resistor-capacitor-inductor shunted Josephson junction (NRCISJJ) model and its application to sEMG (Surface ElectroMyoGraphic) signal encryption through image encrypted technique are reported in this study. Thanks to the numerical simulations and FPGA implementation of the NRCISJJ model, different shapes of chaotic attractors are revealed by varying the parameters. The chaotic behaviour found in the NRCISJJ model is used to encrypt the sEMG signal through image encryption technique. The results obtained are interesting and open up many perspectives.

1. Introduction

Circuits based on Josephson Junction (JJ) devices received particular attention in literature during the past two decades. This great interest is justified not only by the interesting characteristics of JJ device including high working frequency, low power consumption, and ultralow noise but also by their exploitation for constructing important technological devices such as ultrahigh sensitive detectors, high-density computer circuits, quantum-computing devices, superconducting electronic devices (e.g., terahertz pulse generator), and ultrahigh-speed chaotic signal generators [1–8]. Concerning the last application, many works have demonstrated the existence of chaos in several systems using different models of JJ [9–15]. Among them, linear and nonlinear resistor-capacitor-inductor shunted JJ models (LRCISJJ and NRCIJJ) are the most investigated in the relevant literature. This is due to their fascinating properties very suitable for high-frequency applications such as spread spectrum communication systems. Dana et al. characterized the chaotic dynamics in such models [9]. They reported some interesting results on the modulation of chaotic oscillation in such devices by an external sinusoidal signal as information. Control and synchronization of the NRCIJJ

model using the backstepping design method are discussed in [11, 12]. The authors demonstrated that the employed control method is capable to eliminate the chaotic behaviour displayed by the NRCIJJ model and assureed the global asymptotic synchronization between drive-response NRCIJJ models with different system parameters. Remarkable numerical computations were carried out to confirm the feasibility of the developed control technique. Sifeu et al. [16] studied the dynamics and synchronization of the NRCLJJ model. They used the fractional-order form of the model to develop an application to digital cryptography. Implementing chaotic models with electronic devices has some inconveniences due to the limitations of bandwidth of some electronic devices such as operational amplifiers. To overcome these limitations, the implementation of chaotic models is carried out with FPGA and microcontroller devices. In this regard, the authors of [17] analyzed and implemented with FPGA a fractal JJ with unharmonic current-phase relation. They applied the system under scrutiny to chaos-based random number generator. Kadjie et al. [18] discussed the implementation with microcontroller of a NRCIJJ model and its applications in electromechanical engineering. The real electrical signals obtained from the implementation of the considered JJ model have been exploited to power an electromechanical pendulum. The numerical simulations revealed periodic and chaotic behaviours in the resulting system. Lai et al. proposed letter reports. In this letter, the authors constructed an interesting no-equilibrium chaotic system from the Lu system. The most striking feature of the new system is that it has hidden attractors and coexisting attractors [19, 20]. In [21], the authors investigated a 4D extended Lü system which coexists multiple attractors with respect to different initial conditions. Lai et al. [22] reported a new 4D chaotic system with double memristors. The numerical simulation indicated that the system is capable of yielding infinite coexisting attractors.

In recent years, considerable efforts have been devoted to the designing and investigation of image encryption systems. It is well known that image encryption is a useful technique for secure transmission. The objective of every image encryption algorithm is to generate a noisy image's having top-quality capable to keep information secret [23, 24]. Several image encryption algorithms have been proposed in relevant works. For example, some algorithms used single low-dimensional chaotic systems, such as logistic map, tent map, Baker map, and cat map, to encrypt images [25–29]. Wang and Zhang investigated an image encryption algorithm based on genetic recombination and 4D Lorenz-like hyperchaotic systems [30]. Huang et al. [31] developed a color image encryption algorithm using fractional-order chaotic sequences.

Motivated by the above discussions, this study designs and implements on FPGA a chaotic NRCISJJ model and applies it to secure sEMG signal through image encryption technique. The innovation of this study is to show that it is possible to secure a 1D signal using image encryption techniques. To our knowledge, the literature devoted to securing signals by encryption does not mention work on the encryption of EMG signals. On the other hand, this same literature mentions several works on the encryption of other electrophysiological signals (EEG and ECG). This lack of work on sEMG encryption highlights the originality of this study.

The study is articulated around four sections presented as follows. The FPGA implementation of the NRCISJJ model is presented in Section 2. Section 3 focuses on its application to secure surface electromyographic signals through image encryption technique. Finally, the conclusion of the paper is presented in Section 4.

2. FPGA Implementation of the NRCISJJ Model

The NRCISJJ model is described by the following dimensionless rate of equations [11]:

$$\begin{cases} \dfrac{\mathrm{d}x}{\mathrm{d}t} = \dfrac{1}{\beta_c}\left[i - y - g(x)x - \sin(z)\right], \\ \dfrac{\mathrm{d}y}{\mathrm{d}t} = \dfrac{1}{\beta_L}(x - y), \\ \dfrac{\mathrm{d}z}{\mathrm{d}t} = x, \end{cases} \tag{1}$$

where t, x, y, and z represent the dimensionless time, the voltage in the junction, the inductor current, and the phase difference, respectively. The parameter i is an external direct current source and β_C and β_L are capacitive and inductive parameters, respectively. The function $g(x)$ is a piecewise function approximation by current voltage characteristic of the intrinsic junction shunt resistor defined as

$$g(x) = \begin{cases} 0.366, & \text{if } |x| > 2.9, \\ 0.061, & \text{if } |x| \le 2.9. \end{cases} \tag{2}$$

System (1), describing the NRCISJJ model, is designed in Xilinx system generator Simulink integrated in MATLAB. The blocks of Xilinx system generator tool kit used to design system (1) are configured according to IEEE 754 standard as 32 bit (no. of bits) and 16 bit (binary bit) fixed point, where the latency is set to zero. The forward Euler's algorithm is the digital method used to design the integrator of system (1).

By using the Vivado design tool, the register-transfer level (RTL) architecture required for implementation of NRCISJJ model is presented in Figure 1.

Figure 1 is implemented in Kintex 7 XC7K325fFFG676-1 chip. The discretized state equations of system (1) are given by

$$\begin{aligned} x_{m+1} &= x_m + h\frac{\left[i - y_{m-1} - g(x_{m-1})x_{m-1} - \sin(z_{m-1})\right]}{\beta_C}, \\ y_{m+1} &= y_m + h\frac{(x_{m-1} - y_{m-1})}{\beta_L}, \\ z_{m+1} &= z_m + h(x_{m-1}), \end{aligned} \tag{3}$$

where $\beta_R, \beta_L, \beta_C$, and$i$ are the parameter values of system (1) and the step size $h = 0.01$.

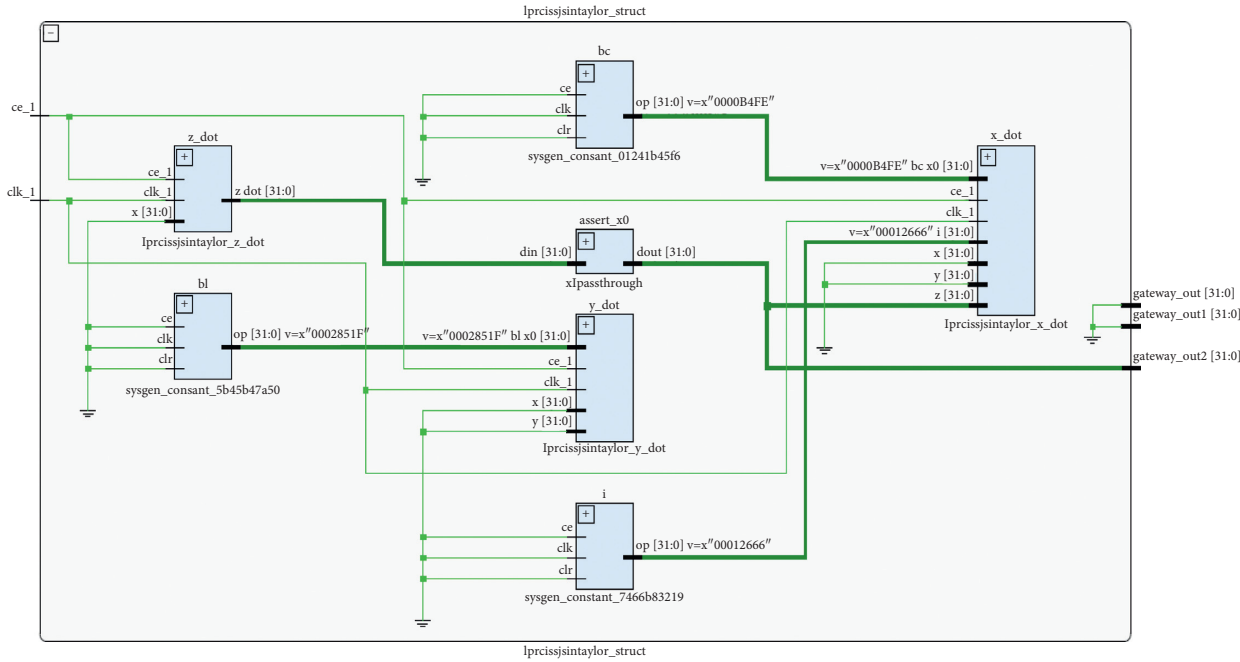

Figure 1: RTL architecture of the NRCISJJ model.

The results of numerical simulations and FPGA implementation of NRCISJJ model are illustrated in Figure 2.

Four different shapes of chaotic attractors are depicted in Figure 2 for given values of parameters i, β_C, and β_L. Moreover, in Figure 2, there is a good qualitative agreement between the numerical simulations and FPGA results.

3. Application of the Chaotic NRCISJJ Model to Secure sEMG Signal Using Chaotic Logistic Map Image Encryption Technique

The proposed encryption technique is based on that used in image encryption by the chaotic logistics map. Innovation takes place in the chaotic sequence. Indeed, the chaotic sequence of the logistic map is replaced in the algorithm by the chaotic sequence of the NRCISJJ model.

The NRCISJJ model is used as a chaotic sequence to apply the sEMG signal encryption technique rather than the chaotic logistic map sequence due to the sensitivity of its key. During the simulation, we found that the key of the NRCISJJ was more sensitive than that of the logistics map. The proposed sEMG signal encryption scheme is shown in Figure 3.

The method presented in Figure 3 consists in transforming the sEMG signal (sEMG_1D) in the form of an image (sEMG_2D). Several works have shown that the manipulation of sEMG in 2D gives better results than sEMG in 1D [32, 33]. The 2D sEMG signal is easily manipulated for pixel swapping. The process of transforming sEMG_1D into sEMG_2D used is described in [34, 35]. Once the signal is transformed into two dimensions as a grayscale image, the encryption algorithm is applied.

The following lines summarize step by step the encrypted proposed scheme of Figure 3.

Step 1 : transform the sEMG_1D signal into sEMG_2D as a grayscale image

Step 2 : generate the chaotic sequence by the chaotic NRCISJJ with the parameters: $i = 1.15$, $\beta_L = 3$, and $\beta_C = 0.707$, and the initial conditions are $(x(0), y(0), z(0)) = (0, 0, 0)$

Step 3 : generate n-iteration with the NRCISJJ model of system (1) to have $h(i)$ for different orbits

Step 4 : match the chaotic sequences with the sEMG_2D image pixels

Step 5 : make a permutation in the lines in N-iteration

Step 6 : make a permutation in the columns in M-iteration and obtain the encrypted sEMG_2D signal

Step 7 : display the encrypted image

Step 8 : transform the sEMG_2D into sEMG_1D and display.

The sEMG signals used are the clinical data acquired from a database. PhysioBank ATM database is used in [36]. In the following, different resolutions of surface EMG_2D are used in Table 1.

KHEIR1, KHEIR2, and JOUVE3 S_EMG 1D signals belong to holy patients, while EMG_MYOPATHY and EMG_HEALTHY S_EMG 1D signals are for not holy patients.

3.1. Key Sensitivity Analysis

3.1.1. Correlation Analysis. The formula for the correlation between two neighboring pixels (w and c, for example) is given by the following relation:

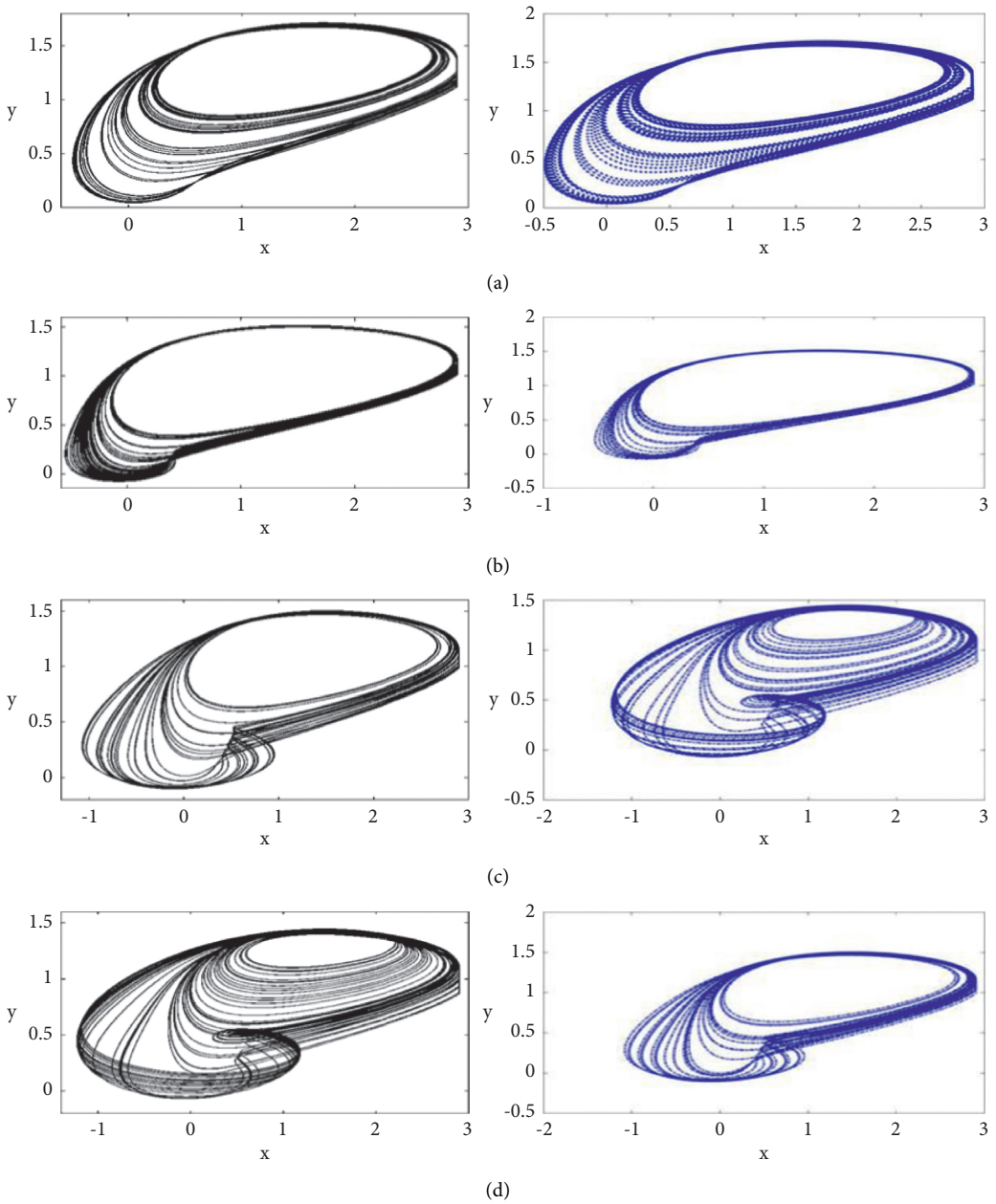

FIGURE 2: 2D phase portraits of numerical simulations and FPGA implementation of the NRCISJJ model for given values of parameter i and β_L: (a) $i = 1.36$ and $\beta_L = 2.07$, (b) $i = 1.15$ and $\beta_L = 2.52$, (c) $i = 1.15$ and $\beta_L = 2.6$, and (d) $i = 1.15$ and $\beta_L = 3$. The other parameter is $\beta_C = 0.707$ and the initial conditions are (x(0), y(0), z(0))=(0, 0, 0).

$$\gamma_{x,y} = \frac{E(y - E(y))(x - E(x))}{\sqrt{D(y)D(x)}},$$

$$E(x) = \frac{1}{T}\sum_{i=1}^{T} x_i, \tag{4}$$

$$D(x) = \frac{1}{T}\sum_{i=1}^{T} (x_i - E(x))^2,$$

where the integer T refers to the total number of adjoining pixels and $D(x)$ and $E(x)$ are the variance and expectation of x, respectively.

Table 2 shows the correlation coefficients of the original sEMG_2D and sEMG_2D encrypted using the proposed approach.

It can be seen from Table 2 that the correlation coefficients of the input images are close to 1, while the correlation coefficients of the cipher images are close to 0, indicating that the pixels of the cipher images are not correlated. These

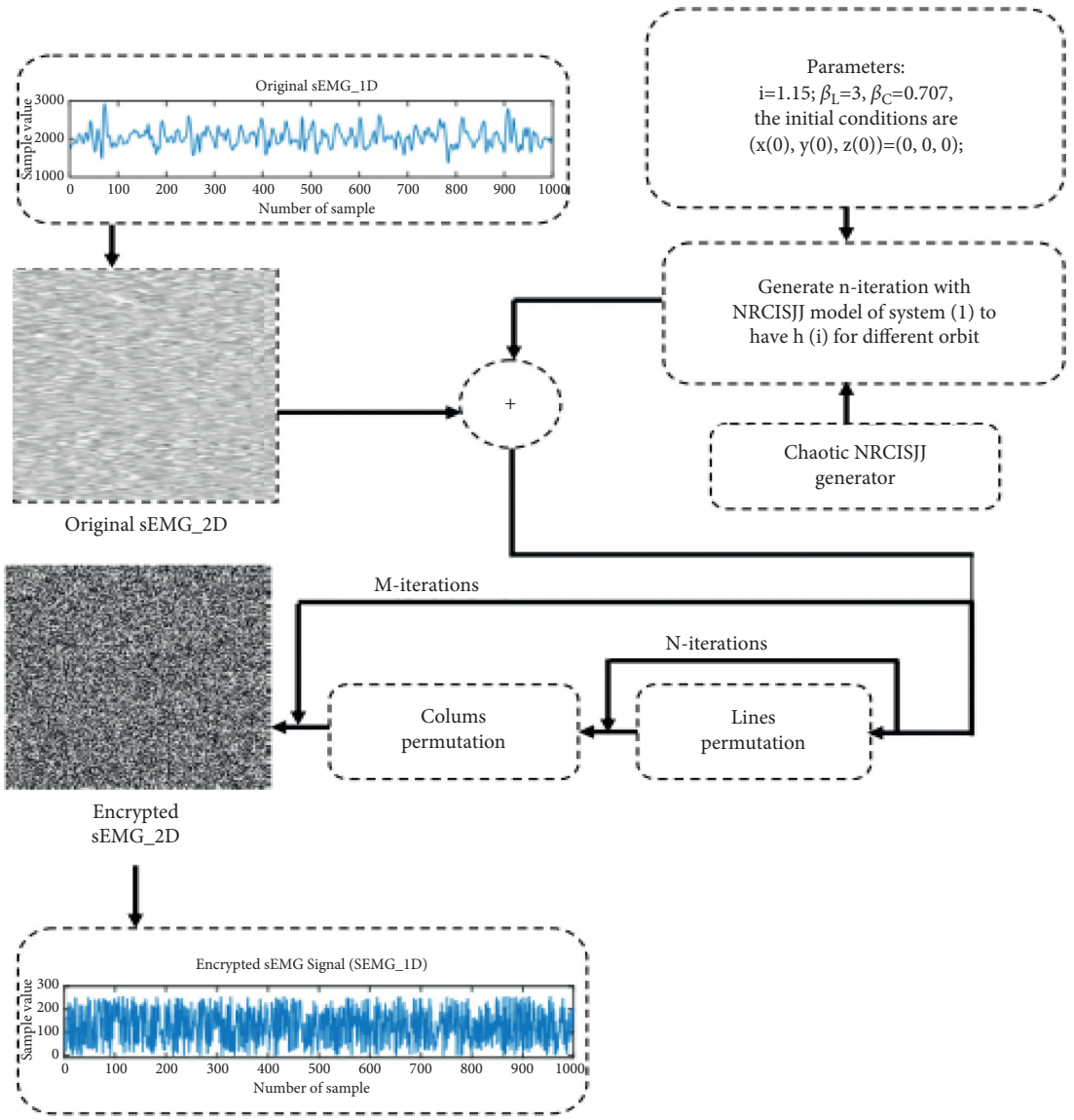

Figure 3: Schematic diagram of the proposed encryption scheme.

Table 1: S_EMG 2D and their resolutions.

S_EMG 1D	S_EMG 2D	RESOLUTION
KHEIR1	KHEIR1_2D	180 ∗ 180
KHEIR2	KHEIR2_2D	180 ∗ 180
JOUVE3	JOUVE3_2D	180 ∗ 180
EMG_MYOPATHY	EMG_MYOPATHY_2D	148 ∗ 148
EMG_HEALTHY	EMG_HEALTHY_2D	53 ∗ 53

results confirm that the proposed algorithm can remove the correlation between adjacent pixels in the encrypted sEMG signals. These results sufficiently show that the encryption algorithm is well suited to EMG signals. Figures 4–8 show a visual representation of the correlation coefficients of the original, encrypted, and decrypted sEMG_2D signal.

From Figures 4 to 8, 200, 300, or even 400 pairs of adjacent pixels are randomly selected from the images to show their adjacent pixel distribution maps. This implies the strong correlation effect in the input and decrypted sEMG_2D signals, while there is a weak correlation effect in the encrypted sEMG_2D signals. These figures verify well that there is no significant correlation between pixels of the encrypted sEMG_2D signals. In addition to the encouraging encryption result offered by the proposed algorithm, Figures 4 to 8 also show that the proposed algorithm gives a decrypted sEMG_2D image very close to the original sEMG_2D image.

Table 2: The correlation coefficient γ of signals (S_EMG 2D).

S_EMG 2D	γ	γ of input signal	Proposed chaotic NRCISJJ
KHEIR1_2D	γ_h	0.9510	−0.0005
	γ_v	−0.0054	0.0028
	γ_d	−0.0050	−0.0009
KHEIR2_2D	γ_h	0.9170	0.0095
	γ_v	0.0017	−0.0012
	γ_d	−0.0009	−0.0078
EMG_MYOPATHY_2D	γ_h	0.4520	−0.0073
	γ_v	0.0158	−0.0069
	γ_d	0.0067	−0.0001
EMG_HEALTHY_2D	γ_h	0.7484	−0.0021
	γ_v	0.0984	−0.0032
	γ_d	0.0852	−0.0113
JOUVE3_2D	γ_h	0.9526	−0.0032
	γ_v	−0.0368	−0.0032
	γ_d	0.0379	−0.0076

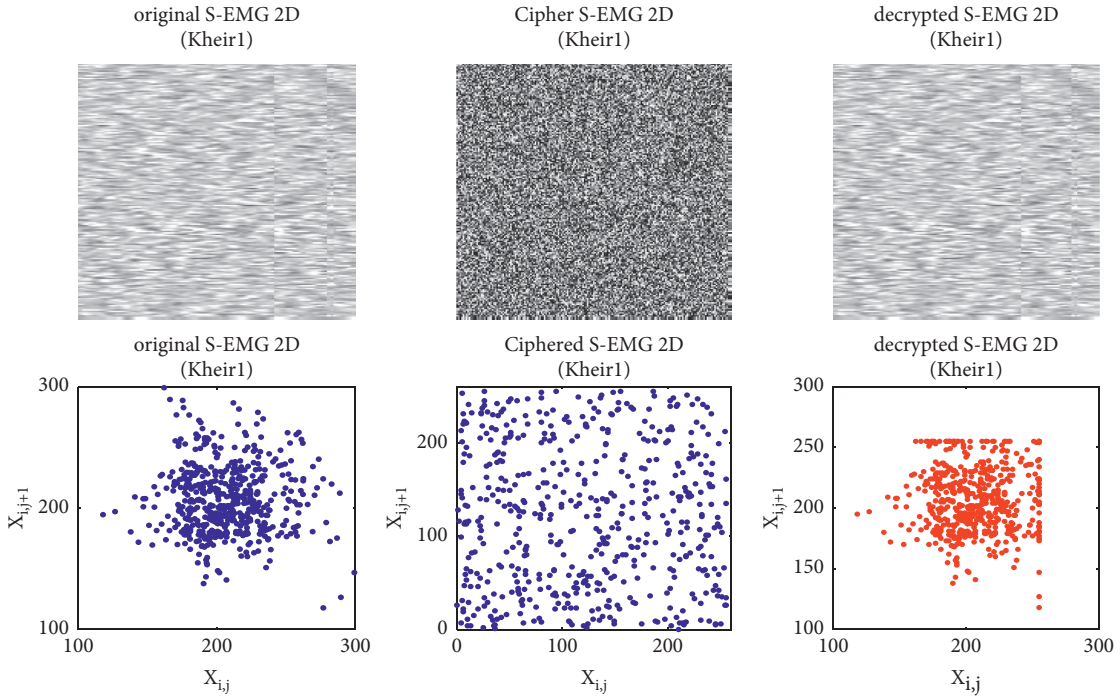

Figure 4: Correlations of KHEIR1_2D. The first column is the input signal with its correlation, the second column is the corresponding cipher signal with its correlation and the third column is the decrypted signal with its correlation.

3.2. Information Entropy. For a grayscale image, the intensity has 2^8 possible types of values, so its ideal IFE is 8. The IFE can be defined by

$$E(n) = \sum_{i=0}^{M-1} p(n_i)\log_2\left(\frac{1}{p(n_i)}\right), \tag{5}$$

where M is the total number of samples $n_i \varepsilon n$, $p(n_i)$ denotes the probability of occurrence of the sample n_i, and log with base 2 signifies the entropy expressed in bits.

When the signal sEMG_1D is transformed into sEMG_2D in the form of an image, the image obtained has the characteristics of a grayscale image. Thus, to have a high security encrypted image, the entropy of the encrypted image must be as high as possible, i.e., very close to 8 [37, 38]. As can be seen in Table 3, the information entropy of the various encrypted sEMG_2D signals is close to 8, as shown in Table 3.

These results of Table 3 once again confirm that the data of the sEMG signals are well encrypted and with a high level of security.

3.3. Resistance to One Bit Changing Attack. To ensure the security of an image encryption scheme against differential scanning, two quantitative measures are used: the NPCR

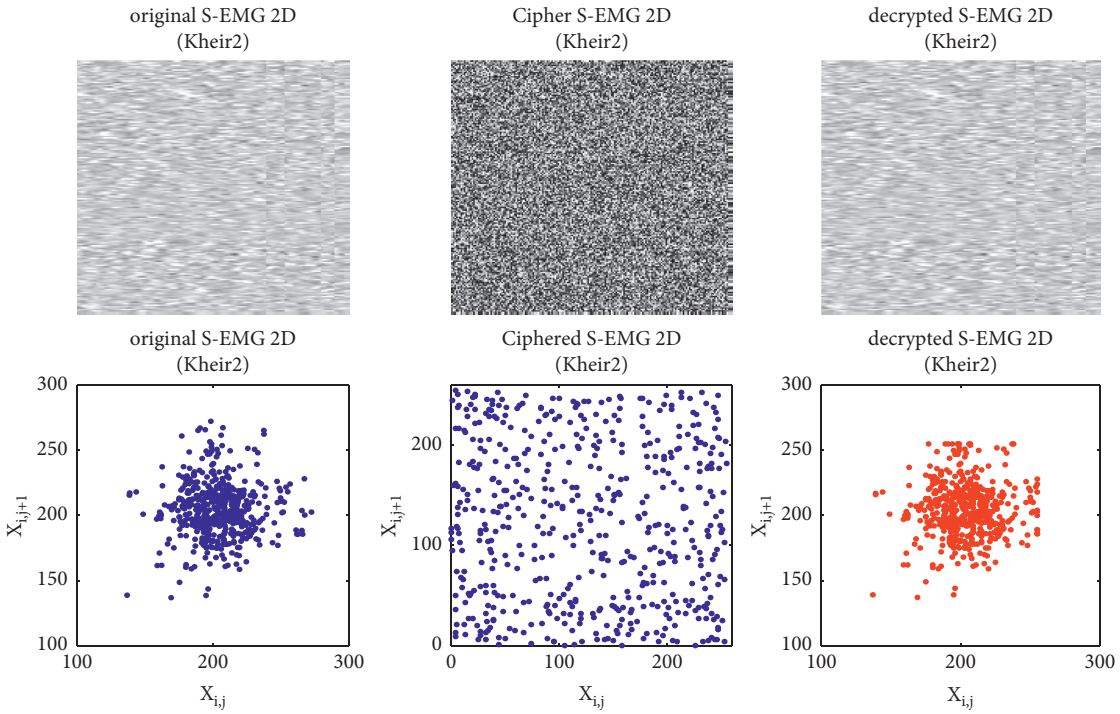

Figure 5: Correlations of KHEIR2_2D. The first column is the input signal with its correlation, the second column is the corresponding cipher signal with its correlation, and the third column is the decrypted signal with its correlation.

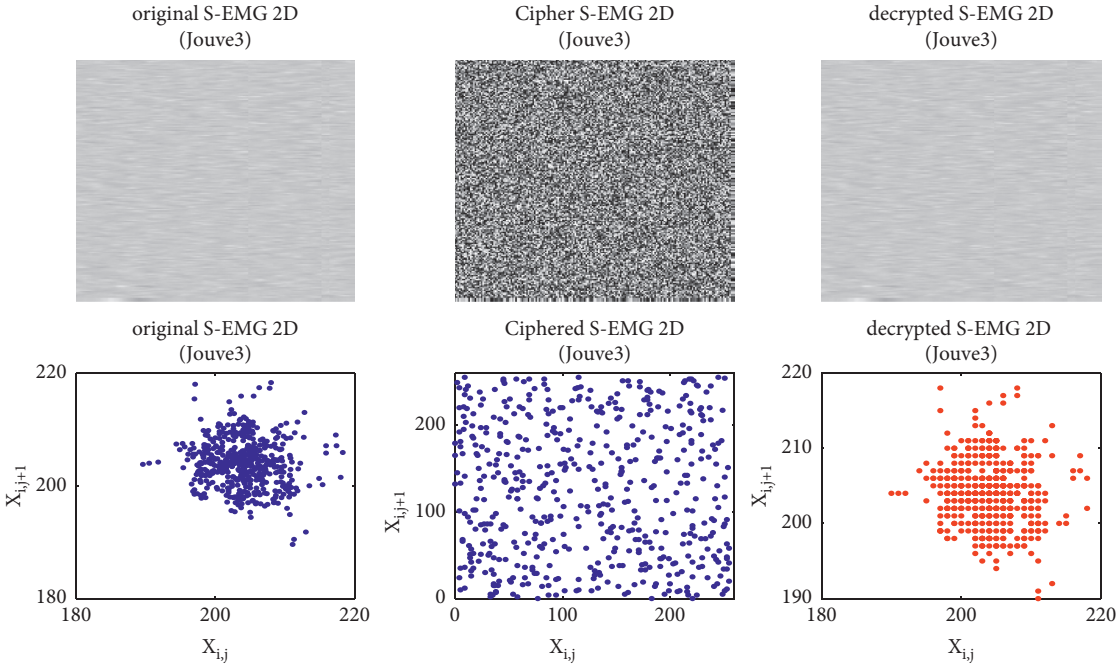

Figure 6: Correlations of JOUVE3_2D. The first column is the input signal with its correlation, the second column is the corresponding cipher signal with its correlation, and the third column is the decrypted signal with its correlation.

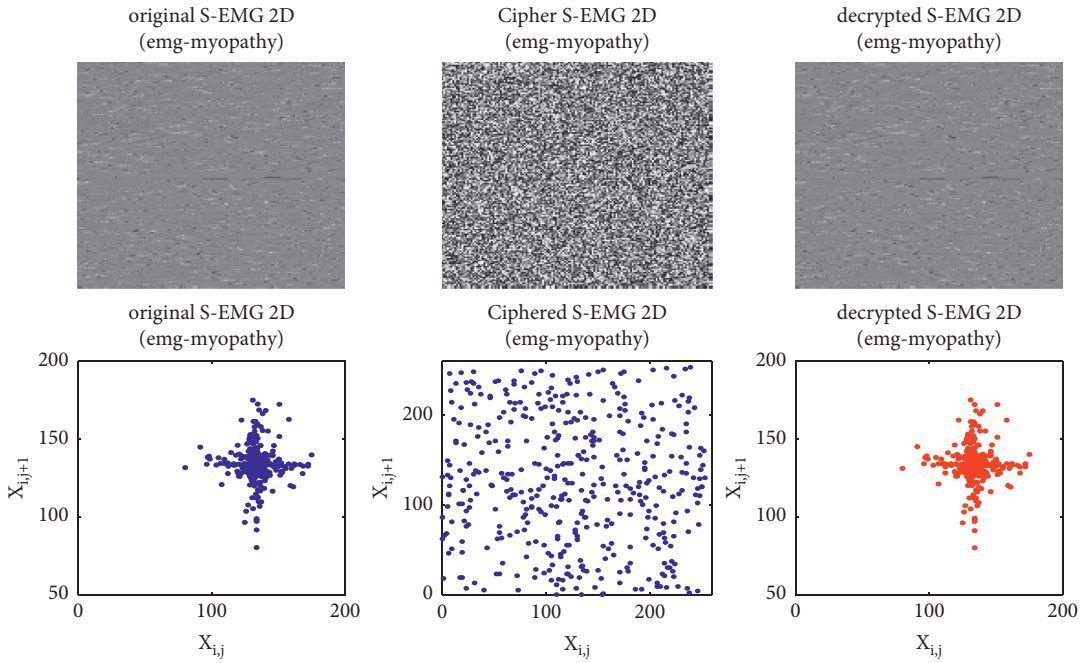

Figure 7: Correlations of MYOPATHY_2D. The first column is the input signal with its correlation, the second column is the corresponding cipher signal with his correlation, and the third column is the decrypted signal with its correlation.

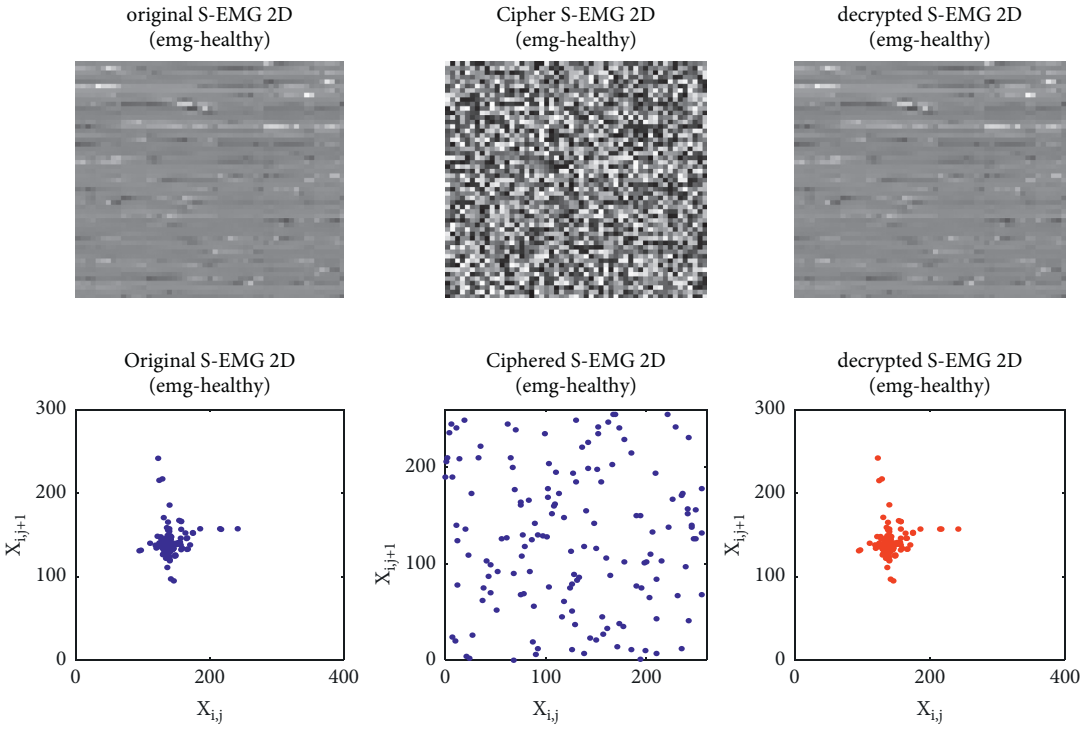

Figure 8: Correlations of HEATHY_2D. The first column is the input signal with its correlation, the second column is the corresponding cipher signal with its correlation, and the third column is the decrypted signal with its correlation.

Table 3: Information entropy performance of cipher S_EMG 2D.

S_EMG 2D	Chaotic NRCISJJ
KHEIR1_2D	7.9941
KHEIR2_2D	7.9936
EMG_MYOPATHY_2D	7.9885
EMG_HEALTHY _2D	7.9388
JOUVE3_2D	7.9923

(number of pixels' change rate) and the UACI (unified average changing intensity). The NPCR represents the rate of different pixels between the two encrypted images, while the UACI represents the difference in average intensity [39].

The formula used to calculate these two percentages is defined as follows [37]:

$$\mathrm{NPCR} = \frac{1}{M \times N} \sum_{i+1}^{M} \sum_{j=1}^{N} \mathrm{DIF}(i, j) \times 100,$$

$$\mathrm{UACI} = \frac{1}{M \times N} \sum_{i+1}^{M} \sum_{j=1}^{N} \frac{\left| C_2(i, j) - C_1(i, j) \right|}{255} \times 100\,(\%),$$

$$\text{with } \mathrm{DIF}(i, j) = \begin{cases} 0, & C_2(i, j) = C_1(i, j), \\ 1, & C_2(i, j) \neq C_1(i, j), \end{cases} \tag{6}$$

where C_2 refers to the crypted image that is encrypted from the original image by changing only one pixel, while C_1 refers to the cipher image encrypted from the same plain image.

When an NPCR > 99.6094%, a UACI > 33.4635% ensures that an image encryption scheme is secure against this attack [40, 41]. Table 4 depicts the values of NPCR and UACI obtained on the sEMG_2D signal.

From the results obtained and presented in Table 4, it appears that all the NPCR values are greater than the optimum value of 99.6094%. As for the values of the UACI, we record two values lower than the optimal value of 33.4635%. Curiously, these two UACI values are obtained on the sEMG signals of patients who are not holy. This observation thus opens another axis of reflection that will furnish our perspective. Apart from these two values, we can conclude that an image encryption scheme is secure against the differential attack.

3.4. Quality Metrics Analysis between Plain and Encrypted. Table 5 shows the analysis of signal quality. After encrypting the signal in 2D, we transform it into 1D to analyze the effect of the encryption on it. The medical personnel who receive the encrypted signal decrypt it for a diagnosis. To avoid misdiagnosis, medical personnel should not receive a corrupt signal. This is why in Table 5 we study the distortion between the original signal and the decrypted signal. This distortion is quantified by the following metrics: the percent root mean square difference (PRD) (%) and the signal to noise ratio (SNR).

3.4.1. Mean Square Error (MSE). The most commonly used quality measure is mean square error (MSE) and is defined by

$$\mathrm{MSE} = \frac{1}{N} \sum_{n=1}^{N} \left(y_O[n] - y_r[n] \right)^2, \tag{7}$$

where $y_O[n]$ is the original surface EMG signal, $y_r[n]$ is the decrypted surface EMG signal, and N is the number of samples of the signal.

3.4.2. Signal-to-Noise Ratio (SNR).

$$\mathrm{SNR} = 10\mathrm{Log}_{10}\left(\frac{\sigma_x^2}{\sigma_e^2} \right). \tag{8}$$

where Log is decimal logarithm. With σ_x^2 as the spectral power of the original SEMG signal and σ_e^2 as the spectral power of the decrypted error.

3.4.3. Percent Root Mean Square Difference (PRD). The PRD (percent root mean square difference) is defined by

$$\mathrm{PRD} = \sqrt{\frac{\sum_{n=0}^{N-1} \left(y_O[n] - y_r[n] \right)^2}{\sum_{n=0}^{N-1} \left(y_O[n] - \mu \right)^2}} \cdot 100\%, \tag{9}$$

where N is the number of samples of the original sEMG signal, μ is the reference value of the DAC (digital analog converter) used for data acquisition s(n) ($\mu = 0$ for EMG signals), $y_r[n]$ is the decrypted sEMG signal, and $y_O[n]$ is the original sEMG signal [34].

Analysis of the values in Table 5 shows that the decrypted sEMG signal resembles the original signal. This can be seen through the value of the PRD which must be as small as possible and that of the SNR must be high. This statement can be verified by observing Figures 9–13.

Figures 9 to 13 present the original, encrypted, and decrypted sEMG signals of the signals KHEIR1, KHEIR2, JOUVE3, MYOPATHY, and HEALTHY, respectively. For each figure, the first line is the input signal, the second line is the corresponding cipher signal, and the third line is the decrypted signal.

3.5. Encryption Time. In telemedicine, the interaction between two health specialists can be in real time. So, the communications must be as fast as possible. Therefore, the encryption and decryption times should be as small as possible. Table 6 shows the encryption and decryption time of the proposed algorithm. The proposed algorithm is implemented in MATLAB R2015a and the "*run and time*" function is used. The characteristics of the machine are as follows:

(i) Name: DESKTOP-FO74VUD

(ii) RAM installed: 8,00 Go (7,85 Go useable)

(iii) Device ID: DD9D7612-CE5F-4069-85ED-6F57D40 3F31C

Table 4: Average performance of NPCR (%) and UACI (%).

S_EMG 2D	NPCR (%)	UACI (%)
KHEIR1_2D	99.9660	35.5353
KHEIR2_2D	99.9599	34.9161
EMG_MYOPATHY_2D	100	24.5620
EMG_HEALTHY _2D	100	25.3572
JOUVE3_2D	99.9568	35.5353

Table 5: Quality metrics analysis.

S_EMG_1D	PRD (%)	SNR (dB)	MSE
KHEIR1_1D	1.66	35.62	1165.37
KHEIR2_1D	0.87	41.24	317.92
EMG_MYOPATHY_1D	3.00	30.46	859.00
EMG_HEALTHY _1D	1.93	34.28	183.29
JOUVE3_1D	0.14	56.90	8.49

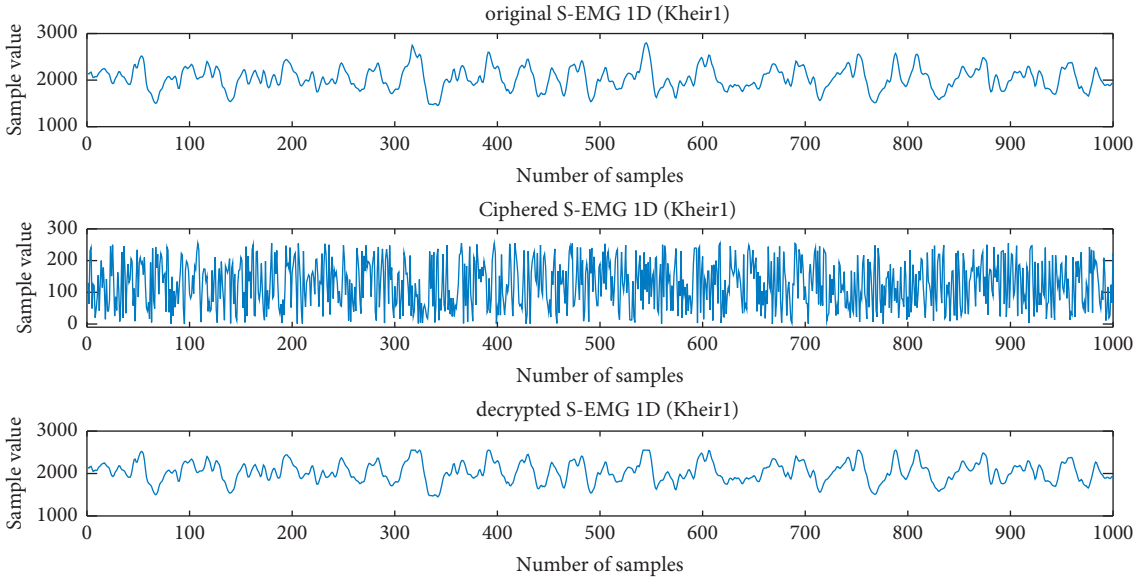

Figure 9: Input signal, cipher signal, and decrypted signal of KHEIR1_1D. The first is the input signal, the second is the corresponding cipher signal, and the third is the decrypted signal.

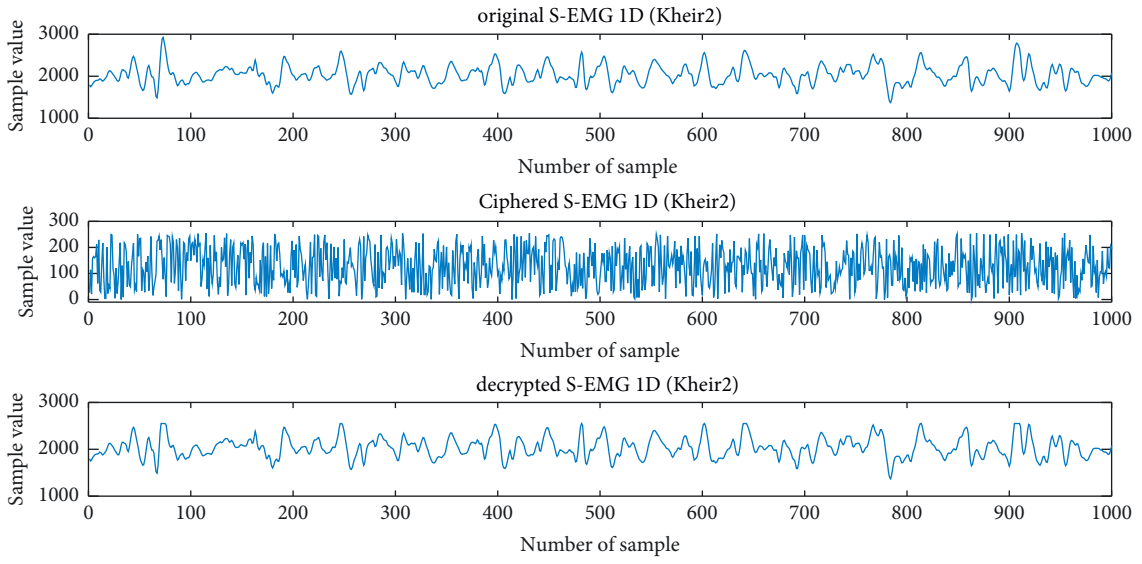

Figure 10: Input signal, cipher signal, and decrypted signal of KHEIR2_1D. The first is the input signal, the second is the corresponding cipher signal, and the third is the decrypted signal.

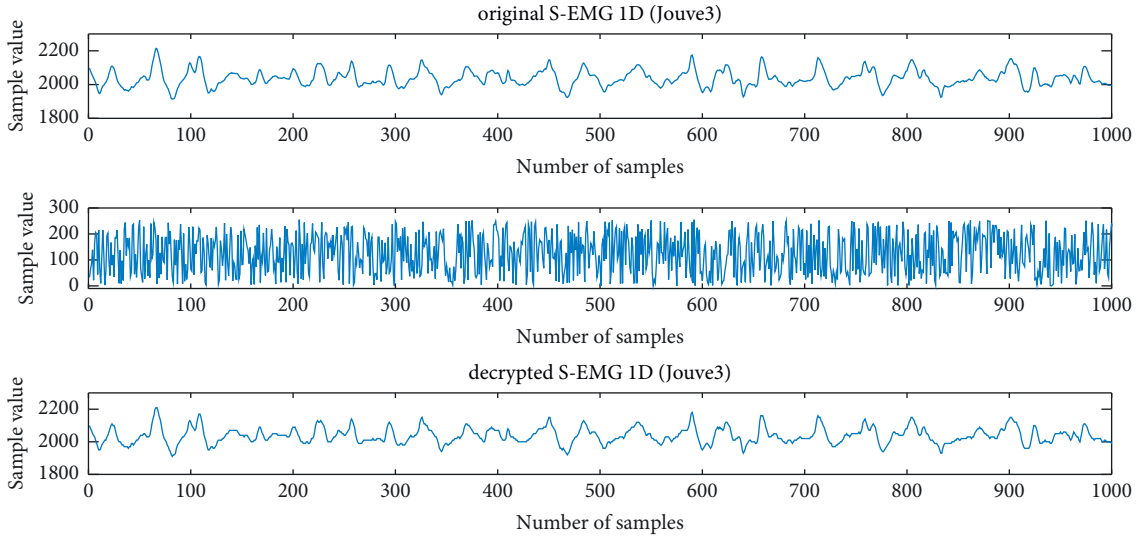

Figure 11: Input signal, cipher signal, and decrypted signal of JOUVE3_1D. The first is the input signal, the second is the corresponding cipher signal, and the third is the decrypted signal.

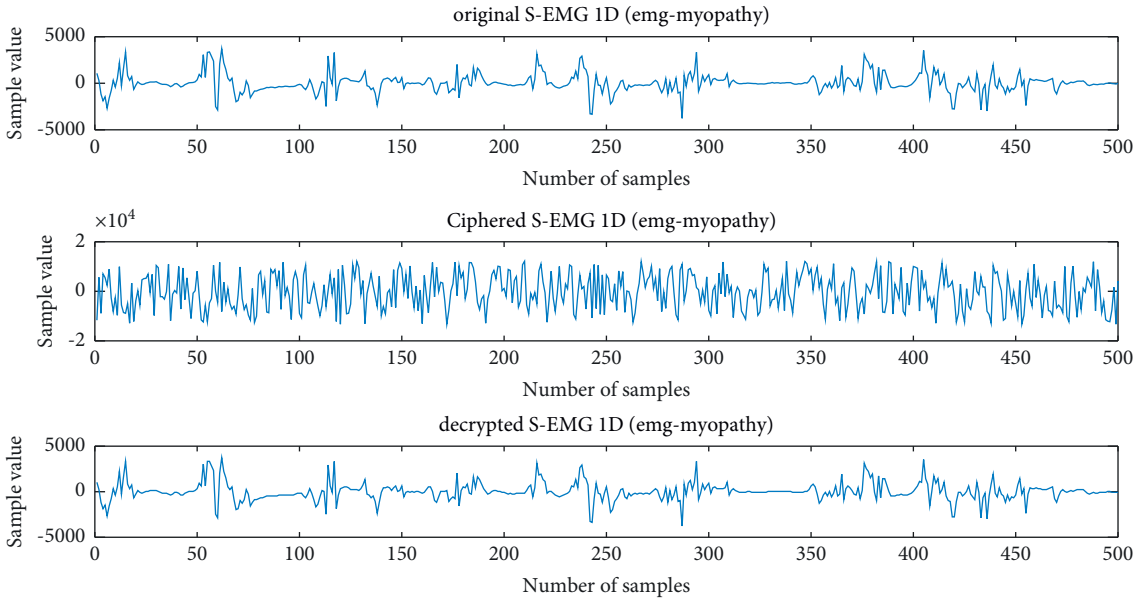

Figure 12: Input signal, cipher signal, and decrypted signal ofMYOPATHY_1D. The first is the input signal, the second is the corresponding cipher signal, and the third is the decrypted signal.

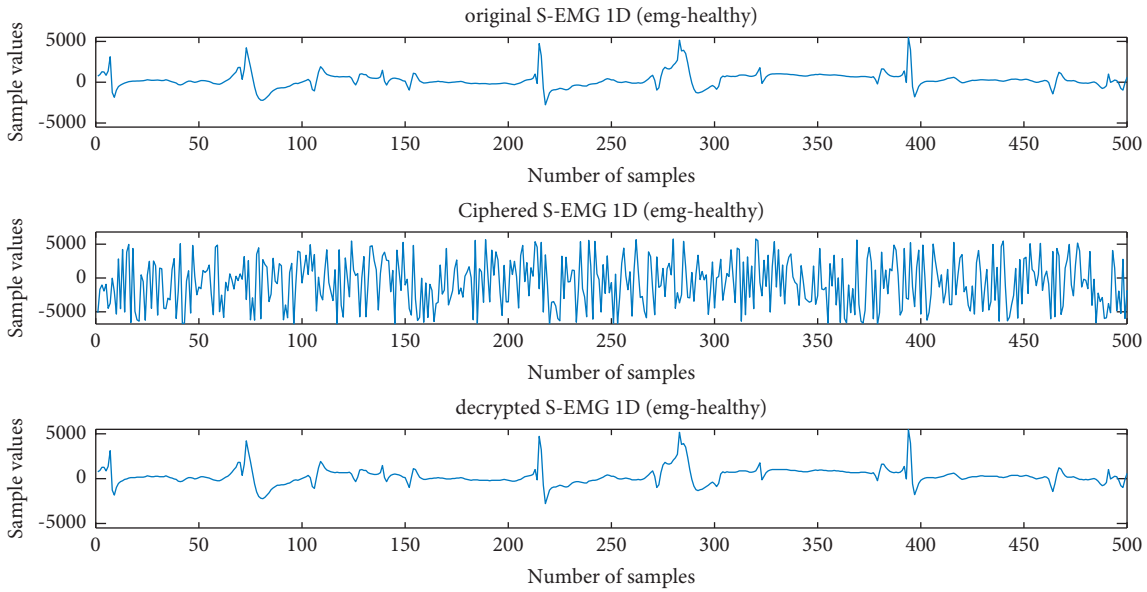

Figure 13: Input signal, cipher signal, and decrypted signal of HEALTY_2D. The first is the input signal, the second is the corresponding cipher signal, and the third is the decrypted signal.

Table 6: Encrypted and decrypted time.

S_EMG 2D	Resolution	Proposed chaotic NRCISJJ	
		Encrypted time (s)	Decrypted time (s)
KHEIR1_2D	180 * 180	0.336	1.701
KHEIR2_2D	180 * 180	0.351	1.676
EMG_MYOPATHY_2D	148 * 148	0.223	1.241
EMG_HEALTHY_2D	53 * 53	0.028	0.169
JOUVE3_2D	180 * 180	0.361	1.757

Table 7: Comparison of the proposed encryption scheme with recent schemes reported in literature, where √ means "achieved" and — means "not achieved."

	[42]	[43]	[44]	[45]	Proposed chaotic NRCISJJ
Clinical signals					
ECG	√	√	—	—	—
BP	√	—	—	—	—
EEG	√	—	√	√	—
EMG	—	—	—	—	√
Acquisition method					
Live sensing	—	—	—	—	—
Database technique	PhysioBank ATM	MIT–BIH	UCI KDD	NTOU	PhysioBank ATM
Encryption	√	√	√	√	√
Compression	—	√	—	—	—
Chaos specifications					
Chaotic map	Logistic map	Not specified	Logistic map	Logistic map	Chaotic NRCISJJ
Lyapunov exponent	√	—	—	—	—
Security analysis					
Secret key space	√	—	—	—	—
Correlation	√	—	√	—	√
Autocorrelation	√	—	—	—	√
Secret key sensitivity	√	—	—	√	√
Plain signal sensitivity	√	—	—	—	—
Floating frequency	√	—	—	—	—
Information entropy	√	—	—	—	√
Mean square error	√	—	√	—	√
Pick signal-to-noise ratio	√	—	—	—	—

Table 7: Continued.

	[42]	[43]	[44]	[45]	Proposed chaotic NRCISJJ
Structural similarity index	√	—	—	—	—
Encryption time	√	—	—	√	√
Distortion criteria					
Signal-to-noise ratio	—	—	—	—	√
Percentage residual deviation	—	√	—	√	√

(iv) Product ID: 00330-80000-00000-AA798

(v) System type: 64 bits, processor x64

These times for all signals show that the proposed algorithm is fast. The comparison analyses are presented in Table 7.

4. Conclusion

The field programmable gate array implementation of the nonlinear resistor-capacitor-inductor shunted Josephson junction model and its application to secure surface electromyographic signal were investigated in this study. Different shapes of chaotic attractors were revealed by using numerical simulations and field programmable gate array implementation of the nonlinear resistive-capacitive-inductive shunted Josephson junction model. The aim of this paper was to show that it is possible to encrypt the surface electromyographic signal through image encryption techniques which was achieved. For a first experiment on the encryption of sEMG signals, the results obtained are encouraging. However, it appears that the results are not as powerful as when the encryption technique is applied to surface electromyographic signal of patients with pathology. This can be due to the fact that the signals of holy patients concentrated more information towards the lower frequencies while the signals of pathological patients concentrated the most information towards the higher frequencies. This will be the subject of a study in future works.

Data Availability

The data used to support the findings of this study are included within the article.

Conflicts of Interest

On behalf of all authors, the corresponding author states that there are no conflicts of interest.

Acknowledgments

This work was partially funded by the Center for Nonlinear Systems, Chennai Institute of Technology, India, via funding no. CIT/CNS/2021/RD/064.

References

[1] T. G. Zhou, D. C. Wang, F. L. Liu, L. Fang, X. J. Zhao, and S. L. Yan, "Simulation of chaos in different models of josephson junctions," *Journal of System Simulation*, vol. 22, pp. 666–669, 2010.

[2] S. Das, S. Datta, and D. Sahdev, "Mode-locking, hysteresis and chaos in coupled josephson junctions," *Physica D: Nonlinear Phenomena*, vol. 101, no. 3-4, pp. 333–345, 1997.

[3] C. R. Nayak and V. C. Kuriakose, "Dynamics of coupled josephson junctions under the influence of applied fields," *Physics Letters A*, vol. 365, no. 4, pp. 284–289, 2007.

[4] X.-S. Yang and Q. Li, "A computer-assisted proof of chaos in josephson junctions," *Chaos, Solitons & Fractals*, vol. 27, no. 1, pp. 25–30, 2006.

[5] T. Kawaguchi, "Directed transport and complex dynamics of vortices in a josephson junction network driven by modulated currents," *Physica C: Superconductivity and its Applications*, vol. 470, no. 20, pp. 1133–1136, 2010.

[6] S. Al-Khawaja, "Chaotic dynamics of underdamped josephson junctions in a ratchet potential driven by a quasiperiodic external modulation," *Physica C: Superconductivity and its Applications*, vol. 420, no. 1-2, pp. 30–36, 2005.

[7] M. MacHida, T. Koyama, A. Tanaka, and M. Tachiki, "Theory of the superconducting phase and charge dynamics in intrinsic Josephson-junction systems: microscopic foundation for longitudinal Josephson plasma and phenomenological dynamical equations," *Physica C: Superconductivity*, vol. 331, no. 1, pp. 85–96, 2000.

[8] M. Hayashi, M. Suzuki, J. Onuki, and H. Ebisawa, "Nonlinear dynamics of intrinsic Josephson junctions under an applied current," *Applications*, vol. 463-465, pp. 993–996, 2007.

[9] S. K. Dana, D. C. Sengupta, and K. D. Edoh, "Chaotic dynamics in Josephson junction," *IEEE Transactions on Circuits and Systems I: Fundamental Theory and Applications*, vol. 48, no. 8, pp. 990–996, 2001.

[10] A. B. Cawthorne, C. B. Whan, and C. J. Lobb, "Complex dynamics of resistively and inductively shunted Josephson junctions," *Journal of Applied Physics*, vol. 84, no. 2, pp. 1126–1132, 1998.

[11] U. E. Vincent, A. Ucar, J. A. Laoye, and S. O. Kareem, "Control and synchronization of chaos in RCL-shunted Josephson junction using backstepping design," *Physica C: Superconductivity*, vol. 468, no. 5, pp. 374–382, 2008.

[12] A. N. Njah, K. S. Ojo, G. A. Adebayo, and A. O. Obawole, "Generalized control and synchronization of chaos in RCL-shunted Josephson junction using backstepping design," *Physica C: Superconductivity*, vol. 470, no. 13-14, pp. 558–564, 2010.

[13] S. K. Dana, D. C. Sengupta, and C.-K. Hu, "Spiking and bursting in Josephson junction," *IEEE Transactions on Circuits and Systems II: Express Briefs*, vol. 53, no. 10, pp. 1031–1034, 2006.

[14] M. Canturk and I. N. Askerzade, "Numerical study of I–V characteristics of externally shunted Josephson junctions with unharmonic current-phase relation," *IEEE Transactions on Applied Superconductivity*, vol. 22, Article ID 1400111, 2012.

[15] M. Canturk and I. N. Askerzade, "Chaotic dynamics of externally shunted Josephson junction with Unharmonic CPR," *Journal of Superconductivity and Novel Magnetism*, vol. 26, no. 4, pp. 839–843, 2013.

[16] S. T. Kingni, G. F. Kuiate, R. Kengne, R. Tchitnga, and P. Woafo, "Analysis of a no equilibrium linear resistive-capacitive-inductance shunted Junction model, dynamics, synchronization, and application to digital cryptography in its fractional-order form," *Complexity*, vol. 2017, Article ID 4107358, 12 pages, 2017.

[17] S. T. Kingni, K. Rajagopal, S. Çiçek, A. Cheukem, V. K. Tamba, and G. F. Kuiate, "Dynamical analysis, FPGA implementation and its application to chaos based random number generator of a fractal Josephson junction with unharmonic current-phase relation," *The European Physical Journal B*, vol. 93, no. 3, p. 44, 2020.

[18] A. N. Kadjie, H. Tchakounté, I. Kemajou, and P. Woafo, "Microcontroller-based simulation of a nonlinear resistive-capacitive-inductance shunted Josephson junction model and applications in electromechanical engineering," *International Journal of Nonlinear Sciences and Numerical Stimulation*, vol. 22, 2021.

[19] Q. Lai and Z. Wan, "Modelling and circuit realisation of a new no-," *Electronics Letters*, vol. 56, no. 20, pp. 1044–1046, 2020.

[20] B. Ramakrishnan, A. A. Oumate, M. Tuna, İ. Koyuncu, S. T. Kingni, and K. Rajagopal, "Analysis, FPGA implementation of a Josephson junction circuit with topologically nontrivial barrier and its application to ring-based dual entropy core true random number generator, Eur," *Phys. J. Spec. Top.*, vol. 230, pp. 18–20, 2021.

[21] Q. Lai, B. Norouzi, and F. Liu, "Dynamic analysis, circuit realization, control design and image encryption application of an extended Lü system with coexisting attractors," *Chaos, Solitons & Fractals*, vol. 114, pp. 230–245, 2018.

[22] Q. Lai, Z. Wan, L. K. Kengne, P. D. K. Kuate, and C. Chen, "Two-memristor-based chaotic system with infinite coexisting attractors," *IEEE Transactions On Circuits And Systems—Ii: Express Briefs*, vol. 68, no. 6, 2021.

[23] A. Hamzenejad, S. J. Ghoushchi, V. Baradaran, and A. Mardani, "A robust algorithm for classification and diagnosis of brain disease using local linear approximation and generalized autoregressive conditional heteroscedasticity model," *Advance in Mathematics*, vol. 8, 2020.

[24] C. K. Filelis-Papadopoulos, P. T. Endo, M. Bendechache et al., "Towards simulation and optimization of cache placement on large virtual content distribution networks," *Journal of Computer Science*, vol. 39, Article ID 101052, 2020.

[25] G. Chen, Y. Mao, and C. K. Chui, "A symmetric image encryption scheme based on 3D chaotic cat maps," *Chaos, Solitons & Fractals*, vol. 21, no. 3, pp. 749–761, 2004.

[26] Y. Mao, G. Chen, and S. Lian, "A novel fast image encryption scheme based on 3D chaotic baker maps," *International Journal of Bifurcation and Chaos*, vol. 14, no. 10, pp. 3613–3624, 2004.

[27] N. K. Pareek, V. Patidar, and K. K. Sud, "Image encryption using chaotic logistic map," *Image and Vision Computing*, vol. 24, no. 9, pp. 926–934, 2006.

[28] A. N. Pisarchik, N. J. Flores-Carmona, and M. Carpio-Valadez, "Encryption and decryption of images with chaotic map lattices," *Chaos*, vol. 16, Article ID 033118, 2006.

[29] J. W. Yoon and H. Kim, "An image encryption scheme with a pseudorandom permutation based on chaotic maps," *Communications in Nonlinear Science and Numerical Simulation*, vol. 15, no. 12, pp. 3998–4006, 2010.

[30] X. Wang and H.-l. Zhang, "A novel image encryption algorithm based on genetic recombination and hyper-chaotic systems," *Nonlinear Dynamics*, vol. 83, no. 1-2, pp. 333–346, 2016.

[31] X. Huang, T. Sun, Y. Li, and J. Liang, "A color image encryption algorithm based on a fractional-order hyperchaotic system," *Entropy*, vol. 17, no. 1, pp. 28–38, 2014.

[32] M. H. Trabuco, M. V. C. Costa, and B. Macchiavello, "S-EMG signal compression in one-dimensional and two-dimensional approaches," *IEEE Journal of Biomedical and Health Informatics*, vol. 22, no. 4, pp. 1104–1113, 2018.

[33] E. D. B. F. Lima and W. S. D. Silva Júnior, "SEMG signal compression based on two-dimensional techniques," *BioMedical Engineering Online*, vol. 15, no. 1, 2016.

[34] C. Welba, A. J. O. Okassa, P. N. Eloundou, and P. Ele, "Contribution to S-EMG signal compression in 1D by the combination of the modified discrete wavelet packet transform (MDWPT) and the discrete cosine transform (DCT)," *Journal of Signal and Information Processing*, vol. 11, no. 03, pp. 35–57, 2020.

[35] C. Welba, E. P. Ntsama, and P. Ele, "Exploitation of differential pulse code modulation for compression of EMG signals by a combination of DWT and DCT," *American Journal of Biomedical Engineering*, vol. 4, pp. 25–32, 2014.

[36] "PhysioBank A. T. M.," 2016, https://physionet.org/cgi-bin/atm/ATM.

[37] Y. Jiayin, X. Yaqin, G. Shiyu, Z. Yanqi, and W. Erfu, "Parallel encryption of noisy images based on sequence generator and chaotic measurement matrix," *Complexity*, vol. 18, Article ID 1987670, , 2020.

[38] K. M. Hosny, S. T. Kamal, M. M. Darwish, and G. A. Papakostas, "New image encryption algorithm using hyperchaotic system and fibonacci Q-matrix," *Electronics*, vol. 10, no. 9, 2021.

[39] K. Zhan, D. Wei, J. Shi, and J. Yu, "Cross-utilizing hyperchaotic and DNA sequences for image encryption," *Journal of Electronic Imaging*, vol. 26, no. 1, pp. 13–21, 2017.

[40] A. Beloucif, "Contribution à l'étude des mécanismes cryptographiques; Université de Batna 2, Faculté de mathématiques et d'informatique," *Thèse en vue de l'obtention du diplôme de Doctorat en Informatique*, 2016.

[41] F. Hadji, "Conception et réalisation d'un système décryptage pour les images médicales," *Mémoire présenté pour l'obtention du diplôme de Master Académique*, Université MOHAMED BOUDIAF - M'SILA, 2018.

[42] M. A. Murillo-Escobar, L. Cardoza-Avendano, R. M. Lopez-Gutierrez, and C. Cruz-Hernandez, "A double chaotic layer encryption algorithm for clinical signals in telemedicine," *Journal of Medical Systems*, vol. 41, no. 4, pp. 41–59, 2017.

[43] M. Raeiatibanadkooki, S. R. Quchani, M. KhalilZade, and K. Bahaadinbeigy, "Compression and encryption of ECG signal using wavelet and chaotically huffman code in telemedicine application," *Journal of Medical Systems*, vol. 40, pp. 73–78, 2016.

[44] C.-F. Lin, "Chaotic visual cryptosystem using empirical mode decomposition algorithm for clinical EEG signals," *Journal of Medical Systems*, vol. 40, pp. 1–10, 2016.

[45] C. F. Lin, S. H. Shih, and J. D. Zhu, "Chaos based encryption system for encrypting electroencephalogram signals," *Journal of Medical Systems*, vol. 38, pp. 49–10, 2014.

Hindawi
Complexity
Volume 2022, Article ID 6035593, 11 pages
https://doi.org/10.1155/2022/6035593

Research Article

Experimental Research on Aerated Supercavitation Suppression of Capillary Outlet Throttling Noise

Qianxu Wang,[1] Shouchuan Wang,[1] Huan Zhang,[1] Yuxuan Wang,[1] Junhai Zhou,[1] Panpan Zhao,[1] and Jia-Bao Liu[2]

[1]*Hefei General Machinery Research Institute Co. Let., Hefei 230000, China*
[2]*School of Mathematics and Physics, Anhui Jianzhu University, Hefei 230601, China*

Correspondence should be addressed to Shouchuan Wang; wangsc0731@163.com

Received 4 September 2021; Revised 4 November 2021; Accepted 6 November 2021; Published 19 January 2022

Academic Editor: Jesus M. Munoz-Pacheco

The aim of this work is the reduction of the throttling noise when the capillary is used as a throttling device. Based on the theory of bubble dynamics, two-phase flow, and aerated supercavitation, four different sizes of aerated devices used in refrigerator refrigeration systems are designed. Throttling noise and the temperature and pressure of inlet and outlet of the capillary are measured under stable operation. To compare the noise suppression effects in different groups of experiments, we introduced the cavitation number to analyze, revealed the principle of aerated supercavitation to suppress noise, and combined the results of Fluent simulations to get the relationship between the noise suppression effect and the aerated quality. The experimental results showed that the aerated device can obviously suppress the throttling noise of the capillary outlet, up to 2.63 dB(A), which provides a new way for reducing the capillary throttling noise.

1. Introduction

In household appliances such as refrigerators that use capillary throttling, noise caused by refrigerant flow is a common problem. Although the refrigerant flow rate is low, it still produces noise that affects the user's life and work in a quiet room, and it also brings hidden dangers to food safety as described by [1]. With the improvement of energy efficiency of household appliances approaching the limit, reducing the noise caused by refrigerant flow to improve acoustic comfort has gradually become a new research hotspot. However, the current research mainly focuses on the fundamental generation mechanism of capillary noise [2–4], there is less research on the technical measures to reduce noise.

Refrigeration equipment operates in a cyclic mode, and the capillary outlet throttling noise determines the overall noise level, especially the cavitation noise, as described by [5, 6], but it has not yet attracted attention [7]. Cavitation noise arises from the transition element between the capillary tube and the evaporator. Reference [3] observed that the connection of this transition structure is usually discontinuous, thus creating conditions for the generation of cavitation noise.

Reference [8] found that the cavitation noise of bubbles is closely related to the pressure pulsation. With the deepening of the research on cavitation noise, it was observed that the size of the cavitation noise is determined by the acoustic characteristics of the bubbles in the tube, as described by [9] and [10]. During the study, they found that the flow pattern is affected by the characteristics of the bubble and established a flow pattern diagram to predict the noise. Reference [11] also studied the fundamental mechanism of capillary outlet noise but did not propose approaches to reduce the noise emission.

Compared with studying the mechanism of cavitation noise, how to reduce the noise is more important. Although [12, 13] achieved the purpose of noise reduction by transforming the transition structure, they did not solve the cavitation noise emission from the root of the noise generation. Reference [14] also tried to use structures such as honeycomb cylinders to adjust flow to reduce noise, but it has certain limitations.

Cavitation was also applied to treat aqueous effluents polluted by organic, toxic, and biorefractory contaminants (2020) [15]. Hydrodynamic cavitation was used for the gradual disintegration of activated sludge and the solubilization of the dissolved organic matter (2021) [16]. Giuseppe Mancuso introduced a hydrodynamic cavitation reactor (Ecowirl) based on swirling jet-induced cavitation and found that Ecowirl reactor resulted in being more energy efficient as compared to hole orifice plates, Venturi and other swirling jet-induced cavitation devices.

In this paper, a noise reduction device is designed based on the theory of bubble dynamics, two-phase flow, and aerated supercavitation, and then the influence of aerated quality change on the noise reduction performance is studied. The fundamental mechanism of noise generation and suppression was analyzed, the noise emission was suppressed from the root of noise generation, and effective noise suppression ideas were innovatively proposed.

2. Theoretical Background for the Root Cause of at the Capillary Outlet

In this section, the theories of two-phase flow and bubble dynamics are reviewed for explaining the root causes of the refrigerant-induced noise that arises at the capillary outlet.

2.1. Two-phase Flow Theory. At any position in the area near the outlet of the capillary, it may be liquid phase, gas phase, or an interface between two phases at different moments. Although the fluid will have inhomogeneities, discontinuities, and uncertainties at any position in the space or in a certain time domain, in principle, the basic equations of fluid mechanics can still be used to establish and analyze the calculation relationship of two-phase flow. Using the split-phase flow model (Figure 1), it is assumed that the gas phase and the liquid phase flow completely separately and have different flow rates. Assuming that the flow is a one-dimensional flow, the pressure distribution of the flow section is uniform, and the change of flow velocity and fluid parameters with the radial direction of the pipeline is ignored, the controlled volume studied is shown in Figure 2, and the angle between the flow and the horizontal direction is θ. The governing equations of the separated-flow model for unidirectional flow are given in (1)–(4), which are the continuity equation, momentum equation, and energy equation, respectively.

Continuity equation is as follows:

$$\frac{\partial(\rho_0 A)}{\partial t} + \frac{\partial(\mathrm{GA})}{\partial z} = 0, \tag{1}$$

where

$$\rho_0 = \left[x v_g + (1-x) v_l\right]^{-1}, \tag{2}$$

where x is the dryness, v_g and v_l are the specific volume of the gas and liquid phases, respectively, G is the mass flux, and A is the cross-sectional area of the pipeline.

Momentum equation is as follows:

$$-\frac{\partial p}{\partial z} = \frac{\tau_w l_w}{A} + \frac{1}{A}\frac{\partial}{\partial z}\left\{\mathrm{AG}^2\left[\frac{x^2 v_g}{\alpha} + \frac{(1-x)^2 v_l}{1-\alpha}\right]\right\} + g\left[\alpha\rho_g + (1-x)\rho_l\right]\sin\theta + \frac{\partial G}{\partial t}, \tag{3}$$

where p is the pressure, τ_w is the shear stress, P_w is the wet perimeter of the control body, α is the cavitation fraction, ρ_g and ρ_l are the density of the gas and liquid phases, and z is the axial coordinates, respectively.

Energy equation is as follows:

$$-\frac{\mathrm{d}p}{\mathrm{d}z} = \rho_0\frac{\mathrm{d}E}{\mathrm{d}z} + \frac{\rho_0}{2}\frac{d}{\mathrm{d}z}\left\{G^2\left[\frac{x^3 v_g^2}{\alpha^2} + \frac{(1-x)^3 v_l^2}{(1-\alpha)^2}\right]\right\} + \rho_0 g\,\sin\theta, \tag{4}$$

where E is the internal energy and ρ_0 is the density after gas-liquid is mixed.

When the flow pattern in a pipe is intermittent (slug, churn (forth), and plug flows), at a specific location in the pipeline, x and α irregularly changing with time, the time gradient of pressure drop is a function of dryness and cavitation fraction as shown in (5) [10]:

$$\frac{d}{\mathrm{d}t}\left(\frac{\mathrm{d}p}{\mathrm{d}z}\right) = \frac{d}{\mathrm{d}t}\left[f\left(x(t), \alpha(t), \ldots\right)\right]. \tag{5}$$

This indicates that the pressure of the intermittent flow will fluctuate irregularly, and the pressure fluctuation will act on the pipe wall and then produce obvious vibration and noise. When the flow pattern is annular or bubbly flow, the dryness and cavitation fraction hardly change with time, so the time gradient of pressure drop is very small, and thus the resulting noise sound pressure level is small and basically constant, which is significantly lower than the vibration and noise level of slug flow [5].

2.2. Bubble Dynamics Theory. Bubble dynamics is the theoretical basis for the study of all liquid cavitation phenomena, which has irrelated with cavitation generation methods, cavitation objects, and cavitation shapes. When the molecules in the refrigerant liquid produce thermal movement, temporary microscopic voids will be formed, or they will fracture at the boundary between the solid container wall and the liquid or the boundary between suspended fine particles and the liquid. These weak voids and points constitute the cavitation nucleus necessary for the burst and growth of macroscopic bubble. With the refrigerant flows in the capillary tube, the liquid pressure gradually decreases because of the friction effect in tube, and the saturated liquid refrigerant quickly transforms into a gas-liquid two-phase fluid accompanied by the bubble nucleation process. As the

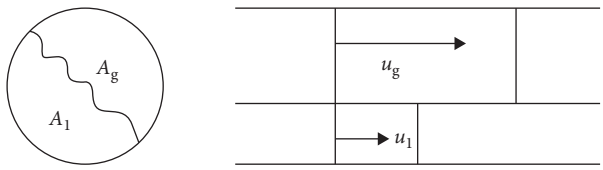

Figure 1: Two-phase and separated-flow model.

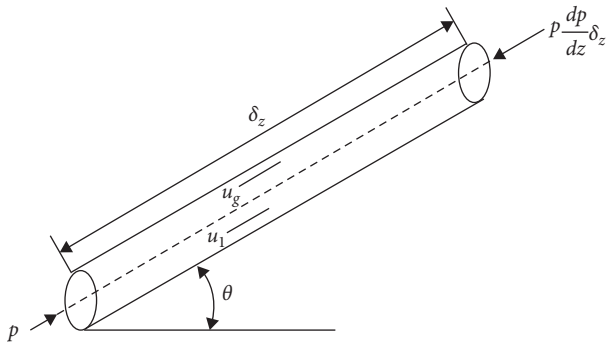

Figure 2: The control volume of the momentum equation of the two-phase and separated-flow model.

superheat of the liquid increases, the nucleation of the inner wall of the pipe and the inside of the liquid will increase significantly. When the static pressure inside the liquid is reduced to a level sufficient to tear the liquid, the cavitation nucleus will inflate, which is called the incipient cavitation [11]. According to the mechanical equilibrium conditions, the pressure in the core can be expressed as

$$P_{g0} = P_0 - P_V + \frac{2S}{R_0}, \tag{6}$$

where P_V is the saturated vapor pressure of the liquid at the corresponding temperature, R_0 is the initial radius of the cavitation nucleus, and S is the surface tension coefficient of the liquid. Regarding bubble frequency, [17] proposed the relationship between bubble radius and natural frequency as showed in

$$f_n = \frac{1}{2\pi R_0}\sqrt{\frac{3\mathrm{kp}}{\rho_l}}. \tag{7}$$

We can observe that the natural frequency of the bubble is closely related to the bubble size. Large bubbles contribute to low frequency, and small bubbles contribute to high frequency.

With the further growth and expansion of the bubble, the bubble will collapse; this process is very rapid and violent. The energy contained in the bubble is released, resulting in strong pressure fluctuations and noise. This process is called bubble collapse. In the refrigeration system, cavitation collapse mainly occurs at the outlet of the capillary tube, and the cavitation noise generated by it makes an important contribution to the flow noise at the outlet of the capillary tube. In order to better describe the characteristics of cavitation, a dimensionless cavitation number σ is introduced in this article:

$$\sigma = \frac{P_\infty - P_V(T_\infty)}{\rho_l u_\infty^2/2}, \tag{8}$$

where P_∞, T_∞, and u_∞ are the hydrostatic pressure, temperature, and velocity on the reference section of the flow field that are not disturbed and ρ_l and P_V are the density of the cavitation liquid medium and the saturated vapor pressure at the corresponding temperature, respectively.

The smaller the cavitation number, the more severe the cavitation degree, but the cavitation intensity is not necessarily high. The cavitation intensity is related to the pressure distribution and flow velocity of the liquid during the flow process and has a direct impact on the cavitation noise. The sound level of the cavitation noise does not rise but falls when it is in the supercavitation state, as described by Arndt [18], which provided a theoretical guidance for reducing capillary flow noise in this paper. The theoretical review shows that the noise induced by refrigerant is closely related to the sound pressure level produced by bubbles. The noise measurement results are mainly introduced in Section 3. The simulation results are combined to analyze the flow field and the noise reduction effect in Section 4. Finally, Section 5 summarizes the paper and outlines future activities.

3. Experimental Methods

3.1. Refrigerator Refrigeration Cycle System. In order to study the flow noise at the outlet of the capillary tube, the paper chooses a refrigerator refrigeration system for experiment. The refrigerator model is Hair BC/BD 103TS. The layout of the refrigeration system is shown in Figure 3. A pressure sensor (PT210B-G1/4) and a temperature sensor (DS18b20) are installed. To measure the inlet and outlet status of the capillary tube, the vortex flow sensor (WL-LWGA-25) is used to measure the mass flow rate. The refrigerant evaporates in the evaporator, takes away the heat, and returns to the compressor. The pressure and temperature of the refrigerant are increased by compression and sent to the condenser. The condensation in the condenser dissipates the heat to the surrounding environment. The refrigerant then flows through the desiccant and the capillary tube and enters the evaporator after throttling, completing the entire cycle. The measurements accuracy is listed in Table 1.

Table 1 lists the experimental measurement data. The data acquisition module is used in conjunction with the software to collect, display, and save the measurement data. The length of the throttling capillary is 3 m, and the inner diameter of the tube is 0.7 mm. The capillary outlet transition tube is shown in Figure 4(a). At the outlet of the capillary, the length of the transition tube is 70 mm, and the capillary extends 20 mm into the transition tube. At the capillary tube outlet, the diameter suddenly expands from 0.7 mm to 6 mm. The optimized transition pipe is equipped with aeration device. As shown in Figure 4(b), four different sizes of aeration devices are designed in this paper, the inner diameters of which are 0.6 mm, 0.8 mm, 1.0 mm, and 1.2 mm, respectively.

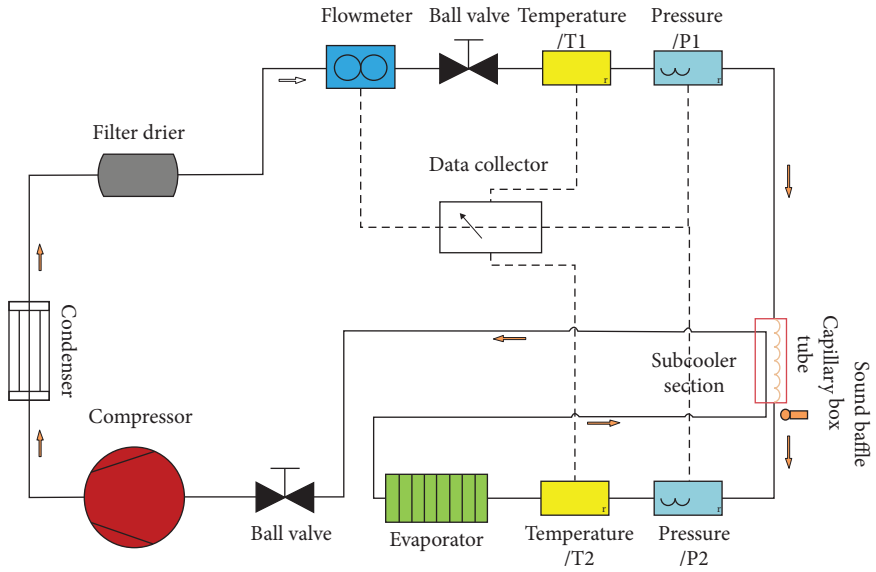

Figure 3: Refrigerator refrigeration system.

Table 1: The calculation parameters of the refrigerator.

Measurand		Value	Uncertainty
Diameter	D_C	0.7 mm	±0.01 mm
	D_S	0.6 mm	±0.01 mm
Length	l_{in}	450 mm	±0.1 mm
	l_{hx}	800 mm	±0.1 mm
	l_c	3050 mm	±0.1 mm
Temperature	T_1	37°C	±0.1°C
	T_2	1°C	±0.1°C
Pressure	P_1	754740 Pa	±100 Pa
	P_2	156960 Pa	±100 Pa
Mass flow	m	0.3 kg h^{-1}	±1%
Capillary roughness		0.00000046	
Refrigerant		R600a	

3.2. Noise Measurement System. The acoustic test system is shown in Figure 5. The portable measurement and analysis system SA-A1 (Japan RION) is used to measure the noise. The 1/2-inch free-field microphone is connected to the host through the preamplifier. The sensitivity of the microphone is −27 (dB re 1 V/Pa)$^{-1}$, the frequency measurement range is 10 Hz to 20000 Hz, and the maximum measurement noise value is 148 dB. The system fully meets the measurement requirements of the experiment. The data measured in the experiment is processed by the SA-A1 system host and supporting software.

There is a sound-proof baffle box in the transition area between the capillary tube and the evaporator, which is covered with sound-absorbing material and also has good heat insulation performance. In order to reduce the presence of moisture that may cause the formation of hoarfrost, the test area was designed to be as small as possible, and the detection area inside the box is $(100 \times 100 \times 100)$ mm^3. In addition, silica gel can dehumidify the enclosed air. The pipe section in the box is not insulated to achieve a better signal-to-noise ratio. The microphone is located 10 mm above the capillary outlet.

For frequencies above 250 Hz, the third-octave band analysis of the background noise measurement corresponds to the inherent noise of the microphone. Below 250 Hz, acoustic disturbances caused by the compressor affect the sound measurements. In order to avoid the necessity of a complex background noise correction, the acoustic analysis is carried out in frequency band of 250 Hz to 16000 Hz. To calculate the A-weighted sound pressure level, the standardized time weighting span "fast" with an exponential average aging time of 125 ms is used.

In a refrigerator, the refrigerant flow cavitation noise frequency is basically the same as the natural frequency of the bubble, and the natural frequency of the bubble can be calculated by (7) as described in [17]. By measuring the noise value under different aeration devices, the correlations between the noise suppression effect and the aeration quality can be obtained.

3.3. Experimental Setup. The refrigerator located on a 5-6 mm thick elastic rubber pad make it run under no load, adjust the thermostat to a medium or strong cold position, and start the

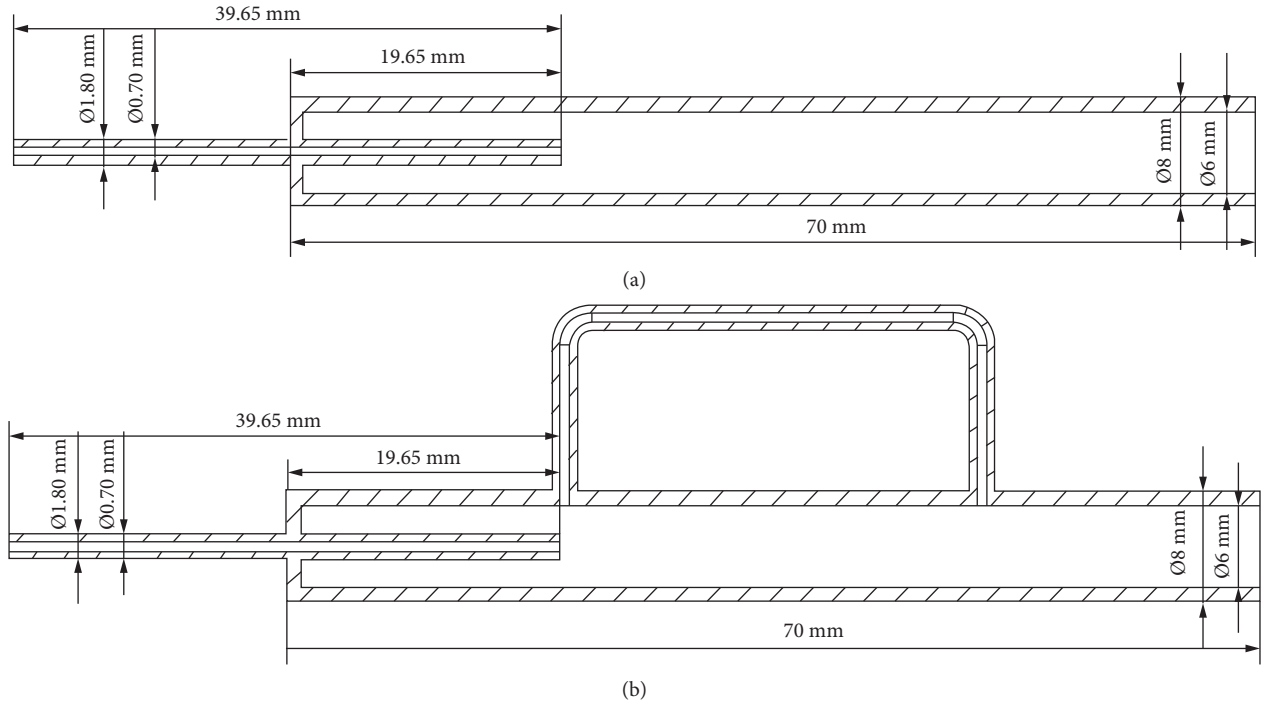

Figure 4: Transition pipe of the refrigeration system. (a) Transition pipe and (b) transition pipe equipped with aeration device.

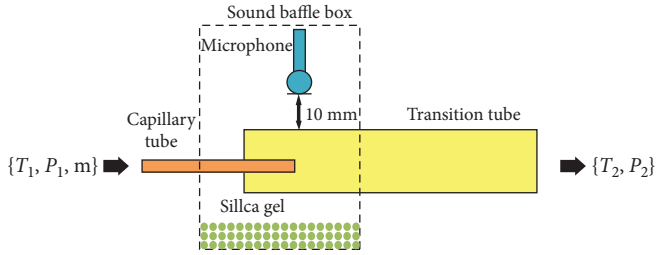

Figure 5: Setup of the sound baffle box around the capillary tube outlet.

test after running for at least 30 minutes. During the test, Because the temperature in the box has reached the set temperature and the machine is stopped, the measurement needs to be interrupted, and the measurement should be performed after the compressor restarts for 3 minutes.

Temperature and pressure sensors are installed at the inlet and outlet of the capillary tube, respectively. Because the refrigerant at the outlet of the condenser is in a supercooled state and single-phase flow, the flowmeter is installed here to measure the refrigerant flow of the refrigeration system. We install aeration devices of different sizes to optimize the transition structure of the refrigerator and repeat the above steps to conduct the experiment. Through the installation of aeration devices, local supercavitation is achieved and the purpose of suppressing refrigerant cavitation is achieved. Four different sizes of aeration devices are used, the inner diameters of which are 0.6 mm, 0.8 mm, 1.0 mm, and 1.2 mm, respectively.

The ambient temperature and humidity are 20.5°C/73%, respectively, and the atmospheric pressure is 1.0118×10^5 Pa. The temperature of the fresh-keeping chamber was set at 6°C.

3.4. Flow Simulation at the Capillary Outlet. Combined with the previous experimental results, the commercial simulation software Fluent was used to simulate the flow at the capillary outlet. As shown in Figure 2, the capillary flow model was established, the mixture multiphase flow model and energy equation was selected, the Schnerr and Sauer cavitation model and the reliable k-e turbulence model were selected, cavitation properties choose tabular-pt-sat, bubble number density of model constants setting is $1e^8$, and turbulent coefficient setting is 0.39. The wall function selected Standard Wall Functions and turbulent viscosity is none. The refrigerant of R600a was selected as the materials in fluid and reference temperature was set to 303 k. The boundary conditions were selected pressure inlet (754740 Pa) and pressure outlet (156960 Pa), total temperature of inlet is set to 303.15 k, and total temperature of outlet is set to 283.15 k. Specification method of turbulence selected k and epsilon, turbulent kinetic energy was set to 0.02 m^2/s^2, and turbulent dissipation rate was set to 1 m^2/s^3. The solution method was set to coupled solution; pseudo transient was selected at the same time. Moment, turbulent

kinetic energy, turbulent dissipation rate, and energy were set to second order upwind; others keep the default settings. Refer to Table 1 for specific parameter settings. Take the capillary inlet and outlet flow rate and its degree of change as the judgment standard to judge whether the entire capillary model calculation process has converged. The calculated residual values are all set to less than 10^{-6}, when the capillary inlet and outlet flow does not change with the time. When the capillary inlet and outlet flow rate changes less than 5%, it can be determined that the capillary model calculation results at this time have converged. The capillary models with 2.79 million grids, 4 million grids, and 6 million grids were calculated, and the three simulation results were compared. The difference between the latter two was less than 0.5%. Finally, 4 million grids were selected to complete the calculation.

4. Results and Analysis

4.1. Noise Reduction of Aerated Supercavitation. A aeration device ($D4 = 0.8$ mm) was selected to verify the noise reduction effect, and the time domain and frequency domain diagrams of the flow noise at the capillary outlet during the stable operation of the refrigerator were obtained, which can be observed from the time domain diagram (Figure 6). When the aeration device was not installed, the overall noise value of the capillary outlet is relatively large, reaching to 26.4 dB(A). After the aeration device was installed, the flow noise of the capillary outlet is significantly lower than the noise of the capillary outlet not equipped with aeration device. The noise fluctuation is more stable, the noise value is only 24.4 dB(A), and the noise suppression value is 2 dB(A). Thus, the aeration device has a significant effect on the flow noise suppression of the capillary outlet.

It can be observed from the frequency distribution (Figure 7) that the maximum noise frequency of the capillary outlet is mainly distributed from 200 Hz to 2000 Hz, indicating that the noise at these frequencies plays a decisive role in the flow noise of the capillary outlet, as also described by [13].

When the refrigeration system is operating stably, the temperature of the capillary outlet was measured with time. From the temperature time domain diagram (Figure 8), it can be observed that the inlet and outlet temperatures of the capillary are 37.5°C/−13.5°C, respectively. After the aeration, the temperature of the capillary inlet and outlet is also 37.5°C/−13.5°C, respectively, indicating that the aeration device has no effect on the temperature of the capillary inlet and outlet, and it does not affect the refrigeration effect of the entire refrigerator refrigeration system.

4.2. The Correlations between Cavitation Noise Frequency and Aeration Quality. The frequency range of refrigerant bubble collapse was calculated to be 200 Hz–2000 Hz; according to (7), the influence of the installation of 4 different aeration devices on the noise frequency of the capillary outlet was measured, and the frequency distribution diagram was obtained as shown in Figure 9. Through analysis, it can be found that the main noise frequency distribution of the capillary outlet under the four working conditions is distributed in 200 Hz–2000 Hz. Combining Figure 7 to analyze, it can be known that the noise at these frequencies is mainly cavitation noise caused by cavitation phenomenon.

By calculating the aeration quality of different aeration devices, the aeration quality of different aeration devices is obtained as shown in Table 2. The size of the aeration device affects the aeration quality, and the aeration quality increases from $1.37 \times 10^{-4}\,\mathrm{kg\,s^{-1}}$ to $5.48 \times 10^{-4}\,\mathrm{kg{\cdot}s^{-1}}$. Despite changing the aeration quality, the maximum noise frequency is still distributed between 200 Hz and 2000 Hz, indicating that the aeration device will not affect the frequency range of cavitation noise.

4.3. The Correlations between Cavitation Noise Suppression Effect and Aeration Quality. The experiment was carried out using the original transition pipe and four transition pipes with different sizes of aeration devices. Moreover, in order to ensure the accuracy of the experiment, the experiment was repeated once. The noise measurement data was analyzed and calculated, and the noise suppression value comparison chart was obtained (Figure 10). Analyzing Figure 10, it can be observed that the experimental results remain unchanged when conducting experiments again. When the aeration quality increases from $1.37 \times 10^{-4}\,\mathrm{kg\,s^{-1}}$ to $5.48 \times 10^{-4}\,\mathrm{kg{\cdot}s^{-1}}$, the value of noise suppression first increases and then decreases. When the diameter of the aeration pipe is $D5 = 1.0$ mm, the aeration quality is $3.84 \times 10^{-4}\,\mathrm{kg{\cdot}s^{-1}}$. Under this condition, the noise suppression value is 2.63 dB(A), which had the best noise suppression effect on the outlet of the refrigerator capillary.

In order to further explain the influence of the aeration quality on the cavitation noise suppression effect, the cavitation number (σ) was introduced to characterize the cavitation phenomenon. Calculate the cavitation number in the local area of the capillary outlet according to (8). The specific value is shown in Table 2. When the cavitation number σ is 0.12 to 0.2, it represented the local cavitation stage. Under this condition, the noise level increases as the cavitation number decreases. and the sound level of cavitation noise did not rise but fell as the cavitation number decreased. When the cavitation number (σ) is below 0.12, it represented the supercavitation status, as confirmed by [18, 19]. From the cavitation number calculated in the paper, it can be clearly observed that the local cavitation number is lower than 0.07 after aeration. Thus, the supercavitation state is locally realized, and the noise level decreases with the decrease of the cavitation number (σ). When $D_5 = 1$ mm, the cavitation number (σ) is 0.057 and the noise level is reduced the most, which is consistent with the results of the previous experimental measurements.

4.4. Simulation Results. Aeration is performed locally on the capillary outlet, and the pressure distribution on the axis of the capillary outlet is shown in Figure 11. The zero point on the x-axis represents the capillary outlet. It can be observed that the aeration device can significantly increase the partial

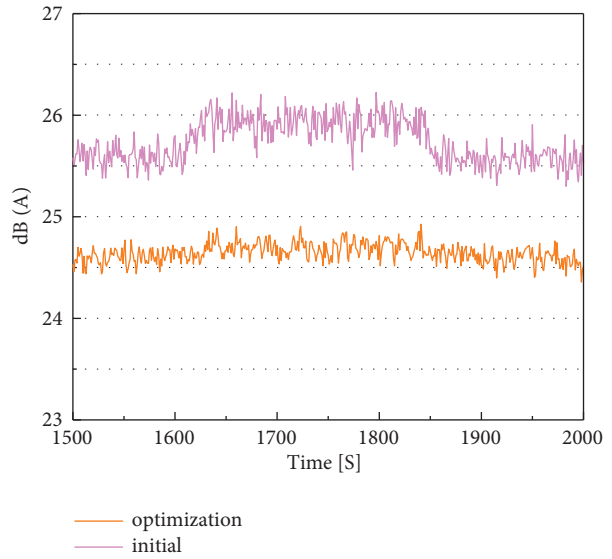

Figure 6: Time domain diagram of the noise of the capillary outlet before and after aeration.

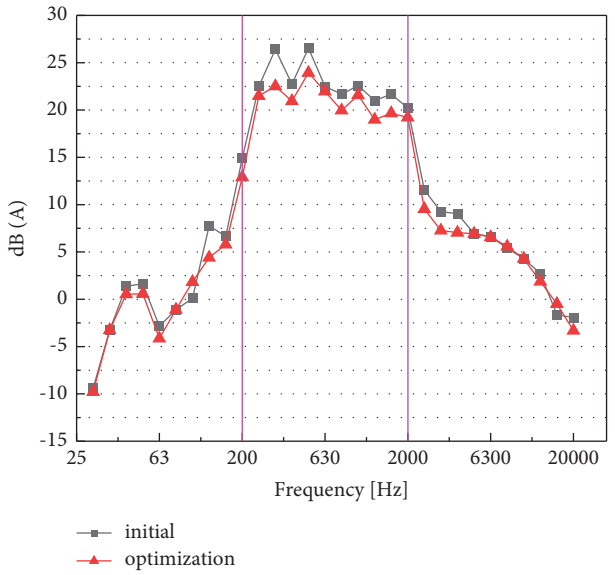

Figure 7: Frequency domain diagram of the noise of capillary outlet before and after aeration.

pressure of the capillary outlet, and it can also be found that $D6 = 1.2$ mm aeration device contributes the most to the local pressure increase, increasing by 800 Pa from Figure 11, indicating that the partial pressure of the capillary outlet is significantly affected by the quality of aeration.

Analyzing the refrigerant gas volume distribution diagram on the outlet axis of the capillary tube (Figure 12), at a position 0 m away from the capillary outlet, the local gas content between the initial transition tube and the four transition tubes with different aeration devices was compared. It is found that the gas content of the local refrigerant at the outlet of the capillary was significantly increased after aeration. When the diameter of the aeration devices is $D6 = 1.2$ mm and the aeration quality is 5.48×10^{-4} kg·s^{-1}, the vapor rate increase is 0.1 under this condition, indicating that the greater is the quality of aeration, the more beneficial it is to increase the local refrigerant vapor rate.

In order to better explain the vapor rate distribution diagram (Figure 12), Figure 12 was divided into four areas I, II, III, and IV. It can be observed that when the aeration device is not installed, the refrigerant bubble gradually grows and matures in the area of II, the gas volume fraction gradually increases from 0.79 to 0.86, then the refrigerant bubble begins to collapse in the III area, the gas volume fraction gradually decreases to 0.80, and finally the collapse is complete in the IV area. The volume fraction gradually stabilized to 0.79. When the aeration amount is 2.43×10^{-4} kg·s^{-1}, the partial pressure of the capillary outlet is increased, but the process of bubble

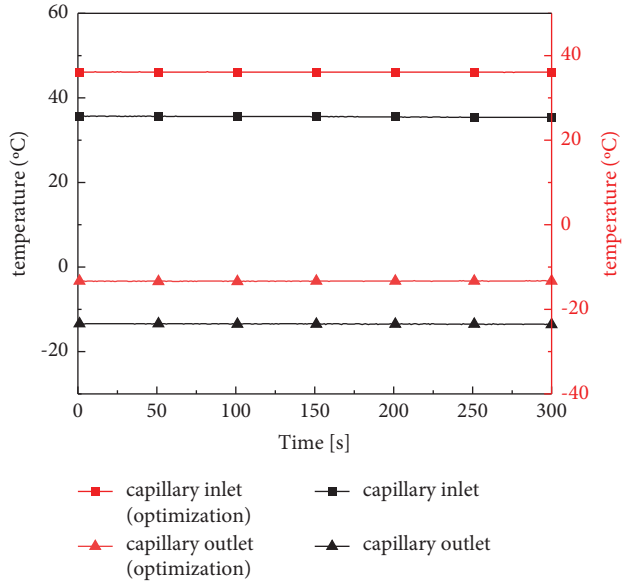

Figure 8: The temperature of the capillary inlet and outlet before and after aeration.

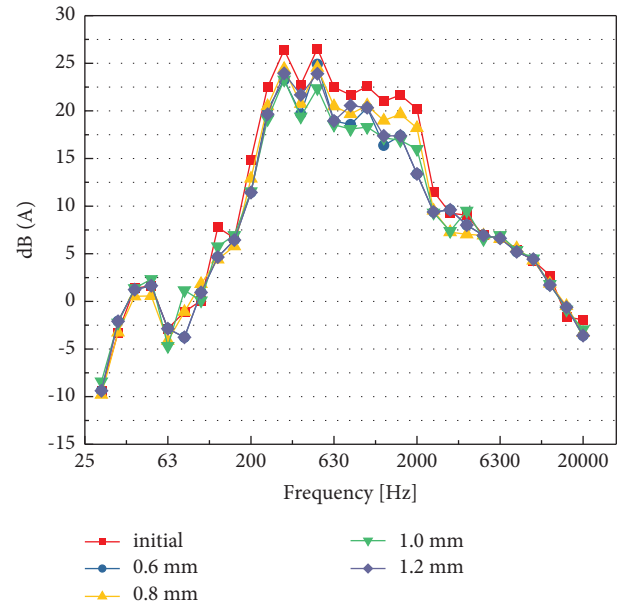

Figure 9: Frequency domain diagram of noise distribution equipped with different sizes of aeration devices.

Table 2: Aeration quality and cavitation number.

Aeration device pipe diameter D (mm)	Aerated amount q (kg·s^{-1})	Cavitation number σ
0.6	1.37×10^{-4}	0.068
0.8	2.43×10^{-4}	0.062
1.0	3.84×10^{-4}	0.057
1.2	5.48×10^{-4}	0.061

growth, maturation, and collapse still occurs, and the gas volume fraction still changes significantly, but when the aeration amount is greater than 2.43×10^{-4} kg·s^{-1} at this time, the bubble growth and collapse process was significantly suppressed, and the gas phase volume fraction remained basically steadily, indicating that the cavitation

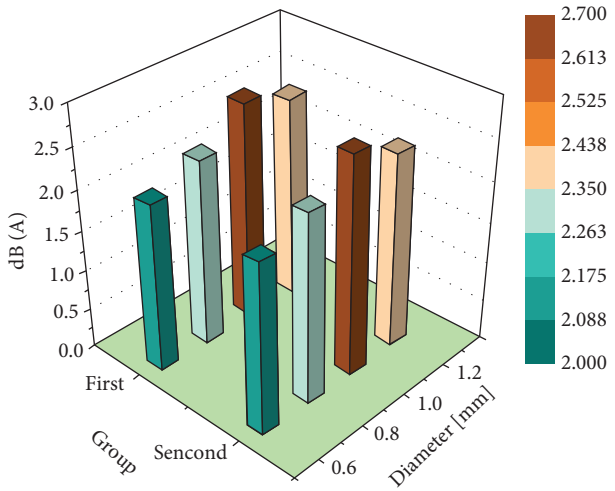

Figure 10: The value of noise suppression aerated different quality refrigerant.

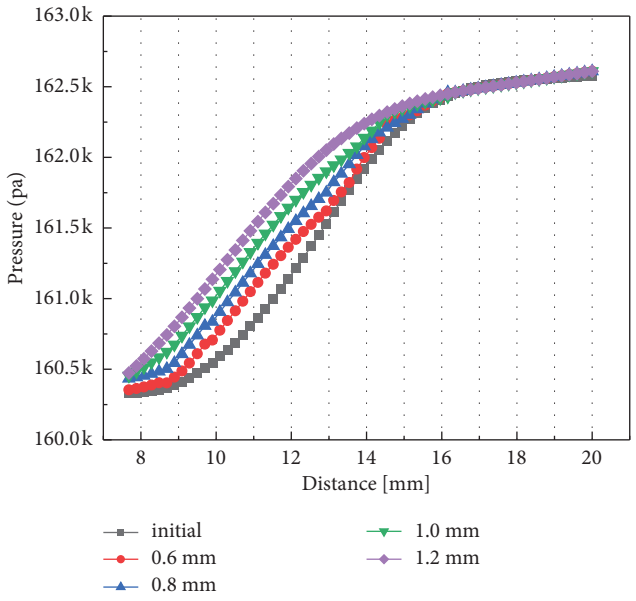

Figure 11: Local pressure distribution at the capillary outlet.

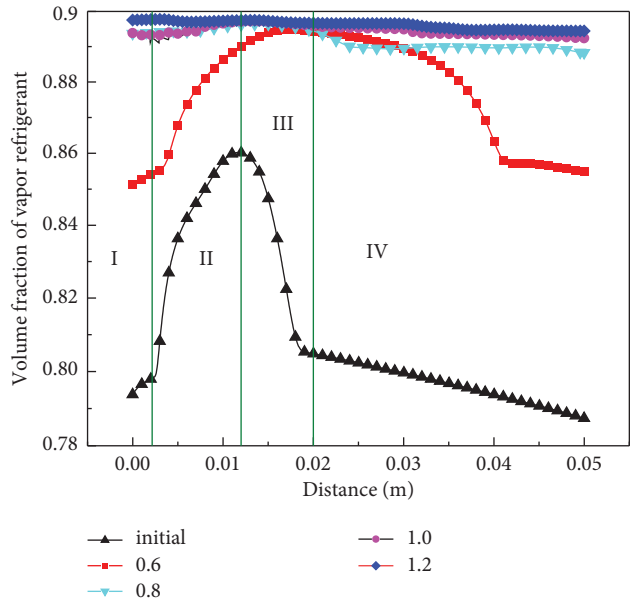

Figure 12: Local refrigerant vapor rate distribution at the outlet of the capillary.

phenomenon was suppressed. Therefore, conclusion can be made that the aeration devices can effectively reduce the cavitation noise.

5. Conclusion

Acoustic investigations are carried out at the outlet of a capillary tube, which serves as a throttling device in a vapor compression cycle. The refrigerator refrigeration system was used to study the flow noise of the capillary outlet, analyze the characteristics of the noise frequency distribution at the capillary outlet, and find that the main noise frequency distribution range of 200 Hz to 2000 Hz at the capillary outlet.

Under the same experimental conditions, aeration devices of different sizes were selected for experiments. By introducing a dimensionless parameter cavitation number σ, the principle of aeration supercavitation noise suppression was explained, and the correlations between noise frequency distribution, noise suppression effect, and aeration quality were found.

Finally, fluent software was used to simulate the flow at the capillary outlet to further verify the experimental results. Through experimental study and analysis, it is determined that cavitation noise is the main contributor to the capillary outlet throttling noise, and the feasibility of noise reduction of the aeration device is verified. At the same time, the suppression effect of different sizes of aeration devices on the noise value was obtained; it can reach up to 2.63 dB(A). Moreover, the aeration device has no negative influence on the evaporation temperature and normal operation of the refrigerator. The aeration device can significantly increase the local pressure, form supercavitation, and suppress the cavitation noise.

The previous article only proves that the aeration device can reduce the flow noise at the capillary outlet (2021). Based on the previous article, this article further studies the influence of different aeration quality on the noise suppression effect. The relationship between aeration quality and noise suppression lays a theoretical foundation for the application of aeration devices.

The noise generation process is very complicated and cannot be determined according to the given initial conditions. When the supercavitation state is reached, the cavitation noise decreases with the decrease of the cavitation number. In this paper, the internal diameter $D = 1.0$ aeration device is selected to achieve the best noise suppression effect. However, for different initial conditions, the influence of the aeration device size change on the cavitation number is different; this is the study of chaos.

The research in this article also provided reference value for noise suppression of other throttling devices.

Abbreviations

E: Internal energy (kJ)
D: Inner diameter (mm)
L: Length (mm)
T: Temperature (°C)
P: Pressure (Pa)
R: Radius (mm)
S: Liquid surface tension coefficient
M: Mass flow (kg s^{-1})
X: Dryness
U: Velocity (m s^{-1})
v: Specific volume
G: Mass flux (kg s^{-1})
A: Pipe cross-sectional area (m^2)
P: Density (kg m^{-3})
Z: Axial coordinates (m)
Q: Aeration amount (kg s^{-1})

Greek symbols
Σ: Cavitation number
A: Vacuole share
T: Shear stress
Λ: Capillary roughness

Subscripts
C: Capillary
S: Compressor suction pipe
W: Control body
O: Gas-liquid two-phase
V: Liquid saturated steam
∞: Reference section
in: Capillary before exchanging heat with compressor suction pipe
hx: Capillary exchanging heat with compressor suction pipe
1: Capillary inlet
2: Capillary outlet
3: 0.8 mm diameter aeration device
4: 1.0 mm diameter aeration device
5: 1.2 mm diameter aeration device
6: 1.4 mm diameter aeration device.

Data Availability

The figure and table data used to support the findings of this study are available from the corresponding author upon request.

Conflicts of Interest

The authors declare that they have no known competing financial interesting or personal relationships that could have appeared to influence the work reported in this paper.

References

[1] W. Hofstetter Richard, E. Copp Brennan, and I. Lukic, "Acoustic noise of refrigerators promote increased growth rate of the gray mold Botrytis cinereal," *Journal of Food Safety*, vol. 40, no. 6, 2020.

[2] D. Hartmann and C. Melo, "An experimental study on the capillary tube flow and its effect on the acoustic behavior of household refrigeators," in *Proceedings of the 15th International Refrigeration and Air Conditioning Conference*, pp. 1367–1378, IRAC, West Lafayette, Indiana, 14 July 2014.

[3] T. Tannert and U. Hesse, "Noise effects in capillary tubes caused by refrigerant flow," in *Proceedings of the 16th International Refrigeration and Air Conditioning Conference*, pp. 1562–1572, IRAC, West Lafayette, Indiana, 11 July 2016.

[4] Y.-Z. Wu, Z. Rui-Qi, X.-L. Cao, and G. Yan, "Combined nucleation theory and models for refrigerant flow in a capillary tube," *Journal of Xi'an Jiaotong University*, vol. 36, no. 7, pp. 661–664, 2002.

[5] H. S. Han, W. B. Jeong, M. S. Kim, and T. H. Kim, "Analysis of the root causes of refrigerant-induced noise in refrigerators," *Journal of Mechanical Science and Technology*, vol. 23, no. 12, pp. 3245–3256, 2009.

[6] H. S. Han, W. B. Jeong, M. S. Kim, S. Y. Lee, and M. Y. Seo, "Reduction of the refrigerant-induced noise from the evaporator-inlet pipe in a refrigerator," *International Journal of Refrigeration*, vol. 33, no. 7, pp. 1478–1488, 2010.

[7] Q. Wang, Y. Liu, Y. Yao, and Yu Zhang, "Experimental study of vapor supercavitation suppression of capillary outlet jet noise[J]," *Journal of Mathematics*, vol. 2021, Article ID 9936291, 10 pages, 2021.

[8] K. Tatsumi, "Study on noise caused by slug flow through a capillary tube (in Japanese)[J]," *Transactions of the Japan Society of Mechanical Engineers: Serie Bibliographique*, vol. 64, no. 611, pp. 2392–2397, 1997.

[9] H. S. Han, W. B. Jeong, and M. S. Kim, "Frequency characteristics of the noise of R600a refrigerant flowing in a pipe with intermittent flow pattern," *International Journal of Refrigeration*, vol. 34, no. 6, pp. 1497–1506, 2011.

[10] M. S. Kim, W. B. Jeong, and H. S. Han, "Development of noise pattern map for predicting refrigerant-induced noise in refrigerators," *Journal of Mechanical Science and Technology*, vol. 28, no. 9, pp. 3499–3510, 2014.

[11] J. Ruebeling and S. Grohmann, "Flow-induced noise generation at the outlet of a capillary tube[J]," *International Journal of Refrigeration*, vol. 111, 2020.

[12] B. Demirtekin and A. S. Sarigül, "Flow-induced noise in refrigerators (conference paper)," in *Proceedings of the International Noise Conference*, Institute of Noise Control Engineering, Hamburg, Germany, August 2016.

[13] X. I. A. Yu-bo, L. I. U. Yong-hui, L. I. U. Yi-cai, Y. Ma, C. Xiao, and T. Wu, "Experimental study on reducing the noise of horizontal household freezers," *Applied Thermal Engineering*, vol. 68, no. 1/2, pp. 107–114, 2014.

[14] G. Kim and S. Song, "Noise reduction of refrigerant two-phase flow using flow conditioners near the electric expansion valve," *Journal of Mechanical Science and Technology*, vol. 34, no. 2, pp. 719–725, 2020.

[15] C. Earls Brennen, *Cavitation and Bubble dynamics*, Jiangsu University Press, Zhenjiang, China, 2013.

[16] J. Cai, *Application of Liquid Cavitation technology[M]*, Science Press, Beijing, China, 2019.

[17] M. Minnaert, "XVI.On musical air-bubbles and the sounds of running water," *The London, Edinburgh, and Dublin Philosophical Magazine and Journal of Science*, vol. 16, no. 104, pp. 235–248, 1933.

[18] R. E. A. Arndt, "Recent advances in cavitation research," *Advances in Hydroscience*, vol. 12, pp. 1–78, 1981.

[19] Y. A. N. Chang-qi, *Gas-liquid Two-phase flow[M]*, pp. 38–64, Harbin Engineering University Press, Harbin, China, 2017.

Hindawi
Complexity
Volume 2021, Article ID 8752161, 18 pages
https://doi.org/10.1155/2021/8752161

Research Article

The Transmission Dynamics of Hepatitis B Virus via the Fractional-Order Epidemiological Model

Tahir Khan,[1,2,3] Zi-Shan Qian,[4] Roman Ullah,[5] Basem Al Alwan,[6] Gul Zaman,[2] Qasem M. Al-Mdallal,[7] Youssef El Khatib,[7] and Khaled Kheder[8]

[1]*Department of Computing, Muscat College, Muscat, Oman*
[2]*Department of Mathematics, University of Malakand, Dir (L), Chakdara, Pakhtunkhwa, Pakistan*
[3]*Department of Mathematics and Statistics, Woman University Swabi, Khyber Pakhtunkhwa, Pakistan*
[4]*School of Physical Sciences, University of California, Irvine, California 92617, USA*
[5]*General Requirements Department, CAS Sohar, , University of Technology and Applied Sciences, Muscat, Oman*
[6]*Chemical Engineering Department, College of Engineering, King Khalid University, Abha 61411, Saudi Arabia*
[7]*Department of Mathematical Sciences, UAE University, P.O. Box 15551, Al-Ain, UAE*
[8]*Civil Engineering Department, College of Engineering, King Khalid University, Abha 61411, Saudi Arabia*

Correspondence should be addressed to Qasem M. Al-Mdallal; q.almdallal@uaeu.ac.ae

Received 6 September 2021; Accepted 2 November 2021; Published 27 December 2021

Academic Editor: Mustafa Cagri Kutlu

We investigate and analyze the dynamics of hepatitis B with various infection phases and multiple routes of transmission. We formulate the model and then fractionalize it using the concept of fractional calculus. For the purpose of fractionalizing, we use the Caputo–Fabrizio operator. Once we develop the model under consideration, existence and uniqueness analysis will be discussed. We use fixed point theory for the existence and uniqueness analysis. We also prove that the model under consideration possesses a bounded and positive solution. We then find the basic reproductive number to perform the steady-state analysis and to show that the fractional-order epidemiological model is locally and globally asymptotically stable under certain conditions. For the local and global analysis, we use linearization, mean value theorem, and fractional Barbalat's lemma, respectively. Finally, we perform some numerical findings to support the analytical work with the help of graphical representations.

1. Introduction

Hepatitis B virus causes inflammation of the liver. It results from a noncytopathic virus which is called the hepatitis B virus (HBV). Characteristic of HBV is its high tissue and species specificity, as well as a unique genomic organization and replication mechanism. The infection of HBV has multiple phases: acute and chronic. The acute one refers to the first six months whenever there is an exposure of some one to the virus. Usually, in this period, the immune system has the capability to vanish the infection, while for some severe cases, it may also lead to the serious stage and so results in the lifelong illness. This is also known as the chronic stage. It could be noted that whenever HBsAg is positive for a person for a period of more than 6 months, it shows that it has a chronic illness. In case of the chronic stage, often, the individual has no history of the acute stage. This infection may also lead to the scarring of the liver, become liver failure, and produce liver cancer [1]. Hepatitis B virus is transferred by many ways: blood (razors, sharing of blades, tooth brushes, etc.) and semen and vaginal [2–5]. One of the other key sources of transmission is from the infected mother to her child called vertical transmission [6]. Worldwide, there are millions of infected population according to the WHO, in which only 93 millions are infected in China [7, 8]. Vaccines are available to immunize from the HBV which are very effective and almost provide permanent immunity [9, 10].

Mathematical modeling of infectious diseases has a vast field and has a rich literature, which plays a significant role to explore the dynamics and suggest the control mechanism. Since hepatitis B is one of the life-threatening and leading causes of death, it obtained the attention of various researches,

and consequently, many epidemiological models were developed (see [11–15]). Anderson and May presented a study in the form of a simple model to investigate the influence of carriers on the transmission of hepatitis B [16]. Williams et al. presented and analyzed the hepatitis B dynamics in the United Kingdom [17]. Moreover, a model was presented by Medley et al. to forecast a mechanism for eliminating hepatitis B from New Zealand [18]. In a similar way, a model that evaluates the effectiveness of the vaccination programme with the effect of age in China was presented by Zhao et al. [19]. Bakare et al. proposed the analysis of control by using an SIR epidemic model [20]. More epidemic models were investigated with control strategies by Kamyad et al. [21]. Onyango developed a model to study the multiple endemic solutions [22]. Similarly, Zhang et al. studied the dynamics of hepatitis B in Xinjiang [23]. Very recently, Khan et al. [24, 25] and Nana-Kyere et al. [26] formulated some epidemiological models to study different parameters' influences on the disease transmission and to suggest some control measures for the elimination of the infection. The study of fractional calculus obtained the attention of researchers and is growing rapidly. This analysis has been used to capture the axioms of inherited and the memory of various natural and physical phenomena occurring in different fields of science and technology. Numerous classical models have been proved with less accuracy in case of predicting the future dynamics of a system. However, models having fractional order are more useful to allocate and detain the missing information [27, 28]. It could also be stated that the classical derivative does not provide the dynamics between two different points [29, 30].

It is noted that hepatitis B virus transmission is influenced by different factors, i.e., various phases, routes of transmission, etc. Especially, the carriers are significant. The chronic carriers have no symptoms while transmitting the infection. Moreover, it could also be noted that the increased development of fractional calculus and fractional-order epidemiological models are more suitable than the classical order epidemic models and complex dynamics of hepatitis B; we therefore investigate a hepatitis B virus transmission epidemic model with various infection phases and multiple routes of transmission. Moreover, we also use the fractional calculus to fractionalize the model under consideration which has not yet been studied to the best of our knowledge. Once we formulate the model, we then study the existence analysis as well as uniqueness to prove the well-posedness and biological feasibility of the problem under consideration. For this analysis, the fixed point theory will be used. We also prove that the solutions of the proposed system are bounded and positive. We then discuss the steady state of the proposed model and investigate that the model under consideration is locally and globally asymptotically stable. For local stability analysis, we use the method of linearization, mean value theorem, and fractional Barbalat's lemma. Finally, some numerical simulations will be performed to support the analytical work and show the difference between the classical and fractional order.

2. Preliminaries

Here, we describe the fundamental concepts related to the fractional calculus which are helpful to obtain our results.

Definition 1 (see [30]). Let us assume a function $\varphi(t)$ such that $\phi \in H^1(0,T), T>0$; if $\alpha>0$ and $n-1<\alpha<n$, $n\in\mathbb{N}$, then the Caputo and Caputo–Fabrizio derivative of the fractional order (α) are defined, respectively, as

$$ {}^{C}D^{\alpha}_{0,t}\{\varphi(t)\} = \frac{1}{\Gamma(n-\alpha)}\int_0^t (t-x)^{n-\alpha-1}\varphi^n(x)\mathrm{d}x \tag{1}$$

and

$$ {}^{CF}D^{\alpha}_{0,t}\{\varphi(t)\} = \frac{K(\alpha)}{(1-\alpha)}\int_0^t \varphi'(y)\exp\left(\frac{\alpha(y-t)}{1-\alpha}\right)\mathrm{d}y. \tag{2}$$

In equations (1) and (2), C and CF represent, respectively, Caputo and Caputo–Fabrizio, while $t>0$ and $K(\alpha)$ represent the normalization function such that $K(1)=0=K(0)$.

Definition 2 (see [30]). If $0<\alpha<1$ and $\varphi(t)$ varies with time t, then the Riemann–Liouville integral of order (α) is defined as

$$ {}^{RL}J^{\alpha}_{0,t}\{\varphi(t)\} = \frac{1}{\Gamma(\alpha)}\int_0^t (t-y)^{\alpha-1}\varphi(y)\mathrm{d}y, \tag{3}$$

while the integral of order (α) in the Caputo–Fabrizio-Caputo (CF) sense is defined by

$$ {}^{CF}J^{\alpha}_{0,t}\{\varphi(t)\} = \frac{2(1-\alpha)\varphi(t)}{(2-\alpha)K(\alpha)} + \frac{2\alpha}{(2-\alpha)K(\alpha)}\int_0^t \varphi(y)\mathrm{d}y. \tag{4}$$

3. Model Formulation

We formulate the model keeping in view the characteristics of hepatitis B virus and so distribute the total population symbolized by $T(t)$ into different compartmental population sizes, i.e., susceptible $S(t)$, acute $A(t)$, chronic $C(t)$, recovered/immune $R(t)$, and vaccinated $V(t)$. We also define some constraints for the proposed problem:

a_1: all the variables (S, A, C, R, and V) and the parameters (Π, ζ, β, ρ, ϑ, η, σ, p, γ, ε, and τ) are nonnegative in the epidemic problem that is under consideration.

a_2: the successfully vaccinated portion η of the susceptible individuals goes to the recovered class.

a_3: the contact of susceptible with acute infected as well as with chronically infected is, respectively, denoted by β and $\rho\beta$, which lead to the acute portion with probability p and go to chronic with probability $(1-p)$, where this assumption is based on the hypothesis that some of the individuals have no history of acute illness.

a_4: since some of the individuals got recovery in the acute stage and it leads to the chronic stage for some severe cases, therefore, a natural recovery with probability q has been proposed, while $(1-q)$ leads to the chronic stage.

a_5: the recovery under treatment (τ) is taken of the chronic population.

a_6: the disease-induced death rate (ε) occurs in the chronic stage only.

a_7: the newborn rate is Π and assumed to be susceptible, while getting successful vaccination (ζ) leads to the vaccinated class.

In light of these assumptions, we develop a model as presented in the following:

$$\begin{cases} \dfrac{dS(t)}{dt} = (1-\zeta)\Pi - \beta S(t)A(t) - \rho\beta S(t)C(t) - (\vartheta+\eta)S(t) + \sigma V(t), \\ \dfrac{dA(t)}{dt} = p\{\beta S(t)A(t) + \rho\beta S(t)C(t)\} - (\vartheta+\gamma)A(t), \\ \dfrac{dC(t)}{dt} = (1-p)\{\beta S(t)A(t) + \rho\beta S(t)C(t)\} + q\gamma A(t) - (\vartheta+\varepsilon+\tau)C(t), \\ \dfrac{dR(t)}{dt} = (1-q)\gamma A(t) + \eta S(t) + \tau C(t) - \vartheta R(t), \\ \dfrac{dV(t)}{dt} = \zeta\Pi - (\vartheta+\sigma)V(t) \end{cases} \tag{5}$$

with initial population sizes

$$S(0) > 0, A(0) \geq 0, C(0) \geq 0, R(0) > 0, V(0) > 0, \tag{6}$$

where ζ is the proportion of successful vaccination individuals and Π is the newborn rate. Similarly, the transmission rate of hepatitis B is denoted by β, while the reduced transmission rate is ρ. Moreover, ϑ and η are, respectively, the natural death rate and permanent recovered individuals' rate. We also symbolize the recovery rate of acute and chronic hepatitis B individuals by γ and τ, respectively. The disease-induced death rate is represented by ε, while those individuals who lose their immunity are represented by σ.

We extend the reported model by equation (5) to the associated fractional-order $(\alpha < 0 < \alpha < 1)$ version by taking into account the Caputo–Fabrizio-Caputo (*CF*) operator. We therefore replace the derivatives in the problem under consideration with a fractional derivative to maintain the dimension of both sides of the equations of the proposed model taking the α power of each parameter which becomes

$$\begin{cases} {}^{CF}D^{\alpha}_{0,t}(S(t)) &= (1-\zeta^{\alpha})\Pi^{\alpha} - \beta^{\alpha}S(t)A(t) - \rho^{\alpha}\beta^{\alpha}S(t)C(t) - (\vartheta^{\alpha}+\eta^{\alpha})S(t) + \sigma^{\alpha}V(t), \\ {}^{CF}D^{\alpha}_{0,t}(A(t)) &= p\{\beta^{\alpha}S(t)A(t) + \rho^{\alpha}\beta^{\alpha}S(t)C(t)\} - (\vartheta^{\alpha}+\gamma^{\alpha})A(t), \\ {}^{CF}D^{\alpha}_{0,t}(C(t)) &= (1-p)\{\beta^{\alpha}S(t)A(t) + \rho^{\alpha}\beta^{\alpha}S(t)C(t)\} + q\gamma^{\alpha}A(t) - (\vartheta^{\alpha}+\epsilon^{\alpha}+\tau^{\alpha})C(t), \\ {}^{CF}D^{\alpha}_{0,t}(R(t)) &= (1-q)\gamma^{\alpha}A(t) + \eta^{\alpha}S(t) + \tau^{\alpha}C(t) - \vartheta^{\alpha}R(t), \\ {}^{CF}D^{\alpha}_{0,t}(V(t)) &= \zeta^{\alpha}\Pi^{\alpha} - (\vartheta^{\alpha}+\sigma^{\alpha})V(t). \end{cases} \tag{7}$$

We now discuss the existence and uniqueness of the above fractional-order epidemiological model (7) in the following section.

4. Existence and Uniqueness

This section is devoted to the existence and uniqueness analysis of the solution of fractional-order epidemiological model (7). We use the concept of fixed point theory and prove the solution existence and uniqueness. For this analysis, transforming the proposed system into an integral equation, we obtain

$$\begin{aligned}
S(t) &= S(0) + {}^{CF}J_{0,t}^{\alpha}\{(1-\zeta^{\alpha})\Pi^{\alpha} - \beta^{\alpha}S(t)A(t) - \rho^{\alpha}\beta^{\alpha}S(t)C(t) - (\vartheta^{\alpha}+\eta^{\alpha})S(t) + \sigma^{\alpha}V(t)\},\\
A(t) &= A(0) + {}^{CF}J_{0,t}^{\alpha}\{p\{\beta^{\alpha}S(t)A(t) + \rho^{\alpha}\beta^{\alpha}S(t)C(t)\} - (\vartheta^{\alpha}+\gamma^{\alpha})A(t)\},\\
C(t) &= C(0) + {}^{CF}J_{0,t}^{\alpha}\{(1-p)\{\beta^{\alpha}S(t)A(t) + \rho^{\alpha}\beta^{\alpha}S(t)C(t)\} + q\gamma^{\alpha}A(t) - (\vartheta^{\alpha}+\varepsilon^{\alpha}+\tau^{\alpha})C(t)\},\\
R(t) &= R(0) + {}^{CF}J_{0,t}^{\alpha}\{(1-q)\gamma^{\alpha}A(t) + \eta^{\alpha}S(t) + \tau^{\alpha}C(t) - \vartheta^{\alpha}R(t)\},\\
V(t) &= V(0) + {}^{CF}J_{0,t}^{\alpha}\{\zeta^{\alpha}\Pi^{\alpha} - (\vartheta^{\alpha}+\sigma^{\alpha})V(t)\}.
\end{aligned} \tag{8}$$

Taking the CF fractional integral of both sides of the above system leads to the assertions as given in the following:

$$\begin{aligned}
S(t) &= S(0) + \frac{2(1-\alpha)}{K(\alpha)(2-\alpha)}\left\{(1-\varsigma^{\alpha})\Pi^{\alpha} - \beta^{\alpha}S(y)A(y) - \rho^{\alpha}\beta^{\alpha}S(t)C(t) - \left(\vartheta^{\alpha}+\eta^{\alpha}\right)S(t) + \sigma^{\alpha}V(t)\right\}\\
&\quad + \frac{2\alpha}{K(\alpha)(2-\alpha)}\int_0^t\left\{(1-\varsigma^{\alpha})\right\} - \beta^{\alpha}S(y)A(y) - \rho^{\alpha}\beta^{\alpha}S(y)C(y) - \left(\vartheta^{\alpha}+\eta^{\alpha}\right)S(y) + \sigma^{\alpha}V(y)dy,\\
A(t) &= A(0) + \frac{2(1-\alpha)}{K(\alpha)(2-\alpha)}\left\{p\{\beta^{\alpha}S(t)A(t) + p^{\alpha}\beta^{\alpha}S(t)C(t)\} - \left(\vartheta^{\alpha}+\gamma^{\alpha}\right)S(t)\right\}\\
&\quad + \frac{2\alpha}{K(\alpha)(2-\alpha)}\int_0^t\left\{p\{\beta^{\alpha}S(y)A(y) + p^{\alpha}\beta^{\alpha}S(y)C(y)\} - \left(\vartheta^{\alpha}+\gamma^{\alpha}\right)A(y)\right\}dy,\\
B(t) &= B(0) + \frac{2(1-\alpha)}{K(\alpha)(2-\alpha)}\left\{(1-p)\{\beta^{\alpha}S(t)A(t) + p^{\alpha}\beta^{\alpha}S(t)C(t)\} + q\gamma^{\alpha}A(t) - \left(\vartheta^{\alpha}+\varepsilon^{\alpha}+\tau^{\alpha}\right)C(t)\right\}\\
&\quad + \frac{2\alpha}{K(\alpha)(2-\alpha)}\int_0^t\left\{(1-p)\{\beta^{\alpha}S(y)A(y) + p^{\alpha}\beta^{\alpha}S(y)C(y)\} - q\gamma^{\alpha}A(t) - \left(\vartheta^{\alpha}+\varepsilon^{\alpha}+\tau^{\alpha}\right)C(y)\right\}dy,\\
R(t) &= R(0) + \frac{2(1-\alpha)}{K(\alpha)(2-\alpha)}\{(1-q)\gamma^{\alpha}A(t) + \eta^{\alpha}S(t) + \tau^{\alpha}C(t) - \vartheta^{\alpha}R(t)\}\\
&\quad + \frac{2\alpha}{K(\alpha)(2-\alpha)}\int_0^t\{(1-q)\gamma^{\alpha}A(y) + \eta^{\alpha}S(y) + \tau^{\alpha}C(y) - \vartheta^{\alpha}R(y)\}dy,\\
V(t) &= V(0) + \frac{2(1-\alpha)}{K(\alpha)(2-\alpha)}\{\varsigma^{\alpha}\Pi^{\alpha} - (\vartheta^{\alpha}+\sigma^{\alpha})V(t)\}\\
&\quad + \frac{2\alpha}{K(\alpha)(2-\alpha)}\int_0^t\{\varsigma^{\alpha}\Pi^{\alpha} - (\vartheta^{\alpha}+\sigma^{\alpha})V(t)\}dy.
\end{aligned} \tag{9}$$

Let ℓ_1, ℓ_2, ℓ_3, ℓ_4, and ℓ_5 be the kernels, and they are defined by

$$\begin{aligned}
\ell_1(S(t),t) &= \{(1-\zeta^\alpha)\Pi^\alpha - \beta^\alpha S(t)A(t) - \rho^\alpha\beta^\alpha S(t)C(t) - (\vartheta^\alpha + \eta^\alpha)S(t) + \sigma^\alpha V(t)\},\\
\ell_2(A(t),t) &= \{p\{\beta^\alpha S(t)A(t) + \rho^\alpha\beta^\alpha S(t)C(t)\} - (\vartheta^\alpha + \gamma^\alpha)A(t)\},\\
\ell_3(C(t),t) &= \{(1-p)\{\beta^\alpha S(t)A(t) + \rho^\alpha\beta^\alpha S(t)C(t)\} + q\gamma^\alpha A(t) - (\vartheta^\alpha + \varepsilon^\alpha + \tau^\alpha)C(t)\},\\
\ell_4(R(t),t) &= \{(1-q)\gamma^\alpha A(t) + \eta^\alpha S(t) + \tau^\alpha C(t) - \vartheta^\alpha R(t)\},\\
\ell_5(V(t),t) &= \{\zeta^\alpha\Pi^\alpha - (\vartheta^\alpha + \sigma^\alpha)V(t)\}.
\end{aligned} \tag{10}$$

Theorem 1. *The above kernels ℓ_1, ℓ_2, ℓ_3, ℓ_4, and ℓ_5 satisfy axioms of Lipschitz conditions.*

Proof. Let us assume that S and S_1, A and A_1, C and C_1, R and R_1, and V and V_1 are, respectively, the two functions for the kernels ℓ_1, ℓ_2, ℓ_3, ℓ_4, and ℓ_5, so we establish the following system:

$$\begin{aligned}
\ell_1(S(t),t) - \ell_1(S_1(t),t) &= \{(1-\zeta^\alpha)\Pi^\alpha - \beta^\alpha(S-S_1)A(t) - \rho^\alpha\beta^\alpha(S-S_1)C(t) - (\vartheta^\alpha + \eta^\alpha)(S-S_1) + \sigma^\alpha V(t)\},\\
\ell_2(A(t),t) - \ell_2(A_1(t),t) &= \{p\{\beta^\alpha S(t)(A-A_1) + \rho^\alpha\beta^\alpha S(t)C(t)\} - (\vartheta^\alpha + \gamma^\alpha)(A-A_1)\},\\
\ell_3(C(t),t) - \ell_3(C_1(t),t) &= \{(1-p)\{\beta^\alpha S(t)A(t) + \rho^\alpha\beta^\alpha S(t)(C-C_1)\} + q\gamma^\alpha A(t) - (\vartheta^\alpha + \varepsilon^\alpha + \tau^\alpha)C(t)\},\\
\ell_4(R(t),t) - \ell_4(R_1(t),t) &= \{(1-q)\gamma^\alpha A(t) + \eta^\alpha S(t) + \tau^\alpha C(t) - \vartheta^\alpha(R-R_1)\},\\
\ell_5(V(t),t) - \ell_5(V_1(t),t) &= \{\zeta^\alpha\Pi^\alpha - (\vartheta^\alpha + \sigma^\alpha)(V-V_1)\}.
\end{aligned} \tag{11}$$

Cauchy's inequality application leads to the following system:

$$\begin{aligned}
\left\|\ell_1(S(t),t) - \ell_1(S_1(t),t)\right\| &= \left\|(1-\zeta^\alpha)\Pi^\alpha - \beta^\alpha(S-S_1)A(t) - \rho^\alpha\beta^\alpha(S-S_1)C(t) - (\vartheta^\alpha + \eta^\alpha)(S-S_1) + \sigma^\alpha V(t)\right\|,\\
\left\|\ell_2(A(t),t) - \ell_2(A_1(t),t)\right\| &= \left\|p\{\beta^\alpha S(t)(A-A_1) + \rho^\alpha\beta^\alpha S(t)C(t)\} - (\vartheta^\alpha + \gamma^\alpha)(A-A_1)\right\|,\\
\left\|\ell_3(C(t),t) - \ell_3(C_1(t),t)\right\| &= \left\|(1-p)\{\beta^\alpha S(t)A(t) + \rho^\alpha\beta^\alpha S(t)(C-C_1)\} + q\gamma^\alpha A(t) - (\vartheta^\alpha + \varepsilon^\alpha + \tau^\alpha)C(t)\right\|,\\
\left\|\ell_4(R(t),t) - \ell_4(R_1(t),t)\right\| &= \left\|(1-q)\gamma^\alpha A(t) + \eta^\alpha S(t) + \tau^\alpha C(t) - \vartheta^\alpha(R-R_1)\right\|,\\
\left\|\ell_5(V(t),t) - \ell_5(V_1(t),t)\right\| &= \left\|\zeta^\alpha\Pi^\alpha - (\vartheta^\alpha + \sigma^\alpha)(V-V_1)\right\|.
\end{aligned} \tag{12}$$

Recursively, we obtain

$$\begin{aligned}
S(t) &= \frac{2(1-\alpha)\ell_1(S_{n-1}(t),t)}{(2-\alpha)K(\alpha)} + \frac{2\alpha}{(2-\alpha)K(\alpha)}\int_0^t \ell_1(S_{n-1}(y),y)\mathrm{d}y,\\
A(t) &= \frac{2(1-\alpha)\ell_2(A_{n-1}(t),t)}{(2-\alpha)K(\alpha)} + \frac{2\alpha}{(2-\alpha)K(\alpha)}\int_0^t \ell_2(A_{n-1}(y),y)\mathrm{d}y,\\
C(t) &= \frac{2(1-\alpha)\ell_3(C_{n-1}(t),t)}{(2-\alpha)K(\alpha)} + \frac{2\alpha}{(2-\alpha)K(\alpha)}\int_0^t \ell_3(C_{n-1}(y),y)\mathrm{d}y,\\
R(t) &= \frac{2(1-\alpha)\ell_4(R_{n-1}(t),t)}{(2-\alpha)K(\alpha)} + \frac{2\alpha}{(2-\alpha)K(\alpha)}\int_0^t \ell_4(R_{n-1}(y),y)\mathrm{d}y,\\
V(t) &= \frac{2(1-\alpha)\ell_5(V_{n-1}(t),t)}{(2-\alpha)K(\alpha)} + \frac{2\alpha}{(2-\alpha)K(\alpha)}\int_0^t \ell_5(V_{n-1}(y),y)\mathrm{d}y.
\end{aligned} \tag{13}$$

The norm application with majorizing and the difference between successive terms imply

$$\begin{aligned}
\|U_n(t)\| = \|S_n(t) - S_{1,(n-1)}(t)\| &\le \frac{2(1-\alpha)}{K(\alpha)(2-\alpha)} \left\| \ell_1(S_{n-1}(t), t) - \ell_1\left(S_{1,(n-2)}(t), t\right) \right\| \\
&+ \frac{2(1-\alpha)}{K(\alpha)(2-\alpha)} \left\| \int_0^t \left[\ell_1(S_{n-1}(y), y) - \ell_1\left(S_{1,n-2}(y), y\right) \right] \mathrm{d}y \right\|, \\
\|W_n(t)\| = \|A_n(t) - A_{1,(n-1)}(t)\| &\le \frac{2(1-\alpha)}{K(\alpha)(2-\alpha)} \left\| \ell_2(A_{n-1}(t), t) - \ell_2\left(A_{1,(n-2)}(t), t\right) \right\| \\
&+ \frac{2(1-\alpha)}{K(\alpha)(2-\alpha)} \left\| \int_0^t \left[\ell_2(A_{n-1}(y), y) - \ell_2\left(A_{1,n-2}(y), y\right) \right] \mathrm{d}y \right\|, \\
\|X_n(t)\| = \|C_n(t) - C_{1,(n-1)}(t)\| &\le \frac{2(1-\alpha)}{K(\alpha)(2-\alpha)} \left\| \ell_3(C_{n-1}(t), t) - \ell_3\left(C_{1,(n-2)}(t), t\right) \right\| \\
&+ \frac{2(1-\alpha)}{K(\alpha)(2-\alpha)} \left\| \int_0^t \left[\ell_3(C_{n-1}(y), y) - \ell_3\left(C_{1,n-2}(y), y\right) \right] \mathrm{d}y \right\|, \\
\|Y_n(t)\| = \|R_n(t) - R_{1,(n-1)}(t)\| &\le \frac{2(1-\alpha)}{K(\alpha)(2-\alpha)} \left\| \ell_4(R_{n-1}(t), t) - \ell_4\left(R_{1,(n-2)}(t), t\right) \right\| \\
&+ \frac{2(1-\alpha)}{K(\alpha)(2-\alpha)} \left\| \int_0^t \left[\ell_4(R_{n-1}(y), y) - \ell_4\left(R_{1,n-2}(y), y\right) \right] \mathrm{d}y \right\|, \\
\|Z_n(t)\| = \|V_n(t) - S_{1,(n-1)}(t)\| &\le \frac{2(1-\alpha)}{K(\alpha)(2-\alpha)} \left\| \ell_5(V_{n-1}(t), t) - \ell_5\left(S_{1,(n-2)}(t), t\right) \right\| \\
&+ \frac{2(1-\alpha)}{K(\alpha)(2-\alpha)} \left\| \int_0^t \left[\ell_4(V_{n-1}(y), y) - \ell_5\left(V_{1,n-2}(y), y\right) \right] \mathrm{d}y \right\|,
\end{aligned} \tag{14}$$

where

$$\begin{aligned}
\sum_{i=0}^{\infty} U_i(t) &= S_n(t), \\
\sum_{i=0}^{\infty} W_i(t) &= A_n(t), \\
\sum_{i=0}^{\infty} X_i(t) &= B_n(t), \\
\sum_{i=0}^{\infty} Y_i(t) &= R_n(t), \\
\sum_{i=0}^{\infty} Z_i(t) &= V_n(t).
\end{aligned} \tag{15}$$

Since the kernels $\ell_1, \ldots, \ell_5$ satisfy the Lipschitz conditions,

$$\begin{aligned}
\left\|U_n(t)\right\| &= \left\|S_n(t) - S_{1,n-1}(t)\right\| \le \frac{2(1-\alpha)}{K(\alpha)(2-\alpha)}\tau_1\left\|S_{n-1}(t) - S_{1,n-2}(t)\right\| \\
&+ \frac{2\alpha}{(2-\alpha)K(\alpha)}\tau_2\int_0^t \left\|S_{n-1}(y) - S_{1,n-2}(y)\right\|\mathrm{d}y, \\
\left\|W_n(t)\right\| &= \left\|A_n(t) - A_{1,n-1}(t)\right\| \le \frac{2(1-\alpha)}{K(\alpha)(2-\alpha)}\tau_3\left\|A_{n-1}(t) - A_{1,n-2}(t)\right\| \\
&+ \frac{2\alpha}{(2-\alpha)K(\alpha)}\tau_4\int_0^t \left\|A_{n-1}(y) - A_{1,n-2}(y)\right\|\mathrm{d}y, \\
\left\|X_n(t)\right\| &= \left\|C_n(t) - C_{1,n-1}(t)\right\| \le \frac{2(1-\alpha)}{K(\alpha)(2-\alpha)}\tau_5\left\|C_{n-1}(t) - C_{1,n-2}(t)\right\| \\
&+ \frac{2\alpha}{(2-\alpha)K(\alpha)}\tau_6\int_0^t \left\|C_{n-1}(y) - C_{1,n-2}(y)\right\|\mathrm{d}y, \left\|Y_n(t)\right\| \\
\left\|Z_n(t)\right\| &= \left\|V_n(t) - V_{1,n-1}(t)\right\| \le \frac{2(1-\alpha)}{K(\alpha)(2-\alpha)}\tau_9\left\|V_{n-1}(t) - V_{1,n-2}(t)\right\| \\
&+ \frac{2\alpha}{(2-\alpha)K(\alpha)}\tau_{10}\int_0^t \left\|V_{n-1}(y) - V_{1,n-2}(y)\right\|\mathrm{d}y.
\end{aligned} \tag{16}$$

Theorem 2. *The solution of fractional-order epidemiological model (7) exists.*

Proof. The use of equation (15) with the recursive scheme implies

$$\begin{aligned}
\left\|U_n(t)\right\| &\le \|S(0)\| + \left\{\left(\frac{2\tau_1(1-\alpha)}{K(\alpha)(2-\alpha)}\right)^n\right\} + \left\{\left(\frac{2\tau_2\alpha t}{K(\alpha)(2-\alpha)}\right)^n\right\}, \\
\left\|W_n(t)\right\| &\le \|A(0)\| + \left\{\left(\frac{2\tau_3(1-\alpha)}{K(\alpha)(2-\alpha)}\right)^n\right\} + \left\{\left(\frac{2\tau_4\alpha t}{K(\alpha)(2-\alpha)}\right)^n\right\}, \\
\left\|X_n(t)\right\| &\le \|(0)\| + \left\{\left(\frac{2\tau_5(1-\alpha)}{K(\alpha)(2-\alpha)}\right)^n\right\} + \left\{\left(\frac{2\tau_6\alpha t}{K(\alpha)(2-\alpha)}\right)^n\right\}, \\
\left\|Y_n(t)\right\| &\le \|R(0)\| + \left\{\left(\frac{2\tau_7(1-\alpha)}{K(\alpha)(2-\alpha)}\right)^n\right\} + \left\{\left(\frac{2\tau_8\alpha t}{K(\alpha)(2-\alpha)}\right)^n\right\}, \\
\left\|Z_n(t)\right\| &\le \|V(0)\| + \left\{\left(\frac{2\tau_9(1-\alpha)}{K(\alpha)(2-\alpha)}\right)^n\right\} + \left\{\left(\frac{2\tau_{10}\alpha t}{K(\alpha)(2-\alpha)}\right)^n\right\}.
\end{aligned} \tag{17}$$

We investigate that equation (17) is the solution of model (7); therefore, we make the following substitutions:

$$\begin{aligned}
S(t) &= S_n(t) - Y_{1,n}(t), \\
A(t) &= A_n(t) - Y_{2,n}(t), \\
B(t) &= B_n(t) - Y_{3,n}(t), \\
R(t) &= R_n(t) - Y_{4,n}(t), \\
V(t) &= V_n(t) - Y_{5,n}(t),
\end{aligned} \tag{18}$$

where $Y_{1,n}(t), Y_{2,n}(t), Y_{3,n}(t), Y_{4,n}(t)$, and $Y_{5,n}(t)$ denote the remainder terms of the series. So,

$$\begin{aligned}
S(t) - S_{n-1}(t) &= \frac{2(1-\alpha)\ell_1\big(S(t) - \Pi_{1,n}(t)\big)}{K(\alpha)(2-\alpha)} + \frac{2\alpha}{K(\alpha)(2-\alpha)}\int_0^t \ell_1\big(S(y) - Y_{1,n}(y)\big)\mathrm{d}y,\\
A(t) - A_{n-1}(t) &= \frac{2\ell_2\big(A(t) - Y_{2,n}(t)\big)(1-\alpha)}{K(\alpha)(2-\alpha)} + \frac{2\alpha}{K(\alpha)(2-\alpha)}\int_0^t \ell_2\big(A(y) - Y_{1,n}(y)\big)\mathrm{d}y,\\
C(t) - C_{n-1}(t) &= \frac{2\ell_3\big(C(t) - Y_{2,n}(t)\big)(1-\alpha)}{K(\alpha)(2-\alpha)} + \frac{2\alpha}{K(\alpha)(2-\alpha)}\int_0^t \ell_2\big(C(y) - Y_{1,n}(y)\big)\mathrm{d}y,\\
R(t) - R_{n-1}(t) &= \frac{2\ell_4\big(R(t) - Y_{2,n}(t)\big)(1-\alpha)}{K(\alpha)(2-\alpha)} + \frac{2\alpha}{K(\alpha)(2-\alpha)}\int_0^t \ell_4\big(R(y) - Y_{1,n}(y)\big)\mathrm{d}y,\\
V(t) - V_{n-1}(t) &= \frac{2\ell_5\big(V(t) - Y_{2,n}(t)\big)(1-\alpha)}{K(\alpha)(2-\alpha)} + \frac{2\alpha}{K(\alpha)(2-\alpha)}\int_0^t \ell_5\big(V(y) - Y_{1,n}(y)\big)\mathrm{d}y.
\end{aligned} \tag{19}$$

Applying norm on both sides and the Lipschitz axiom,

$$\begin{aligned}
&\left\|S(t) - \frac{2(1-\alpha)\ell_1(S(t),t)}{(2-\alpha)K(\alpha)} - S(0) - \frac{2\alpha}{(2-\alpha)K(\alpha)}\int_0^t \ell_1(S(y),y)\mathrm{d}y\right\|\\
&\quad\le \left\|\Upsilon_{1,n}(t)\right\|\left\{1 + \left(\frac{2(1-\alpha)\tau_1}{(2-\alpha)K(\alpha)} + \frac{2\alpha\tau_2 t}{(2-\alpha)K(\alpha)}\right)\right\},\\
&\left\|A(t) - \frac{2(1-\alpha)\ell_2(A(t),t)}{(2-\alpha)K(\alpha)} - A(0) - \frac{2\alpha}{(2-\alpha)K(\alpha)}\int_0^t \ell_2(A(y),y)\mathrm{d}y\right\|\\
&\quad\le \left\|\Upsilon_{2,n}(t)\right\|\left\{1 + \left(\frac{2(1-\alpha)\tau_3}{(2-\alpha)K(\alpha)} + \frac{2\alpha\tau_4 t}{(2-\alpha)K(\alpha)}\right)\right\},\\
&\left\|C(t) - \frac{2(1-\alpha)\ell_3(S(t),t)}{(2-\alpha)K(\alpha)} - C(0) - \frac{2\alpha}{(2-\alpha)K(\alpha)}\int_0^t \ell_3(C(y),y)\mathrm{d}y\right\|\\
&\quad\le \left\|\Upsilon_{3,n}(t)\right\|\left\{1 + \left(\frac{2(1-\alpha)\tau_5}{(2-\alpha)K(\alpha)} + \frac{2\alpha\tau_6 t}{(2-\alpha)K(\alpha)}\right)\right\},\\
&\left\|R(t) - \frac{2(1-\alpha)\ell_4(R(t),t)}{(2-\alpha)K(\alpha)} - R(0) - \frac{2\alpha}{(2-\alpha)K(\alpha)}\int_0^t \ell_4(R(y),y)\mathrm{d}y\right\|\\
&\quad\le \left\|\Upsilon_{4,n}(t)\right\|\left\{1 + \left(\frac{2(1-\alpha)\tau_7}{(2-\alpha)K(\alpha)} + \frac{2\alpha\tau_8 t}{(2-\alpha)K(\alpha)}\right)\right\},\\
&\left\|V(t) - \frac{2(1-\alpha)\ell_5(S(t),t)}{(2-\alpha)K(\alpha)} - V(0) - \frac{2\alpha}{(2-\alpha)K(\alpha)}\int_0^t \ell_5(V(y),y)\mathrm{d}y\right\|\\
&\quad\le \left\|\Upsilon_{5,n}(t)\right\|\left\{1 + \left(\frac{2(1-\alpha)\tau_9}{(2-\alpha)K(\alpha)} + \frac{2\alpha\tau_{10} t}{(2-\alpha)K(\alpha)}\right)\right\}.
\end{aligned} \tag{20}$$

Taking lim as t approaches ∞, we get

$$
\begin{aligned}
S(t) &= \frac{2(1-\alpha)\ell_1(S(t),t)}{K(\alpha)(2-\alpha)} + \frac{2\alpha}{K(\alpha)(2-\alpha)}\int_0^t \ell_1(S(y),y)\mathrm{d}y + S(0),\\
A(t) &= \frac{2(1-\alpha)\ell_2(A(t),t)}{(2-\alpha)K(\alpha)} + \frac{2\alpha}{(2-\alpha)K(\alpha)}\int_0^t \ell_2(A(y),y)\mathrm{d}y + A(0),\\
C(t) &= \frac{2(1-\alpha)\ell_3(C(t),t)}{(2-\alpha)K(\alpha)} + \frac{2\alpha}{(2-\alpha)K(\alpha)}\int_0^t \ell_3(C(y),y)\mathrm{d}y + C(0),\\
R(t) &= \frac{2(1-\alpha)\ell_4(R(t),t)}{(2-\alpha)K(\alpha)} + \frac{2\alpha}{(2-\alpha)K(\alpha)}\int_0^t \ell_4(R(y),y)\mathrm{d}y + R(0),\\
V(t) &= \frac{2(1-\alpha)\ell_5(V(t),t)}{(2-\alpha)K(\alpha)} + \frac{2\alpha}{(2-\alpha)K(\alpha)}\int_0^t \ell_5(R(y),y)\mathrm{d}y + V(0),
\end{aligned}
\tag{21}
$$

which proves the conclusion that the solution of the proposed epidemiological model as reported by equation (7) exists. □

Theorem 3. *The proposed epidemiological model described by equation (7) possesess a unique solution.*

Proof. On the contradiction basis, we assume that $(S^+(t), A^+(t), B^+(t), R^+(t), V^+(t))$ is another solution of model (7); then,

$$
\begin{aligned}
S(t) - S^+(t) &= \frac{2(1-\alpha)\{\ell_1(S(t),t) - \ell_1(S^+(t),t)\}}{K(\alpha)(2-\alpha)}\\
&\quad + \frac{2\alpha}{K(\alpha)(2-\alpha)}\int_0^t \{\ell_1(S(y),y) - \ell_1(S^+(y),y)\}\mathrm{d}y,\\
A(t) - A^+(t) &= \frac{2(1-\alpha)\{\ell_2(S(t),t) - \ell_2(S^+(t),t)\}}{K(\alpha)(2-\alpha)}\\
&\quad + \frac{2\alpha}{K(\alpha)(2-\alpha)}\int_0^t \{\ell_2(A(y),y) - \ell_2(A^+(y),y)\}\mathrm{d}y,\\
C(t) - C^+(t) &= \frac{2(1-\alpha)\{\ell_3(S(t),t) - \ell_3(C^+(t),t)\}}{K(\alpha)(2-\alpha)}\\
&\quad + \frac{2\alpha}{K(\alpha)(2-\alpha)}\int_0^t \{\ell_3(C(y),y) - \ell_3(C^+(y),y)\}\mathrm{d}y,\\
R(t) - R^+(t) &= \frac{2(1-\alpha)\{\ell_4(R(t),t) - \ell_1(R^+(t),t)\}}{K(\alpha)(2-\alpha)}\\
&\quad + \frac{2\alpha}{K(\alpha)(2-\alpha)}\int_0^t \{\ell_4(R(y),y) - \ell_4(R^+(y),y)\}\mathrm{d}y,\\
V(t) - V^+(t) &= \frac{2(1-\alpha)\{\ell_5(V(t),t) - \ell_5(V^+(t),t)\}}{K(\alpha)(2-\alpha)}\\
&\quad + \frac{2\alpha}{K(\alpha)(2-\alpha)}\int_0^t \{\ell_5(V(y),y) - \ell_5(V^+(y),y)\}\mathrm{d}y.
\end{aligned}
\tag{22}
$$

Majorizing the above equations, we obtain

$$\begin{aligned}
\left\|S(t)-S^{+}(t)\right\| &= \frac{2(1-\alpha)\left\|\ell_1(S(t),t)-\ell_1(S^{+}(t),t)\right\|}{K(\alpha)(2-\alpha)} \\
&\quad + \frac{2\alpha}{K(\alpha)(2-\alpha)}\int_0^t \left\|\ell_1(S(y),y)-\ell_1(S^{+}(y),y)\right\|\mathrm{d}y, \\
\left\|A(t)-A^{+}(t)\right\| &= \frac{2(1-\alpha)\left\|\ell_2(A(t),t)-\ell_2(A^{+}(t),t)\right\|}{K(\alpha)(2-\alpha)} \\
&\quad + \frac{2\alpha}{K(\alpha)(2-\alpha)}\int_0^t \left\|\ell_2(A(y),y)-\ell_2(A^{+}(y),y)\right\|\mathrm{d}y, \\
\left\|C(t)-C^{+}(t)\right\| &= \frac{2(1-\alpha)\left\|\ell_3(C(t),t)-\ell_3(C^{+}(t),t)\right\|}{K(\alpha)(2-\alpha)} \\
&\quad + \frac{2\alpha}{K(\alpha)(2-\alpha)}\int_0^t \left\|\ell_3(C(y),y)-\ell_3(C^{+}(y),y)\right\|\mathrm{d}y, \\
\left\|R(t)-R^{+}(t)\right\| &= \frac{2(1-\alpha)\left\|\ell_4(R(t),t)-\ell_4(R^{+}(t),t)\right\|}{K(\alpha)(2-\alpha)} \\
&\quad + \frac{2\alpha}{K(\alpha)(2-\alpha)}\int_0^t \left\|\ell_4(R(y),y)-\ell_4(R^{+}(y),y)\right\|\mathrm{d}y, \\
\left\|V(t)-V^{+}(t)\right\| &= \frac{2(1-\alpha)\left\|\ell_5(V(t),t)-\ell_5(V^{+}(t),t)\right\|}{K(\alpha)(2-\alpha)} \\
&\quad + \frac{2\alpha}{K(\alpha)(2-\alpha)}\int_0^t \left\|\ell_5(V(y),y)-\ell_5(V^{+}(y),y)\right\|\mathrm{d}y.
\end{aligned} \tag{23}$$

Using Theorems 1 and 2, one may obtain

$$\begin{aligned}
\left\|S(t)-S^{+}(t)\right\| &\le \frac{2\tau_1\psi_1(1-\alpha)}{K(\alpha)(2-\alpha)} + \left(\frac{2\tau_2\alpha\phi_2 t}{K(\alpha)(2-\alpha)}\right)^n, \\
\left\|A(t)-A^{+}(t)\right\| &\le \frac{2\tau_3(1-\alpha)\psi_3}{K(\alpha)(2-\alpha)} + \left(\frac{2\tau_4\alpha\phi_4 t}{K(\alpha)(2-\alpha)}\right)^n, \\
\left\|C(t)-C^{+}(t)\right\| &\le \frac{2(1-\alpha)\tau_5\psi_5}{K(\alpha)(2-\alpha)} + \left(\frac{2\alpha\tau_6\phi_6 t}{K(\alpha)(2-\alpha)}\right)^n, \\
\left\|R(t)-R^{+}(t)\right\| &\le \frac{2\tau_7\psi_7(1-\alpha)}{K(\alpha)(2-\alpha)} + \left(\frac{2\alpha\tau_8\phi_8 t}{K(\alpha)(2-\alpha)}\right)^n, \\
\left\|V(t)-V^{+}(t)\right\| &\le \frac{2\tau_9\psi_9(1-\alpha)}{K(\alpha)(2-\alpha)} + \left(\frac{2\alpha\tau_{10}\phi_{10} t}{K(\alpha)(2-\alpha)}\right)^n.
\end{aligned} \tag{24}$$

The inequalities as reported by equation (24) hold for every value of n; thus, we obtain

$$\begin{aligned} S(t) &= S^{+}(t), \\ A(t) &= A^{+}(t), \\ B(t) &= B^{+}(t), \\ R(t) &= R^{+}(t), \\ V(t) &= V^{+}(t). \end{aligned} \tag{25}$$

We now discuss the positivity as well as the boundedness of model (7) to show the well-posedness of the problem. Furthermore, we define a certain region for the dynamics of the proposed problem which is positively invariant. For this, the following lemmas have been explored. □

Lemma 1. *Since $(S(t), A(t), C(t), R(t), V(t))$ are the solutions of model (7), let us consider that the model possesses nonnegative initial conditions; then, the solutions $(S(t), A(t), C(t), R(t), V(t))$ are nonnegative for all $t \geq 0$.*

Proof. We assume a general fractional-order (ω) model of system (7) as

$$\begin{cases} {}^{G}D^{\omega}_{0,t}(S(t)) &= (1-\zeta^{\alpha})\Pi^{\alpha} - \beta^{\alpha}S(t)A(t) - \rho^{\alpha}\beta^{\alpha}S(t)C(t) - (\vartheta^{\alpha}+\eta^{\alpha})S(t) + \sigma^{\alpha}V(t), \\ {}^{G}D^{\omega}_{0,t}(A(t)) &= p\{\beta^{\alpha}S(t)A(t) + \rho^{\alpha}\beta^{\alpha}S(t)C(t)\} - (\vartheta^{\alpha}+\gamma^{\alpha})A(t), \\ {}^{G}D^{\omega}_{0,t}(C(t)) &= (1-p)\{\beta^{\alpha}S(t)A(t) + \rho^{\alpha}\beta^{\alpha}S(t)C(t)\} + q\gamma^{\alpha}A(t) - (\vartheta^{\alpha}+\varepsilon^{\alpha}+\tau^{\alpha})C(t), \\ {}^{G}D^{\omega}_{0,t}(R(t)) &= (1-q)\gamma^{\alpha}A(t) + \eta^{\alpha}S(t) + \tau^{\alpha}C(t) - \vartheta^{\alpha}R(t), \\ {}^{G}D^{\omega}_{0,t}(V(t)) &= \zeta^{\alpha}\Pi^{\alpha} - (\vartheta^{\alpha}+\sigma^{\alpha})V(t), \end{cases} \tag{26}$$

where G represents the fractional-order operator under consideration and ω is the order. So, equation (26) becomes

$$\begin{aligned} &{}^{G}D^{\omega}_{0,t}(S(t))|_{\kappa(S)} = (1-\zeta^{\omega})\Pi^{\omega} > 0, \; {}^{G}D^{\omega}_{0,t}(A(t))|_{\kappa(A)} = p\{\beta^{\omega}S(t)A(t) + \rho^{\omega}\beta^{\omega}S(t)C(t)\} \geq 0, \\ &{}^{G}D^{\omega}_{0,t}(C(t))|_{\kappa(C)} = (1-p)\{\beta^{\omega}S(t)A(t) + \rho^{\omega}\beta^{\omega}S(t)C(t)\} + q\gamma^{\omega}A(t) \geq 0, \\ &{}^{G}D^{\omega}_{0,t}(R(t))|_{\kappa(R)} = (1-q)\gamma^{\omega}A(t) + \eta^{\omega}S(t) + \tau^{\omega}C(t) > 0, \; {}^{G}D^{\omega}_{0,t}(V(t))|_{\kappa(V)} = \zeta^{\alpha}\Pi^{\alpha} > 0, \end{aligned} \tag{27}$$

where $\kappa(\xi) = \{\xi = 0 \text{ and } S, A, C, R, V \text{ contained in } C(R_{+} \times R_{+})\}$ and $\xi \in \{S, A, C, R, V\}$. By following [31], we conclude that the solutions $(S(t), A(t), C(t), R(t), V(t))$ are positive for all nonnegative t. □

Lemma 2. *Let Ω be the region for dynamics of model (7) within it which is positively invariant; then,*

$$\Omega = \left\{ (S(t), A(t), C(t), R(t), V(t)) \in R^{4}_{+} : S + A + C + R + V \leq \left(\frac{\Pi}{\vartheta}\right)^{\omega} \right\}. \tag{28}$$

Proof. Since N represents the total population, therefore, it implies that

$${}^{G}D^{\omega}_{0,t}(T(t)) + \vartheta^{\omega}T(t) \leq \Pi^{\omega}. \tag{29}$$

The solution of equation (29) gives

$$T(t) \leq T(0)E_{\omega}(-\vartheta^{\omega}t^{\omega}) + \left(\frac{\Pi}{\vartheta}\right)^{\omega}(1 - E_{\omega}(-\vartheta^{\omega}t^{\omega})), \tag{30}$$

where $E(.)$ is the Mittag-Leffler function such that $E_{\omega}(Z) = \sum_{n=0}^{\infty} Z^{n}/\Gamma(\omega i + 1)$. Note that, in equation (30), whenever time increases with no bound, $T(t) \longrightarrow (\Pi/\vartheta)^{\omega}$. Hence, if $T(0) \leq (\Pi/\vartheta)^{\omega}$, then $T(t) \leq (\Pi/\vartheta)^{\omega}$ for all $t > 0$, while if $T(0) > (\Pi/\vartheta)^{\omega}$, then T goes into the feasible region Ω and will never leave. So, it could be concluded that the dynamics of the fractional-order epidemiological model can be studied in the feasible region Ω. □

5. Steady-State Analysis

The proposed epidemiological model (7) of the hepatitis B virus is examined for the equilibria: disease-free and endemic states. Let D_1 be the disease-free equilibrium of the proposed model; then, for analyzing this point, the population under consideration is assumed to be infection free. Thus, the system reported by equation (7) has a disease-free equilibrium $D_1 = (S^0, A^0, C^0, R^0, V^0)$, where $S^0 = q_4^{\alpha}(1-\zeta^{\alpha}) + \sigma^{\alpha}\zeta^{\alpha}/q_1^{\alpha}q_4^{\alpha}$, $A^0 = C^0 = 0$, $R^0 = \eta^{\alpha}\Pi^{\alpha}q_4^{\alpha}(1-\zeta^{\alpha}) + \sigma^{\alpha}\zeta^{\alpha}/\vartheta^{\alpha}q_1^{\alpha}q_4^{\alpha}$, and $V^0 = \zeta^{\alpha}\Pi^{\alpha}/q_4^{\alpha}$, and $q_1 = \vartheta^{\alpha} + \eta^{\alpha}$, $q_2 = \vartheta^{\alpha} + \gamma^{\alpha}$, $q_3 = \vartheta^{\alpha} + \varepsilon^{\alpha} + \tau^{\alpha}$, and $q_4 = \vartheta^{\alpha} + \sigma^{\alpha}$. Now, to calculate the basic reproductive number, we assume $X = (A, C)^{T}$; then, system (7) yields

$$\left.\frac{dX}{dt}\right|_{D_1} = F - V, \tag{31}$$

where

$$F = \begin{bmatrix} p\beta^{\alpha}S^{0} & p\rho^{\alpha}\beta^{\alpha}S^{0} \\ (1-p)\beta^{\alpha}S^{0} & (1-p)\rho^{\alpha}\beta^{\alpha}S^{0} \end{bmatrix},$$
$$V = \begin{bmatrix} q_2 & 0 \\ -q\gamma^{\alpha} & q_3 \end{bmatrix}. \tag{32}$$

Therefore, the basic reproductive number is the spectral radius of $\rho(FV^{-1})$, i.e., $R_0 = R_1 + R_2 + R_3$, where

$$R_1 = \frac{p\beta^{\alpha}S^{0}}{q_2},$$
$$R_2 = \frac{\rho^{\alpha}\beta^{\alpha}S^{0}(1-p)}{q_3}, \tag{33}$$
$$R_3 = \frac{p\gamma^{\alpha}\rho^{\alpha}\beta^{\alpha}qS^{0}}{q_2q_3}.$$

Let D_2 be the endemic equilibrium, and assume that $S = S^*$, $A = A^*$, $C = C^*$, $R = R^*$, and $V = V^*$ at the steady state of the proposed model; then, the solution of the resultant algebraic equations will lead to the endemic equilibrium. Thus, regarding the local as well as global analysis of the proposed model, we have the following stability results.

Theorem 4. *If $R_0 < 1$, then the disease-free equilibrium D_1 of the proposed model (7) is locally asymptotically stable, while if $R_0 > 1$, then the endemic equilibrium D_2 is locally asymptotically stable.*

Proof. The linearizable version of the proposed hepatitis B model (7) around D_1 leads to a matrix given by

$$J|_{D_1} = \begin{pmatrix} -q_1 & -\beta^{\alpha}S^{0} & -\rho^{\alpha}\beta^{\alpha}S^{0} & 0 & \sigma^{\alpha} \\ 0 & p\beta^{\alpha}S^{0} - q_2 & p\rho^{\alpha}\beta^{\alpha}S^{0} & 0 & 0 \\ 0 & (1-p)\beta^{\alpha}S^{0} + q\gamma & (1-p)\rho^{\alpha}\beta^{\alpha}S^{0} - q_3 & 0 & 0 \\ \eta^{\alpha} & (1-q)\gamma^{\alpha} & \tau^{\alpha} & -\vartheta^{\alpha} & 0 \\ 0 & 0 & 0 & 0 & -q_4 \end{pmatrix}. \tag{34}$$

The characteristic equation of the matrix $J|_{D_1}$ takes the following form:

$$\omega^5 + a_1\omega^4 + a_2\omega^3 + a_3\omega^2 + a_4\omega + a_5, \tag{35}$$

where

$$\begin{aligned}
a_1 &= q_1 + q_4 + \vartheta^{\alpha} + q_2(1-R_1) + q_3(1-R_2),\\
a_2 &= q_1q_4 + (q_1+q_4)\{\vartheta^{\alpha} + q_2(1-R_1) + q_3(1-R_2)\}\\
&\quad + q_2q_3(1-R_0) + q_3\vartheta^{\alpha}(1-R_2) + q_2\vartheta^{\alpha}(1-R_1),\\
a_3 &= (q_1+q_4)\{q_2\vartheta^{\alpha}(1-R_1) + q_3\vartheta^{\alpha}(1-R_2) + q_2q_3(1-R_0)\}\\
&\quad + q_1q_4\{\vartheta^{\alpha} + q_2(1-R_1) + q_3(1-R_2)\} + q_2q_3\vartheta^{\alpha}(1-R_0),\\
a_4 &= q_1q_4\{q_2q_3(1-R_0) + q_2\vartheta^{\alpha}(1-R_1) + q_3\vartheta^{\alpha}(1-R_2)\} + (q_1+q_4)q_2q_3\vartheta^{\alpha}(1-R_0),\\
a_5 &= q_1q_4q_2q_3\vartheta^{\alpha}(1-R_0).
\end{aligned} \tag{36}$$

It could be noted that the real parts of the eigenvalues of the above matrix $J|_{D_1}$ are negative whenever Routh–Hurwitz criteria, i.e., H: $\{a_i > 0, \text{for } i = 1,2,3,4,5, a_1a_2a_3 - a_3^2 - a_1^2a_4 > 0 \text{ and } (a_1a_4 - a_5)(a_1a_2a_3 - a_3^2 - a_1^2a_4) - a_5(a_1a_2 - a_3)^2 - a_1a_5^2 > 0\}$, hold. So,

$$\begin{aligned}
a_1a_2a_3 - a_3^2 - a_1^2a_4 &= \{q_1 + q_4 + \vartheta^{\alpha} + q_2(1-R_1) + q_3(1-R_2)\}\{q_1q_4 + (q_1+q_4)\{\vartheta^{\alpha} + q_2(1-R_1)\\
&\quad + q_3(1-R_2)\} + q_2q_3(1-R_0) + q_3\vartheta^{\alpha}(1-R_2) + q_2\vartheta^{\alpha}(1-R_1)\}\{(q_1+q_4)\{q_2\vartheta^{\alpha}(1-R_1)\\
&\quad + q_3\vartheta^{\alpha}(1-R_2) + q_2q_3(1-R_0)\} + q_1q_4(\vartheta^{\alpha} + q_2(1-R_1) + q_3(1-R_2))\\
&\quad + q_2q_3\vartheta^{\alpha}(1-R_0)\} - \{(q_1+q_4)\{q_2\vartheta^{\alpha}(1-R_1) + q_3\vartheta^{\alpha}(1-R_2) + q_2q_3(1-R_0)\}\\
&\quad + q_1q_4\{\vartheta^{\alpha} + q_2(1-R_1) + q_3(1-R_2)\} + q_2q_3\vartheta^{\alpha}(1-R_0)\}^2 - (q_1 + q_4 + \vartheta^{\alpha}\\
&\quad + q_2(1-R_1) + q_3(1-R_2))^2\{q_1q_4(q_2(1-R_1) + q_3(1-R_2) + q_2q_3(1-R_0)) + (q_1+q_4)q_2q_3\vartheta^{\alpha}(1-R_0)\},
\end{aligned} \tag{37}$$

and

$$
\begin{aligned}
&(a_1a_4-a_5)\left(a_1a_2a_3-a_3^2-a_1^2a_4\right)-a_5\left(a_1a_2-a_3\right)^2-a_1a_5^2\\
&=\left\{\begin{array}{c}(q_1+q_4+\vartheta^\alpha+q_2(1-R_1)+q_3(1-R_2))\\ (q_1q_4(q_2\vartheta^\alpha(1-R_1)+q_3\vartheta^\alpha(1-R_2)+q_2q_3(1-R_0))+(q_1+q_4)q_2q_3(1-R_0)+(q_1+q_4)q_2q_3\vartheta^\alpha(1-R_0))\\ -q_1q_4q_2q_3\vartheta^\alpha(1-R_0)\end{array}\right\}\\
&\left\{\begin{array}{c}(q_1+q_4+\vartheta^\alpha+q_2(1-R_1)+q_3(1-R_2))\{q_1q_4+(q_1+q_4)\{\vartheta^\alpha+q_2(1-R_1)+q_3(1-R_2)\}+q_2q_3(1-R_0)+q_3\vartheta^\alpha(1-R_2)+q_2\vartheta^\alpha(1-R_1)\}\\ \{(q_1+q_4)\{q_2\vartheta^\alpha(1-R_1)+q_3\vartheta^\alpha(1-R_2)+q_2q_3(1-R_0)\}+q_1q_4\{\vartheta^\alpha+q_2(1-R_1)+q_3(1-R_2)\}+q_2q_3\vartheta^\alpha(1-R_0)\}\\ -\{(q_1+q_4)\{q_2\vartheta^\alpha(1-R_1)+q_3\vartheta^\alpha(1-R_2)+q_2q_3(1-R_0)\}+q_1q_4(\vartheta^\alpha+q_2(1-R_1)+q_3(1-R_2))+q_2q_3\vartheta(1-R_0)\}^2\\ -\{q_1+q_4+\vartheta+q_2(1-R_1)+q_3(1-R_2)\}^2(q_1q_4(q_2\vartheta^\alpha(1-R_1)+q_3\vartheta^\alpha(1-R_2)+q_2q_3(1-R_0))+(q_1+q_4)q_2q_3\vartheta^\alpha(1-R_0))\end{array}\right\}\\
&-q_1q_2q_3q_4\vartheta^\alpha(1-R_0)\left\{\begin{array}{c}(q_1+q_4+\vartheta^\alpha+q_2(1-R_1)+q_3(1-R_2))\\ \{q_1q_4+(q_1+q_4)\{\vartheta^\alpha+q_2(1-R_1)+q_3(1-R_2)\}+q_2q_3(1-R_0)+q_3\vartheta^\alpha(1-R_2)+q_2\vartheta^\alpha(1-R_1)\}\\ -(q_1+q_4)\{q_2\vartheta^\alpha(1-R_1)+q_3\vartheta^\alpha(1-R_2)+q_2q_3(1-R_0)\}-q_1q_4(\vartheta^\alpha+q_2\vartheta^\alpha(1-R_1)+q_3\vartheta^\alpha(1-R_2))\\ -q_2q_3\vartheta^\alpha(1-R_0)\end{array}\right\}^2\\
&-(q_1+q_4+\vartheta^\alpha+q_2(1-R_1)+q_3(1-R_2))q_1^2q_4^2q_2^2q_3^2\vartheta^{2\alpha}(1-R_0)^2.
\end{aligned}
\tag{38}
$$

Clearly, we observe that all the coefficients a_i for $i = 1, 2, 3, 4, 5$ are positive whenever $R_0 < 1$, and if $a_1a_2a_3 - a_3^2 - a_1^2a_4$ and $(a_1a_4 - a_5)(a_1a_2a_3 - a_3^2 - a_1^2a_4) - a_5(a_1a_2 - a_3)^2 - a_1a_5^2$ are positive, then it implies that the Routh–Hurwitz criteria hold, and so, the disease-free state D_1 is stable. In a similar fashion, it can proved that the disease endemic state D_2 of the proposed model (7) is stable. □

Theorem 5. *If $R_0 \le 1$, then the disease-free equilibrium D_1 of the proposed model (7) is globally asymptotically stable, while if $R_0 > 1$, then the endemic equilibrium D_2 is globally asymptotically stable.*

Proof. Let $\chi(t) = (S(t), A(t), C(t), R(t), V(t))$, and we claim that it has a finite limit whenever t approaches to ∞; then, the last equation of model (7) looks like

$$
{}^{CF}D_{0,t}^{\alpha}V(t) = \zeta^\alpha\Pi^\alpha - q_4V(t). \tag{39}
$$

Since for $t \ge 0$ and for any φ, $\varphi \le \varphi e^t$, by following the mean value theorem and the result as stated by Theorem 3.1 in [32], equation (39) implies that

$$
\|V(t)\| \le aC\ \exp^{\left[-\{q_4\}^{1/\alpha}+1\right]t}, \tag{40}
$$

where $a = \|V_0\|e^{-T} + KT^\alpha e^{-T}/\alpha\Gamma(\alpha) + \zeta^\alpha\Pi^\alpha$, $t \ge T$, and C is a positive constant, and consequently, we obtain

$$
\lim_{t\longrightarrow\infty} V(t) \le C(\zeta\Pi)^\alpha. \tag{41}
$$

Similarly, the first equation of the proposed fractional-order model (7) can be rewritten as

$$
{}^{CF}D_{0,t}^{\alpha}S(t) \le (1-\zeta^\alpha)\Pi^\alpha - q_1\ S(t) + \sigma^\alpha V(t). \tag{42}
$$

Let $b = \|S_0\|e^{-T} + KT^\alpha e^{-T}/\alpha\Gamma(\alpha) + (1-\zeta^\alpha)\Pi^\alpha + \sigma^{\alpha V(t)}$; then,

$$
\|S(t)\| \le bC\ \exp^{\left[-\{q_1\}^{1/\alpha}+1\right]t}, \tag{43}
$$

which implies that

$$
\lim_{t\longrightarrow\infty} S(t) \le C\left((1-\zeta^\alpha)\Pi^\alpha\right) + \lim_{t\longrightarrow\infty}\sigma^\alpha\ V(t), \tag{44}
$$

or equivalently, equation (44) may take the form after using equation (41) in equation (44) such that

$$
\lim_{t\longrightarrow\infty} S(t) \le C\Pi^\alpha. \tag{45}
$$

In a similar fashion, lim of $A(t)$, $C(t)$, and $R(t)$ can be shown. Moreover, we assume that

$$
\lim_{t\longrightarrow\infty}\chi(t) = \left(S_\infty, A_\infty, C_\infty, R_\infty, V_\infty\right), \tag{46}
$$

and

$$\phi(\chi) = \begin{pmatrix} \phi_1(\chi) \\ \phi_2(\chi) \\ \phi_3(\chi) \\ \phi_4(\chi) \\ \phi_5(\chi) \end{pmatrix} = \begin{pmatrix} (1-\zeta^\alpha)\Pi^\alpha - \beta^\alpha S(t)A(t) - \rho^\alpha\beta^\alpha S(t)C(t) - q_1 S(t) + \sigma^\alpha V(t) \\ p\{\beta^\alpha S(t)A(t) + \rho^\alpha\beta^\alpha S(t)C(t)\} - q_2 A(t) \\ (1-p)\{\beta^\alpha S(t)A(t) + \rho^\alpha\beta^\alpha S(t)C(t)\} + q\gamma^\alpha A(t) - q_3 C(t) \\ (1-q)\gamma^\alpha A(t) + \eta^\alpha S(t) + \tau^\alpha C(t) - \vartheta^\alpha R(t) \\ \zeta^\alpha\Pi^\alpha - q_4 V(t) \end{pmatrix}. \tag{47}$$

Thus, in light of the mean value theorem, there exist positive constants C_1 and C_2 such that

$$\|\phi(\chi)\| \leq C_1 + C_2\|\chi\|. \tag{48}$$

So, Theorems 2.1 and 3.1 in [33] imply that ${}^{CF}D^{\alpha}_{0,t}(S(t), A(t), C(t), R(t), V(t))$ is uniformly continuous. Thus, Barbalat's lemma (for details, see [34]) implies that

$$\lim_{t\longrightarrow\infty}{}^{CF}D^{\alpha}_{0,t}(\chi(t)) = (0,0,0,0,0). \tag{49}$$

Consequently,

$$\begin{cases} (1-\zeta^\alpha)\Pi^\alpha - \beta^\alpha S(t)A(t) - \rho^\alpha\beta^\alpha S(t)C(t) - q_1 S(t) + \sigma^\alpha V(t) = 0, \\ p\{\beta^\alpha S(t)A(t) + \rho^\alpha\beta^\alpha S(t)C(t)\} - q_2 A(t) = 0, \\ (1-p)\{\beta^\alpha S(t)A(t) + \rho^\alpha\beta^\alpha S(t)C(t)\} + q\gamma^\alpha A(t) - q_3 C(t) = 0, \\ (1-q)\gamma^\alpha A(t) + \eta^\alpha S(t) + \tau^\alpha C(t) - \vartheta^\alpha R(t) = 0, \\ \zeta^\alpha\Pi^\alpha - q_4 V(t) = 0. \end{cases} \tag{50}$$

Therefore, $(S_\infty, A_\infty, C_\infty, R_\infty, V_\infty)$ is an equilibrium point of the proposed fractional-order epidemiological model (7), and by a similar argument as stated by Theorem 3.1 in [35], we conclude that

$$\begin{aligned} \lim_{t\longrightarrow\infty}(\chi(t)) &= D_1, \\ \lim_{t\longrightarrow\infty}(\chi(t)) &= D_2. \end{aligned} \tag{51}$$

Hence, the disease endemic state D_2 does not exist whenever $R_0 < 1$, and so, $\lim\chi(t) = D_1$ as t approaches ∞, and if $R_0 = 1$, then $D_2 = D_1$ and $\lim\chi(t) = D_1$ as t approaches ∞, while on the contrary, if $R_0 > 1$, then D_2 exists, and thus, $\lim\chi(t) = D_2$ as t tends to ∞. □

6. Numerical Simulation

In this section, the numerical simulations are carried out to understand the temporal dynamical behavior corresponding with hepatitis B virus fractional-order epidemiological model (7). This is very important to show the feasibility of the reported work and investigate the validity of the analytical work using large-scale numerical simulation. It is important to point out that, unlike traditional numerical analysis, there are not as many options to choose schemes for the numerical analysis of the fractional-order epidemiological model simulations [36]. Thus, there is a need of extensive research in order to develop new schemes and techniques that are both convergent and robust in the field of

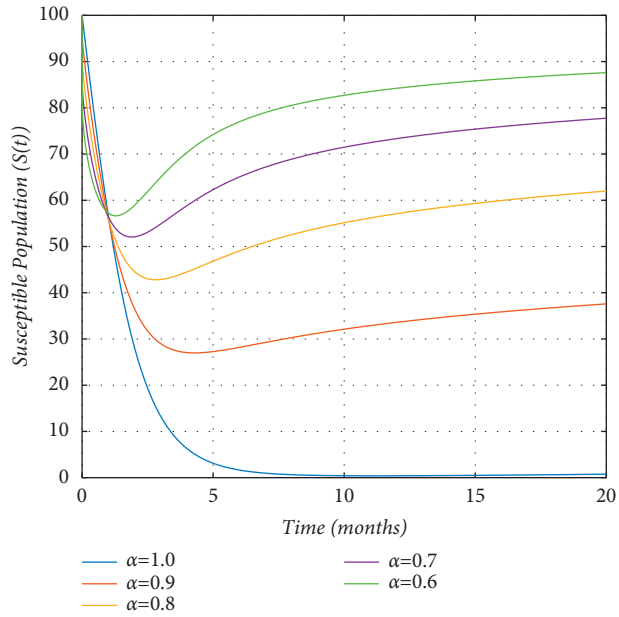

FIGURE 1: The graph shows the dynamics of the susceptible population $(S(t))$ for different values of the fractional-order parameter (α), and the initial population sizes are $(100, 90, 80, 70, 60)$.

fractional calculus. By following the numerical schemes as reported in [37, 38], we assume $[0, t]$ interval of simulation and $h = 10^{-3}$ is the time step for integration, and $n = T/h$, $n \in \mathbb{N}$, and $u = 0, 1, 2, \ldots, n$. So, the scheme may take the following structure:

$$
\begin{aligned}
{}^{CF}S_{u+1} &= S(0) + (1-\alpha)\{(1-\zeta^{\alpha})\Pi^{\alpha} - \beta^{\alpha}S(t)A(t) - \rho^{\alpha}\beta^{\alpha}S(t)C(t) - (\vartheta^{\alpha} + \eta^{\alpha})S(t) + \sigma^{\alpha}V(t)\} \\
&\quad + \alpha h \sum_{k=0}^{u} \{(1-\zeta^{\alpha})\Pi^{\alpha} - \beta^{\alpha}S(t)A(t) - \rho^{\alpha}\beta^{\alpha}S(t)C(t) - (\vartheta^{\alpha} + \eta^{\alpha})S(t) + \sigma^{\alpha}V(t)\}, \\
{}^{CF}A_{u+1} &= A(0) + (1-\alpha)\{p\{\beta^{\alpha}S(t)A(t) + \rho^{\alpha}\beta^{\alpha}S(t)C(t)\} - (\vartheta^{\alpha} + \gamma^{\alpha})A(t)\} \\
&\quad + \alpha h \sum_{k=0}^{u} \{p\{\beta^{\alpha}S(t)A(t) + \rho^{\alpha}\beta^{\alpha}S(t)C(t)\} - (\vartheta^{\alpha} + \gamma^{\alpha})A(t)\}, \\
{}^{CF}C_{u+1} &= C(0) + (1-\alpha)\{(1-p)\{\beta^{\alpha}S(t)A(t) + \rho^{\alpha}\beta^{\alpha}S(t)C(t)\} + q\gamma^{\alpha}A(t) - (\vartheta^{\alpha} + \varepsilon^{\alpha} + \tau^{\alpha})C(t)\} \\
&\quad + \alpha h \sum_{k=0}^{u} \{(1-p)\{\beta^{\alpha}S(t)A(t) + \rho^{\alpha}\beta^{\alpha}S(t)C(t)\} + q\gamma^{\alpha}A(t) - (\vartheta^{\alpha} + \varepsilon^{\alpha} + \tau^{\alpha})C(t)\}, \\
{}^{CF}R_{u+1} &= (1-\alpha)\{(1-q)\gamma^{\alpha}A(t) + \eta^{\alpha}S(t) + \tau^{\alpha}C(t) - \vartheta^{\alpha}R(t)\} \\
&\quad + \alpha h \sum_{k=0}^{u} \{(1-q)\gamma^{\alpha}A(t) + \eta^{\alpha}S(t) + \tau^{\alpha}C(t) - \vartheta^{\alpha}R(t)\} + R(0), \\
{}^{CF}V_{u+1} &= (1-\alpha)\{\zeta^{\alpha}\Pi^{\alpha} - (\vartheta^{\alpha} + \sigma^{\alpha})V(t)\} + V(0) \\
&\quad + \alpha h \sum_{k=0}^{u} \{\zeta^{\alpha}\Pi^{\alpha} - (\vartheta^{\alpha} + \sigma^{\alpha})V(t)\}.
\end{aligned}
\tag{52}
$$

Furthermore, the parameters' value is assumed with biological feasibility; that is, $\zeta = 0.4$, $\Pi = 0.0975$, $\vartheta = 0.00000456$, $\varepsilon = 0.3454$, $\beta = 0.022$, $\rho = 0.048$, $p = 0.5$, $q = 0.5$, $\gamma = 0.45$, $\eta = 0.8613$, $\tau = 0.1428$, and $\sigma = 0.06$, and

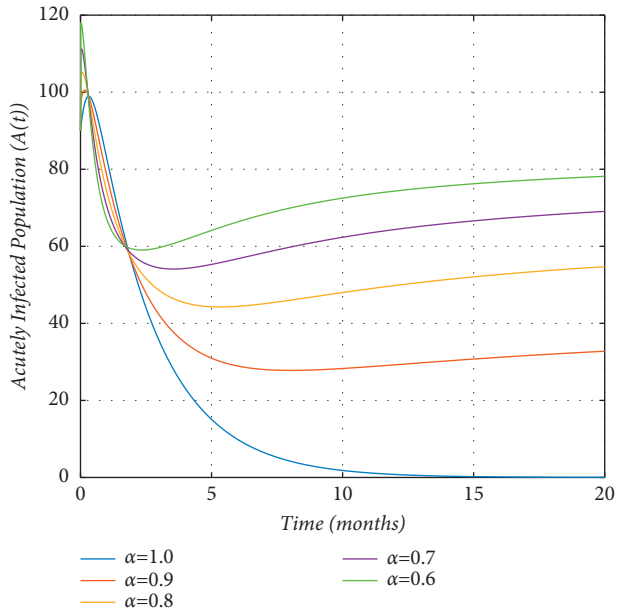

Figure 2: The graph visualizes the dynamics of the acutely infected population ($A(t)$) for different values of the fractional-order parameter (α), and the initial population sizes are $(100, 90, 80, 70, 60)$.

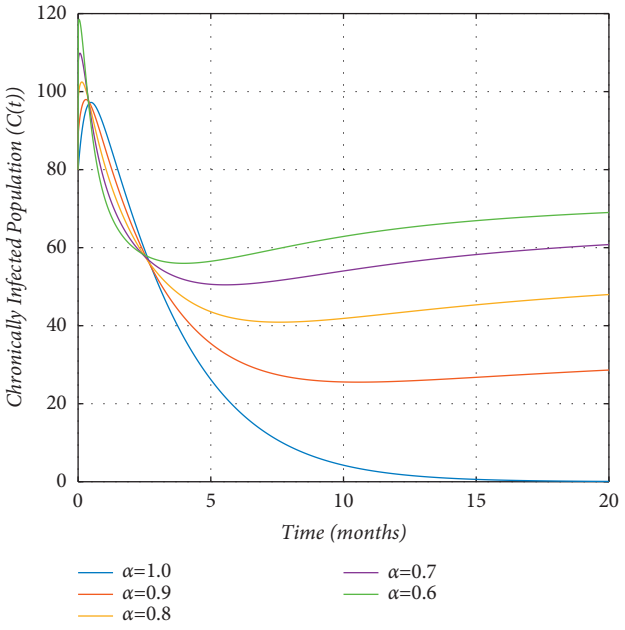

Figure 3: The graph demonstrates the dynamics of the chronically infected population against different values of the fractional-order parameter (α), and the initial sizes of the population are $(100, 90, 80, 70, 60)$.

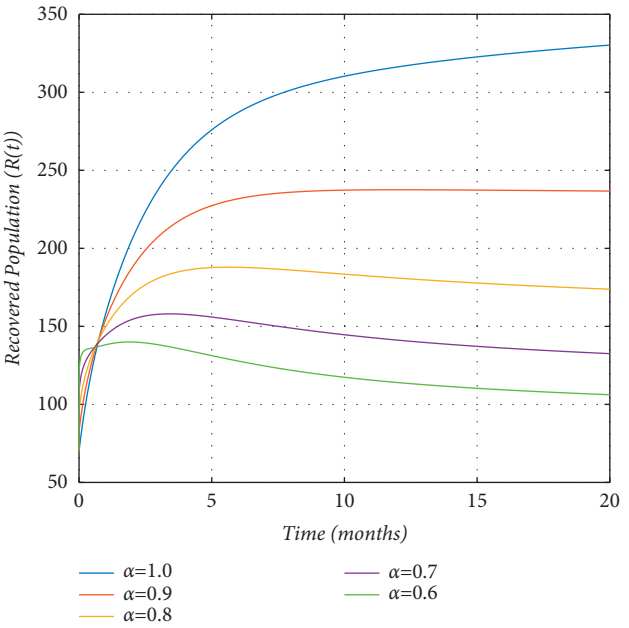

Figure 4: The graph demonstrates the dynamics of the recovered population against different values of the fractional-order parameter (α), and the initial sizes of the population are $(100, 90, 80, 70, 60)$.

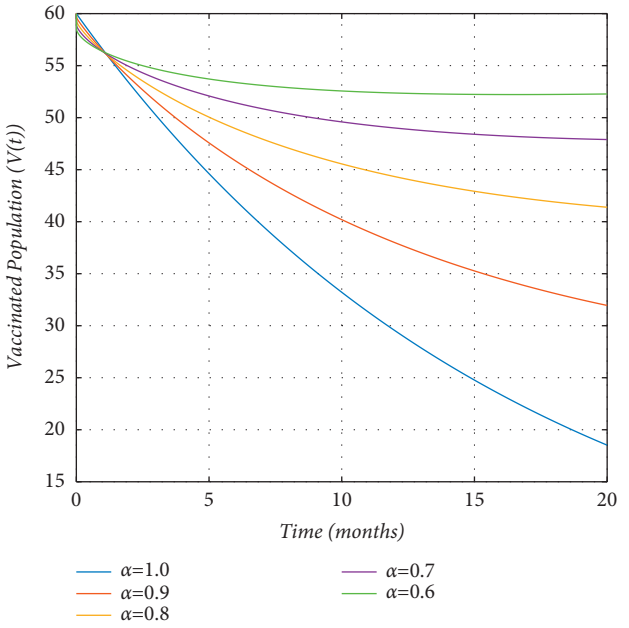

Figure 5: The graph demonstrates the dynamics of the vaccinated population against different values of the fractional-order parameter (α), and the initial sizes of the population are $(100, 90, 80, 70, 60)$.

the initial sizes of compartmental populations are $(100, 90, 80, 70, 60)$.

By the execution of the above scheme with the stated parameters' value as above along the initial sizes of populations, we obtain the results as depicted in Figures 1–5. These graphs visualize the dynamical behaviors of the susceptible, the acutely and chronically infected, the recovered, and the vaccinated groups of populations. More precisely, the dynamics of the susceptible individuals for different values of the fractional-order parameter (α) is shown in Figure 1, which demonstrates that if the value of α increases, then the ratio of the susceptible individuals

decreases. This shows that the fractional-order parameter and the susceptible population are inversely proportional to each other. Similarly, the acutely and chronically infected population are also inversely proportional to the fractional-order parameter (α) as shown in Figures 2 and 3, respectively, while the dynamics of recovered individuals reveals that there is a direct relation between the fractional-order parameter (α) and the recovered population, i.e., whenever the value of α increases, the size of the recovered population also increases as depicted in Figure 4. The dynamics of the vaccinated group of population is described in Figure 5, which demonstrates that the fractional-order parameter (α) has a negative impact on the dynamics of the vaccinated population, i.e., whenever the value of α increases, the size of the population group $V(t)$ decreases. This analysis reveals that the CF fractional-order model presents more valuable outputs regarding the behavior of compartmental populations which usually could not be obtained in case of the classical model.

7. Conclusion

The work carried out in this study consists of a new epidemiological model related to dynamics of hepatitis B virus transmission. We used the CF operator and investigated the dynamics of hepatitis B virus. We formulated the proposed model first and then fractionalized by using the Caputo–Fabrizio operator with dimensional balance in respect of involved epidemic parameters. We used the fixed point theory and rigorously showed that the model under the CF operator possesses a unique solution. We also discussed biological as well as mathematical feasibility of the proposed model by proving that the solutions of the model are bounded and positive. Moreover, the basic reproductive number is calculated, and the stability analysis of the steady states of the proposed fractional-order epidemiological model is shown. At the end, we presented some numerical simulations to show the relation between compartmental populations and the fractional-order operator. Thus, the major findings of this study show that the CF fractional-order operator is the best choice instead of the classical order.

Data Availability

No data were used to support this study.

Conflicts of Interest

The authors declare that they have no conflicts of interest.

Acknowledgments

This research work was funded by the Deanship of Scientific Research, King Khalid University (Project no. RGP.2/204/42), Abha, K. S. A. The author, Basem Al Alwan, therefore, acknowledges with thanks to the DSR and the Chemical Engineering Department in the College of Engineering (KKU) for the financial and technical support. The authors would also like to acknowledge and express their gratitude to the United Arab Emirates University, Al Ain, UAE, for providing financial support (Grant no. 12S086).

References

[1] J. Mann and M. Roberts, "Modelling the epidemiology of hepatitis B in New Zealand," *Journal of Theoretical Biology*, vol. 269, no. 1, pp. 266–272, 2011.

[2] D. Lavanchy, "Hepatitis B virus epidemiology, disease burden, treatment, and current and emerging prevention and control measures," *Journal of Viral Hepatitis*, vol. 11, no. 2, pp. 97–107, 2004.

[3] A. S. Lok, E. J. Heathcote, and J. H. Hoofnagle, "Management of hepatitis B: 2000-Summary of a workshop," *Gastroenterology*, vol. 120, no. 7, pp. 1828–1853, 2001.

[4] B. J. McMahon, "Epidemiology and natural history of hepatitis B," *Seminars in Liver Disease*, vol. 25, no. 1, pp. 3–8, 2005.

[5] M.-H. Chang, "Hepatitis B virus infection," *Seminars in Fetal and Neonatal Medicine*, vol. 12, no. 3, pp. 160–167, 2007.

[6] S. Thornley, C. Bullen, and M. Roberts, "Hepatitis B in a high prevalence New Zealand population: a mathematical model applied to infection control policy," *Journal of Theoretical Biology*, vol. 254, no. 3, pp. 599–603, 2008.

[7] M. K. Libbus and L. M. Phillips, "Public health management of perinatal hepatitis B virus," *Public Health Nursing*, vol. 26, no. 4, pp. 353–361, 2009.

[8] R. Williams, "Global challenges in liver disease," *Hepatology*, vol. 44, no. 3, pp. 521–526, 2006.

[9] J. E. Maynard, M. A. Kane, and S. C. Hadler, "Global control of hepatitis B through vaccination: role of hepatitis B vaccine in the expanded programme on immunization," *Clinical Infectious Diseases*, vol. 11, no. 3, pp. S574–S578, 1989.

[10] C. W. Shepard, E. Simard, L. Finelli, A. Fiore, and B. Bell, "Hepatitis B virus infection: epidemiology and vaccination," *Epidemiologic Reviews*, vol. 28, no. 1, pp. 112–125, 2006.

[11] K. Wang, A. Fan, and A. Torres, "Global properties of an improved hepatitis B virus model," *Nonlinear Analysis: Real World Applications*, vol. 11, no. 4, pp. 3131–3138, 2010.

[12] M. A. Safi and A. B. Gumel, "The effect of incidence functions on the dynamics of a quarantine/isolation model with time delay," *Nonlinear Analysis: Real World Applications*, vol. 12, no. 1, pp. 215–235, 2011.

[13] A. Rachah and D. F. M. Torres, "Mathematical modelling, simulation, and optimal control of the 2014 Ebola outbreak in West Africa," *Discrete Dynamics in Nature and Society*, vol. 2015, Article ID 842792, 9 pages, 2015.

[14] H. S. Rodrigues, M. T. T. Monteiro, and D. F. M. Torres, "Vaccination models and optimal control strategies to dengue," *Mathematical Biosciences*, vol. 247, pp. 1–12, 2014.

[15] P. Rodrigues, C. J. Silva, and D. F. M. Torres, "Cost-effectiveness analysis of optimal control measures for tuberculosis," *Bulletin of Mathematical Biology*, vol. 76, no. 10, pp. 2627–2645, 2014.

[16] R. Anderson and R. May, *Infectious Diseases Of Humans: Dynamics And Control*, Oxford University Press, Oxford, UK, 1992.

[17] J. R. Williams, D. J. Nokes, G. F. Medley, and R. M. Anderson, "The transmission dynamics of hepatitis B in the UK: a mathematical model for evaluating costs and effectiveness of immunization programmes," *Epidemiology and Infection*, vol. 116, no. 1, pp. 71–89, 1996.

[18] G. F. Medley, N. A. Lindop, W. J. Edmunds, and D. J. Nokes, "Hepatitis-B virus endemicity: heterogeneity, catastrophic

dynamics and control," *Nature Medicine*, vol. 7, no. 5, pp. 619–624, 2001.
[19] S. Zhao, Z. Xu, and Y. Lu, "A mathematical model of hepatitis B virus transmission and its application for vaccination strategy in China," *International Journal of Epidemiology*, vol. 29, no. 4, pp. 744–752, 2000.
[20] E. A. Bakare, A. Nwagwo, and E. Danso-Addo, "Optimal control analysis of an sir epidemic model with constant recruitment," *International Journal of Applied Mathematical Research*, vol. 3, no. 3, p. 273, 2014.
[21] A. V. Kamyad, R. Akbari, A. A. Heydari, and A. Heydari, "Mathematical modeling of transmission dynamics and optimal control of vaccination and treatment for hepatitis b virus," *Computational and Mathematical Methods in Medicine*, vol. 2014, Article ID 475451, 15 pages, 2014.
[22] N. O. Onyango, "Multiple endemic solutions in an epidemic hepatitis B model without vertical transmission," *Applied Mathematics*, vol. 2014, Article ID 516242, 2014.
[23] T. Zhang, K. Wang, and X. Zhang, "Modeling and analyzing the transmission dynamics of hbv epidemic in xinjiang, China," *PloS one*, vol. 10, no. 9, Article ID e0138765, 2015.
[24] T. Khan and G. Zaman, "Classification of different hepatitis B infected individuals with saturated incidence rate," *SpringerPlus*, vol. 5, no. 1, p. 1082, 2016.
[25] T. Khan, G. Zaman, and M. I. Chohan, "The transmission dynamic and optimal control of acute and chronic hepatitis B," *Journal of Biological Dynamics*, vol. 11, no. 1, pp. 172–189, 2017.
[26] S. Nana-Kyere, J. Ackora-Prah, E. Okyere, S. Marmah, and T. Afram, "Hepatitis b optimal control model with vertical transmission," *Applications of Mathematics*, vol. 7, no. 1, pp. 5–13, 2017.
[27] A. Atangana, "Modelling the spread of covid-19 with new fractal-fractional operators: can the lockdown save mankind before vaccination?" *Chaos, Solitons & Fractals*, vol. 136, Article ID 109860, 2020.
[28] A. Atangana and S. İğret Araz, "Nonlinear equations with global differential and integral operators: existence, uniqueness with application to epidemiology," *Results in Physics*, vol. 20, Article ID 103593, 2021.
[29] S. G. Samko, *Fractional Integrals and Derivatives, Theory and Applications*, Minsk; Nauka I Tekhnika, New York, NY, USA, 1987.
[30] D. Baleanu, Z. B. Güvenç, and J. T. Machado, *New Trends in Nanotechnology and Fractional Calculus Applications*, Springer, Manhattan, NY, USA, 2010.
[31] X. Yang, L. Chen, and J. Chen, "Permanence and positive periodic solution for the single-species nonautonomous delay diffusive models," *Computers & Mathematics with Applications*, vol. 32, no. 4, pp. 109–116, 1996.
[32] L. Kexue and P. Jigen, "Laplace transform and fractional differential equations," *Applied Mathematics Letters*, vol. 24, no. 12, pp. 2019–2023, 2011.
[33] W. Lin, "Global existence theory and chaos control of fractional differential equations," *Journal of Mathematical Analysis and Applications*, vol. 332, no. 1, pp. 709–726, 2007.
[34] F. Wang and Y. Yang, "Correction: fractional order BARBALAT'S lemma and its applications in the stability of fractional order nonlinear systems," *Mathematical Modelling and Analysis*, vol. 22, no. 4, pp. 503–513, 2017.
[35] K. Hattaf, N. Yousfi, and A. Tridane, "Mathematical analysis of a virus dynamics model with general incidence rate and cure rate," *Nonlinear Analysis: Real World Applications*, vol. 13, no. 4, pp. 1866–1872, 2012.
[36] H. Ramos, Z. Kalogiratou, T. Monovasilis, and T. E. Simos, "An optimized two-step hybrid block method for solving general second order initial-value problems," *Numerical Algorithms*, vol. 72, no. 4, pp. 1089–1102, 2016.
[37] D. Baleanu, A. Jajarmi, and M. Hajipour, "On the nonlinear dynamical systems within the generalized fractional derivatives with Mittag-Leffler kernel," *Nonlinear Dynamics*, vol. 94, no. 1, pp. 397–414, 2018.
[38] C. Li and F. Zeng, *Numerical Methods for Fractional Calculus*, Chapman and Hall/CRC, Boca Raton, FL, USA, 2019.

Hindawi
Complexity
Volume 2021, Article ID 4558400, 16 pages
https://doi.org/10.1155/2021/4558400

Research Article

Synchronization of Chaotic Systems: A Generic Nonlinear Integrated Observer-Based Approach

Muhammad Majid Hussain,[1] **Muhammad Siddique**,[2] **Ziyad M. Almohaimeed**,[3] **Romaisa Shamshad**,[2] **Rizwan Akram**,[3] **and Naeem Aslam**[2]

[1]*Department of Electrical and Electronic Engineering, University of South Wales, Pontypirdd CF37 1DL, UK*
[2]*Department of Electrical Engineering & Computer Science, NFC Institute of Engineering and Technology (NFC-IET), Multan 66000, Pakistan*
[3]*Department of Electrical Engineering, College of Engineering, Qassim University, P.O.Box 6677, Qassim 51452, Saudi Arabia*

Correspondence should be addressed to Muhammad Siddique; msiddique@nfciet.edu.pk and Rizwan Akram; rizwanakram75@qec.edu.sa

Received 3 October 2021; Revised 3 November 2021; Accepted 6 November 2021; Published 2 December 2021

Academic Editor: Jawad Ahmad

The purpose of this research is to study the synchronization of two integrated nonlinear systems with time delay and disturbances. A nonlinear system is a system in which the difference in output is not relative to the difference in input. A new control methodology for synchronization of the two chaotic systems master and slave is recognized by means of the unique integrated chaotic synchronous observer and the integrated chaotic adaptive synchronous observer. The instantaneous approximation states of the master and slave systems are accomplished by means of methods for suggesting observers for every one of the master and slave systems and by the production of error signals between these approximated states. This approximated synchronization error signal and state approximation errors meet at the origin by means of methods involving a particular observer-based feedback control signal to ensure synchronization and state approximation. Using Lyapunov stability theory, adaptive and nonadaptive laws for control systems, and nonlinear properties, the intermingling conditions for state approximation errors and approximated synchronization errors are established as nonlinear matrix inequalities. A solution to the resulting inequality constraints using a two-step linear matrix inequality (LMI)-based approach is introduced, giving essential and adequate conditions to extract values from the controller gain and observer gain matrices. Simulation of the suggested synchronization procedure for Fitz-Hugh–Nagumo neuronal systems is demonstrated to expand the viability of the suggested observer-based control techniques.

1. Introduction

In nature, most real systems are nonlinear. To better understand the performance of distinctive nonlinear systems, it is significant and interesting to study the synchronization between two systems. Synchronization, perceived as a procedure that normally happens, has a notable effect in different areas of science, design, and engineering, even in public activities. Nonlinear system synchronization is an interesting field amid specialisations in various trains of thought because of its various uses relating to design and innovation. Researchers stepped into the universe of nonlinear systems in 1988, and various papers were published on the subject [1, 2]. Nonlinear systems do not obey the principle of superposition and their output is not directly proportional to their input. Pecora and Carroll were responsible for the earliest effective work on the subject, introducing an experiment for synchronization of nonlinear systems under various initial conditions. Pecora and Carroll published a seminal paper [3] in the field of nonlinear synchronization. In this study, they described that certain nonlinear chaotic systems can be made to synchronize by linking them with common signals. The criterion for this is the sign of the sub-Lyapunov exponents. We apply these ideas to a real set of synchronizing chaotic circuits. Subsequently, scientists have developed numerous nonlinear

synchronization strategies. The process of synchronization is where the determined system (slave system) comes to be in parallel with the master system (driving system), meaning that the synchronized system moves in a specific way, following the direction of a synchronizing system [4, 5]. The background of this article outlines that many different methodologies have been used, including the Runge–Kutta model-based nonlinear observer [6], linear feedback control (LFC) [7], and delay-range dependent methodologies [8, 9]. Adaptive schemes using fuzzy disturbance observers [10], robust adaptive methodology [11, 12], reduced-order and full-order output-related observers [13], synchronization with Huygens' coupling [14], adaptive generalized projective synchronization (GPS) [15], stepwise sliding mode observer techniques [16], evolutionary algorithms [17], backstepping techniques [18], and nonlinear synchronism of undefined inputs, as well as Takagi–Sugeno fuzzy [19], have all been implemented for the coordination of chaos systems. All of these defined methods of synchronization of nonlinear modules show their robustness to different technologies such as neural networks [20], biological systems [21], secure communication [22, 23], robotics [24], optics and lasers [25], information science [26], and chemical reaction [27]. Observer-based synchronization methods are progressively pertinent to the condition, where the master and slave situations are unknown [28]. Research specialists are consistently investigating such methods with various kinds of observers for different applications, for example, synchronous chaos in coupled systems [29], comprehensive projective synchronization procedures dependent on state approximation of hyperchaotic modules without computing Lyapunov proponents, and nonlinear-based protective communication, using decreased-order and stepwise sliding state observers. Nevertheless, previous statements of observer-dependent synchronization methods do not explain the integrated chaotic synchronized (ICS) observer and integrated chaotic adaptive synchronized (ICAS) observer-dependent control strategies shown in this article. The primary disadvantage of the strategies previously mentioned, as opposed to the ICS and ICAS observer-dependent control techniques, is their appropriateness for the lower degree of synchronization of the two nonlinear modules with inaccessible state vectors. An error concurrent observer-dependent synchronization method was suggested in a recent work [30]. However, the technique is only used in nonlinear modules for which the general error module is adaptable to a direct composition of several error parameters. This is widely used in applications to secure communications. The numerous forms of chaotic synchronization include synchronization of Lur'e master and slave system. The work behind this synchronization of the chaotic Lur'e system was controlled in different ways. The absolute stability theory and different circumstances have been established. The objective of this research paper is to synchronize the unbalanced master pendulum system and slave system using a robust feedback technique and the LMI-based method for the synchronization of the chaotic dynamical pendulum system and output feedback controller technique. The main contribution and the objectives of the paper are (i) development of robust adaptive feedback control for delay containing chaotic systems, (ii) the mitigation of the effect of the disturbances using novel integrated adaptive observers, and (iii) a sufficient condition for the existence of observer and controller gains for the synchronization of chaotic systems. The closed-loop error is minimized after very little time and the system becomes stable, so the disturbance input effect reduces. To validate our research results, we have considered the example of the phase-locked loop system.

2. System Description

Synchronization of nonlinear systems is a subject matter. It means that synchronization of the dynamics of those systems occur, containing nonlinearities in their dynamics. Mathematical representations of nonlinear systems, which will be synchronized, contain both types of nonlinearities mentioned. Following this discussion, it is necessary to consider the generalized model of nonlinear master and slave chaotic (nonlinear) system equations (1) and (2), defined by state space representation when disturbance and adaptation are zero. $dm = 0$; $ds = 0$.

$$\begin{aligned}\dot{x}_m(t) &= Ax_m(t) + A_d x_m(t-\tau) + f\left(x_m(t)\right) + f_d\left(x_m(t-\tau)\right) + Bg\left(x_m(t)\right)\theta_m \\ &\quad + Bg_d\left(x_m(t-\tau)\right)\theta_{m,d} + d_m,\ y_m(t) = Cx_m(t),\end{aligned} \tag{1}$$

$$\begin{aligned}\dot{x}_s(t) &= Ax_s(t) + A_d x_s(t-\tau) + f\left(x_s(t)\right) + f_d\left(x_s(t-\tau)\right) + Bg\left(x_s(t)\right)\theta_s \\ &\quad + Bg_d\left(x_s(t-\tau)\right)\theta_{s,d} + d_s + Bu(t), \\ y_s(t) &= Cx_s(t),\end{aligned} \tag{2}$$

where $xm(t) \in \mathrm{Rn}$ and $xs(t) \in \mathrm{Rn}$ are the state vectors for the master and slave systems, respectively. Similarly, $\mathrm{ym(t)} \in \mathrm{Rm}$ and $\mathrm{ys(t)} \in \mathrm{Rm}$ are the output vectors. A, $\in R^{n\times n}$, B, $\in \mathrm{R}^{n\times 1}$, and C, $\in R$, $m \times n$ are real constant matrices. The vector functions $f(\mathrm{x(t)}) \in \mathrm{Rn}$ and $g(x(t)) \in \mathrm{R}^{1\times p}$ are the nonlinear functions $(\tau - \mathrm{t})$. Nonlinear function time delay, $qm(t) \in \mathrm{Rp}$ and $qs(t) \in \mathrm{Rp}$ are the unknown parameters in the dynamics of the chaotic oscillators, and $\mathrm{u(t)} \in \mathrm{Rl}$ is the control input.

3. Integrated Adaptive Observer-Dependent Synchronization

If unknown parameters such as θ_m, θ_s, $\theta_{m,d}$, $\theta_{s,d} \in R^p$ are present in the master (M) and slave (S) nonlinear systems, then the control law will not be applicable for the synchronization of both systems. In such cases, we will use adaptation laws with a choice of control law:

$$\begin{aligned} u(t) = \psi(\hat{x}_m(t), \hat{x}_s(t))\Psi(\hat{x}_m(t), \hat{x}_s(t)) = F(\hat{x}_m(t) - \hat{x}_s(t)) + g(\hat{x}_m(t))\hat{\theta}_m(t) - g(\hat{x}_s(t))\hat{\theta}_s(t) \\ + g_d(\hat{x}_m(t-\tau))\hat{\theta}_{m,d}(t-\tau) - g_d(\hat{x}_s(t-\tau))\hat{\theta}_{s,d}(t-\tau), \end{aligned} \tag{3}$$

where $\hat{\theta}_m(t) \in R^p$, $\hat{\theta}_s(t) \in R^p$, $\hat{\theta}_{m,d}(t-\tau) \in R^p$, $\hat{\theta}_{s,d}(t-\tau) \in R^p$, and θ_m, θ_s, $\theta_{m,d}$, and $\theta_{s,d}, \in R^p$ are the unknown parameter estimates. For the estimation of both system states under unspecified parameters, coupled adaptive observers are the best to use:

$$\begin{aligned} \dot{\hat{x}}_m(t) = A\hat{x}_m(t) + A_d\hat{x}_m(t-\tau) + f(\hat{x}_m(t)) + f_d(\hat{x}_m(t-\tau)) + Bg(\hat{x}_m(t))\hat{\theta}_m(t) + Bg_d(\hat{x}_m(t-\tau))\hat{\theta}_{m,d}(t-\tau) \\ + L_m(y_m(t) - \hat{y}_m(t)) - \frac{1}{2}BF(\hat{x}_m(t) - \hat{x}_s(t)), \end{aligned} \tag{4}$$

$$\begin{aligned} \dot{\hat{x}}_s(t) = A\hat{x}_s(t) + A_d\hat{x}_s(t-\tau) + f(\hat{x}_s(t)) + f_d(\hat{x}_s(t-\tau)) + Bg(\hat{x}_s(t))\hat{\theta}_s(t) + Bg_d(\hat{x}_s(t-\tau))\hat{\theta}_{s,d}(t-\tau) \\ + L_s(y_s(t) - \hat{y}_s(t)) - \frac{1}{2}BF(\hat{x}_m(t) - \hat{x}_s(t)) + Bu(t), \end{aligned} \tag{5}$$

where $L_m \in R^{n\times m}$ and $L_s \in R^{n\times m}$ are the observer gain matrices. With the help of equation (3), we can manage the model structure of the slave (S) observer given as

$$\begin{aligned} \dot{\hat{x}}_s(t) = A\hat{x}_s(t) + A_d\hat{x}_s(t-\tau) + f(\hat{x}_s(t)) + f_d(\hat{x}_s(t-\tau)) + Bg(\hat{x}_s(t))\hat{\theta}_s(t) \\ + Bg_d(\hat{x}_s(t))\hat{\theta}_{s,d}(t-\tau) + L_s(y_s(t) - \hat{y}_s(t)) + \frac{1}{2}BF(\hat{x}_m(t) - \hat{x}_s(t)) + Bu_g(t), \\ u_g(t) = g(\hat{x}_m(t))\hat{\theta}_m(t) - g(\hat{x}_s(t))\hat{\theta}_s(t) + g_d(\hat{x}_m(t-\tau))\hat{\theta}_{m,d}(t-\tau) - g_d(\hat{x}_s(t-\tau))\hat{\theta}_{s,d}(t-\tau), \end{aligned} \tag{6}$$

where $u(t)$ is a nonlinear element. Also, in addition, we define

$$\begin{aligned} e_m(t) &= x_m(t) - \hat{x}_m(t), \\ e_s(t) &= x_s(t) - \hat{x}_s(t), \\ e_0(t) &= \hat{x}_m(t) - \hat{x}_s(t), \\ \psi(t) &= f(x(t)) - f(\hat{x}(t)), \\ \psi_d(t,\tau) &= f_d(x(t-\tau)) - f_d(\hat{x}(t-\tau)), \\ \psi_g(t) &= Bg(x_m(t))\theta_m - Bg(\hat{x}_m(t))\hat{\theta}_m(t), \\ \psi_{(g,d)}(t,\tau) &= Bg_d(x(t-\tau))\theta_d - Bg_d(\hat{x}(t-\tau))\hat{\theta}_d(t-\tau). \end{aligned} \tag{7}$$

4. Synchronization Feedback Control

The (M) and (S) chaotic frameworks can be made clear through the use of their particular observers. These observers for the (M) and (S) frameworks produce evaluations of the conditions of the particular framework. The two approximates of the (M) and (S) frameworks are authorized to make up for a similar performance. This is finished by applying the recommended control holding the approximated conditions of the drive and reaction frameworks. The suggested control coordinates related approximated conditions of the two frameworks with the end goal that approximated the synchronization error, for example, $e_s(t) = x_s(t) - \hat{x}_s(t)$ deals to zero. When it occurs, the conditions of the (M) and (S) observers remain synchronized. Subsequently, (M) and (S) observers are called synchronous observers. Presently,

taking the derivative of both sides of the master, slave, and output error equation, we acquire

$$\dot{e}_m(t) = Ae_m(t) + A_d e_m(t-\tau) + \psi_m(t) + \psi_{dm}(t) + \psi_{gm}(t) + \psi_{(g,d)m}(t) - L_m C e_m(t) + d_m + \frac{1}{2}BFe_o(t), \tag{8}$$

$$\dot{e}_s(t) = Ae_s(t) + A_d e_s(t-\tau) + \psi_s(t) + \psi_{ds}(t) + \psi_{gs}(t) + \psi_{(g,d)s}(t) - L_s C e_s(t) - \frac{1}{2}BFe_o(t) + d_s - Bu_g(t), \tag{9}$$

where $u_g(t)$ is the nonlinear part of the proposed control law, i.e.,

$$u_g(t) = g(\hat{x}_m(t))\hat{\theta}_m(t) - g(\hat{x}_s(t))\hat{\theta}_s(t) + g_d(\hat{x}_m(t-\tau))\hat{\theta}_{m,d}(t-\tau) - g_d(\hat{x}_s(t-\tau))\hat{\theta}_{s,d}(t-\tau), \tag{10}$$

$$\dot{e}_o(t) = Ae_o(t) + A_d e_o(t-\tau) + \psi_o(t) + \psi_{do}(t) + L_m C e_m(t) - L_s C e_s(t) - BFe_o(t). \tag{11}$$

The assumption considers $B^T P_m C^\perp = 0$, $B^T P_s C^\perp = 0$, and $B^T P_o C^\perp = 0$, where $C^\perp$ stands for the orthogonal projection on the null of C. If the above assumption holds, solving $B^T P_m - R_m C = 0$, $B^T P_s - R_s C = 0$, and $B^T P_o - R_o C = 0$ matrices, R_m, R_s, and R_o can be delegated. Adaptive controller design is provided using ICAS observers.

5. Theorem

The given observer and controller are then able to gain matrices $F \in R^{l\times n}$, $L_m \in R^{n\times m}$, and $L_s \in R^{n\times m}$ an appropriate state for synchronization of the (M) and (S) systems (1) and (2) with undefined dynamics $\theta_m \in R^p$, $\theta_s \in R^p$, $\theta_{m,d} \in R^p$, and $\theta_{s,d} \in R^p$ which concern with the assumption, applying the control law and ICAS observers (4)-(5), together with the law of adaptation:

$$\begin{aligned}
\dot{\hat{\theta}}_m(t) &= -\Theta_m g^T(\hat{x}_m(t))R_m(y_m(t) - C\hat{x}_m(t)), \quad \Theta_m > 0,\\
\dot{\hat{\theta}}_s(t) &= -\Theta_s g^T(\hat{x}_s(t))R_s(y_s(t) - C\hat{x}_s(t)), \quad \Theta_s > 0,\\
\dot{\hat{\theta}}_{m,d}(t-\tau) &= -\Theta_{m,d} g_d^T(\hat{x}_m(t-\tau))R_m y_m(t-\tau)) - C\hat{x}_m(t-\tau)), \quad \Theta_{m,d} > 0,\\
\dot{\hat{\theta}}_{s,d}(t-\tau) &= -\Theta_{s,d} g_d^T(\hat{x}_s(t-\tau))R_s y_s(t-\tau)) - C\hat{x}_s(t-\tau)), \quad \Theta_{s,d} > 0.
\end{aligned} \tag{12}$$

These are the adaptation rate $\dot{\hat{\theta}}_m$, $\dot{\hat{\theta}}_s$, $\dot{\hat{\theta}}_{m,d}$, and $\dot{\hat{\theta}}_{s,d}$ of proper quantities, with P_m, P_s, and P_o positive-definite matrices. The scalars are $\alpha_1 > 0$, $\alpha_2 > 0$, $\alpha_3 > 0, \alpha_4 > 0, \alpha_5 > 0, \alpha_6 > 0, \beta_1 > 0$, $\beta_{12} > 0$, $\beta_3 > 0$, and $\beta_4 > 0$ so that the inequality matrix is satisfied:

$$\begin{bmatrix}
\Phi_{11_{9\times9}} & \Phi_{12_{9\times9}} & \Phi_{13_{9\times7}}\\
\Phi_{21_{9\times9}} & \Phi_{22_{9\times9}} & \Phi_{23_{9\times7}}\\
\Phi_{31_{9\times9}} & \Phi_{32_{9\times9}} & \Phi_{33_{7\times7}}
\end{bmatrix}_{25*25}, \tag{13}$$

where

$$\begin{aligned}
\zeta_{11,m} &= A^T P_m + P_m A - C^T L_m^T P_m + R_m + R_{1m} + R_{2m} + (\tau_2 - \tau_1)Q_m + \alpha_1 L_f^2 + \alpha_2 L_{f,d}^2 + \beta_1 L_{gm}^2 + \beta_2 L_{gm,d}^2,\\
\zeta_{11,s} &= A^T P_s + P_s A - C^T L_s^T P_s + R_s + R_{1s} + R_{2s} + (\tau_2 - \tau_1)Q_s + \alpha_3 L_f^2 + \alpha_4 L_{f,d}^2 + \beta_3 L_{gs}^2 + \beta_4 L_{gs,d}^2,\\
\zeta_{11,o} &= A^T P_o + P_o A - P_o B^T F^T - P_o BF + (\tau_2 - \tau_1)Q_o + R_o + R_{1o} + R_{2o} + \alpha_5 L_f^2 + \alpha_6 L_{f,d}^2.
\end{aligned} \tag{14}$$

Proof. The balanced state for synchronization of (M) and (S) modules is adopted as follows. By considering $\widetilde{\theta}_m(t) = \theta_m - \widehat{\theta}_m(t)$ and $\widetilde{\theta}_m(t-\tau) = \theta_m - \widehat{\theta}_m(t-\tau)$ and assuming $g_m(x_m(t)) = Bg(x_m(t))\theta_m$, $g_s(x_s(t)) = Bg(x_s(t))\theta_s$, $g_{dm}(x_m(t-\tau)) = Bg(x_m(t-\tau))\theta_{dm}$, and $g_{ds}(x_s(t-\tau)) = Bg(x_s(t-\tau))\theta_{ds}$ and further utilizing some mathematical manipulation, we can derive

$$\begin{aligned}
Bg(x_m(t))\theta_m - Bg(\widehat{x}_m(t))\widehat{\theta}_m(t) &= g_m(x_m(t)) - g_m(\widehat{x}_m(t)) + Bg(\widehat{x}_m(t))\widetilde{\theta}_m(t),\\
Bg(x_m(t-\tau))\theta_m - Bg(\widehat{x}_m(t-\tau))\widehat{\theta}_m(t-\tau) &= g_{dm}(x_m(t-\tau)) - g_{dm}(\widehat{x}_m(t-\tau)) + Bg(\widehat{x}_m(t-\tau))\widetilde{\theta}_m(t-\tau),\\
Bg(\widehat{x}_s(t))\widehat{\theta}_s(t) &= g_s(x_s(t)) - g_s(\widehat{x}_s(t)) + Bg(\widehat{x}_s(t))\widetilde{\theta}_s(t),\\
Bg(x_s(t-\tau))\theta_s - Bg(\widehat{x}_s(t-\tau))\widehat{\theta}_s(t-\tau) &= g_{ds}(x_s(t-\tau)) - g_{ds}(\widehat{x}_s(t-\tau)) + Bg(\widehat{x}_s(t-\tau))\widetilde{\theta}_s(t-\tau).
\end{aligned} \tag{15}$$

By letting

$$\begin{aligned}
\widetilde{\psi}_{g,m\widehat{m}}(t) &= g_m^T(x_m(t)) - g_m^T(\widehat{x}_m(t)),\\
\widetilde{\psi}_{g,s\widehat{s}}(t) &= g_s^T(x_s(t)) - g_s^T(\widehat{x}_s(t)),\\
\widetilde{\psi}_{(g,d),m\widehat{m}}(t,\tau) &= g_{dm}(x_m(t-\tau)) - g_{dm}(\widehat{x}_m(t-\tau)),\\
\widetilde{\psi}_{(g,d),s\widehat{s}}(t,\tau) &= g_{ds}(x_s(t-\tau)) - g_{ds}(\widehat{x}_s(t-\tau)),
\end{aligned} \tag{16}$$

we obtain from equation (8)

$$\begin{aligned}
\dot{e}_m(t) = {} & Ae_m(t) + A_d e_m(t-\tau) + \psi_m(t) + \psi_{dm}(t) + \widetilde{\psi}_{g,m\widehat{m}}(t) + \widetilde{\psi}_{(g,d),m\widehat{m}}(t,\tau)\\
& + Bg(\widehat{x}_m(t))\widetilde{\theta}_m(t) + Bg(\widehat{x}_m(t-\tau))\widetilde{\theta}_m(t-\tau)\\
& - L_m C e_m(t) + d_m + \frac{1}{2}BFe_o(t).
\end{aligned} \tag{17}$$

Thus, it is certain to acquire from equation (9)

$$\begin{aligned}
\dot{e}_s(t) = {} & Ae_s(t) + A_d e_s(t-\tau) + \psi_s(t) + \psi_{ds}(t) + \widetilde{\psi}_{g,s\widehat{s}}(t)\\
& + \widetilde{\psi}_{(g,d),s\widehat{s}}(t,\tau) + Bg(\widehat{x}_s(t))\widetilde{\theta}_s(t) + Bg(\widehat{x}_s(t-\tau))\widetilde{\theta}_s(t-\tau)\\
& - L_s C e_s(t) - \frac{1}{2}BFe_o(t) + d_s - Bu_g(t),
\end{aligned} \tag{18}$$

Using equation (11), we have

$$\dot{e}_o(t) = (A - BF)e_o(t) + A_d e_o(t-\tau) + \psi_o(t) + \psi_{do}(t) + L_m C e_m(t) - L_s C e_s(t). \tag{19}$$

With the help of the Lyapunov function, the theorem is a proof that

$$\begin{aligned}
V(t,e) = {} & e_m^T(t)P_m e_m(t) + \int_{-\tau_2}^{-\tau_1}\int_{t+\beta}^{t} e_m^T(\alpha)Q_m e_m(\alpha)d\alpha d\beta + \int_{-\tau}^{0} e_m^T(t+\sigma)R_m \\
& \times e_m(t+\sigma)d\sigma + \int_{-\tau_1}^{0} e_m^T(t+\sigma)R_{1m}e_m(t+\sigma)d\sigma + \int_{-\tau_2}^{0} e_m^T(t+\sigma)R_{2m} \\
& \times e_m(t+\sigma)d\sigma + \left[\int_{-\tau_2}^{-\tau_1} e_m(t+\sigma)d\sigma\right]^T W_m \left[\int_{-\tau_2}^{-\tau_1} e_m(t+\sigma)d\sigma\right] \\
& + e_s^T(t)P_s e_s(t) + \int_{-\tau_2}^{-\tau_1}\int_{t+\beta}^{t} e_s^T(\alpha)Q_s e_s(\alpha)d\alpha d\beta + \int_{-\tau}^{0} e_s^T(t+\sigma)R_s \\
& \times e_s(t+\sigma)d\sigma + \int_{-\tau_1}^{0} e_s^T(t+\sigma)R_{1s}e_s(t+\sigma)d\sigma + \int_{-\tau_2}^{0} e_s^T(t+\sigma)R_{2s} \\
& \times e_s(t+\sigma)d\sigma + \left[\int_{-\tau_2}^{-\tau_1} e_s(t+\sigma)d\sigma\right]^T W_s \left[\int_{-\tau_2}^{-\tau_1} e_s(t+\sigma)d\sigma\right] \\
& + e_o^T(t)P_o e_o(t) + \int_{-\tau_2}^{-\tau_1}\int_{t+\beta}^{t} e_o^T(\alpha)Q_o e_o(\alpha)d\alpha d\beta + \int_{-\tau}^{0} e_o^T(t+\sigma)R_o \\
& \times e_o(t+\sigma)d\sigma + \int_{-\tau_1}^{0} e_o^T(t+\sigma)R_{1o}e_o(t+\sigma)d\sigma + \int_{-\tau_2}^{0} e_o^T(t+\sigma)R_{2o} \\
& \times e_o(t+\sigma)d\sigma + \left[\int_{-\tau_2}^{-\tau_1} e_o(t+\sigma)d\sigma\right]^T W_o \left[\int_{-\tau_2}^{-\tau_1} e_o(t+\sigma)d\sigma\right] \\
& + \tilde{\theta}_m^T(t)\Theta_m^{-1}\tilde{\theta}_m(t) + \tilde{\theta}_s^T(t)\Theta_s^{-1}\tilde{\theta}_s(t) + \\
& \tilde{\theta}_{m,d}^T(t-\tau)\Theta_{m,d}^{-1}\tilde{\theta}_{m,d}(t-\tau) + \tilde{\theta}_{s,d}^T(t-\tau)\Theta_{s,d}^{-1}\tilde{\theta}_{s,d}(t-\tau).
\end{aligned} \tag{20}$$

Taking the time derivative of the Lyapunov energy function, equation (15) can be written as

$$\begin{aligned}
\dot{V}(t,e) = {} & \dot{e}_m^T(t)P_m e(t) + e_m^T(t)P_m\dot{e}_m(t) + (\tau_2-\tau_1)e_m^T(t)Qe_m(t) - \int_{t-\tau_2}^{t-\tau_1} e_m^T(\sigma) \\
& \times Qe_m(\sigma)d\sigma + e_m^T(t)Re_m(t) - (1-\dot{\tau})e_m^T(t-\tau)Re_m(t-\tau) + e_m^T(t)R_1e_m(t) \\
& - e_m^T(t-\tau_1)R_1e_m(t-\tau_1) + e_m^T(t)R_2e_m(t) - e_m^T(t-\tau_2)R_2e_m(t-\tau_2) \\
& + [e_m(t-\tau_1) - e_m(t-\tau_2)]^T W\left[\int_{t-\tau_2}^{t-\tau_1} e_m(\sigma)d\sigma\right] + \left[\int_{t-\tau_2}^{t-\tau_1} e_m(\sigma)d\sigma\right]^T \\
& \times W[e_m(t-\tau_1) - e_m(t-\tau_2)] \\
& \dot{e}_s^T(t)P_s e(t) + e_s^T(t)P_s\dot{e}_s(t) + (\tau_2-\tau_1)e_s^T(t)Qe_s(t) - \int_{t-\tau_2}^{t-\tau_1} e_s^T(\sigma) \\
& \times Qe_s(\sigma)d\sigma + e_s^T(t)Re_s(t) - (1-\dot{\tau})e_s^T(t-\tau)Re_s(t-\tau) + e_s^T(t)R_1e_s(t) \\
& - e_s^T(t-\tau_1)R_1e_s(t-\tau_1) + e_s^T(t)R_2e_s(t) - e_s^T(t-\tau_2)R_2e_s(t-\tau_2) \\
& + [e_s(t-\tau_1) - e_s(t-\tau_1)]^T W\left[\int_{t-\tau_2}^{t-\tau_1} e_s(\sigma)d\sigma\right] + \left[\int_{t-\tau_2}^{t-\tau_1} e_s(\sigma)d\sigma\right]^T \\
& \times W[e_s(t-\tau_1) - e_s(t-\tau_1)] \\
& \dot{e}_o^T(t)P_o e(t) + e_o^T(t)P_o\dot{e}_o(t) + (\tau_2-\tau_1)e_o^T(t)Qe_o(t) - \int_{t-\tau_2}^{t-\tau_1} e_o^T(\sigma) \\
& \times Qe_o(\sigma)d\sigma + e_o^T(t)Re_o(t) - (1-\dot{\tau})e_o^T(t-\tau)Re_o(t-\tau) + e_o^T(t)R_1e_o(t) \\
& - e_o^T(t-\tau_1)R_1e_o(t-\tau_1) + e_o^T(t)R_2e_o(t) - e_o^T(t-\tau_2)R_2e_o(t-\tau_2) \\
& + [e_o(t-\tau_1) - e_o(t-\tau_2)]^T W\left[\int_{t-\tau_2}^{t-\tau_1} e_o(\sigma)d\sigma\right] + \left[\int_{t-\tau_2}^{t-\tau_1} e_o(\sigma)d\sigma\right]^T \\
& \times W[e_o(t-\tau_1) - e_o(t-\tau_2)] \\
& + 2\tilde{\theta}_m^T(t)\Theta_m^{-1}\dot{\tilde{\theta}}_m(t) + 2\tilde{\theta}_s^T(t)\Theta_s^{-1}\dot{\tilde{\theta}}_s(t) \\
& + 2\tilde{\theta}_{m,d}^T(t-\tau)\Theta_{m,d}^{-1}\dot{\tilde{\theta}}_{m,d}(t-\tau) + 2\tilde{\theta}_{s,d}^T(t-\tau)\Theta_{s,d}^{-1}\dot{\tilde{\theta}}_{s,d}(t-\tau).
\end{aligned} \tag{21}$$

Assume $d_m = d_s = 0$.

From equation (21), clearly, $\dot{V}(t) < 0$ is guaranteed if $1 < 0$ is fulfilled. Thus, the em(t), es(t), and eo(t) error signals are asymptotically steady. Accordingly, the (M)-(S) systems in equations (1) and (2) are synchronized, which concludes the proof. □

Theorem 1. *It gives the result of the synchronization problem for the (M)-(S) nonlinear systems with the requirement that F is the controller gain matrix and Lm and Ls are the observer gain matrices. To remove this restriction, we have suggested a solution for the approximation values of Lm, Ls, and F, using a convex routine solution. Now, we set out*

a methodology for solving the inequality matrix with the help of the two-step LMI-based approach:

$$\Phi_{11}=\begin{bmatrix}
\zeta_{11,m} & A_dP_m & 0 & 0 & 0 & 0 & 0 & 0 & 0\\
A_d^TP_m & -(1-\tau)R & 0 & 0 & 0 & 0 & 0 & 0 & 0\\
* & * & -R_{1m} & 0 & W_m & 0 & 0 & 0 & 0\\
* & * & * & -R_{2m} & -W_m & 0 & 0 & 0 & 0\\
* & * & W_m & -W_m & -\dfrac{1}{\tau_2-\tau_1}Q_m & 0 & 0 & 0 & 0\\
* & * & * & * & * & \zeta_{11,s} & A_dP_s & 0 & 0\\
* & * & * & * & * & A_d^TP_s & -(1-\tau)R & 0 & 0\\
* & * & * & * & * & * & * & -R_{1s} & 0\\
* & * & * & * & * & * & * & * & -R_{2s}
\end{bmatrix},$$

$$\Phi_{22}=\begin{bmatrix}
-\dfrac{1}{\tau_2-\tau_1}Q_s & 0 & 0 & 0 & 0 & 0 & 0 & 0 & 0\\
* & \zeta_{11,o} & A_dP_o & 0 & 0 & 0 & 0 & 0 & 0\\
* & A_d^TP_o & -(1-\tau)R & 0 & 0 & 0 & 0 & 0 & 0\\
* & * & * & -R_{1o} & 0 & W_o & 0 & 0 & 0\\
* & * & * & * & -R_{2o} & -W_o & 0 & 0 & 0\\
* & * & * & W_o & -W_o & -\dfrac{1}{\tau_2-\tau_1}Q_0 & 0 & 0 & 0\\
* & * & * & * & * & * & -\alpha_1I_n & 0 & 0\\
* & * & * & * & * & * & * & -\alpha_2I_n & 0\\
* & * & * & * & * & * & * & * & -\beta_1I_n
\end{bmatrix},$$

$$\Phi_{33}=\begin{bmatrix}
-\beta_2I_n & 0 & 0 & 0 & 0 & 0 & 0\\
* & -\alpha_3I_n & 0 & 0 & 0 & 0 & 0\\
* & * & -\alpha_4I_n & 0 & 0 & 0 & 0\\
* & * & * & -\beta_3I_n & 0 & 0 & 0\\
* & * & * & * & -\beta_4I_n & 0 & 0\\
* & * & * & * & * & -\alpha_5I_n & 0\\
* & * & * & * & * & * & -\alpha_6I_n
\end{bmatrix},$$

$$\Phi_{12}=\begin{bmatrix} 0 & 0.5P_mBF+L_m^TC^TP_o & 0\ 0\ 0\ 0 & P_m & P_m & P_m \\ 0 & 0 & 0\ 0\ 0\ 0 & 0 & 0 & 0 \\ 0 & 0 & 0\ 0\ 0\ 0 & 0 & 0 & 0 \\ 0 & 0 & 0\ 0\ 0\ 0 & 0 & 0 & 0 \\ 0 & 0 & 0\ 0\ 0\ 0 & 0 & 0 & 0 \\ 0 & 0.5P_sBF-L_s^TC^TP_o & 0\ 0\ 0\ 0 & 0 & 0 & 0 \\ 0 & 0 & 0\ 0\ 0\ 0 & 0 & 0 & 0 \\ W_s & 0 & 0\ 0\ 0\ 0 & 0 & 0 & 0 \\ -W_s & 0 & 0\ 0\ 0\ 0 & 0 & 0 & 0 \end{bmatrix},$$

$$\Phi_{13}=\begin{bmatrix} P_m & 0 & 0 & 0 & 0 & 0 & 0 \\ 0 & 0 & 0 & 0 & 0 & 0 & 0 \\ 0 & 0 & 0 & 0 & 0 & 0 & 0 \\ 0 & 0 & 0 & 0 & 0 & 0 & 0 \\ 0 & 0 & 0 & 0 & 0 & 0 & 0 \\ 0 & P_s & P_s & P_s & P_s & 0 & 0 \\ 0 & 0 & 0 & 0 & 0 & 0 & 0 \\ 0 & 0 & 0 & 0 & 0 & 0 & 0 \\ 0 & 0 & 0 & 0 & 0 & 0 & 0 \end{bmatrix},$$

$$\Phi_{21}=\begin{bmatrix} * & * & * & * & * & * & W_s & -W_s \\ 0.5P_mB^TF^T+L_mCP_o & * & * & * & * & 0.5P_mB^TF^T+L_sCP_o & * & * & * \\ * & * & * & * & * & * & * & * \\ * & * & * & * & * & * & * & * \\ * & * & * & * & * & * & * & * \\ * & * & * & * & * & * & * & * \\ P_m & * & * & * & * & * & * & * \\ P_m & * & * & * & * & * & * & * \\ P_m & * & * & * & * & * & * & * \end{bmatrix},$$

(22)

$$\Phi_{23} = \begin{bmatrix} 0 & 0 & 0 & 0 & 0 & 0 & 0 \\ 0 & 0 & 0 & 0 & 0 & P_o & P_o \\ 0 & 0 & 0 & 0 & 0 & 0 & 0 \\ 0 & 0 & 0 & 0 & 0 & 0 & 0 \\ 0 & 0 & 0 & 0 & 0 & 0 & 0 \\ 0 & 0 & 0 & 0 & 0 & 0 & 0 \\ 0 & 0 & 0 & 0 & 0 & 0 & 0 \\ 0 & 0 & 0 & 0 & 0 & 0 & 0 \\ 0 & 0 & 0 & 0 & 0 & 0 & 0 \end{bmatrix},$$

$$\Phi_{31} = \begin{bmatrix} P_m & * & * & * & * & * & * & * & * \\ * & * & * & * & * & P_s & * & * & * \\ * & * & * & * & * & P_s & * & * & * \\ * & * & * & * & * & P_s & * & * & * \\ * & * & * & * & * & P_s & * & * & * \\ * & * & * & * & * & * & * & * & * \\ * & * & * & * & * & * & * & * & * \end{bmatrix} \quad (23)$$

$$\Phi_{32} = \begin{bmatrix} * & * & * & * & * & * & * & * & * \\ * & * & * & * & * & * & * & * & * \\ * & * & * & * & * & * & * & * & * \\ * & * & * & * & * & * & * & * & * \\ * & * & * & * & * & * & * & * & * \\ * & * & * & * & * & * & * & * & * \\ * & P_o & * & * & * & * & * & * & * \\ * & P_o & * & * & * & * & * & * & * \end{bmatrix}.$$

6. Simulation and Results

Simulation of the suggested methods for the synchronization of the (M) and (S) systems with undefined parameters, as planned in Theorem 1, is shown in the accompanying simulation outcomes for FHN (Fitz-Hugh–Nagumo) (M)-(S) designs. The suggested methodology was completed with the help of simulation work using MATLAB software and FHN numerical models. FHN is generally utilized in genetic systems, such as brain stimulation therapy, considering the performance of neurons in electricity. It helps in investigating symptoms and diseases of the brain, including tremors resulting from disorders of the brain's neurons. This kind of infection occurs in various parts of the brain. The FHN system is defined below:

$$\begin{aligned} \dot{X}_{m1} &= \left(X_{m1}^2 - X_{m1}\right)\left(1 - R_1 X_{m1}\right) - X_{m2} + I_o \dot{X}_{m2} = BX_{m2}, \\ \dot{X}_{si} &= \left(X_{si}^2 - X_{si}\right)\left(1 - R_i X_{si}\right) - X_{si} + I_o \dot{X}_{si+1} = BX_{si+1}, \\ I_o &= \left(\frac{m}{\omega}\right) Cos(\omega t), \end{aligned} \quad (24)$$

where I_o is the current in the above equation, $m = 0.099$, $\omega = 2\pi f$, and $f = 0.128$. Chaotic systems are sensitive to initial conditions. By changing the value of initial conditions, the phase portrait, i.e., behaviour of nonlinear chaotic systems, changes. The initial conditions for the (M) and (S) systems are $X_{s1(0)} = 0.399$ and $X_{si+1(0)} = 0.099$. The other parameters are $B = 1.01$, $R_1 = 10.09$, and $R_2 = 9.89$.

The phasor picture and individual reactions to the nonlinear chaotic performance of the (M)-(S) FHN system are exposed in Figure 1. For the (M)-(S) systems, various initial conditions are used. Different error signals are designed between the master system with its observer and the slave system with its observer and introduced in Figures 2(a) and 2(b), for Theorem 1, respectively. Figure 3 describes the error signal between the (M) observer state and the (S) observer state. The simulation results are given for a nonadaptive control strategy under three different conditions. First, neuron behaviour with the help of the FHN system is generalized. In neurons, membrane potential is not the same in all living beings. It can be standardized using methods for an alternative scaling factor, so this is pertinent for all types of neurons. Second, the numerical articulations of the FHN system are, for the most part, dependent on the ordinary membrane potential. Third, standardized potential usage gain matrices must be controlled to finally synchronize (M)-(S) systems.

The FHN model is related to the matrices, as indicated by the nonlinear chaotic master and slave systems:

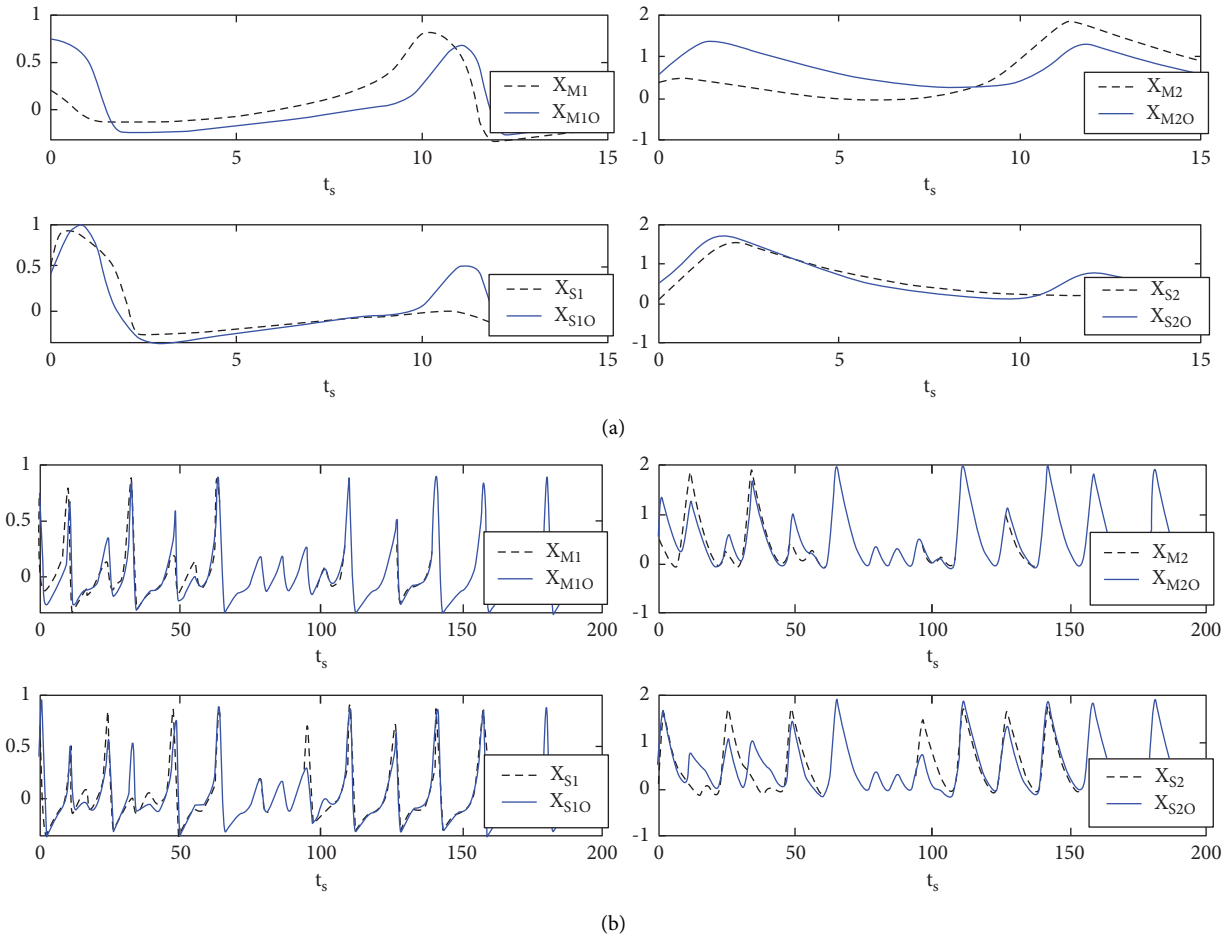

Figure 1: (a) Standardized potential of the master and (b) four slave systems and their respective observers of Theorem 1.

$$S_i = \begin{bmatrix} -1.00 & -1.00 \\ 1.00 & 0.00 \end{bmatrix},$$

$$X = \begin{bmatrix} 1.00 \\ 0.00 \end{bmatrix},$$

$$Y = \begin{bmatrix} 1.00 \\ 0.00 \end{bmatrix}, \tag{25}$$

$$F(x(t)) = \begin{bmatrix} 11.00x_1^{\,2} + 10.00x_1^{\,3} + \left(\frac{m}{\omega}\right)Cos(\omega t) \\ 0.00 \end{bmatrix}.$$

By using the adaptive scheme, synchronizing the (M)-(S) systems according to Theorem 1, Lm and Ls are the gain matrices for the observer's master and slave systems, respectively. By varying the values of these observers gain matrices Lm and Ls and control gain matrix F, the effectiveness and efficiency of proposed control methodology may vary. After some empirical analysis, the values of the observer gain matrices and controller gain matrix are chosen. These Lm, Ls, and F values are chosen as follows:

$$L_m = \begin{bmatrix} 1.32 \\ 0.00 \end{bmatrix},$$

$$L_{si} = \begin{bmatrix} 1.32 \\ 0.00 \end{bmatrix}, \tag{26}$$

$$F = [1.000.00],$$

$$\xi = F\left(\hat{x}_m(t) - \hat{x}_{si}(t)\right).$$

Figure 4 represents the result of the controller. In equation (26), ξ is the controlling function, which controls the behaviour of the (M)-(S) system. Theorem 1 illustrates this in Figure 1, which shows the standardized potential of the (M)-(S) system with its observers. In Figure 5, Theorem 1 illustrates the observer recovery variables for the (M)-(S) systems. Figure 6 explains the error signals between the (M) system and its master observer and between the (S) system and its slave observer. Lm and Ls are the gain matrices for the observer's respective master and slave systems, potentially influencing the master error em(t) and slave error es(t). "F" can clearly affect eoi(t). In the unlikely event where we

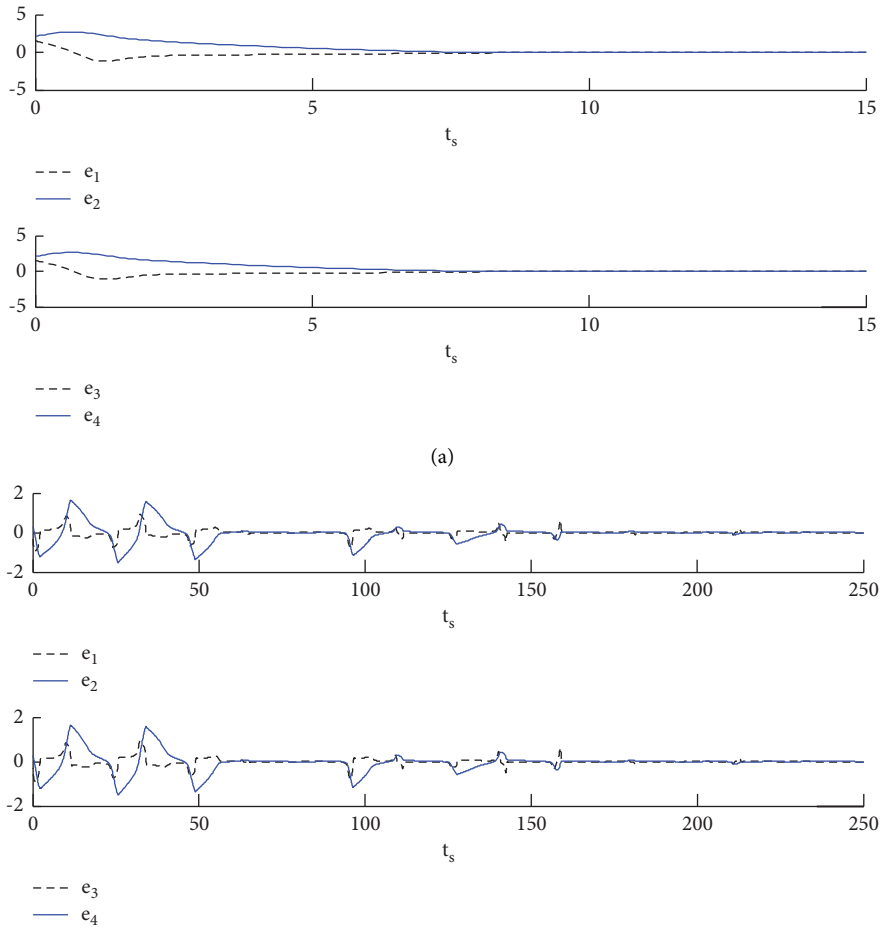

Figure 2: (a) Error between the states of the master and (b) the slave system for Theorem 1.

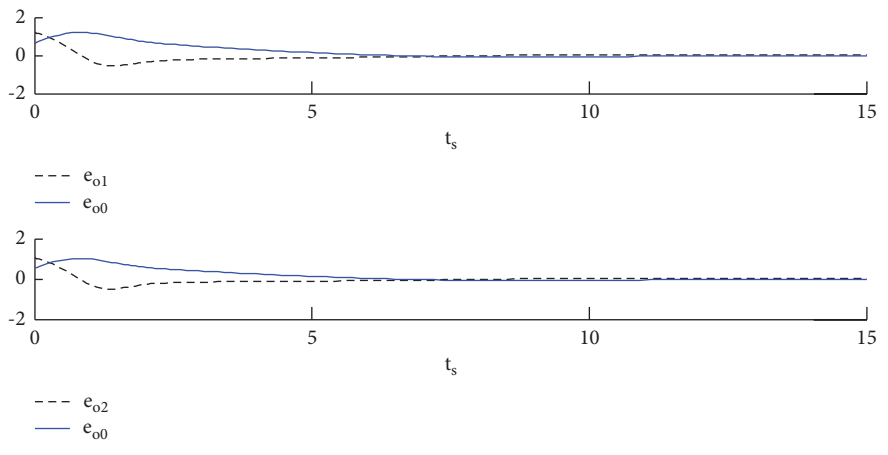

Figure 3: Continued.

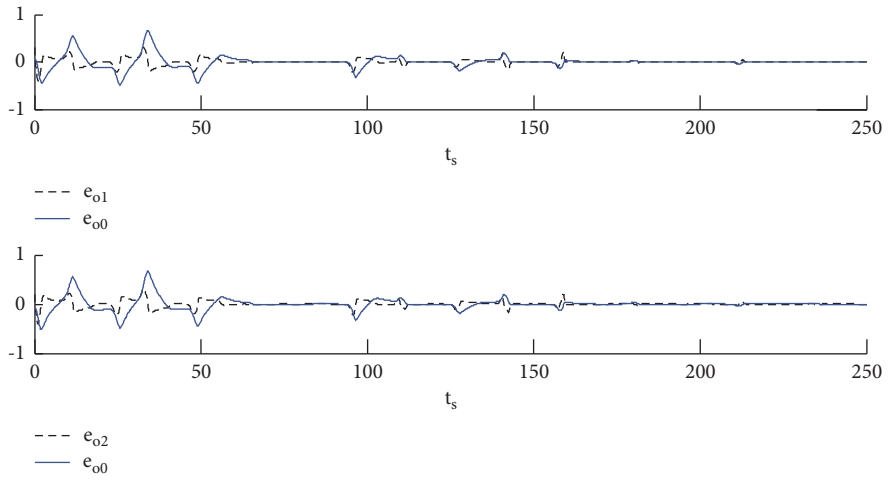

(b)

Figure 3: (a) Error between the master observer states and (b) that corresponding to the states of slave observers of Theorem 1.

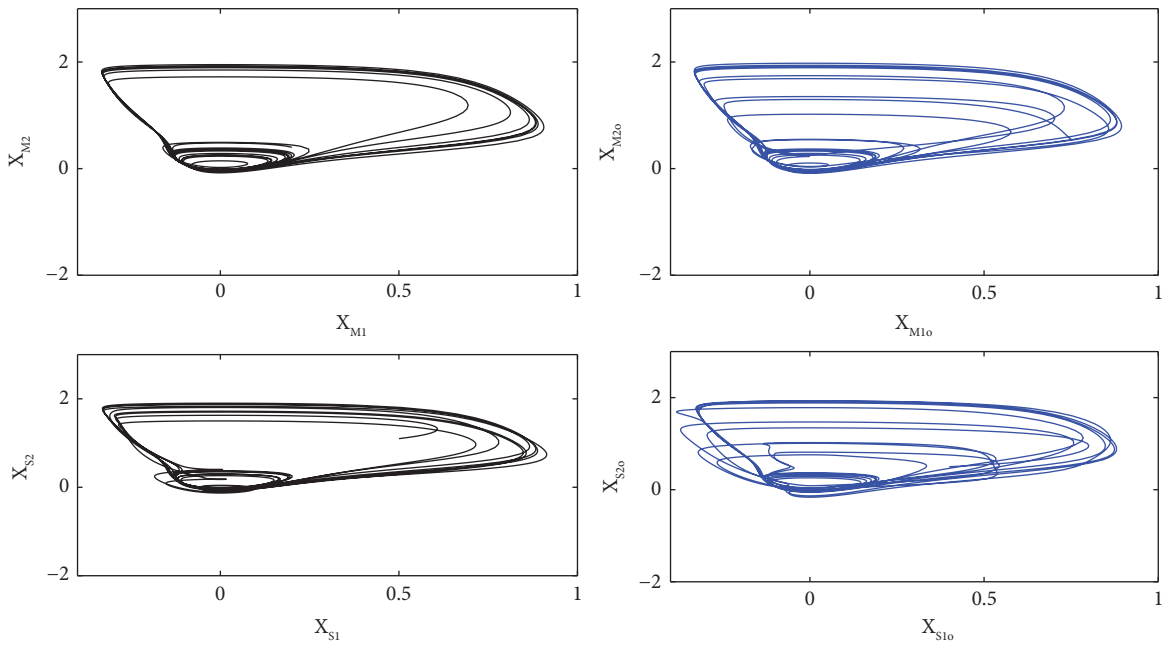

Figure 4: Phase portraits of master and slave systems of Theorem 1.

change the gain matrices' standards, these straightforwardly influence the synchronizing time. In Figure 2, Theorem 1 shows the error signals between master and slave states. Finally, Figure 3 describes the error signals between the (M) observer state and (S) observer states.

For the representation of the degree of synchronization statistically [31, 32], error-based DOS criteria are defined as follows:

$$DOS(\tilde{e}) = 1 - \frac{\tilde{e}_2}{\tilde{e}_{2,max}\left(\sqrt{\int_0^t \tilde{e}^2 dt} / \sqrt{\int_0^t \tilde{e}^2 dt}\,|_{max}\right)}, \quad (27)$$

where $\tilde{e}_2$ and $\tilde{e}_{2,\max}$ are the 2-norm of error $\tilde{e}$ and the maximum value of the norm, respectively. Note that the minimum and maximum values of degree of synchronization ($DOS(\tilde{e})$) are 0 and 1, respectively. The maxima occurs for the minimum synchronization error, that is, $\tilde{e}_2 = 0$. While the minima occurs for $\tilde{e}_2 = \tilde{e}_{2,\max}$, when synchronization error is maximum. It is worth mentioning that the maximum value $\tilde{e}_{2,max}$ can be achieved by selecting either $L_m = L_s = [\,0 \;\; 0\,]^T$ for any particular value of F or by utilitarian of $F = [\,0 \;\; 0\,]$ with some fixed values of L_m and L_s. Degree of synchronization is calculated for nonadaptive case to show the effect of variations in L_m, L_s, and F. Tables 1 and

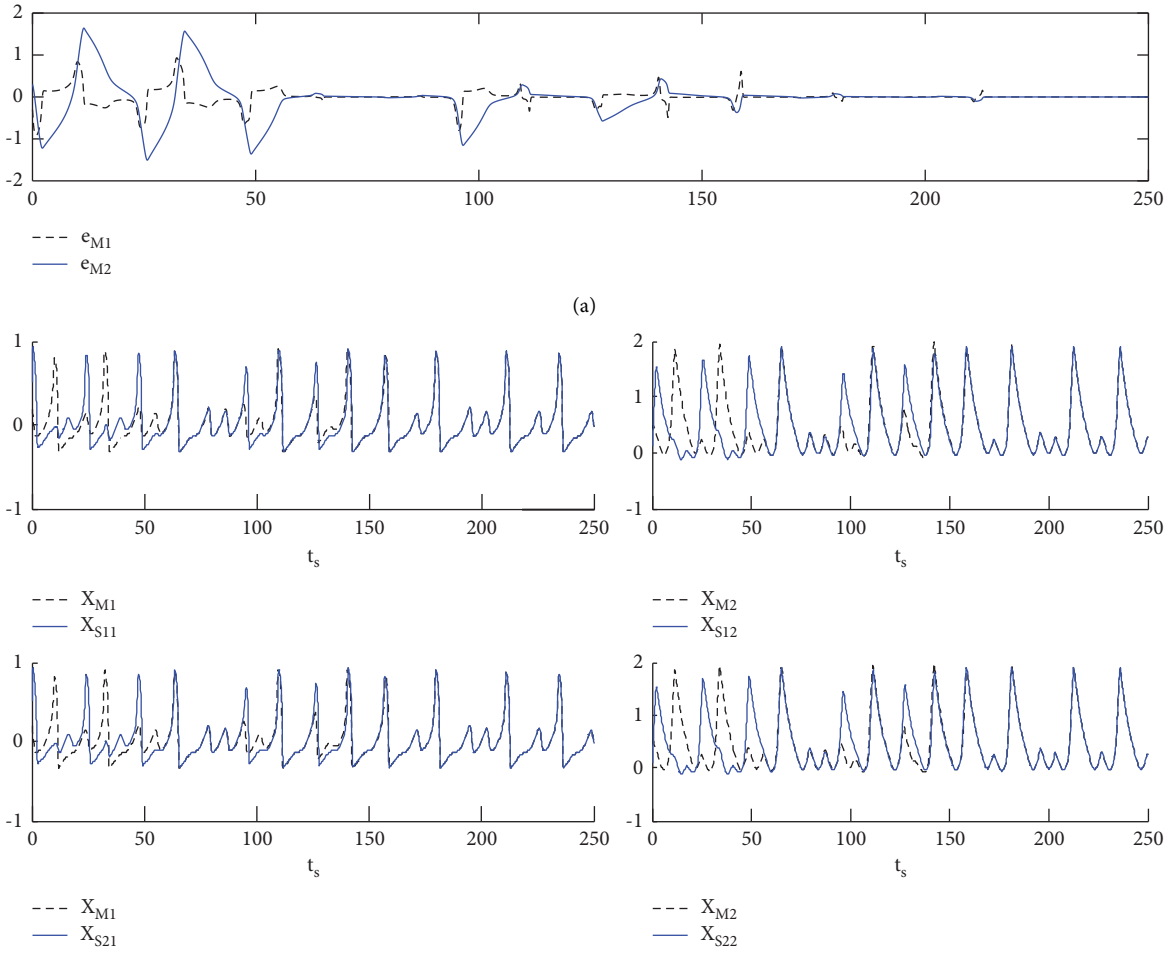

Figure 5: (a) Master and slave systems and (b) their respective observer recovery variables of Theorem 1.

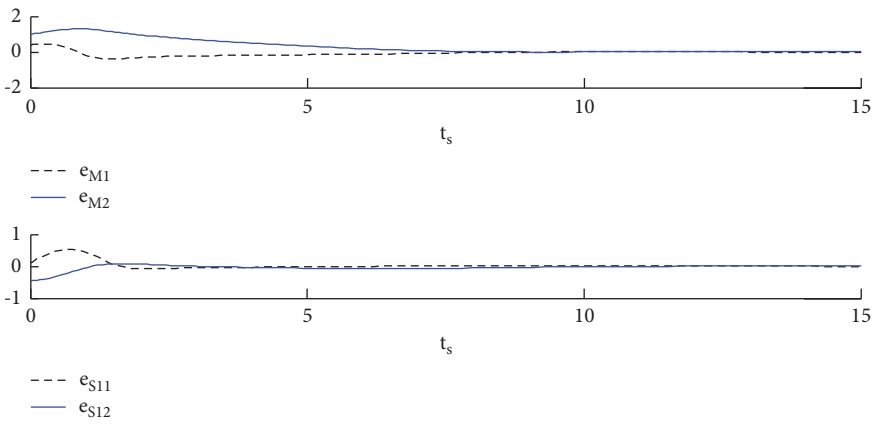

Figure 6: Continued.

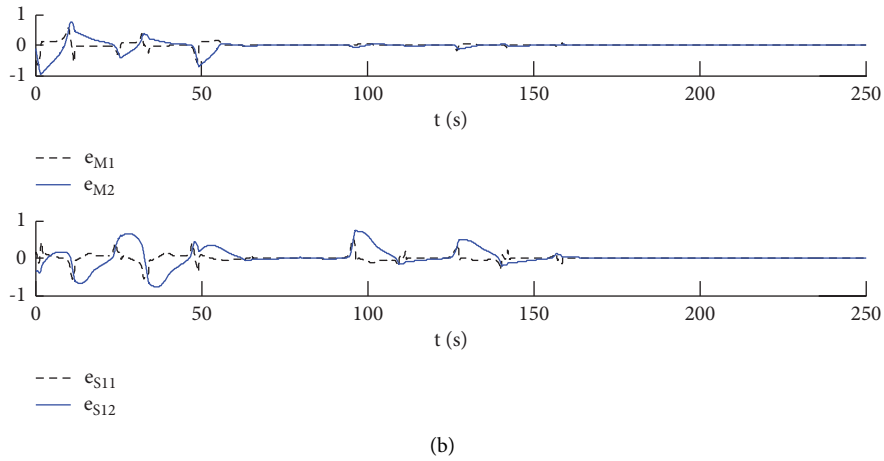

(b)

Figure 6: (a) Errors between the corresponding states of master and (b) master observer and slave observer for Theorem 1.

Table 1: DOS for different values of Lm = Ls and fixed $F = [1\ 0]$.

Serial no.	$L_m = L_s$	$\|\| e_{m1} \|\|$	DoS
1	$[0\ 0]^T$	31.5261	0
2	$[0.1\ 0]^T$	28.2900	0.102648
3	$[0.14\ 0]^T$	13.5245	0.5710063
4	$[0.15\ 0]^T$	8.4689	0.731369
5	$[5\ 0]^T$	0.0470	0.998509
6	$[20\ 0]^T$	0.0131	0.999584
7	$[100\ 0]^T$	0.0095	0.999699

Table 2: DOS for different values of $L_m = L_s$ and fixed $F = [1.3\ 0]^T$.

Serial no.	$L_m = L_s$	$\|\| e_{m1} \|\|$	DoS
1	$[0\ 0]^T$	3.0379	0
2	$[0.2\ 0]^T$	2.4210	0.203068
3	$[0.5\ 0]^T$	0.8489	0.391389
4	$[1\ 0]^T$	0.4706	0.84509
5	$[5\ 0]^T$	0.1324	0.956417
6	$[20\ 0]^T$	0.0165	0.994569
7	0.0052	0.0095	0.998288

2 demonstrate the effect of $L_m = L_s$ and Fon the DOS, respectively. It can be concluded that increase in the entries of L_m and F can increase the degree of synchronization errors $e_{m1}(t)$ and $e_{o1}(t)$, respectively.

7. Conclusion

Synchronization of the two nonlinear systems, as well as chaotic frameworks with time delay, uncertainties, and disturbance, are recognized in this research study. A controller is designed utilizing the robust adaptive input control hypothesis. Along with the laws of adaptation for the approximation of boundaries, the planned delay rate-dependent controller ensures the synchronization of chaos, bringing synchronization errors to zero. The simulations using MATLAB confirm the adequacy of the proposed strategy. This is despite the fact that the model considered is for complex nonlinear chaotic framework with time delays with undefined elements. The result is also significant for its moderately simple, nonlinear frameworks with defined elements and consistent delays. As far as the future work is concerned, the distributed systems' synchronization of nonlinear systems can be considered. New methodologies can be sought for the distributed nonlinear systems having network delays with varying parameters.

Data Availability

The data used to support the findings of this study are available within the article. The raw data used to support the findings of this study are available from the corresponding author upon request.

Conflicts of Interest

The authors declare no conflicts of interest.

Acknowledgments

The authors would like to thank the Deanship of Scientific Research, Qassim University, for funding the publication of this project.

References

[1] T. L. Carroll, L. M. Pecora, and F. J. Rachford, "Chaotic transients and multiple attractors in spin-wave experiments," *Physical Review Letters*, vol. 59, no. 25, pp. 2891–2894, 1987.

[2] L. M. Pecora, "Derivation and generalization of the suhl spin-wave instability relations," *Physical Review B*, vol. 37, no. 10, pp. 5473–5477, 1988.

[3] T. L. Carroll and L. M. Pecora, "Synchronizing chaotic circuits," *IEEE Transactions on Circuits and Systems*, vol. 38, no. 4, pp. 453–456, 1991.

[4] M. Chadli and I. Zelinka, "Chaos synchronization of unknown inputs Takagi-Sugeno fuzzy: application to secure communications," *Computers & Mathematics with Applications*, vol. 68, no. 12, pp. 2142–2147, 2014.

[5] J. M. G. Miranda, *Synchronization and Control of Chaos: An Introduction for Scientists and Engineers*, Imperial College Press, London, UK, 2004.

[6] S. Beyhan, "Runge-Kutta model-based nonlinear observer for synchronization and control of chaotic systems," *ISA Transactions*, vol. 52, no. 4, pp. 501–509, 2013.

[7] M. T. Yassen, "Controlling chaos and synchronization for new chaotic system using linear feedback control," *Chaos, Solitons & Fractals*, vol. 26, no. 3, pp. 913–920, 2005.

[8] M. Rehan and K. S. Hong, "Robust synchronization of delayed chaotic fitzhugh-nagumo neurons under external electrical stimulation," *Computational and Mathematical Methods in Medicine*, vol. 2021, Article ID 230980, 11 pages, 2012.

[9] M. H. Zaheer, M. Rehan, G. Mustafa, and M. Ashraf, "Delay-range-dependent chaos synchronization approach under varying time-lags and delayed nonlinear coupling," *ISA Transactions*, vol. 53, no. 6, pp. 1716–30, 2014.

[10] S. C. Jeong, D. H. Ji, J. H. Park, and S. C. Won, "Adaptive synchronization for uncertain chaotic neural networks with mixed time delays using fuzzy disturbance observer," *Applied Mathematics and Computation*, vol. 219, no. 11, pp. 5984–5995, 2013.

[11] C.-C. Yang, "Adaptive control and synchronization of identical new chaotic flows with unknown parameters via single input," *Applied Mathematics and Computation*, vol. 216, no. 4, pp. 1316–1324, 2010.

[12] C.-C. Yang, "Adaptive synchronization of Lü hyperchaotic system with uncertain parameters based on single-input controller," *Nonlinear Dynamics*, vol. 63, no. 3, pp. 447–454, 2011.

[13] A. Abdullah, "Synchronization and secure communication of uncertain chaotic systems based on full-order and reduced-order output-affine observers," *Applied Mathematics and Computation*, vol. 219, no. 19, pp. 10000–10011, 2013.

[14] J. Pena Ramirez, R. H. B. Fey, and H. Nijmeijer, "Synchronization of weakly nonlinear oscillators with Huygens' coupling," *Chaos: An Interdisciplinary Journal of Nonlinear Science*, vol. 23, no. 3, Article ID 033118, 2013.

[15] E. S. Kuetche Mbe, H. B. Fotsin, J. Kengne, and P. Woafo, "Parameters estimation based adaptive Generalized Projective Synchronization (GPS) of chaotic Chua's circuit with application to chaos communication by parametric modulation," *Chaos, Solitons & Fractals*, vol. 61, pp. 27–37, 2014.

[16] J. Yang and F. Zhu, "Synchronization for chaotic systems and chaos-based secure communications via both reduced-order and step-by-step sliding mode observers," *Communications in Nonlinear Science and Numerical Simulation*, vol. 18, no. 4, pp. 926–937, 2013.

[17] B. Liu, L. Wang, Y.-H. Jin, D.-X. Huang, and F. Tang, "Control and synchronization of chaotic systems by differential evolution algorithm," *Chaos, Solitons & Fractals*, vol. 34, no. 2, pp. 412–419, 2007.

[18] A. N. Njah, "Tracking control and synchronization of the new hyperchaotic liu system via backstepping techniques," *Nonlinear Dynamics*, vol. 61, no. 2, pp. 1–9, 2010.

[19] G. Hussain, M. Siddique, M. M. Hussain, M. T. Hassan, and N. Aslam, "Synchronization of n-non-linear slave systems with master system using non-adaptive and adaptive coupled observers," *Energies*, vol. 14, no. 11, p. 3190, 2021.

[20] P. N. Steinmetz, A. Roy, P. J. Fitzgerald, S. S. Hsiao, K. O. Johnson, and E. Niebur, "Attention modulates synchronized neuronal firing in primate somatosensory cortex," *Nature*, vol. 404, no. 6774, pp. 187–190, 2000.

[21] R. E. Mirollo and S. H. Strogatz, "Synchronization of pulse-coupled biological oscillators," *SIAM Journal on Applied Mathematics*, vol. 50, no. 6, pp. 1645–1662, 1990.

[22] R. L. Filali, M. Benrejeb, and P. Borne, "On observer-based secure communication design using discrete-time hyperchaotic systems," *Communications in Nonlinear Science and Numerical Simulation*, vol. 19, no. 5, pp. 1424–1432, 2014.

[23] M. Siddique, M. Hussain, M. Rehan, and M. M. Hussain, "Robust-adaptive synchronization of drive and response systems using coupled chaotic adaptive synchronous observers," *IEEE Conference on Systems, Process and Control (ICSPC)*, pp. 24–29, 2017.

[24] A. Rodriguez-Angeles and H. Nijmeijer, "Mutual synchronization of robots via estimated state feedback: a cooperative approach," *IEEE Transactions on Control Systems Technology*, vol. 12, no. 4, pp. 542–554, 2004.

[25] L. Poinkam Meffo, P. Woafo, and S. Domngang, "Cluster states in a ring of four coupled semiconductor lasers," *Communications in Nonlinear Science and Numerical Simulation*, vol. 12, no. 6, pp. 942–952, 2007.

[26] L. Kuhnert, K. I. Agladze, and V. I. Krinsky, "Image processing using light-sensitive chemical waves," *Nature*, vol. 337, no. 6204, pp. 244–247, 1989.

[27] Y.-N. Li, L. Chen, Z.-S. Cai, and X.-z. Zhao, "Experimental study of chaos synchronization in the Belousov-Zhabotinsky chemical system," *Chaos, Solitons & Fractals*, vol. 22, no. 4, pp. 767–771, 2004.

[28] Ö Morgül and E. Solak, "Observer based synchronization of chaotic systems," *Physical Review. E, Statistical Physics, Plasmas, Fluids, and Related Interdisciplinary Topics*, vol. 54, no. 5, pp. 4803–4811, 1996.

[29] J. F. Heagy, T. L. Carroll, and L. M. Pecora, "Synchronous chaos in coupled oscillator systems," *Physical Review E*, vol. 50, no. 3, pp. 1874–1885, 1994.

[30] S. Wen, Z. Zeng, and T. Huang, "Observer-based synchronization of memristive systems with multiple networked input and output delays," *Nonlinear Dynamics*, vol. 78, no. 1, pp. 541–554, 2014.

[31] M. Gerster, R. Berner, J. Sawicki et al., "FitzHugh-Nagumo oscillators on complex networks mimic epileptic-seizure-related synchronization phenomena," *Chaos: An Interdisciplinary Journal of Nonlinear Science*, vol. 30, no. 12, Article ID 123130, 2020.

[32] X. Sun, S. Wandelt, and A. Zhang, "On the degree of synchronization between air transport connectivity and COVID-19 cases at worldwide level," *Transport Policy*, vol. 105, pp. 115–123, 2021.